electronics

Energy Harvesting and Energy Storage Systems

Edited by

Shailendra Rajput, Moshe Averbukh and Noel Rodriguez
Printed Edition of the Special Issue Published in *Electronics*

MDPI

Energy Harvesting and Energy Storage Systems

Energy Harvesting and Energy Storage Systems

Editors

Shailendra Rajput
Moshe Averbukh
Noel Rodriguez

MDPI

Editors

Shailendra Rajput
Department of Electrical
Engineering and Electronics
Ariel University
Ariel
Israel

Moshe Averbukh
Department of Electrical
Engineering and Electronics
Ariel University
Ariel
Israel

Noel Rodriguez
Department of Electronics and
Computer Technology
University of Granada
Granada
Spain

For citation purposes, cite each article independently as indicated on the article page online and as indicated below:

LastName, A.A.; LastName, B.B.; LastName, C.C. Article Title. *Journal Name* **Year**, *Volume Number*, Page Range.

Contents

About the Editors

Shailendra Rajput

Dr. Shailendra Rajput is an Associate Professor at University Centre for Research & Development, Chandigarh University, Mohali, India. He is also affiliated with the Department of Electrical and Electronic Engineering, Ariel University, Israel as Research Fellow. He was a postdoctoral fellow at Ariel University, Israel (September 2017-April 2021) and Xi'an Jiaotong University, China (May 2015-July 2017). He achieved B.Sc. and M.Sc. degrees from the Dr. Hari Singh Gour University, Sagar, India, in 2006 and 2008, respectively. He achieved a Ph.D. degree from the Department of Physics, Birla Institute of Technology, Ranchi, India, in 2014. His main research work is associated with Energy harvesting, Solar energy, Energy storage, Ferroelectricity, Piezoelectricity, and biomedical application of electromagnetic waves.

Moshe Averbukh

Dr. Moshe Averbukh is Head of Laboratory Electrical Storage Systems at Ariel University. In 1972, he received B.Sc. and M.Sc. degrees (Summa Cum Laude) from the University of Mining (Moscow) and a Ph.D. degree in 1984 from the Institute of Mining Academy of Science USSR (Moscow). His primary research is focused on energy harvesting, solar energy, energy storage, electrochemical devices, and induction motors.

Noel Rodriguez

Prof. Noel Rodriguez received the Electronics Engineer degree (B.Sc.+M.Eng.) by the University of Granada in 2004 obtaining the first national award of university education. In 2008, he received a double Ph.D. by the University of Granada and the National Polytechnic Institute of Grenoble (France) with the extraordinary award. At the present time, he holds a Tenured Professor position at the University of Granada being also head of the Pervasive Electronics Advanced Research Laboratory (PEARL). His research lines cover the development of applications based on Laser-Induced Graphene; the development of new transduction platforms for sensors; the investigation of new elemental devices for its application in the neuromorphic field; the development of new memory cells; and the low-power energy conversion. He has participated in 25 research projects (including National and Internationals), co-authored 15 international patents.

Preface to "Energy Harvesting and Energy Storage Systems"

Energy harvesting or the process of acquiring energy from the surrounding environment has been a continuous human endeavor throughout history. The research and development on energy harvesting and energy storage methodology are growing very rapidly. Hence, it is necessary to summarize recent advances in energy harvesting and energy storage systems. This book covers various aspects of optimization algorithms, evaluations of wind energy turbines, electrostatic vibration energy transducers, battery management systems, thermoelectric generators, distribution networks, issues of renewable energy micro-grid interfacing, fuzzy-logic-controller-based direct power controls, parameter estimations of fuel cells, and ultra-low-power supercapacitors. This book is beneficial for young researchers (Bachelor, Masters, and Doctoral students), who are new to this area. We would like to take this opportunity to thank all of the authors for their excellent efforts, as well as the reviewers for their insightful remarks and suggestions.

Shailendra Rajput, Moshe Averbukh, and Noel Rodriguez
Editors

MDPI

Editorial

Energy Harvesting and Energy Storage Systems

Shailendra Rajput [1,2,*] **, Moshe Averbukh** [1] **and Noel Rodriguez** [3]

1   Department of Electrical Engineering and Electronics, Ariel University, Ariel 40700, Israel; mosheav@ariel.ac.il
2   Department of Physics, University Centre for Research & Development, Chandigarh University, Mohali 140431, India
3   Department of Electronics and Computer Technology, University of Granada, 18011 Granada, Spain; noel@ugr.es
*   Correspondence: shailendrara@ariel.ac.il

Sustainable development systems are based on three pillars: economic development, environmental stewardship, and social equity. One of the guiding principles for finding the balance between these pillars is to limit the use of non-renewable energy sources. A promising method to resolve this challenge is harvesting energy from the ambient environment and converting it into electrical power. The contemporary development of novel energy generation technologies, such as solar, wind, and thermal energy, is in high demand to facilitate the replacement of fossil fuel energy resources with cleaner renewable sources. Energy harvesting systems have emerged as a prominent research area, and have continued to develop at a rapid pace.

Modern technologies, including portable electronic devices, electrical transportation, communication systems, and smart medical equipment, need efficient energy storage systems. Electrical energy storage devices are also used for smart grid control, grid stability, and peak-power saving, as well as for frequency and voltage regulation. Electricity generated from renewable sources (e.g., solar power and wind energy) cannot always deliver an immediate response to demand because of fluctuating power supplies. Hence, preserving the harvested electrical energy for future requirements has been suggested. The present status of electrical energy storage technologies is far from the necessary demands.

In this Special Issue, thirteen papers are published, covering various aspects of optimization algorithms, evaluations of wind energy turbines, electrostatic vibration energy transducers, battery management systems, thermoelectric generators, distribution networks, issues of renewable energy micro-grid interfacing, fuzzy-logic-controller-based direct power controls, parameter estimations of fuel cells, and ultra-low-power supercapacitors.

Sharma et al. [1] proposed a hybrid version of the whale optimization algorithm (WOA) and particle swarm optimization (PSO) algorithm (WOAPSO) for the parameter optimization of PV cells. The exploitation ability of PSO with adaptive weight function was exploited in the pipeline mode with a WOA to enhance the ability and convergence speed of the basic PSO. The performance of the proposed hybrid algorithm was compared with six different optimization algorithms in terms of the root mean square error and rate of convergence. The simulation result showed that the proposed hybrid algorithm not only produced optimized parameters at different irradiation levels, but also estimated the minimum root mean square error, even at a low level of irradiation.

The tunicate swarm algorithm (TSA) was employed to estimate the Photowatt-PWP201 PV panel module parameters under standard temperature conditions [2]. It was concluded that the TSA is an effective and robust technique to estimate the unknown optimized parameters of the solar PV module model under standard operating conditions. The simulation results were compared with four different pre-existing optimization algorithms: the gravitational search algorithm (GSA); a hybrid of the particle swarm optimization and gravitational search algorithm (PSOGSA); the sine cosine algorithm (SCA); and the whale

optimization algorithm (WOA). The comparison of results broadly demonstrated that the TSA outperforms the existing optimization algorithms in terms of the root mean square error (RMSE) and convergence rate.

Greenberg et al. [3] evaluated wind energy turbines using the volatility of wind and price. In their study, the real options analysis approach for the valuation of wind energy turbines was applied. It was hypothesized that the real options analysis (ROA) method is better than the alternative due to the nature of wind energy production uncertainties.

Ishida and Tanzawa proposed an integrated AC–DC converter in 1 V CMOS for electrostatic vibration energy transducer with an open circuit voltage of 10 V [4]. The proposed AC–DC converter did not require external components for rectification and power conversion. It can be integrated in the same IoT chip with a small overhead area of 0.1 mm^2. This converter can provide a better option for electrostatic energy harvesting where the cost is the highest priority.

Koketsu and Tanzawa designed a charge pump circuit and system with input impedance modulation for a flexible-type thermoelectric generator with high-output impedance [5]. The circuit system was also measured with a flexible-type TEG and a thermal source. The system converted thermal energy into power to 30 μW at 2.5 V. By adding a full-bridge rectifier between the energy transducer and the proposed converter, the control circuit could work even with other energy transducers such as piezoelectric or electrostatic vibration energy transducers with an AC equivalent voltage source and high-output impedance.

Lee et al. [6] proposed a battery efficiency calculation formula to manage battery states. The proposed battery efficiency calculation formula used the charging time, charging current, and battery capacity. An algorithm that can accurately determine the battery state was proposed by applying the proposed state of charge (SoC) and state of health (SoH) calculations. To reduce the initial error of the Coulomb counting method (CCM), the SoC could be calculated accurately by applying the battery efficiency to the open circuit voltage (OCV). During the charging and discharging process, the internal resistance of a battery increases and the constant current (CC) charging time decreases. The SoH can be predicted from the CC charging time of the battery and the battery efficiency, as proposed in this paper. Furthermore, a safe system was implemented during charging and discharging by applying a fault diagnosis algorithm to reduce the efficiency of the battery. The validity of the proposed BMS algorithm was demonstrated by applying it in a 3 kW ESS.

An ultra-low-power CMOS supercapacitor storage unit for energy harvesting applications was presented by Gogolou et al. [7]. The ultra-low current consumption of only 432 nA at 2.3 V proves that the proposed storage unit is ideal for energy harvesting systems, even for cases with a small input power range. Furthermore, extra modes can be added to the topology with the usage of external controls, expanding the operational capabilities of the proposed unit. For instance, the control of an additional charging unit for the backup battery is a highly beneficial mode that will be added in future studies.

Satish et al. [8] proposed a novel three-phase harmonic power flow algorithm for unbalanced radial distribution networks in the presence of D-STATCOM devices. This method used the basic concepts of circuit theory, which can easily be understood. In this study, the linear loads were modeled as a series combination of resistance and reactance, and non-linear loads were modeled as constant current sources, with the magnitude and angle obtained from the current spectra. The harmonic current injections from the D-STATCOM were assumed to be zero. The proposed FPFA and HPFA were tested on the IEEE-13 bus URDN, and the results were found to be in accordance with the literature. Test studies were carried on the IEEE−13 bus and IEEE−34 bus URDN, and the results of the case studies showed that there was an improvement in the fundamental voltage profile, a reduction in the fundamental and harmonic power loss, and a reduction in THD% with the integration of D-STATCOM devices.

Sharma et al. [9] introduced a novel opposition-based arithmetic optimization algorithm (OBAOA) for identifying the unspecified parameters of PEM fuel cells. The proposed algorithm was tested using ten benchmark test functions (seven unimodal and three mul-

timodal). Furthermore, the convergence graph, as well as the I-V and P-V characteristic curves, supported the precision of the anticipated algorithm. The proposed OBAOA technique was easy to implement, with low computational complexity. The performance of the proposed algorithm was verified using the Friedman ranking test. The proposed formulation will pique the attention of both researchers and practitioners in the fuel cell community, due to its capacity to solve problems effectively.

Ahmad et al. [10] proposed a fuzzy logic controller (FLC)-based direct power control (DPC) method for photovoltaic (PV) cells, which was modelled by modulating microgrids' point of common coupling (PCC) voltage. They also introduced a modified grid synchronization method through the direct power calculation of PCC voltage and current, instead of using a conventional phase-locked loop (PLL) system.

Singh et al. [11] employed the sooty tern optimization (STO) algorithm for the parameter extraction of solar modules. They implemented the STO algorithm with a single-diode model on an R.T.C France solar panel and an SS2018 polycrystalline PV module. It was concluded that the STO is an efficient and reliable technique for estimating the unknown optimum parameters of a solar PV module model under typical operating conditions.

El-Ela et al. [12] discussed the economic and environmental issues of renewable energy micro-grid interfacing. The stochastic behavior of renewable resources increases the need to determine the optimum operation of microgrids. The optimal operation of a typical microgrid aims to simultaneously minimize the operational costs and the accompanying emission pollutants over a daily scheduling horizon.

Ammar et al. [13] reviewed energy-harvesting-driven edge devices using task-offloading approaches. This paper includes a literature review of state-of-the-art joint energy-harvesting and task-offloading approaches in fog edge computing systems, research efforts on task offloading in fog edge computing, and the design of patient-centered care systems. The authors investigated energy-harvesting technologies and energy-storage strategies for IoMT devices.

We would like to take this opportunity to appreciate and thank all authors for their outstanding contributions, and the reviewers for their fruitful comments and feedback. We are thankful to the Editorial Board of the *Electronics* journal for the opportunity to edit this Special Issue. Special appreciation should also be given to the Editorial Office staff for their hard and precise work in maintaining a rigorous peer-review schedule and ensuring the timely publication of this Special Issue.

Conflicts of Interest: The authors declare no conflict of interest.

References

1. Sharma, A.; Sharma, A.; Averbukh, M.; Jately, V.; Azzopardi, B. An Effective Method for Parameter Estimation of a Solar Cell. *Electronics* **2021**, *10*, 312. [CrossRef]
2. Sharma, A.; Dasgotra, A.; Tiwari, S.K.; Sharma, A.; Jately, V.; Azzopardi, B. Parameter Extraction of Photovoltaic Module Using Tunicate Swarm Algorithm. *Electronics* **2021**, *10*, 878. [CrossRef]
3. Greenberg, D.; Byalsky, M.; Yahalom, A. Valuation of Wind Energy Turbines Using Volatility of Wind and Price. *Electronics* **2021**, *10*, 1098. [CrossRef]
4. Ishida, Y.; Tanzawa, T. A Fully Integrated AC-DC Converter in 1 V CMOS for Electrostatic Vibration Energy Transducer with an Open Circuit Voltage of 10 V. *Electronics* **2021**, *10*, 1185. [CrossRef]
5. Koketsu, K.; Tanzawa, T. Design of a Charge Pump Circuit and System with Input Impedance Modulation for a Flexible-Type Thermoelectric Generator with High-Output Impedance. *Electronics* **2021**, *10*, 1212. [CrossRef]
6. Lee, J.; Kim, J.-M.; Yi, J.; Won, C.-Y. Battery Management System Algorithm for Energy Storage Systems Considering Battery Efficiency. *Electronics* **2021**, *10*, 1859. [CrossRef]
7. Gogolou, V.; Kozalakis, K.; Koutroulis, E.; Doumenis, G.; Siskos, S. An Ultra-Low-Power CMOS Supercapacitor Storage Unit for Energy Harvesting Applications. *Electronics* **2021**, *10*, 2097. [CrossRef]
8. Satish, R.; Vaisakh, K.; Abdelaziz, A.Y.; El-Shahat, A. A Novel Three-Phase Harmonic Power Flow Algorithm for Unbalanced Radial Distribution Networks with the Presence of D-STATCOM Devices. *Electronics* **2021**, *10*, 2663. [CrossRef]
9. Sharma, A.; Khan, R.A.; Sharma, A.; Kashyap, D.; Rajput, S. A Novel Opposition-Based Arithmetic Optimization Algorithm for Parameter Extraction of PEM Fuel Cell. *Electronics* **2021**, *10*, 2834. [CrossRef]

10. Ahmad, S.; Mekhilef, S.; Mokhlis, H.; Karimi, M.; Pourdaryaei, A.; Ahmed, T.; Jhuma, U.K.; Afzal, S. Fuzzy Logic-Based Direct Power Control Method for PV Inverter of Grid-Tied AC Microgrid without Phase-Locked Loop. *Electronics* **2021**, *10*, 3095. [CrossRef]

11. Singh, A.; Sharma, A.; Rajput, S.; Mondal, A.K.; Bose, A.; Ram, M. Parameter Extraction of Solar Module Using the Sooty Tern Optimization Algorithm. *Electronics* **2022**, *11*, 564. [CrossRef]

12. Abou El-Ela, A.A.; El-Sehiemy, R.A.; Allam, S.M.; Shaheen, A.M.; Nagem, N.A.; Sharaf, A.M. Renewable Energy Micro-Grid Interfacing: Economic and Environmental Issues. *Electronics* **2022**, *11*, 815. [CrossRef]

13. Ben Ammar, M.; Ben Dhaou, I.; El Houssaini, D.; Sahnoun, S.; Fakhfakh, A.; Kanoun, O. Requirements for Energy-Harvesting-Driven Edge Devices Using Task-Offloading Approaches. *Electronics* **2022**, *11*, 383. [CrossRef]

Article

Valuation of Wind Energy Turbines Using Volatility of Wind and Price

Doron Greenberg [1], Michael Byalsky [2] and Asher Yahalom [3,4,*]

1   Department of Economics & Business Administration, Ariel University, Ariel 40700, Israel;
    dorongre@ariel.ac.il
2   Department of Economics, The Hebrew University of Jerusalem, Jerusalem 91905, Israel;
    michael.byalsky@mail.huji.ac.il
3   Department of Electrical & Electronics Engineering, Ariel University, Ariel 40700, Israel
4   Princeton Plasma Physics Laboratory, Princeton University, Princeton, NJ 08543, USA
*   Correspondence: asya@ariel.ac.il

Abstract: The limitedness of the nonrenewable local energy resources in Israel, even in the background of the later gas fields' findings, continues to force the state to devote various efforts towards 'green' energy development. These efforts include installations, both for the solar and for wind energy, thus improving the diversity of energy sources. While the standard discounted cash flow (DCF) method using the net present value (NPV) criterion is extensively adopted to evaluate investments, the standard DCF method is inappropriate for the rapidly changing investment climate and for the managerial flexibility in investment decisions. In recent years, the real options analysis (ROA) technique has been widely applied in many studies for the valuation of renewable energy investment projects. Taking into account the above background, we apply, in this study, the real options analysis approach for the valuation of wind energy turbines and apply it to the analysis of wind energy economic potential in Israel, which is the context of our work. We hypothesize that due to nature of wind energy production uncertainties, the ROA method is better than the alternative. The novelty of this paper includes the following: real world wind statistics of the Merom Golan site in Israel (velocity 3.73 m/s, with a standard deviation of 2.03 m/s), a realistic power generation estimation (power generation of 1205.84 kW with a standard deviation of about 0.5% in annual value which is worth about 1.3 M$ per annum), and an economic model to evaluate the profitability of such a project. We thus discuss the existing challenges of diversifying renewable energy sources in Israel by adding wind installations. Our motivation is to introduce a method which will allow investors and officials to take into account uncertainties when deciding in investing in such wind installations. The outcomes of the paper, which are obtained using the method of Weibull statistics and the Black–Scholes ROA technique, include the result that market price volatility adds to the uncertainties much more than any wind fluctuations, provided that the analysis is integrated over a long enough time.

Keywords: wind energy; renewable resources; Black–Scholes model

1. Introduction

Even during prolonged global economic crisis, the worldwide wind power ascent continues. The world's wind power capacity, according to the Global Wind Energy Council (GWEC) report, added 39.1 GW in 2010, growing by 24% during the year, 40.6 GW in 2011, growing by 20.5% per year, and 44.8 GW in 2012 (18.8% growth during the year: 78% growth in the last three years). Thus, the total installations at the end of 2012 provide up to 282.6 GW. A huge part of this power was produced in China—first place globally, with 75.3 GW, or 26.7% of the world product (about 30% of the world year's additions), the and USA—60.0 GW, or 21.2% of the world product, while Germany, Spain, and India (3rd–5th places) produced 25.7% together [1].

Wind energy is now a significant participant in the world's energy market. The 2012 global wind power market grew by more than 10% compared to 2011, representing investments of about 56 billion €. The main markets of wind energy are situated in Asia, North America, and Europe, each of which installs 13–15 GW of new capacity each year. About half a million people are now employed, corresponding to the European Wind Energy Association (EWEA) publication, by the wind industry around the world [2].

Considering the growing Israeli energy market, even nowadays, when plentiful sources of traditional nonrenewable energy such as the vast gas fields that were found in the Mediterranean Sea off the coast of Israel, Tamar (Tamar gas field [3]), and Leviathan (Leviathan gas field [4]), with the estimated quantity of 356 and 450 billion cubic meters, respectively, the possibility of their exhaustion still forces the state, as other numerous political entities, to devote significant efforts towards 'green' energy research and development. This is also important from the point of view of reducing carbon emission and global warming. These efforts are undertaken primarily for developing solar energy, but also recently for wind energy facilities. Yet, the wind power amount produced in Israel is rather small compared to the continuously growing global market; however, the recent steps undertaken by the state are destined to make the situation better.

Israel currently operates a wind farm in Asanyia mountain in the Golan Heights with an installed capacity of 6 MW (10 turbines reaching a height 50 m (blades included), each with a power capacity of 600 kW), this is the typical consumption of about five thousand families. The duty cycle of the wind farm reaches 97%, and electricity production is worth 1 million US$ a year. Indeed, the wind energy potential of Israel is rather restricted due to moderate or poor wind velocities in most areas and the restricted number of areas with high average wind speed. In many areas worthy of wind energy development, one is encountered by the opposition of green groups on landscape conservation grounds and the influence of the facility on local and migrating birds. Nevertheless, satisfying the Israel Ministry of Environmental Protection (IMEP) directions, the state of Israel continues efforts towards the development of additional farms with a 50 MW capacity [5].

As it is emphasized in a document issued by the Israeli Parliament (Knesset), a better estimate, based on the wind turbines' technical development, gives a value of more than 500 MW for the Israeli potential wind energy potential capacity [6]. One of the prospective areas for the development of efficient wind technology, considering its climatic characteristics, is the region of Ariel city in Samaria [7], the current research, however, is devoted to another region [8].

While the generic discounted cash flow (DCF) approach using the net present value (NPV) criterion is generally adopted to evaluate investments, the DCF method is inappropriate for a rapidly changing investment situation (Dixit and Pindyck [9]; Herath and Park [10]; Lee and Shih [11]) and does not consider managerial flexibility in investment decisions (Hayes and Abernathy [12]; Hayes and Garvin [13]; Trigeorgis and Mason [14]; Trigeorgis [15]). In the current study, we consider a two-stage approach—one turbine at the first stage and a field of 50 at the second stage, along with the possibility to withdraw at the second stage. Hence, the scenario is a one in which managerial flexibility can be practiced.

Currently, the real option analysis method is widely applied in many studies for the valuation of renewable energy investment projects, for example, Lee and Shih [11] and Kumbaroğlu, Madlener, and Demirel [16]. See also Boomsma, Meade, and Fleten [17] and Menegaki [18]. We thus apply in this paper the real options analysis method for the evaluation of the economic value of wind energy turbines in a specific location. In particular, we analyze the value of the investment opportunities that add value to the investment due to managerial flexibility (in the case of energy market price drop, one may abandon the investment). It is worth mentioning that the option valuation method has become more sophisticated by using approaches such as the binomial lattice, the mean reverting jump-diffusion method, and stochastic volatility model. It is also used for other types of hazards such as technological risks (Deng [18]; Menegaki [19]; Siddiqui, Marnay, and Wiser [20]), which may include a change in the wind regime, in our case, or

power output reduction of the turbine. See also Davis and Owens [21] and Baringo and Conejo [22].

The reasons for the current study are as follows, we are interested in estimating the profitability of a Merom Golan wind facility. For this:

(1)   We calculate the revenue from Merom Golan due to electric energy production.
(2)   We show that, taking into account the annual energy production, fluctuations are rather small; this is contrasted with rather large fluctuations when one considers the data over a daily basis.
(3)   This is then integrated into two economic models; one is the standard discounted cash flow and the other is the real options analysis.
(4)   We finally show that, because of energy price volatility and despite small technical fluctuations, the correct estimation of the investment is given by the real options analysis, which takes into account the ability of the investors to abort their investment after the first stage.

The main purpose of this paper is to study the effect of energy value fluctuations on the assessment of the profitability of wind turbine facilities using the real option analysis method. The economic output of a wind turbine installation is a function of its electric energy output [23–25] and the value of market energy. The electric energy output is a function of the turbine used and wind speed statistics. The turbine used can be chosen to have an optimal cut-in velocity (the wind speed level at which the turbine starts to generate electricity), and the cut-out velocity (the speed level at which the facility hits its alternator limit and stops producing more power output following increases in wind velocity) [26]. For a more technical discussion, we refer the reader to the results of our previous studies on wind power production, devoted to the technological appropriateness and environmental relevance issues [7,27]. See also [28,29]. While the total annual energy output of the turbine facility can be known to a high certainty, the market prices of energy may vary indeterminately, and thus should be considered as the most serious investment risk. To evaluate the financial risk correctly, we suggest employing the real option analysis method, which is the subject of the current study. In a wider sense, our manuscript contributes to the risk analysis of Grossman, which is the way a "decentralized economy allocates risk and investment resources when information is dispersed" [30] (p. 773).

In this paper, we shall describe the various sources of the uncertainties in determining the economic value of a wind installation. Both in terms of technical parameters, such as wind velocity change, and the effect on the power output of the turbine. Additionally, in terms of the market value of the power generated, which is dependent on the value of competing power generation methods. We then combine the uncertainties to produce the economic value of the installation using the real option analysis evaluation techniques. On comparing the different sources of uncertainty, we show that the uncertainty in the market value of electric power significantly dominates the technical uncertainties.

The structure of the paper is as follows: in the "Materials and Methods" section we describe the methods of this work, which are the Weibull statistics of wind and the Black–Scholes analysis of the real option technique. In the "Results" section we describe the Weibull fit for the site of installation, deriving the relevant parameters; we also introduce the economic model in terms of its parameters and emphasize the difference between the DCF and ROA methods for evaluation. Next, in the "Discussion" section, we estimate the power production and power uncertainty for different turbines and compare this with the economic uncertainty of energy prices, determining that the latter is much larger. Finally, in the "Conclusion" section, we summarize our conclusions underlining the dominance of market price fluctuations over technical fluctuations and the benefit of using the ROA method over the DCF method for a better economic evaluation of the wind energy facility expedience.

2. Materials and Methods

In this study we concentrated on the wind speed distribution in the Golan heights area, using the information available from the meteorological service of the Israel Ministry of Transport [31], gathered by the Merom Golan meteorological station, one of the 84 Israeli meteorological facilities, which is situated at the relevant area [32], for the year 2014. The file used includes 52,066 data points gathered during the specified period. This includes sample values of the wind speed, one observation for every 10 min or 144 values per day (except for some non-significant missing values) [33]. We describe the data analytically using the Weibull probability density function (PDF). This is commonly accepted as the most appropriate function describing the wind speed statistical frequencies at a given location in most world locations. These data are essential for the planning of the wind turbine optimal choice [7].

The Weibull PDF is determined, in addition to a random variable X, representing here the wind speed, by two parameters, which are location dependent. They are a shape parameter k (dimensionless) and a scale parameter λ (m/s for the wind speed), which, together, determine the following PDF form:

$$f(x; \lambda, k) = \begin{cases} \frac{k}{\lambda} \left(\frac{x}{\lambda}\right)^{k-1} e^{-\left(\frac{x}{\lambda}\right)^k}, & x \geq 0 \\ 0, & x = 0 \end{cases}$$

Both PDF parameters are important for choosing the best location for the appropriate wind turbine, which imply the wind farm's economic value [34].

The wind velocity determines the electric power output. We will evaluate the power output based on wind statistics and turbine characteristics in the results section. As the electric power is sold to the users, the remaining question in evaluating the value of the installation is how much money the user will pay for their power consumption, in other words, "what is the market value of the power?", which reflects on the economic value of the installation. In the following, we describe the methods used for such evaluation.

While the generic discounted cash flow (DCF) approach using the net present value (NPV) criterion is generally adopted to evaluate investments, the DCF method is inappropriate for a rapidly changing investment situation (Dixit and Pindyck [20]; Herath and Park [21]; Lee and Shih [11]) and does not consider managerial flexibility in investment decisions (Hayes and Abernathy [23]; Hayes and Garvin [24]; Trigeorgis and Mason [25]; Trigeorgis [26]). In the current study, we consider a two-stage approach—one turbine at the 1st stage and a field of 50 at the 2nd stage; along with the possibility to withdraw at the 2nd stage. Hence, the scenario is a one in which managerial flexibility can be practiced.

Currently, the real option analysis method is widely applied in many studies for the valuation of renewable energy investment projects, for example Lee and Shih [11] and Kumbaroğlu, Madlener, and Demirel [27]. See also Boomsma, Meade, and Fleten [28] and Menegaki [29]. We thus apply in this paper the real options analysis method for the evaluation of the economic value of wind energy turbines in a specific location. In particular, we analyze the value of the investment opportunities that add value to the investment due to managerial flexibility (in the case of energy market price drop, one may abandon the investment). It is worth mentioning that the option valuation method has become more sophisticated by using approaches such as the binomial lattice, the mean reverting jump-diffusion method, and stochastic volatility model. It is also used for other types of hazards such as technological risks (Deng [30], Menegaki [29], Siddiqui, Marnay, and Wiser [31]), which may include a change in the wind regime, in our case, or power output reduction of the turbine. See also Davis and Owens [32] and Baringo and Conejo [33].

However, we decided to adopt the basic Black–Scholes equation of a financial market [35] because we were focused on the underestimated value of the option to abort the investment in an environment where it is not possible to foresee the standard deviation using numerical tools.

In this study, we analyzed the possibility of installing additional turbines in the Asanyia mountain in the Golan Heights in order to extract profit from wind-generated power. We have partly based our study on the known results of wind turbine construction and use in Israel [36], while part of the numbers presented here are rather rough estimates. The decision to construct a field, which is a collection of many turbines, can be divided into two stages: in the 1st stage we build one unit. After building and operating this single unit for few years and gaining confidence in the technical and financial output, the 2nd stage, regarding the decision of building the entire turbine field, is made, based on electricity price at this stage as well as the future predicted energy evaluation.

We evaluate the uncertainty over future electricity market price as an economic value of an underlying asset of a real option using the Black–Scholes equation [35]:

$$C = S_0\, N(d_1) - K\, e^{-rT} N(d_2)$$

where

$$d_1 = \frac{\ln(S_0/K) + (r + \sigma^2/2)T}{\sigma\sqrt{T}},$$
$$d_2 = \frac{\ln(S_0/K) + (r - \sigma^2/2)T}{\sigma\sqrt{T}} = d_1 - \sigma\sqrt{T}.$$

We use the following notations: C is the call option value, S_0 is the market price of the underlying asset, K is the exercise price, r is the annual risk-free return, T is the duration of the period (the number of years) till exercising the real option (constructing the entire turbine field), and σ is the annualized standard deviation (StD) of the return of the underlying asset. N is the symbol of the Gaussian cumulative probability density function (CDF).

3. Results

3.1. Wind Energy Statistics

Several various methods exist for fitting the observed data of the given location [37] to the PDF. We used the method of the maximum likelihood estimators for PDF fitting [38]. The corresponding Weibull PDF for the wind speed distribution at the Merom Golan site, together with their distribution histogram, is shown below at Figure 1. (The authors are willing to share their data set in Excel format with those who wish to replicate the results of this research).

The figure demonstrates visually that low and moderate winds are widespread, with a tight condensation at the primary segment, which means that storms are just rare. It should be noticed that the distribution approximation by a Weibull PDF in this case is not perfect, although we could nevertheless obtain the wind principal statistical parameters approximately based on it.

Estimated annual parameters of the wind Weibull distribution were found to be $k = 1.7228$ and $\lambda = 4.1206$ m/s. In addition, we calculated (excess) kurtosis (a measure of the PDF sharpness) to be 2.1757, and skewness (a measure of the PDF asymmetry) as 0.0574, which were calculated to demonstrate the specific type of the Weibull PDF.

The main meaningful statistical parameter for the planning of the wind turbine installation, the speed mean, was obtained at 3.73 m/s, with standard deviation of 2.03 m/s, during the given period, with a positive right-skewed tail. This finding, in accordance with the Israeli Cooperative for Renewable Energy conclusions [39], indicates the possibility of wind energy exploitation in the investigated region.
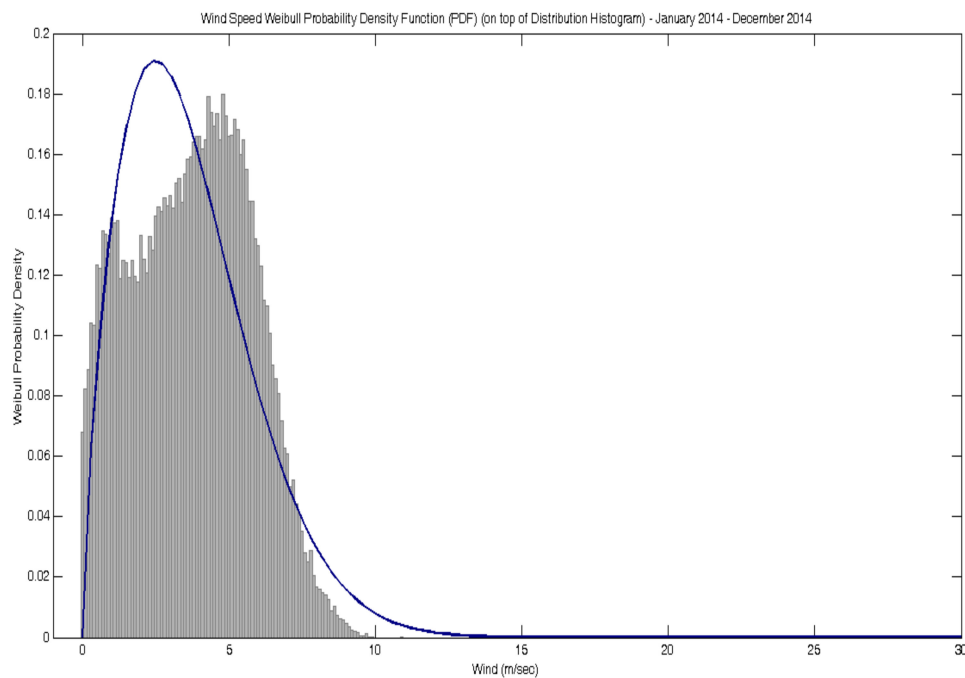
Figure 1. The Weibull PDF diagram for the Merom Golan wind speed distribution (on top of the distribution histogram).

3.2. Economical Model

All the used figures were elaborated in accordance with a proposed scenario as in Table 1 below, where the real figures can be introduced according to the data of each project (all prices are given in millions of US$):

Table 1. Input data for the Black–Scholes option value calculation.

Data for the Black–Scholes Option Value	
Cost of the first stage's one turbine building	50
Annual turbine's profit in the second stage	0.2
Present value of 50 turbines' profit over 20 years = stock price now (S_0)	114.7
Cost of the second stage for each turbine construction	1.2
Number of turbines in the second stage (entire field)	50
Cost of the second stage's 50 turbines = exercise price of option (K)	60
Number of periods to exercise in years (T)	2
Compounded risk-free interest rate (r)	0.02
Standard deviation of prices of energy or electricity (annualized σ)	0.031

We apply here the technique of real option valuation, as illustrated in Brealey et al. [40] (p. 584), where we have replaced:

(1) The stock price with the current value of the field, S_0 = 114.7 million $US, which is the present value of 20 years of future operation with an annual profit of 0.2 million $US per turbine for a field of 50 turbines, discounted with 6% annual cost of capital;

(2) The number of periods to exercise in years (T), with the number of years between the confirmation of the first stage (one unit) to the decision on the second stage (the field).

We have therefore calculated, at first, the call value, based on the annual StD estimation of 0.031, as 57.05 million $US. This StD estimation of 0.031 is based on the data of the Electric Power Monthly report of the U.S. Energy Information Administration (EIA), Table 5.3 "Average Retail Price of Electricity to Ultimate Customers" [41].

Our assumption of the first unit's building cost is equal, as mentioned above, to 50 million $US, where such high expenses of the first turbine's launching include, among others,

research and development to adapt the turbine to the specific area under consideration and the cost of connecting it to the power grid, subtracted by the profit from operation.

We stress that the current work is based on assumed values, and, in this sense, it is an exercise in applying the real option technique. Future work will depend on a more realistic estimation of both the investment costs in infrastructure and current energy prices.

Hence, the results indicate that the investment in the first turbine stage is warranted, and the fact that there is the option to follow-on adds significant value to the investment. It follows that the net profit of the first stage is $57.05 - 50 = 7.05$ million \$US for the standard deviation value of 0.031, according to the following data of Table 2 (in a column for the case of StD = 0.031), which includes the intermediate values and the option to follow-on:

Table 2. Intermediate and output data for the Black–Scholes option value.

Intermediate and Output Data for Two Assumptions on StD		
StD	0.031	0.40
$\sigma\sqrt{T}$	0.0438	0.5657
d1	15.7146	1.4990
d2	15.6707	0.9333
Delta N(d1) Normal CDF	0.5123	0.9331
Value of the Call Option to Follow-On	**57.05**	**59.48**

For comparison with a scenario lacking an option to abandon, the project value is estimated as the present discounted value of a difference between (i.e., the earnings from) the future cash flow raised from the second stage realization subtracted by the second stage building cost, which is subtracted additionally by the first stage building cost.

Applying to our numerical example, this yields just the negative benefit, meaning merely loss, of the $(114.7 - 60)/1.06^2 - 50 = -1.3$ million \$US.

However, using StD of 0.031 yields a profit of 7.05 million \$US, as was calculated above. This is so because one can make a choice to abandon the project while it is still underway. This is the economic meaning of the real option.

4. Discussion

It is difficult to determine the direction and intensity of energy prices in the future. For example, the U.S. Energy Information Administration in its "Independent Statistics & Analysis" publication, "The Availability and Price of Petroleum and Petroleum Products Produced in Countries other than Iran" in its May–June 2015 update states the following:

"The uncertainty on both the supply and demand side of the market could result in large future price movements [underlined by the authors]. The possible lifting of sanctions on Iran could move additional supply on to the world market and reduce prices, while an unexpected supply disruption at a time of low surplus production capacity may push prices higher. Meanwhile, if a slowdown in global economic activity from current levels occurred, it would reduce demand and result in higher-than-expected inventory builds, moving prices lower" [42]. This can be seen from the graph from the same source in Figure 2, where the spread between production and consumption has been widening since July 2014.

In addition to the world energy price uncertainty, in Israel, there are at least four other sources for price uncertainty:

(a)   the possibility of military conflict;
(b)   the discovery of gas on Israel's shore;
(c)   the adoption of gas by the industry; for example, Foenicia—a glass manufacturer that was recently close to bankruptcy due to lack of gas turned to become profitable [43]; and
(d)   the discovery of oil in the Golan Heights [44].
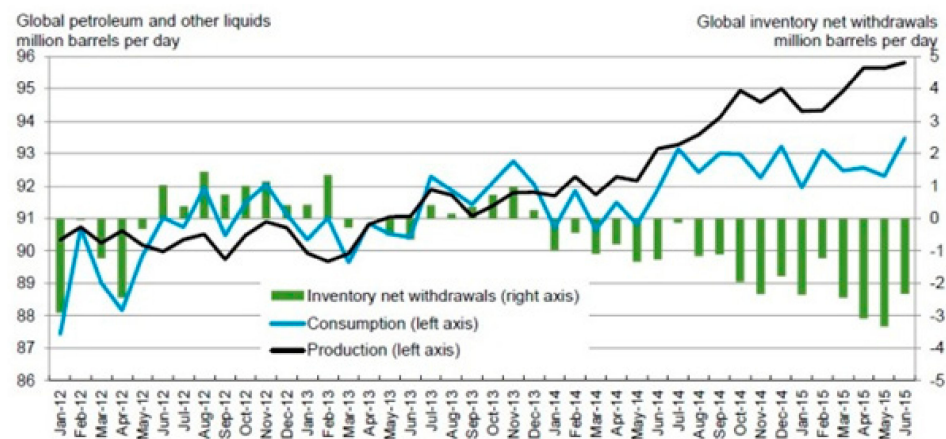
Figure 2. Global petroleum and other liquids production, consumption and inventory net withdrawals, January 2012–June 2015 [20].

While it is still difficult with all these sources of uncertainty to determine the direction and intensity of the change of energy price, we must consider, thus, the possibility of high volatility in price. To this end, we will consider hereafter the possibility of high volatility taken to be StD = 40% per annum.

Calculating the call value based on the annual StD estimation of 0.4 yields 59.48 million \$US (compared to 57.05 million \$US based on StD of 0.031). It follows that the net profit of the first stage increased to $59.48 - 50 = 9.48$ million \$US (see Table 2, a column for the case of StD = 0.40). It would be worth noticing here that the main statistical parameters of the wind speed in the Merom Golan area, the mean and the StD, are observed with a tendency towards stability, without any significant divergence over the period of the last few years, 2009–2014, as it follows from the calculated data in Table 3:

Table 3. Wind speed mean and StD at Merom Golan for the last period.

Year	2009	2010	2011	2012	2013	2014
Speed mean (m/s)	3.89	3.69	3.63	3.70	3.80	3.62
StD (m/s)	2.10	2.12	2.00	2.03	2.05	1.99
Number of Samples	2919	2920	2920	9774	2896	2898
StD/$\sqrt{n}$ (m/s)	0.039	0.039	0.037	0.021	0.038	0.037

The expectation value of an annual average is the same as the expectation value for one sample, but the standard deviation of the annual average is equal to the standard deviation of one sample divided by the square root of the annual number of samples (see Appendix A for a mathematical justification). Thus, the standard deviation of the annual average of wind speed is between 0.6–1.1%, and can be further reduced by more sampling. A six year average based on 24,327 samples will be 3.72 m/s, with only 0.4% standard deviation. The power curves of available turbines are described in [45], from which three examples are analyzed in this paper and are depicted in Figure 3.
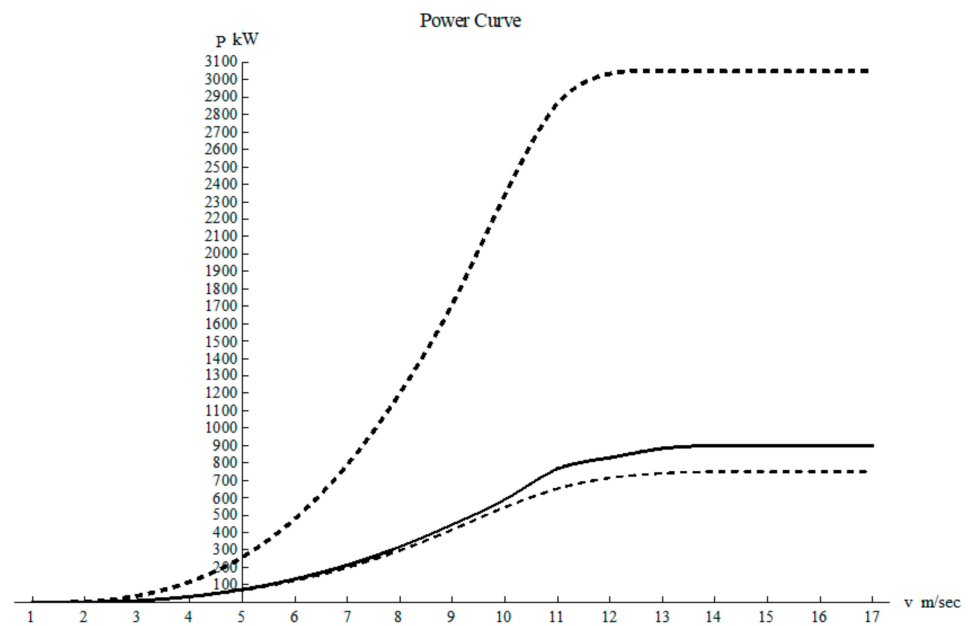
Figure 3. Power curves of wind turbines [45]. The dashed thick curve is the power curve of Enercon's model E101/3000 turbine, the thick line is the power curve of AWE's model 54–900 turbine, and the dashed curve is the power curve of EWT's model Directwind 52/750 turbine.

The wind speeds described in Table 3 are for a height of 10 m, for different heights, we apply the velocity to height connection [46]:

$$v(h) = v_{10} \left(\frac{h}{10} \right)^a$$

in which $v(h)$ is the velocity at height h, v_{10} is the velocity at a height of 10 m, and a is Hellmann's exponent, which, for a neutral air above human inhabited areas, is about 0.34. Among the turbines analyzed, the largest is Enercon's model E101/3000 turbine with a radius of 50.5 m. Hence, we will assume from now on that the hub of the turbine is 60 m. Table 4 will summarize the area and radii of the turbines under study:

Table 4. Wind turbine geometric parameters.

Turbine	Enercon's E101/3000	AWE's 54–900	EWT's Directwind 52/750
Area (m^2)	8012	2290	2083
Radius (m)	50.5	27	25.75

For this height, we obtain a six year speed average of 6.84 m/s. The eleven year average of the power and the standard deviation obtained for each turbine are depicted in Table 5, the total number of samples in this analysis was 31,292 based on the wind data from Merom Golan.

Table 5. Wind turbine power for eleven years of data acquisition.

Turbine	Enercon's E101/3000	AWE's 54–900	EWT's Directwind 52/750
Average Power (kW)	1205.84	325.84	289.70
Power StD (kW)	1125.94	309.10	264.99
Power StD/$\sqrt{n}$ (kW)	6.36	1.75	1.50
%(StD/$\sqrt{n}$)/Average	0.52	0.54	0.52
Annual Revenue (SH)	5,133,695	1,387,218	1,233,357
Annual Revenue ($)	1,327,909	358,825	319,027

The standard deviation of average power for all turbines investigated is much lower than the standard deviations of energy price appearing in Table 2. Hence, a long-term project can ignore the risks connected with the standard deviation of wind speed. A formal proof for this decisive circumstance is given in Appendix B.

This circumstance determines the fact of non-relevancy of the speed variance over a prolonged period of time for the wind turbine economic value; this should be compared to the significance of the energy prices for the turbine economic value.

Table 5 also contains the annual economic value of the turbine based on the current price of energy for consumers in Israel, which is 0.486 SH for kW hour on 11 September, 2015, the exchange rate for the same date is 3.866 SH for one US$. We assume that the turbine owner will need to pay for transmission and distribution, hence the more conservative estimate of an annual profit of 0.2 million $US per turbine quoted in the previous section. In practice, the price is determined by governmental authorities who strike a balance between the interest of other producers, the cost of transmission and distribution, and the public interest in clean energy.

We previously concluded that the advantage of using ROA over DCF is most significant when the market prices are volatile, and less so when the energy prices are stable. However, the change in wind speed is a small fraction of the value of the wind installation volatility, and this alone cannot justify the use of the ROA method. However, the fluctuations of the market energy prices is reason enough.

5. Conclusions

Traditional calculation for an uncertain cash flow applies just to the expected values of the cash flow from the project without the possibility of abandoning the project. Given our empirical assumptions, this yields a loss of 1.3 million $US instead of profit, meaning the project becomes not worthwhile.

Nevertheless, applying the real option analysis, which reveals the value of the option to abandon the second stage running as well, we turn the project to just become profitable and worthwhile. The value of the real option increases depending on the volatility to be either 57.05 million $US or 59.50 million $US, depending on future volatility, and the profit is either 7.05 million $US or 9.48 million $US, respectively.

Finally, for civil engineering projects with volatility in input and mainly in output prices, it is important to consider the option to abandon the project from the beginning, as this option may turn the project to be profitable.

We underline that, for wind installations, the main volatility is due to energy market prices and less because of wind speed uncertainties, which average out on an annual time scale.

To conclude, we underline that our work contains the following innovative elements, which were not published before:

1.	Weibull statistics of the wind in Merom Golan based on data gathered for several years was obtained, thus deriving the relevant parameters needed for our work.
2.	Using the empiric wind data and power curves of commercial wind turbines to choose the best wind turbine for the Merom Golan site.

3. Using the above data, we calculated the revenue from Merom Golan due to electric energy production.
4. It was shown that, taking into account the annual energy production, fluctuations are rather small; this is contrasted with rather large fluctuations when one considers the data over a daily basis.
5. This was integrated into two economic models; one is the standard discounted cash flow and the other is the real options analysis. We have shown that, because of energy price volatility and despite small technical fluctuations, the correct estimation of the investment is given by the real options analysis, which takes into account the ability of the investors to abort their investment after the first stage.

We thus make the following policy recommendation, which is particularly relevant in the current era of high energy price fluctuations (for example on 15 April 2020, the US WTI Crude was 19.87 US$, today (20 February 2021) it is 59.24 $. This is more than 40% difference, which is discussed in the current work). We recommend investors and policy makers to use real options analysis rather than standard discounted cash flow, and take advantage of the ability to abort an unprofitable endeavor.

Future directions in this research area include the analysis of real economic parameters that are not just rough estimates, and the use of more accurate analysis using approaches such as the binomial lattice, the mean reverting jump-diffusion method, and the stochastic volatility model.

Appendix A

Consider a random process $X(t)$, which is sampled at times t_i, each sample $X_i = X(t_i)$ is a random variable. We will assume that the process is stationary in the sense that each random variable has the same expectation value:

$$E[X_i] = E[X_j] = \overline{X} \quad \forall\, i, j \tag{A1}$$

and standard deviation:

$$\sigma_{x_i} = \sigma_{x_j} = \sigma_x \quad \forall\, i, j \tag{A2}$$

We will also assume that the random variables are independent. Thus the covariance satisfies $C_{x_i x_j} = 0$, $\forall\, i \neq j$. Let us now average n samples as:

$$X_a = \frac{1}{n} \sum_{i=1}^{n} X_i. \tag{A3}$$

This implies that the expectation value of the average will be the same as that of the samples:

$$E[X_a] = E\left[\frac{1}{n} \sum_{i=1}^{n} X_i\right] = \frac{1}{n} \sum_{i=1}^{n} E[X_i] = \frac{1}{n} \sum_{i=1}^{n} \overline{X} = \overline{X} \tag{A4}$$

However, the standard deviation of X_a will be much smaller, since:

$$\sigma_{X_a}^2 = E\left[(X_a - \overline{X_a})^2\right] = \frac{1}{n^2} E\left[\sum_{i,j}^n (X_i - \overline{X_i})(X_j - \overline{X_j})\right]$$
$$= \frac{1}{n^2} \sum_{i,j}^n C_{x_i x_j} = \frac{1}{n^2} \sum_i^n C_{x_i x_i} = \frac{1}{n^2} \sum_i^n \sigma_{X_i}^2 = \frac{1}{n^2} \sum_i^n \sigma_X^2 = \frac{\sigma_X^2}{n} \tag{A5}$$

Hence:

$$\sigma_{X_a} = \frac{\sigma_X}{\sqrt{n}}. \tag{A6}$$

Additionally, for a large amount of samples:

$$\lim_{n \to \infty} \sigma_{X_a} = \lim_{n \to \infty} \frac{\sigma_X}{\sqrt{n}} = 0. \tag{A7}$$

Appendix B

The revenue R is the product of En, the energy produced, and C, the price of energy. For a small amount of energy dEn, dR is equal to:

$$dR = C \, dEn \tag{A8}$$

The gain G is defined as the revenue per unit time:

$$G = \frac{dR}{dt} = C \frac{dEn}{dt} = CP \tag{A9}$$

in which $P = \frac{dEn}{dt}$ is the power. Thus the expectation of the gain is the correlation of the price and the power.

$$E[G] = E[CP] = R_{CP}. \tag{A10}$$

Since the price is a random process, which is largely independent of the power and is dependent, among other things, on the price of other energy sources and administrative decisions, we will assume that C and P are independent random variables, hence:

$$E[G] = \overline{C} \cdot \overline{P} \tag{A11}$$

in which $E[C] = \overline{C}$ is the average price and $E[P] = \overline{P}$ is the power average. The variance of the gain, as its standard deviation square, is thus:

$$\sigma_G^2 = E\left[G^2\right] - \overline{G}^2 = E\left[C^2 P^2\right] - \overline{C}^2 \overline{P}^2 = E\left[C^2\right] E[P^2] - \overline{C}^2 \overline{P}^2 \tag{A12}$$

However, since

$$E\left[C^2\right] = \sigma_C^2 + \overline{C}^2, \quad E\left[P^2\right] = \sigma_P^2 + \overline{P}^2 \tag{A13}$$

it follows that:

$$\sigma_G^2 = \left(\sigma_C^2 + \overline{C}^2\right)\left(\sigma_P^2 + \overline{P}^2\right) - \overline{C}^2 \overline{P}^2 = \sigma_C^2 \sigma_P^2 + \overline{C}^2 \sigma_P^2 + \overline{P}^2 \sigma_C^2 \tag{A14}$$

Hence:

$$\frac{\sigma_G^2}{\overline{G}^2} = \frac{\sigma_C^2}{\overline{C}^2} + \frac{\sigma_P^2}{\overline{P}^2}\left(1 + \frac{\sigma_C^2}{\overline{C}^2}\right) \tag{A15}$$

Thus, if $\frac{\sigma_P^2}{\overline{P}^2} \ll \frac{\sigma_C^2}{\overline{C}^2}$, and since necessarily $\frac{\sigma_C^2}{\overline{C}^2} < 1$, we can write:

$$\frac{\sigma_G^2}{\overline{G}^2} \cong \frac{\sigma_C^2}{\overline{C}^2}. \tag{A16}$$

However, notice that power fluctuations are not small, it is only the power average fluctuations over many samples that are small (see Appendix A), hence a more sophisticated approach is needed. We notice that the typical time for the change of power is much shorter than the typical time for the change of price. For example, we can assume that price changes once a month while power is sampled every ten min. We define ΔT as a duration for which the price remains constant. Next, we calculate the revenue for the total duration T:

$$R_T = \int_0^{R_T} dR = \int_0^T CP dt \tag{A17}$$

We now divide the duration T to the subduration of intervals ΔT, and integrate R as follows:

$$R_T = \sum_{n=1}^N \int_{T_{n-1}}^{T_n} CP dt \tag{A18}$$

In the above, $T_n - T_{n-1} = \Delta T$, and $T_0 = 0$, $T_N = T$. Since C is constant for ΔT intervals, we can write:

$$R_T = \sum_{n=1}^N C_n \int_{T_{n-1}}^{T_n} P dt \tag{A19}$$

Let us further divide the duration ΔT into subdurations $\Delta t = \frac{\Delta T}{M}$, in which M is a large enough number; we may now write:

$$\int_{T_{n-1}}^{T_n} P dt = \sum_{i=1}^M \int_{T_{ni-1}}^{T_{ni}} P dt \tag{A20}$$

In the above, $T_{ni} - T_{ni-1} = \Delta t$, and $T_{n0} = T_{n-1}$, $T_{nM} = T_n$. If M is large enough, we may write approximately:

$$\int_{T_{n-1}}^{T_n} P dt \cong \sum_{i=1}^M \Delta t P_{ni} = \frac{\Delta T}{M} \sum_{i=1}^M P_{ni} = \Delta T P_{na}. \tag{A21}$$

where P_{na} is an average in the sense of (A3), hence the fluctuations of P_{na} are small enough. The total revenue is therefore:

$$R_T = \Delta T \sum_{n=1}^N C_n P_{na} = \Delta T \sum_{n=1}^N G_{na} \tag{A22}$$

Thus the revenue is proportional to the sum of the average gains G_{na}, which, according to Equations (A14) and (A15), have fluctuations that are a result of the dominant price fluctuations and the negligible power fluctuations.

References

1. Global Wind Energy Council; Gwec.net. The Global Status of Wind Power in 2012 [Electronic Version]. Available online: http://www.gwec.net/index.php?id=180 (accessed on 15 September 2013).
2. European Wind Energy Association. Global Wind Energy Statistics [Electronic Version]. Available online: http://www.ewea.org/statistics/global-statistics/ (accessed on 16 September 2013).
3. Tamar Gas Field. Available online: http://en.wikipedia.org/wiki/Tamar_gas_field (accessed on 22 February 2015).
4. Leviathan Gas Field. Available online: http://en.wikipedia.org/wiki/Leviathan_gasfield (accessed on 22 February 2015).
5. Israel Ministry of Environmental Protection. Renewable Energy [Electronic Version]. Available online: http://www.sviva.gov.il (accessed on 31 July 2009).
6. Lotan, O. *Wind Energy Power Generation*; Background Paper, 21.09.05; Knesset, Research and Information Center: Jerusalem, Israel, 2005. (In Hebrew)
7. Byalsky, M.; Yahalom, A. Modeling of the Wind Energy Use Efficiency. In Proceedings of the 4th Annual International Conference on Qualitative and Quantitative Economics Research (QQE 2014), GSTF, Phuket, Thailand, 28–29 April 2014.

8. Greenberg, D.; Byalsky, M.; Yahalom, A. On the Wind Turbines Assessment by Real Options Technique in Israel. In Proceedings of the Seventh International Conference on Bioenvironment, Biodiversity and Renewable Energies, Lisbon, Portugal, 26–30 June 2016.

9. Dixit, A.K.; Pindyck, R.S. The options approach to capital investment. In *Real Options and Investment under Uncertainty-Classical Readings and Recent Contributions*; MIT Press: Cambridge, UK, 1995; pp. 105–115.

10. Herath, H.S.B.; Park, C.S. Economic Analysis of R&D projects: An options approach. *Eng. Econ.* **1999**, *44*, 1–35. [CrossRef]

11. Lee, S.C.; Shih, L.H. Renewable energy policy evaluation using real option model—The case of Taiwan. *Energy Econ.* **2010**, *32*, 67–78. [CrossRef]

12. Hayes, R.H.; Abernathy, W.J. Managing our way to economic decline. *Harv. Bus. Rev. U. S.* **1980**, *58*, 67–77.

13. Hayes, R.H.; Garvin, D. Managing as it tomorrow mattered. *Harv. Bus. Rev.* **1982**, *60*, 70–79.

14. Trigeorgis, L.; Mason, S.P. Valuing managerial flexibility and strategy in resource. *Midl. Corp. Financ. J.* **1987**, *5*, 14–21.

15. Trigeorgis, L. *Real Option: Managerial Flexibility and Strategy, Resource Allocation*, 2nd ed.; Parager Publisher: Westport, MA, USA, 1997.

16. Kumbaroğlu, G.; Madlener, R.; Demirel, M. A real options evaluation model for the diffusion prospects of new renewable power generation technologies. *Energy Econ.* **2008**, *30*, 1882–1908. [CrossRef]

17. Boomsma, T.K.; Meade, N.; Fleten, S.E. Renewable energy investments under different support schemes: A real options approach. *Eur. J. Oper. Res.* **2012**, *220*, 225–237. [CrossRef]

18. Deng, S. *Stochastic Models of Energy Commodity Prices and Their Applications: Mean-Reversion with Jumps and Spikes*; the POWER Working Papers Series, PWP-073; University of California Energy Institute: Berkeley, CA, USA, 2000.

19. Menegaki, A. Valuation for renewable energy: A comparative review. *Renew. Sustain. Energy Rev.* **2008**, *12*, 2422–2437. [CrossRef]

20. Siddiqui, A.S.; Marnay, C.; Wiser, R.H. Real options valuation of US federal renewable energy research, development, demonstration, and deployment. *Energy Policy* **2007**, *35*, 265–279. [CrossRef]

21. Davis, G.A.; Owens, B. Optimizing the level of renewable electric R&D expenditures using real options analysis. *Energy Policy* **2003**, *31*, 1589–1608.

22. Baringo, L.; Conejo, A.J. Strategic Wind Power Investment. *IEEE Trans. Power Syst.* **2014**, *29*, 1250–1260. [CrossRef]

23. Astolfi, D. Wind Turbine Operation Curves Modelling Techniques. *Electronics* **2021**, *10*, 269. [CrossRef]

24. Alturki, F.A.; MH Farh, H.; Al-Shamma'a, A.A.; AlSharabi, K. Techno-Economic Optimization of Small-Scale Hybrid Energy Systems Using Manta Ray Foraging Optimizer. *Electronics* **2020**, *9*, 2045. [CrossRef]

25. Ahmed, D.; Ebeed, M.; Ali, A.; Alghamdi, A.S.; Kamel, S. Multi-Objective Energy Management of a Micro-Grid Considering Stochastic Nature of Load and Renewable Energy Resources. *Electronics* **2021**, *10*, 403. [CrossRef]

26. Gray, P.; Johnson, L. *Wind Energy System*; Prentice Hall: Upper Saddle River, NJ, USA, 1985.

27. Ditkovich, Y.; Kuperman, A.; Yahalom, A.; Byalsky, M. A Generalized Approach to Estimating Capacity Factor of Fixed Speed Wind Turbines. *IEEE Trans. Sustain. Energy* **2012**, *3*, 607–608. [CrossRef]

28. Ditkovich, Y.; Kuperman, A.; Yahalom, A.; Byalsky, M. Site-Dependent Wind Turbine Performance Index. *Int. J. Renew. Energy Res.* **2013**, *3*, 592–594.

29. Ditkovich, Y.; Kuperman, A.; Yahalom, A.; Byalsky, M. Alternative Approach to Wind Turbine Performance Index Assessment. *J. Energy Eng.* **2014**, *140*, 06014001. [CrossRef]

30. Grossman, S.J. Dynamic Asset Allocation and the Informational Efficiency of Markets. *J. Financ.* **1995**, *50*, 773–787. [CrossRef]

31. The Israel Meteorological Service Site. Available online: http://www.ims.gov.il/ims/all_tahazit/ (accessed on 26 May 2015).

32. The Israel Meteorological Stations' Characteristics. Available online: https://data.gov.il/sites/data.gov.il/files/metadata1 0minutesIMS7.XLSX (accessed on 1 June 2015).

33. The Government Information Data Bases' Site. Available online: https://data.gov.il/ims/7 (accessed on 3 June 2015).

34. Reliability Engineering. Weibull Statistics. Available online: http://www.weibull.nl/weibullstatistics.htm (accessed on 30 December 2013).

35. Black, F.; Scholes, M. The pricing of options and corporate liabilities. *J. Political Econ.* **1973**, *81*, 637–654. [CrossRef]

36. Golan Wind Energy [Electronic Version]. Available online: http://www.wind-golan.com/ (accessed on 14 February 2015).

37. Bhattacharya, P.; Bhattacharjee, R. A study on Weibull distribution for estimating the parameters. *J. Appl. Quant. Methods* **2010**, *5*, 234–241. [CrossRef]

38. "Weibull Parameter Estimates", MathWorks Documentation Center [Electronic Version]. Available online: www.mathworks.com/help/toolbox/stats/wblfit.html (accessed on 18 August 2013).

39. Levy, H. Installation of Small Wind Turbines for the Electricity Generation. In Israeli Cooperative for Renewable Energy (in Hebrew): 2013. [Electronic Version]. Available online: http://ecoop.org.il/index.php?option=com_content&view=article&id=88&Itemid=135 (accessed on 30 December 2013).

40. Brealey, R.A.; Myers, S.C.; Allen, F. *Principles of Corporate Finance*, 10th ed.; McGraw-Hill/Irwin: New York, NY, USA, 2011.

41. Electricity. Electric Power Monthly Report of the U.S. Energy Information Administration (EIA). Available online: http://www.eia.gov/electricity/?fm&t=epmt_5_03 (accessed on 24 September 2015).

42. The Availability and Price of Petroleum and Petroleum Products Produced in Countries Other Than Iran. In No. 23 in a Series of Reports Required by Section 1245(d)(4)(A) of the National Defense Authorization Act for Fiscal Year 2012. 2012. Available online: http://www.eia.gov/analysis/requests/ndaa/pdf/ndaa.pdf (accessed on 6 October 2015).

43. Finally: Phoenicia Factory from Nazareth Ilit Is Connected to the Natural Gas (in Hebrew), Globes. Available online: http://www.globes.co.il/news/article.aspx?did=1001006735 (accessed on 3 February 2015).

44. Huge Oil Discovery on Golan Heights, Globes. Available online: http://www.globes.co.il/en/article-huge-oil-discovery-on-golan-heights-1001071698 (accessed on 7 October 2015).

45. Carrillo, C.; Obando Montaño, A.F.; Cidrás, J.; Díaz-Dorado, E. Review of power curve modelling for wind turbines. *Renew. Sustain. Energy Rev.* **2013**, *21*, 572–581. Available online: http://grupo_ene.webs.uvigo.es/ (accessed on 17 September 2015). [CrossRef]

46. Kaltschmitt, M.; Streicher, W.; Wiese, A. *Renewable Energy: Technology, Economics, and Environment*; Springer Science & Business Media: Berlin, Germany, 2007; p. 55. ISBN 978-3-540-70947-3.

Article

Renewable Energy Micro-Grid Interfacing: Economic and Environmental Issues

Adel A. Abou El-Ela [1], Ragab A. El-Sehiemy [2],* , Sohir M. Allam [1], Abdullah M. Shaheen [3] , Nadia A. Nagem [1] and Adel M. Sharaf [4]

[1] Electrical Engineering Department, Faculty of Engineering, Menoufiya University, Shebin el Kom 32512, Egypt; draaa50@hotmail.com (A.A.A.E.-E.); sohir.allam.sa@gmail.com (S.M.A.); nadyaali88@yahoo.com (N.A.N.)
[2] Department of Electrical Engineering, Faculty of Engineering, Kafrelsheikh University, Kafrelsheikh 33516, Egypt
[3] Department of Electrical Engineering, Faculty of Engineering, Suez University, Suez 43533, Egypt; abdullahshaheen2015@gmail.com
[4] Sharaf Energy Systems Inc., Fredeticton, NB E3C 2P2, Canada; profdramsharaf@icloud.com
* Correspondence: elsehiemy@eng.kfs.edu.eg

Abstract: This paper presents a study on the technical, economic, and environmental aspects of renewable energy resources-based distributed generation units (DGs). These units are connected to the medium-voltage network to create a new structure called a microgrid (MG). Renewable energies, especially wind and solar, are the most important generation units among DGs. The stochastic behavior of renewable resources increases the need to find the optimum operation of the MG. The optimal operation of a typical MG aims to simultaneously minimize the operational costs and the accompanied emission pollutants over a daily scheduling horizon. Several renewable DGs are investigated in the MG, consisting of biomass generators (BGs), wind turbines (WTs), and photovoltaics (PV). For the proposed operating strategy of the MG, a recent equilibrium optimization (EO) technique is developed and is inspired by the mass balance models for a control volume that are used to estimate their dynamic and equilibrium states. The uncertainties of wind speed and solar irradiation are considered via the Weibull and Beta-probability density functions (PDF) with different states of mean and standard deviation for each hour, respectively. Based on the developed EO, the hourly output powers of the PV, WT, and BGs are optimized, as are the associated power factors of the BGs. The proposed MG operating strategy based on the developed EO is tested on the IEEE 33-bus system and the practical large-scale 141-bus system of AES-Venezuela in the metropolitan area of Caracas. The simulation results demonstrate the significant benefits of the optimal operation of a typical MG using the developed EO by minimizing the operational costs and emissions while preserving the penetration level of the DGs by 60%. Additionally, the voltage profile of the MG operation for each hour is highly enhanced where the minimum voltage at each hour is corrected within the permissible limit of [0.95–1.05] Pu. Moreover, the active power losses per hour are greatly reduced.

Keywords: distributed generation; microgrid; equilibrium optimization technique; wind turbines; photovoltaics; biomass generators

1. Introduction

Due to the continuous increase in power demand and rapid depletion of fossil fuels, researchers all over the world have no other option but to look for alternative energy sources by utilizing small-scale distributed power generation (DG) and energy storage systems (ESS) [1]. However, due to the inherent intermittency and volatility of renewable energy sources (RESs), its large-scale integration into the power system will increase the regulation

burden and affect the security operation of the main grid. The microgrid is defined as small-scale controllable electrical distribution systems, which have the important advantage of operating either islanded or interconnected to the main grid. Microgrids (MGs) are usually composed of Distributed Energy Resources (DERs), ESSs, and controllable loads [2]. The DERs are based on conventional resources, such as diesel generators and RESs such as photovoltaics (PV) and wind turbines (WT) [3–6]. There are two modes of operation for MGs. In a grid-connected operation, the MGs draw/supply power from/to the grid based on load and generation conditions with regard to the market prices. On the other hand, it will be disconnected from the grid to provide electricity to associated critical loads in the event of faults [7].

In the first mode of operation, the MGs should be operated economically and reliably, where a supervisory control and data acquisition (SCADA) system is activated to monitor, control, and dispatch all DERs to guarantee the economic and secure operation of the MGs. For this targeted operation of the MGs, various conventional and artificial intelligent programming techniques were applied for dispatching the DERs [8]. In [9–12], the operation of distribution systems was optimally controlled via DERs commitment, Capacitor Banks (CBs) switching, SVC, and reconfiguration using the jellyfish search algorithm and manta ray foraging optimization algorithm, respectively. In both studies, the wasted energy of power losses was minimized considering the daily load variations, but the uncertainties of the DERs were not taken into account. In [13], the optimal operation and energy management method for a hybrid MG including photovoltaics, wind turbines, a pump as a turbine system, and a diesel generator was introduced, with a study on day-ahead scheduling. The optimal energy management minimizes the fuel cost of diesel generators, the daily operating cost, as well as the balance between the generation and load for both warm and cold days using an imperialist competitive algorithm. In [14], a hybrid ant lion optimization with a bat algorithm was utilized for the power management of the MG considering a droop controller strategy. The main target of this droop controller was stabilized by the MG by minimizing the errors of real and reactive power under a power shortage and power maximum. In [15], an optimal energy scheduling mechanism was presented in multi-MGs in order to minimize the total operational costs of their committed DERs. This study provided different DERs types and their associated uncertainties in a multi-MG system, but the linked lines and their losses were completely ignored. In [16], a Tabu search algorithm was applied for the design of the MG system components with minimum investment, operation, and emission costs. This study utilized the Monte Carlo simulation to deal with the uncertainties due to load forecasting and the random outages of the units. However, the uncertainties due to the intermittent sources of WTs and PVs were not taken into consideration where their outputs were directly evaluated from the daily wind velocity and solar irradiance, respectively. In [17], particle swarm optimization (PSO) was dedicated to minimize the MG operational costs considering the variations in loadings, DGs, and requirements of stable grid operational constraints.

Despite that, only the fuel costs of the committed DGs were handled where the quadratic cost models were utilized for the fuel cells and the micro turbines. In [18], a manta ray foraging optimizer was developed to optimally solve the economic dispatch problem with wind power inclusion considering the valve point effects of the generators, while the wind power effects were ignored in [19,20]. However, the environmental impacts of this operation were not considered. In [21], an artificial ecosystem-based optimizer was applied considering the demand side management for minimizing the techno-economic evaluations of hybrid energy systems. In [22], an optimal operational strategy was presented for MGs including hydrogen storage to integrate RESs and decrease the emissions. In [23], in off-grid MG simulation and tests, an adaptable energy management strategy relying on a mixed energy systems has been provided to preserve the stable operating condition of the off-grid MG and lengthen the lifetime of batteries.

In [24], a harmony search algorithm was combined with differential evolution for the optimal operation of MGs. Added to that, an optimal operation of MGs was considered

with WTs, PVs, battery energy storage (BES) systems, electric vehicles (EVs), and demand response for minimizing the total operating costs [25]. In this study, Sparse Nonlinear OPTimizer (SNOPT) solver was utilized using Generalized Algebraic Modeling Systems (GAMS) software. In both studies [24,25], the outputs of WTs and PVs were directly evaluated from the hourly wind velocity and solar irradiance, respectively. Therefore, the uncertainties due to the intermittent sources require an effective handling procedure. In [26,27] a moth flame optimization algorithm was employed for the optimal operation of a hybrid energy system including WTs, PVs, gas turbines, and energy storage.

In [28], an optimal MG operation strategy was presented to minimize the fuel costs and the produced emissions. In this study, the DER uncertainties were considered via the probability distributions and confidence. However, the application was limited to a very small number of sources where linear programming and quadratic programming (QP) were utilized as solvers. In [29], RES was allocated and optimized in a distribution system using Mixed Integer-Linear Programming (MILP) and was solved by FICO® XPRESS optimization software. In [30], the Energy Storage (ES) and RES were integrated using MILPmethod.

Recently, a new effective optimization algorithm of Equilibrium optimizer (EO) was presented [31]. EO provides strong exploratory and exploitative search mechanisms to adjust solutions at random, assisting in local minima avoidance in the optimization process, which is a common drawback of many optimization algorithms [31]. EO was efficiently used for solving the optimal power flow (OPF) problem in the AC power systems [32] and hybrid AC/DC power grids [33]. In [34,35], EO was utilized for handling the economic and the combined economic environmental dispatch problems, respectively, considering the power constraints, effects of the valve point, transmission losses, and ramp rate limits. In [36], an adaptive EO was developed for an optimal allocation procedure of biomass DGs to enhance the performance of the distribution systems and to reduce the related environmental emissions. In [37], EO was used to deal with the energy management optimization (EMO) in the MG considering the variations of WTs, PVs, and load demand for cost minimization and voltage magnitude improvements. In [38], an improved EO integrated for with optimal allocation of multiple PV units with batteries has been described. In [39], EO was utilized for the EMO considering the energy storage devices and the emissions from the associated DERs. In [40], EO was employed for estimating the undefined parameters for the lithium-ion batteries. In [41], EO was employed for identifying the prediction of oil breakdown voltage considering the barrier impact.

In this paper, an optimal operating strategy based on EO is developed for the techno-economic and environmental optimization scheme for MGs with multiple RESs. For this target, two objective functions are represented for minimizing the generation costs and minimizing the emissions of environmental pollution caused by them. The proposed algorithm is tested on two systems in order to verify its effectiveness and efficiency. The two systems are IEEE 33-bus and a practical large-scale 141-bus system of AES-Venezuela in the metropolitan area of Caracas. Added to that, EO is compared with other recent algorithms of DE and RAO algorithms. The main contributions of this paper can be summarized as follows:

- Proposing an operational optimization problem of MG incorporating PV, WT, and BG with consideration of the uncertainties of PV and wind as RESs.
- Simultaneously minimizing the operational costs and the accompanied pollutants.
- Hourly load variations over a 24-h scheduling horizon are handled.
- EO technique is employed with higher performance compared to DE and RAO.
- The validity of the proposed methodology is validated on a large-scale 141-bus real distribution system.

Four additional rest sections of the current paper are organized thusly: Section 2 shows the mathematical formulation of the MG operation. The EO algorithm is developed in Section 3. Section 4 reveals the simulation results on the two small and large scale tested distribution systems. Section 5 concludes the paper findings.

2. Problem Formulation

DGs based on renewable energies are the main technologies that greatly affect the operation of the MG units. Because of their stochastic nature, optimal MG operation has to effectively handle their types and associated uncertainties in hourly basis. In this section, an optimization scheme is presented for the techno-economic and environmental operation of MGs that are established with several DGs based on renewable energies, including PV/WT/BG considering hourly variable load demand.

2.1. Types of DGs

Four types of the DG resources are classified based on their ability to deliver active and reactive powers [42–44]. In the first type, the DG units supply active power only. In Type-2, the DG units provide reactive power only. The DG units in Type 3 inject real and reactive power. The 4th type of DG units injects the active power and consumes reactive power. In this work, the WT model is considered Type-4. The related reactive power to be consumed by these units is obtained by [45].

$$Q_{DG,i} = \left(0.05 + 0.04 P_{DG,i}^2 \right) \tag{1}$$

where $P_{DG,i}$ and $Q_{DG,i}$ are the active and reactive powers of the *DG* unit i, respectively.

2.2. Modeling of Renewable Energy Sources
2.2.1. Photovoltaic DGs

The small-scale PV DGs are the most common renewable sources in the MGs. PV modules are usually modeled using single, double, and triple diode-equivalent circuits [46,47]. Unfortunately, the produced power is intermittent and varied in each hour with high uncertainty levels due to their dependency on the solar irradiances. Therefore, they should be treated with an effective way for each hour where the uncertainty of solar irradiance is modeled by the Beta Probability Density Function (PDF). Consequently, in each hour, different states of the solar irradiance are considered to generate its Beta-PDF. For each state of solar irradiance s, the output power from the PV module, $P_{pv0}(s)$, can be expressed as follows [48,49]:

$$FF = \frac{V_{MPP} \times I_{MPP}}{V_{OC} \times I_{SC}} \tag{2}$$

where

$$P_{pv0}(s) = N \times FF \times V_y \times I_y \tag{3}$$

$$V_y = V_{OC} - K_v \times T_{cy} \tag{4}$$

$$I_y = s \left[I_{sc} + K_i \times (T_{cy} - 25) \right] \tag{5}$$

$$T_{cy} = T_A + s \left(\frac{N_{OT} - 20}{0.8} \right) \tag{6}$$

$$f_b(s) = \left\{ \begin{array}{ll} \frac{\Gamma(\alpha+\beta)}{\Gamma(\alpha)\,\Gamma(\beta)} \, s^{(\alpha-1)} \, (1-s)^{(\beta-1)} & 0 \leq s \leq 1, \alpha, \beta \geq 0 \\ 0 & otherwise \end{array} \right\} \tag{7}$$

$$\beta = (1-\mu) \left(\frac{\mu\,(1+\mu)}{\sigma^2} - 1 \right) \tag{8}$$

$$\alpha = \frac{\mu \times \beta}{1 - \mu} \tag{9}$$

$$\rho(s) = \int_{s_1}^{s_2} f_b(s) \, ds \tag{10}$$

$$P_{pv}(t) = \int_0^1 P_{pv0}(s)\rho(s)ds \qquad (11)$$

where N is the module number; s is the solar irradiance kW/m^2; K_i and K_v are current and voltage temperature coefficients (A/°C and V/°C), respectively; T_{cy} and T_A are cell and ambient temperatures (°C), respectively; N_{OT} is the nominal operating temperature of the cell in °C; *FF* is the fill factor; V_{oc} and I_{sc} are the open circuit voltage (V) and short circuit current (A), respectively; V_{MPP} and I_{MPP} are the voltage and current at the maximum power point, respectively; $f_b(s)$ is the Beta-PDF of s; α and β are the parameters of the Beta-PDF; μ and σ are the mean and standard deviation of the random variable s, respectively; s_1 and s_2 are the solar irradiance limits of state (s); and $\rho(s)$ is the probability of the solar irradiance state (s) during any specific hour.

Figure 1 describes in detail the calculation of the total average power at each hour including the uncertainties of solar irradiance. As shown, the related uncertainties are modeled using Beta-PDF where the day is split into 24-h periods, each of which is 1 hr. From the collected historical data, the mean and standard deviation of the hourly solar irradiance of the day is estimated. For each hour, different states of the solar irradiance among the Beta-PDF with equal steps are taken. In this study, each hour has 20 states for solar irradiance with a step of 0.05 kW/m^2. Accordingly, the PV output power is obtained for each state using Equation (3). Besides, the probability of the solar irradiance state (s) is estimated using Equation (10). Thus, the average output power of the PV module at any specific hour can be obtained using Equation (11) [48]. This study considers that a PV unit is associated with the type of converter that can deliver active power only (i.e., unity power factor) as the standard IEEE 1547 [50].
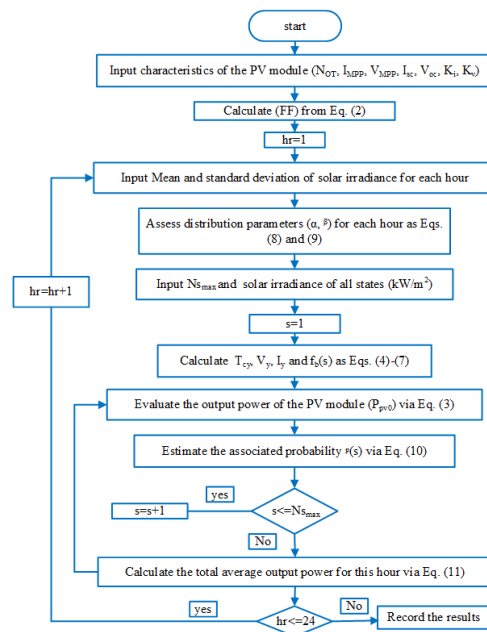
Figure 1. Evaluation of PV output power considering the uncertainties in solar irradiance.

2.2.2. Wind Turbine DGs

The WT-DGs are renewable sources, as well, where their produced powers are intermittent and varied in each hour with high uncertainty levels due to the dependency on wind speed. Generally, the power output from WT is calculated as Equation (12) [51]:

$$
P_W(v) = \begin{cases} 0 & 0 \leq v \leq v_{ci} \\ P_r \times \left(\frac{v - v_{ci}}{v_r - v_{ci}} \right) & v_{ci} \leq v \leq v_r \\ P_r & v_r \leq v \leq v_{co} \\ 0 & v \geq v_{co} \end{cases} \tag{12}
$$

where v_{co} and v_{ci} are the cut-out and cut-in wind speeds of Wind Turbines (WT), respectively; v is the average wind speed of the hour; v_r is nominal operating wind speed of WT; and P_r is the maximum power generated by the WT.

For the WT-DGs, the uncertainty of wind speed is modeled by the Weibull-PDF. The Weibull-PDF $f(v)$ is formulated as in Equations (13)–(15) [52,53]:

$$
f(v) = \frac{K}{C} \left(\frac{v}{C} \right)^{K-1} exp \left(\frac{-v}{C} \right)^{K} \tag{13}
$$

$$
K = \left(\frac{\sigma}{v_m} \right)^{-1.086} \tag{14}
$$

$$
C = \frac{v_m}{\Gamma \left(1 + \frac{1}{k} \right)} \tag{15}
$$

where K and C are the shape and scale indexes of the Weibull-PDF; v_m is the mean wind speed; and σ is the standard deviation.

Based on that, in each hour, different states of the wind speeds are generated. Accordingly, the output power of the WT-DG is obtained for each state using Equation (12). Besides, the probability of the wind speed for each state is estimated using Equation (16).

$$
\rho(v) = \int\limits_{vw_1}^{vw_2} f(v) dv \tag{16}
$$

where $\rho(v)$ is the probability of wind speed in each state whereas vw_1 and vw_2 are the regarding limits of the wind speed.

Thus, the average output power of the WT-DG for each hour is calculated using Equation (17) [48].

$$
P_w(t) = \int\limits_{1}^{25} P_w(v) \rho(v) dv \tag{17}
$$

Figure 2 describes in detail the calculation of the total average power at each hour including the uncertainties of wind speed, where each hour has 20 states for wind speed with a step of 5% of the maximum wind speed.

2.2.3. Biomass DGs

The biomass generators (BGs) are firm generation DGs. The resulted BGs power is constant with no associated uncertainties in its rated value. The BG active and reactive powers at bus i can be expressed as in [36]:

$$
Q_{BG,i} = a_i \times P_{BG,i} \tag{18}
$$

$$
a_i = \pm tan \left(cos^{-1}(PF_{BG,i}) \right) \tag{19}
$$

where $Q_{BG,i}$ and $P_{BG,i}$ are the reactive and active powers associated with BG unit i, respectively. $PF_{BG,i}$ refers to the lag/lead operating biomass power factor, and a_i takes positive or negative signs for the BG when supplying and consuming reactive powers, respectively.
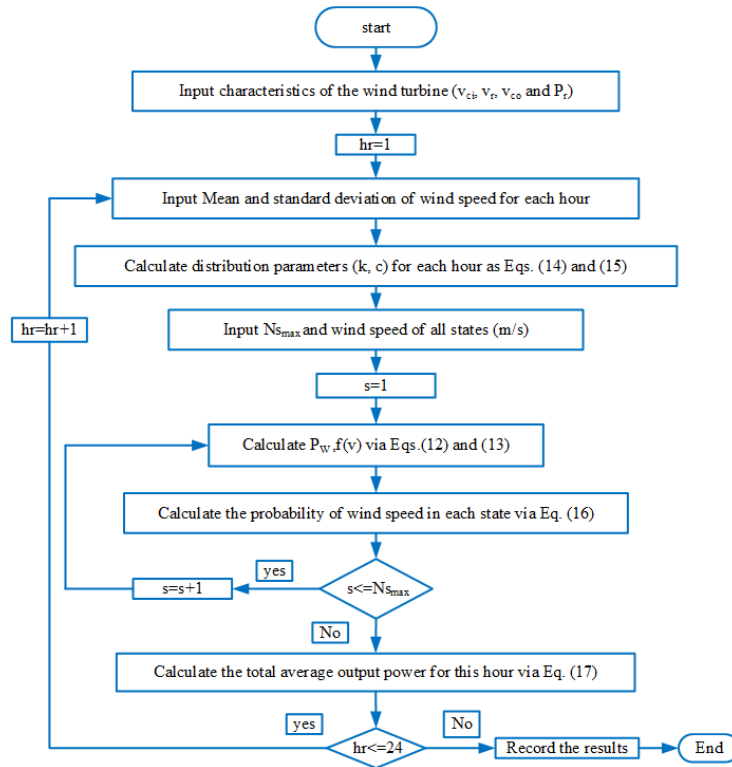
Figure 2. Evaluation of WT output power considering the uncertainties in wind speed.

2.3. Techno-Economic and Environmental Optimization Scheme of MGs

The optimal operation of a typical MG is investigated to reduce the economical operational costs and the accompanied pollutants simultaneously over a 24-h scheduling horizon.

2.3.1. Objective Function

Nowadays, the environmental emission reduction comes with great importance in order to reduce emission levels [54]. In this work, the goal is to optimize two conflicting cost functions simultaneously, which are the operating cost and the emissions of the WT, PV, BG, and grid. The objective function is modeled as follows:

$$Min\left[OC_t(P_{BDG}, P_w, P_{pv}, P_{grid}) + H.E_t(P_{BDG}, P_w, P_{pv}, P_{grid})\right] \tag{20}$$

where OC_t and E_t are the total operational and emission costs in the MG for each hour (*t*), which are functions of the output powers of the renewable sources and grid; P_{BG} is the output of BGs; P_w is the scheduled output of WT units; P_{pv} is the scheduled output of PV units; P_{grid} is the grid output power; and H is the price penalty factor ($/Ton CO_2). The price penalty factor was used [55], which is the ratio between the maximum fuel cost and the maximum emission of the associated generator

The total operational cost function is expressed in Equation (21) as

$$OC_t = \sum_{i=1}^{N_w} C_{pw,i,t} + \sum_{i=1}^{N_{pv}} C_{pv,i,t} + C_{BG}\sum_{i=1}^{N_{BG}} P_{BG,i,t} + C_{grid}P_{grid,t} \tag{21}$$

The total emission cost function can be expressed in Equation (22) as follows:

$$E_t = E_w\sum_{i=1}^{N_w} P_{w,i,t} + E_{pv}\sum_{i=1}^{N_{pv}} P_{pv,i,t} + E_{BG}\sum_{i=1}^{N_{BG}} P_{BG,i,t} + E_{grid}P_{grid,t} \tag{22}$$

where N_w is the number of WT units; N_{pv} is the number of PV units; N_{BG} is the number of BG units; C_{pw} is the operational costs of WT (\$); C_{pv} is the operational costs of PV units (\$); C_{BG} is the cost coefficients of the operation and maintenance of BG; C_{grid} is the cost coefficients related to grid; and E_w, E_{pv}, E_{BG}, and E_{grid} are the emission coefficients related to WT, PV, BG, and the grid, respectively.

2.3.2. Operational Costs

First, for the WT-DGs, the operational cost is the summation of two parts. The first part refers to the cost of the actual output power of the WT. The second part is the penalty cost of unavailable wind output power that refers to the deviation between the available and scheduled wind powers. At time *t*, the total operational costs of each WT (*i*) can be represented, as in [56], as

$$C_{pw,i,t} = \begin{cases} c_w P_{w,i,t} + c_{pw}(P_{wav,i,t} - P_{w,i,t}), & if\ P_{w,i,t} < P_{wav,i,t} \\ c_w P_{w,i,t} + c_{rw}(P_{w,i,t} - P_{wav,i,t}), & if\ P_{w,i,t} > P_{wav,i,t} \end{cases} \quad (23)$$

where $C_{pw,i,t}$ is the total operating cost of the wind, c_w is the operational cost of the wind output (\$/kW), c_{pw} is the penalty costs for under-estimation power of the WT (\$/kW), $P_{wav,i,t}$ is the available *i*th WT power at time t (kW), and c_{rw} is the reserve cost for over-estimation wind turbine power (\$/kW).

Second, for the PV units, the operational costs for each unit (*i*) at each time (*t*) are described as in [56]:

$$C_{pv,i,t} = \begin{cases} c_{pv} P_{v,i,t} + c_{ppv}(P_{pv\_av,i,t} - P_{pv,i,t}), & if\ P_{pv,i,t} < P_{pv\_av,i,t} \\ c_{pv} P_{v,i,t} + c_{rpv}(P_{pv,i,t} - P_{pv\_av,i,t}), & if\ P_{pv,i,t} > P_{pv\_av,i,t} \end{cases} \quad (24)$$

where $C_{pv,i,t}$ is the total operating cost of the PV, c_{pv} is the operational cost of the PV units (\$/kW), c_{ppv} and c_{rpv} are, respectively, the penalty costs for under-estimation and over-estimated powers (\$/kW), and $P^{pv\_av,i,t}$ is the available power that can be produced (kW).

The first parts of Equations (23) and (24) represent the cost based on the actual PV and WT generation power, while the second part represents the costs due to under-estimation or over-estimation. The under-estimation costs are related to penalties due to the generated PV, and WT output power is less than the scheduled one, whereas the over-estimation costs are related to the reserve costs in case the scheduled output power is greater than the available generated power for both PV and WT.

2.4. Constraints

For the optimal operating strategy in MGs, different equality and inequality constraints have to be maintained as presented in Equations (25)–(31). Equations (25) and (26) represent the active and reactive power balance constraints mentioned as P_s and Q_s that are the supplied active and reactive power by the main feeder and the active and reactive power losses denoted by P_{Tloss} and Q_{Tloss} in the MG, respectively [57,58]. Equations (27)–(29) present the allowable limits of the output powers of different RERs. Equation (30) represents the output power for BG; PV and WT units must follow their operating limits. The power factor (PF) limits for each BG are maintained as in [59]. The bus voltage (*V*) limits should be in the range of [0.95–1.05] for each bus *j* [59], as presented in Equation (31). Equation (32) preserves the thermal capacity of the branches below their maximum thermal capacity for each branch [60,61]. Equation (33) gives the penetration bounds of the total renewable sources capacity in the system (KP) as [62,63]:

$$\left(P_s + \sum_{n=1}^{N_{BG}} P_{BG,n} + \sum_{n=1}^{N_w} P_{w,n} + \sum_{n=1}^{N_{pv}} P_{pv,n} \right)_t = (P_{Tloss} + P_{load})_t \qquad t = 1, 2, \ldots \ldots 24 \quad (25)$$

$$\left(Q_s + \sum_{n=1}^{N_{BG}} Q_{BG,n} + \sum_{n=1}^{N_w} Q_{w,n} \right)_t = (Q_{Tloss} + Q_{load})_t \qquad t = 1,2,\ldots\ldots 24 \qquad (26)$$

$$0 \le P_{BG,i,t} \le P_{BG,max} \qquad i = 1,2,\ldots\ldots N_{BG},\ t = 1,2,\ldots\ldots 24 \qquad (27)$$

$$0 \le P_{pv,i,t} \le P_{pv,max} \qquad i = 1,2,\ldots\ldots N_{pv},\ t = 1,2,\ldots\ldots 24 \qquad (28)$$

$$0 \le P_{w,i,t} \le P_{w,max} \qquad i = 1,2,\ldots\ldots N_w,\ t = 1,2,\ldots\ldots 24 \qquad (29)$$

$$PF_{BG,min} \le PF_{BG,i,t} \le PF_{BG,max} \qquad i = 1,2,\ldots\ldots N_{BG},\ t = 1,2,\ldots\ldots 24 \qquad (30)$$

$$V_{j,min} \le V_{j,t} \le V_{j,max} \qquad j = 1,2,\ldots\ldots nbus,\ t = 1,2,\ldots\ldots 24 \qquad (31)$$

$$I_{br,t} \le I_{br,max} \qquad br = 1,2,\ldots\ldots n_{br},\ t = 1,2,\ldots\ldots 24 \qquad (32)$$

$$\left\{ \sum_{i=1}^{N_{BG}} P_{BG,i} + \sum_{i=1}^{N_w} P_{w,i} + \sum_{i=1}^{N_{pv}} P_{pv,i} \right\}_t \le KP \left\{ \sum_{n=1}^{n_{bus}} P_{load,n} \right\}_t,\ t = 1,2,\ldots\ldots 24 \qquad (33)$$

3. Equilibrium Optimization for Optimal Operation Strategy in MGs

EO Algorithm

The dynamic balance of mass on the control volume is a key source of inspiration for the EO technique. The following three steps can be used to explain its mathematical model:

Step 1: Initialization: In the starting of the optimization process, the EO randomly generates the population. The initial concentrations are calculated using uniform random initialization based on the particle number, population, and dimensions, as in Equation (34) [64]:

$$C_{i,initial} = C_{i,min} + rand_i(C_{i,max} - C_{i,min}), \qquad i = 1,2,\ldots\ldots N_i \qquad (34)$$

where $C_{i,initial}$ refers to the initial vector for each particle (*i*), $C_{i,min}$ and $C_{i,max}$ are the lower and upper bounds of the control variables, $rand_i$ refers to a random distributed vector in [0,1], and N_i is the number of particles.

In this step, the fitness of the initialized particles is estimated, and the best scores are used to find the nominee solutions.

Step 2: Equilibrium pool and candidates: In this step, the EO finds the particle's equilibrium state. The algorithm reaches a near-optimal solution at its equilibrium state. It assigns the best four particles in the population at equilibrium candidates and the fifth one containing the average of the previous best four particles. The pool of equilibrium (Ceq, pool) that helps the EO features in their exploitation and exploration operations is expressed by these five equilibrium candidates.

Step 3: Updating the concentration: The evaluation process for updating each concentration vector (*C*) is carried out as

$$\vec{C} = \overrightarrow{C_{eq}} + (\vec{C} - \overrightarrow{C_{eq}})\vec{F} + \frac{\vec{G}}{\lambda \vec{V}}(1 - \vec{F}) \qquad (35)$$

where C_{eq} is a randomly generated vector ($C_{eq,\ pool}$) from the pool of equilibrium; λ is a random vector [0,1]; *G* is the generation rate; *V* stands for the volume unit, which is equal to one [31]; and *F* is an exponential term that helps the EO algorithm in achieving a balance between the exploration and extraction phases. It can be determined as follows:

$$\vec{F} = e^{-\vec{\lambda}(t - t_o)} \qquad (36)$$

where t_0 is the initial start time, and the time (*t*) depends on the number of iterations (*Iter*) as follows:

$$t = \left[1 - \frac{Iter}{Max\_iter} \right]^{[a_2 * Iter/Max\_iter]} \qquad (37)$$

where *Iter* and *Max_iter* are the initial and maximum iteration numbers, respectively; and a_2 is a constant value equal to 1 that is used to monitor exploitation potential [31]. The following formula can be considered to boost the developed technique's exploration and exploitation abilities.

$$\vec{t_o} = \frac{1}{\vec{\lambda}} \ln\left[-a_1 sign(\vec{r} - 0.5)(1 - e^{-\vec{\lambda}t})\right] + t \tag{38}$$

where a_1 is a constant value of 2 that is used to control exploration ability [31], *r* is a random vector in the range of 0 to 1, and the term ($sign(r - 0.5)$) affects exploration and exploitation directions. The generation rate (*G*) is calculated as follows:

$$\vec{G} = \overrightarrow{G_{cp}}\left(\overrightarrow{C_{eq}} - \vec{\lambda}\vec{C}\right)\vec{F} \tag{39}$$

$$\overrightarrow{G_{cp}} = \left\{ \begin{array}{ll} 0.5r_1 & r_2 \geq G_p \\ 0 & r_2 \leq G_p \end{array} \right\} \tag{40}$$

where G_{cp} is the control parameter of the generation rate that is used to update the EO technique, G_P is the generation probability that equals 0.5 [31], and r_1 and r_2 are random numbers in the range [0,1]. Figure 3 shows the EO based optimal operation procedure of MG in the tested distribution systems.
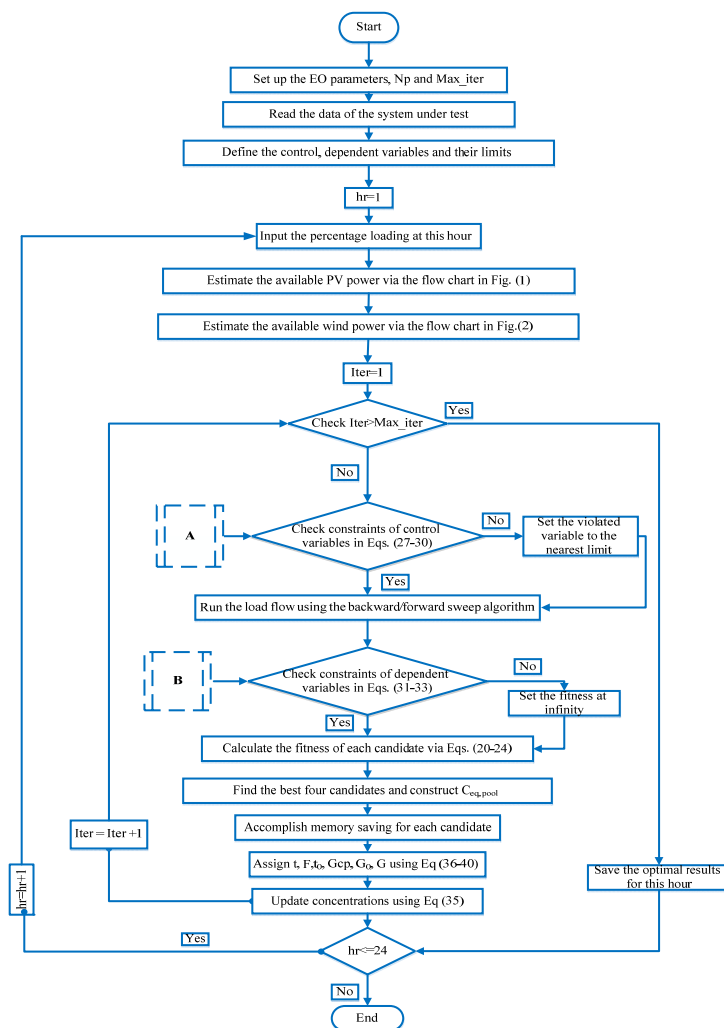
Figure 3. Flowchart of the optimal proposed operation procedure of MG.

4. Simulation Results

The EO is applied to determine the optimal operation of MG to achieve technical and economic benefits with respecting the associated operational and emission costs for two distribution systems. For the optimal operation, the control variables are the active power resulted from different RERs, including BGs, wind, and PV, and the power factor of BGs.

4.1. Test Systems

Two test systems are considered to apply the proposed operation strategy. The 1st test system is the 12.66 kV IEEE 33-bus distribution system. It contains 33-node and 32 branches whilst its total active and reactive demand is 3715 kW + 2300 kVAr [65]. Figure 4 displays the first MG configuration where this system includes 1.1 MW-WT connected at bus 3, and five PV generators with ratings of 20, 25, 30, 40, and 50 kW are connected at buses 13, 17, 20, 27, and 33, respectively. In addition to that, four BGs with ratings of 400, 500, 700, and 1000 kVA are installed at buses 15, 25, 9, and 31, respectively [36].
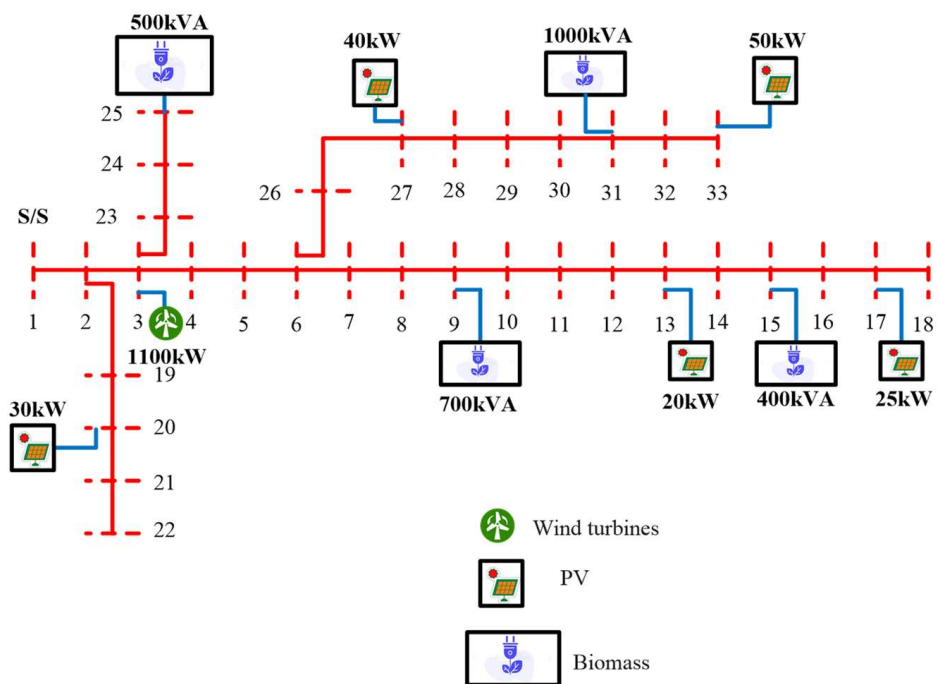
Figure 4. First MG configuration.

The 12.47 kV AES-Venezuela in the metropolitan area of Caracas that is modeled by 141-node is considered the large-scale test system. The total peak load is 12.19 MW + 6.2894 MVAR [66,67]. Figure 5 displays the second MG configuration where the 141-bus system is modified to include one WT with a capacity of 3 MW connected at bus 50, and five PV generators with ratings of 40, 50, 60, 80, and 100 kW are connected at buses 60, 70, 80, 90, and 100, respectively. Added to that, four BGs with ratings of 650, 2500, 3500, and 2000 kVA are installed at buses 109, 16, 78, and 63, respectively [36]. For both studied systems, the load profile is taken into consideration where Figure 6 describes this hourly loading as a percentage of the peak load [68].
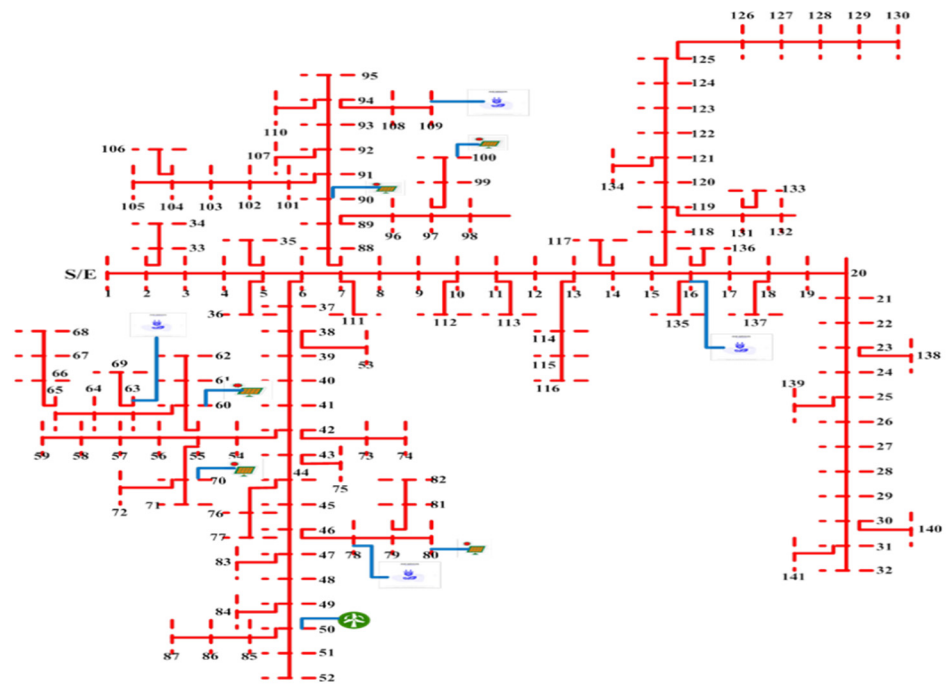
Figure 5. Second MG configuration.
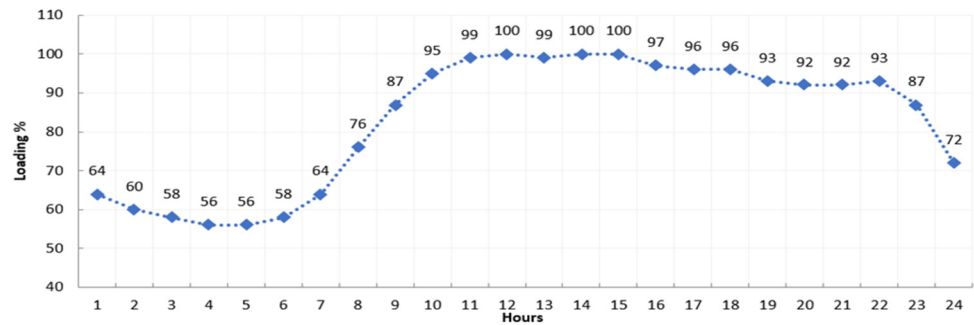
Figure 6. Daily load demand profile.

Also, the maximum iterations number equals 400 for the tested systems. The particles number is considered to be 50 for IEEE 33-bus and 100 for the large scale 141-bus system. The numbers of iterations and particles are considered the same for all competitive algorithms for a fair assessment of their performance. Additionally, the allowable number of the RERs units, BGs, wind, and PV are assumed as 4, 1, and 5, respectively. The maximum penetration level is limited by 60% of the load demand [69].Table 1 shows the data of operational costs and the emission for the shared energy sources in the microgrid.

Table 1. Operational costs as well as emissions of the renewable sources and the grid.

Energy Source	CO$_2$ Emission (Ton Co$_2$/MWh)	Operational Costs ($/MWh)
BG	E_{BG} = 0.733 [36]	c_{BG} = 46 [36]
Grid	E_{grid} = 0.91 [36]	c_{grid} = 76 [36]
PV	E_{pv} = 0.045 [70]	c_{pv} = 6 [71]
WT	E_w = 0.016 [72]	c_w = 7 [71]
Price penalty factor	H = 10 $/Ton Co$_2$ [73]	

4.2. Cases Studied

In this paper, three different cases studied are performed for each system, and these cases are described as follows:

Case 1: this is considered the basic system condition without adding DGs units.

Case 2: in this case, the MG is operated without considering the optimal control settings of BGs, WT, and PV with daily load variations.

Case 3: this case develops the optimal operation of the MG with optimal control settings by using the EO algorithm for BGs, WT, and PV, simultaneously with considering the daily load variations.

4.3. Simulation Results of 33-Bus Test System

4.3.1. Case 1: Without DGs

In the first case, the hourly load flow is carried out at each loading hour of the 33-bus system without DGs installations. At the peak loading (hour 12) and without DGs units, the initial power losses equal 211.2 kW. Bus 18 has a minimum voltage that equals 0.9038 p.u. as in [65].

4.3.2. Case 2: MG without Optimal Control on BGs, Wind, and PV with Daily Load Variation

In the second case, MG is operated without optimal control on DGs whereas the WTs and PVs generate its available power, and the BGs generate its full capacity at a unity power factor. For the small-scale PV DGs, the Beta-PDF is used to model the uncertainty of the solar irradiance and the evaluation of PV output power is performed as described in Figure 1 considering the uncertainties in solar irradiance. From the collected historical data, the mean and standard deviations of the hourly solar irradiance of the day are estimated. Based on that, the Beta-PDF is generated for each hour. Consequently, 20 different states of solar irradiance among the Beta-PDF are taken with equal step sizes of 0.05 kW/m^2 for each hour. Figure 7 displays their produced powers from each PV source at each hour. There is no power output to be generated from the PV sources in the first and last five hours in the morning and evening since there are no solar irradiances at these hours. Additionally, the highest output of each PV source occurred at 12 pm, with 55.2, 55.3%, 55.4%, 55.2% and 55.3% from their installed capacities for the PV sources at buses 13, 17, 20, 27, and 33, respectively.
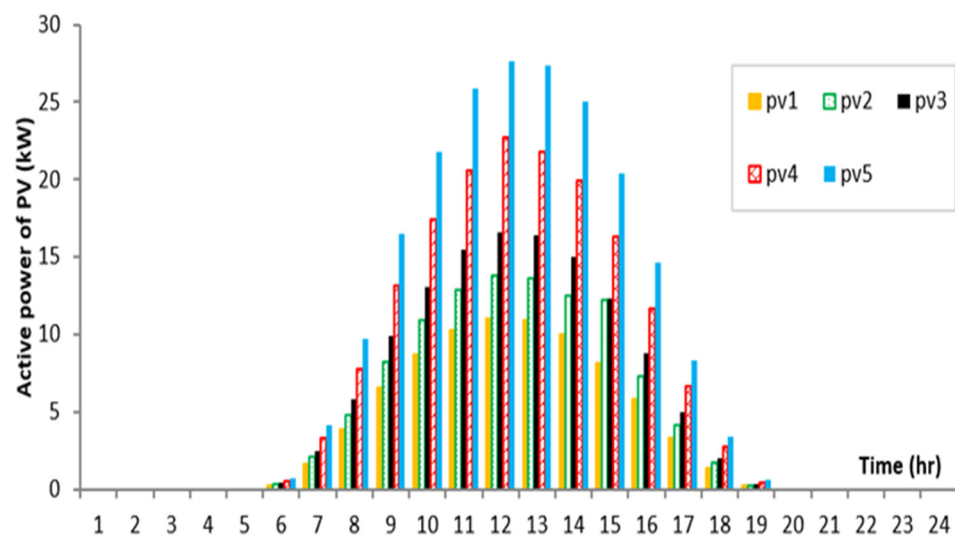
Figure 7. Scheduled output power from each PV at each hour for the first MG.

For the WT-DGs, the Weibull-PDF is used to model the uncertainty of the wind speed and the evaluation of WT output power, considering that the uncertainties in wind speed is

performed as described in Figure 2. For each hour, the mean and standard deviations of the hourly wind speed of the day are estimated, and the associated Weibull-PDF is generated. Similarly, 20 states of the wind speed, for each hour, are considered where the step is 1.25 m/s. Figure 8 displays the hourly active and reactive powers that are produced from the WT source at bus 3. The type 4 distributed generation, WT-DG, is used in this study to deliver the active power and to consume reactive power using the induction generators at a fixed speed. At hour 18, the WT-DG produces the highest active power with 692.1 kW and consumes the highest reactive power with 69.16 kVAr. Thus, it is operated with 62.92% from its full capacity. At hour 7, the WT-DG is operated with 36.53% from its full capacity, where it produces the least active power with 401.8 kW and consumes the least reactive power with 56.45 kVAr.
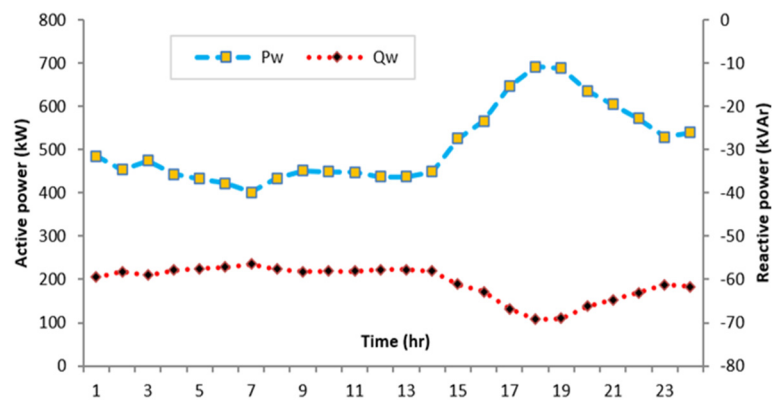
Figure 8. Scheduled active and reactive power from wind at each hour for the first MG system.

On the other side, the BGs are operated at full capacity without optimal control. By running the load flow algorithm for these hourly circumstances, Figure 9 shows the total active power of each type of DG and the summation of loads and the hourly power losses. Then, Figure 9 concludes the following findings:

- During nine hours (1–8 and 24), the sign of the grid power is negative. At these hours, the DGs generated power in the MG is greater than the loads and the MG power losses so that the excess power is back to the grid bus. Consequently, there is surplus active power to be generated from the DGs in the MG and injected to the grid bus. The maximum extra power is reached at hour 4 with 913.438 kW, whilst the minimum surplus power is reached at hour 8 with 191.873 kW.
- During the other 15 h, the MG absorbs active power from the grid bus. The maximum absorbed power is reached at hour 14 with 655.4086 kW, whilst the minimum absorbed power is reached at hour 23 with 160.7345 kW.
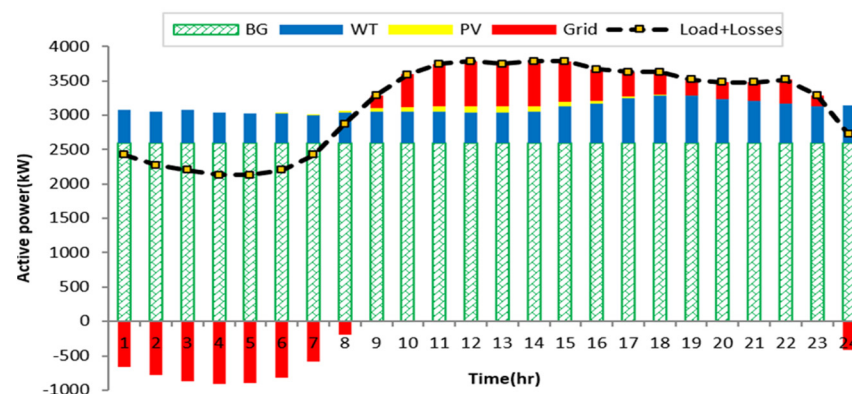
Figure 9. Results of the first MG operation without optimal control.

4.3.3. Case 3: MG with Optimal Control on BGs, WT, and PV Simultaneously with Daily Load Variation

In the third case, the EO algorithm is applied to operate the economical solution of MG considering the emission concerns by simultaneously minimizing the hourly operational costs and the accompanied pollutants. Added to that, the assessment of EO performance is carried out compared with other optimization algorithms such as DE [74] and RAO [75] techniques at different hours. The convergence comparisons between the developed EO, DE, and RAO algorithms at hours 6 and 12 are described in Figure 10 where the associated outcomes of them are tabulated in Tables 2 and 3 at hours 6 and 12, respectively. At hour 6 (Table 2), the developed EO achieves the minimum objective function of $124.4644, whereas DE and RAO algorithms acquire objective functions of $127.5425 and $124.6005, respectively. Similarly, at hour 12 (Table 3), the developed EO achieves the minimum objective function of $224.2039, whereas the DE and RAO algorithms acquire objective functions of $234.7754 and $224.2165, respectively.

(**a**) At hour 6   (**b**) At hour 12
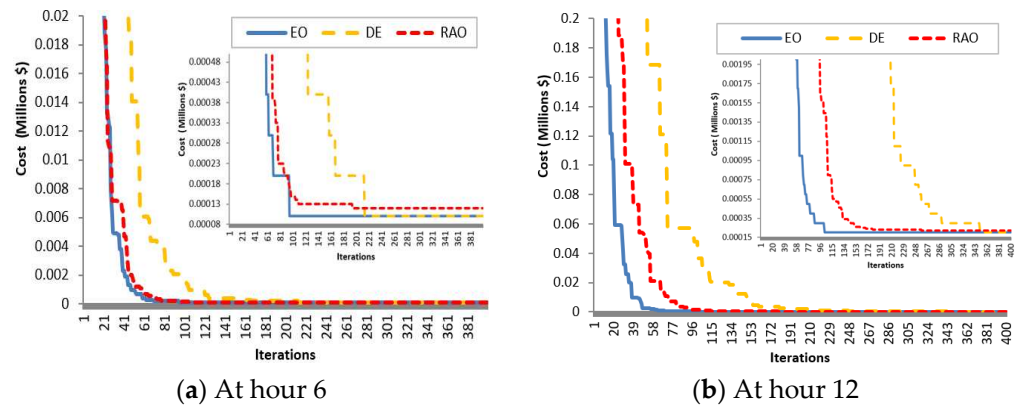
Figure 10. Convergence curves of EO, DE and RAO for the first MG at hours 6 and 12, respectively.

Table 2. Optimal operations of MG at hour 6 using EO, DE, and RAO algorithms.

	EO	DE	RAO
P_w (kW)	423.1	423.1	423.1
Q_w (kVAR)	−57.1605 *	−57.1605 *	−57.1605 *
P_{pv} (kW)	0.2696, 0.3378, 0.4059, 0.5392, 0.6755	0.2697, 0.3379, 0.4058, 0.5392, 0.6755	0.2696, 0.3378, 0.4059, 0.5392, 0.6755
kW P_{BG} (Power factor)	304.0531 (0.8508), 0.043 (0.8514), 70.7528 (0.9895), 492.6431 (0.925)	391.616 (0.9878), 330.0176 (0.8794), 83.1291 (0.85), 55.6774 (0.9869)	315.214 (0.9889), 213.145 (0.8535), 1.449 (0.8521), 337.6556 (0.8501)
P_{grid} (kW)	879.0094	888.9166	879.1928
Pu V_{min} (bus)	0.9761(18)	0.9795(33)	0.9796(33)
$PTloss$ (kW)	17.1294	19.9847	17.2843
C_{BG} ($)	39.9046	39.5802	39.9033
C_w ($)	2.9619	3.2674	3.0122
C_{PV} ($)	0.0197	2.3282	0.0915
C_{grid} ($)	66.8047	67.5577	66.8187
E_{BG} ($)	6.7057	6.6512	6.7055
E_{grid} ($)	7.999	8.0891	8.0007
E_{pv} ($)	0.001	0.001	0.001
E_w ($)	0.0677	0.0677	0.0677
OC_t ($)	109.691	112.7335	110
E_t ($)	14.7734	14.809	14.7748
Objective function ($)	124.4644	127.5425	124.6005

* negative sign means that wind consumes reactive power.

Table 3. Optimal operation of MG at hour 12 using EO, DE, and RAO algorithms.

	EO	DE	RAO
P_w (kW)	437.4	437.4002	437.4
Q_w (kVAR)	−57.6528 *	−57.6528 *	−57.6528 *
P_{pv} (kW)	11.0451, 13.8367, 16.6283, 22.0901, 27.6733	11.0452, 13.8367, 16.6281, 22.09, 27.6733	11.0451, 13.8367, 16.6283, 22.0901, 27.6733
kW P_{BG} (Power factor)	853.2986 (0.8537), 243.3503 (0.8663), 17.8781 (0.8866), 585.7994 (0.85)	853.9887(0.9), 400.0 (1), 347.2767 (0.85),	848.6954 (0.8505), 312.6636 (0.8506), 126.229 (0.85), 410.301 (0.85)
P_{grid} (kW)	1520	1640	1517.6
Pu V_{min} (bus)	0.9787 (18)	0.9533 (18)	0.9774 (18)
$PTloss$ (kW)	31.3311	57.7494	29.1443
C_{BG} ($)	78.215	73.6582	78.1029
C_W ($)	3.0618	4.7979	3.143
C_{PV} ($)	0.5477	4.0274	0.5887
C_{grid} ($)	115.3172	124.8536	115.3362
E_{BG} ($)	13.1435	12.3778	13.1247
E_{grid} ($)	13.8077	14.9496	13.81
E_{pv} ($)	0.0411	0.0411	0.0411
E_w ($)	0.07	0.07	0.07
OC_t ($)	197.1416	207.337	197.1708
E_t ($)	27.0623	27.4384	27.0457
Objective function ($)	224.2039	234.7754	224.2165

* negative sign means that wind consumes reactive power.

Based on the developed EO, the output powers of the PV, WT, and BGs are optimized besides the associated power factors of the BGs. Figure 11a shows the percentage apparent power of the BGs at buses 15, 25, 9, and 31 for each hour, whereas Figure 11b displays the hourly optimized value of the power factor. From Figure 11a,b:

- The first BG at bus 31 is operating within range [40:100] % of its capacity to inject apparent power demand to the MG during the day. Similarly, the second BG at bus 15 is operating within range [60:100] % of its capacity during the day excluding hour 6.
- Both BG1 and BG2 at buses 31 and 15 are approximately operating at a power factor of 0.85, which has the minimum power factor to be considered, and so their injected reactive power is directly proportional to their scheduled output power.
- Both BG3 and BG4 at buses 25 and 9 produce very small apparent power at the first five hours, respectively, which has the smallest loadings. Then, their output powers increase through the loading increases, whereas BG3 at bus 25 is operating with 100% of its capacity at hour 6. Added to that, BG4 at bus 9 is operating with 100% of its capacity at hours 12, 14, 17, and 18.
- BG3 at bus 25 is operating at a varied power factor through the day. BG4 at bus 9 is operating at a varied power factor at the first nine hours with low loading values, whilst its power factor is nearly fixed at 0.85 for the next hours.

(**a**) Percentage apparent power
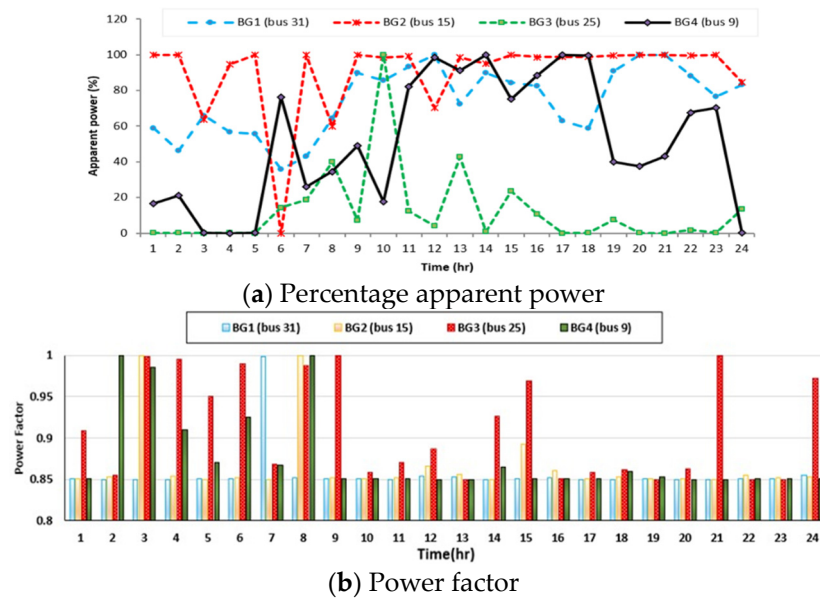
(**b**) Power factor

Figure 11. Hourly Percentage apparent power and power factor for each BG for the first MG system.

To study the hourly power balance operation of the MG, Figure 12 illustrates the total active power for each type of DG and the summation of loads and hourly power losses. This figure leads to the following findings:

- The total generation equals to the loads and power losses at each hour, where the summations of the output powers from the BGs are varied, which is optimally controlled by the developed EO algorithm at each hour.
- The developed EO algorithm optimizes the output powers from WT and PV sources at their available outputs to make use of their environmentally friendly characteristics.
- During the day, there are no excess powers in the MG back to the grid bus. The MG was supplied with the active power from the grid bus. The maximum supplied power is achieved at hour 12 with 1520 kW, whilst the minimum supplied power is reached at hour 5 with 843.97 kW.
- As a result, the supplied power represents 40.58% and 40.34% referred to the loading and power losses at hours 12 and 5, respectively. Therefore, the total produces power from the DGs with 59.42% and 59.66% referred to the loading and power losses at hours 12 and 5, respectively.
- Nevertheless, the penetration of the total DGs power production in the MG does not exceed the penetration limit of 60%.

To assess the voltage quality of the MG operation for each hour, Figure 13 displays the minimum voltage at each hour for the three cases studied. It is shown that the minimum voltage is corrected in cases 2 and 3 where, when the voltages at all hours are below the permissible limit of 0.95 Pu in the case (case 1), the highest minimum voltage occurs at bus 18 at hour 5, whereas the least minimum voltage occurs at the same bus at hour 15. At both hours, the voltage profiles at all MG buses are described in Figure 14. The voltage profile at each bus is improved at light loading at hour 5. At this loading hour, the minimum voltage at bus 18 is corrected from 0.9495 to 0.9877 Pu, which exceeds the minimum limit of 0.95 Pu in case 3; consequently, this improvement represents 4.02%. Additionally, the voltage profile at each bus is improved at peak loading at hour 15, where the minimum voltage at bus 18 is improved with 7.822% and corrects the voltage from 0.9038 to 0.9745 Pu, which exceeds the minimum limit of 0.95 Pu in case 3.
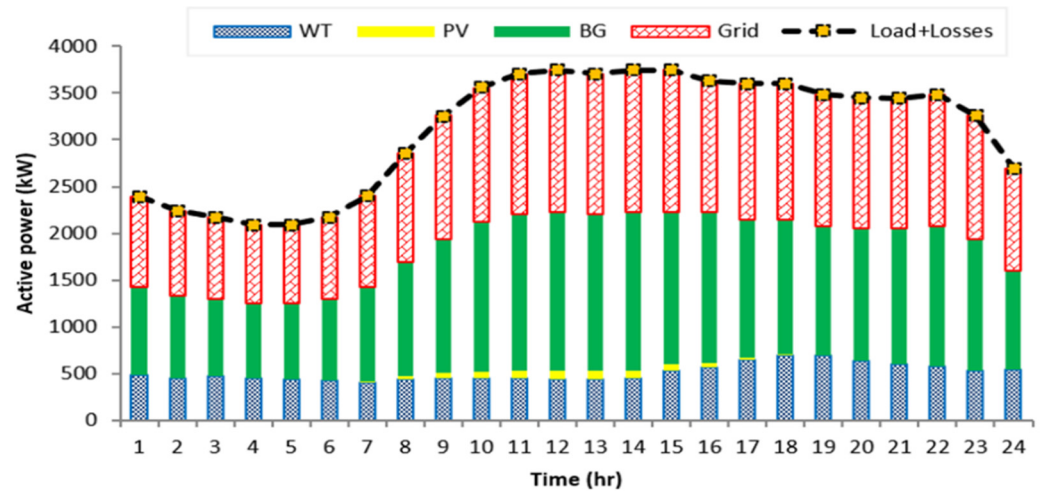
Figure 12. Results of the optimal operation of the first MG.
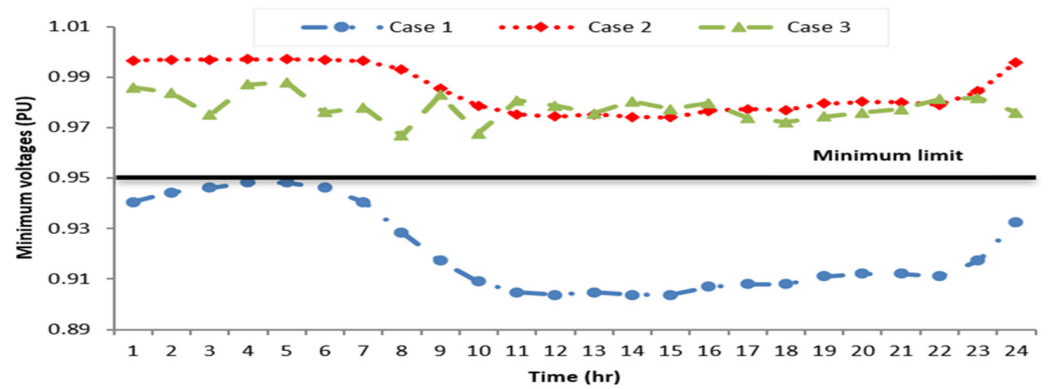
Figure 13. Minimum voltage at each hour for different cases studied of the first MG.

(**a**) At hour 5

(**b**) At hour 15
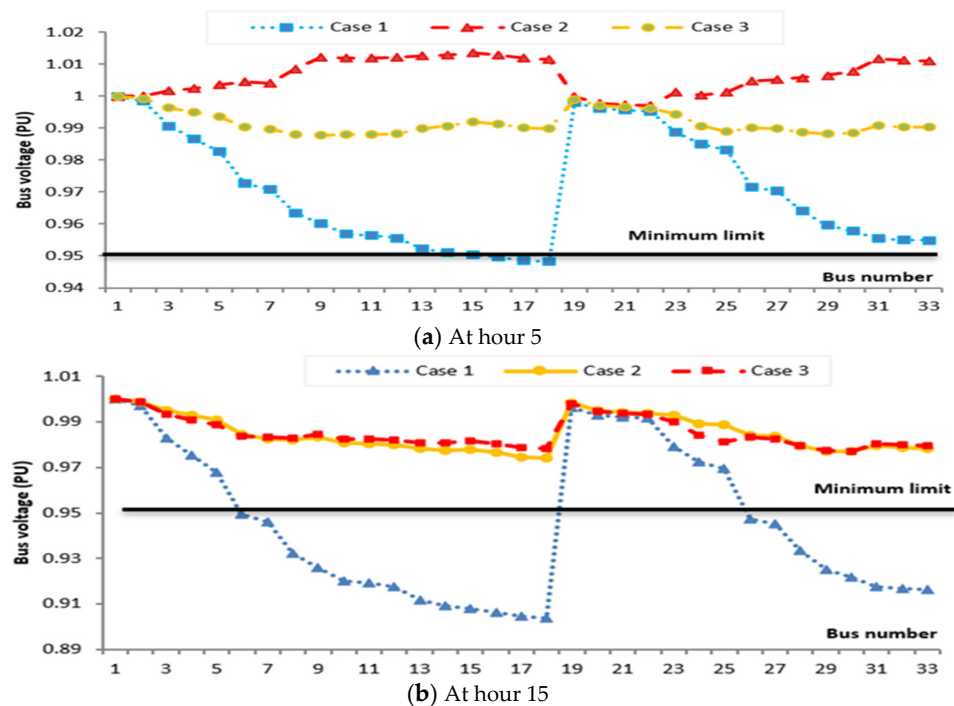
Figure 14. Voltage profile for the first MG at light and peak loading at hours 5 and 15, respectively.

In addition, Figure 15 shows the hourly active power losses for the three cases that are greatly reduced from case 1 to cases 2 and 3, whereas the optimal operating strategy based on the developed EO algorithm in case 3 provides the minimum power losses at each hour through the day. Compared to case 1, the percentages of the reduction in power losses that are achieved by case 3 reach 81.9, 79.6, 73.7, 80.6, 80.9, 74.2, 71.8, 75.5, 84.9, 83.7, 85.3, 85.2, 85.5, 85.2, 84.2, 84.8, 82.1, 81.1, 82.4, 83.1, 83.7, 84.5, 84.3, and 79.8% for hours 1–24, respectively. Compared to case 2, the percentages of the reduction in power losses that are achieved by case 3 reach 41.9, 48.5, 48.6, 61.7, 61.8, 48.6, 31.6, 19.5, 22.3, 18.7, 19.7, 19.4, 19.9, 19.4, 18.3, 19.4, 16.7, 15.7, 17.6, 20.3, 19.1, 19.7, 21.3, and 27.6% for hours 1–24, respectively.
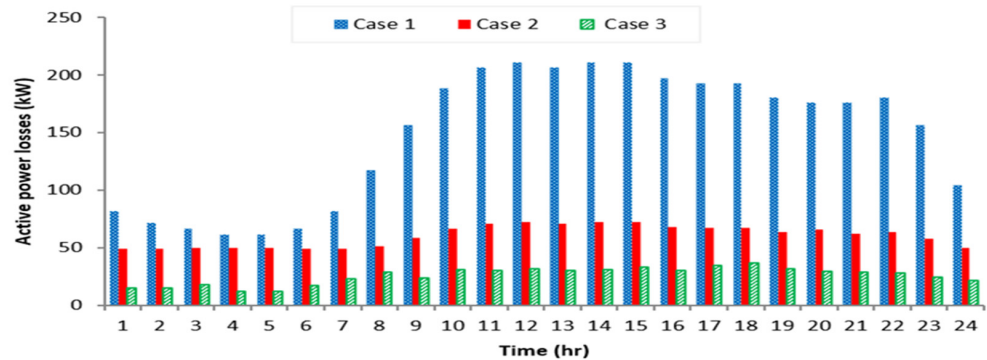
Figure 15. Active power losses at each hour for different cases for the first MG.

Additionally, the hourly operational costs and the associated emissions of the distributed energy sources in the MG for the cases studied are depicted in Figure 16. As shown, the operational costs and the associated emissions in the MG at each hour are greatly reduced from case 1 to cases 2 and 3. Despite that case 2 provides the least operational costs and the emissions in the MG in comparison to case 3, the penetration limit of the total output of the DGs in the MG exceeds the limits of the 60% penetration ratio, as detailed in Figure 9. In Figure 9, the penetration level in case 2 exceeds 100% at nine hours, where it reaches 129.96, 136.83, 143.25, 146.15, 145.67, 140.93, 126.89, 108.86, and 117.60% at hours 1–8 and 24, respectively.

(**a**) MG operational costs
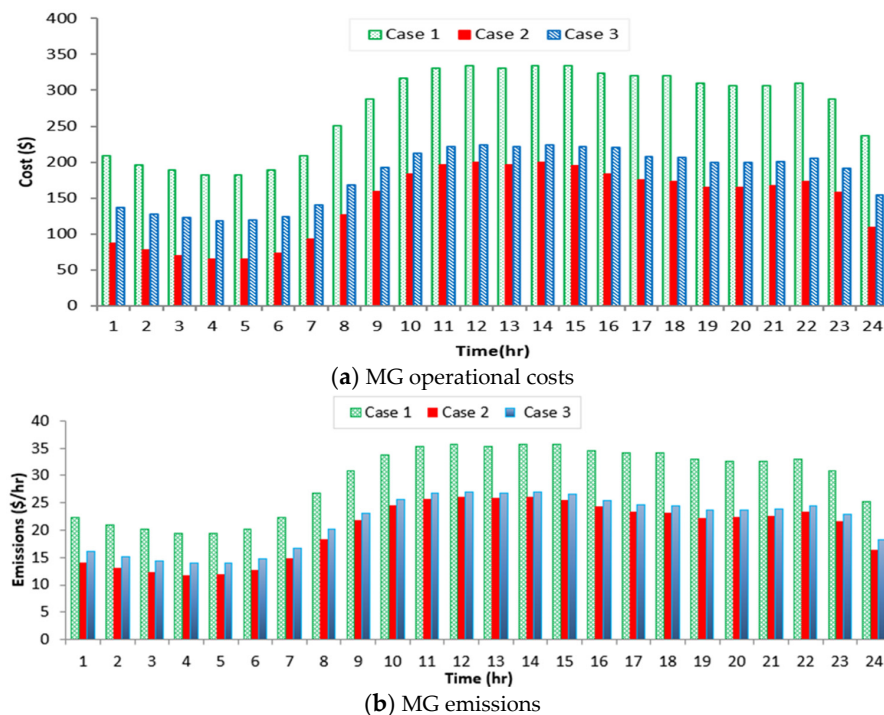
(**b**) MG emissions

Figure 16. Hourly optimal operational costs and the associated emissions in the MG for the first MG.

4.4. Simulation Results of a Large-Scale 141-Bus Test System

In this subsection, the proposed solution methodology is applied on a large-scale 141-bus system. Three cases studied are investigated. The system's initial power loss (without DGs) was 603.821 kW, where bus 87 has the minimum voltage that is 0.9294 Pu. In the 2nd case, the resulted uncertainties of the solar irradiance and wind speed are modeled by Beta-PDF and Weibull-PDF for the PV and WT sources, respectively. Therefore, the PV output power is evaluated at buses 60, 70, 80, 90, and 100. The active and reactive powers are hourly produced from the WT source at bus 50, as displayed in Figure 17.
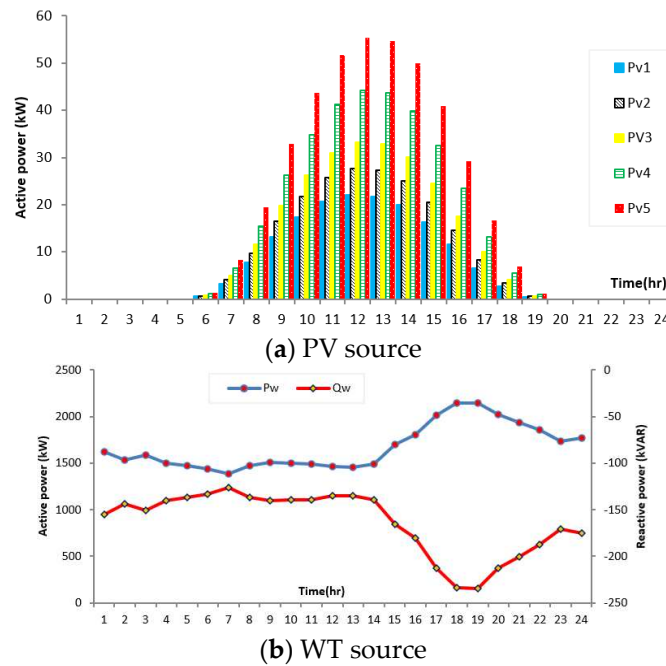
(**b**) WT source

Figure 17. Hourly produced active and reactive power from PV and WT sources for the second MG.

On the other side, the BGs are operated at their full capacity without optimal control. By running the load flow algorithm for these hourly circumstances, Figure 18 shows the total active power of each type of DG and the summation of loads and losses at each hour. During 9 h (1–8 and 24), there is surplus active power to be generated from the DGs in the MG and injected to the grid bus, where the generated power from the DGs in the MG is greater than the loads and the power losses so that the excess power is back to the grid bus. In the other 15 h, the MG absorbs active power from the grid bus.
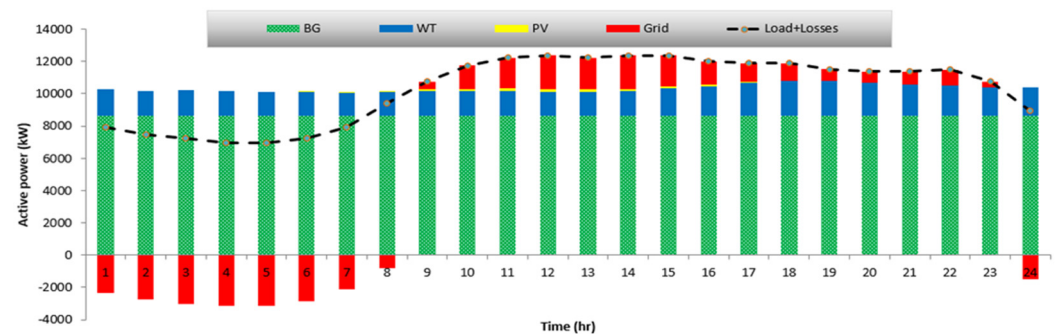
Figure 18. Results of the second MG operation without optimal control.

In the third case, the developed EO algorithm is applied to optimally operate the MG in order to minimize the operational costs and the accompanied pollutants simultaneously over a 24-h scheduling horizon. Based on the developed EO, the output powers of the PV, WT, and BGs are optimized besides the associated power factors of the BGs. Figure 19a

shows the percentage apparent power of the BGs at buses 109, 16, 78, and 63 for each hour, whereas Figure 19b displays the hourly optimized value of the power factor.
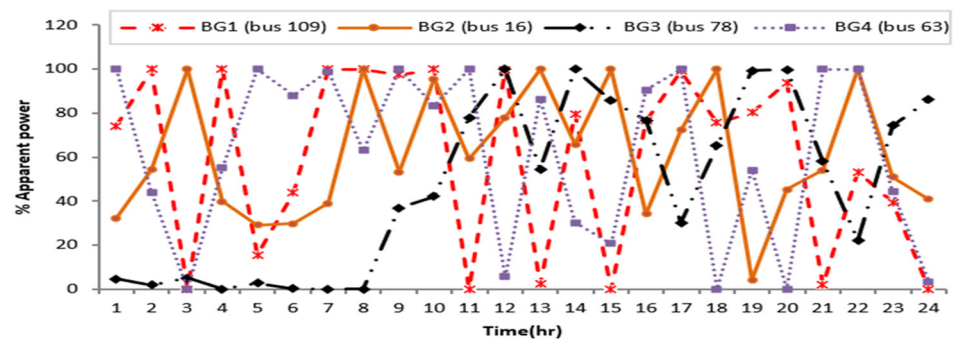
(**a**) Percentage of scheduled apparent power referred to its capacity,
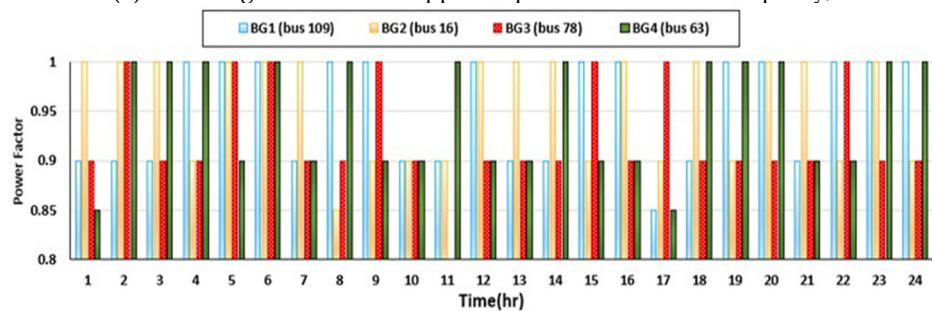
(**b**) Power factor.

Figure 19. Hourly apparent power and power factor of each BG for case 3 for the second MG.

To describe the power balance operation of the MG for each hour, Figure 20 illustrates the total active power of each type of DG and the summation of loads and power losses at each hour. At each hour, the generated grid power is always higher than 40% of summation loads and power losses whereas the penetration level of 60% is preserved by means of the developed EO algorithm.
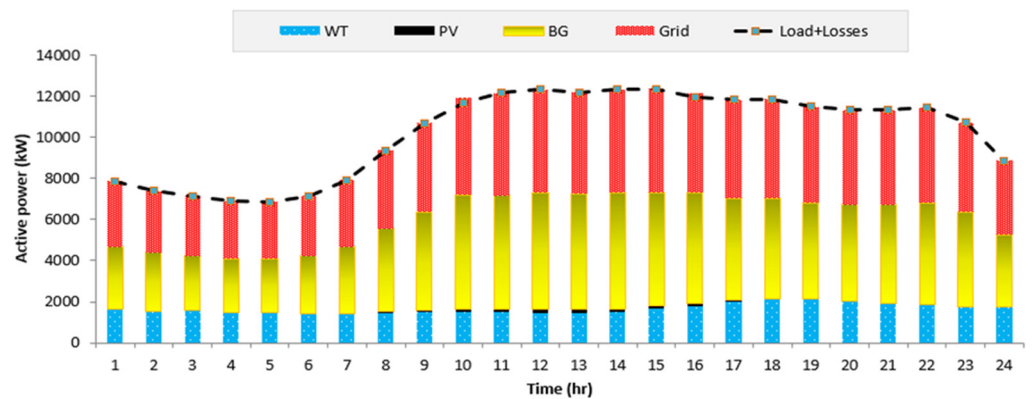
Figure 20. Results of the optimal operation for the second MG.

For each hour, Figure 21 displays the minimum voltage for the three-cases studied. For hours 8–23, the minimum voltages are corrected in cases 2 and 3. In addition, in cases 2 and 3, the minimum voltages at all hours are above the permissible limit of 0.95 Pu. In the initial case (case 1), the highest minimum voltage occurs at bus 87 at hour 5, whereas the least minimum voltage occurs at the same bus at hour 15. At both hours, the voltage profile at all MG buses is described in Figure 22. However, the voltage profile at each bus is improved at light loading at hour 5. At this loading hour, bus 87 has the minimum voltage level in case 3. It is declined from 0.9616 to 0.9914 Pu. Additionally, the voltage profile at each bus is corrected at peak loading at hour 15, where the bus 87 has the minimum voltage

level in case 3 that is declined from 0.9294 to 0.9772 Pu which exceeds the minimum limit of 0.95 Pu; consequently, this improvement represents 5.14%.
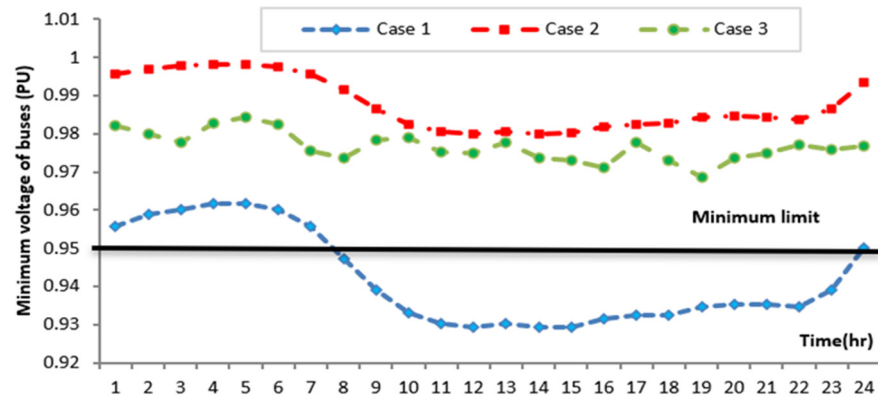
Figure 21. Minimum voltage profiles for different cases studied at each hour **for** the second MG.

(**a**) At hour 5.

(**b**) At hour 15.
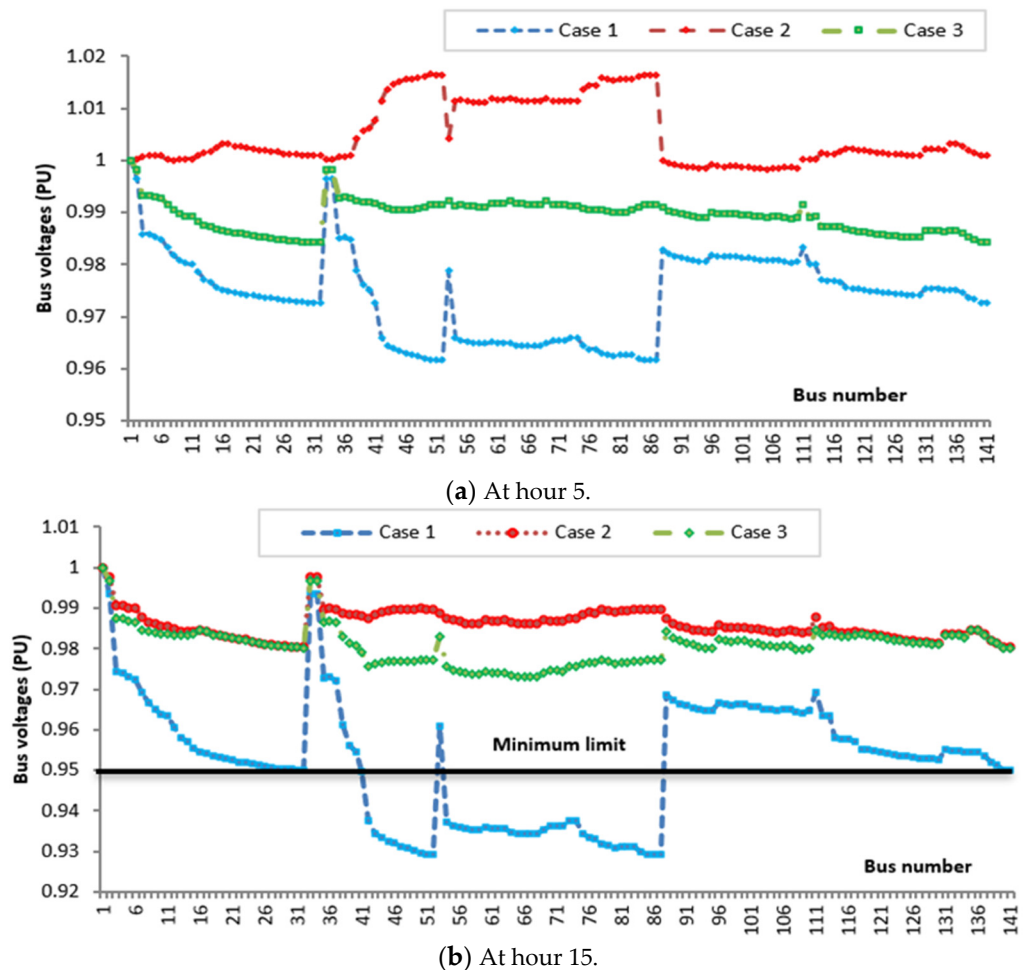
Figure 22. Bus voltage profiles for different cases studied at hours 5 and 15 for the second MG.

Moreover, the active power losses at each hour for the three cases studied are depicted in Figure 23. The power losses at each hour are greatly reduced from case 1 to cases 2 and 3, whereas the optimal operating strategy based on the developed EO algorithm in case 3 provides the minimum power losses at each hour through the day. Compared to case 1, the percentages of the reduction in power losses that are achieved by case 3 reached 78.9, 67.3, 58.0, 70.0, 77.1, 64.8, 49.5, 72.5, 79.9, 84.1, 80.2, 79.3, 80.6, 80.4, 73.8, 80.7, 79.9, 75.6, 73.4, 77.7,

80.4, 80.9, 77.2, and 71.3% for hours 1–24, respectively. Compared to case 2, the percentages of the reduction in power losses that are achieved by case 3 reached 66.7, 54.9, 48.3, 65.3, 73.2, 54.2, 13.3, 32.4, 38.9, 46.7, 32.0, 28.0, 32.8, 32.2, 11.9, 37.7, 38.5, 27.0, 23.7, 34.9, 41.9, 41.5, 34.1, and 42.6% for hours 1–24, respectively.
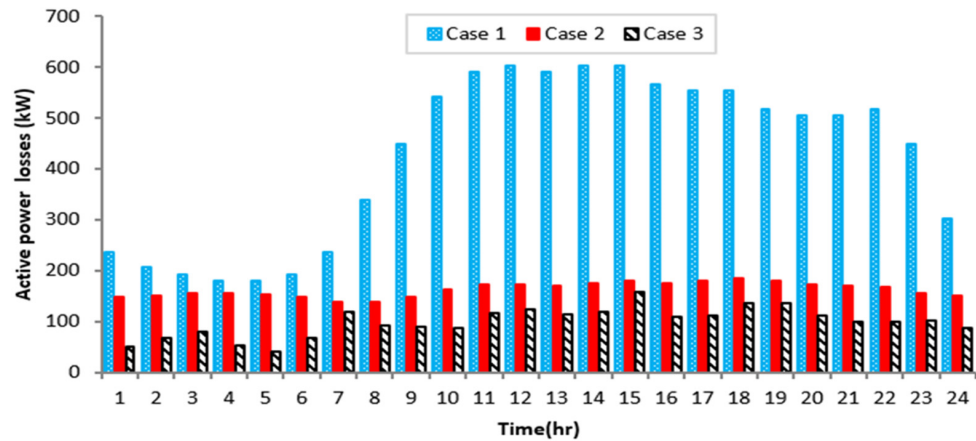
Figure 23. Active power losses for different cases studied at each hour for the second MG.

Additionally, the operational costs and the associated emissions of the distributed energy sources in the MG at each hour for the three cases studied are depicted in Figure 24. However, the operational costs and the associated emissions in the MG at each hour are greatly reduced from case 1 to cases 3 and 2. Despite case 2 providing the least operational costs and the emissions in the MG in comparison to case 3, the penetration limit of the total output of the DGs in the MG exceeds the limits of the 60% penetration ratio, as described by Figure 18.

(**a**) MG operational costs
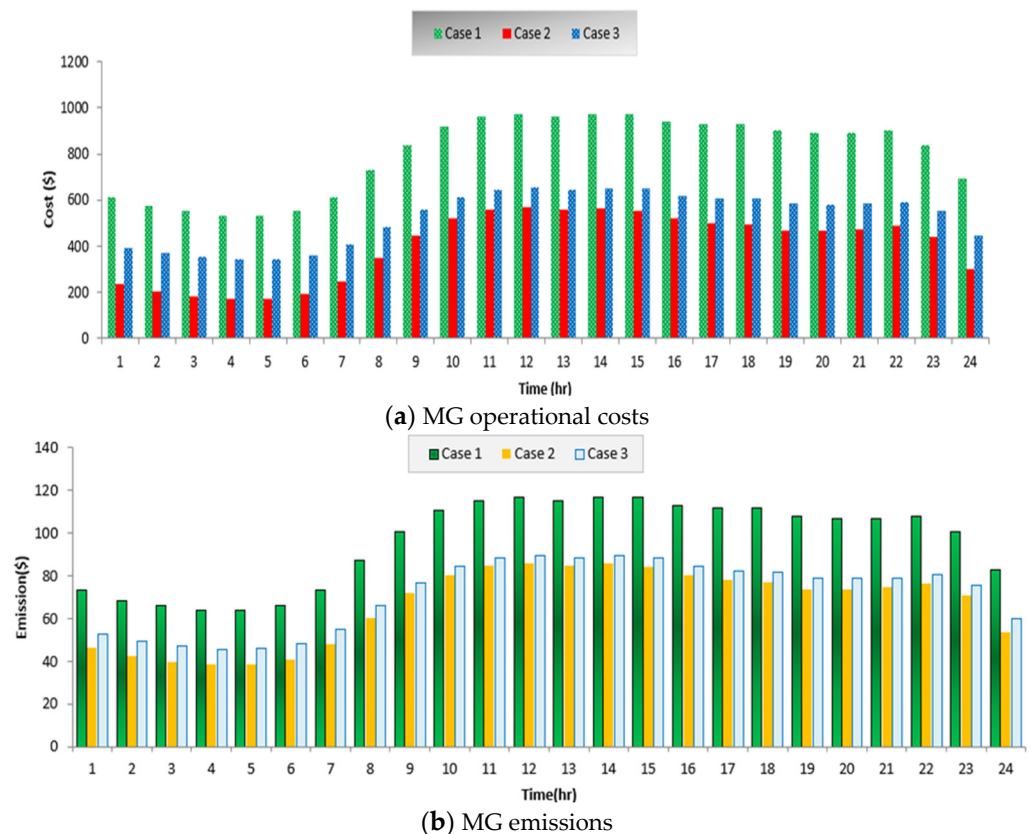
(**b**) MG emissions

Figure 24. Hourly optimal operational costs and the associated emissions in the second MG.

5. Conclusions

- The optimal operating strategy based on the developed equilibrium optimization (EO) technique has been presented and is proposed in order to minimize the operational costs and the accompanied pollutants simultaneously over a 24-h scheduling horizon.
- Several renewable DGs have been investigated in the understudy MG, consisting of biomass generators (BG), wind turbines (WTs), and photovoltaics (PV).
- The uncertainties of wind speed and solar irradiation have been considered via Weibull and Beta-PDF with different states of mean and standard deviation at each hour, respectively.
- The developed EO methodology has been tested on the IEEE 33-bus system and the practical large-scale 141-bus system of AES-Venezuela in the metropolitan area of Caracas to verify its effectiveness and efficiency.
- Added to that, the optimal operation of MG using the developed EO has been compared with other recent algorithms of DE and RAO algorithms.
- Based on the developed EO, the hourly output powers of the PV, WTs, and BGs are optimized, as are the associated power factors of the BGs.
- Significant benefits of the optimal operation of a typical MG using the developed EO have been demonstrated by minimizing the operational costs and emissions while preserving the penetration level of the DGs by 60%.
- The voltage profiles of the MG operation for every hour have been greatly improved, with the minimum voltage adjusted within the permitted limit of [0.95–1.05] p.u.
- The active power losses per hour have been significantly decreased.

References

1. Shahooei, Z.; Martin, L.; Nehrir, H.; Bahramipanah, M. A Novel Agent-Based Power Management Scheme for Smart Multiple-Microgrid Distribution Systems. *Energies* **2022**, *15*, 1774. [CrossRef]
2. Konneh, K.V.; Adewuyi, O.B.; Lotfy, M.E.; Sun, Y.; Senjyu, T. Application Strategies of Model Predictive Control for the Design and Operations of Renewable Energy-Based Microgrid: A Survey. *Electronics* **2022**, *11*, 554. [CrossRef]
3. Guoping, Z.; Weijun, W.; Longbo, M. An Overview of Microgrid Planning and Design Method. In Proceedings of the 2018 IEEE 3rd Advanced Information Technology, Electronic and Automation Control Conference (IAEAC), Chongqing, China, 12–14 October 2018; pp. 326–329. [CrossRef]
4. Su, W.; Wang, J. Energy Management Systems in Microgrid Operations. *Electr. J.* **2012**, *25*, 8. [CrossRef]
5. Shaheen, A.M.; Elattar, E.E.; El-Sehiemy, R.A.; Elsayed, A.M. An Improved Sunflower Optimization Algorithm-Based Monte Carlo Simulation for Efficiency Improvement of Radial Distribution Systems Considering Wind Power Uncertainty. *IEEE Access* **2020**, *9*, 2332–2344. [CrossRef]
6. Bayoumi, A.S.; El-Sehiemy, R.A.; Mahmoud, K.; Lehtonen, M.; Darwish, M.M.F. Assessment of an Improved Three-Diode against Modified Two-Diode Patterns of MCS Solar Cells Associated with Soft Parameter Estimation Paradigms. *Appl. Sci.* **2021**, *11*, 1055. [CrossRef]
7. Sood, V.K.; Ali, M.Y.; Khan, F. Energy Management System of a Microgrid Using Particle Swarm Optimization (PSO) and Communication System. In *Lecture Notes in Electrical Engineering*; Springer: Berlin/Heidelberg, Germany, 2020; p. 625.

8. Vera, Y.E.G.; Dufo-López, R.; Bernal-Agustín, J.L. Energy Management in Microgrids with Renewable Energy Sources: A Literature Review. *Appl. Sci.* **2019**, *9*, 3854. [CrossRef]

9. Shaheen, A.M.; Elsayed, A.M.; Ginidi, A.R.; Elattar, E.E.; El-Sehiemy, R.A. Effective Automation of Distribution Systems with Joint Integration of DGs/ SVCs Considering Reconfiguration Capability by Jellyfish Search Algorithm. *IEEE Access* **2021**, *9*, 92053–92069. [CrossRef]

10. Shaheen, A.M.; Elsayed, A.M.; El-Sehiemy, R.A.; Ginidi, A.R.; Elattar, E. Optimal management of static volt-ampere-reactive devices and distributed generations with reconfiguration capability in active distribution networks. *Int. Trans. Electr. Energy Syst.* **2021**, *31*, e13126. [CrossRef]

11. Elattar, E.E.; Shaheen, A.M.; El-Sayed, A.M.; El-Sehiemy, R.A.; Ginidi, A.R. Optimal Operation of Automated Distribution Networks Based-MRFO Algorithm. *IEEE Access* **2021**, *9*, 19586–19601. [CrossRef]

12. Shaheen, A.M.; El-Sehiemy, R.A. Optimal allocation of capacitor devices on MV distribution networks using crow search algorithm. *CIRED Open Access Proc. J.* **2017**, *2017*, 2453–2457. [CrossRef]

13. Bidgoli, M.A.; Payravi, A.R.; Ahmadian, A.; Yang, W. Optimal day-ahead scheduling of autonomous operation for the hybrid micro-grid including PV, WT, diesel generator, and pump as turbine system. *J. Ambient Intell. Humaniz. Comput.* **2021**, *12*, 961–977. [CrossRef]

14. Sridhar, N.; Kowsalya, M. Enhancement of power management in micro grid system using adaptive ALO technique. *J. Ambient Intell. Humaniz. Comput.* **2021**, *12*, 2163–2182. [CrossRef]

15. Funde, N.; Dhabu, M.; Deshpande, P. CLOES: Cross-layer optimal energy scheduling mechanism in a smart distributed multi-microgrid system. *J. Ambient Intell. Humaniz. Comput.* **2020**, *11*, 4765–4783. [CrossRef]

16. Hosseinnia, H.; Nazarpour, D.; Talavat, V. Multi-objective optimization framework for optimal planning of the microgrid (MG) under employing demand response program (DRP). *J. Ambient Intell. Humaniz. Comput.* **2018**, *10*, 2709–2730. [CrossRef]

17. Maulik, A.; Das, D. Optimal operation of microgrid using four different optimization techniques. *Sustain. Energy Technol. Assess.* **2017**, *21*, 100–120. [CrossRef]

18. Shaheen, A.M.; Ginidi, A.R.; El-Sehiemy, R.A.; Elattar, E.E. Optimal economic power and heat dispatch in Cogeneration Systems including wind power. *Energy* **2021**, *225*, 120263. [CrossRef]

19. Ginidi, A.; Elsayed, A.; Shaheen, A.; Elattar, E.; El-Sehiemy, R. An Innovative Hybrid Heap-Based and Jellyfish Search Algorithm for Combined Heat and Power Economic Dispatch in Electrical Grids. *Mathematics* **2021**, *9*, 2053. [CrossRef]

20. El-Sehiemy, R.; Elsayed, A.; Shaheen, A.; Elattar, E.; Ginidi, A. Scheduling of Generation Stations, OLTC Substation Transformers and VAR Sources for Sustainable Power System Operation Using SNS Optimizer. *Sustainability* **2021**, *13*, 11947. [CrossRef]

21. Omotoso, H.O.; Al-Shaalan, A.M.; Farh, H.M.H.; Al-Shamma'a, A.A. Techno-Economic Evaluation of Hybrid Energy Systems Using Artificial Ecosystem-Based Optimization with Demand Side Management. *Electronics* **2022**, *11*, 204. [CrossRef]

22. Zhu, Z.; Weng, Z.; Zheng, H. Optimal Operation of a Microgrid with Hydrogen Storage Based on Deep Reinforcement Learning. *Electronics* **2022**, *11*, 196. [CrossRef]

23. Wu, X.; Li, S.; Gan, S.; Hou, C. An Adaptive Energy Optimization Method of Hybrid Battery-Supercapacitor Storage System for Uncertain Demand. *Energies* **2022**, *15*, 1765. [CrossRef]

24. Reddy, S.S.; Park, J.Y.; Jung, C.M. Optimal operation of microgrid using hybrid differential evolution and harmony search algorithm. *Front. Energy* **2016**, *10*, 355–362. [CrossRef]

25. Reddy, S.S. Optimal Operation of Microgrid considering Renewable Energy Sources, Electric Vehicles and Demand Response. In Proceedings of the 1st International Conference on Sustainable Energy and Future Electric Transportation (SeFet 2019), Hyderabad, India, 14–16 February 2019; EDP Sciences: Les Ulis, France, 2019; Volume 7, p. 01007.

26. Wang, Y.; Li, F.; Yu, H.; Wang, Y.; Qi, C.; Yang, J.; Song, F. Optimal operation of microgrid with multi-energy complementary based on moth flame optimization algorithm. *Energy Sources Part A Recover. Util. Environ. Eff.* **2020**, *42*, 785–806. [CrossRef]

27. Elsakaan, A.A.; El-Sehiemy, R.A.; Kaddah, S.S.; Elsaid, M.I. Optimal economic–emission power scheduling of RERs in MGs with uncertainty. *IET Gener. Transm. Distrib.* **2020**, *14*, 37–52. [CrossRef]

28. Balasubramaniam, K.; Hadidi, R.; Makram, E. Optimal operation of microgrids under conditions of uncertainty. In Proceedings of the 2015 IEEE Power & Energy Society General Meeting, Denver, CO, USA, 26–30 July 2015; pp. 1–5. [CrossRef]

29. Andrychowicz, M. Optimization of distribution systems by using RES allocation and grid development. In Proceedings of the 15th International Conference of European Energy Market, Łodź, Poland, 27–29 June 2018.

30. Andrychowicz, M. RES and ES Integration in Combination with Distribution Grid Development Using MILP. *Energies* **2021**, *14*, 383. [CrossRef]

31. Faramarzi, A.; Heidarinejad, M.; Stephens, B.; Mirjalili, S. Equilibrium optimizer: A novel optimization algorithm. *Knowl.-Based Syst.* **2020**, *191*, 105190. [CrossRef]

32. Nusair, K.; Alhmoud, L. Application of Equilibrium Optimizer Algorithm for Optimal Power Flow with High Penetration of Renewable Energy. *Energies* **2020**, *13*, 6066. [CrossRef]

33. Abdul-Hamied, D.T.; Shaheen, A.M.; Salem, W.A.; Gabr, W.I.; El-Sehiemy, R.A. Equilibrium optimizer based multi dimensions operation of hybrid AC/DC grids. *Alex. Eng. J.* **2020**, *59*, 4787–4803. [CrossRef]

34. Agnihotri, S.; Atre, A.; Verma, H.K. Equilibrium optimizer for solving economic dispatch problem. In Proceedings of the PIICON 2020—9th IEEE Power India International Conference, Sonepat, India, 28 February–1 March 2020.

35. El-Shorbagy, M.A.; Mousa, A.A. Constrained Multiobjective Equilibrium Optimizer Algorithm for Solving Combined Economic Emission Dispatch Problem. *Complexity* **2021**, *2021*, 6672131. [CrossRef]
36. El-Ela, A.A.A.; Allam, S.M.; Shaheen, A.M.; Nagem, N.A. Optimal allocation of biomass distributed generation in distribution systems using equilibrium algorithm. *Int. Trans. Electr. Energy Syst.* **2020**, *31*, e12727. [CrossRef]
37. Ahmed, D.; Ebeed, M.; Ali, A.; Alghamdi, A.; Kamel, S. Multi-Objective Energy Management of a Micro-Grid Considering Stochastic Nature of Load and Renewable Energy Resources. *Electronics* **2021**, *10*, 403. [CrossRef]
38. El-Ela, A.A.A.; El-Seheimy, R.A.; Shaheen, A.M.; Wahbi, W.A.; Mouwafi, M.T. PV and battery energy storage integration in distribution networks using equilibrium algorithm. *J. Energy Storage* **2021**, *42*, 103041. [CrossRef]
39. El Sayed, S.; Al Otaibi, S.; Ahmed, Y.; Hendawi, E.; Elkalashy, N.; Hoballah, A. Probabilistic Modeling and Equilibrium Optimizer Solving for Energy Management of Renewable Micro-Grids Incorporating Storage Devices. *Energies* **2021**, *14*, 1373. [CrossRef]
40. Shaheen, A.M.; Hamida, M.A.; El-Sehiemy, R.A.; Elattar, E.E. Optimal parameter identification of linear and non-linear models for Li-Ion Battery Cells. *Energy Rep.* **2021**, *7*, 7170–7185. [CrossRef]
41. Ghoneim, S.S.M.; Alharthi, M.M.; El-Sehiemy, R.A.; Shaheen, A.M. Prediction of Transformer Oil Breakdown Voltage with Barriers Using Optimization Techniques. *Intell. Autom. Soft Comput.* **2022**, *31*, 1593–1610. [CrossRef]
42. El-Fergany, A. Optimal allocation of multi-type distributed generators using backtracking search optimization algorithm. *Int. J. Electr. Power Energy Syst.* **2015**, *64*, 1197–1205. [CrossRef]
43. Hien, N.C.; Mithulananthan, N.; Bansal, R. Location and Sizing of Distributed Generation Units for Loadabilty Enhancement in Primary Feeder. *IEEE Syst. J.* **2013**, *7*, 797–806. [CrossRef]
44. Gözel, T.; Hocaoglu, M.H. An analytical method for the sizing and siting of distributed generators in radial systems. *Electr. Power Syst. Res.* **2009**, *79*, 912–918. [CrossRef]
45. El-Fergany, A. Multi-objective Allocation of Multi-type Distributed Generators along Distribution Networks Using Backtracking Search Algorithm and Fuzzy Expert Rules. *Electr. Power Compon. Syst.* **2015**, *44*, 252–267. [CrossRef]
46. Ginidi, A.; Ghoneim, S.M.; Elsayed, A.; El-Sehiemy, R.; Shaheen, A.; El-Fergany, A. Gorilla Troops Optimizer for Electrically Based Single and Double-Diode Models of Solar Photovoltaic Systems. *Sustainability* **2021**, *13*, 9459. [CrossRef]
47. Said, M.; Shaheen, A.M.; Ginidi, A.R.; El-Sehiemy, R.A.; Mahmoud, K.; Lehtonen, M.; Darwish, M.M.F. Estimating Parameters of Photovoltaic Models Using Accurate Turbulent Flow of Water Optimizer. *Processes* **2021**, *9*, 627. [CrossRef]
48. Atwa, Y.M.; El-Saadany, E.F.; Salama, M.M.A.; Seethapathy, R. Optimal Renewable Resources Mix for Distribution System Energy Loss Minimization. *IEEE Trans. Power Syst.* **2009**, *25*, 360–370. [CrossRef]
49. Soroudi, A.; Aien, M.; Ehsan, M. A Probabilistic Modeling of Photo Voltaic Modules and Wind Power Generation Impact on Distribution Networks. *IEEE Syst. J.* **2011**, *6*, 254–259. [CrossRef]
50. IEEE. IEEE application guide for IEEE std 1547TM, IEEE standard for interconnecting distributed resources with electric power systems. *IEEE* **2009**, 1–217. [CrossRef]
51. Ahmed, A.; Nadeem, M.F.; Sajjad, I.A.; Bo, R.; Khan, I. Optimal Allocation of Wind DG with Time Varying Voltage Dependent Loads Using Bio-Inspired: Salp Swarm Algorithm. In Proceedings of the 2020 3rd International Conference on Computing, Mathematics and Engineering Technologies (iCoMET), Sukkur, Pakistan, 3–4 March 2020; pp. 1–7. [CrossRef]
52. Murty, V.V.S.N.; Kumar, A. Optimal Energy Management and Techno-economic Analysis in Microgrid with Hybrid Renewable Energy Sources. *J. Mod. Power Syst. Clean Energy* **2020**, *8*, 929–940. [CrossRef]
53. Rehman, W.U.; Khan, M.F.N.; Sajjad, I.A.; Afzaal, M.U. Probabilistic generation model for grid connected wind DG. *J. Renew. Sustain. Energy* **2019**, *11*, 045301. [CrossRef]
54. Bentouati, B.; Khelifi, A.; Shaheen, A.M.; El-Sehiemy, R.A. An enhanced moth-swarm algorithm for efficient energy management based multi dimensions OPF problem. *J. Ambient Intell. Humaniz. Comput.* **2021**, *12*, 9499–9519. [CrossRef]
55. Raglend, I.J.; Veeravalli, S.; Sailaja, K.; Sudheera, B.; Kothari, D. Comparison of AI techniques to solve combined economic emission dispatch problem with line flow constraints. *Int. J. Electr. Power Energy Syst.* **2010**, *32*, 592–598. [CrossRef]
56. Eladl, A.A.; El Desouky, A.A. Optimal economic dispatch for multi heat-electric energy source power system. *Int. J. Electr. Power Energy Syst.* **2019**, *110*, 21–35. [CrossRef]
57. Shaheen, A.; Elsayed, A.; Ginidi, A.; El-Sehiemy, R.; Elattar, E. Reconfiguration of electrical distribution network-based DG and capacitors allocations using artificial ecosystem optimizer: Practical case study. *Alex. Eng. J.* **2021**, *61*, 6105–6118. [CrossRef]
58. El-Ela, A.A.A.; El-Sehiemy, R.A.; Shaheen, A.M.; Elllien, A.R. Multiobjective coyote optimization algorithm for techno-economic simultaneous placement of DGs and FCLs in distribution networks. *Int. Trans. Electr. Energy Syst.* **2021**, *31*, e13050. [CrossRef]
59. Talaat, H.E.; Al-Ammar, E. Optimal allocation and sizing of Distributed Generation in distribution networks using Genetic Algorithms. In Proceedings of the 11th International Conference on Electrical Power Quality and Utilisation, Lisbon, Portugal, 17–19 October 2011; pp. 1–6.
60. Shaheen, A.; Elsayed, A.; Ginidi, A.; El-Sehiemy, R.; Elattar, E. A heap-based algorithm with deeper exploitative feature for optimal allocations of distributed generations with feeder reconfiguration in power distribution networks. *Knowl.-Based Syst.* **2022**, *241*, 108269. [CrossRef]
61. Shaheen, A.M.; Elsayed, A.M.; Ginidi, A.R.; El-Sehiemy, R.A.; Elattar, E.E. Improved Heap-Based Optimizer for DG Allocation in Reconfigured Radial Feeder Distribution Systems. *IEEE Syst. J.* **2022**, 1–10. [CrossRef]

62. Shaheen, A.M.; Elsayed, A.M.; El-Sehiemy, R.A.; Kamel, S.; Ghoneim, S.S.M. A modified marine predators optimization algorithm for simultaneous network reconfiguration and distributed generator allocation in distribution systems under different loading conditions. *Eng. Optim.* **2021**, 1–22. [CrossRef]

63. Shaheen, A.M.; El-Sehiemy, R.A.; Kamel, S.; Elattar, E.E.; Elsayed, A.M. Improving Distribution Networks' Consistency by Optimal Distribution System Reconfiguration and Distributed Generations. *IEEE Access* **2021**, *9*, 67186–67200. [CrossRef]

64. Abdel-Basset, M.; Chang, V.; Mohamed, R. A novel equilibrium optimization algorithm for multi-thresholding image segmentation problems. *Neural Comput. Appl.* **2020**, 1–34. [CrossRef]

65. Kefayat, M.; Ara, A.L.; Niaki, S.N. A hybrid of ant colony optimization and artificial bee colony algorithm for probabilistic optimal placement and sizing of distributed energy resources. *Energy Convers. Manag.* **2015**, *92*, 149–161. [CrossRef]

66. Khodr, H.; Olsina, F.; Jesus, P.D.O.-D.; Yusta, J. Maximum savings approach for location and sizing of capacitors in distribution systems. *Electr. Power Syst. Res.* **2008**, *78*, 1192–1203. [CrossRef]

67. Nasef, A.; Shaheen, A.; Khattab, H. Local and remote control of automatic voltage regulators in distribution networks with different variations and uncertainties: Practical cases study. *Electr. Power Syst. Res.* **2022**, *205*, 107773. [CrossRef]

68. Grigg, C.; Wong, P.; Albrecht, P.; Allan, R.; Bhavaraju, M.; Billinton, R.; Chen, Q.; Fong, C.; Haddad, S.; Kuruganty, S.; et al. The IEEE Reliability Test System-A report prepared by the Reliability Test System Task Force of the Application of Probability Methods Subcommittee. *IEEE Trans. Power Syst.* **1999**, *14*, 1010–1020. [CrossRef]

69. Shaheen, A.M.; El-Sehiemy, R.A. Optimal Coordinated Allocation of Distributed Generation Units/ Capacitor Banks/ Voltage Regulators by EGWA. *IEEE Syst. J.* **2021**, *15*, 257–264. [CrossRef]

70. Shafei, M.A.R.; Anwar, Y.A.; Ibrahim, D.K. Sharm El-Sheikh 5 MW PV Plant Performance, Environmental Impact and Grid Connection Parameters. In Proceedings of the 2019 21st International Middle East Power Systems Conference (MEPCON), Cairo, Egypt, 17–19 December 2019; pp. 790–795.

71. Basu, M. Combined heat and power dynamic economic dispatch with demand side management incorporating renewable energy sources and pumped hydro energy storage. *IET Gener. Transm. Distrib.* **2019**, *13*, 3771–3781. [CrossRef]

72. Owens, E.; Chapman, S. Valuing the Greenhouse Gas Emissions from Wind Power. *Int. J. Energy Eng.* **2013**, *3*, 41–54. [CrossRef]

73. Soroudi, A.; Ehsana, M.; Zareipour, H. A practical eco-environmental distribution network planning model including fuel cells and non-renewable distributed energy resources. *Renew. Energy* **2011**, *36*, 179–188. [CrossRef]

74. Shaheen, A.M.; El-Sehiemy, R.A.; Farrag, S.M. A reactive power planning procedure considering iterative identification of VAR candidate buses. *Neural Comput. Appl.* **2017**, *31*, 653–674. [CrossRef]

75. Rao, R.V. Rao algorithms: Three metaphor-less simple algorithms for solving optimization problems. *Int. J. Ind. Eng. Comput.* **2020**, *11*, 107–130. [CrossRef]

Article

Requirements for Energy-Harvesting-Driven Edge Devices Using Task-Offloading Approaches

Meriam Ben Ammar [1,2,3,*] , **Imed Ben Dhaou** [4,5,6] , **Dhouha El Houssaini** [1] , **Salwa Sahnoun** [2,3] , **Ahmed Fakhfakh** [2,3] and **Olfa Kanoun** [1]

1 Measurements and Sensor Technology, Faculty of Electrical Engineering and Information Technology, Chemnitz University of Technology, W206, 09126 Chemnitz, Germany; dhouha.el-houssaini@etit.tu-chemnitz.de (D.E.H.); Olfa.Kanoun@etit.tu-chemnitz.de (O.K.)
2 National School of Electronics and Telecommunications of Sfax, University of Sfax, Sfax 3018, Tunisia; salwa.sahnoun@enetcom.usf.tn (S.S.); ahmed.fakhfakh@enetcom.usf.tn (A.F.)
3 Laboratory of Signals, Systems, Artificial Intelligence and Networks, Digital Research Center of Sfax, University of Sfax, Sfax 3038, Tunisia
4 Department of Computer Science, Hekma School of Engineering, Computing and Informatics, Dar Al-Hekma University, Jeddah 22246-4872, Saudi Arabia; imed.bendhaou@utu.fi
5 Department of Computing, University of Turku, FI-20014 Turku, Finland
6 Department of Technology, Higher Institute of Computer Sciences and Mathematics, University of Monastir, Monastir 5000, Tunisia
* Correspondence: meriam.ben-ammar@etit.tu-chemnitz.de

Abstract: Energy limitations remain a key concern in the development of Internet of Medical Things (IoMT) devices since most of them have limited energy sources, mainly from batteries. Therefore, providing a sustainable and autonomous power supply is essential as it allows continuous energy sensing, flexible positioning, less human intervention, and easy maintenance. In the last few years, extensive investigations have been conducted to develop energy-autonomous systems for the IoMT by implementing energy-harvesting (EH) technologies as a feasible and economically practical alternative to batteries. To this end, various EH-solutions have been developed for wearables to enhance power extraction efficiency, such as integrating resonant energy extraction circuits such as SSHI, S-SSHI, and P-SSHI connected to common energy-storage units to maintain a stable output for charge loads. These circuits enable an increase in the harvested power by 174% compared to the SEH circuit. Although IoMT devices are becoming increasingly powerful and more affordable, some tasks, such as machine-learning algorithms, still require intensive computational resources, leading to higher energy consumption. Offloading computing-intensive tasks from resource-limited user devices to resource-rich fog or cloud layers can effectively address these issues and manage energy consumption. Reinforcement learning, in particular, employs the Q-algorithm, which is an efficient technique for hardware implementation, as well as offloading tasks from wearables to edge devices. For example, the lowest reported power consumption using FPGA technology is 37 mW. Furthermore, the communication cost from wearables to fog devices should not offset the energy savings gained from task migration. This paper provides a comprehensive review of joint energy-harvesting technologies and computation-offloading strategies for the IoMT. Moreover, power supply strategies for wearables, energy-storage techniques, and hardware implementation of the task migration were provided.

Keywords: energy harvesting; IoMT devices; energy autonomous; wearables; energy-storage; energy management; fog edge computing; task offloading; deep learning; reinforced learning; IoMT

1. Introduction

With the spread of Internet of Medical Things (IoMT) applications, more intelligent services are presently emerging in the healthcare and medical areas, such as remote patient monitoring [1,2], telemedicine [3], biometrics scanners [4] and vital signs monitoring [5,6].

In general, the IoMT comprises different and heterogeneous smart devices, such as wearables, wireless sensors, and medical monitors, which can be applied to the human body, at home or in hospitals to provide better and more efficient remote monitoring. By combining information technology with medical information, wearable devices can perform better monitoring of medical and healthcare applications, resulting in reduced complexity and enhanced efficiency. With the use of the IoMT, physicians and healthcare responsible are also able to access different and real-time medical databases, which ensures a better understanding and identification of their patients' health issues.

The IoMT presents an application of the Internet of Things (IoT) in the field of medical and healthcare. The IoT comprises physical network devices equipped with sensors, software, and network connections that facilitate data collection and transmission. It can integrate cloud services and fog centers, where complex and efficient data processing is carried out with high processing capabilities. Considering the basic concepts of the IoT, the general layer architecture of IoMT is illustrated in Figure 1. It comprises four main layers, namely the sensing layer, the edge layer, the fog layer and the cloud layer. In the sensing layer, the wireless sensors and medical devices are installed along with different actuators. They are responsible for sensing medical and physiological information, and executing specific controlling and monitoring requests such as laser positioning and equipment maintenance. The raw data collected from the end devices are collected and transmitted to the edge devices, where data processing, reduction and analysis are carried out. Devices with edge computing processors provide improved security while operating at a low power level. Within the fog layer, local area networks are installed, where the data are transmitted from endpoints to a gateway, where it is then transmitted to sources for processing and return transmission. By the end, data are transmitted to the cloud layer, which can access several IoT devices at the same time. It permits real-time and continuous data processing with higher computational capabilities. However, even though wearable devices are becoming more powerful and affordable, machine-learning-based tasks that typically require more computation resources may overload them with higher data communications and, therefore, higher energy consumption.
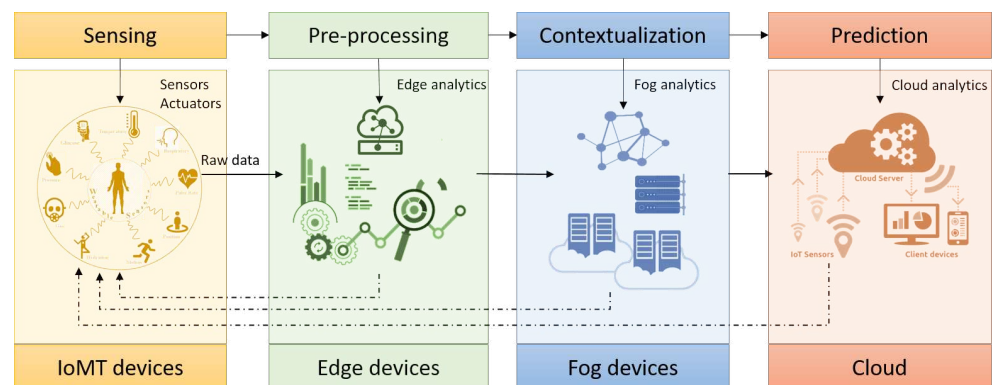
Figure 1. General layers architecture of IoMT system.

Therefore, it becomes imperative to offload some tasks from resource-constrained edge devices to co-located edge devices, such as the fog. Applications that require intensive computation resources are often offloaded to cloud servers to be processed, which improves IoT device capabilities. Cloud computing, by contrast, may cause high latency response times, privacy and security issues. As a solution, some studies proposed to offload tasks to a Mobile Edge Computing (MEC) server via edge devices that can be placed near end devices and process some computational capacity. Thus, transmission latencies are reduced, and reliability and security are enhanced. Even though computation offloading over fog edge computing or MEC has reduced the energy consumption of IoMT devices to a certain degree, their energy limitations remain a key concern. However, most devices are powered by batteries, which limits their energy resources and operating times. Similarly,

computation performance may be affected if not enough battery energy is available for task transmission. A larger battery or more frequent recharging can address this problem. In contrast, the small size of IoMT devices makes it difficult to equip them with larger batteries or to recharge their batteries frequently. To address these challenges, energy-harvesting technologies have been identified as promising techniques to increase battery life and achieve energy-autonomous systems. Figure 2 shows the general architecture of an IoMT system with the integration of EH-supplied systems and considering the task-offloading aspect. The IoMT system includes various types of sensors used, most likely activity sensors (presented in red circles in Figure 2), physiological sensors (presented in green circles in Figure 2). Sensor are placed over the human body within a network, where each sensor is responsible for monitoring certain physical information. The sensor data are gathered in the base station to be transmitted to the next IoT layer, which can be either an access point, a gateway or a mobile device. Later, the collected data are transported to the fog layer and then the cloud. Communication can be established between different installed devices over the different layers. During the communication, information related to the actual status of the corresponding devices, such as the residual energy level, neighbor list and reception acknowledgement could be shared. This information care is used later to decide upon the most appropriate device for task offloading. Offloading involves sharing details about which device will be best suited to execute the current task, the type of task that will be executed, and how it will be executed. Task offloading can occur at different levels of the IoMT system, such as from the WBAN to the gateway and from the gateway to the fog, to the cloud.
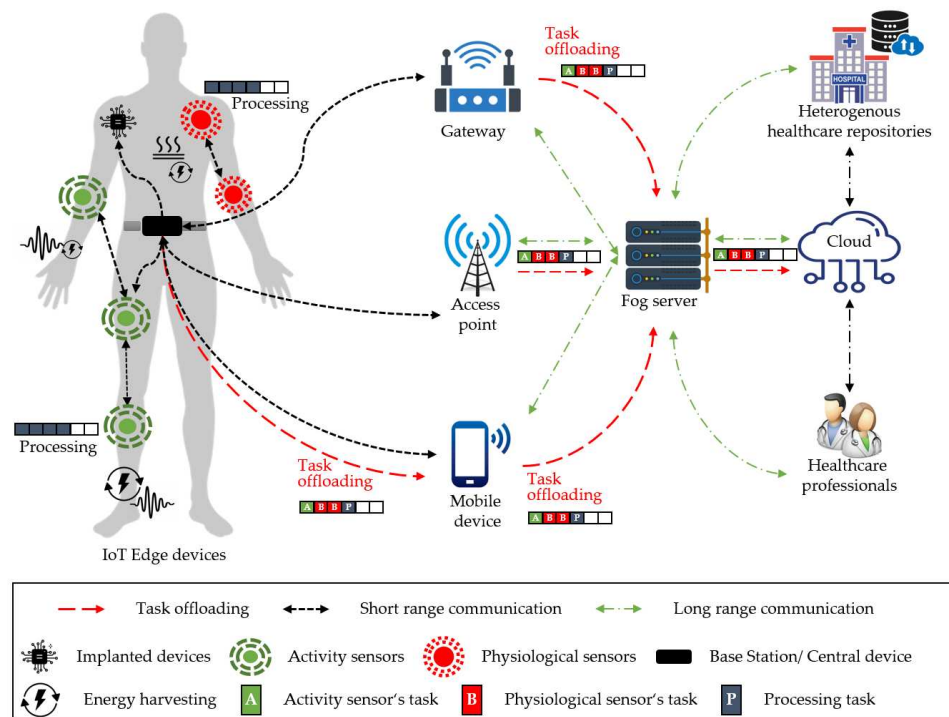
Figure 2. General architecture of an IoMT system based on energy harvesting and with consideration of task offloading.

Within the framework of IoT for medical applications, continuous data transmission takes place over the different layers of the network. Therefore, different sensor and communication technologies are used for sensing and transmitting data in real time, enabling fast calculations and optimal decision-making. It is crucial to satisfy the trade-off between the energy consumption, computational capability and data transmission for a real-time and accurate operation. Several schemes for energy efficiency and management are required to respond to these challenges. In general they can be classified into four main categories:

- Resources allocation ensures a better allocation and management of the available resources, mainly radio and energy resources.
- Energy harvesting and transfer provide a sustainable energy supply, which are harvested from ambient resources. In the case of wearable systems, the energy can even be harvested from the human activities, such as breathing and movement.
- Hardware systems are explored during the development and design of wireless nodes and devices with consideration of the minimum energy consumption.
- Network installation enables the definition of appropriate infrastructures that maximize energy efficiency and ensure the data transmission and computational capabilities.

In this direction, it is important to investigate energy-efficient solutions for IoMT system, where intensive tasks and data processing are realized in a strict execution time. In particular, the communication and data transmissions need more attention, especially in the case of limited energy sources and computation capabilities. In this direction, investigations into energy-harvesting solutions along with task-offloading concepts present a promising solution to deal with excessive demands for a stable communication and data transmission. The contributions of this paper are:

- We provide a literature review of the state-of-the-art joint energy-harvesting and task-offloading approaches in fog edge computing systems.
- We compare the state-of-the-art related surveys based on specific key features.
- We investigate energy-harvesting technologies and energy-storage strategies for IoMT devices.
- We survey recent research efforts on task offloading in fog edge computing and related design considerations.
- We review existing approaches for the design of patient-centered care system.

The paper is organized as follows. Section 2 surveys research efforts related to joint energy harvesting and task-offloading approaches in fog edge computing systems. Section 3 presents the task-offloading approaches for fog edge computing, and deep-reinforcement learning-based algorithms. Section 4 highlights the related design considerations and challenges for EH driven task offloading. Section 5 reviews possibilities of energy supply, energy-storage strategies and recent trends in energy harvesting. Section 6 presents requirements for patient-centered care system. Finally, Section 7 concludes the paper.

2. Related Works

Recently, task offloading in fog edge computing systems has gained considerable attention due to the increasing development of IoMT devices. In [7], the authors developed a deep-learning-based, Internet of Medical Things-enabled edge computing framework for tackling COVID-19. It detects various COVID-19 symptoms and generates reports and alerts for medical decision support. Results indicate that the system can be used to effectively manage in-home health during a pandemic. Nevertheless, improvements to the system accuracy were needed as well as implementations with real subjects. In [8] a joint optimization framework was also proposed for IoT fog computing to achieve optimal resource allocation. The results show that the proposed framework enhanced the performance of IoT-based network systems. In [9] authors investigated delay-sensitive task offloading in edge-enabled healthcare services. A priority-aware service provisioning was proposed, allowing edge server computing resources to handle hard-deadline tasks earlier than soft-deadline tasks which have a lower priority and can tolerate longer delays over hard-deadline tasks. In contrast, the authors plan to examine how hard-deadline tasks can be placed in remote healthcare applications where ensuring high reliability is a crucial requirement.

When focusing on the increasing number of tasks that require high computational capability and consequently more energy, mobile devices need effective mechanisms to figure out which tasks to perform locally and which to migrate to the cloud. The authors in [10] discussed different computational offloading techniques. They consider the offloading either to a fog node or a cloud. They both have their trade-offs. The cloud, as an example,

is rich in terms of resources, but offloading computational tasks to cloud servers can lead to security and privacy issues and it is also far away from mobile nodes. In contrast, fog is nearby but has limited resources. Hence, offloading to a cloud or fog consumes different amounts of energy and increases computation performance. In this context, the authors proposed an energy consumption-oriented algorithm to reduce energy consumption when offloading tasks. Initially, they compute the consumed energy when offloading the task to the fog compared to the cloud. Afterwards, they evaluated which entity would be preferred for the task based on the computation requirements. Based on these factors, the task is then offloaded to the desired entity.

Energy harvesting is a promising technology for converting ambient (solar, wind, etc.) and human energy (motion, breath) into electrical power, enabling communication systems to achieve energy-autonomous and efficient communications. In [11] the joint offloading and resource allocation issues in energy harvesting small cell networks is addressed to maximize the number of tasks performed by edge servers while reducing their energy and delay costs. In [12], the authors proposed a deep-reinforcement-learning-based framework for online offloading to reduce the computational complexity in large EH-driven networks. The proposed algorithm can successfully improve offloading behavior by implementing a deep neural network that learns binary offloading decisions based on past offloading experiences. In contrast, a distributed implementation of the proposed algorithm is still needed to enable the users to make offloading decisions in a distributed manner via a learning process. Similarly, a reinforcement-learning-based privacy-aware offloading scheme for a healthcare IoT device supplied by energy harvesting was proposed in [13]. The offloading policy applied on the edge device can be determined by considering the privacy level, energy consumption, and computation latency at each time slot. In [14], the authors investigated computation offloading and resource allocation issues with multiple energy harvesting supplied mobiles. All mobile devices initially harvest energy from RF signals and then use it to perform their own tasks locally or offload them to a MEC server. Some other offloading schemes can also achieve self-sustaining operations. In [15], for instance, the state-of-the-art of methodologies for task offloading in MEC and wireless power transfer to end nodes were recently described. The authors demonstrated the effective use of the Wireless Power Transfer (WPT) technique to charge end mobile phones which have gained more popularity in MEC. However, the increasing demand for computing resources may degrade the performance of MEC. Accordingly, they highlighted the influence of making decisions between task-offloading implementations and offloading locations on the power consumption of MEC devices.

Energy-efficient appliances have become prevalent in various fields and industries, including health care. Therefore, energy management is an effective technique for evaluating the energy efficiency of different devices. By contrast, the surveyed contributions lack discussions of joint energy-harvesting technologies, fog edge computing, and energy management techniques which are vital for IoMT devices.

Table 1 compares the state-of-the-art-related surveys based on specific key features.

Table 1. Comparison between state-of-the-art surveys.

Reference	Fog Edge Computing	Task Offloading	Energy Harvesting	Energy Storage
[16–18]	✓	-	-	-
[19,20]	✓	✓	-	-
This work	✓	✓	✓	✓

3. Principles of Task Offloading

3.1. Pre-IoT Age

Task or computation-offloading theory emerged to respond with the need to speed up task processing in hardware. Task migration in a distributed system aims at balancing

the load among available processors without a drastic increase in the communication overhead [21,22]. Two classes of algorithms have been devised: static and dynamic. Communication protocol plays a pivotal role in balancing the load among processors. Three types of control models have been articulated for load balancing: centralized, distributed, and hybrid [23].

In a multicore/multiprocessor system, task offloading has been used to speed up the execution of multitasks, given a process P_1 that can be decomposed into n independent processes, $P1, n$ and M cores. Each process k requires an execution time $t_{k,m}$ on the mth core, such that $m \in \{1, \ldots, M\}$ and $k \in \{1, \ldots, n\}$ (see Appendix A). The energy dissipated by the mth core to run the kth process is $E_{k,m}$. The task offloading seeks an offloading algorithm that assigns tasks such that the execution time is met at the lowest possible energy consumption, i.e., the offloading should solve the following optimization problem.

$$
\begin{aligned}
\min \quad & \sum_{m=1}^{M} \sum_{i=1}^{n} \delta_{i,m} E_{i,m} \\
\text{s.t.} \quad & \sum_{k=1}^{n} t_{k,m} \leq t_{,,} \\
& n \leq M
\end{aligned}
\tag{1}
$$

where $\delta_{i,m} \begin{cases} 1 & \text{if } P_i \text{ runs on processor } m \\ 0 & \text{else} \end{cases}$.

The authors of [24] devised an offloading strategy that moves the computationally demanding task from CPU to GPU. They further demonstrated this strategy by considering the implementation of a signature-matching intrusion detection system. This approach has been generalized to cover the multicore architecture with and without accelerators.

Offloading can be used to balance the load among cores or processors in a multiprocessor system. This is often regarded as task migration that aims at moving the task execution from one core/processor using a given performance metric: power consumption, thermal energy, and dark silicon [25]. Communication-driven task migration attempts to migrate tasks to adjacent cores.

3.2. Post IoT Age

The Internet of Things, IoT, is the new trend in connectivity spawned from progress in sensors, embedded systems, and communication technologies. It is a three-tier architecture that is composed of a perception/sensors layer, connectivity layer, and application layer [26].

Mobile edge computing, MEC, is a new frontier in computing technologies. Multitude factors have contributed to the emergence of edge computing. Traditionally, cloud computing has been the dominant technology for the storage and processing of big data. Conventional task-offloading techniques have been proposed to migrate computationally intensive tasks/applications to cloud servers for processing. The offloading decision is aimed at either reducing end-user power consumption or increasing system performance [27]. However, the offloading strategies devised for cloud computing are not adequate in today's technologies for the following reasons: (1) Cloud servers cannot sustain the real-time processing of critical tasks, (2) the growing need for data protection and privacy, (3) the exponential increase in the number of IoT devices, and (4) the rising concern of the power consumption of data centers [28]. It has been reported that in the US, data centers consume up to 2.2% of all utility power [29]. According to the International Energy Agency (IEA), nearly 1% of global energy is consumed by data centers (roughly 250 TWh).

Edge computing, EC, addresses the shortcomings of cloud computing by bringing cloud-like services and operations close to the user. Task-offloading techniques have also been developed for edge computing. Fog computing is a term coined by CISCO and emerged after edge computing [30,31]. Fog-computing architecture, as illustrated in Figure 3, is composed of IoT end devices, fog devices that can perform processing and

storage (such as micro cloudlet and gateways), and cloud layer (typically data centers and cloud servers) [32,33].
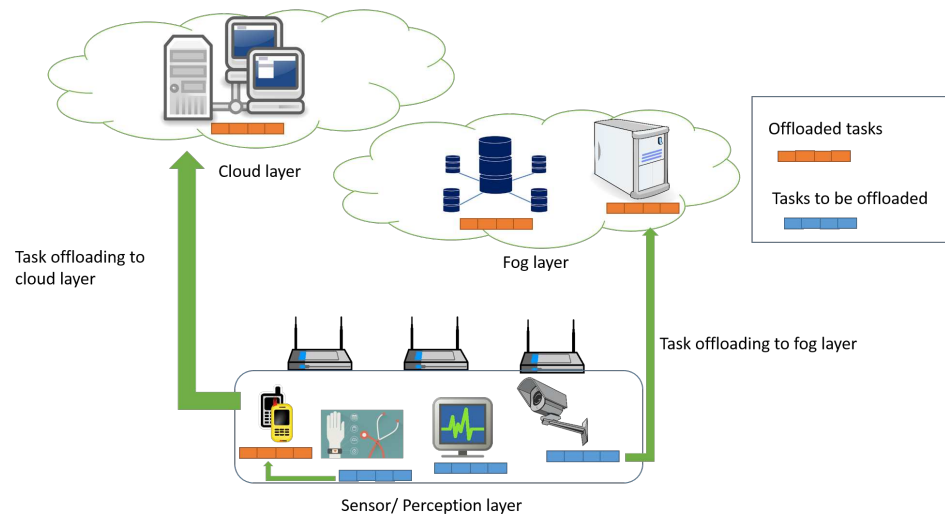
Figure 3. Offloading strategies using fog-computing paradigm. The fog layer is composed of cloudlets (small-scale data centers),and storage (fog servers). The cloud layer houses data centers and servers.

In the realm of the fog-computing paradigm, task offloading has become a hierarchical approach in which an offloading algorithm can execute the task locally using a specialized core, or nearby on an edge device, or remotely on fog or cloud nodes.

Task migration to near or far end nodes needs to account for the cost of the communication protocol: power and delay. In the context of fog computing, the offloading algorithm needs to solve the following optimization algorithm.

$$
\begin{aligned}
\min \quad & \sum_{m=1}^{M} \sum_{i=1}^{n} \delta_{i,m} (E_{i,m} + EC_{i,m}) \\
\text{s.t.} \quad & \sum_{k=1}^{n} (t_{k,m} + \tau_{k,m}) \leq t,, \\
& n \leq M
\end{aligned}
\tag{2}
$$

where $EC_{i,m}$ is the energy consumed to transmit data of task P_i to processor m, and $\tau_{k,m}$ is the latency to transmit task data to the processor m. Those parameters depend on the type of the communication protocol as well as the load of the remote processor that will execute the task.

3.3. Offloading Algorithms

The offloading algorithms aim to find a suitable processor (locally or remotely) to execute a task given a certain constraint. In wearables, offloading can be done at two stages: from wearables to edge devices or from edge device to fog/cloud devices [34]. The offloading device keeps on checking the estimated available power and compares it with the forested power demands. The offloading algorithms are invoked whenever the power demands exceed the available power (harvested and stored) and the energy consumed by the communication unit is less than the energy consumed by task processing. This concept is illustrated in Figure 4. Offloading can be combined with advanced techniques for power management such as sleep, dynamic voltage and frequency scaling (DVFS), and approximated computing [35].
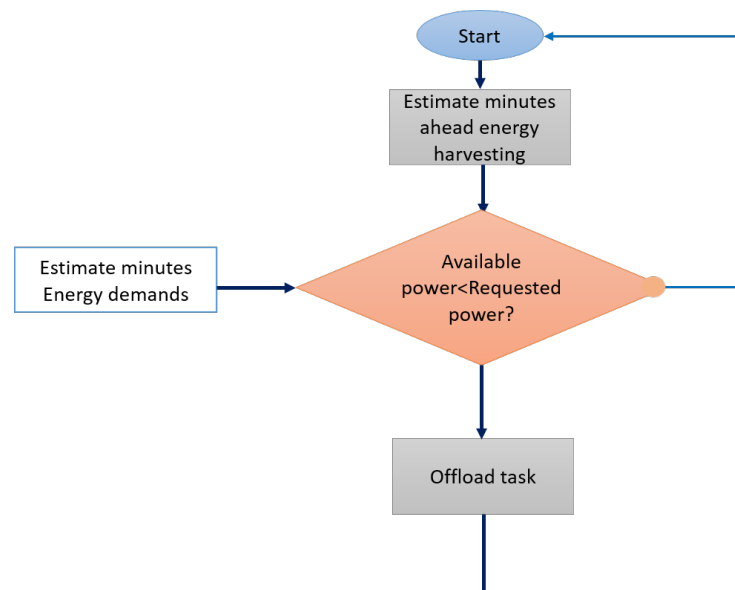
Figure 4. Principles of energy-aware offloading algorithm.

3.3.1. Algorithm Classification

Numerous offloading algorithms for fog computing have recently been proposed. Those algorithms belong to two categories: learning and non-learning. Table 2 summarizes the types of offloading algorithms proposed recently.

Table 2. Recently proposed offloading algorithm.

Reference	Algorithm Type	Optimization Problem	Objective
[36]	Heuristic	Approximation algorithm	Reduce energy consumption of wearables
[37]	Heuristic	Mixed-integer nonlinear programming	Joint scheduling and offloading
[38]	Coalition game theory	merge and split	maxi- mize the total numbers of computed bits
[39]	Evolutionary	genetic algorithm	joint optimization of load balance and propagation delay
[40]	Deterministic	Iterative	balance relays energy
[41]	Reinforcement learning	decentralized partially observable Markov decision process	Maximizing IoT utility and satisfying delay requirements
[42]	Reinforcement learning	Deep Deterministic Policy Gradient	Maximizing task completion rate and reducing task latency
[43,44]	Reinforcement learning	Q-deep learning	Reduce computation latency

3.3.2. Deep-Reinforcement Learning

In recent years, much attention has been given to deep-reinforcement learning (DRL) in task offloading. Reinforcement learning, RL, is a branch of artificial intelligence in which an agent interacts with the environment and learns using two functions: reward and punishment. Punishment is a negative reward. In RL, the learning cycle is not based on a training dataset; instead, the agent interacts with the environments with no prior knowledge and obtains immediate feedback based on its performance. The environment is modeled as a Markovian Decision Process (MDP). In RL an experience is defined as the triple (s_t, a_t, r_t), where s_t, a_t, and r_t are, respectively the state, action and reward at the time

t. The agent determines the action based on a policy, $\pi(s)$. Q-learning algorithm is an offline policy that estimates $\pi(s)$ with guaranteed convergence. The mapping between the policy and the state at a given time t is given by (3) [45]

$$Q(s_t, a_t) = Q(s_t, a_t) + \alpha(r_t + \gamma \max_a Q(s_{t+1}, a_t) - Q(s_t, a_t)), \tag{3}$$

where α is the learning rate, and γ is the discount rate. In RL, the agent tends to maximize the rewards. This concept is illustrated in Figure 5.
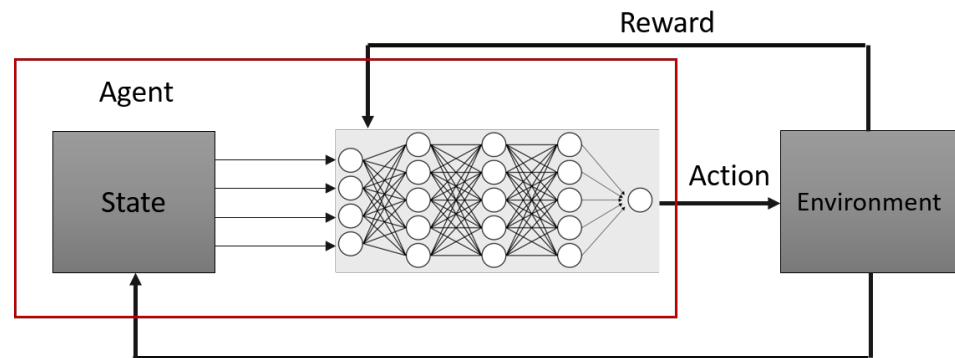
Figure 5. Principles of DRL.

Offloading algorithms-based Q-Learning has been devised in many published reports such [11,43,44,46–48].

In [46], the authors devised a dynamic computation-offloading strategy for an MEC system using Markov decision process theory. The authors considered IoT devices with energy-harvesting techniques. The optimal offloading is achieved using a low-complex after-state learning method.

The problem of task offloading in the context of MEC has been formulated in [47] as a constrained Markov decision process (CMDP). The authors applied Lagrangian primal-dual optimization and devised a deep-reinforcement learning algorithm to solve the relaxed CMDP.

Dynamic computational offloading for MEC systems with EH-enabled IoT devices considering multiple offloading servers has been studied and solved in [48]. The authors elaborated an offloading algorithm using deep Q-learning techniques.

Hardware implementation of the Q-learning algorithm received scant attention. Most of the reported implementation focuses on designing an accelerator using FPGA technology. The lowest power consumption has been reported to be 37 mW for a Q-matrix of dimensions eight states and four policies [49].

The work of [41] considered task offloading with energy harvesting for an IoT MEC system. The offloading problem has been formulated as a decentralized partially observable Markov decision process. They further reduced the computational complexity by searching for an approximated solution using an RL decentralized offloading algorithm. The results, obtained using Matlab simulations, showed that the proposed reduces both average delay and average energy consumption.

To this end, it is crucial to identify the power consumption during different activities of the end devices, in particular data processing, data transmission and communication. In the following section, specific design considerations for task offloading are presented, which may influence the power consumption and the latency of the software and hardware components of the IoMT systems. The main focus is attributed to the choice of the communication protocols for IoT devices with consideration of the energy consumption.

4. Design Considerations for the Task Offloading

With respect to the general architecture of IoMT, Wireless Body Area Networks (WBANs) [38,50,51] are installed where various types of sensors are used, most likely

activity sensors (e.g., accelerometer), physiological sensors (e.g., heart rate, ECG and body temperature) and environmental sensors (e.g., humidity and air pressure) (see Figure 1). Various types of applications are recognized with enhanced sensing and communication capability, such as biomedical and wearable solutions for health monitoring, human activities control, organ implantation monitoring and remote surgical interventions. These applications require a high data rate, low latency and high quality of services (QoS) [39,40,52], in order to ensure precise, real-time and secure medical applications. With the integration of the IoMT, it is more challenging to identify the most appropriate strategy that enables efficient handling of the intensive and continuous requests from the installed wireless devices on the human body promptly. Moreover, wireless sensor nodes are battery powered, where the lifetime of the battery is directly dependent of the number of executed tasks along the process. Due to this, it is important to increase the computation capacity of battery-powered devices when performing intensive computing tasks while ensuring real-time intervention and data transmission. In this context, the choice of suitable data transmission and communication protocols has a strong influence on the evaluation of the task-offloading algorithm in terms of processing time, energy consumption and computation. In the following, an overview of the most common communication protocols is provided.

4.1. Communication Protocols

The general architecture of IoMT is reported in Figure 1. The provided architecture is composed of three main layers: (1) the things/devices layer, where the WBAN is installed, along with the gateway devices, (2) the fog layer, and (3) the cloud layer [53,54]. Different communication technologies can be identified within each layer, which enable transmission of the data from the end devices to the end user.

In the first layer, different sensor nodes are installed on the body, which build the WBAN. Sensor nodes can be implantable, wearable or mobile, placed for example in the hand of the patient. In this type of network the communication between sensors is carried out within a short range of 2 to 3 m. These devices, basically, require small power sources with respect to the safety and security of the user. Therefore, with respect to the low power specification and small communication range, the standard Industrial Scientific and Medical (ISM) band is sufficient to cover the installed nodes [55,56]. Various communication technologies are supported in the ISM band, such as ZigBee, Bluetooth and Wi-Fi. Moreover, alternative communication technology is introduced such as the Intra-Body Communication (IBC) technology [57,58]. Through IBC, the human body is used as a transmission medium, enabling power-saving, and thus improving the robustness and security of communications. Due to these advantages, IBC has been included as a third physical layer in the IEEE 802.15.6 standard for wireless body area networks designated as Human Body Communication (HBC) [59]. A central device, refereed also as base station, is responsible for collecting sensor data and forwarding them to the next communication layer. Accordingly, intermediate devices are installed as a bridge between the small interconnected WBAN and the exterior local network, namely the Wireless Local Area Network (WLAN). In this case, local gateways are used such as mobile devices, access points or simple mid-layer gateways. Typically, they provide a bridge between the IoT edge devices and the fog and cloud servers. They enable the passing of data from the discrete sensor network to the other cloud and application layers. On one side, common communication technologies can be initiated between the WBAN' nodes and the intermediate gateways, such as the Wi-Fi and Bluetooth. In the other side, communication with the fog and cloud server can be realized through 5G, Wi-Fi or GPR [60,61]. To this end, data communication and storage are carried out over this layer, whereas in the IoT layer, installed wireless devices are periodically transmitting information. Sensor devices remain awake for a specific time frame from time to time to transmit the required information.

Within the second layer, local servers and gateway devices for the fog network are placed. These devices enable the processing of the collected data. Excessive and complex

processing and data-mining algorithms can be carried out at this stage. Later, the collected data are redirected to the cloud layer for further processing. In the case of the cloud or fog layer, more powerful and long-range protocols are required, namely the LoRaWAN, Sigfox, NB-IoT and LTW-M [62], which ensure a better coverage range with a minimum of 1 km in urban deployment and 10 km in rural deployment. Moreover, the fog layer is in connection with healthcare experts responsible, which permits a reduction to the time delay of the interpretation and execution of specific tasks and decisions. In the third layer, powerful data storage and computation resources are installed. In this instance data analysis, decision-making and urgent intervention can be recognized. In addition, the cloud layer permits the incorporation of various and heterogeneous healthcare systems, which enables a real-time and continuous access to the current patient, equipment and planned tasks supervision and monitoring. Basically, this layer consists of cloud-based resources that will store the data generated by the medical infrastructure and be used to perform analytical work as needed in the future [54]. An overview of the common communication technologies used in WBANs is presented in Table 3 [63,64].

Table 3. Comparison between communication technologies used in the WBANs.

Criteria	Range in m	Data Rate	Frequency	Standard	Energy Consumption
Bluetooth [65,66]	<10	1–3 Mbits/s	2.4 GHz	IEEE 802.15.1-	<30 mA
NFC [67]	0.1	424 Kbit/s	13.56 MHz	ISO/IEC 1800-3	<15 mA
RFID [68,69]	<12	100 Mbit/s	LF: 125–135 KHz, HF: 13.56 MHz, UHF: 868–930 MHz, Microwave 2.45, 5.8 GHz,	ISO/IEC 1800	-
BLE [66]	10–300	125 Mbit/s	2.4 GHz	IEE 802.15.1	<15 mA, 10–100 mW
ZigBee [66,70]	10–500	250 Kbit/s	2.4 GHz	IEEE 802.15.4	<16 mA, 10–100 mW
Wi-Fi [64,70]	100	11 Mbit/s	2.4, 5 GHz	IEEE 802.11 a/b/g	-
LoRaWAN [71,72]	∼5 in urban 20 in rural	56 bits/s UL 296 bits/s DL	868, 434, 915 MHz	LPWAN	Sleep: 7.66 µA to 34 mA Tx: 133 mA Rx: 16.3 mA
Sigfox [73,74]	∼10 km in urban ∼40 km in rural	100 bits/s UL 60 bits/s DL	868, 434, 915 MHz	LPWAN, UNB	Sleep: ∼1 µA, Tx: 49 mA Rx: 19 mA
NB-IoT [75–77]	∼1 km in urban ∼10 km in rural	220 Kbits/s	Licensed LTE	LPWAN	Sleep: 13 mW Tx: 716 mW, Rx: 21 mW

4.2. Energy Consumption of Wireless Nodes

Typically, in the task-offloading paradigm, computing tasks are created by end devices (e.g., wireless sensor nodes, central devices). Therefore, the energy requirement at the level of the wireless node, as well as the network, are emphasized. Therefore, characterizing the energy consumption of the end device is crucial to create a balance between the energy requirement, demands and consumption. Essentially, the wireless sensor node is composed of four main units: energy management unit, communication unit, data processing unit and sensing unit. The energy management unit is responsible for converting the energy retrieved from either the battery or the energy-harvesting circuit into a suitable energy level, which can be used to supply the electronics of the node. Using energy harvesting helps to reduce the dependency on the battery power by extending the lifetime of the node itself [78]. The communication unit contains the radio transceiver module used for wireless communication. The processing unit is the core of the node, where all data processing and node activity is carried out. The last unit contains the embedded sensors, which can be either passive or active and are responsible for the sensing and actuating tasks. Basically, the effective lifetime of the node is dependent on the available, residual energy and the required amount of energy to successfully carry out the assigned task. Consequently, the total energy consumption is deducted in relation to the energy supply and energy consumption during data processing and communication. Considering the

energy provided by the harvesting module and the module consumption, the effective residual energy at a time instance *t* is estimated in accordance with the consumed, harvested and residual energy amounts of the previous time instance.

$$E_{Res}(t) = E_{Res}(t-1) - E_{Cons} + E_{Harv} \tag{4}$$

$E_{Res}(t)$, $E_{Res}(t-1)$, E_{Cons} and E_{Harv} are the residual energy of the node at a time instance *t*, the residual energy at a time instance $(t-1)$, energy consumption and the energy of the harvesting module, respectively (see Appendix A).

The general definition of the energy consumption within a sensor node is presented in Equation (5).

$$E_{Cons} = E_{Transceiver} + E_{System} + E_{Sensing} \tag{5}$$

where $E_{Transceiver}$, E_{System} and $E_{Sensing}$ are the energy consumed during the reception and transmission of data packet, energy consumed within the coding and decoding activities and the energy consumed during sensing activities, respectively.

With respect to the standard energy consumption model, the $E_{Transceiver}$ is presented based on the transmitter and receiver electronic definition as presented in Equations (7) and (9). The total energy consumption, within the radio module during data transmission, becomes:

$$E_{Cons} = E_{R_x} + E_{T_x} + E_{System} + E_{Sensing} \tag{6}$$

The energy of transmission and reception are dependent on the number of transmitted data bits over a distance *d*, where E_{elec} is the electrical energy of the circuitry needed to transmit or to receive a *l* bit data packet. *d* is the distance between the receiver and transmitter.

$$E_{T_x} = \begin{cases} E_{elec} \times l + E_{fs} \times l \times d^2, & d \leq d_T \\ E_{elec} \times l + E_{amp} \times l \times d^4, & d > d_T \end{cases} \tag{7}$$

The distance between both transmitter and receiver is dependent on the medium access and therefore, it is defined based on ϵ_f and ϵ_{amp}, which present the energy consumption factor for free space and for the multipath radio models, respectively. The threshold distance d_T is defined as:

$$d_T = \sqrt{\frac{\epsilon_{fs}}{\epsilon_{amp}}} \tag{8}$$

The energy consumption during the reception is defined based on the number of communicated bits *l*, which is defined in Equation (9). The list of the used parameters with their typical values is illustrated in Appendix A.

$$E_{R_x}(l) = E_{elec} \times l \tag{9}$$

Eventually, the effective energy consumption of a wireless node depends strongly on how often it sends and receives data packets, and processes sensor information.

Task offloading offers a promising solution to reduce the workload on the installed devices, by adopting specific algorithms where the task realization is offloaded to devices with efficient energy sources and computation capabilities. In the context of WBANs and wearable solutions, intensive computing is mitigated from the wireless sensor to the edge and from the cloud to the fog. It presents an efficient solution to manage the intensive communication and computation in a limited energy source environment. Moreover, by adopting an energy-harvesting solution, the energy of the system can be kept available to carry out the assigned tasks in real time and continuously, which remains challenging for different applications, such as in the case of real-time and continuous pulse monitoring [79], motion tracking [80], exoskeleton manipulation [81] and the maintenance and monitoring of implantable devices [82]. To this end, providing continuous and efficient power supply to wearable and implantable devices presents a highly addressed challenge in recent

research [83–85]. As part of this, integrating energy-harvesting technologies with task-offloading approaches allows end devices to endure for a long time to support long-term task processing [86–88].

5. Power Supply for Wearables with Task Offloading Capabilities

Task-offloading approaches can be efficiently combined with energy harvesting to address the issue of insufficient battery capacity and limited computation resources in IoMT devices and consequently increase the operating time of wearable devices. This is referred to as joint energy harvesting and task offloading. Using this technology, users can extract energy, convert it into useful energy, store it in the appropriate energy-storage device, and use that energy to perform the corresponding local computing and offloading tasks [15,89–91].

As depicted in Figure 4, the offloading algorithm reacts based on two estimations: The energy harvested/stored and the energy demands. Energy harvesting from ambient sources is considered a promising solution that can be used to provide power supply for IoMT devices and thus replace batteries. The most commonly used harvesters for the supply of wearable devices are piezoelectric harvesters, thermoelectric generators, RF harvesters, and solar cells. Table 4 illustrates the amount of power that can be harnessed from different sources, along with some advantages and limitations associated with each.

Ambient light presents the highest power density among other sources, with the possibility of harvesting indoor and outdoor. However, it has limited application due to its restricted availability.

Table 4. Available power from different energy sources (literature survey).

Energy Source	Harvested Power	Advantages	Disadvantages
Mechanical energy			
Human (motion)	$4\,\mu W/cm^2$	High power density	Depending on the source properties
Industry (vibrations)	$100\,\mu W/cm^2$		
Thermal energy			
Human (heat)	$25\,\mu W/cm^2$	Widely available	Limitation of power density
Industry	1–$10\,mW/cm^2$		
Ambient light			
Indoor	$10\,\mu W/cm^2$	High power density	Intermittent
Outdoor	$10\,mW/cm^2$		
Radio frequency			
GSM	$0.1\,\mu W/cm^2$	Widely available	Power dependent on distance between RF source-harvester
Wi-Fi	$0.001\,mW/cm^2$		

5.1. Thermoelectric Generators

Energy can be derived from heat using thermoelectric generators (TEGs) based on the thermoelectric effect. It is also known as the Seebeck effect, according to which electricity is generated by the temperature gradient between two conductors. A TEG can be attached to the body to convert the temperature difference between a body skin and the surrounding environment into voltage. This concept was launched in 1999, where the first wristwatch supplied by body heat was invented [92]. TEGs can be used as an efficient power supply for wearable devices when the human body and the surrounding environment have a temperature difference of 5 to 10 degrees.

The electric potential of a TEG is expressed by Equation (10)

$$V_{TEG} = S \cdot \Delta T \tag{10}$$

where *S* is the Seebeck coefficient of the material used and (ΔT) is the temperature difference across the TEG.

A thermally powered wearable device that incorporates an accelerometer to sense falls was developed in [93]. In this application, the device generated 520 μW of output power at 15 °C, which charged a capacitor and a power management unit, included to link the thermal source and a sensor node.

An in-depth analysis of thermoelectric generation technology was recently presented in [94], illustrating the working principles of TEGs and their applications. Nevertheless, the development of thermoelectric materials with acceptable power factors remains a major challenge, for which various techniques have been investigated to achieve better efficiencies.

5.2. Kinetic Energy Harveters

In contrast to solar or thermal energy, a kinetic energy source is not dependent on location or time. Kinetic harvesters are based on the extraction of vibration or motion and the conversion of the mechanical energy into electrical power through one or a combination of different transduction mechanisms. The most common ones are piezoelectric, electromagnetic, electrostatic, and triboelectric. These harvesters are classified related to their transduction mechanisms. Unlike other means of transduction, piezoelectric harvesters directly convert human motion changes into electrical signals without any requirements for further external input. Piezoelectric (PE) harvesters operate through the piezoelectric effect. When a force is applied to a PE element, a mechanical strain is developed, causing the material to exhibit changes in its polarization, causing the accumulation of electrical charges across the piezoelectric material. The changes in charge distribution produce an electric field depending on the applied force, frequency of oscillation, and geometry of the harvester.

Electromagnetic kinetic energy harvesters operate based on Faraday's law induction which states that once a conductor moves through an electric field, a current is induced. A system of springs, magnets and coils are used in electromagnet energy-harvesting systems. Coil number and magnetic mass are the main determinants of the output power of these energy harvesters. Therefore, reducing their size, weight and complexity is challenging. As example, the authors of [95] demonstrated the effectiveness of a frequency-converted electromagnetic harvester which extracts energy mainly from human limb motion. A power density of 0.33 mW/cm^3 was achieved in this work using low-frequency human vibration to power wearable devices at extremely low frequencies.

5.3. Flexible Piezoelectric Generators

The body is an excellent source of significant amounts of mechanical energy which can be produced from several biological processes, including walking, heartbeat, breathing and muscle movements. Thanks to their high flexibility, piezoelectric nanogenerators (PENGs) can convert this mechanical stress into electrical charges through nanostructured piezoelectric materials when stretched, pressed or flexed. In addition, this technology can potentially be integrated with other energy-harvesting mechanisms, resulting in hybrid energy-harvesting solutions. The simple architecture of PENGs makes them attractive and considered to be the most promising energy harvesters for wearable devices and microsystems. The materials used in piezoelectricity are diverse, including crystals, ceramics, and polymers. The converter needs to be attached to a part of the body subjected to strong compressive stress to maximize the piezoelectric effect. PENGs can provide enough power to supply devices with power consumption ranging from microwatts to milliwatts, which best fits the wearable sensor range as seen in Table 5 where the energy consumption of typical wearable sensors is presented.

Table 5. Energy consumption of typical medical sensors.

Wearable Sensors	Voltage Range	Power Consumption	Description
Optical heart rate sensors - BH1790GLC optical heart rate sensor [96]	1.7–3.6 V	720 µW	Measures the pulse waves that occur when the heart pumps blood.
Blood pressure sensors - Capacitive tactile sensor [97]	1.8–3.3 V	1.2–4.6 mW	Measures the pressure exerted by the circulating blood on the walls of blood vessels.
Glucometers - Implantable RFID glucose monitoring sensor [98]	1.0 V–1.2 V	50 µW	Measures the average blood glucose concentration.
Pulse oximeter sensors -MAX30102 pulse oximetry [99]	1.8 V–3.3 V	<1 mW	It attaches to a body part, most commonly to a finger to measure the oxygen saturation level of the circulating arterial blood.

Flexible Piezoelectric generators can be modeled as sinusoidal current sources I_P in parallel with parasitic capacitances C_P and internal resistances R_P when excited by sinusoidal vibrations at their resonant frequencies. Since the piezoelectric transducer can deliver an alternating irregular AC current rather than direct current (DC), an electronic interface is essential to enable voltage compatibility between the piezoelectric element and the load. The electronic interface greatly influences the energy-harvesting effectiveness [100], which has driven a variety of research efforts to develop PENG-compatible energy management interfaces [101]. Implementing these circuits is mostly intended to allow the user to use irregular AC power harnessed by piezoelectric transducers (PTs) to supply loads such as wearable sensors. The rectification stage of PEH systems is usually coupled with a DC-DC converter [100] to scale the rectified voltage to match the application's requirements.

One limitation of the classic AC-DC energy-harvesting circuits when implemented with PEts is that negative output power is produced because the output current and voltage could not keep the same phase, leading to a loss of an amount of the harvested energy. P-SSHI and S-SSHI have been proposed to overcome this limitation. The main difference between the circuits is how we connect the switch S and the inductor L, either in series, so we are talking about SSHI or in parallel to deal with P-SSHI. When the vibration occurs, the switch S remains open, allowing the current to flow through the circuit to the storage element Cr. If the piezoelectric element's voltage drops below a certain threshold, the switch S will automatically close, inverting the voltage across the PE element and therefore stopping current flow. This means that the switch is kept closed until a full inversion of the PEt's voltage has been achieved. Nevertheless, this voltage inversion causes an electrical damping that opposes the mechanical vibrations on the piezoelectric material. This effect is known as Synchronized Switch Damping (SSD). It can significantly affect the overall conversion efficiency, and it is consequently the main limitation of both P-SSHI and S-SSHI circuits. Figures 6 and 7 display the P-SSHI and S-SSHI energy-harvesting interfaces, respectively.
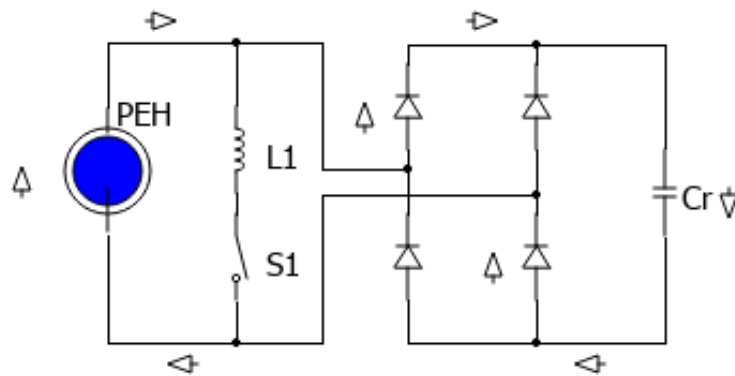
Figure 6. Schematic of P-SSHI energy extraction interface.
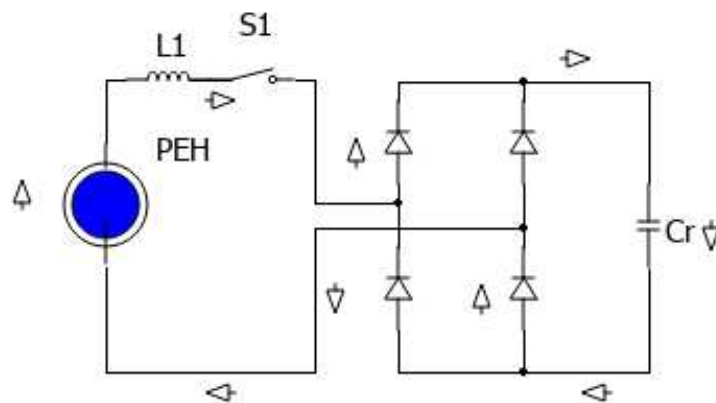
Figure 7. Schematic of S-SSHI energy extraction interface.

SECE circuit, displayed in Figure 8, mainly prevents the SSD effect, which is the main limitation of P-SSHI and S-SSHI circuits. This effect is caused by the direct connection between the output load and the piezoelectric transducer during the hole vibration phase. When the PEH generates the voltage, the switch S will be closed, and the energy will be stored in the inductor L as seen in the figure.
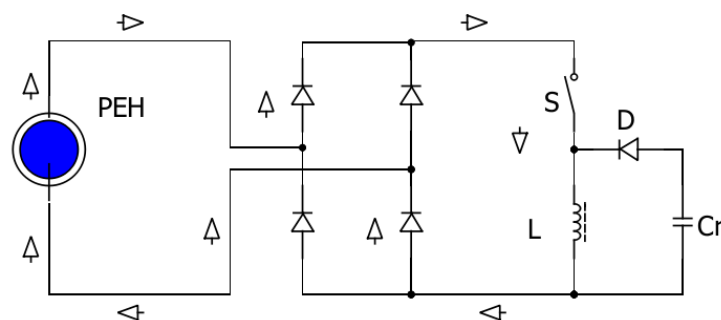
Figure 8. Schematic of SECE energy extraction interface when the switch S is closed.

When the vibration stops, the voltage across the piezoelectric element falls to zero, and the switch S will open immediately. Consequently, the energy accumulated in the inductor will be directly transferred to the storage capacitor and the load. One limitation for this interface is the complexity when compared to the simple architecture and switching strategy that characterize SSHI circuits.

The control of the integrated switches was a common limitation for the reviewed interfaces, so several researchers were focusing on developing self-powered resonant energy-harvesting circuits. In [102], authors demonstrated an optimized self-powered P-

SSHI circuit that can automatically switch once the voltage exceeds its maximum threshold. In addition, this technology can potentially be integrated with other energy-harvesting mechanisms, resulting in hybrid harvesting solutions [103].

5.4. Energy-Storage Techniques

Using energy harvesting to achieve battery-free operation has gained high interest. However, any interruption in the energy-harvesting source will affect the wearable device's operation. Therefore, an energy-storage mechanism is still required to maintain a smooth power supply for charge loads and serve as a backup whenever the energy source is unavailable.

The harnessed energy can be stored before being supplied to the MCU, or the power can be delivered directly. The decision of whether implementing a storage element in a wearable device considers different factors:

- Placement of the device: implant or outside.
- Energy source: type
- Requirements of the application: either it needs a sustainable supply for the wearable device or a non-critical usage.

Batteries and super capacitors are the two main solutions for energy storage. Energy storage for wearable devices must comply with several requirements. First, the storage element needs to be rechargeable to avoid frequent battery replacements, which can be inconvenient in several cases. In pacemakers, as an example, surgery needs to be performed every eight years to replace their lithium batteries [104]. As a second requirement, the storage device needs to be capable of supporting long-term application with minimal impact on battery parameters.

The following Table 6 compares two storage mechanisms, batteries and capacitors.

Table 6. Comparison between different storage techniques for energy harvesters in IoMT devices

Comparison	Conventional Batteries	Supercapacitors
Storage mechanism	Chemical	Physical
Energy storage	High	Limited
Recharging cycles	100 s	Millions
Charging time	Hours	Sec-minutes
Impedance	Low-high	Low
Physical size	Large	Medium
Capacity	0.3–2500 mAH	10–100 µAH

They differ mostly in the number of charging cycles since capacitors can reach millions of cycles. In addition, capacitors require only a few seconds for charging, so the charging time is very fast compared to batteries. In contrast, supercapacitors cannot be used in AC and high frequency circuits and have lower capacity than batteries, but this can satisfy the requirements of some low-power applications. One more limitation for using batteries as a storage element is that the battery is susceptible to leakage, leading to chemical poisoning, especially when used in implants. Batteries can leak chemicals when overcharged or heated (above 60 °C). This can lead to chemical burns risking human beings. Due to their advantages over batteries, super capacitors are a promising alternative to store energy. In a super capacitor, thin dielectric layers and electrodes hold power at the electrode–electrolyte interface to be accessed when needed. Thanks to their high pulse power capacity, they can also handle small power surges. Super capacitors' excellent cycle lifetime also makes them ideally suited to act as energy-storage components in energy-harvesting-based sustainable power systems.

5.5. Recent Energy-Harvesting Solutions for Wearables

The human body can be a versatile source of energy harvesting [105,106]. Energy can be harvested from everyday activities, such as breathing, arm motion, walking, running,

or pedaling, without performing a specific workout. The body can produce mechanical energy through various body zones movements, such as the elbow, the knee, the ankle or the heels. The performance of three vibrating generators was studied in [107] at nine different body locations for a person walking on a treadmill. The results indicate that the energy generated at lower-body locations (hip, knee, and ankle) is four times greater than the energy generated at upper-body locations. Additionally, body heat offers promising possibilities for supplying wearable systems. Based on the Seeback effect, a flexible TEG generated 4.95 mW of body heat and was used for a wearable multi-sensing bracelet [108]. A energy-autonomous, multi-sensing bracelet can operate under varying conditions, including human motion. The amount of energy in such systems is highly dependent on the temperature difference between the human body and the ambient environment [109]. Several studies have shown that physiological activities, such as blood pressure, heart motion and breathing, can regularly provide wearable devices with energy supply. In [110], cardiac contractions are used to supply low-powered pacemakers. When powered by a constant heartbeat of 90 bpm, the harvester can deliver 11.1 j of electrical energy. Because of the small size and weight requirement, energy extraction from the human body is much more complicated than energy harvesting from machines [111]. The available power is often weak and difficult to use, such as human kinetic energy, which typically has a low frequency and a low amplitude.

Recently, thermoelectric nanogenerators (TENGs) were demonstrated as a conventional technique for rehabilitation in [112]. As an exercise gaming device, a wearable TENG-based rehabilitation device (Rehab-TENG) was developed. The device was used to control a game on a laptop by flexing and extending the arm. It is an effective way of testing the motor function of an impaired arm. Rehab-TENG is also used as an energy harvester in an exercise system where the patient moves an impaired arm to store energy in a capacitor. It is possible to assess the level of deficiency by measuring the charging rate of the storage element, which consequently enhances patients' motivation for exercising more repetitive movements of the impaired body zone. This, in turn, speeds up recovery. Furthermore, the authors suggested using the Rehab-TENG device as an autonomous home exercise and monitoring system, which is particularly relevant during pandemics, therefore reducing the necessity for hospital visits for rehabilitation.

An emerging trend in energy-harvesting technologies for IoMT is developing biocompatible wearable harvesters, such as textiles, footwear, or watches, which are energy-autonomous, lightweight, flexible, and have more computational resources for better performance. Consequently, various energy-saving approaches were proposed to mitigate the problem of excessive energy demands during the operation of devices. Task offloading is a promising and effective technique that extends the operating time of wearables by migrating the energy intensive task to edge device. Task-offloading algorithms attempts to solve an optimization problem by looking for a suitable remote processor to perform the offloading, taking into consideration the overheads caused by the communication link (energy and latency). Real-time implementation of task offloading for wearables is still in its infancy.

6. Value-Based Healthcare System and Personalized Healthcare

The legacy health care system is staff-centric. Driven by the need to transform the healthcare system to be patient- and personnel-centric, numerous governments have proposed a transformation strategy. For instance, in Saudi Arabia, the government has identified eight challenges that the current health care system should cope with. Those challenges are: (1) the continued growth and aging of the population, (2) the prevalence of avoidable injuries and non-communicable diseases beyond the international standard, (3) the inadequacy and inconsistency of primary care, (4) wide-scale disparity in the quality of care, (5) a significant deficiency in value and quality, (6) the system is resource-, staff-, and institution-centric, (7) insufficient use of digital integrated systems, and (8) the growing need to decrease government spending in health care systems [113].

The value-based healthcare system is a new framework adopted by many governments to improve healthcare services and user experience through the improvement of patient healthcare outcomes at the lowest possible cost, i.e., the value is determined as the ratio of outcomes to cost [114]. Preventive medicine and early intervention lowers the cost associated with the hospitalization of patients. Healthcare 4.0, a new paradigm shift in the health industry, has transformed healthcare from an institution-centered to a patient-centered system [115].

Wearables are cornerstone technologies in Healthcare 4.0. The design of patient-centered care mandates the inclusion of the user requirements to identify functional and non-functional requirements [35]. Surveys, focus groups, and interviews are common ways to capture user requirements. In [116], the authors devised a cost-efficient system for the monitoring of the sedentary level of senior citizens. The system requirements and guidelines have been gathered from a literature review. The system is then evaluated using a mixed approach: focus group, interview, and observations. The system is refined through the feedback provided by the end-user. The authors reported that: (1) the majority of the respondents are interested in receiving a feedback on the level of their physical activity at the end of the day, (2) nearly 58% of participants showed interest in a system that integrates games with physical activity, and (3) virtually 83% of the participants showed interest in profiling their daily activities and receiving alerts when their physical activities are low.

The user requirements for the wearables targeting Chinese seniors are the focus of the work described in [117]. Those requirements have been classified under the following three categories: healthcare requirements, privacy and security requirements, and commodity requirements.

7. Conclusions

Wearable devices are the heart of IoMT. Energy-harvesting techniques can achieve energy-autonomous wearable devices. However, handling tasks that require intensive computing resources limits their performance. To overcome these limitations, energy-aware task-offloading approaches were proposed to reduce the device energy consumption and improve computation resources. This paper surveys recent works on joint task offloading and energy-harvesting techniques in the IoMT. In addition, possibilities of power supply for medical sensors and energy-storage strategies are investigated.

Joint task offloading and energy harvesting is still an active area of research. The offloading is meaningful at two possible levels: from wearables (IoT end device) to edge devices (IoT high-end or middle-end device), or from edge devices to fog nodes. An off-policy-based reinforcement learning algorithm has been often proposed in the literature. Nevertheless, its hardware implementation has received scant attention.

Future work will focus on the efficient hardware implementation of joint energy harvesting and reinforcement learning-based task offloading for wearable devices. Nevertheless, privacy and security might affect the offloading strategy when applied to wearables; this topic was not considered in this study.

Abbreviations

EH	Energy Harvesting
SSHI	Synchronized Switch Harvesting on Inductor
P-SSHI	Parallel Synchronized Switch Harvesting on Inductor
S-SSHI	Serial Synchronized Switch Harvesting on Inductor
SECE	Synchronized Electrical Charge Extraction
SEH	Standard Energy Harvesting (Bridge rectifier)
SSD	Synchronized Switch Damping
EWMA	Exponentially Weighted Moving Average
HBC	Human Body Communication
IoT	Internet of Things
IoMT	Internet of Medical Things
MCU	Micro-Controller Unit
MEC	Mobile Edge Computing
QoS	Quality of Service
WBANs	Wireless Body Area Networks
WSNs	Wireless Sensor Networks
PENGs	Piezoelectric nanogenerators
PEH	Piezoelectric energy harvesting
FPEGs	Flexible Piezoelectric Generators
PEt	Piezoelectric transducer
TEG	Thermoelectric Generator

Appendix A

Table A1. List of parameters with their typical values.

Parameter	Explanation	Typical Value/Range	Unit
$E_{Res}(t)$	Residual energy at a time instance t	NA	J
$E_{Res}(t-1)$	Residual energy at a time instance $(t-1)$	NA	J
E_{Cons}	Energy consumption	NA	J
E_{Harv}	Energy of the harvesting module	NA	J
$E_{Transceiver}$	Consumed energy of transmission	NA	J
E_{System}	Consumed energy of coding and decoding	NA	J
$E_{Sensing}$	Consumed energy of the sensing	NA	J
E_{R_x}	Consumed energy of the reception	NA	J
E_{T_x}	Consumed energy of the transmission	NA	J
E_{elec}	Electrical energy of the circuitry	Based on initial assumption (e.g., 50 nJ)	J
d	Distance between transmitter and receiver	Related to the realized scenario	m
d_T	Threshold distance between transmitter and receiver	1 m	m
l	Size of the data packet	Depends on the ADC of the processor	bits
ϵ_f	Energy consumption factor for free space	Depends on the	$pJ/bit/m^2$
ϵ_{amp}	Energy consumption factor for multipath radio models	propagation loss	$pJ/bit/m^4$
M	Number of cores	8	-
n	Number of tasks	maximum value is 6	-
α	the learning rate	10^{-4}	-
γ	the discount rate	0.85	-

References

1. Farias, F.A.C.d.; Dagostini, C.M.; Bicca, Y.d.A.; Falavigna, V.F.; Falavigna, A. Remote patient monitoring: A systematic review. *Telemed. E-Health* **2020**, *26*, 576–583. [CrossRef] [PubMed]
2. Tian, S.; Yang, W.; Grange, J.M.L.; Wang, P.; Huang, W.; Ye, Z. Smart healthcare: Making medical care more intelligent. *Glob. Health J.* **2019**, *3*, 62–65. [CrossRef]
3. Gatouillat, A.; Badr, Y.; Massot, B.; Sejdić, E. Internet of Medical Things: A Review of Recent Contributions Dealing With Cyber-Physical Systems in Medicine. *IEEE Internet Things J.* **2018**, *5*, 3810–3822. [CrossRef]
4. Yang, W.; Wang, S.; Sahri, N.M.; Karie, N.M.; Ahmed, M.; Valli, C. Biometrics for Internet-of-Things Security: A Review. *Sensors* **2021**, *21*, 6163. [CrossRef]
5. Swaroop, K.N.; Chandu, K.; Gorrepotu, R.; Deb, S. A health monitoring system for vital signs using IoT. *Internet Things* **2019**, *5*, 116–129. [CrossRef]
6. Ali, M.; Ali, A.A.; Taha, A.E.; Dhaou, I.B.; Gia, T.N. Intelligent Autonomous Elderly Patient Home Monitoring System. In Proceedings of the ICC 2019—2019 IEEE International Conference on Communications (ICC), Shanghai, China, 20–24 May 2019; pp. 1–6. [CrossRef]
7. Rahman, M.A.; Hossain, M.S. An Internet of medical things-enabled edge computing framework for tackling COVID-19. *IEEE Internet Things J.* **2021**, *8*, 15847–15854. [CrossRef]
8. Zhang, H.; Xiao, Y.; Bu, S.; Niyato, D.; Yu, F.R.; Han, Z. Computing resource allocation in three-tier IoT fog networks: A joint optimization approach combining Stackelberg game and matching. *IEEE Internet Things J.* **2017**, *4*, 1204–1215. [CrossRef]
9. Mukherjee, M.; Kumar, V.; Maity, D.; Matam, R.; Mavromoustakis, C.X.; Zhang, Q.; Mastorakis, G. Delay-sensitive and Priority-aware Task Offloading for Edge Computing-assisted Healthcare Services. In Proceedings of the GLOBECOM 2020—2020 IEEE Global Communications Conference, Taipei, Taiwan, 7–11 December 2020; pp. 1–5. [CrossRef]
10. Zhao, X.; Zhao, L.; Liang, K. An energy consumption oriented offloading algorithm for fog computing. In *International Conference on Heterogeneous Networking for Quality, Reliability, Security and Robustness*; Springer: Berlin/Heidelberg, Germany, 2016; pp. 293–301.
11. Zhang, Z.; Yu, F.R.; Fu, F.; Yan, Q.; Wang, Z. Joint offloading and resource allocation in mobile edge computing systems: An actor-critic approach. In Proceedings of the 2018 IEEE Global Communications Conference (GLOBECOM), Abu Dhabi, United Arab Emirates, 9–13 December 2018; IEEE: Piscataway, NJ, USA, 2018; pp. 1–6.
12. Huang, L.; Feng, X.; Zhang, C.; Qian, L.; Wu, Y. Deep reinforcement learning-based joint task offloading and bandwidth allocation for multi-user mobile edge computing. *Digit. Commun. Netw.* **2019**, *5*, 10–17. [CrossRef]
13. Min, M.; Wan, X.; Xiao, L.; Chen, Y.; Xia, M.; Wu, D.; Dai, H. Learning-based privacy-aware offloading for healthcare IoT with energy harvesting. *IEEE Internet Things J.* **2018**, *6*, 4307–4316. [CrossRef]
14. Wang, F.; Zhang, X. Dynamic computation offloading and resource allocation over mobile edge computing networks with energy harvesting capability. In Proceedings of the 2018 IEEE International Conference on Communications (ICC), Kansas City, MO, USA, 20–24 May 2018; IEEE: Piscataway, NJ, USA, 2018; pp. 1–6.
15. Mustafa, E.; Shuja, J.; Jehangiri, A.I.; Din, S.; Rehman, F.; Mustafa, S.; Maqsood, T.; Khan, A.N. Joint wireless power transfer and task offloading in mobile edge computing: A survey. *Clust. Comput.* **2021**, 1–20. [CrossRef]
16. Engineer, M.; Tusha, R.; Shah, A.; Adhvaryu, D.K. Insight into the Importance of Fog Computing in Internet of Medical Things (IoMT). In Proceedings of the 2019 International Conference on Recent Advances in Energy-Efficient Computing and Communication (ICRAECC), Nagercoil, India, 7–8 March 2019; pp. 1–7. [CrossRef]
17. Hartmann, M.; Hashmi, U.S.; Imran, A. Edge computing in smart health care systems: Review, challenges, and research directions. *Trans. Emerg. Telecommun. Technol.* **2019**, e3710. [CrossRef]
18. Omoniwa, B.; Hussain, R.; Javed, M.A.; Bouk, S.H.; Malik, S.A. Fog/Edge Computing-Based IoT (FECIoT): Architecture, Applications, and Research Issues. *IEEE Internet Things J.* **2019**, *6*, 4118–4149. [CrossRef]
19. Aazam, M.; Zeadally, S.; Flushing, E.F. Task offloading in edge computing for machine learning-based smart healthcare. *Comput. Netw.* **2021**, *191*, 108019. [CrossRef]
20. Islam, A.; Debnath, A.; Ghose, M.; Chakraborty, S. A survey on task offloading in Multi-access Edge Computing. *J. Syst. Archit.* **2021**, *118*, 102225. [CrossRef]
21. Ryou, J.C.; Wong, J. A task migration algorithm for load balancing in a distributed system. In Proceedings of the Twenty-Second Annual Hawaii International Conference on System Sciences. Volume II: Software Track, Kailua-Kona, HI, USA, 3–6 January 1989; Volume 2, pp. 1041–1048. [CrossRef]
22. Suen, T.; Wong, J. Efficient task migration algorithm for distributed systems. *IEEE Trans. Parallel Distrib. Syst.* **1992**, *3*, 488–499. [CrossRef]
23. Jiang, Y. A Survey of Task Allocation and Load Balancing in Distributed Systems. *IEEE Trans. Parallel Distrib. Syst.* **2016**, *27*, 585–599. [CrossRef]
24. Jacob, N.; Brodley, C. Offloading IDS Computation to the GPU. In Proceedings of the 2006 22nd Annual Computer Security Applications Conference (ACSAC'06), Miami Beach, FL, USA, 11–15 December 2006; pp. 371–380. [CrossRef]
25. Liu, C.; Tang, F.; Hu, Y.; Li, K.; Tang, Z.; Li, K. Distributed Task Migration Optimization in MEC by Extending Multi-Agent Deep Reinforcement Learning Approach. *IEEE Trans. Parallel Distrib. Syst.* **2021**, *32*, 1603–1614. [CrossRef]

26. Sun, L.; Jiang, X.; Ren, H.; Guo, Y. Edge-Cloud Computing and Artificial Intelligence in Internet of Medical Things: Architecture, Technology and Application. *IEEE Access* **2020**, *8*, 101079–101092. [CrossRef]

27. Kumar, K.; Liu, J.; Lu, Y.H.; Bhargava, B. A survey of computation offloading for mobile systems. *Mob. Netw. Appl.* **2013**, *18*, 129–140. [CrossRef]

28. Jalali, F.; Hinton, K.; Ayre, R.; Alpcan, T.; Tucker, R.S. Fog Computing May Help to Save Energy in Cloud Computing. *IEEE J. Sel. Areas Commun.* **2016**, *34*, 1728–1739. [CrossRef]

29. Zhang, X.; Lu, J.J.; Qin, X.; Zhao, X.N. A high-level energy consumption model for heterogeneous data centers. *Simul. Model. Pract. Theory* **2013**, *39*, 41–55. [CrossRef]

30. Naha, R.K.; Garg, S.; Georgakopoulos, D.; Jayaraman, P.P.; Gao, L.; Xiang, Y.; Ranjan, R. Fog Computing: Survey of Trends, Architectures, Requirements, and Research Directions. *IEEE Access* **2018**, *6*, 47980–48009. [CrossRef]

31. Aazam, M.; Zeadally, S.; Harras, K.A. Offloading in fog computing for IoT: Review, enabling technologies, and research opportunities. *Future Gener. Comput. Syst.* **2018**, *87*, 278–289. [CrossRef]

32. Ud Din, I.; Guizani, M.; Hassan, S.; Kim, B.S.; Khurram Khan, M.; Atiquzzaman, M.; Ahmed, S.H. The Internet of Things: A Review of Enabled Technologies and Future Challenges. *IEEE Access* **2019**, *7*, 7606–7640. [CrossRef]

33. Kumari, A.; Tanwar, S.; Tyagi, S.; Kumar, N. Fog computing for Healthcare 4.0 environment: Opportunities and challenges. *Comput. Electr. Eng.* **2018**, *72*, 1–13. [CrossRef]

34. Yang, Y.; Geng, Y.; Qiu, L.; Hu, W.; Cao, G. Context-Aware Task Offloading for Wearable Devices. In Proceedings of the 2017 26th International Conference on Computer Communication and Networks (ICCCN), Vancouver, BC, Canada, 31 July–3 August 2017; pp. 1–9. [CrossRef]

35. Ben Dhaou, I.; Ebrahimi, M.; Ben Ammar, M.; Bouattour, G.; Kanoun, O. Edge Devices for Internet of Medical Things: Technologies, Techniques, and Implementation. *Electronics* **2021**, *10*, 2104. [CrossRef]

36. Kalantarian, H.; Sideris, C.; Mortazavi, B.; Alshurafa, N.; Sarrafzadeh, M. Dynamic Computation Offloading for Low-Power Wearable Health Monitoring Systems. *IEEE Trans. Biomed. Eng.* **2017**, *64*, 621–628. [CrossRef]

37. Geng, Y.; Yang, Y.; Cao, G. Energy-Efficient Computation Offloading for Multicore-Based Mobile Devices. In Proceedings of the IEEE INFOCOM 2018—IEEE Conference on Computer Communications, Honolulu, HI, USA, 16–19 April 2018; pp. 46–54. [CrossRef]

38. Wang, L.; Shao, H.; Li, J.; Wen, X.; Lu, Z. Optimal Multi-User Computation Offloading Strategy for Wireless Powered Sensor Networks. *IEEE Access* **2020**, *8*, 35150–35160. [CrossRef]

39. Jiang, J.; Zhang, X.; Li, S. A Task Offloading Method with Edge for 5G-Envisioned Cyber-Physical-Social Systems. *Secur. Commun. Netw.* **2020**, *2020*, 8867094. [CrossRef]

40. Liao, Y.; Yu, Q.; Han, Y.; Leeson, M. Relay-Enabled Task Offloading Management for Wireless Body Area Networks. *Appl. Sci.* **2018**, *8*, 1409. [CrossRef]

41. Tang, Q.; Xie, R.; Yu, F.R.; Huang, T.; Liu, Y. Decentralized computation offloading in IoT fog computing system with energy harvesting: A dec-POMDP approach. *IEEE Internet Things J.* **2020**, *7*, 4898–4911. [CrossRef]

42. Li, Y.; Qi, F.; Wang, Z.; Yu, X.; Shao, S. Distributed Edge Computing Offloading Algorithm Based on Deep Reinforcement Learning. *IEEE Access* **2020**, *8*, 85204–85215. [CrossRef]

43. Gao, Z.; Hao, W.; Han, Z.; Yang, S. Q-Learning-Based Task Offloading and Resources Optimization for a Collaborative Computing System. *IEEE Access* **2020**, *8*, 149011–149024. [CrossRef]

44. Zhang, K.; Zhu, Y.; Leng, S.; He, Y.; Maharjan, S.; Zhang, Y. Deep Learning Empowered Task Offloading for Mobile Edge Computing in Urban Informatics. *IEEE Internet Things J.* **2019**, *6*, 7635–7647. [CrossRef]

45. Sutton, R.S.; Bach, F.; Barto, A.G. *Reinforcement Learning*, 2nd ed.; MIT Press Ltd.: Cambridge, MA, USA, 2018.

46. Wei, Z.; Zhao, B.; Su, J.; Lu, X. Dynamic Edge Computation Offloading for Internet of Things With Energy Harvesting: A Learning Method. *IEEE Internet Things J.* **2019**, *6*, 4436–4447. [CrossRef]

47. Zhang, K.; Samaan, N. Optimized Look-Ahead Offloading Decisions Using Deep Reinforcement Learning for Battery Constrained Mobile IoT Devices. In Proceedings of the 2020 IEEE International Conference on Smart Cloud (SmartCloud), Washington, DC, USA, 6–8 November 2020; pp. 181–186. [CrossRef]

48. Zhang, J.; Du, J.; Wang, J.; Shen, Y. Hybrid Decision Based Deep Reinforcement Learning For Energy Harvesting Enabled Mobile Edge Computing. In Proceedings of the 2020 International Wireless Communications and Mobile Computing (IWCMC), Limassol, Cyprus, 15–19 June 2020; pp. 2100–2105. [CrossRef]

49. Spanò, S.; Cardarilli, G.C.; Di Nunzio, L.; Fazzolari, R.; Giardino, D.; Matta, M.; Nannarelli, A.; Re, M. An Efficient Hardware Implementation of Reinforcement Learning: The Q-Learning Algorithm. *IEEE Access* **2019**, *7*, 186340–186351. [CrossRef]

50. Rawat, P.; Singh, K.D.; Chaouchi, H.; Bonnin, J.M. Wireless sensor networks: A survey on recent developments and potential synergies. *J. Supercomput.* **2013**, *68*, 1–48. [CrossRef]

51. Jung, J.; Lee, W.; Kim, H. Cooperative Computing System for Heavy-Computation and Low-Latency Processing in Wireless Sensor Networks. *Sensors* **2018**, *18*, 1686. [CrossRef]

52. Zhou, G.D.; Yi, T.H. Recent Developments on Wireless Sensor Networks Technology for Bridge Health Monitoring. *Math. Probl. Eng.* **2013**, *2013*, 947867. [CrossRef]

53. Razdan, S.; Sharma, S. Internet of Medical Things (IoMT): Overview, Emerging Technologies, and Case Studies. *IETE Tech. Rev.* **2021**, 1–14. [CrossRef]

54. Vishnu, S.; Ramson, S.J.; Jegan, R. Internet of Medical Things (IoMT)—An overview. In Proceedings of the 2020 5th International Conference on Devices, Circuits and Systems (ICDCS), Coimbatore, India, 5–6 March 2020; IEEE: Piscataway, NJ, USA, 2020. [CrossRef]

55. Alabidi, E.S.; Kamarudin, M.; Rahman, T.; Khalily, M.; Abdulrahman, A.; Jamlos, M.; Jais, M. Radiation characteristics improvement of monopole antenna for WBAN applications. *Int. J. Multimed. Ubiquitous Eng* **2014**, *9*, 53–64. [CrossRef]

56. Al Islam, N.; Arifin, F. Performance analysis of a miniaturized implantable PIFA antenna for WBAN at ISM band. In Proceedings of the 2016 3rd International Conference on Electrical Engineering and Information Communication Technology (ICEEICT), Dhaka, Bangladesh, 22–24 September 2016; IEEE: Piscataway, NJ, USA, 2016; pp. 1–5.

57. Asan, N.B.; Hassan, E.; Perez, M.D.; Joseph, L.; Berggren, M.; Voigt, T.; Augustine, R. Fat-Intrabody Communication at 5.8 GHz Including Impacts of Dynamics Body Movements. 2019. Available online: http://www.diva-portal.org/smash/record.jsf?pid=diva2:1353288 (accessed on 10 January 2022).

58. Čuljak, I.; Lučev Vasić, Ž.; Mihaldinec, H.; Džapo, H. Wireless Body Sensor Communication Systems Based on UWB and IBC Technologies: State-of-the-Art and Open Challenges. *Sensors* **2020**, *20*, 3587. [CrossRef] [PubMed]

59. Álvarez-Botero, G.A.; Hernández-Gómez, Y.K.; Telléz, C.E.; Coronel, J.F. Human body communication: Channel characterization issues. *IEEE Instrum. Meas. Mag.* **2019**, *22*, 48–53. [CrossRef]

60. Windha M.V.; Iskandar; Hendrawan; Arifianto, M.S. Wireless Sensor Network on 5G Network. In Proceedings of the 2018 4th International Conference on Wireless and Telematics (ICWT), Bali, Indonesia, 12–13 July 2018; pp. 1–5. [CrossRef]

61. Papadopoulos, G.Z.; Kritsis, K.; Gallais, A.; Chatzimisios, P.; Noel, T. Performance evaluation methods in ad hoc and wireless sensor networks: A literature study. *IEEE Commun. Mag.* **2016**, *54*, 122–128. [CrossRef]

62. Aldahdouh, K.A.; Darabkh, K.A.; Al-Sit, W. A survey of 5G emerging wireless technologies featuring LoRaWAN, Sigfox, NB-IoT and LTE-M. In Proceedings of the 2019 International Conference on Wireless Communications Signal Processing and Networking (WiSPNET), Chennai, India, 21–23 March 2019; IEEE: Piscataway, NJ, USA, 2019; pp. 561–566.

63. Arefin, M.T.; Ali, M.H.; Haque, A.F. Wireless body area network: An overview and various applications. *J. Comput. Commun.* **2017**, *5*, 53–64. [CrossRef]

64. Vallejos de Schatz, C.H.; Medeiros, H.P.; Schneider, F.K.; Abatti, P.J. Wireless medical sensor networks: Design requirements and enabling technologies. *Telemed. E-Health* **2012**, *18*, 394–399. [CrossRef]

65. Reich, O.; Hübner, E.; Ghita, B.; Wagner, M.; Schäfer, J. Performance Evaluation of Bluetooth in a Wireless Body Area Network for Practical Applications. In Proceedings of the 2020 IEEE 11th Sensor Array and Multichannel Signal Processing Workshop (SAM), Hangzhou, China, 8–11 June 2020; pp. 1–5. [CrossRef]

66. Georgakakis, E.; Nikolidakis, S.A.; Vergados, D.D.; Douligeris, C. An analysis of bluetooth, zigbee and bluetooth low energy and their use in wbans. In *International Conference on Wireless Mobile Communication and Healthcare*; Springer: Berlin/Heidelberg, Germany, 2010; pp. 168–175.

67. Coskun, V.; Ozdenizci, B.; Ok, K. A survey on near field communication (NFC) technology. *Wirel. Pers. Commun.* **2013**, *71*, 2259–2294. [CrossRef]

68. Bouhassoune, I.; Saadane, R.; Chehri, A. Wireless Body Area Network Based on RFID System for Healthcare Monitoring: Progress and Architectures. In Proceedings of the 2019 15th International Conference on Signal-Image Technology Internet-Based Systems (SITIS), Sorrento, Italy, 26–29 November 2019; pp. 416–421. [CrossRef]

69. Liu, H.; Bolic, M.; Nayak, A.; Stojmenovi, I. Integration of RFID and wireless sensor networks. In *Encyclopedia on Ad Hoc and Ubiquitous Computing: Theory and Design of Wireless Ad Hoc, Sensor, and Mesh Networks*; World Scientific: Singapore, 2010; pp. 319–347.

70. Tang, M.; Jin, Y.; Yao, L. WiFi-ZigBee Coexistence Based on Collision Avoidance for Wireless Body Area Network. In Proceedings of the 2017 3rd International Conference on Big Data Computing and Communications (BIGCOM), Chengdu, China, 10–11 August 2017; pp. 245–250. [CrossRef]

71. Casals, L.; Mir, B.; Vidal, R.; Gomez, C. Modeling the energy performance of LoRaWAN. *Sensors* **2017**, *17*, 2364. [CrossRef]

72. Haxhibeqiri, J.; Van den Abeele, F.; Moerman, I.; Hoebeke, J. LoRa scalability: A simulation model based on interference measurements. *Sensors* **2017**, *17*, 1193. [CrossRef]

73. Gomez, C.; Veras, J.C.; Vidal, R.; Casals, L.; Paradells, J. A sigfox energy consumption model. *Sensors* **2019**, *19*, 681. [CrossRef]

74. Lavric, A.; Petrariu, A.I.; Popa, V. Long Range SigFox Communication Protocol Scalability Analysis Under Large-Scale, High-Density Conditions. *IEEE Access* **2019**, *7*, 35816–35825. [CrossRef]

75. Lauridsen, M.; Krigslund, R.; Rohr, M.; Madueno, G. An empirical NB-IoT power consumption model for battery lifetime estimation. In Proceedings of the 2018 IEEE 87th Vehicular Technology Conference (VTC Spring), Porto, Portugal, 3–6 June 2018; IEEE: Piscataway, NJ, USA, 2018; pp. 1–5.

76. Migabo, E.M.; Djouani, K.D.; Kurien, A.M. The Narrowband Internet of Things (NB-IoT) Resources Management Performance State of Art, Challenges, and Opportunities. *IEEE Access* **2020**, *8*, 97658–97675. [CrossRef]

77. Díaz Zayas, A.; Rivas Tocado, F.J.; Rodríguez, P. Evolution and Testing of NB-IoT Solutions. *Appl. Sci.* **2020**, *10*, 7903. [CrossRef]

78. Tan, Y.K.; Panda, S.K. Review of Energy Harvesting Technologies for Sustainable WSN. *Sustain. Wirel. Sens. Netw.* **2010**, 15–43. [CrossRef]

79. Park, D.Y.; Joe, D.J.; Kim, D.H.; Park, H.; Han, J.H.; Jeong, C.K.; Park, H.; Park, J.G.; Joung, B.; Lee, K.J. Self-powered real-time arterial pulse monitoring using ultrathin epidermal piezoelectric sensors. *Adv. Mater.* **2017**, *29*, 1702308. [CrossRef] [PubMed]

80. Zeng, Y.; Xiang, H.; Zheng, N.; Cao, X.; Wang, N.; Wang, Z.L. Flexible triboelectric nanogenerator for human motion tracking and gesture recognition. *Nano Energy* **2022**, *91*, 106601. [CrossRef]

81. Zhu, M.; Sun, Z.; Chen, T.; Lee, C. Low cost exoskeleton manipulator using bidirectional triboelectric sensors enhanced multiple degree of freedom sensory system. *Nat. Commun.* **2021**, *12*, 2692. [CrossRef]

82. Bian, S.; Zhu, B.; Rong, G.; Sawan, M. Towards wearable and implantable continuous drug monitoring: A review. *J. Pharm. Anal.* **2021**, *11*, 1–14. [CrossRef]

83. Zou, Y.; Bo, L.; Li, Z. Recent progress in human body energy harvesting for smart bioelectronic system. *Fundam. Res.* **2021**, *1*, 364–382. [CrossRef]

84. Liu, L.; Guo, X.; Liu, W.; Lee, C. Recent Progress in the Energy Harvesting Technology—From Self-Powered Sensors to Self-Sustained IoT, and New Applications. *Nanomaterials* **2021**, *11*, 2975. [CrossRef]

85. Jiang, D.; Shi, B.; Ouyang, H.; Fan, Y.; Wang, Z.L.; Li, Z. Emerging implantable energy harvesters and self-powered implantable medical electronics. *ACS Nano* **2020**, *14*, 6436–6448. [CrossRef] [PubMed]

86. Zhao, Y.; Luo, X. Task Offloading Policy for Nodes with Energy Harvesting Capabilities. In Proceedings of the 2019 IEEE 90th Vehicular Technology Conference (VTC2019-Fall), Honolulu, HI, USA, 22–25 September 2019; pp. 1–5. [CrossRef]

87. Zhang, Y.; He, J.; Guo, S. Energy-Efficient Dynamic Task Offloading for Energy Harvesting Mobile Cloud Computing. In Proceedings of the 2018 IEEE International Conference on Networking, Architecture and Storage (NAS), Chongqing, China, 11–14 October 2018; pp. 1–4. [CrossRef]

88. Guo, M.; Li, Q.; Peng, Z.; Liu, X.; Cui, D. Energy harvesting computation offloading game towards minimizing delay for mobile edge computing. *Comput. Netw.* **2021**, *204*, 108678. [CrossRef]

89. Sun, Y.; Song, C.; Yu, S.; Liu, Y.; Pan, H.; Zeng, P. Energy-Efficient Task Offloading Based on Differential Evolution in Edge Computing System with Energy Harvesting. *IEEE Access* **2021**, *9*, 16383–16391. [CrossRef]

90. Min, M.; Xiao, L.; Chen, Y.; Cheng, P.; Wu, D.; Zhuang, W. Learning-based computation offloading for IoT devices with energy harvesting. *IEEE Trans. Veh. Technol.* **2019**, *68*, 1930–1941. [CrossRef]

91. Khan, P.W.; Abbas, K.; Shaiba, H.; Muthanna, A.; Abuarqoub, A.; Khayyat, M. Energy efficient computation offloading mechanism in multi-server mobile edge computing—An integer linear optimization approach. *Electronics* **2020**, *9*, 1010. [CrossRef]

92. Kawata, M.; Takakura, A. Thermoelectrically Powered Wrist Watch. US Patent 5,889,735, 30 March 1999.

93. Hoang, D.C.; Tan, Y.K.; Chng, H.B.; Panda, S.K. Thermal energy harvesting from human warmth for wireless body area network in medical healthcare system. In Proceedings of the 2009 International conference on power electronics and drive systems (PEDS), Taipei, Taiwan, 2–5 November 2009; IEEE: Piscataway, NJ, USA, 2009; pp. 1277–1282.

94. Jouhara, H.; Żabnieńska-Góra, A.; Khordehgah, N.; Doraghi, Q.; Ahmad, L.; Norman, L.; Axcell, B.; Wrobel, L.; Dai, S. Thermoelectric generator (TEG) technologies and applications. *Int. J. Thermofluids* **2021**, *9*, 100063. [CrossRef]

95. Halim, M.A.; Cho, H.; Park, J.Y. Design and experiment of a human-limb driven, frequency up-converted electromagnetic energy harvester. *Energy Convers. Manag.* **2015**, *106*, 393–404. [CrossRef]

96. Surangsrirat, D.; Dumnin, S.; Samphanyuth, S. Heart Rate, Skin Temperature and Skin Humidity and their Relationship to Accumulated Fatigue. In Proceedings of the 2019 3rd International Conference on Bio-engineering for Smart Technologies (BioSMART), Paris, France, 24–26 April 2019; IEEE: Piscataway, NJ, USA, 2019; pp. 1–4.

97. Kirstein, K.U.; Sedivy, J.; Salo, T.; Hagleitner, C.; Vancura, T.; Baltes, H. A CMOS-based tactile sensor for continuous blood pressure monitoring. In Proceedings of the 30th European Solid-State Circuits Conference, Leuven, Belgium, 23 September 2004; IEEE: Piscataway, NJ, USA, 2004; pp. 463–466.

98. Xiao, Z.; Tan, X.; Chen, X.; Chen, S.; Zhang, Z.; Zhang, H.; Wang, J.; Huang, Y.; Zhang, P.; Zheng, L.; et al. An implantable RFID sensor tag toward continuous glucose monitoring. *IEEE J. Biomed. Health Inform.* **2015**, *19*, 910–919. [CrossRef]

99. Shruthi, P.; Resmi, R. Heart rate monitoring using pulse oximetry and development of fitness application. In Proceedings of the 2019 2nd International Conference on Intelligent Computing, Instrumentation and Control Technologies (ICICICT), Kannur, India, 5–6 July 2019; IEEE: Piscataway, NJ, USA, 2019; Volume 1, pp. 1568–1570.

100. Ammar, M.B.; Sahnoun, S.; Fakhfakh, A.; Kanoun, O. Design of a DC-DC Boost Converter of Hybrid Energy Harvester for IoT Devices. In Proceedings of the 2020 IEEE 6th World Forum on Internet of Things (WF-IoT), New Orleans, LA, USA, 2–16 June 2020; IEEE: Piscataway, NJ, USA, 2020; pp. 1–4.

101. Ammar, M.B.; Bouattour, G.; Bouhamed, A.; Sahnoun, S.; Fakhfakh, A.; Kanoun, O. AC-DC Single Phase Rectifiers for Nanocomposite based Flexible Piezoelectric Energy Harvesters. In Proceedings of the 2021 18th International Multi-Conference on Systems, Signals & Devices (SSD), Monastir, Tunisia, 22–25 March 2021; IEEE: Piscataway, NJ, USA, 2021; pp. 228–234.

102. Zouari, M.; Naifar, S.; Götz, M.; Derbel, N.; Kanoun, O. An optimized self-powered P-SSHI circuit for piezoelectric energy harvesting. In Proceedings of the 2017 IEEE International Instrumentation and Measurement Technology Conference (I2MTC), Turin, Italy, 22–25 May 2017; IEEE: Piscataway, NJ, USA, 2017; pp. 1–6.

103. Kanoun, O.; Bradai, S.; Khriji, S.; Bouattour, G.; El Houssaini, D.; Ben Ammar, M.; Naifar, S.; Bouhamed, A.; Derbel, F.; Viehweger, C. Energy-aware system design for autonomous wireless sensor nodes: A comprehensive review. *Sensors* **2021**, *21*, 548. [CrossRef]

104. Mallela, V.S.; Ilankumaran, V.; Rao, N.S. Trends in cardiac pacemaker batteries. *Indian Pacing Electrophysiol. J.* **2004**, *4*, 201.

105. Khalid, S.; Raouf, I.; Khan, A.; Kim, N.; Kim, H.S. A review of human-powered energy harvesting for smart electronics: Recent progress and challenges. *Int. J. Precis. Eng. Manuf.-Green Technol.* **2019**, *6*, 821–851. [CrossRef]

106. Zhou, M.; Al-Furjan, M.S.H.; Zou, J.; Liu, W. A review on heat and mechanical energy harvesting from human–Principles, prototypes and perspectives. *Renew. Sustain. Energy Rev.* **2018**, *82*, 3582–3609. [CrossRef]

107. von Buren, T.; Mitcheson, P.; Green, T.; Yeatman, E.; Holmes, A.; Troster, G. Optimization of inertial micropower Generators for human walking motion. *IEEE Sensors J.* **2006**, *6*, 28–38. [CrossRef]

108. Yuan, J.; Zhu, R. Self-Powered Wearable Multi-Sensing Bracelet with Flexible Thermoelectric Power Generator. In Proceedings of the 2019 20th International Conference on Solid-State Sensors, Actuators and Microsystems & Eurosensors XXXIII (TRANSDUCERS & EUROSENSORS XXXIII), Berlin, Germany, 23–27 June 2019; IEEE: Piscataway, NJ, USA, 2019; pp. 1431–1434.

109. Nozariasbmarz, A.; Collins, H.; Dsouza, K.; Polash, M.H.; Hosseini, M.; Hyland, M.; Liu, J.; Malhotra, A.; Ortiz, F.M.; Mohaddes, F.; et al. Review of wearable thermoelectric energy harvesting: From body temperature to electronic systems. *Appl. Energy* **2020**, *258*, 114069. [CrossRef]

110. Zurbuchen, A.; Pfenniger, A.; Stahel, A.; Stoeck, C.T.; Vandenberghe, S.; Koch, V.M.; Vogel, R. Energy harvesting from the beating heart by a mass imbalance oscillation generator. *Ann. Biomed. Eng.* **2013**, *41*, 131–141. [CrossRef]

111. Magno, M.; Boyle, D. Wearable energy harvesting: From body to battery. In Proceedings of the 2017 12th International Conference on Design & Technology of Integrated Systems In Nanoscale Era (DTIS), Palma de Mallorca, Spain, 4–6 April 2017; IEEE: Piscataway, NJ, USA, 2017; pp. 1–6.

112. Bhatia, D.; Jo, S.H.; Ryu, Y.; Kim, Y.; Kim, D.H.; Park, H.S. Wearable triboelectric nanogenerator based exercise system for upper limb rehabilitation post neurological injuries. *Nano Energy* **2021**, *80*, 105508. [CrossRef]

113. Health Sector Transformation Strategy. V.3. 2019. Available online: https://www.moh.gov.sa/en/Ministry/vro/Documents/Healthcare-Transformation-Strategy.pdf (accessed on 10 January 2022).

114. Walraven, J.; Jacobs, M.S.; Uyl-de Groot, C.A. Leveraging the Similarities Between Cost-Effectiveness Analysis and Value-Based Healthcare. *Value Health* **2021**, *24*, 1038–1044. [CrossRef]

115. Wehde, M. Healthcare 4.0. *IEEE Eng. Manag. Rev.* **2019**, *47*, 24–28. [CrossRef]

116. Tirkel, T.; Edan, Y.; Khvorostianov, N.; Bar-Haim, S. SIT LESS: A prototype home-based system for monitoring older adults sedentary behavior. *Assist. Technol.* **2020**, *32*, 79–91. [CrossRef]

117. Peng, G.; Sepulveda Garcia, L.M.; Nunes, M.; Zhang, N. Identifying user requirements of wearable healthcare technologies for Chinese ageing population. In Proceedings of the 2016 IEEE International Smart Cities Conference (ISC2), Trento, Italy, 12–15 September 2016; pp. 1–6. [CrossRef]

Article

An Effective Method for Parameter Estimation of a Solar Cell

Abhishek Sharma [1,*], Abhinav Sharma [2,*], Moshe Averbukh [3], Vibhu Jately [4] and Brian Azzopardi [4]

1   Department of Research and Development, University of Petroleum and Energy Studies, Dehradun 248007, India
2   Department of Electrical and Electronics Engineering, School of Engineering, University of Petroleum and Energy Studies, Dehradun 248007, India
3   Department of Electrical and Electronics Engineering, Ariel University, Ariel 40700, Israel; mosheav@ariel.ac.il
4   Institute of Engineering and Transport, Malta College of Arts, Science and Technology (MCAST), Paola PLA9032, Malta; vibhu.jately@mcast.edu.mt (V.J.); brian.azzopardi@mcast.edu.mt (B.A.)
*   Correspondence: abhishek_sharma@ddn.upes.ac.in (A.S.); abhinav.sharma@ddn.upes.ac.in (A.S.)

Abstract: Parameter extraction of the photovoltaic cell is a highly nonlinear complex optimization problem. This article proposes a new hybrid version of whale optimization and particle swarm optimization algorithm to optimize the photovoltaic cell parameters. The exploitation ability of particle swarm optimization with adaptive weight function is implemented in the pipeline mode with a whale optimization algorithm to improve its exploitation capability and convergence speed. The performance of the proposed hybrid algorithm is compared with six different optimization algorithms in terms of root mean square error and rate of convergence. The simulation result shows that the proposed hybrid algorithm produces not only optimized parameters at different irradiation levels (i.e., 1000 W/m^2, 870 W/m^2, 720 W/m^2, and 630 W/m^2) but also estimates minimum root mean square error even at a low level of irradiations. Furthermore, the statistical analysis validates that the average accuracy and robustness of the proposed algorithm are better than other algorithms. The best values of root mean square error generated by the proposed algorithm are 7.1700×10^{-4} and 9.8412×10^{-4} for single-diode and double-diode models. It is observed that the estimated parameters based on the optimization process are highly consistent with the experimental data.

Keywords: photovoltaic; parameter extraction; single-diode model; double-diode model; swarm intelligence

1. Introduction

The depletion of fossil fuel resources and resulting environmental impact due to their usages embarks the need for alternate energy resources [1]. Solar energy is one of the most promising alternative sources for fossil fuel. The free access to the energy of sunlight can be extracted employing the photovoltaic (PV) panels. The rapid adoption of solar energy by the domestic and industrial sector makes it a vital source to be explored [2]. Despite the very low operational and maintenance cost, there are various limitations for efficient energy generation. An enormous amount of research has been performed and carried out to better the power output from the PV panels [3,4]. The major limitation in the execution and implementation of the solar PV power plants is the very high capital cost for installation [5]. PV cells are having nonlinear current-voltage (I-V) and power-voltage (P-V) characteristics curves with some operational limitations [6]. This non-linearity makes it difficult for any probability and approximation to increase efficiency. Every PV panel can operate at maximum efficiency, as defined by the manufacturer, only if the practical parameters (voltage-current) are somewhat close to or coinciding with the maximum power point (MPP). The real behaviour of PV panels rather different from the optimal conditions, due to the non-linearity of I-V characteristics of solar cells makes it essential to determine the MPP in each moment. It could be done through simulation techniques for better operational efficiency [7]. This technology is ensured by the model of the equivalent

circuit having several inherent parameters. However, the parameters provided by the PV panel manufacturer don't specify the model parameters. The given information states the open-circuit voltage (V_{oc}), short circuit current (I_{sc}), and current at maximum power point (I_{mpp}) under standard test conditions (i.e., 1000 W/m^2, 25 °C). The practical parameters vary at every instant with a change in weather conditions. The aging effects of PV also alter the parameters of the equivalent circuit [3,8,9].

The core unit of the PV system is a solar cell, and it is of utmost priority to extract the parameters for a close analysis of the PV panel performance around its MPP. The simulation study of cells combined all together give the performance analysis of entire PV panels [8,10]. The equivalent circuit for the single- and double-diode model for parameter extraction is the recent and most widely used approach. The method of parameter extraction can be bifurcated into two major categories: analytical and optimization methods [11–15]. Although the analytical methods are the simplest and yields result quickly, but it misses the accuracy under normal day conditions with variable lighting. The deterministic ways of parameter extraction such as Newton-Raphson, nonlinear least square, Lambert W-functions [16], iterative curve fitting [17], conductivity method [18] and the Levenberg-Marquardt algorithm [19] have many boundaries such as continuity, differentiability, and convexity related to objective functions. The boundary conditions further impose limitations on the usage of the above analytical methods, as they obtain local minima when dealing with multi-modal problems. Thus, analytical methods are not suitable to extract the parameters.

To get more accurate and precise parameters from nonlinear implicit equations with high accuracy, evolutionary algorithms [20] were proposed. The bio-related algorithms are more accurate and powerful optimization algorithms to simplify nonlinear transcendental equations as it doesn't include complex mathematics. Although, researchers have developed number of metaheuristic algorithm but there is no algorithm that provides optimal solution to all sets of problems which has also been proven by No free lunch theorem. This has motivated researchers to design new algorithms to efficiently solve complex science and engineering problems. A gradient-based optimizer (GBO) [20] inspired from the gradient-based Newton's method, Harris-Hawk optimizer (HHO) [21] inspired from cooperative behavior and chasing style of the Harris Hawks Heap-based optimizer (HBO) [22] inspired from corporate rank hierarchy and slime mould algorithm (SMA) [23] inspired from diffusion and foraging conduct of slime mould are some of the recently developed metaheuristic algorithms. Some of the recent optimization algorithms used for parameter extraction are the genetic algorithm (GA) [24], differential evolution (DE) [25], simulated annealing (SA) [26], pattern search (PS) [27], harmony search (HS) [28], cuckoo search (CS) [29], flower pollination algorithm [30], bacterial foraging optimization (BFO) [31], bird mating [32], and artificial bee swarm optimization (ABSO) [33]. The proposed algorithms suffer from the problem of premature convergence. The primary disadvantage of GA is that it involves wide parameter optimization search space which makes the system quite complicated and slow. The problem of large search space was overcome by implementing PSO. However, it imposed the problem of the randomly chosen initial parameter value. The value exchange in SA between the cooling timetable and the original temperature makes it less popular. There is a likelihood that PSO will choose an incorrect pattern, leading to premature convergence or no convergence. PSO with reverse barrier restriction for series resistance (Rs), shunt resistance (Rsh), and diode ideality factor (a) is suggested for fast and coherent convergence of optimization issue to global optima, considering the temperature impact to reduce the modeling errors in differential evolution [31–35]. Although the BFO technique offers excellent outcomes but involving too many parameters that have complicated the scheme and imposed a computational strain. Authors in [36], implemented improved teaching-learning based optimization (ITLBO), where a good trade-off is established between the exploration and exploitation by eliminating the worst learner. This increases the global search ability of the population in a defined search space. A hybridization approach is carried out by the researchers in [34] for parameter

extraction of solar PV cell. In this approach, the hybridization of two algorithms are implemented, the firefly and pattern search. The exploration phase is completed by the firefly algorithm during the first half iteration and then the pattern search algorithm takes control of the population for the exploitation phase. A new opposition-based learning approach is incorporated with whale optimization and shuffled complex evolutionary algorithm for optimization of solar cell parameters [35,36]. This approach is tested on unimodal as well as on multimodal benchmark functions and simulation results clearly show the robustness of the algorithms.

The whale optimization algorithm (WOA) [37] and particle swarm optimization (PSO) [38] are the two most prominent used metaheuristics techniques as available in the literature. However, they differ from each other in the search mechanism for the best solution in a defined search space. WOA mimics the social behaviour of humpback whales while PSO mimics the searching behaviour of the birds in a group. It is shown by many previous research studies that WOA is good at exploring [39] the search space but suffers from a slow convergence rate due to low exploitation ability while PSO don't have good capability in exploring [40] the search space but have good local search capability. the convergence speed of the algorithm. In [41], the author proposed a chaotic WOA (CWOA) to improve maps utilized their dynamic behavior to prevent an optimization algorithm to trap in local optima and improves its global search capability. In [42], the author proposed Levy flight trajectory based WOA (LWOA) to improve the accuracy and convergence speed of the algorithm. Levy flight allowed for the algorithm to get rid of local optima and prevents premature convergence.

There are certain complex and non-convex optimization problems that are not solved by continuous metaheuristic therefore, in [43], the author proposed binary WOA (BWOA). In [44], the author proposed a modified WOA that includes whale memory and new random search agent to enhance the exploitation capability of the algorithm. In [45], the author improved the exploration capability of WOA and proposed three modified WOA which are based on opposition-based learning, exponentially decreasing parameters, and re-initialization of the worst particles. The hybridization of metaheuristic algorithms is another approach to improve the exploration and exploitation capability of population based stochastic algorithm. Furthermore, researchers have proposed hybrid approach grey wolf optimization (HAGWO) [46], WOA-CBO (colliding bodies optimization) [47], memetic-WOA (MWOA) [48], WOA-SA (simulated annealing) [39], WOA-MFO (moth flame optimization) [49], Sine-Cosine (SC-WOA) [50], WOA-PS (Pattern Search) [51], and Brain Storm (BS-WOA) [52–54] to improve the global and local search capability of WOA.

According to the literature survey, WOAPSO has not yet been implemented for the parameter extraction of the solar cell (and it cannot be used to establish a PV parameter estimation technique that can overcome all existing techniques). Therefore, this research paper aims to anticipate a new parameter estimation algorithm for solar cell/module. The novelty of the proposed study is that the exploitation capability of WOA is significantly improved by incorporating the exploitation capability of PSO with adaptive weight in sequential mode. As a result, equivalent circuit parameters converge equally good to the true values with minimum error. The proposed WOAPSO algorithm's performance is measured based on convergence analysis, robustness, reliability, and statistical analysis for three PV models at diverse operating conditions.

The manuscript is organized as follows: the problem formulation and mathematical model for solar PV cell/module are presented in Section 2. Section 3 gives a brief introduction of the WOA, PSO, and proposed WOAPSO algorithm and discussed its implementation to estimate the optimized value of unknown parameters of a single-diode, double-diode, and PV module model. In Section 4, the simulation results of the WOAPSO algorithm are discussed and compared with pre-existing metaheuristic algorithms. Finally, Section 5 provides a conclusive remark to summarize the paper.

2. Methodology

In this section, the equivalent circuits of a photovoltaic solar cell are formulated using a single-diode and double-diode models. These equivalent circuit models are used to describe the current-voltage characteristics of a solar cell.

2.1. PV Panel Model

The equivalent circuit of PV panel module is shown in Figure 1. The relation between current and voltage at output terminal for the PV panel module is expressed as:

$$I_l/N_p = I_p - I_{SD}\left[exp\left(\frac{q\left(V_l/N_s + R_s I_l/N_p\right)}{a_1 k_B T}\right) - 1\right] - \frac{V_l/N_s + R_s I_l/N_p}{R_{sh}} \tag{1}$$

where N_s and N_p represents the number of solar cells connected in series and parallel respectively. It is clearly depicted from Figure 1 that only five parameters (I_p, I_{SD}, a_1, R_s and R_{sh}) are needed to be estimated for minimum value of the RMSE.
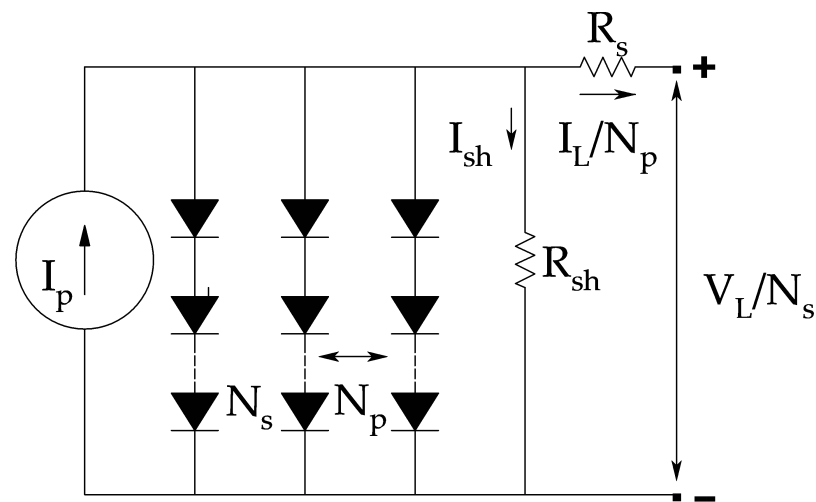
Figure 1. Equivalent circuit of PV panel module model.

2.2. Objective Function

The key purpose of this work is to optimize the unknown parameters for both the models (SDM and DDM) and to reduce the error between experimental and estimated data. The objective function for error used here is same as the authors have used previously in as:

$$\text{RMSE} = \sqrt{\frac{1}{k}\sum_{N=1}^{k} f(V_l, I_l, X)} \tag{2}$$

where V_l and I_l are the measured voltage and current of PV module. The parameter '*k*' stands for the number of experimental data set. The best solution found by WOAPSO is represented by a vector *X*. For the single-diode model:

$$\begin{cases} f_{single}(V_l, I_l, X) = I_p - I_{SD}\left[exp\left(\frac{q(V_l + I_l R_s)}{a_1 k_B T}\right) - 1\right] - \frac{V_l + I_l R_s}{R_{sh}} - I_l \\ \left(X = I_p, I_{SD}, a_1, R_s, R_{sh}\right) \end{cases} \tag{3}$$

For the double-diode model:

$$\begin{cases} f_{double}(V_l, I_l, X) = I_p - I_{SD1}\left[exp\left(\frac{q(V_l + I_l R_s)}{a_1 k_B T}\right) - 1\right] \\ \quad - I_{SD2}\left[exp\left(\frac{q(V_l + I_l R_s)}{a_2 k_B T}\right) - 1\right] - \frac{V_l + I_l R_s}{R_{sh}} - I_l \\ \left(X = I_p, I_{SD1}, I_{SD2}, a_1, a_2, R_s, R_{sh}\right) \end{cases} \tag{4}$$

For the PV panel module model:

$$
\begin{cases}
f_{single}(V_l,\ I_l,\ X) = \ I_p - I_{SD}\left[exp\left(\dfrac{q\left(\frac{V_l}{N_s}+\frac{R_sI_l}{N_p}\right)}{a_1 k_B T}\right) - 1\right] \\[2em]
\qquad\quad -\dfrac{V_l/N_s + R_s I_l/N_p}{R_{sh}} - I_l/N_p \\[1em]
\qquad\qquad \left(X = \ I_p,\ I_{SD},\ a_1,\ R_s,\ R_{sh}\ \right)
\end{cases}
\tag{5}
$$

2.3. Hybrid Algorithm

The hybridization of the metaheuristic algorithm plays a vital role in improving their performance. The fundamental principle of hybridization is to blend the best features of two or more metaheuristic algorithms to improve search capability, accuracy, and convergence speed of an individual algorithm. A hybrid algorithm is also known as a memetic algorithm. In the last few years, researchers have proposed different strategies for hybridizing metaheuristic algorithms. The three most explored methodologies of hybridization are multi-stage, sequential and parallel.

In the multi-stage methodology, one of the algorithms globally explores the search space and the second algorithm locally discovers the optimal solution. In sequential search, both the algorithms run sequentially and find the optimal solution in the search space. In the parallel mode, both the algorithms run parallel on the same population of the defined problem.

2.3.1. Particle Swarm Optimization (PSO)

Particle swarm optimization is a nature inspired stochastic optimization technique proposed by J. Kennedy and R. C. Eberhard in 1995. It is a population-based computationally inexpensive technique that is inspired by the social behaviour of fish schooling and bird flocking. The methodology of the algorithm is that the swarm of particles fly in the search space and finds the optimal solution by updating their own best solution and the best solution obtained by the swarms. The swarm is randomly initialized as particles in N-dimensional search space with position x_i and velocity v_i. The position of the particles represents the probable solution, and the velocity represents the rate of change of position of the particle concerning the current position. The particles change their positions with respect to the positions of the best particle. The velocity update equations are given by:

$$
v_i^d(t+1) = w \times v_i^d(t) + c_1 \times r_1 \times \left(pbest_i^d(t) - x_i^d(t)\right) + c_2 \times r_2 \times \left(gbest^d - x_i^d\right)
\tag{6}
$$

$$
x_i^d(t+1) = x_i^d(t) + v_i^d(t+1)
\tag{7}
$$

where $v_i^d(t)$ and $x_i^d(t)$ represents the velocity and position of ith particle in dth dimension at tth iteration, $v_i^d(t+1)$ and $x_i^d(t+1)$ is the velocity and position of the ith particle in dth dimension at $(t+1)$th iteration. $pbest_i^d$ represents the current best position of the particles and $gbest^d$ represents the best position among all the particles in dth dimension, c_1 and c_2 are the acceleration parameter, r_1 and r_2 are the random number in the range [0, 1] and w is the inertial weight vector which maintains balance between exploration and exploitation.

2.3.2. Whale Optimization Algorithm (WOA)

The whale optimization algorithm is a population-based optimization algorithm that mimics the social behaviour of humpback whales and was proposed by Mirjalili and Lewis in 2016. Humpback whales are long in size and have an interesting food searching capability: they attack their prey (krill and small fishes) by a bubble-net hunting strategy. WOA is inspired by this hunting behaviour, and works in three phases. First, it searches for prey then encircles the prey and lastly, attacks the prey. Humpback whales swim around the prey either following a shrinking path or through a spiral movement. A probability factor p assumed to be 50% simultaneously choose either of the two movements.

Shrinking Movement

Initially in the exploration phase, humpback whales search around a prey chosen randomly in the search space with the following mathematical model:

$$\vec{D} = \left| \vec{C} \times \vec{X}_{rand} - \vec{X} \right| \tag{8}$$

$$\vec{X}(t+1) = \vec{X}_{rand} - \vec{A} \times \vec{D} \tag{9}$$

where t is the current iteration and $(t + 1)$th is the next iteration, $\vec{X}_{rand}$ is the random position of the prey, $\vec{A}$ and $\vec{C}$ are the coefficient vectors and is defined as:

$$\vec{A} = 2\vec{a}\,\vec{r} - \vec{a} \tag{10}$$

$$\vec{C} = 2 \times \vec{r} \tag{11}$$

where $\vec{a}$ is decreased from 2 to 0 over the course of iterations and $\vec{r}$ is the random number in the range [0, 1]. In the exploitation phase the position of whales are updated based on the position of the best search prey $\vec{X}^*$. Mathematically it is defined as:

$$\vec{D} = \left| \vec{C} \times \vec{X}^* - \vec{X} \right| \tag{12}$$

$$\vec{X}(t+1) = \vec{X}^* - \vec{A} \times \vec{D} \tag{13}$$

Spiral Movement

In the spiral movement of the humpback whale, first the distance is evaluated between the whale located at (X, Y) and best search prey located at (X^*, Y^*). Once the distance is evaluated then the helix-shaped movement of whale around the prey is defined with following mathematical equation:

$$\vec{X}(t+1) = \vec{D'} \cdot e^{bl} \cdot \cos(2\pi l) + \vec{X}^*(t) \tag{14}$$

where $\vec{D'} = |\vec{X}^*(t) - \vec{X}(t)|$ is the distance between the whale and best searched prey, b is the constant which maintains the shape of the logarithmic spiral and l is the random number defined in the range [−1, 1].

In WOA, coefficient vector 'A' maintains the balance in exploration and exploitation, when the value of $p < 0.5$ and $A > 1$ then the positions are updated by Equations (9) and (13) while when $p < 0.5$ and $A < 1$ the positions are updated by Equations (13) and (14) and when the $p \geq 0.5$ then the positions are updated using Equation (14).

2.3.3. Hybrid WOAPSO Algorithm

In this section, the principle of the proposed hybrid WOAPSO algorithm is briefly addressed. In general, the performance of any optimization technique while solving any NLP problem is affected by premature convergence and slow rate of convergence. Some algorithms better explore the search space and have a slow convergence rate while some algorithms less diversely explore the search space and did not find the optimal solution. Maintaining the balance between exploration and exploitation is a critical issue in any optimization algorithm. WOA has good exploration capability but exploitation depends on evaluating the distance between the whale and the best position of the prey, and if the distance is large then it takes more time to converge. While PSO has fast rate of convergence but it is prone to premature convergence due to weakness in global search capability. Since in PSO, if the global best solution gets trapped in local optima, then the rest of the particles

do not explore the search space and follow the global best solution, and become trapped in local optima. Therefore, it can be concluded that WOA is good at exploring the search space, but suffers from a slow convergence rate while PSO doesn't have good capability in exploring the search space but have good local search capability. The aim of the proposed hybrid algorithm is to enhance the exploitation capability of WOA by embedding the PSO algorithm to find an optimal solution around the region explored by WOA. The proposed approach is mixed, co-evolutionary in which PSO is used as a component of WOA and thus the hybrid approach utilizes the strength of both the algorithms to avoid the premature convergence and local optima. Figure 2 depicts the process flow chart of the proposed algorithm. The mathematical model of the proposed algorithm is illustrated in the following steps:

Step 1: Initialize the random population of search agents with position and velocity defined as:

$$X_i = \left(x_i^1, \ldots \ldots \ldots x_i^d, \ldots \ldots \ldots x_i^n \right), \ for \ i = 1, 2, \ldots \ldots \ldots \ldots N \qquad (15)$$

$$V_i = \left(v_i^1, \ldots \ldots \ldots v_i^d, \ldots \ldots \ldots v_i^n \right), \ for \ i = 1, 2, \ldots \ldots \ldots \ldots N \qquad (16)$$

Step 2: Calculate the fitness of each search agent. If the problem is the minimization problem, then $\overrightarrow{X^*}$ is the position corresponding to the minimum fitness and for maximization problem $\overrightarrow{X^*}$ is the position corresponding to the maximum fitness. $\overrightarrow{X^*}$ is the best search agent.

Step 3: Update the constant parameters A, C, using Equations (10) and (11) and l lying between [–1, 1] and p is the probability between 0 and 1.

Step 4: If $p < 0.5$ and $|A| \geq 1$, then select the random position of search agent (X*) in search space and update the position of search agent using Equations (9) and (13).

Else if $p < 0.5$ and $|A| < 1$, then update the position of search agent using Equations (13) and (14).

Else $p > 0.5$, then update the position of search agent using Equation (14).

Step 5: Update the velocity of search agent based on the best position of search agent (X*) in the search space using the following equation:

$$v_i^d(t+1) = w \times v_i^d(t) + c_1 \times r_1 \times \left(X^* - x_i^d(t) \right) \qquad (17)$$

Step 6: Update the position of the particles using Equation (17).

Step 7: Go to step 3 until the termination criteria is met. The algorithm terminates when either maximum number of iterations or minimum error criteria is attained.

Step 8: In the last iteration the returned value of $\overrightarrow{X^*}$ represents the global minimum and the position corresponding to it represents the solution of the problem.

2.3.4. Implementation of WOAPSO for Parameter Extraction
Single-Diode Model

Initialize the population of search agents of fifth order dimension in the search space. The fifth order dimension represents the photovoltaic current (I_p), series resistance (R_s), shunt resistance (R_{sh}), diode saturation current (I_{SD}) and diode ideality factor (a_1). The range of these parameters are [0–1, 0.001–0.5, 0–100, 0.01–0.5, 1–2].

Regulate the fitness of all agents in the search space using Equation (3).

Update the position of the agents at every iteration using WOAPSO. The algorithm is designed to work in the minimization mode thus the location of particles that acquire minimum cost represents the optimized parameters of SDM with minimum RMSE.
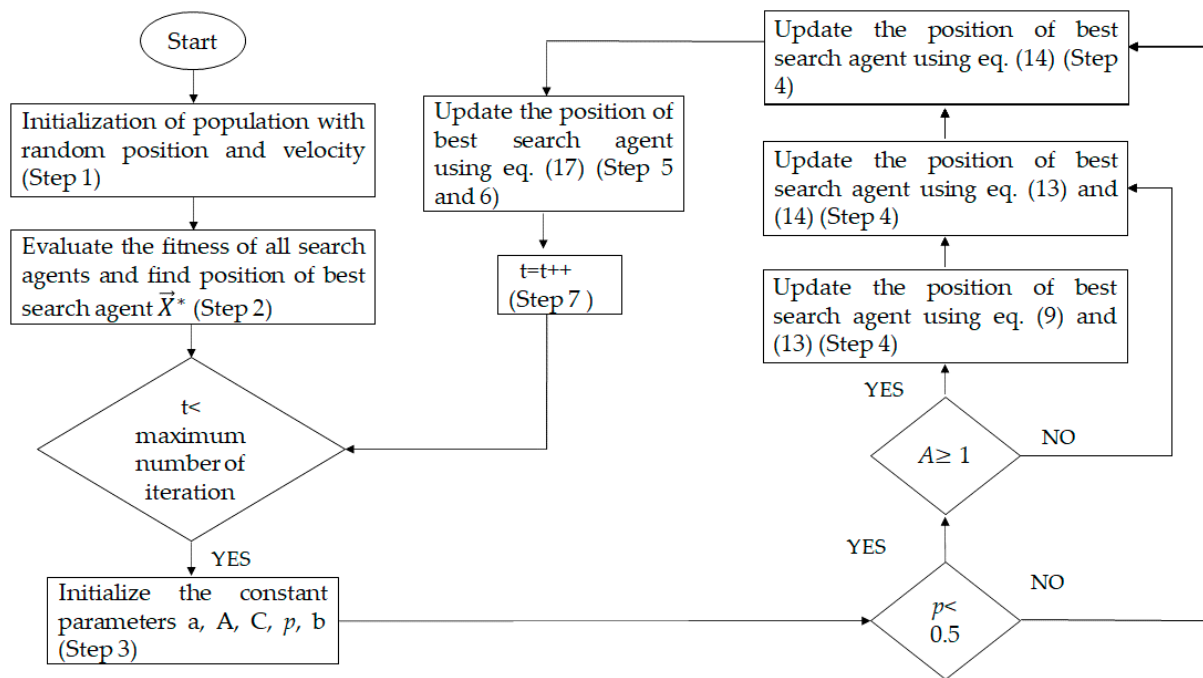
Figure 2. Flowchart of proposed hybrid version of whale optimization and particle swarm optimization WOAPSO algorithm.

Double-Diode Model

Initialize population of search agents of seventh-order dimension in the search space. The seventh-order dimension represents the photovoltaic current (I_p), series resistance (R_s), shunt resistance (R_{sh}), diode saturation currents (I_{SD}, I_{SD1}), and diode ideality factor (a_1, a_2). The range of these parameters are [0–1, 0.001–0.5, 0–100, 0.01–0.5, 0.01–0.5, 1–2, 1–2].

Regulate the fitness of all agents in the search space using Equation (4).

Update the position of all agents at every iteration using WOAPSO. The algorithm is designed to work in the minimization mode. Thus, the location of particles having minimum cost represents the parameters of the double-diode model with minimum RMSE.

3. Results

In this section, the feasibility of the proposed new hybrid WOAPSO was tested and evaluated using mainly two types of PV devices: one PV cell (R.T.C France solar cell) and one PV module (SS2018P) at different solar irradiation. As a result, the retrieved PV cell and module parameters were monitored and used to create simulated I-V data for each device type. The accuracy and reliability of the WOAPSO were assessed by comparing the techniques published in the literature with the existing art. The efficiency of the proposed method is evaluated based on distinct empirical tools such as the individual absolute error (IAE), the relative error (RE), the precision of the curve fitting, and the global minimum convergence patterns. The experimental values of current and voltage are taken from [55] by using R.T.C France solar cell at standard temperature condition i.e., 1000 W/m² at 33 °C. The SS2018P PV module is composed of 36 polycrystalline cells connected in series and generate the I-V data under different irradiance levels i.e., 1000 W/m², 870 W/m², 720 W/m² and 630 W/m². The data collection consists of a total of 20 I-V measurements for solar cell and 27 for PV module. The values of current and voltage for solar PV module (SS2018P) are measured across variable resistive load (0.1–250 Ω, 2 A). The measured value of voltage and current at different irradiance level is presented in supplementary materials. For a reasonable comparison, the search ranges (i.e., upper and lower bound) for each parameter are tabulated in Table 1, which are the same as those being used by investigators

in [27]. The proposed WOAPSO algorithm is implemented on MATLAB 2018a platform with Intel ® core ™ i7-HQ CPU, 2.4 GHz, 16 GB RAM Laptop. In order to conduct the experiment, the sample size, and the estimated number of objective function evaluations are set at 30 and 50,000, respectively. Furthermore, a minimum of 30 separate runs are carried out to prevent the contingency.

Table 1. Range of parameters for SDM, DDM and PV Module.

Parameter	SDM/DDM		SS2018P PV Module	
	Lower Bound	Upper Bound	Lower Bound	Upper Bound
I_p (A)	0	1	0	10
I_{sd}, I_{sd1} (µA)	0.01	0.5	0	50
R_s (Ω)	0.001	0.5	0.001	2
R_{sh} (Ω)	0	100	0	2000
a, a_1, a_2	1	2	0	100

3.1. Parameter Estimation of Single-Diode Model Using WOAPSO

Only five parameters (I_p, I_{sd}, a, R_s, R_{sh}) are required to be estimated for a single-diode model. Table 2 signifies the values of parameters optimized by WOAPSO and RMSE for the comparison. The WOAPSO algorithm provides the lowest RMSE of 7.1700×10^{-4} than others (Table 2 and Table S2). Here RMSE values are acquired as the index for the evaluation of results with previously existing algorithms implemented by the researchers.

Table 2. Comparison of WOAPSO with different parameter estimation methods for SDM.

Algorithms	I_{ph} (A) ± SD	I_{sd} (µA) ± SD	R_s (Ω) ± SD	R_{sh} (Ω) ± SD	a ± SD	RMSE
GSA	0.7607 ± 0.0053	0.05 ± 0.0265	0.0339 ± 0.0076	63.7784 ± 4.304	1.5486 ± 0.0042	1.2012×10^{-3}
SCA	0.7595 ± 0.0209	0.002 ± 0.034	0.0519 ± 0.0229	90.0685 ± 4.517	1.2641 ± 0.140	1.9123×10^{-3}
GWO	0.7695 ± 0.0038	1 ± 0.193	0.0269 ± 0.0037	47.9136 ± 16.872	1.6232 ± 0.0311	9.4095×10^{-4}
PSO	0.7383 ± 0.023	1 ± 0.023	0.0501 ± 0.0053	25.1251 ± 3.213	1.6605 ± 0.024	1.4320×10^{-3}
WOA	0.7573 ± 0.0019	0.016 ± 0.0056	0.053 ± 0.0028	58.5839 ± 0.354	1.2476 ± 0.0043	9.9529×10^{-4}
PSOGSA	0.7677 ± 0.0071	0.01 ± 0.006	0.0522 ± 0.0066	18.4587 ± 37.62	1.218 ± 0.0349	1.2400×10^{-3}
WOAPSO	0.7597 ± 0.0012	0.499 ± 0.004	0.0342 ± 0.0007	83.0131 ± 0.027	1.5483 ± 0.001	7.1700×10^{-4}

The characteristics curve of current-voltage and power-voltage for a single-diode model is redrawn based on the best optimized parameters obtained by implementing the WOAPSO algorithm and depicted in Figure 3. It is observed that the calculated data obtained by the WOAPSO is very effectively in keeping with the experimental data set, under S.T.C (i.e., 1000 w/m^2 and 33 °C), all over the voltage range. The error relating the measurement results for each of 20 pair points is determined by IAE and RE, which is calculated by using Equations (18) and (19), respectively.

$$IAE = |I_{measured} - I_{simulated}| \tag{18}$$

$$RE = (I_{measured} - I_{simulated})/I_{measured} \tag{19}$$
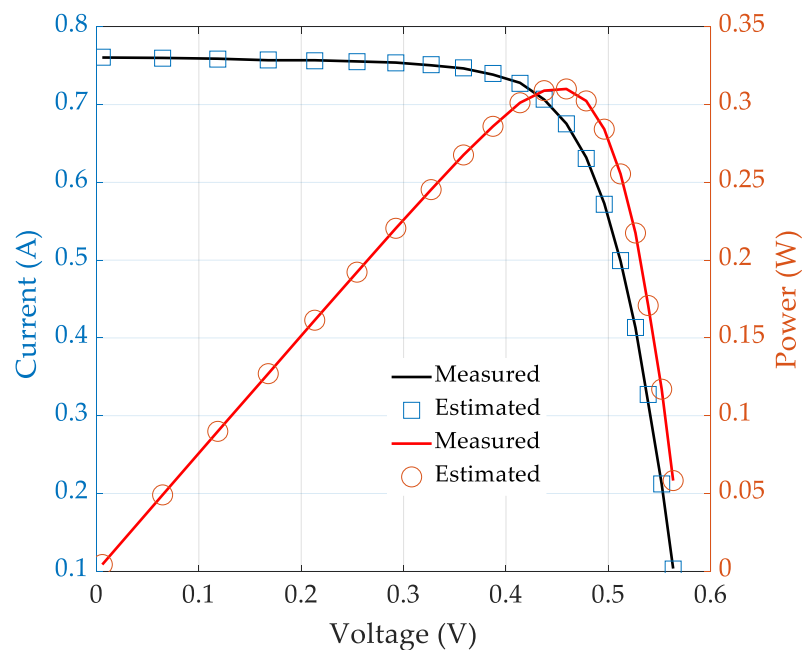
Figure 3. I-V and P-V characteristics curve for estimated and experimental values for single-diode model of R.T.C France solar cell.

3.2. WOAPSO for Parameter Estimation of Double-Diode Model

In the case of DDM, the seven parameters (I_p, I_{sd}, I_{sd1}, a_1, a_2, R_s, R_{sh}) are required to be optimized. The values of optimized parameters and minimum of RMSE are presented in Table 3. The characteristics curve in terms of current-voltage and power-voltage for the double-diode model is redrawn based on the best optimized parameters (Figure 4). It can be observed that the estimated data based on optimized parameters are in keeping with the experimental data set.

Table 3. Comparison of WOAPSO with different parameter estimation methods for DDM.

| Algorithms	I_{ph} (A) ± SD	I_{sd1} (μA) ± SD	I_{sd2} (μA) ± SD	R_s (Ω) ± SD	R_{sh} (Ω) ± SD	a_1 ± SD	a_2 ± SD	RMSE
GSA	0.7641 ± 0.0079	0.05 ± 0.177	0.001 ± 0.1191	0.0344 ± 0.0091	37.780 ± 1.21	1.9943 ± 0.1756	1.5492 ± 0.1076	2.03×10^{-3}
SCA	0.7623 ± 0.0097	0.0012 ± 0.059	0.001 ± 0.046	0.0595 ± 0.0067	52.4903 ± 24.02	2 ± 0.3030	1.2197 ± 0.2088	3.18×10^{-3}
GWO	0.7609 ± 0.0026	0.3156 ± 0.0052	0.0001 ± 0.008	0.0323 ± 0.0015	65.6799 ± 6.5859	1.9426 ± 0.0625	1.5312 ± 0.0272	1.60×10^{-3}
PSO	0.7676 ± 0.0016	0.0216 ± 0.027	0.0947 ± 0.234	0.0335 ± 0.012	54.9501 ± 5.4630	1.4606 ± 0.203	1.8363 ± 0.0137	2.90×10^{-3}
WOA	0.76354 ± 0.0019	0.169 ± 0.0017	0.163 ± 0.0011	0.0410 ± 0.0022	35.7342 ± 0.7539	2 ± 0.034	1.4420 ± 0.0036	4.30×10^{-3}
PSOGSA	0.7611 ± 0.0041	0.432 ± 0.0171	0.01 ± 0.0021	0.0347 ± 0.0042	61.72 ± 18.7135	1.9 ± 0.0183	1.5489 ± 0.0144	1.48×10^{-1}
WOAPSO	0.7601 ± 0.0007	0.5 ± 0.0020	0.5 ± 0.0027	0.0311 ± 0.0005	100 ± 0.4345	1.5755 ± 0.0043	1.7314 ± 0.0015	9.8412×10^{-4}
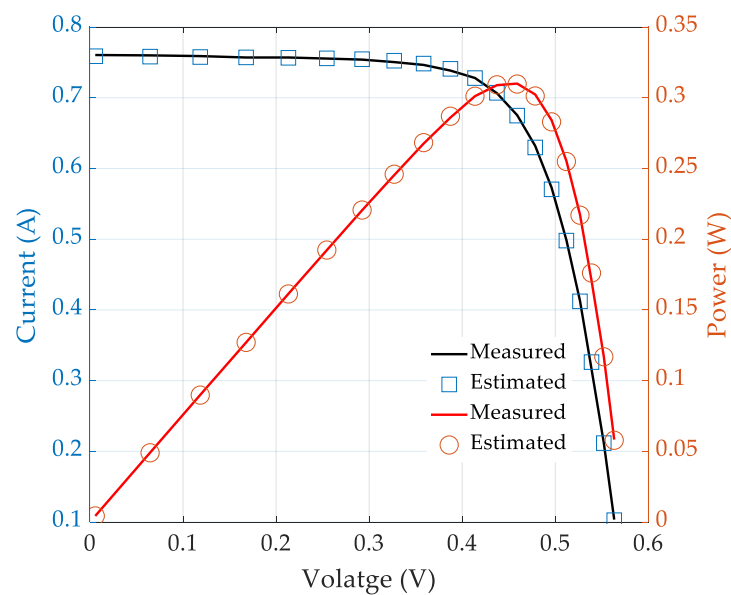
Figure 4. I-V and P-V characteristics curve for estimated and experimental values for double-diode model of R.T.C France solar cell.

3.3. WOAPSO for Parameter Estimation of SS2018P PV Module

In order to further evaluate the efficiency of the proposed WOAPSO algorithm, parameters for SS2018P PV module were also estimated at different level of irradiance by utilizing the SDM model. The optimal value of five parameters (I_p, I_{sd}, a, R_s, R_{sh}) for SDM of solar PV module at distinct levels of irradiance and constant temperature of 25 °C is presented in Table 4 and Tables S7–S9. The characteristics curve of current-voltage and power-voltage for solar PV module is redrawn based on best optimized parameters obtained by implementing the WOAPSO algorithm at a different level of irradiance, i.e., 1000 W/m^2, 870 W/m^2, 720 W/m^2, and 630 W/m^2 and is depicted in Figure 5. It is found that the calculated data obtained by the WOAPSO is very effectively in keeping with the experimental data set. The curve of IAE between experimental and estimated values at 1000 W/m^2, 870 W/m^2, 720 W/m^2, and 630 W/m^2, is shown in Figure 6.

Table 4. Comparison of proposed WOAPSO with different parameter estimation methods for SS2018P PV module (1000 W/m^2).

Parameters	Algorithms						
	GSA	**SCA**	**GWO**	**PSO**	**WOA**	**PSOGSA**	**WOAPSO**
I_{ph} (A)	1.0959 ± 0.0037	1.1742 ± 0.011	1 ± 0.024	1.1796 ± 1.009	1.181 ± 0.0103	1.168 ± 0.053	1.1707 ± 0.0025
I_{sd} (µA)	0.001 ± 0.2246	0.0092 ± 0.388	0.001 ± 0.0759	0.001 ± 0.707	0.019 ± 1.034	0.001 ± 1.358	0.0074 ± 0.0348
R_s (Ω)	0.001 ± 0.0253	0.0011 ± 0.0187	0.001 ± 0.0022	0.0022 ± 0.583	0.0024 ± 0.007	0.0075 ± 0.0342	0.2 ± 0.0017
R_{sh} (Ω)	455.5284 ± 13.67	139.676 ± 19.5323	100 ± 0.842	1308.079 ± 2.466	18.166 ± 10.71	2000 ± 4.63	177.219 ± 0.026
a	53.5976 ± 0.2493	1.4147 ± 1.021	1.2628 ± 0.0399	1.2429 ± 0.252	1.289 ± 0.6784	1.246 ± 0.24	1.3939 ± 0.0068
RMSE	1.68×10^{-1}	1.51×10^{-3}	1.59×10^{-1}	5.13×10^{-3}	7.82×10^{-4}	3.22×10^{-3}	7.6714×10^{-4}
CPU time (s)	17	12.45	9.3	10	7.56	13.17	7.81
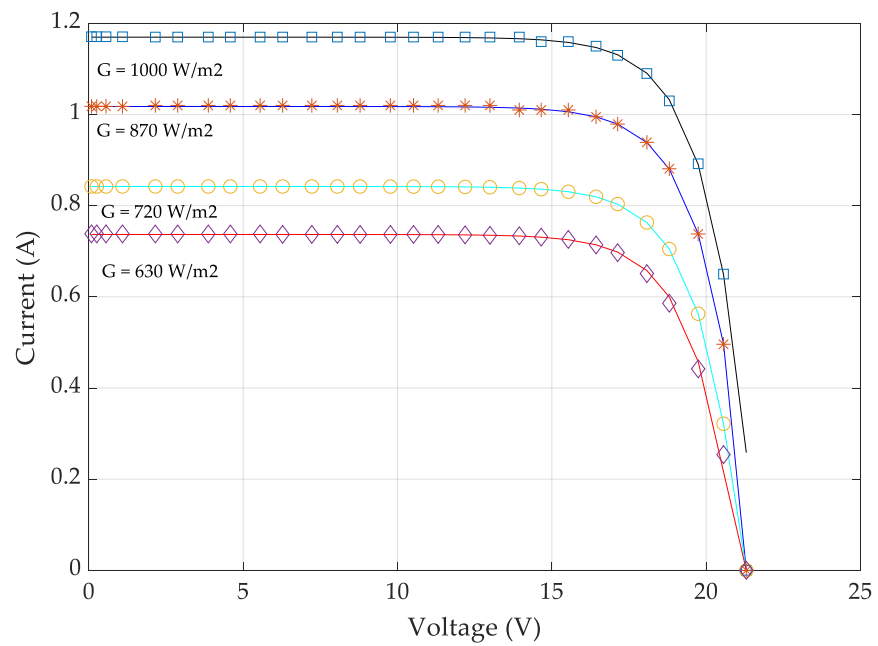
(**a**)
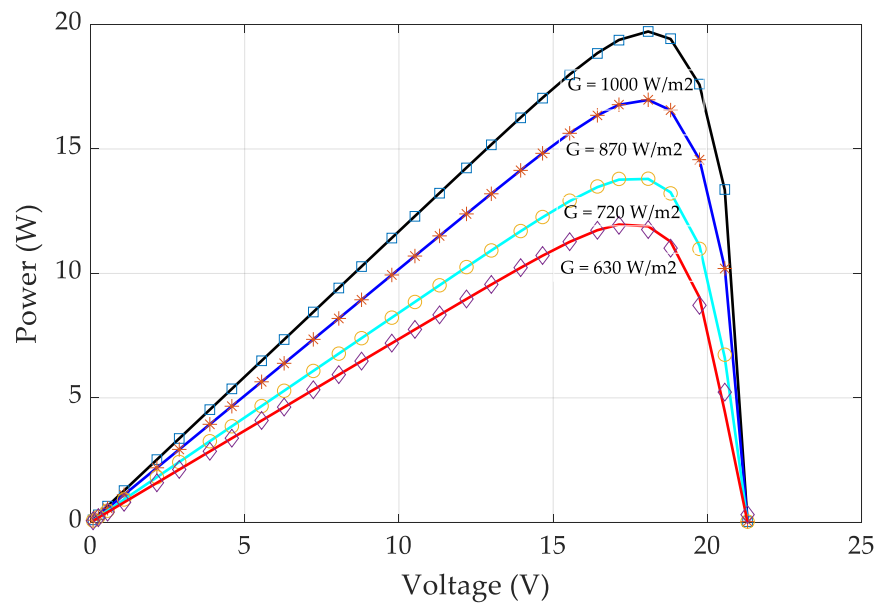
(**b**)

Figure 5. Characteristics curve of simulated and experimental values at different level of irradiance (**a**) I-V curve and (**b**) P-V curve for single-diode model of SS2018P PV module. Symbols represent the estimated data while the solid lines represent the measured data.
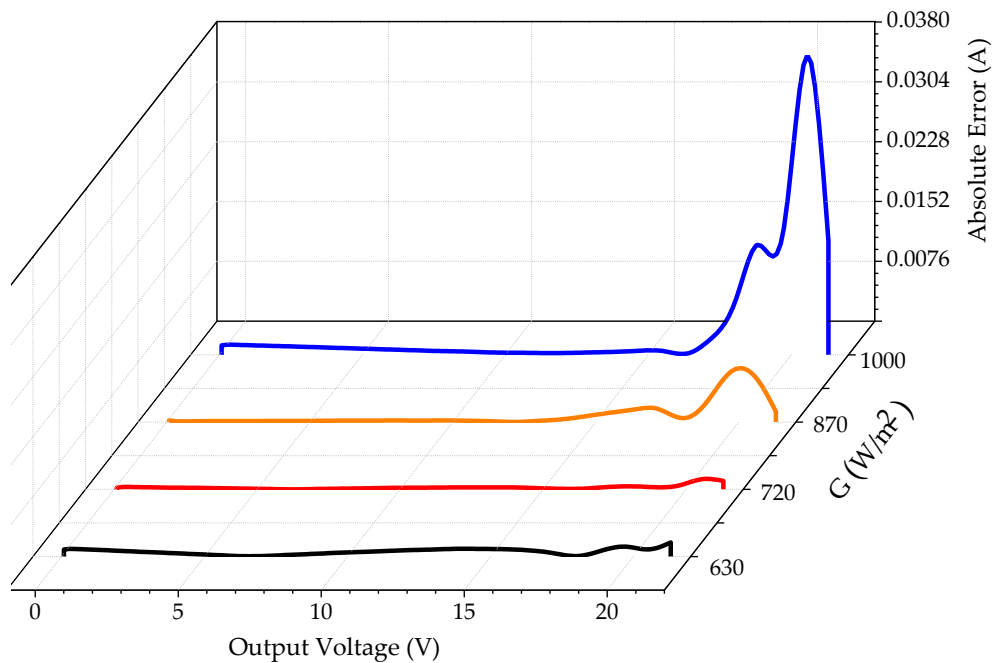
Figure 6. Internal absolute error between measured and simulated current for single-diode model of SS2018P PV module at different level of irradiance.

3.4. Convergence Analysis

To analyze the computational competence of WOAPSO, the convergence curves of the single-diode model, double-diode model, and PV module is presented in Figure 7. It is depicted that the proposed WOAPSO algorithm outperforms the GSA, SCA, GWO, PSO, WOA, PSOGSA algorithms in terms of convergence speed and generates a precise solution for the identical number of function evaluations (i.e., 50,000).

(**a**)
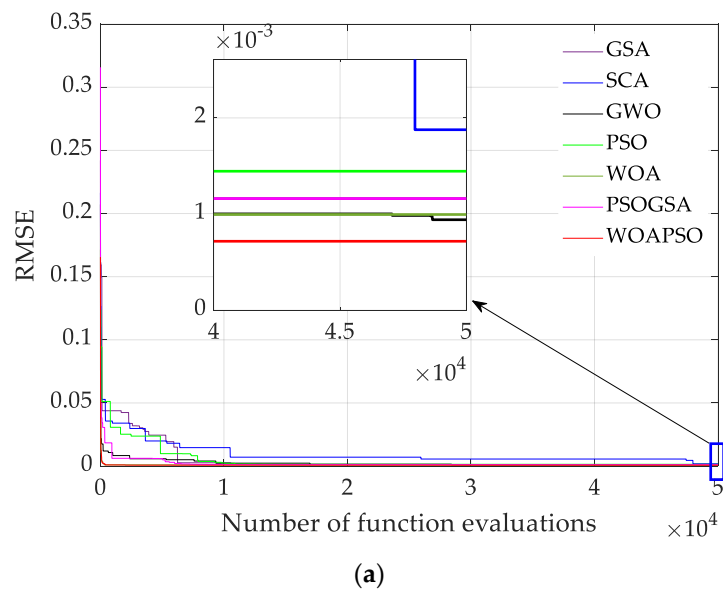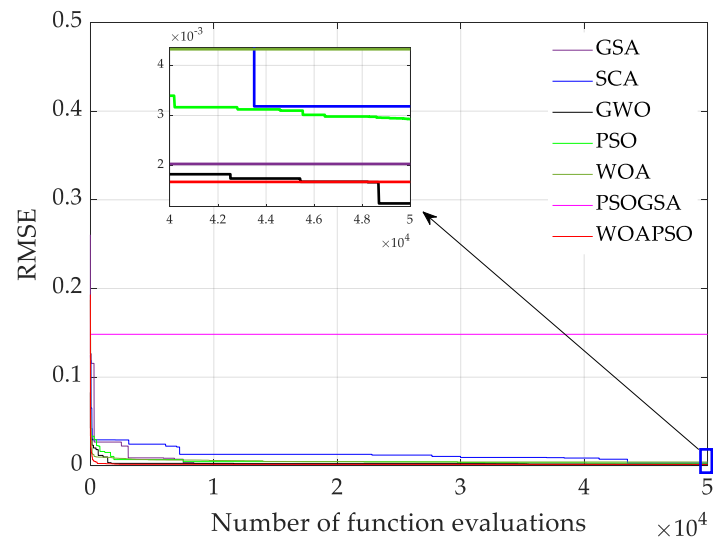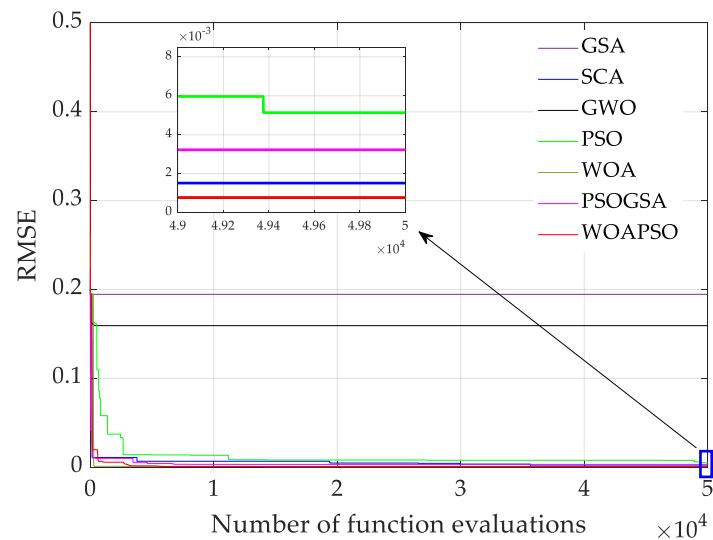
Figure 7. *Cont.*

Figure 7. Convergence curve of WOAPSO and other six algorithms for (**a**) single-diode model (**b**) double-diode model of R.T.C France solar cell and (**c**) single-diode model of SS2018P PV module.

3.5. Robustness and Statistical Analysis

This section presents statistical evaluation based on mean, minimum, maximum, and standard deviation of RMSE for all previously implemented methods, and a comparison with respect to precision and consistency of the distinct algorithms in a total of thirty runs and depicted in Table 5. The mean of RMSE is calculated to evaluate the precision of algorithms, and the standard deviation is calculated to evaluate the consistency of the parameter estimation methods.

Table 5. Statistical results of RMSE of different algorithms for all three models.

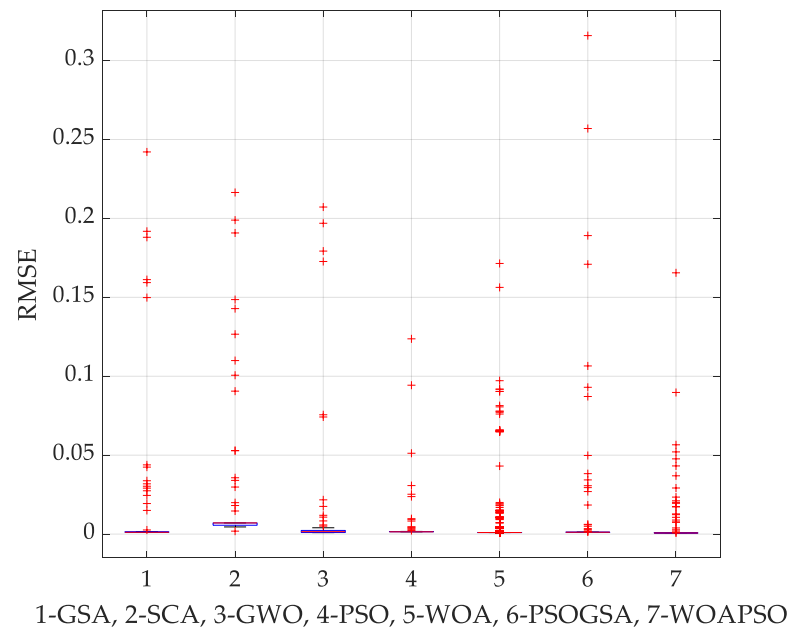| Model	Algorithm	RMSE			
		Min	**Mean**	**Max**	**SD**
Single-diode model	GSA	1.2012×10^{-3}	5.4701×10^{-3}	2.4211×10^{-1}	1.3129×10^{-3}
	SCA	1.9123×10^{-3}	9.6515×10^{-3}	2.1642×10^{-1}	9.4066×10^{-3}
	GWO	9.4095×10^{-4}	1.0441×10^{-3}	1.3506×10^{-3}	1.4050×10^{-5}
	PSO	1.4320×10^{-3}	1.2534×10^{-3}	1.4074×10^{-3}	1.1520×10^{-4}
	WOA	9.9529×10^{-4}	9.2032×10^{-4}	7.1240×10^{-3}	9.0250×10^{-3}
	PSOGSA	1.2400×10^{-3}	1.7660×10^{-3}	5.2460×10^{-3}	1.9880×10^{-3}
	WOAPSO	7.1701×10^{-4}	7.8030×10^{-4}	1.3436×10^{-3}	2.4290×10^{-6}
Double-diode model	GSA	2.0330×10^{-3}	4.7041×10^{-3}	2.6058×10^{-1}	1.5796×10^{-3}
	SCA	3.1800×10^{-3}	1.7932×10^{-3}	1.2470×10^{-1}	7.7256×10^{-2}
	GWO	1.6000×10^{-3}	2.6901×10^{-3}	8.2830×10^{-2}	2.6995×10^{-3}
	PSO	2.9000×10^{-3}	4.9713×10^{-3}	3.3402×10^{-2}	3.5833×10^{-2}
	WOA	4.3000×10^{-3}	5.2967×10^{-3}	1.8698×10^{-2}	3.9481×10^{-3}
	PSOGSA	1.4812×10^{-1}	1.4833×10^{-1}	1.4732×10^{-1}	1.0977×10^{-2}
	WOAPSO	9.8412×10^{-4}	1.2481×10^{-3}	1.9312×10^{-3}	1.0581×10^{-3}
SS2018P module model	GSA	1.6877×10^{-1}	1.9462×10^{-1}	2.0011×10^{-1}	4.4500×10^{-3}
	SCA	1.5149×10^{-3}	5.2657×10^{-3}	2.0345×10^{-1}	1.0058×10^{-2}
	GWO	1.5938×10^{-1}	1.5940×10^{-1}	5.2494×10^{-1}	1.6793×10^{-2}
	PSO	5.1329×10^{-2}	1.2512×10^{-2}	2.6323×10^{-1}	1.9334×10^{-2}
	WOA	7.8164×10^{-4}	1.8268×10^{-3}	2.1078×10^{-2}	1.3639×10^{-3}
	PSOGSA	3.2258×10^{-3}	3.9510×10^{-3}	2.2333×10^{-1}	4.0336×10^{-3}
	WOAPSO	7.6714×10^{-4}	7.4601×10^{-4}	7.5388×10^{-4}	7.4516×10^{-5}

The statistical results presented in Table 5 indicate that WOAPSO is the most accurate and reliable parameter optimization technique. As shown in Table 6, based on the Friedman ranking test result, the best ranking is obtained by the WOAPSO, followed by WOA, GWO, GSA, PSOGSA, SCA, and PSO. Also, Figure 8 shows the distribution of results (i.e., RMSE) obtained from the distinct algorithms in 30 runs in the form of a boxplot graph for the SDM, DDM, and PV module. It can be anticipated from Figure 8 that the proposed WOAPSO algorithm delivers the best results in terms of accuracy and reliability compared to the other six algorithms.

Table 6. Ranking of the proposed WOAPSO and other compared algorithms on three PV models according to the Friedman test.

Algorithms	Friedman Ranking	Final Ranking
GSA	3.9	4
SCA	5.91	6
GWO	3.36	3
PSO	6.53	7
WOA	2.05	2
PSOGSA	5.22	5
WOAPSO	1	1

(**a**)

(**b**)

Figure 8. *Cont.*

1-GSA, 2-SCA, 3-GWO, 4-PSO, 5-WOA, 6-PSOGSA, 7-WOAPSO
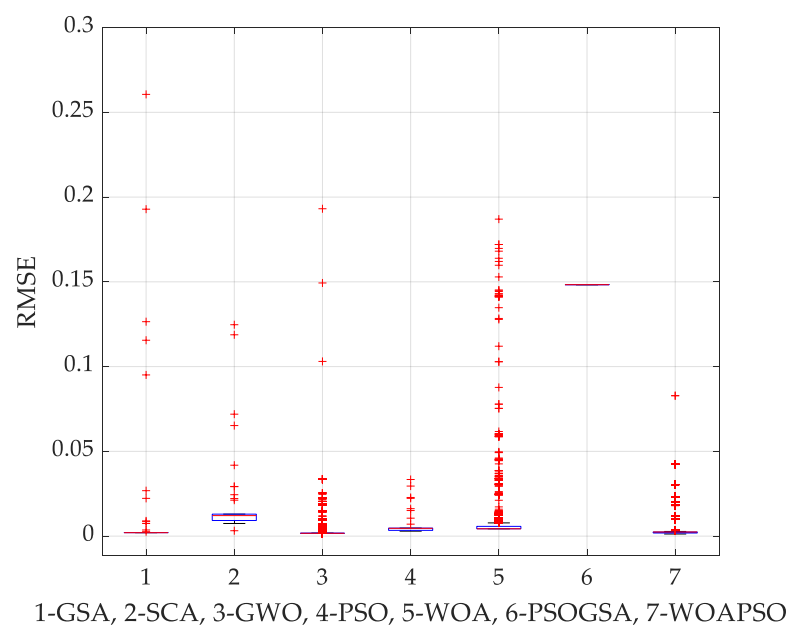
(**c**)

Figure 8. Boxplot graph of best RMSE in 30 runs for (**a**) single diose model (**b**) double-diode model (**c**) polycrystalline SS2018P PV module.

4. Discussion

To evaluate the reliability of the WOAPSO, the proposed hybrid algorithm is compared with six well established metaheuristics algorithms, i.e., GSA [56], SCA [57], GWO [58], PSO [59], WOA [37], PSOGSA [60] as well as other algorithms existing in the literature. It is observed that the estimated parame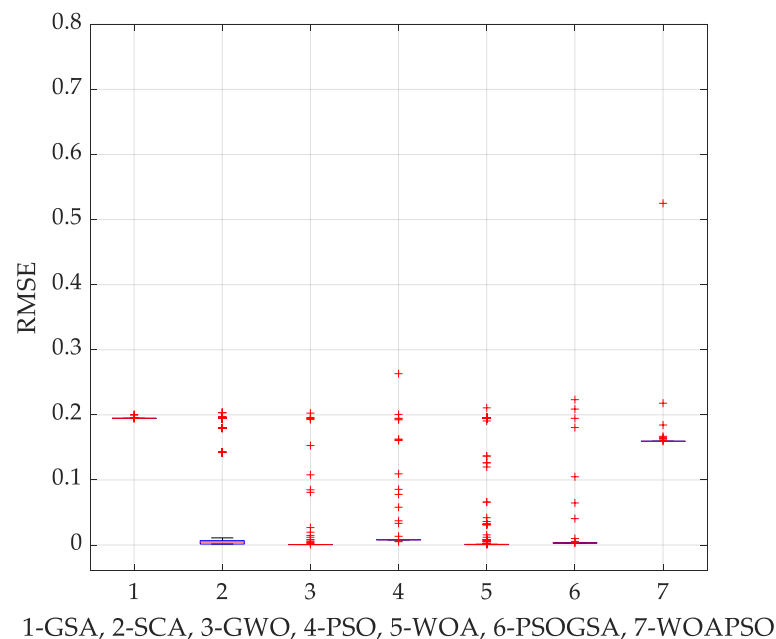ters based on the optimization process are highly consistent with the experimental data for SDM, DDM, and SS2018P PV module.

For SDM, the hybrid WOAPSO algorithm generates the lowest RMSE values (7.1700×10^{-4}) compared to the GSA, SCA, GWO, PSO, and WOA, PSOGSA algorithms (Table 2). The RMSE of the proposed WOAPSO algorithm is also compared with previously studied algorithms (Table S2). It is noted that the hybrid WOAPSO algorithm provides the lowest RMSE values than that of others. Table S3 represents the absolute IAE for SDM analysis. The magnitude of IAE for different observations is less than 0.0018 (Table S3), which indicates that the parameters optimized by the WOAPSO are very precise.

In the case of DDM analysis, the MLBSA, EHHO, IJAYA, and GOTLBO algorithms produce the best value of RMSE (Table S4). However, WOAPSO generates the third-best value of RMSE (9.8412×10^{-4}), which is very close to MLBSA (9.8249×10^{-4}), EHHO (9.8360×10^{-4}), IJAYA (9.8293×10^{-4}), and GOTLBO (9.8317×10^{-4}). However, the computational cost in terms of function evaluation is 1/3 of MLBSA, EHHO, IJAYA, and GOTLBO. Moreover, WOAPSO shows superiority over other algorithms in terms of RMSE (Table 3). For DDM, the magnitude of IAE for different observations is depicted in Table S5. It is noticed that the IAE values are less than 0.0097, which demonstrates the accuracy of optimized parameters produced by WOAPSO.

For the SS2018P PV module, the hybrid WOAPSO algorithm produces the lowest RMSE values compared to the GSA, SCA, GWO, PSO, WOA, and PSOGSA algorithms. The IAE magnitudes for different observations (at 1000 W/m^2) are less than 0.0018 (Table S6). More importantly, the computational time for WOAPSO is less than other algorithms (Table 4). The average execution time of each algorithm on the three PV models is calculated and illustrated in Figure 9. The WOAPSO algorithm requires less time (about 26.1 s)

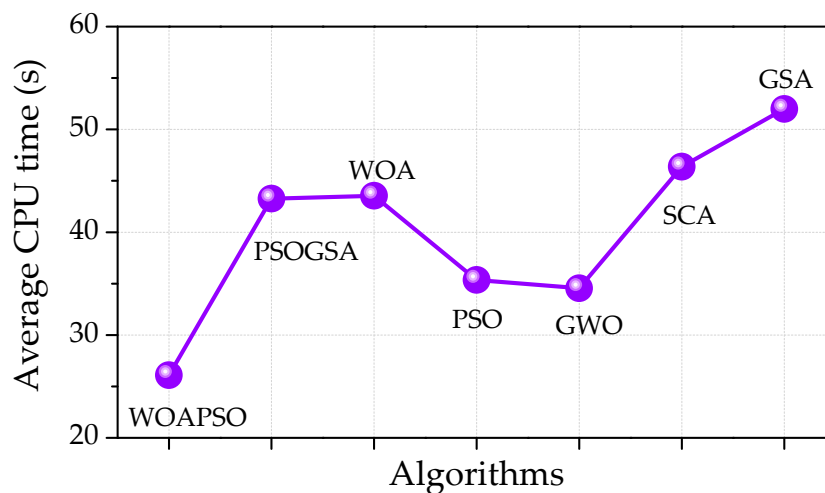than GWO, PSO, SCA, WOA, and PSOGSA, while GSA has the worst execution time of approximately 52 s.

Figure 9. Comparison of the execution time.

Furthermore, the Friedman ranking test is also performed for all algorithms and depicted in Table 6. Table 6 shows that the proposed WOAPSO algorithm significantly outperforms the GSA, SCA, GWO, PSO, WOA, PSOGSA algorithms for all three models, i.e., single-diode, double-diode, and PV module models.

5. Conclusions

In this study, the hybridization of whale optimization and particle swarm optimization algorithm (WOAPSO) is anticipated. The exploitation ability of PSO is only implemented in pipeline mode when WOA stops to improve the best-found solution. The collaboration of both metaheuristic algorithms can establish an effective balance between exploitation and exploration ability. The proposed technique is further used to estimate the parameter of three PV cell models, i.e., single-diode, double-diode, and SS108P PV panel module model at different operating conditions. It should be noted that this suggested technique is, for the first time, intended to track the estimation of parameters for photovoltaic models reliably. The major conclusions are classified as follows:

- The proposed WOAPSO is relatively accurate and reliable at delivering the solution in terms of RMSE as compared with other algorithms such as GSA, SCA, GWO, PSO, WOA, PSOGSA, and existing algorithms in the literature.
- The I-V and P-V characteristic curves and IAE results indicate that WOAPSO can generate the optimized value of estimated parameters for all the models of solar PV cell as compared with other algorithms.
- The statistical analysis clearly depicts the robustness of the proposed WOAPSO technique on parameter estimation problem at different operating conditions.
- The convergence curves demonstrate that the best values of estimated parameters are obtained by WOAPSO, and RMSE is 7.1700×10^{-4} and 9.8412×10^{-4} in the case of single- and double-diode respectively.
- At different irradiation levels (i.e., $1000 \, \text{W/m}^2$, $870 \, \text{W/m}^2$, $720 \, \text{W/m}^2$, and $630 \, \text{W/m}^2$), the proposed WOAPSO algorithm is best in producing optimized parameters (I_p, I_{sd}, a, R_s, R_{sh}) and minimum value of RMSE for PV module even at a low level of irradiation ($630 \, \text{W/m}^2$).

The proposed WOAPSO algorithm has limitation for DDM analysis. The RMSE value (9.8412×10^{-4}) of WOAPSO algorithm is lower than that of recently developed metaheuristics algorithms (MLBSA, EHHO, IJAYA, and GOTLBO algorithms).

The WOAPSO is an efficient and robust technique to estimate the unknown optimized parameters of the solar PV model at different operating conditions. For future study, the implementation of proposed WOAPSO to solve the other problems related to energy optimization such as economic load dispatch, energy scheduling and optimization of PV array configuration may also be interesting for scientists and research scholars.

Supplementary Materials: The supplementary materials are available online at https://www.mdpi.com/2079-9292/10/3/312/s1.

Author Contributions: Conceptualization: A.S. (Abhishek Sharma), and A.S. (Abhinav Sharma); methodology and formal analysis: A.S. (Abhishek Sharma) and M.A.; investigation, A.S. (Abhinav Sharma); writing—original draft preparation, A.S. (Abhishek Sharma); writing—review and editing, A.S. (Abhinav Sharma), M.A. and V.J.; supervision, M.A. and B.A.; fund acquisition: B.A. All authors have read and agreed to the published version of the manuscript.

Conflicts of Interest: The authors declare no conflict of interest.

Abbreviations

The following abbreviations and nomenclature are used in this manuscript:

I_p	Photo Diode Current
I_{sd}	Reverse Saturation Current
R_s	Series Resistance
R_{sh}	Shunt Resistance
a	Diode Ideality Factor
RMSE	Root Mean Square Error
PV	Photo Voltaic
I-V	Current-Voltage
P-V	Power-Voltage
MPP	Maximum Power Tracking
V_{oc}	Open Circuit Voltage
I_{mpp}	Maximum Power Point Current
I_{sc}	Short Circuit Current
GBO	Gradient Based Optimizer
HHO	Harris-Hawk optimizer
HBO	Heap-Based Optimizer
SMA	Slime Mould Algorithm
GA	Genetic Algorithm
DE	Differential Evaluation
SA	Simulating Annealing
PS	Pattern Search
HS	Harmony Search
CS	Cooku Search
FPA	Flower Pollination Algorithm
BFO	Bacterial Foraging Algorithm
BM	Bird Mating
ABSO	Artificial Bee Swarm Optimization
PSO	Particle Swarm Optimization
ITLBO	Improved Teaching-Learning Based Optimization
WOA	Whale Optimization Algorithm
CWOA	Chaotic Whale Optimization Algorithm

LWOA	Levy flight trajectory based WOA
BWOA	Binary Whale Optimization Algorithm
HAGWO	Hybrid Approach Grey Wolf Optimization
WOA-CBO	Whale Optimization Algorithm Colliding Bodies Optimization
MWOA	Memetic Whale Optimization Algorithm
WOA-SA	Whale Optimization Algorithm-Simulated Annealing
WOA-MFO	Whale Optimization Algorithm-Moth Flame Optimization
SC-WOA	Sine-Cosine Whale Optimization Algorithm
WOA-PS	Whale Optimization Algorithm- Pattern Search
BS-WOA	Brainstorm- Whale Optimization Algorithm
SDM	Single-diode Model
DDM	Double-diode Model
IAE	Internal Absolute Error
RE	Relative Error
GSA	Gravitational Search Algorithm
SCA	Sine Cosine Algorithm
GWO	Grey Wolf Optimization
PSOGSA	Particle Swarm Optimization Gravitational Search Algorithm
MLBSA	Multiple Learning Backtracking Search Algorithm
EHHO	Enriched Harris Hawks Optimization
IJAYA	Improved Jaya Algorithm
GOTLBO	Generalized Opposition-Based Teaching Learning Based Optimization

References

1. Panwar, N.L.; Kaushik, S.C.; Kothari, S. Role of renewable energy sources in environmental protection: A review. *Renew. Sustain. Energy Rev.* **2011**, *15*, 1513–1524. [CrossRef]
2. Gielen, D.; Boshell, F.; Saygin, D.; Bazilian, M.D.; Wagner, N.; Gorini, R. The role of renewable energy in the global energy transformation. *Energy Strategy Rev.* **2019**, *24*, 38–50. [CrossRef]
3. Rajput, S.; Averbukh, M.; Yahalom, A.; Minav, T. An Approval of MPPT Based on PV Cell's Simplified Equivalent Circuit During Fast-Shading Conditions. *Electronics* **2019**, *8*, 1060. [CrossRef]
4. Jordehi, A.R. Parameter estimation of solar photovoltaic (PV) cells: A review. *Renew. Sustain. Energy Rev.* **2016**, *61*, 354–371. [CrossRef]
5. Aryanpur, V.; Atabaki, M.S.; Marzband, M.; Siano, P.; Ghayoumi, K. An overview of energy planning in Iran and transition pathways towards sustainable electricity supply sector. *Renew. Sustain. Energy Rev.* **2019**, *112*, 58–74. [CrossRef]
6. Armghan, H.; Ahmad, I.; Armghan, A.; Khan, S.; Arsalan, M. Backstepping based nonlinear control for maximum power point tracking in photovoltaic system. *Sol. Energy* **2018**, *159*, 134–141.
7. Ram, J.P.; Manghani, H.; Pillai, D.S.; Babu, T.S.; Miyatake, M.; Rajasekar, N. Analysis on solar PV emulators: A review. *Renew. Sustain. Energy Rev.* **2018**, *81*, 149–160. [CrossRef]
8. Youssef, A.; El-Telbany, M.; Zekry, A. The role of artificial intelligence in photovoltaic systems design and control: A review. *Renew. Sustain. Energy Rev.* **2017**, *78*, 72–79. [CrossRef]
9. Gomes, R.C.M.; Vitorino, M.A.; de Rossiter Corrêa, M.B.; Fernandes, D.A.; Wang, R. Shuffled complex evolution on photovoltaic parameter extraction: A comparative analysis. *IEEE Trans. Sustain. Energy* **2016**, *8*, 805–815. [CrossRef]
10. Chin, V.J.; Salam, Z.; Ishaque, K. Cell modelling and model parameters estimation techniques for photovoltaic simulator application: A review. *Appl. Energy* **2015**, *154*, 500–519. [CrossRef]
11. Brano, V.L.; Ciulla, G. An efficient analytical approach for obtaining a five parameters model of photovoltaic modules using only reference data. *Appl. Energy* **2013**, *111*, 894–903. [CrossRef]
12. Louzazni, M. An analytical mathematical modeling to extract the parameters of solar cell from implicit equation to explicit form. *Appl. Sol. Energy* **2015**, *51*, 165–171. [CrossRef]
13. Batzelis, E.I.; Papathanassiou, S.A. A method for the analytical extraction of the single-diode PV model parameters. *IEEE Trans Sustain. Energy* **2015**, *7*, 504–512. [CrossRef]
14. Khan, F.; Baek, S.H.; Kim, J.H. Wide range temperature dependence of analytical photovoltaic cell parameters for silicon solar cells under high illumination conditions. *Appl. Energy* **2016**, *183*, 715–724. [CrossRef]
15. Tao, Y.; Bai, J.; Pachauri, R.K.; Sharma, A. Parameter extraction of photovoltaic modules using a heuristic iterative algorithm. *Energy Convers. Manag.* **2020**, *224*, 113386. [CrossRef]
16. Gao, X.; Cui, Y.; Hu, J.; Xu, G.; Yu, Y. Lambert W-function based exact representation for double diode model of solar cells: Comparison on fitness and parameter extraction. *Energy Convers. Manag.* **2016**, *127*, 443–460. [CrossRef]
17. Villalva, M.G.; Gazoli, J.R.; Ruppert Filho, E. Comprehensive approach to modeling and simulation of photovoltaic arrays. *IEEE Trans. Power Electron.* **2009**, *24*, 1198–1208. [CrossRef]

18. Chegaar, M.; Ouennoughi, Z.; Hoffmann, A. A new method for evaluating illuminated solar cell parameters. *Solid-State Electron.* **2001**, *45*, 293–296. [CrossRef]

19. Abdallah, R.; Natsheh, E.; Juaidi, A.; Samara, S.; Manzano-Agugliaro, F. A Multi-Level World Comprehensive Neural Network Model for Maximum Annual Solar Irradiation on a Flat Surface. *Energies* **2020**, *13*, 6422. [CrossRef]

20. Ahmadianfar, I.; Bozorg-Haddad, O.; Chu, X. Gradient-based optimizer: A new Metaheuristic optimization algorithm. *Inf. Sci.* **2020**, *540*, 131–159. [CrossRef]

21. Heidari, A.A.; Mirjalili, S.; Faris, H.; Aljarah, I.; Mafarja, M.; Chen, H. Harris hawks optimization: Algorithm and applications. *Future Gener. Comput. Syst.* **2019**, *97*, 849–872. [CrossRef]

22. Askari, Q.; Saeed, M.; Younas, I. Heap-based optimizer inspired by corporate rank hierarchy for global optimization. *Expert Syst. Appl.* **2020**, *161*, 113702. [CrossRef]

23. Li, S.; Chen, H.; Wang, M.; Heidari, A.A.; Mirjalili, S. Slime mould algorithm: A new method for stochastic optimization. *Future Gener. Comput. Syst.* **2020**, *111*, 300–323. [CrossRef]

24. Ismail, M.S.; Moghavvemi, M.; Mahlia, T.M.I. Characterization of PV panel and global optimization of its model parameters using genetic algorithm. *Energy Convers. Manag* **2013**, *73*, 10–25. [CrossRef]

25. Ishaque, K.; Salam, Z.; Mekhilef, S.; Shamsudin, A. Parameter extraction of solar photovoltaic modules using penalty-based differential evolution. *Appl. Energy* **2012**, *99*, 297–308. [CrossRef]

26. El-Naggar, K.M.; AlRashidi, M.R.; AlHajri, M.F.; Al-Othman, A.K. Simulated annealing algorithm for photovoltaic parameters identification. *Sol. Energy* **2012**, *86*, 266–274. [CrossRef]

27. AlHajri, M.F.; El-Naggar, K.M.; AlRashidi, M.R.; Al-Othman, A.K. Optimal extraction of solar cell parameters using pattern search. *Renew. Energy* **2012**, *44*, 238–245. [CrossRef]

28. Askarzadeh, A.; Rezazadeh, A. Parameter identification for solar cell models using harmony search-based algorithms. *Sol. Energy* **2012**, *86*, 3241–3249. [CrossRef]

29. Ma, J.; Ting, T.O.; Man, K.L.; Zhang, N.; Guan, S.U.; Wong, P.W. Parameter estimation of photovoltaic models via cuckoo search. *J. Appl. Math.* **2013**, *2013*, 1–8. [CrossRef]

30. Yousri, D.; Babu, T.S.; Allam, D.; Ramachandaramurthy, V.K.; Beshr, E.; Eteiba, M.B. Fractional Chaos Maps with Flower Pollination Algorithm for Partial Shading Mitigation of Photovoltaic Systems. *Energies* **2019**, *12*, 3548. [CrossRef]

31. Subudhi, B.; Pradhan, R. Bacterial foraging optimization approach to parameter extraction of a photovoltaic module. *IEEE Trans. Sustain. Energy* **2017**, *9*, 381–389. [CrossRef]

32. Askarzadeh, A.; Rezazadeh, A. Extraction of maximum power point in solar cells using bird mating optimizer-based parameters identification approach. *Sol. Energy* **2013**, *90*, 123–133. [CrossRef]

33. Askarzadeh, A.; Rezazadeh, A. Artificial bee swarm optimization algorithm for parameters identification of solar cell models. *Appl. Energy* **2013**, *102*, 943–949. [CrossRef]

34. Beigi, A.M.; Maroosi, A. Parameter identification for solar cells and module using a Hybrid Firefly and Pattern Search Algorithms. *Sol. Energy* **2018**, *171*, 435–446. [CrossRef]

35. Abd Elaziz, M.; Oliva, D. Parameter estimation of solar cells diode models by an improved opposition-based whale optimization algorithm. *Energy Convers. Manag* **2018**, *171*, 1843–1859. [CrossRef]

36. Chen, Y.; Chen, Z.; Wu, L.; Long, C.; Lin, P.; Cheng, S. Parameter extraction of PV models using an enhanced shuffled complex evolution algorithm improved by opposition-based learning. *Energy Procedia* **2019**, *158*, 991–997. [CrossRef]

37. Mirjalili, S.; Lewis, A. The whale optimization algorithm. *Adv. Eng. Softw.* **2016**, *95*, 51. [CrossRef]

38. Eberhart, R.; Kennedy, J. A new optimizer using particle swarm theory. In Proceedings of the Sixth International Symposium on Micro Machine and Human Science, Nagoya, Japan, 4–6 October 1995.

39. Mafarja, M.M.; Mirjalili, S. Hybrid whale optimization algorithm with simulated annealing for feature selection. *Neurocomputing* **2017**, *260*, 302–312. [CrossRef]

40. Laskar, N.M.; Guha, K.; Chatterjee, I.; Chanda, S.; Baishnab, K.L.; Paul, P.K. HWPSO: A new hybrid whale-particle swarm optimization algorithm and its application in electronic design optimization problems. *Appl. Intell.* **2019**, *49*, 265–291. [CrossRef]

41. Kaur, G.; Arora, S. Chaotic whale optimization algorithm. *J. Comput. Des. Eng.* **2018**, *5*, 275–284. [CrossRef]

42. Ling, Y.; Zhou, Y.; Luo, Q. Lévy flight trajectory-based whale optimization algorithm for global optimization. *IEEE Access* **2017**, *5*, 6168–6186. [CrossRef]

43. Reddy, K.S.; Panwar, L.; Panigrahi, B.K.; Kumar, R. Binary whale optimization algorithm: A new metaheuristic approach for profit-based unit commitment problems in competitive electricity markets. *Eng. Optim.* **2019**, *51*, 369–389. [CrossRef]

44. Pandey, H.M. A Modified Whale Optimization Algorithm with Multi-Objective Criteria for Optimal Robot Path Planning. Available online: http://www.datascience.manchester.ac.uk/media/1669/a-modified-whale-optimization-algorithm-with-multi-objective-criteria-for-optimal-robot-path-planning.pdf (accessed on 26 January 2021).

45. Salgotra, R.; Singh, U.; Saha, S. On some improved versions of whale optimization algorithm. *Arab. J. Sci. Eng.* **2019**, *44*, 9653–9691. [CrossRef]

46. Singh, N.; Hachimi, H. A new hybrid whale optimizer algorithm with mean strategy of grey wolf optimizer for global optimization. *Math. Comput. Appl.* **2018**, *23*, 14. [CrossRef]

47. Kaveh, A.; Rastegar Moghaddam, M. A hybrid WOA-CBO algorithm for construction site layout planning problem. *Sci. Iran.* **2018**, *25*, 1094. [CrossRef]

48. Xu, Z.; Yu, Y.; Yachi, H.; Ji, J.; Todo, Y.; Gao, S. A novel memetic whale optimization algorithm for optimization. In *International Conference on Swarm Intelligence*; Springer: Cham, Switzerland, 2018; pp. 384–396.

49. Abd El Aziz, M.; Ewees, A.A.; Hassanien, A.E. Whale optimization algorithm and moth-flame optimization for multilevel thresholding image segmentation. *Expert Syst. Appl.* **2017**, *83*, 242–256. [CrossRef]

50. Khalilpourazari, S.; Khalilpourazary, S. SCWOA: An efficient hybrid algorithm for parameter optimization of multi-pass milling process. *J. Ind. Prod. Eng.* **2018**, *35*, 135–147. [CrossRef]

51. Bentouati, B.; Chaib, L.; Chettih, S. A hybrid whale algorithm and pattern search technique for optimal power flow problem. In Proceedings of the 8th International Conference on Modelling, Identification and Control (ICMIC), Algiers, Algeria, 15–17 November 2016; pp. 1048–1053.

52. Revathi, S.T.; Ramaraj, N.; Chithra, S. Brainstorm-based Whale Optimization Algorithm for privacy-protected data publishing in cloud computing. *Clust. Comput.* **2019**, *22*, 3521–3530. [CrossRef]

53. Kang, T.; Yao, J.; Jin, M.; Yang, S.; Duong, T. A Novel Improved Cuckoo Search Algorithm for Parameter Estimation of Photovoltaic (PV) Models. *Energies* **2018**, *11*, 1060. [CrossRef]

54. Sheng, H.; Li, C.; Wang, H.; Yan, Z.; Xiong, Y.; Cao, Z.; Kuang, Q. Parameters Extraction of Photovoltaic Models Using an Improved Moth-Flame Optimization. *Energies* **2019**, *12*, 3527. [CrossRef]

55. Easwarakhanthan, T.; Bottin, J.; Bouhouch, I.; Boutrit, C. Nonlinear minimization algorithm for determining the solar cell parameters with microcomputers. *Int. J. Sol. Energy* **1986**, *4*, 1–12. [CrossRef]

56. Rashedi, E.; Nezamabadi-Pour, H.; Saryazdi, S. GSA: A gravitational search algorithm. *Inf. Sci.* **2009**, *179*, 2232. [CrossRef]

57. Mirjalili, S. SCA: A sine cosine algorithm for solving optimization problems. *Knowl. Based Syst.* **2016**, *96*, 120–133. [CrossRef]

58. Mirjalili, S.; Mirjalili, S.M.; Lewis, A. Grey wolf optimizer. *Adv. Eng. Softw.* **2014**, *69*, 46–61. [CrossRef]

59. Kennedy, J.; Eberhart, R. Particle swarm optimization. In Proceedings of the International Conference on Neural Networks (ICNN'95), Perth, WA, Australia, 27 November–1 December 1995; pp. 1942–1948.

60. Mirjalili, S. Hybrid Particle Swarm Optimization and Gravitational Search Algorithm for Multilayer Perceptron Learning. Ph.D. Thesis, Universiti Teknologi Malaysia, Johor, Malaysia, 2011.

Parameter Extraction of Photovoltaic Module Using Tunicate Swarm Algorithm

Abhishek Sharma [1], Ankit Dasgotra [1] , Sunil Kumar Tiwari [1], Abhinav Sharma [2], Vibhu Jately [3,*] and Brian Azzopardi [3]

[1] Research and Development Department, University of Petroleum and Energy Studies, Dehradun 248007, India; abhishek15491@gmail.com (A.S.); dasgotraa@gmail.com (A.D.); suniltiwari.me.utu@gmail.com (S.K.T.)

[2] Department of Electrical and Electronics Engineering, School of Engineering, University of Petroleum and Energy Studies, Dehradun 248007, India; abhinav.sharma@ddn.upes.ac.in

[3] MCAST Energy Research Group, Institute of Engineering and Transport, Malta College of Arts, Science and Technology, Paola PLA9032, Malta; brian.azzopardi@mcast.edu.mt

* Correspondence: vibhu.jately@mcast.edu.mt

Abstract: In the renewable energy sector, the extraction of parameters for solar photovoltaic (PV) cells is a widely studied area of research. Parameter extraction is a non-linear complex optimization problem for solar PV cells. In this research work, the authors have implemented the Tunicate swarm algorithm (TSA) to estimate the optimized value of the unknown parameters of a PV cell/module under standard temperature conditions. The simulation results have been compared with four different, pre-existing optimization algorithms: gravitational search algorithm (GSA), a hybrid of particle swarm optimization and gravitational search algorithm (PSOGSA), sine cosine (SCA), and whale optimization (WOA). The comparison of results broadly demonstrates that the TSA algorithm outperforms the existing optimization algorithms in terms of root mean square error (RMSE) and convergence rate. Furthermore, the statistical results confirm that the TSA algorithm is a better algorithm in terms of average robustness and precision. The Friedman ranking test is also carried out to demonstrate the competency and reliability of the implemented approach.

Keywords: photovoltaic; TSA; parameter extraction; single-diode model; double-diode model; swarm intelligence

1. Introduction

Solar energy is emerged as a potential renewable source of energy. For the eighth year in a row, solar power has received the greatest proportion of groundbreaking investment opportunities in renewable energy sources. Because of the high investment cost of PV-generating installations, it is necessary to estimate the behavior of the PV-system from the designing phase to assure efficient utilization of solar energy in electricity generation [1,2]. Solar energy is also reflected as an extremely capable renewable resource owing to its usage and non-polluting nature [1–3]. Moreover, its modularity and scalability have added to its extensive acceptance in power systems through different photovoltaic (PV) configurations [4]. For simulating, controlling, and evaluating the photovoltaic systems, modeling of the solar-cell installation must be done. Whenever photovoltaics start operating, the solar-cell parameters could be utilized for accounting for the detectability and analysis [3]. However, the practical aspect is that photovoltaic devices are majorly bare compared to several outer atmospheric belongings, and its photovoltaic arrays do not last always efficiently which will harm the production of sun-based devices [4]. Accordingly, this is a critical estimation of the practical performance of photovoltaic arrays in the process to achieve, enhance, and simulate these types of systems/devices. With this aim, we frequently use a reliable prototype to measure current and voltage files [5].

The importance of photovoltaics is estimated to be a major stimulating topic by scientists/researchers and firms to progress energy adaption and reduce costs [6–8]. To boost the systematic performance of photovoltaics, modeling the photovoltaic cells and their segments is a crucial part. The non-linear dimensions and sporadic nature of meteorologic static make it difficult to identify cell constraints [9]. Furthermore, the production firms require assurance of the performance of photovoltaic units for approx. twenty-five years; photovoltaic arrangements are dependent on location and unavoidably undergo degradation, along with possible occurrences of electrical faults. So, we can considerably work on a systematic model that predicts the practical behavior of the photovoltaic cell in possible working conditions [10].

Generally, PV systems are vulnerable to outside atmospheric aspects such as temperature and irradiance, which affect the effectiveness of solar energy [11]. Thus, it is essential to generate current–voltage modeling setups for enhancing and controlling PV arrangements [12]. Generally, single, double, and triple diode models are majorly used for photovoltaic cells [13–15], and are extensively used to specify the current–voltage connections. Parameters of the photovoltaics help to determine the accurateness and dependability of the models. However, due to unbalanced operational cases, such as faults and aging, the models' parameters are not accessible. Therefore, the development of an active methodology to accurately extract these parameters turn out to be critical. The single diode model (SDM) is majorly used in the approximation of these constraints because of ease and acceptance. The double diode model (DDM) is expected to be as accurate as SDM, especially in lower solar irradiance; nevertheless, it desires to exist for a long consuming time [16–20]. To get more accurate and precise parameters from nonlinear implicit equations with high accuracy, evolutionary algorithms [21–31] were proposed. The bio-related algorithms are more accurate and powerful optimization algorithms for simplifying nonlinear transcendental equations, as they do not include complex mathematics. In the proposed work, TSA is implemented for the parameter extraction of the solar cell/module, and the results clearly show the superiority of the TSA over particle swarm optimization (PSO). The reason for this is that PSO has the problem of getting stuck in the local optima solution due to poor exploration capabilities for searching for the optimal solution in the search space, while the searching mechanism of TSA provides a good trade-off between exploration and exploitation capabilities [18]. Hence, TSA provides a more optimal solution as compared with PSO and other existing algorithms.

In this manuscript, we have discussed, initially, the problem formulation followed by a mathematical model for solar PV cell/module, as presented in Section 2. In Section 3, a brief introduction of the TSA algorithm is discussed and is implemented to estimate the optimized value of the unknown parameters of a PV module model. In Section 4, the simulation results of the TSA algorithm are discussed and compared with those of pre-existing metaheuristic algorithms. Section 5 entails the discussion and finally, the manuscript is concluded in Section 6.

2. Problem Statement

In a photovoltaic solar cell, the parallel circuits are formulated using single-diode and double-diode models. In the solar cell, the correlation between the current and voltage is represented using equivalent circuit models.

2.1. Photovoltaic Panel Module Model

The equivalent circuit of PV panel module is shown in Figure 1. The relation between the current and voltage at the output terminal for the PV panel module is expressed as:

$$I_l/N_p = I_p - I_{SD}\left[exp\left(\frac{q\left(V_l/N_s + R_s I_l/N_p\right)}{ak_B T}\right) - 1\right] - \frac{V_l/N_s + R_s I_l/N_p}{R_{sh}} \tag{1}$$

where N_s and N_p represent the number of solar cells connected in series and parallel, respectively. I_l stands for cell current in the output, I_p represents the photogenerated current, I_{SD} stands for the reverse saturation current. V_l, a, R_s, k_B, T and q are the cell output voltage, diode ideality constant, series resistance, Boltzmann constant (1.381×10^{-23} J/K), junction temperature (°K), and electron charge (1.602×10^{-19} C), respectively. It is depicted in Figure 1 that only five parameters (I_p, I_{SD}, a, R_s and R_{sh}) are needed to be estimated for the minimum value of RMSE.
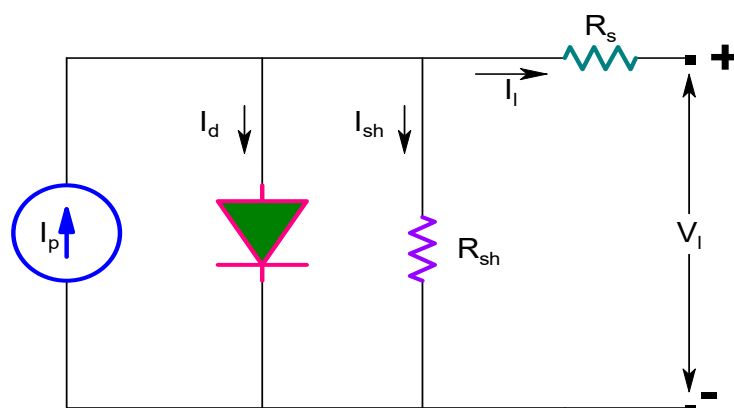

Figure 1. Single diode model of photovoltaic panel module.

2.2. Objective Function

The key deliverables in this work are the optimization of unknown specifications for both SDM and DDM models to reduce the error between the experimental and estimated data. The objective function for error used here is the same as the one that authors have used previously in [23–25]:

$$\text{RMSE} = \sqrt{\frac{1}{k} \sum_{N=1}^{k} f(V_l, I_l,)} \tag{2}$$

where V_l and I_l are the measured voltage and current of the PV module. The parameter k stands for the number of experimental data sets. The best solution found by the TSA is represented by a vector X.

For the PV panel module model,

$$\left(f_{single}(V_l,\ I_l,\ X) = I_p - I_{SD}\left[exp\left(\frac{q\left(\frac{V_l}{N_s} + \frac{R_s I_l}{N_p}\right)}{a_1 k_B T}\right) - 1\right] - \frac{\frac{V_l}{N_s} + \frac{R_s I_l}{N_p}}{R_{sh}} - \frac{I_l}{N_p} \right) \\ \left(X = I_p,\ I_{SD},\ a,\ R_s,\ R_{sh}\right) \tag{3}$$

3. Tunicate Swarm Algorithm

In [6], authors have proposed a new metaheuristic algorithm known as the Tunicate swarm algorithm. These are visible from a few meters' distance and create a pale blue–green bioluminescent light which is intense in nature. These are cylindrically shaped and must open at one end only when they grow to the size of a few millimeters. Each tunic consists of growing a gelatinous tunic which helps to join all individuals. These tunicates are opened at one end only, and they grow up to a few millimeters in size. In every tunicate, a gelatinous tunic grows, which helps all the individuals to join. Each tunicate, through atrial syphons, generates jet propulsion from its opening by receiving water from the adjacent sea. To understand the actions of jet propulsion using the mathematical model, the tunicate should fulfill three conditions: prevent collisions between candidate solutions, step more toward the location of the best solution, and stick close to the best solution. Figure 2 depicts the process flow chart of TSA for parameter extraction.
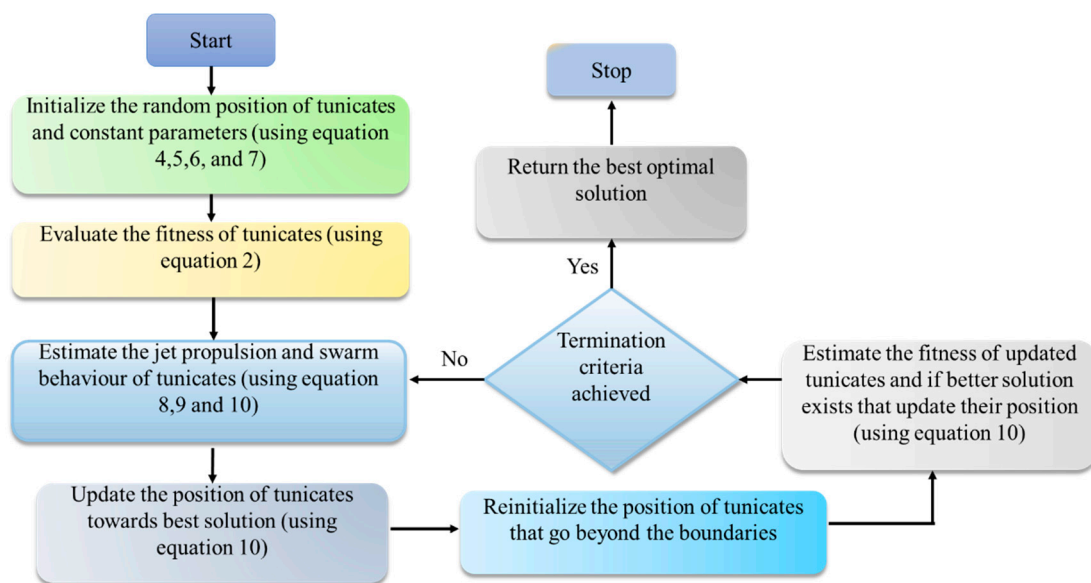
Figure 2. Process flow diagram of the Tunicate swarm algorithm (TSA).

3.1. Prevent Collisions between Candidate Solutions

We initialize the parameters $\vec{A}$ (constant), gravity force ($\vec{G}$), water flow advection in the deep ocean ($\vec{F}$), social force $\vec{M}$ and the maximum number of iterations:

$$\vec{A} = \frac{\vec{G}}{\vec{M}} \tag{4}$$

$$\vec{G} = c_2 + c_3 - \vec{F} \tag{5}$$

$$\vec{F} = 2 \times c_1 \tag{6}$$

$$M = \lfloor P_{min} + c_1 \times P_{max} - P_{min} \rfloor \tag{7}$$

where, c_1, c_2, c_3 are random numbers in the range [0,1], and P_{min} and P_{max} are considered as 1 and 4, respectively.

3.2. Step More toward the Location of the Best Solution

The search agents are moved in the direction of the finest neighbors after successfully preventing a conflict with the neighbors:

$$\vec{PD} = \left| \vec{FS} - rand \times \vec{P}_p(x) \right| \tag{8}$$

where $\vec{PD}$ is the total distance between the search agent and food source, *rand* is the random number in the range [0,1], x indicates the current iteration, $\vec{FS}$ indicates the position of the food source, and $\vec{P}_p(x)$ is the position of the tunicates.

3.3. Stick Close to the Best Solution

The search agent could even establish its position as the leading search agent.

$$\vec{P}_p(x) = \begin{cases} \vec{FS} + \vec{A} \times \vec{PD}, & if\ rand \geq 0.5 \\ \vec{FS} - \vec{A} \times \vec{PD}, & if\ rand\ < 0.5 \end{cases} \tag{9}$$

The position of all the tunicates is updated with respect to the position of the first two tunicates as follows:

$$\vec{P}_p(x+1) = \frac{\vec{P}_p(x) + \vec{P}_p(x+1)}{2 + c_1} \tag{10}$$

where $\vec{P}_p(x+1)$ represents the updated position of the tunicates.

3.4. Implementation of TSA for Parameter Extraction

Step 1. Initialize the population of search agents of the fifth order dimension in the search space. The fifth order dimension represents the photovoltaic current (I_p), series resistance (R_s), shunt resistance (R_{sh}), diode saturation current (I_{SD}), and diode ideality factor (*a*). The range of these parameters are [0–10, 0.001–2, 0–2000, 0–50, 0–100].

Step 2. Regulate the fitness of all agents in the search space using Equation (2).

Step 3. Update the position of the agents at every iteration using TSA. The algorithm is designed to work in the minimization mode; thus, the location of the particles that acquire minimum costs represents the optimized parameters of SDM with minimum RMSE.

4. Results and Discussion

We analyzed the feasibility of the TSA algorithm and evaluated it using mainly one polycrystalline PV module (Photowatt-PWP201) under standard temperature conditions (i.e., 1000 W/m^2 at 30 °C). As a result, the retrieved PV module parameters were monitored and used to create simulated I-V data. The reliability of the WOAPSO is evaluated and compared with six metaheuristics algorithms, i.e., GSA [7], SCA [8], GWO [9], PSO [10], WOA [11], PSOGSA [12], as well as other algorithms existing in the literature. For the experiment, the sample size and the objective function evaluations are set between 30 and 50,000, respectively. Furthermore, a minimum of 30 separate runs are carried out to prevent contingency.

The efficiency of the proposed method is evaluated based on distinct empirical tools such as the internal absolute error (IAE), the Relative Error (RE), the precision of the curve fitting, and the global minimum convergence patterns. The experimental values of current and voltage are taken from [13] by using Photowatt-PWP201 (Photowatt, Bourgoin-Jallieu, France). The Photowatt-PWP201 PV module is composed of 36 polycrystalline cells arranged in a series to generate current-voltage data under standard temperature conditions. The data collection consists of a total of 23 for the PV module. For a reasonable comparison, the search ranges (i.e., upper and lower bound) for each parameter are tabulated in Table 1, which are the same as those being used by investigators in [13–15]. The TSA algorithm is implemented on the MATLAB 2018a (MathWorks, Mexico) platform with Intel ® core ™ i7-HQ CPU, 2.4 GHz, 16 GB RAM laptop.

Table 1. Range of parameters for solar photovoltaic (PV) module.

Parameters	Photowatt-PWP201 PV Module	
	Lower Bound	**Upper Bound**
I_p (A)	0	10
I_{sd} (μA)	0	50
R_s (Ω)	0.001	2
R_{sh} (Ω)	0	2000
a	0	100

4.1. TSA for Parameter Extraction of Photowatt-PWP201 PV Module

This section discusses the evaluation efficiency of the TSA algorithm. Parameters of the Photowatt-PWP201 PV module were estimated under standard temperature conditions by utilizing the SDM model. The optimal values of the five parameters (I_p, I_{sd}, *a*, R_s, R_{sh}) for SDM of the solar PV module are presented in Table 2. The characteristics curves of current-voltage (I-V) and power-voltage (P-V) are redrawn by implementing the TSA algorithm

under optimized parameters. Figure 3 demonstrates the estimated and experimental I-V and P-V characteristics curves. It can be observed that the estimated parameters show good agreement with the measured ones, which proves the efficient performance of the TSA.

Table 2. Comparison of TSA with other parameter estimation methods for Photowatt-PWP201 PV Module.

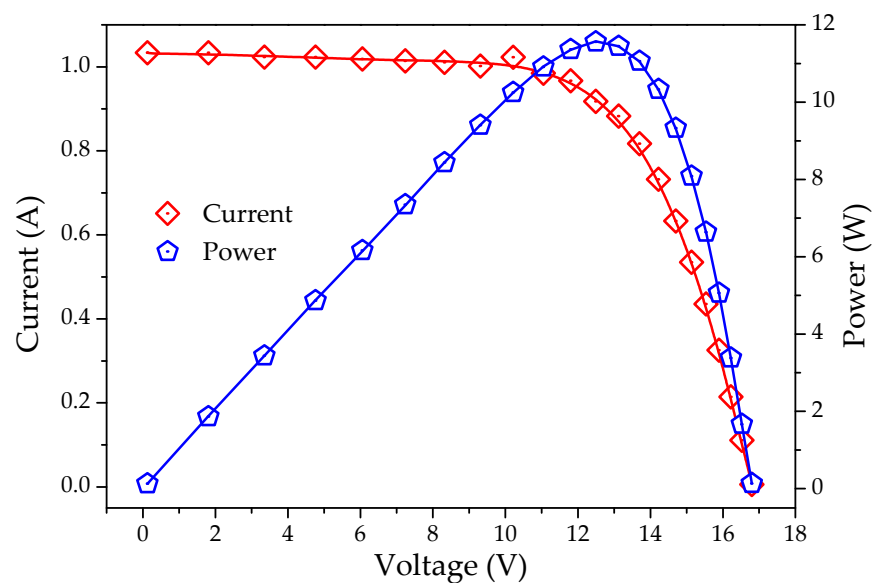| Algorithms	I_{ph} (A)	R_s (Ω)	R_{sh} (Ω)	I_{sd} (μA)	a	RMSE
WOAPSO [18]	1.5032	0.0213	668.27	0.024	1.502	8.86×10^{-4}
GSA	0.0278	2	1201.097	0.050	58.4588	8.80×10^{-3}
PSOGSA	0.0218	0.6430	1100.437	0.01	79.7893	7.156×10^{-3}
SCA	1.0063	0.0496	1107.399	0.039	1.0532	1.28×10^{-2}
WOA	0.0264	0.0113	588.5011	0.0424	1.4496	9.54×10^{-4}
TSA	0.0261	0.0017	2000	0.053	1.4727	5.06×10^{-4}

Figure 3. Current-Voltage (I-V) and Power-Voltage (P-V) characteristics curve for estimated and experimental values for single-diode model of Photowatt-PWP201 PV Module. Symbols represent measured data, and optimized data are represented by solid lines.

Table 3 represents the Internal absolute error (IAE) between the estimated and experimental data sets. Every determined value of IAE (at 1000 W/m^2 and 30 °C) is less than 0.0195, which indicates that the parameters optimized by the TSA are very precise. The error relating to the measurement results for each of the 23 pair points is determined by the IAE and Relative Error (RE). The IAE and RE values are calculated using Equations (11) and (12). The curve of IAE and RE between experimental and estimated values is shown in Figure 4.

$$\text{IAE} = |I_{measured} - I_{simulated}| \tag{11}$$

$$\text{RE} = \frac{(I_{measured} - I_{simulated})}{I_{measured}} \tag{12}$$

Table 3. The calculated current and absolute error results of TSA (Tunicate swarm algorithm) for solar PV (Photovoltaic) module.

| Observations	V_L (V)	I_L (A)	I_{sim} (A)	IAE (A)	$P_{measured}$ (W)	$P_{simulted}$ (W)	IAE (W)
1	0.1246	1.0345	1.0335	0.001	0.1288	0.1256	0.0032
2	0.1248	1.0315	1.0335	0.002	0.1287	0.1226	0.0061
3	1.8093	1.03	1.0335	0.0035	1.8635	1.8765	0.013
4	3.3511	1.026	1.0234	0.0026	3.4382	3.4354	0.0028
5	4.7622	1.022	1.0234	0.0014	4.8669	4.8766	0.0097
6	6.0538	1.018	1.019	0.001	6.1627	6.1456	0.0171
7	7.2364	1.0155	1.0142	0.0013	7.3485	7.3256	0.0229
8	8.3189	1.014	1.011	0.003	8.4353	8.4453	0.01
9	9.3097	1.01	1.002	0.008	9.4027	9.4124	0.0097
10	10.2163	1.0035	1.023	0.0195	10.252	10.245	0.007
11	11.0449	0.988	0.985	0.003	10.9123	10.9234	0.0111
12	11.8018	0.963	0.967	0.004	11.3651	11.3554	0.0097
13	12.4929	0.9255	0.918	0.0075	11.5621	11.5722	0.0101
14	13.1231	0.8725	0.883	0.0105	11.4499	11.445	0.0049
15	13.6983	0.8075	0.8173	0.0098	11.0613	11.0521	0.0092
16	14.2221	0.7265	0.7324	0.0059	10.3323	10.321	0.0113
17	14.6995	0.6345	0.633	0.0015	9.3268	9.313	0.0138
18	15.1346	0.5345	0.535	0.0005	8.0894	8.0754	0.014
19	15.5311	0.4275	0.4356	0.0081	6.6395	6.6367	0.0028
20	15.8929	0.3185	0.3256	0.0071	5.0618	5.0524	0.0094
21	16.2229	0.2085	0.2145	0.006	3.3824	3.3724	0.01
22	16.5241	0.101	0.111	0.01	1.6689	1.6564	0.0125
23	16.7987	0.008	0.006	0.002	0.1343	0.1347	0.0004
Sum of IAE				0.0594			0.0927
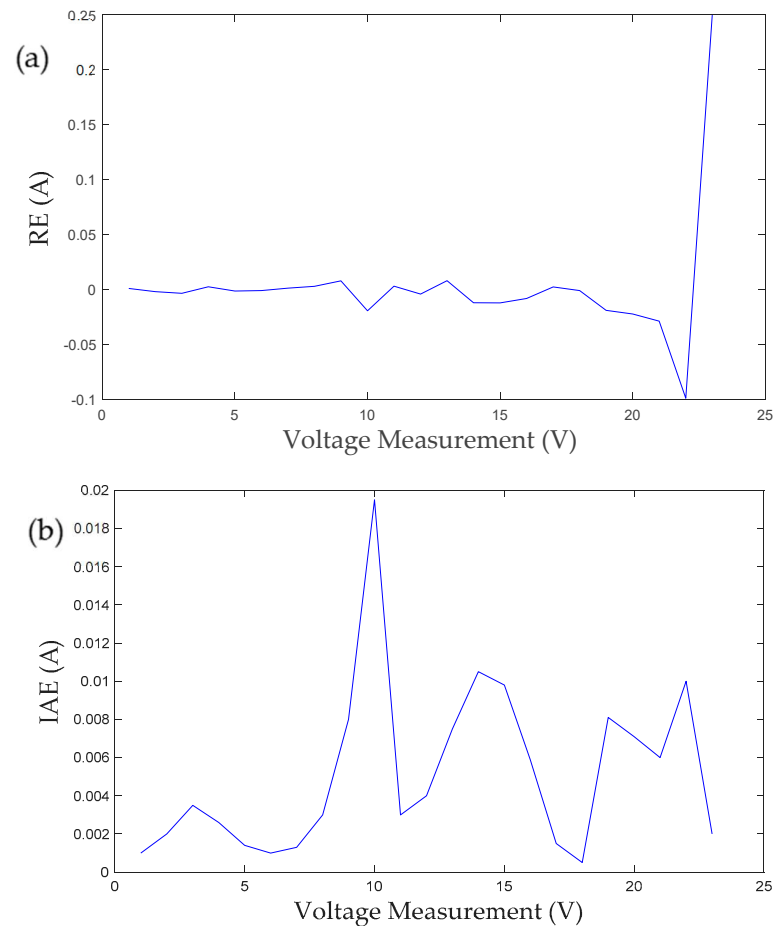
Figure 4. (**a**) Internal absolute error and (**b**) relative error curve between measured and estimated current for Photowatt-PWP201 PV Module.

4.2. Convergence Analysis

The convergence analysis was performed to examine the computational competence of the TSA. The convergence curves of the solar PV module are presented in Figure 5. It is depicted in Figure 5 that the TSA algorithm outperforms the GSA, PSOGSA, SCA, and WOA algorithms in terms of convergence speed and generates a precise solution for the identical number of function evaluations (i.e., 50,000).
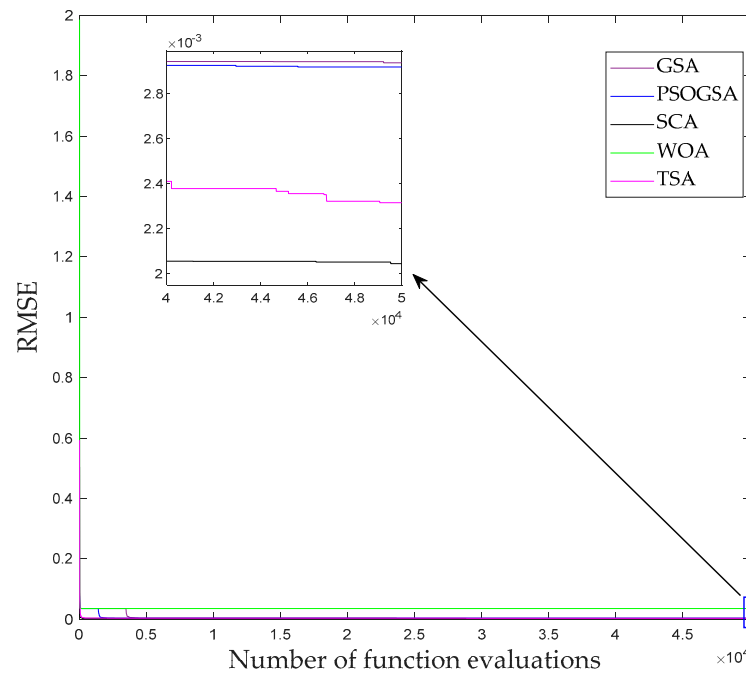

Figure 5. Convergence curve of TSA (Tunicate swarm algorithm) and the other four algorithms for single-diode model of Photowatt-PWP201 PV (Photovoltaic) Module.

4.3. Robustness and Statistics Analysis

This section presents the statistical evaluation based on mean, minimum, maximum, and standard deviation of the RMSE for all previously implemented methods and comparison concerning precision and consistency of the distinct algorithms in a total of thirty runs, as depicted in Table 4. The mean of the RMSE is calculated to evaluate the precision of the algorithms, and the standard deviation is calculated to evaluate the consistency of the parameter estimation methods.

Table 4. Statistical results of the root mean square error (RMSE) of different algorithms for Photowatt-PWP201 PV Modules.

Photowatt-PWP201 Module Model	Algorithm	RMSE			
		Min	**Mean**	**Max**	**SD**
	GSA	8.80×10^{-3}	2.65×10^{-1}	2.08×10^{-1}	5.85×10^{-3}
	PSOGSA	7.156×10^{-3}	6.47×10^{3}	2.83×10^{-1}	1.81×10^{-2}
	SCA	1.28×10^{-2}	2.26×10^{1}	6.35×10^{-1}	1.78×10^{-2}
	WOA	9.54×10^{-4}	2.35×10^{2}	2.63×10^{-1}	2.83×10^{-2}
	TSA	5.06×10^{-4}	1.45×10^{3}	2.34×10^{-2}	1.25×10^{-3}

In Table 4, it is depicted that the proposed TSA algorithm significantly outperforms the GSA, PSOGSA, SCA, and WOA algorithms for the solar PV module model. The statistical results presented in Table 4 indicate that TSA is the most accurate and reliable parameter optimization technique.

5. Discussion

The TSA algorithm is successfully developed and implemented for parameter extraction of the polycrystalline Photowatt-PWP201 PV module. The I-V and P-V curves obtained by the optimization process show excellent accord with the measured data. The IAE values (both current and power) validate the exactness of the optimized parameters. The statistical evaluation confirms that the standard deviation is very small, which confirms that the TSA is an accurate and useful parameter estimation technique. The average execution time of every algorithm on the Photowatt-PWP201 PV module is established and introduced in Figure 6. Compared to GSA, PSOGSA, SCA, and WOA, TSA requires a much lower time of about 11 s, while PSOGSA has the worst execution time of about 40 s. The Friedman ranking test results are shown in Figure 7. The best ranking is obtained by the TSA, followed by SCA, WOA, GSA, and PSOGSA.
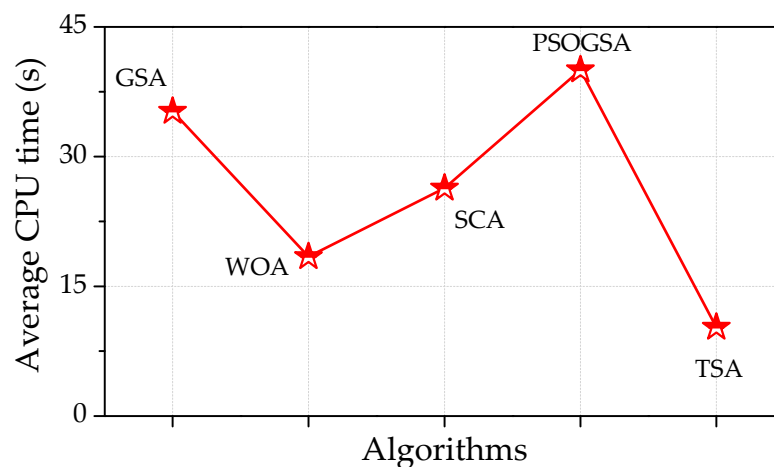

Figure 6. Comparison of the execution time of different metaheuristic algorithms.
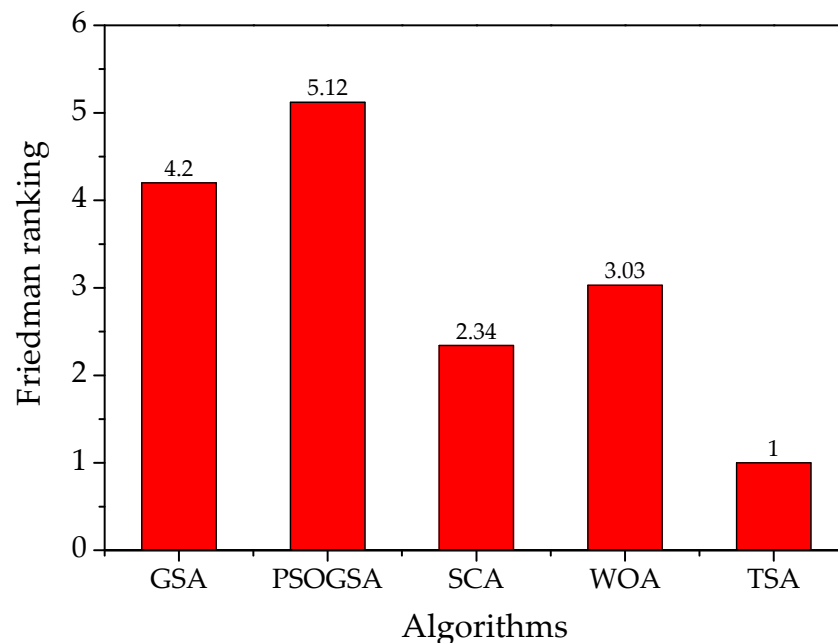

Figure 7. Ranking of TSA (Tunicate swarm algorithm) and other compared algorithms on Photowatt-PWP201 PV panel module according to the Friedman test.

6. Conclusions

In this research investigation, TSA was employed to estimate the Photowatt-PWP201 PV panel module parameters under standard temperature conditions. It should be noted

the TSA technique is, for the first time, intended to reliably track the estimation of parameters for photovoltaic models. The observations based on the experimental findings are defined as follows:

- TSA is relatively accurate and reliable at delivering the solution in terms of the RMSE compared with other algorithms such as GSA, PSOGSA, SCA, and WOA.
- The I-V and P-V characteristic curves and IAE results indicate that TSA can generate the optimized value of the estimated parameters for all the solar PV cell models compared with other algorithms.
- The statistical analysis depicts the robustness of the TSA technique in parameter estimation problems under standard operating conditions.
- The convergence curves demonstrate that the TSA obtains the best estimated parameters in terms of RMSE (5.06×10^{-4}).
- From the above discussion, it can be concluded that the TSA is an effective and robust technique to estimate the unknown optimized parameters of the solar PV module model under standard operating conditions.

Author Contributions: Conceptualization: A.S. (Abhishek Sharma), and A.S. (Abhinav Sharma); methodology and formal analysis: A.S. (Abhishek Sharma) and V.J.; investigation, A.S. (Abhinav Sharma) and S.K.T.; writing—original draft preparation, A.S. (Abhishek Sharma) and A.D.; writing—review and editing, A.S. (Abhinav Sharma), A.D. and S.K.T.; supervision, V.J. and B.A.; fund acquisition: B.A. All authors have read and agreed to the published version of the manuscript.

Data Availability Statement: The data presented in this study are available on request from the corresponding author.

Conflicts of Interest: The authors declare no conflict of interest.

Abbreviations and Symbols

The following abbreviations and nomenclature are used in this manuscript:

I_p	Photo Diode Current
I_{sd}	Reverse Saturation Current
R_s	Series Resistance
R_{sh}	Shunt Resistance
A	Diode Ideality Factor
RMSE	Root Mean Square Error
PV	Photovoltaic
I-V	Current-Voltage
P-V	Power-Voltage
MPPT	Maximum Power Point Tracking
V_{oc}	Open Circuit Voltage
I_{mpp}	Maximum Power Point Current
I_{sc}	Short Circuit Current
PSO	Particle Swarm Optimization
WOA	Whale Optimization Algorithm
SDM	Single diode Model
DDM	Double diode Model
IAE	Internal Absolute Error
RE	Relative Error
GSA	Gravitational Search Algorithm
SCA	Sine Cosine Algorithm
PSOGSA	Particle Swarm Optimization Gravitational Search Algorithm

References

1. Coello, C.; Lamont, G.; van Veldhuizen, D. *Evolutionary Algorithms for Solving Multi-Objective Problems*; Springer: New York, NY, USA, 2007.
2. Khanna, V.; Das, B.K. A Method to Model the Maximum Power Output of Photovoltaic Modules Using Statistical Analysis and Matlab-Simulink Simulation; A Method to Model the Maximum Power Output of Photovoltaic Modules Using Statistical Analysis and Matlab-Simulink Simulation. 2018. Available online: http://www.academia.edu/download/59389096/a-method-to-model-the-maximum-power-output-of-simulation-IJERTV7IS05022020190525-102639-p9gz0d.pdf (accessed on 7 October 2020).
3. Chen, X.; Yu, K.; Du, W.; Zhao, W.; Liu, G. Parameters identification of solar cell models using generalized oppositional teaching learning based optimization. *Energy* **2016**, *99*, 170–180. [CrossRef]
4. KYu, K.; Liang, J.; Qu, B.; Chen, X.; Wang, H. Parameters identification of photovoltaic models using an improved JAYA optimization algorithm. *Energy Convers. Manag.* **2017**, *150*, 742–753. [CrossRef]
5. Merchaoui, M.; Sakly, A.; Mimouni, M.F. Particle swarm optimisation with adaptive mutation strategy for photovoltaic solar cell/module parameter extraction. *Energy Convers. Manag.* **2018**, *175*, 151–163. [CrossRef]
6. Kaur, S.; Awasthi, L.K.; Sangal, A.; Dhiman, G. Tunicate Swarm Algorithm: A new bio-inspired based metaheuristic paradigm for global optimization. *Eng. Appl. Artif. Intell.* **2020**, *90*. [CrossRef]
7. Rashedi, E.; Nezamabadi-Pour, H.; Saryazdi, S. GSA: A Gravitational Search Algorithm. *Inf. Sci.* **2009**, *179*, 2232–2248. [CrossRef]
8. Mirjalili, S. SCA: A Sine Cosine Algorithm for solving optimization problems. *Knowl.-Based Syst.* **2016**, *96*, 120–133. [CrossRef]
9. Mirjalili, S.; Mirjalili, S.M.; Lewis, A. Grey Wolf Optimizer. *Adv. Eng. Softw.* **2014**, *69*, 46–61. [CrossRef]
10. Kennedy, C. Review of Mid-to High-Temperature Solar Selective Absorber Materials. 2002. Available online: https://www.osti.gov/biblio/15000706 (accessed on 6 September 2020).
11. Mirjalili, S.; Lewis, A. The Whale Optimization Algorithm. *Adv. Eng. Softw.* **2016**, *95*, 51–67. [CrossRef]
12. Mirjalili, S. Hybrid Particle Swarm Optimization and Gravitational Search Algorithm for Multilayer Perceptron Learning. Ph.D. Thesis, Universiti Teknologi Malaysia, Skudai, Malaysia, 2011.
13. AlHajri, M.; El-Naggar, K.; AlRashidi, M.; Al-Othman, A. Optimal extraction of solar cell parameters using pattern search. *Renew. Energy* **2012**, *44*, 238–245. [CrossRef]
14. Gong, X.; Kulkarni, M. Design optimization of a large scale rooftop photovoltaic system. *Sol. Energy* **2005**, *78*, 362–374. [CrossRef]
15. Chellaswamy, C.; Ramesh, R. Parameter extraction of solar cell models based on adaptive differential evolution algorithm. *Renew. Energy* **2016**, *97*, 823–837. [CrossRef]
16. Bayoumi, A.; El-Sehiemy, R.; Mahmoud, K.; Lehtonen, M.; Darwish, M.M.F. Assessment of an Improved Three-Diode against Modified Two-Diode Patterns of MCS Solar Cells Associated with Soft Parameter Estimation Paradigms. *Appl. Sci.* **2021**, *11*, 1055. [CrossRef]
17. Mughal, M.A.; Ma, Q.; Xiao, C. Photovoltaic Cell Parameter Estimation Using Hybrid Particle Swarm Optimization and Simulated Annealing. *Energies* **2017**, *10*, 1213. [CrossRef]
18. Sharma, A.; Sharma, A.; Averbukh, M.; Jately, V.; Azzopardi, B. An Effective Method for Parameter Estimation of a Solar Cell. *Electronics* **2021**, *10*, 312. [CrossRef]
19. Elazab, O.S.; Hasanien, H.M.; Alsaidan, I.; Abdelaziz, A.Y.; Muyeen, S.M. Parameter Estimation of Three Diode Photovoltaic Model Using Grasshopper Optimization Algorithm. *Energies* **2020**, *13*, 497. [CrossRef]
20. Oliva, D.; Ewees, A.A.; Aziz, M.A.E.; Hassanien, A.E.; Peréz-Cisneros, M. A Chaotic Improved Artificial Bee Colony for Parameter Estimation of Photovoltaic Cells. *Energies* **2017**, *10*, 865. [CrossRef]
21. Stornelli, V.; Muttillo, M.; de Rubeis, T.; Nardi, I. A New Simplified Five-Parameter Estimation Method for Single-Diode Model of Photovoltaic Panels. *Energies* **2019**, *12*, 4271. [CrossRef]
22. Al-Taani, H.; Arabasi, S. Solar Irradiance Measurements Using Smart Devices: A Cost-Effective Technique for Estimation of Solar Irradiance for Sustainable Energy Systems. *Sustainability* **2018**, *10*, 508. [CrossRef]
23. Park, C.-Y.; Hong, S.-H.; Lim, S.-C.; Song, B.-S.; Park, S.-W.; Huh, J.-H.; Kim, J.-C. Inverter Efficiency Analysis Model Based on Solar Power Estimation Using Solar Radiation. *Processes* **2020**, *8*, 1225. [CrossRef]
24. Bocca, A.; Bergamasco, L.; Fasano, M.; Bottaccioli, L.; Chiavazzo, E.; Macii, A.; Asinari, P. Multiple-Regression Method for Fast Estimation of Solar Irradiation and Photovoltaic Energy Potentials over Europe and Africa. *Energies* **2018**, *11*, 3477. [CrossRef]
25. Kiani, A.T.; Nadeem, M.F.; Ahmed, A.; Khan, I.; Elavarasan, R.M.; Das, N. Optimal PV Parameter Estimation via Double Exponential Function-Based Dynamic Inertia Weight Particle Swarm Optimization. *Energies* **2020**, *13*, 4037. [CrossRef]
26. Ramadan, A.; Kamel, S.; Korashy, A.; Yu, J. Photovoltaic cells parameter estimation using an enhanced teaching–learning-based optimization algorithm. *Iran. J. Sci. Technol. Trans. Electr. Eng.* **2020**, *44*, 767–779. [CrossRef]
27. Kiani, A.T.; Nadeem, M.F.; Ahmed, A.; Sajjad, I.A.; Raza, A.; Khan, I.A. Chaotic inertia weight particle swarm optimization (CIWPSO): An efficient technique for solar cell parameter estimation. In Proceedings of the 2020 3rd International Conference on Computing, Mathematics and Engineering Technologies (iCoMET), Sindh, Pakistan, 29–30 January 2020; pp. 1–6.
28. Halko, S.; Halko, . Research of electrical and physical characteristics of the solar panel on the basis of cogeneration photoelectric modules. *a aΛ'ΟΟΣ* **2020**, *2*, 39–44. [CrossRef]
29. El-Hameed, M.A.; Elkholy, M.M.; El-Fergany, A.A. Three-diode model for characterization of industrial solar generating units using Manta-rays foraging optimizer: Analysis and validations. *Energy Convers. Manag.* **2020**, *219*, 113048. [CrossRef]

30. Abdulrazzaq, A.K.; Bognár, G.; Plesz, B. Evaluation of different methods for solar cells/modules parameters extraction. *Sol. Energy* **2020**, *196*, 183–195. [CrossRef]
31. Babich, V.; Lobel, R.; Şafak, Y. Promoting Solar Panel Investments: Feed-in-Tariff vs. Tax-Rebate Policies. *Manuf. Serv. Oper. Manag.* **2020**, *22*, 1148–1164. [CrossRef]

Article

Parameter Extraction of Solar Module Using the Sooty Tern Optimization Algorithm

Abha Singh [1], Abhishek Sharma [2,3], Shailendra Rajput [2], Amit Kumar Mondal [4], Amarnath Bose [5,*] and Mangey Ram [6]

[1] Department of Basic Science, College of Science and Theoretical Study, Saudi Electronic University, Dammam-Female Branch, Dammam 32242, Saudi Arabia; asingh@seu.edu.sa

[2] Department of Electrical and Electronic Engineering, Ariel University, Ariel 40700, Israel; abhishek_sharma@ddn.upes.ac.in (A.S.); shailendrara@ariel.ac.il (S.R.)

[3] Department of Research & Development, University of Petroleum and Energy Studies, Dehradun 248007, India

[4] Department of Mechatronics Engineering, School of Engineering & Information Technology, Manipal Academy of Higher Education, Dubai 345050, United Arab Emirates; amit.mondal@manipaldubai.com

[5] Sustainability Cluster, School of Engineering (SOE), University of Petroleum & Energy Studies, Dehradun 248007, India

[6] Department of Mathematics, Computer Science and Engineering, Graphic Era (Deemed to be University), Dehradun 248002, India; drmrswami@geu.ac.in

* Correspondence: abose@ddn.upes.ac.in

Abstract: Photovoltaic module parameter estimation is a critical step in observing, analyzing, and optimizing the efficiency of solar power systems. To find the best value for unknown parameters, an efficient optimization strategy is required. This paper presents the implementation of the sooty tern optimization (STO) algorithm for parameter assessment of a solar cell/module. The simulation findings were compared to four pre-existing optimization algorithms: sine cosine (SCA) algorithm, gravitational search algorithm (GSA), hybrid particle swarm optimization and gravitational search algorithm (PSOGSA), and whale optimization (WOA). The convergence rate and root mean square error evaluations show that the STO method surpasses the other studied optimization techniques. Additionally, the statistical results show that the STO method is superior in average resilience and accuracy. The superior performance and reliability of the STO method are further validated by the Friedman ranking test.

1. Introduction

Recently, clean energy usage has increased significantly as demand for all other fuels declined because of environmental concerns. As a result,, the scientific community made substantial efforts to harvest energy from different ambient sources [1–5]. Solar energy harvesting has become the most ideal option since it surpasses all traditional nonrenewable and renewable resources [6]. As a result, the worldwide solar electricity sector is expanding significantly, with a current value of more than $10 billion each year [6–8].

Solar energy is converted into electrical energy by employing photovoltaic (PV) panels [9]. Numerous PV panels are linked together in serial and/or parallel arrangements to create bulky solar energy plants equipped with maximum power point tracking (MPPT) systems to increase power generation. The primary goal of MPPT systems is to regulate the parameters of the PV system to generate optimum power [9]. The rapid deviation of electrical energy production is a well-known property of solar plants [9]. Many solar facilities are linked to local grids, and their operation at the same time as the grids causes voltage instability in distribution lines [10]. Hence, stable and maximized power generation from

solar plants is an essential requirement of the green energy movement. To obtain maximum power density, both theoretical and experimental studies were performed to optimize the parameters of PV panels [4,11–13]. Single, double, and triple diode models of PV cells are widely employed to identify the current-voltage parameters [14–16]. These parameters are helpful for determining the accuracy and steadiness of the models. However, parameter assessment is not an easy task because of unbalanced operational cases such as faults and ageing. In most cases, the single diode model is employed because of ease and acceptance. On the other hand, the double diode model is anticipated to be more than the three-diode model accurate in case of lower solar irradiance.

Different types of algorithms were proposed and studied to get more accurate and precise parameters from nonlinear implicit equations with high accuracy [17–33]. The merits and demerits of these algorithms are categorized because of the trade-off between exploration and exploitation capabilities [17]. Some became caught in local optima solutions because of a lack of exploration capabilities for finding an optimal solution in the search space. Heuristic and deterministic are the two main groups of algorithms. Heuristic algorithms contain particle swarm optimization (PSO) [18], cuckoo search algorithm [19], harmony search [20], cat swarm optimization (CSO) [21], differential evolution (DE) [22], artificial bee colony [23], chaos CPSO [24], simulated annealing [25], biogeography-based optimization algorithm with mutation strategies [26], genetic algorithms [27], improved adaptive differential evolution [28], pattern search [29], generalized opposition-based teaching-learning-based optimization [30], and Nelder–Mead modified PSO [31]. The Lambert W-functions [32], least squares [33], iterative curve-fitting methods [34], conductivity method [35], Levenberg–Marquardt algorithm [36], Newton–Raphson, and nonlinear least square are categorized as deterministic algorithms. The applicability of deterministic algorithms is restricted because of continuity, differentiability, and convexity related to objective functions. These algorithms are likewise sensitive to the starting solution and settle at local optima in most cases. Because they do not include difficult mathematics, biorelated algorithms are more realistic and robust optimization methods for simplifying complex transcendental equations.

The sooty tern optimization (STO) algorithm mimics the attack and migration behavior of sooty terns (birds of tropical oceans). This algorithm provides a good balance between exploration and exploitation strategy and thus reaches optimal solution without getting trapped in a local solution. These benefits allow researchers to apply the STO for parameter extraction of a solar module. The key purposes of this research investigation are as follows:

- To first present the experimental results that verify the performance of the STO in handling the parameter extraction problem of the solar module.
- To use two test cases—R.T.C France solar cell and SS2018P polycrystalline PV module—to evaluate the effectiveness of the STO and compare it with other metaheuristic algorithms.
- To use the experimental results to comprehensively confirm that STO is competitive compared to other existing methods in literature.

This study utilizes the STO algorithm for the parameter assessment of PV cells/modules. Initially, the mathematical model for PV cell/module and problem formulation is discussed. At the second stage, the STO algorithm is briefly introduced and used to assess the optimal magnitude of undetermined parameters. Next, the output results are examined with a measured dataset, and the algorithm is compared to pre-existing metaheuristic algorithms. Section 5 contains the discussion and conclusion of manuscript.

2. Problem Formulation and Methodology

2.1. Mathematical Modeling of Solar Panels

Figure 1 depicts the PV panel's comparable circuit model. At the output terminal, the correlation between voltage (V_l) and current (I_l) is expressed as:

$$I_l = I_p - I_{sd} \left[exp \left(\frac{q \left(V_l/N_s + R_s I_l/N_p \right)}{a\, k_B T} \right) - 1 \right] - \frac{V_l/N_s + R_s I_l/N_p}{R_{sh}} \tag{1}$$

where N_p and N_s denote the count of solar cells interconnected in parallel and series combinations. The k_B is the Boltzmann constant (1.3806×10^{-23} m^{2}kgK^{-1}s^{-2}), T is the cell/module temperature, q is elementary charge, I_p is photovoltaic current, I_{sd} is diode saturation current, R_s series resistance, R_{sh} shunt resistance, and a is the module quality factor. Only five parameters (I_p, I_{sd}, a, R_s, R_{sh}) are required to calculate the minimum value of root mean square error (RMSE).
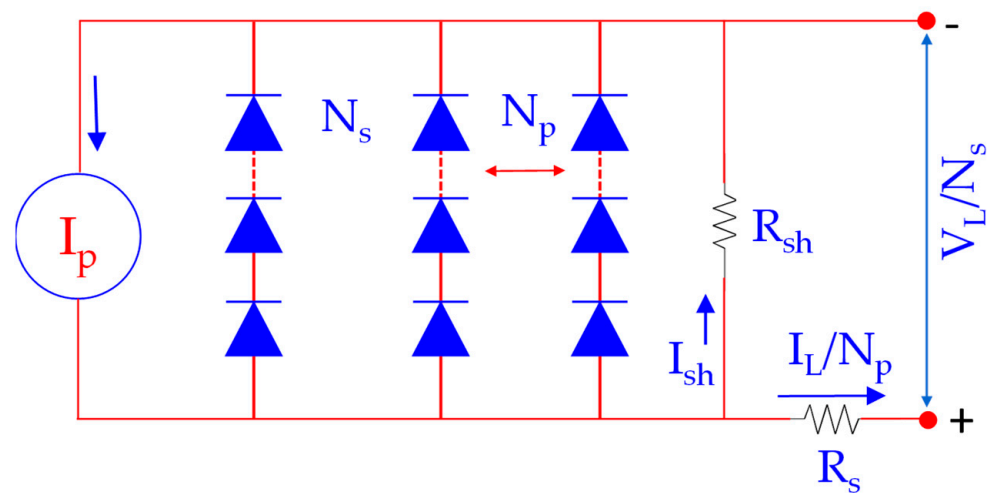

Figure 1. PV panel module equivalent circuit.

2.2. Objective Function

The main objective of the presented study is to lessen the variance among experimental and estimated data by optimizing unknown parameters for the single-diode model. Unknown parameters (I_p, I_{sd}, a, R_s, R_{sh}) are employed as decision variables during the optimization process. The accumulative squared variation between calculated and observed data is applied as an objective function. The error objective function is denoted as follows [37,38]:

$$\text{RMSE} = \sqrt{\frac{1}{k} \sum_{N=1}^{k} f(V_l, I_l, X)^2} \tag{2}$$

where V_l and I_l denote the observed value of voltage and current of the PV module. The range of experimental datasets is specified by the parameter 'k' and the algorithm's best answer is indicated by a vector X. In the case of the PV panel module:

$$\left(\begin{array}{c} f_{single}(V_l,\, I_l,\, X) = I_p - I_{sd} \left[exp \left(\frac{q \left(\frac{V_l}{N_s} + \frac{R_s I_l}{N_p} \right)}{a_1 k_B T} \right) - 1 \right] - \frac{\frac{V_l}{N_s} + \frac{R_s I_l}{N_p}}{R_{sh}} - \frac{I_l}{N_p} \\ \left(X = I_p,\, I_{sd},\, a,\, R_s,\, R_{sh} \right) \end{array} \right) \tag{3}$$

3. Sooty Tern Optimization

The sooty tern optimization (STO) algorithm was proposed in 2019 [39,40]. The algorithm is inspired by the attacking behavior of sooty tern birds. Generally, sooty terns live in groups. They employ their intelligence to locate and attack a target. The most

notable characteristics of sooty terns are their migrating and assaulting behaviors. The following provide insights into sooty tern birds:

- Sooty terns travel in groups during migration. To avoid collisions, the initial positions of sooty terns are different.
- In a group, sooty terns with low fitness levels can nevertheless travel the same distance that the fittest among them can.
- Sooty terns with low fitness can upgrade their preliminary locations on the basis of the fittest sooty tern.

3.1. Migration Behavior

A sooty tern must meet three requirements during a migration:

Collision avoidance: SA is used to compute a new search agent location to avoid collisions with its neighborhood search agents (i.e., sooty terns).

$$\vec{C}_{st} = s_A \cdot \vec{P}_{st}(z) \tag{4}$$

where $\vec{C}_{st}$ denotes the position of a sooty tern that does not collide with other terns. $\vec{P}_{st}$ represents the current location of the sooty tern. z signifies the current iteration, and s_A denotes the migration of a sooty tern in the solution space.

Converge in the direction of best neighbor: Following collision evasion, the search agents converge in the path of the finest neighbor.

$$\vec{M}_{st} = C_B \cdot \vec{P}_{st}(z)\left(\vec{P}_{bst}(z) - \vec{P}_{st}(z)\right) \tag{5}$$

where $\vec{M}_{st}$ denotes a different position of a search agent (i.e., sooty tern). $\vec{P}_{bst}(z)$ shows the best location of a search agent, and C_B signifies the random variable and can be computed as follows:

$$C_B = 0.5\, R_{and} \tag{6}$$

where R_{and} represents any arbitrary number in the range of 0 and 1.

Updating corresponding to best search agent: Finally, the sooty tern can revise its location in relation to the best search agent.

$$\vec{D}_{st} = \vec{C}_{st} + \vec{M}_{st} \tag{7}$$

where $\vec{D}_{st}$ signifies the difference between the search agent and the best fittest search agent.

3.2. Attacking Behavior

Sooty terns can modify their speed and attack angle during migration. They gain altitude by flapping their wings. They produce spherical behavior in the air while attacking prey, which is explained below.

$$x\prime = R_{adius}\sin(i) \tag{8}$$

$$y\prime = R_{adius}\cos(i) \tag{9}$$

$$z\prime = R_{adius}i \tag{10}$$

$$r = ue^{kv} \tag{11}$$

where, R_{adius} denotes the radius of each spiral turn, i signifies the value in the range of $[0 \leq k \leq 2\pi]$, and the u and v are the constant values.

3.3. Execution Steps of STO for Parameter Estimation

Figure 2 illustrates the flowchart of the STO algorithm for optimized parameter estimation of a solar cell/module. The algorithm works as follows:

- **Step 1.** In the search space, begin the population of search agents of the fifth order dimension. The photovoltaic current (I_p), diode saturation current (I_{sd}), series resistance (R_s), shunt resistance (R_{sh}), and diode ideality factor are all represented by the fifth order dimension (*a*).
- **Step 2**. In the search space, control the fitness of all agents using Equation (2).
- **Step 3**. At each iteration, the STO is employed to adjust the position of the agents. Because the algorithm is intended to function in the minimization mode, the location of the particles with the least cost suggests the best SDM parameters with the minimum RMSE.
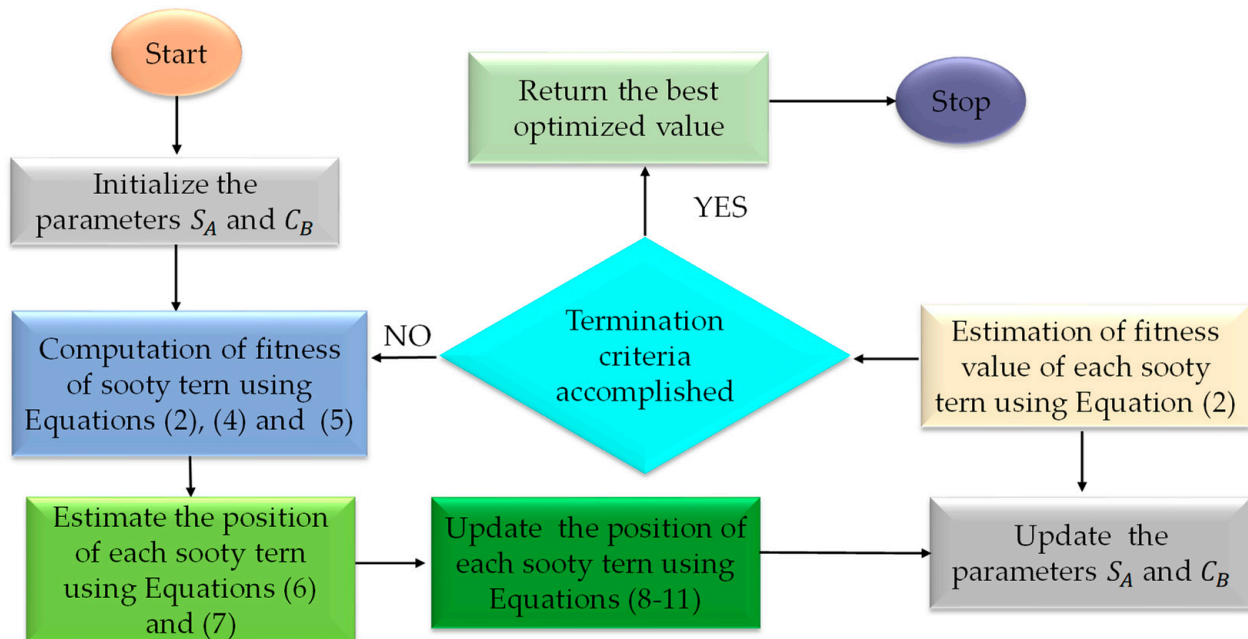

Figure 2. Process flowchart of STO algorithm for parameter estimation of PV cell/module.

4. Results and Discussion

In this section, we examine the validity of the STO algorithm and describe how we tested it under standard temperature conditions (1000 W/m^2 at 25 °C) utilizing primarily one R.T.C France solar cell and polycrystalline PV module (SS2018P). The extracted PV module characteristics were tracked and employed to generate simulated I-V and P-V data sets. The dependability of the STO algorithm was examined and compared to four metaheuristic algorithms: GSA [41], SCA [42], GWO [43], and WOA [44]. The size of the sample and the objective function evaluations for the experiment were fixed to 30 and 50,000, respectively. In addition, at least 30 independent runs were performed to avoid duplication.

The effectiveness of the proposed method was evaluated using several empirical constraints, e.g., internal absolute error (IAE), correctness of the curve-fitting, and global minimum convergence rates. The current and voltage data for the R.T.C France solar cell [45] and the SS2018P polycrystalline PV module [38] were collected experimentally. In the SS2018P PV module, 36 polycrystalline cells were connected serially [38]. Table 1 tabulates the exploration ranges for every parameter (i.e., upper and lower bounds). These ranges were utilized by investigators in this study. The STO algorithm [46] was simulated on a MATLAB 2018a (MathWorks, Mexico, DF, Mexico) platform with an Intel $^®$ core TM i5-HQ CPU running at turbo frequency of 4.8 GHz and 8 GB of RAM.

Table 1. The parameter range for SDM of a solar cell and a PV module.

Parameters	R.T.C France Solar Cell		SS2018P PV Module	
	Lower Bound	**Upper Bound**	**Lower Bound**	**Upper Bound**
I_p(A)	0	1	0	10
R_s(Ω)	0.01	0.5	0.01	2
R_{sh}(Ω)	0.001	100	0.001	2000
I_{sd}(μA)	0	0.5	0	50
a	1	2	1	100

4.1. Parameter Extraction of the R.T.C France Solar Cell

For a single-diode model, five parameters (I_p, I_{sd}, a, R_s, R_{sh}) must be estimated. The values of simulated current and power with their IAE are charted in Table 2. Table 3 shows the values of the STO-optimized parameters and RMSE for comparison. The STO algorithm has the lowest RMSE of 8.6106×10^{-4} when compared to other algorithms. In this case, RMSE values are obtained as an index for evaluating results with previously constructed techniques by the researchers. Figure 3 depicts a redrawn current-voltage (I-V) and power-voltage (P-V) characteristics curve for a single-diode model based on the optimum optimized parameters achieved by executing the STO method. The computed data generated by the STO was found to be very close to the experimental data set across the whole voltage range.

Table 2. The calculated current and absolute error results of the STO for SDM of the R.T.C France solar cell.

Observations	V_l(V)	I_l (A)	$I_{\text{simulated}}$ (A)	IAE (A)	P_{measured} (W)	$P_{\text{simulated}}$ (W)	IAE (W)
1	0.0057	0.7605	0.7817	0.0212	0.0043	0.0044	0.0001
2	0.0646	0.7600	0.7764	0.0164	0.0490	0.0501	0.0010
3	0.1185	0.7590	0.7714	0.0124	0.0899	0.0914	0.0014
4	0.1678	0.7570	0.7669	0.0099	0.1270	0.1287	0.0016
5	0.2132	0.7570	0.7627	0.0057	0.1613	0.1626	0.0012
6	0.2545	0.7555	0.7588	0.0033	0.1922	0.1931	0.0008
7	0.2924	0.7540	0.754	0.0007	0.2204	0.2206	0.0002
8	0.3269	0.7505	0.7501	0.0003	0.2453	0.245	0.0001
9	0.3585	0.7465	0.7441	0.0023	0.2676	0.2667	0.0008
10	0.3873	0.7385	0.7351	0.0033	0.2860	0.2847	0.0012
11	0.4137	0.7280	0.7208	0.0071	0.3011	0.2982	0.0029
12	0.4373	0.7065	0.6987	0.0077	0.3089	0.3055	0.0034
13	0.459	0.6755	0.6648	0.0106	0.3100	0.3051	0.0049
14	0.4784	0.6320	0.6173	0.0146	0.3023	0.2953	0.0070
15	0.496	0.5730	0.5544	0.0185	0.2842	0.2750	0.0091
16	0.5119	0.4990	0.4772	0.0217	0.2554	0.2443	0.0111
17	0.5265	0.4130	0.3857	0.0272	0.2174	0.2030	0.0143
18	0.5398	0.3165	0.2945	0.0219	0.1708	0.1590	0.0118
19	0.5521	0.2120	0.1728	0.0391	0.1170	0.0954	0.0215
20	0.5633	0.1035	0.0582	0.0452	0.0583	0.0328	0.0254
	Sum of IAE			**0.2891**			

4.2. Parameter Extraction of the SS2018P PV Module

To properly assess the efficacy of the STO algorithm, parameters for the SS2018P PV module were computed at 1000 W/m^2 and 25 °C, using the SDM model. The values of simulated current and power with their IAE are tabulated in Table 4. Table 5 shows the optimized value of all five parameters (I_p, I_{sd}, a, R_s, R_{sh}) for SDM of the PV module at standard temperature condition. Figure 4 depicts a redrawn I-V and P-V characteristics curve for a single-diode model based on the optimum optimized parameters achieved by

executing the STO method. It was observed that the simulated data provided by the STO was extremely closely related to the experimental data set.

Table 3. Comparison between the STO and other algorithms for parameter estimation techniques for R.T.C France solar cell.

Algorithms	I_p(A)	R_s(Ω)	R_{sh}(Ω)	I_{sd}(μA)	a	RMSE
STO	0.7850	0.0394	10.9985	0.1770	1.4474	8.6106×10^{-4}
GSA [41]	0.7607	0.0339	63.7784	0.0500	1.5486	1.2012×10^{-3}
SCA [42]	0.7595	0.0519	90.0685	0.002	1.2641	1.9123×10^{-3}
GWO [43]	0.7695	0.0269	47.9136	1	1.6232	9.4095×10^{-4}
WOA [44]	0.7573	0.053	58.5839	0.016	1.2476	9.9529×10^{-4}
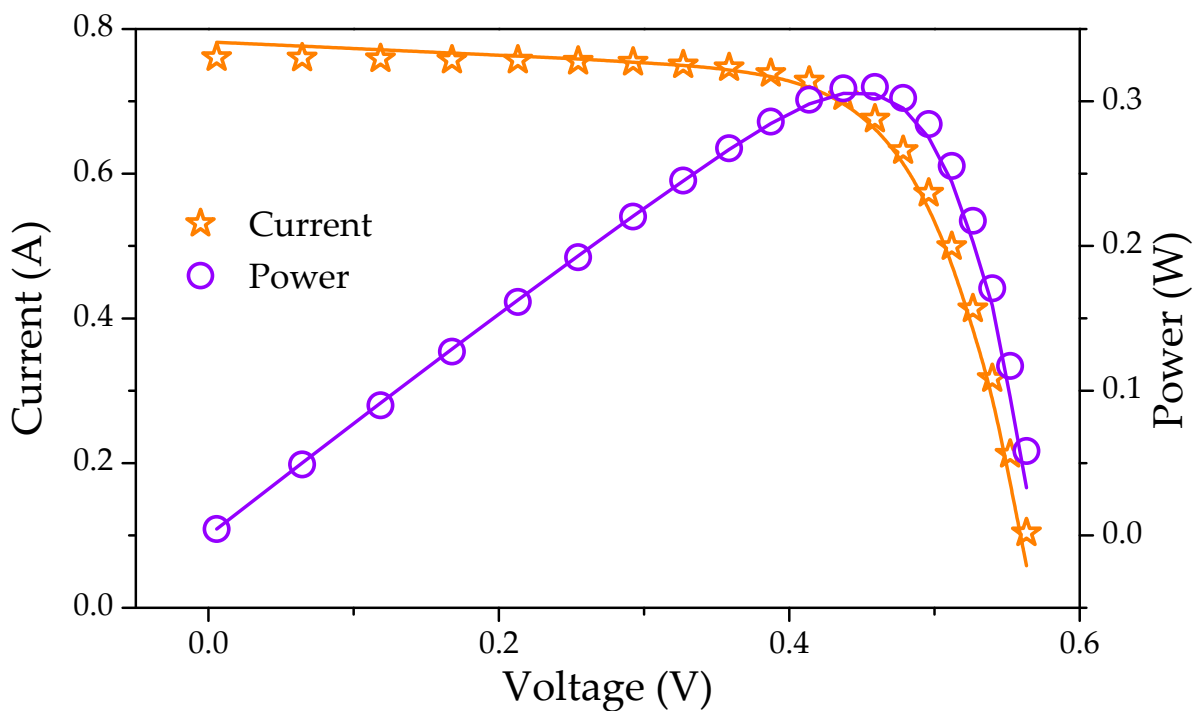
Figure 3. The simulated and experimental I-V and P-V characteristics curves for the single-diode model of the R.T.C France solar cell. Symbols indicate measured data, while solid lines indicate optimized data.

4.3. Convergence Analysis

Figures 5 and 6 depict the convergence curves of the R.T.C France solar cell and the SSS2018 polycrystalline PV cell for examining the computational competency of the STO. The convergence rate analysis shows that the STO algorithm is more accurate than the GSA, SCA, GWO, and WOA algorithms. Thus, the STO algorithm produces a realistic answer for the same amount of evaluation functions (i.e., 50,000).

4.4. Statistical and Robustness Analysis

This subsection offers statistical assessments of the mean, minimum, maximum, and standard deviation (SD) of RMSE for all recently created strategies. The accuracy and reliability comparison of the various algorithms in 30 runs is summarized in Table 6. The RMSE mean and standard deviation were calculated to investigate the durability of the parameter estimation algorithms. According to the statistical data presented in Table 6, the STO is found to be the most precise and trustworthy parameter optimization technique.

Table 4. The simulated current and absolute error results of the STO for SDM of the SS2018 PV module.

Observations	V_l(V)	I_l(A)	$I_{simulated}$ (A)	IAE (A)	$P_{measured}$ (W)	$P_{simulated}$ (W)	IAE (W)
1	0.0844	1.1698	1.2096	0.0397	0.0988	0.1021	0.00336
2	0.2558	1.1697	1.2088	0.0390	0.2993	0.3093	0.0100
3	0.5550	1.1697	1.2075	0.0377	0.6492	0.6702	0.0210
4	1.0896	1.1697	1.2051	0.0353	1.2745	1.3131	0.0386
5	2.1529	1.1697	1.2003	0.0306	2.5183	2.5843	0.0659
6	2.8780	1.1697	1.1971	0.0273	3.3666	3.4454	0.0788
7	3.8696	1.1697	1.1926	0.0229	4.5265	4.6153	0.0888
8	4.5833	1.1697	1.1895	0.0197	5.3613	5.4518	0.0906
9	5.5482	1.1697	1.1851	0.0154	6.4901	6.5757	0.0856
10	6.2780	1.1697	1.1819	0.0121	7.3436	7.4201	0.0765
11	7.2243	1.1697	1.1776	0.0079	8.4505	8.5079	0.0574
12	8.0501	1.1697	1.1739	0.0042	9.4164	9.4506	0.0342
13	8.7878	1.1696	1.1706	0.0009	10.2789	10.2874	0.00852
14	9.7689	1.1696	1.1662	0.0034	11.4259	11.3926	0.0333
15	10.5181	1.1695	1.1627	0.0067	12.3009	12.2302	0.0707
16	11.3167	1.1692	1.1590	0.0102	13.2324	13.1166	0.11160
17	12.1901	1.1688	1.1548	0.0140	14.2485	14.0774	0.1710
18	12.9947	1.1680	1.1506	0.0174	15.1790	14.9522	0.227
19	13.9457	1.1663	1.1449	0.0213	16.2656	15.9678	0.2980
20	14.6556	1.1638	1.1398	0.0240	17.0574	16.7051	0.3520
21	15.5347	1.1583	1.1312	0.0270	17.9941	17.5742	0.4200
22	16.4330	1.1471	1.1177	0.0294	18.8509	18.3673	0.4840
23	17.1324	1.1312	1.1007	0.0305	19.3812	18.8578	0.5230
24	18.0801	1.0907	1.0600	0.0306	19.7206	19.1662	0.5540
25	18.8065	1.0325	1.0033	0.0291	19.4190	18.8700	0.5490
26	19.7423	0.8906	0.8658	0.0248	17.5832	17.0933	0.4900
27	20.5628	0.6493	0.6315	0.0178	13.3533	12.9868	0.3660
28	21.3013	0.2582	0.2516	0.0065	5.5007	5.3614	0.1390
Sum of IAE				**0.5840**			

Table 5. Comparison of the STO with other parameter estimation methods for the SS2018 PV module.

Algorithms	I_p(A)	R_s(Ω)	R_{sh}(Ω)	I_{sd}(μA)	a	RMSE
STO	1.1276	2	2000	0.5000	89.85	6.19×10^{-5}
GSA [41]	1.0959	0.001	455.528	0.0010	53.59	1.68×10^{-1}
SCA [42]	1.1742	0.0011	139.676	0.0092	1.415	1.51×10^{-3}
GWO [43]	1	0.001	100	0.0010	1.263	1.59×10^{-1}
WOA [44]	1.1810	0.0024	18.166	0.0190	1.289	7.82×10^{-4}

In addition to the conventional statistical analysis, we also applied the Friedman rank test [47] to determine the relevance of the presented study. It is a nonparametric test which is employed to decide the rank of algorithms for the analysis of PV modules; lower the rank, better the algorithm. Table 7 illustrates the Friedman ranking test results of different algorithms. The Friedman ranking test results show that the STO has the highest ranking compared to WOA, SCA, GWO and GSA. In the Friedman test, the null hypothesis H_0 (*p*-value > 5%) suggests that there are no noteworthy alterations among the compared algorithms. For all 30 runs, the contrary hypothesis H_1 indicates a significant difference between the compared methods. Each algorithm is ranked in this test depending on its efficiency.
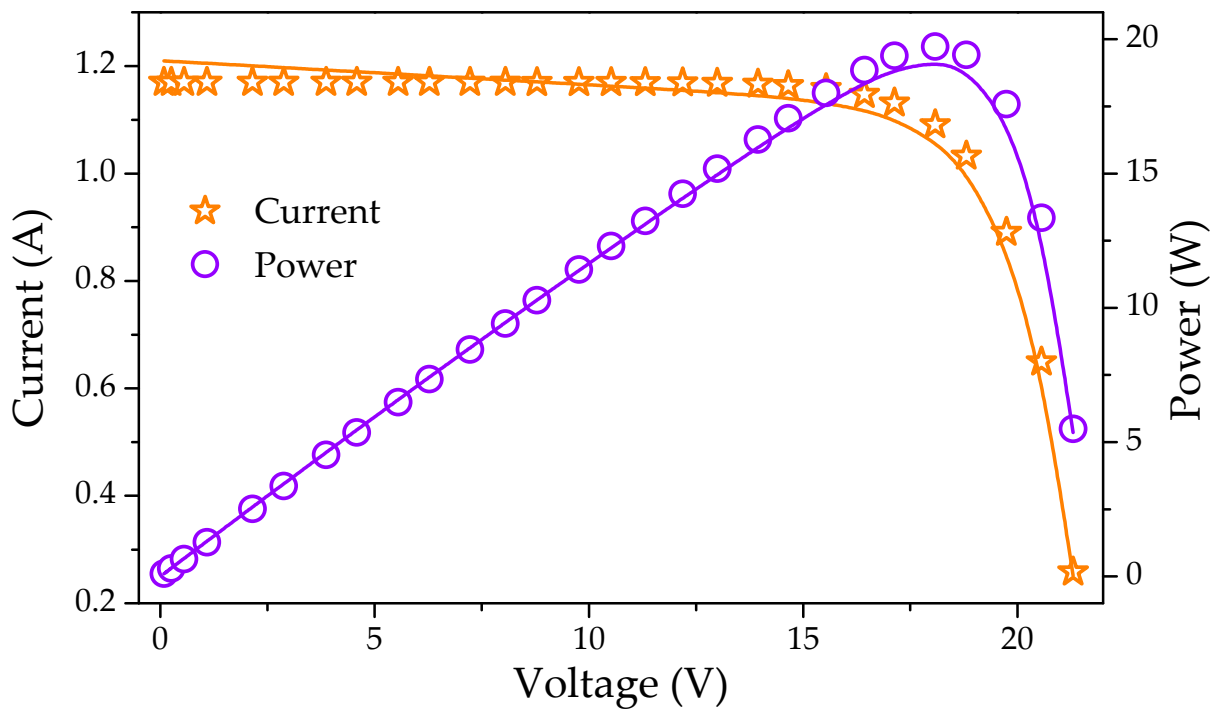
Figure 4. I-V and P-V characteristics curves for anticipated and experimental values for the SS2018 PV module. Symbols indicate measured data, while solid lines indicate optimized data.
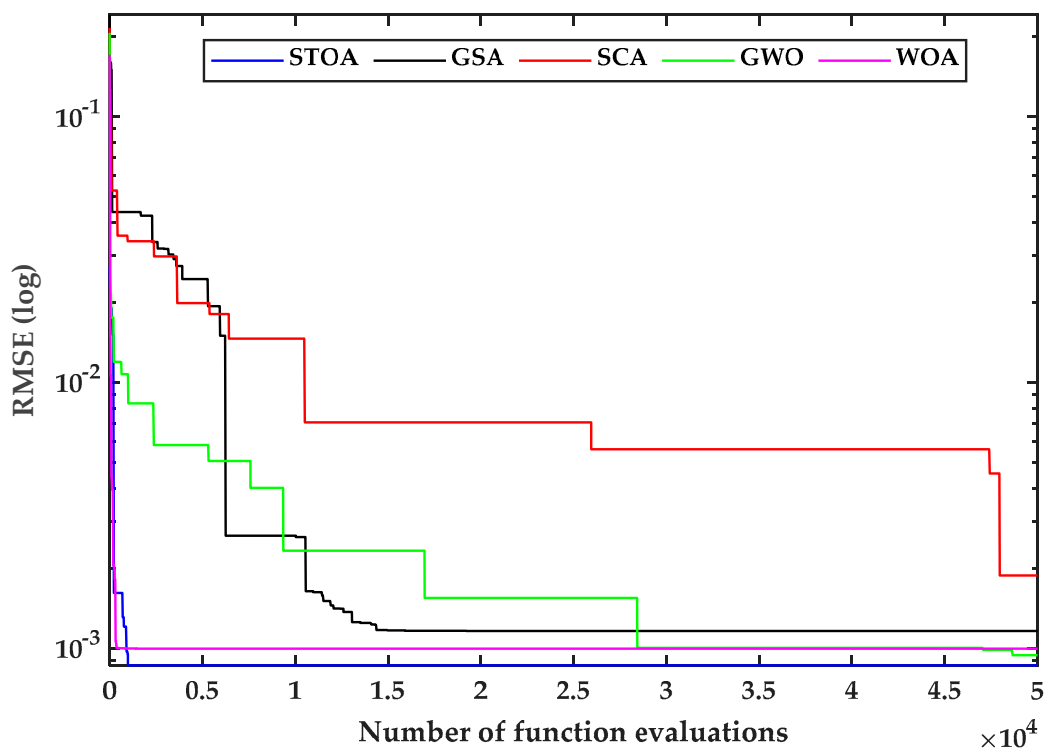

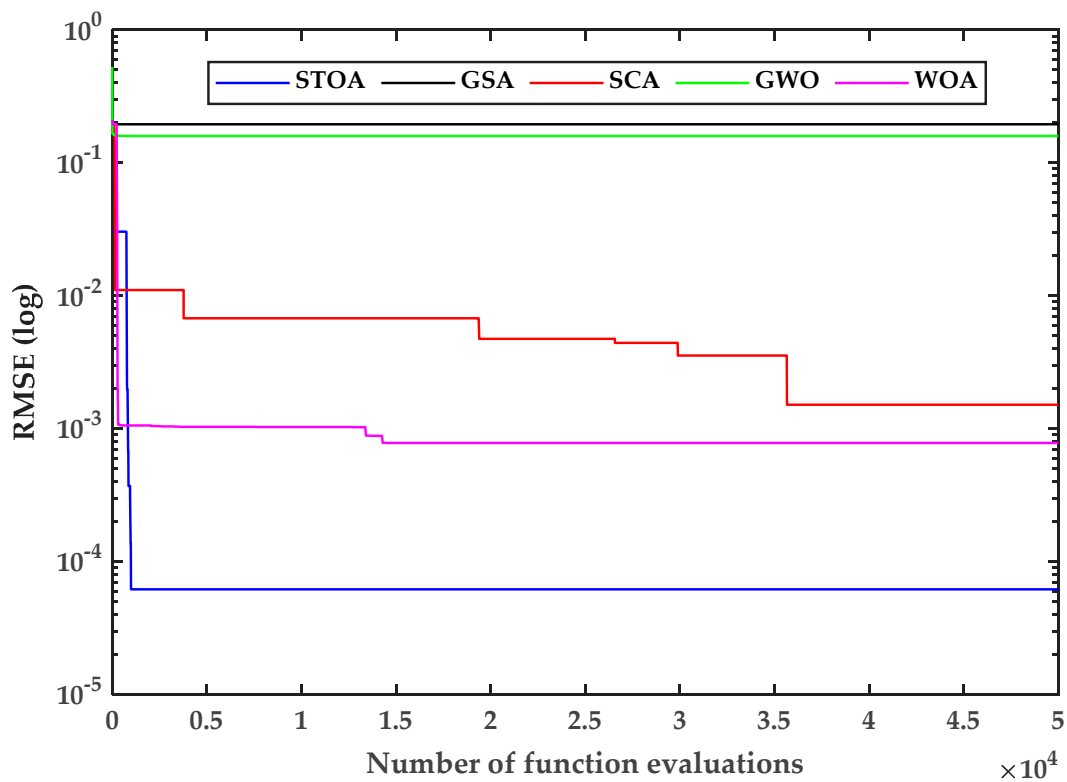**Figure 5.** Convergence plot for the RTC France solar cell.

Figure 6. Convergence plot for the SS2018 PV module.

Table 6. Statistical RMSE results for various techniques for the R.T.C France solar cell and the SS2018 PV module.

	Algorithm	RMSE			
		Minimum	**Mean**	**Maximum**	**SD**
R.T.C France Solar Cell	STO	8.6106×10^{-4}	9.4761×10^{-4}	2.6964×10^{-2}	1.0836×10^{-5}
	GSA [41]	1.2012×10^{-3}	5.4701×10^{-3}	2.4211×10^{-1}	1.3129×10^{-3}
	SCA [42]	1.9123×10^{-3}	9.6515×10^{-3}	2.1642×10^{-1}	9.4066×10^{-3}
	GWO [43]	9.4095×10^{-4}	1.0441×10^{-3}	1.3506×10^{-3}	1.4050×10^{-5}
	WOA [44]	9.9529×10^{-4}	9.2032×10^{-4}	7.1240×10^{-3}	9.0250×10^{-3}
SS2018 PV Module	STO	6.1900×10^{-5}	5.2500×10^{-4}	3.0407×10^{-2}	2.3643×10^{-5}
	GSA [41]	1.6800×10^{-1}	1.9462×10^{-1}	2.0011×10^{-1}	4.4500×10^{-3}
	SCA [42]	1.5100×10^{-3}	5.2657×10^{-3}	2.0345×10^{-1}	1.0058×10^{-2}
	GWO [43]	1.5900×10^{-1}	1.5940×10^{-1}	5.2494×10^{-1}	1.6793×10^{-2}
	WOA [44]	7.8200×10^{-4}	1.8268×10^{-3}	2.1078×10^{-2}	1.3639×10^{-3}

Table 7. Friedman ranking of different algorithms for all modules.

Algorithm	Friedman Ranking	Final Ranking
STO	1	1
GSA [41]	5.12	5
SCA [42]	3.01	3
GWO [43]	4.29	4
WOA [44]	2.03	2

5. Conclusions

In this study, the STO algorithm was employed to assess the parameters of the R.T.C France solar panel and the SS2018 polycrystalline PV module at typical temperature condi-

tions. The single-diode model theory was considered for parameter estimation. We also want to point out that the STO method was being used for the parameter estimation of PV models for the first time. The main observations of this study are as follows:

- The RMSE values confirm that the STO is generally more accurate and trustworthy to generate the best optimized parameters than GSA, SCA, GWO, and WOA.
- The IV and PV characteristic curves as well as IAE results show that the STO can successfully optimize the parameters for different types of PV cells.
- The statistical study illustrates the robustness of the implemented STO technique on the parameter estimation problem in standard operational conditions.
- The convergence curve confirms that the STO obtains the best values of estimated parameters in terms of RMSE of 8.6106×10^{-4} and 6.19×10^{-5} for solar cells and PV modules respectively.

According to the preceding discussion, the STO is an efficient and reliable technique for estimating the unknown optimum parameters of a solar PV module model under typical operating conditions.

References

1. Guzowska, M.K.; Kryk, B.; Michalak, D.; Szyja, P. R&D Spending in the Energy Sector and Achieving the Goal of Climate Neutrality. *Energies* **2021**, *14*, 7875.
2. Rajput, S.; Averbukh, M.; Yahalom, A. Electric power generation using a parallel-plate capacitor. *Int. J. Energy Res.* **2019**, *43*, 3905–3913. [CrossRef]
3. Goldemberg, J. The promise of clean energy. *Energy Policy* **2006**, *34*, 2185–2190. [CrossRef]
4. Sharma, A.; Khan, R.A.; Sharma, A.; Kashyap, D.; Rajput, S. A Novel Opposition-Based Arithmetic Optimization Algorithm for Parameter Extraction of PEM Fuel Cell. *Electronics* **2021**, *10*, 2834. [CrossRef]
5. Buchmayr, A.; Van Ootegem, L.; Dewulf, J.; Verhofstadt, E. Understanding Attitudes towards Renewable Energy Technologies and the Effect of Local Experiences. *Energies* **2021**, *14*, 7596. [CrossRef]
6. Abdul-Ganiyu, S.; Quansah, D.A.; Ramde, E.W.; Seidu, R.; Adaramola, M.S. Techno-economic analysis of solar photovoltaic (PV) and solar photovoltaic thermal (PVT) systems using exergy analysis. *Sustain. Energy Technol. Assess.* **2021**, *47*, 101520. [CrossRef]
7. REN21. *Renewables 2020 Global Status Report—REN21*; REN21: Paris, France, 2020.
8. Doshi, Y. Solar Photovoltaic (PV) Panels Market Overview. Available online: https://www.alliedmarketresearch.com/solar-photovoltaic-panel-market (accessed on 21 October 2021).
9. Rajput, S.; Averbukh, M.; Yahalom, A.; Minav, T. An Approval of MPPT Based on PV Cell's Simplified Equivalent Circuit During Fast-Shading Conditions. *Electronics* **2019**, *8*, 1060. [CrossRef]
10. Rajput, S.; Amiel, I.; Sitbon, M.; Aharon, I.; Averbukh, M. Control the Voltage Instabilities of Distribution Lines using Capacitive Reactive Power. *Energies* **2020**, *13*, 875. [CrossRef]
11. Liu, Y.; Chen, Y.; Wang, D.; Liu, J.; Luo, X.; Wang, Y.; Liu, H.; Liu, J. Experimental and numerical analyses of parameter optimization of photovoltaic cooling system. *Energy* **2021**, *215*, 119159. [CrossRef]
12. Zhang, X.; Zhao, X.; Smith, S.; Xu, J.; Yu, X. Review of R&D progress and practical application of the solar photovoltaic/thermal (PV/T) technologies. *Renew. Sustain. Energy Rev.* **2012**, *16*, 599–617.
13. Su, D.; Jia, Y.; Lin, Y.; Fang, G. Maximizing the energy output of a photovoltaic–thermal solar collector incorporating phase change materials. *Energy Build.* **2017**, *153*, 382–391. [CrossRef]

14. Bayoumi, A.S.; El-Sehiemy, R.A.; Mahmoud, K.; Lehtonen, M.; Darwish, M.M.F. Assessment of an Improved Three-Diode against Modified Two-Diode Patterns of MCS Solar Cells Associated with Soft Parameter Estimation Paradigms. *Appl. Sci.* **2021**, *11*, 1055. [CrossRef]

15. Mughal, M.A.; Ma, Q.; Xiao, C. Photovoltaic Cell Parameter Estimation Using Hybrid Particle Swarm Optimization and Simulated Annealing. *Energies* **2017**, *10*, 1213. [CrossRef]

16. Elazab, O.S.; Hasanien, H.M.; Alsaidan, I.; Abdelaziz, A.Y.; Muyeen, S.M. Parameter Estimation of Three Diode Photovoltaic Model Using Grasshopper Optimization Algorithm. *Energies* **2020**, *13*, 497. [CrossRef]

17. Jordehi, A.R. Parameter estimation of solar photovoltaic (PV) cells: A review. *Renew. Sustain. Energy Rev.* **2016**, *61*, 354–371. [CrossRef]

18. Mittal, A.; Pattnaik, A.; Tomar, A. *Different Variants of Particle Swarm Optimization Algorithms and Its Application: A Review*; Metaheuristic and Evolutionary Computation: Algorithms and Applications; Springer: Singapore, 2021; Volume 916, pp. 131–163.

19. Mareli, M.; Twala, B. An adaptive Cuckoo search algorithm for optimisation. *Appl. Comput. Inform.* **2018**, *14*, 107–115. [CrossRef]

20. Derick, M.; Rani, C.; Rajesh, M.; Farrag, M.; Wang, Y.; Busawon, K. An improved optimization technique for estimation of solar photovoltaic parameters. *Sol. Energy* **2017**, *157*, 116–124. [CrossRef]

21. Guo, L.; Meng, Z.; Sun, Y.; Wang, L. Parameter identification and sen-sitivity analysis of solar cell models with cat swarm optimization algorithm. *Energy Convers. Manage.* **2016**, *108*, 520–528. [CrossRef]

22. Li, S.; Gong, W.; Yan, X.; Hu, C.; Bai, D.; Wang, L. Parameter estimation of photovoltaic models with memetic adaptive differential evolution. *Sol. Energy* **2019**, *190*, 465–474. [CrossRef]

23. Kabalci, Y.; Kockanat, S.; Kabalci, E. A modified ABC algorithm approach for power system harmonic estimation problems. *Electr. Power Syst. Res.* **2018**, *154*, 160–173. [CrossRef]

24. Kiani, A.T.; Nadeem, M.F.; Ahmed, A.; Sajjad, I.A.; Raza, A.; Khan, I.A. Chaotic inertia weight particle swarm optimization (CIWPSO): An efficient technique for solar cell parameter estimation. In Proceedings of the 3rd International Conference on Computing, Mathematics and Engineering Technologies (iCoMET), Sukkur, Pakistan, 29–30 January 2000; pp. 1–6.

25. El-Naggar, K.M.; AlRashidi, M.; AlHajri, M.; Al-Othman, A. Simulated annealing algorithm for photovoltaic parameters identification. *Sol. Energy* **2012**, *86*, 266–274. [CrossRef]

26. Niu, Q.; Zhang, L.; Li, K. A biogeography-based optimization algo-rithm with mutation strategies for model parameter estimation of solar and fuel cells. *Energy Convers. Manage.* **2014**, *86*, 1173–1185. [CrossRef]

27. Jervase, J.A.; Bourdoucen, H.; Al-Lawati, A. Solar cell parameter ex-traction using genetic algorithms. *Meas. Sci. Technol.* **2001**, *12*, 1922. [CrossRef]

28. Gao, X.; Cui, Y.; Hu, J.; Xu, G.; Wang, Z.; Qu, J.; Wang, H. Parameter extraction of solar cell models using improved shuffled complex evolution algorithm. *Energy Convers. Manage.* **2018**, *157*, 460–479. [CrossRef]

29. AlHajri, M.; El-Naggar, K.; AlRashidi, M.; Al-Othman, A. Optimal ex-traction of solar cell parameters using pattern search. *Renew. Energy* **2012**, *44*, 238–245. [CrossRef]

30. Chen, X.; Yu, K.; Du, W.; Zhao, W.; Liu, G. Parameters identification of solar cell models using generalized oppositional teaching learning based optimization. *Energy* **2016**, *99*, 170–180. [CrossRef]

31. Chen, Z.; Wu, L.; Lin, P.; Wu, Y.; Cheng, S. Parameters identification of photovoltaic models using hybrid adaptive Nelder-Mead simplex algorithm based on eagle strategy. *Appl. Energy* **2016**, *182*, 47–57. [CrossRef]

32. Gao, X.; Cui, Y.; Hu, J.; Xu, G.; Yu, Y. Lambert W-function based exact representation for double diode model of solar cells: Comparison on fitness and parameter extraction. *Energy Convers. Manag.* **2016**, *127*, 443–460. [CrossRef]

33. Maouhoub, N. Photovoltaic module parameter estimation using an analytical approach and least squares method. *J. Comput. Electron.* **2018**, *17*, 784–790. [CrossRef]

34. Villalva, M.G.; Gazoli, J.R.; Ruppert Filho, E. Comprehensive approach to modeling and simulation of photovoltaic arrays. *IEEE Trans. Power Electron.* **2009**, *24*, 1198–1208. [CrossRef]

35. Chegaar, M.; Ouennoughi, Z.; Hoffmann, A. A new method for evaluating illumi-nated solar cell parameters. *Solid-State Electron.* **2001**, *45*, 293–296. [CrossRef]

36. Abdallah, R.; Natsheh, E.; Juaidi, A.; Samara, S.; Manzano-Agugliaro, F. A Mul-ti-Level World Comprehensive Neural Network Model for Maximum Annual Solar Irradiation on a Flat Surface. *Energies* **2020**, *13*, 6422. [CrossRef]

37. Sharma, A.; Sharma, A.; Averbukh, M.; Jately, V.; Azzopardi, B. An Effective Method for Parameter Estimation of a Solar Cell. *Electronics* **2021**, *10*, 312. [CrossRef]

38. Sharma, A.; Sharma, A.; Dasgotra, A.; Jately, V.; Ram, M.; Rajput, S.; Averbukh, M.; Azzopardi, B. Opposition-Based Tunicate Swarm Algorithm for Parameter Optimization of Solar Cells. *IEEE Access* **2021**, *9*, 125590–125602. [CrossRef]

39. Dhiman, G.; Kaur, A. STOA: A bio-inspired based optimization algorithm for industrial engineering problems. *Eng. Appl. Artif. Intell.* **2019**, *82*, 148–174. [CrossRef]

40. Ali, H.H.; Fathy, A.; Kassem, A.M. Optimal model predictive control for LFC of multi-interconnected plants comprising renewable energy sources based on recent sooty terns approach. *Sustain. Energy Technol. Assess.* **2020**, *42*, 100844. [CrossRef]

41. Rashedi, E.; Nezamabadi-Pour, H.; Saryazdi, S. GSA: A gravitational search algorithm. *Inf. Sci.* **2009**, *179*, 2232–2248. [CrossRef]

42. Mirjalili, S. SCA: A sine cosine algorithm for solving optimization problems. *Knowl. Based Syst.* **2016**, *96*, 120–133. [CrossRef]

43. Mirjalili, S.; Mirjalili, S.M.; Lewis, A. Grey wolf optimizer. *Adv. Eng. Softw.* **2014**, *69*, 46–61. [CrossRef]

44. Mirjalili, S.; Lewis, A. The whale optimization algorithm. *Adv. Eng. Softw.* **2016**, *95*, 51–67. [CrossRef]

45. Lin, X.; Wu, Y. Parameters identification of photovoltaic models using niche-based particle swarm optimization in parallel computing architecture. *Energy* **2020**, *196*, 117054. [CrossRef]
46. Gaurav, D. Sooty Tern Optimization Algorithm (STOA). 2022. Available online: https://in.mathworks.com/matlabcentral/fileexchange/76667-sooty-tern-optimization-algorithm-stoa (accessed on 19 November 2021).
47. Digalakis, J.G.; Margaritis, K.G. An experimental study of benchmarking functions for genetic algorithms. *Int. J. Comput. Math.* **2002**, *79*, 403–416. [CrossRef]

Article

Fuzzy Logic-Based Direct Power Control Method for PV Inverter of Grid-Tied AC Microgrid without Phase-Locked Loop

Shameem Ahmad [1], Saad Mekhilef [1,2,*], Hazlie Mokhlis [1,*], Mazaher Karimi [3,*], Alireza Pourdaryaei [4,5], Tofael Ahmed [6], Umme Kulsum Jhuma [1] and Suhail Afzal [1,7]

1   Power Electronics and Renewable Energy Research Laboratory (PEARL), Department of Electrical Engineering, Universiti Malaya, Kuala Lumpur 50603, Malaysia; ahmad05shameem@gmail.com (S.A.); umme.jr@gmail.com (U.K.J.); suhailafzal@bzu.edu.pk (S.A.)
2   School of Science, Computing and Engineering Technologies, Swinburne University of Technology, Hawthorn, VIC 3122, Australia
3   School of Technology and Innovations, University of Vaasa, Wolffintie 34, FI-65200 Vaasa, Finland
4   Department of Power and Control, School of Electrical and Computer Engineering, Shiraz University, Shiraz 7194684334, Iran; a.pourdaryaei@gmail.com
5   Department of Electrical and Computer Engineering, University of Hormozgan, Bandar Abbas 7916193145, Iran
6   Department of Electrical and Electronic Engineering, Chittagong University of Engineering and Technology, Chittagong 4349, Bangladesh; tofael@cuet.ac.bd
7   Department of Electrical Engineering, Faculty of Engineering and Technology, Bahauddin Zakariya University, Multan 60800, Pakistan
*   Correspondence: saad@um.edu.my or smekhilef@swin.edu.au (S.M.); hazli@um.edu.my (H.M.); mazaher.karimi@uwasa.fi (M.K.)

Abstract: A voltage source inverter (VSI) is the key component of grid-tied AC Microgrid (MG) which requires a fast response, and stable, robust controllers to ensure efficient operation. In this paper, a fuzzy logic controller (FLC)-based direct power control (DPC) method for photovoltaic (PV) VSI was proposed, which was modelled by modulating MG's point of common coupling (PCC) voltage. This paper also introduces a modified grid synchronization method through the direct power calculation of PCC voltage and current, instead of using a conventional phase-locked loop (PLL) system. FLC is used to minimize the errors between the calculated and reference powers to generate the required control signals for the VSI through sinusoidal pulse width modulation (SPWM). The proposed FLC-based DPC (FLDPC) method has shown better tracking performance with less computational time, compared with the conventional MG power control methods, due to the elimination of PLL and the use of a single power control loop. In addition, due to the use of FLC, the proposed FLDPC exhibited negligible steady-state oscillations in the output power of MG's PV-VSI. The proposed FLDPC method performance was validated by conducting real-time simulations through real time digital simulator (RTDS). The results have demonstrated that the proposed FLDPC method has a better reference power tracking time of 0.03 s along with reduction in power ripples and less current total harmonic distortion (THD) of 1.59%.

Keywords: microgrid; PLL; RTDS; direct power control; fuzzy logic; voltage source inverter

1. Introduction

Fossil fuel resources are frequently used to generate power in conventional power systems, which outcomes in the hasty diminution of fossil fuel, as well as augmented environmental pollution. Renewable energy has arisen as an alternate solution to overcome the environmental and fossil fuel scarcity issues around the world. As a result, modern power systems have undergone vast changes and up-gradation to accommodate renewable energy sources in the power system network. The microgrid (MG) is one of such revolutions, integrating dispatchable and non-dispatchable distributed generation (DG) units through

power electronics devices to power system networks, and providing uninterruptible power to communities [1,2]. MG possesses benefits like low capital cost, a low payback period, and high reliability; however, regarding their operation, there are still numerous technical challenges, including the flexible control of power flow between the utility grid and MG during grid-tied mode, and voltage magnitude and frequency control during islanding operation [3]. In this study, the control strategy that governs the smooth flow of real and reactive power between the MG and the utility grid for efficient operation of grid-tied AC-MG, with multiple DGs, is considered.

Grid-tied voltage source inverters (VSI) are one of the key devices of a MG, which interconnect the DG units of the MG with the main grid, and regulate power flow between them by adopting appropriate power control methods. It has become very important for grid-tied VSI to ensure high power quality and stability, as the penetration level of MG renewable energy resources in modern power grids is increased. The power controllers allow the MG system to attain a fast response and a small steady state rate of error, and to maintain stability during drastic changes [4]. A rotating synchronous reference frame-based trajectory current control scheme is the commonly used strategy to control the output power of a grid-tied VSI. In this scheme, by regulating dq axes currents separately, real and reactive powers are controlled where the decoupling-term-based linear proportional integral (PI) controller can be applied indirectly [4].

To ensure better efficiency, reliability and safety of VSIs used in grid-tied MGs, in the literature based on dq current control schemes (CCSs), various real and reactive power control methods have been proposed. Worku et al. proposed a power control strategy for photovoltaic (PV) and battery storage-based AC-MGs, based on decoupled dq CCS [5]. A rigid power controller was proposed by Safa et al. for a grid-connected VSI, to improve AC-MG power quality [6]. A new power control method, based on the artificial neural network (ANN) to control the power quality of PV-incorporated AC-MGs, was presented by Kaushal et al. [7]. For controlling the VSI of a grid-tied AC-MG, Smadi et al. proposed a compact control strategy based on dq CCS [8]. By cascading the voltage and current controller, a new power control scheme was proposed by Lou et al. for an AC-MG VSI [9]. A power control strategy, based on a sliding mode-integrated dq CCS, was proposed by Abadlia et al. for a hybrid grid-tied PV/hydrogen system [10]. Based on an instantaneous self-tuning technique, another power control scheme was designed by Feng et al. for a grid-tied MG [11]. Adhikari et al., for a maximum power point tracking (MPPT) system-integrated hybrid PV/battery system, proposed a coordinated power control strategy [12]. A coupled harmonic compensation and voltage support method was developed by Mousavi et al., for DG-interfaced VSIs in grid-tied AC-MGs [13]. To regulate the power flow between grid and PV/battery hybrid systems, Go et al. proposed a power control strategy for VSI [14]. A power control and management system for a grid-tied MG was developed by Sedaghati to ensure the optimum operation of MG [15]. For controlling the output power of grid-tied PV-VSI in AC-MGs, a voltage-oriented power coordination strategy was proposed by Tang et al. [16]. A dq axes CCS synchronous reference frame-based power control method was proposed by Ahmad et al. for grid-connected AC-MG's VSIs [17].

Since in the aforementioned methods, Park's transformation has been used during abc to dq transformation, there is a need for phase angle extraction from grid voltages to ensure dq axes currents and grid voltages are in phase with each other [18]. Phase-locked loop (PLL) systems are commonly used for the extraction of grid voltage phase angles, based on arctangent functions [19]. However, the problems with the use of PLL systems are their adverse impact on VSIs' small-signal stability, along with the slowdown of the transient response of the power system parameters, causing high ripples in real and reactive power [20]. Moreover, at low frequencies PLL initiates negative resistance, which deteriorates VSIs stability [21]. PLL also introduces dynamic coupling in VSIs [22]. Furthermore, the power system's dynamic performance is also jeopardized, due to the adoption of low-bandwidth PLLs for improving VSIs' stability and robustness. Another

issue associated with all these controllers is the consideration of two control loops, namely the outer power and inner current control loops, when designing the power control scheme. Due to the presence of two control loops, the computation burden increases. Furthermore, the performances of the above-mentioned control methods are greatly influenced by the accurate tuning of PI controller gains, the conditions of grid voltage, and the comprehensiveness of the current decoupling [23]. In addition, PI controllers cannot eliminate steady state error for sinusoidal signals, and they cannot handle power system non-linearity efficiently. Moreover, due to the existence of multivariable parameters, during dynamic-load variations PI controllers have a poorer performance [24].

In some studies, fuzzy logic controller (FLC)-based control methods have been proposed for VSIs operating in grid-tied or autonomous modes for DG applications. Hasanien et al. proposed an FLC-based control method to maintain the output voltage of VSI for the islanded DG system during load variability and weather uncertainties [24]. A type-2 FLC-based control method was developed by Heydari et al. for VSIs of autonomous naval shipboard microgrids, to damp the steady-state deviations of voltage and frequency [25]. However, in [24,25], FLC controllers were used to control the output voltage and frequency of VSIs during an islanded operation. Thao et al. developed a power control method by combining feedback linearization and FLC, to reduce the fluctuations in the VSI's output active and reactive powers at the steady state, for a grid-tied PV system [26]. Another FLC-based power control method was proposed by Omar et al. to control the output power of grid-connected PV-VSI [27]. Jamma et al. proposed an FLC and ANN combined DPC for controlling the VSI output power of a grid-tied PV system [28]. For a grid-tied PV system VSI, a control method based on FLC and the Levenberg–Marquardt optimization method was proposed by Islam et.al. [29]. Shadoul et.al. proposed an adaptive FLC-based control method for grid-tied PV-VSIs [30]. FLC-based active and reactive power control was proposed by Tahri et al. for a grid-tied PV system's neutral-point-clamped VSI [31]. Teekaraman et al. developed an FLC-based current control method for a grid-tied Z-source VSI [32]. In all these studies [26–32], even though FLC was considered when designing the feedback controller, all the control methods were based on dq CCS where Park Transformation was used for abc to dq transformation, and PLL was implemented to extract the voltage angle. As mentioned earlier, due to the use of the PLL system, the control methods performance deteriorated, and most of the control methods consisted of two control loops. As a result, undesirable ripples were observed in the VSI output powers, and controllers took a longer time to track the reference powers. Furthermore, the performance of all these controllers were validated only for grid-tied PV systems, which are not connected to MGs.

To overcome the issue of double control loops, direct power control (DPC) method was introduced for VSI, where the inner current control loop was omitted. A control method for VSI based on a DPC, to control the output power, was introduced by Gui et al. [33,34]. However, due to the use of the variable switch frequency in this method, undesirable harmonics occurred, which hampered the suitable design of the line filter. The DPC method based on the sliding mode and model predictive controllers were introduced by Gui et al. [35] and Choi et al. [36], respectively, to improve the fast tracking of power references and DPC method robustness. Though power tracking performance was improved, undesirable ripples still existed in real and reactive power, and their performances were not validated for MG applications.

In this paper, to address the problems associated with the previous power controllers of PV-VSI, an FLC-based DPC (FLDPC) method is proposed for AC-MG's photovoltaic (PV) VSI, through modulating MG's point of common coupling (PCC) voltage. The advantages of FLC over conventional PI controllers, is that their design is independent of power system mathematical modelling, and can therefore deal with power system non-linearities effectively, and can easily adopt the dynamic load variation of a power system [24]. For grid-synchronization, instead of using a PLL system, in this study, the direct power calculation of PCC voltage and current grid-synchronization takes place. The proposed FL-DPC method also consists of a feedforward decoupled control, and a feedback FLC method

including the non-linear voltage modulated control. Since the proposed controller excludes Park transformation and PLL, it exhibits a faster and more transient dynamic performance, compared with conventional PLL-PI-integrated CCS-based power control methods. In addition, due to the use of FLC and the elimination of PLL, the steady state oscillation in VSI output power reduced substantially, and the reference power tracking speed became faster. Furthermore, the computational burden was also reduced, since the proposed FLDPC had only a single power control loop, which regulated the instantaneous real and reactive power flow, directly. Moreover, the presence of the feedforward decoupled control eliminated the coupling terms presented in the new control inputs from the nonlinear PCC voltage modulation (PVM), and finally, two individual dynamics of the second order error signals of the real and reactive were obtained, using a feedback FLC strategy. For controlling the bus voltage and frequency of the MG during islanded mode of operation, a V-f control strategy was adopted [37].

The main contribution of this paper is unlike conventional CCS-based VSI; the PV-VSI is modelled based on DPC and PVM theory (PVMT) to control the real and reactive power flow between the AC-MG and the utility grid. The detailed mathematical modelling of the grid synchronization technique, based on the direct power calculation of PCC voltage and current was conducted. The modelling of the FLDPC strategy for PV-VSI, along with feedforward decoupled control is also depicted extensively. Real-time simulations were carried out using a real-time digital simulator (RTDS) for different references of real and reactive power, to test the proposed FLDPC method's performance. Considering real-world scenarios, the performance of the proposed controller was verified by changing the PV generation and load demand simultaneously, during both MG's grid-tied and islanded modes of operation. Finally, to demonstrate the pre-eminence of the proposed FLDPC controller, real-time simulations of different conventional grid-tied MG power control methods were conducted, and their performances were compared with the proposed controller for various parameters of steady-state power oscillations, refence power tracking time and total harmonic distortions (THD) of VSI's output current and voltage.

The organization of the rest of the paper is as follows: in Section 2, the modelling of AC-MG's different components are presented. In Section 3, the mathematical modelling of the DPC and PVMT-based VSI are presented. Section 4 presents the proposed FLDPC method's design strategy. Section 5 presents the results obtained through the real-time simulations, along with a detailed discussion and comparative study. Finally, a conclusion of this study is presented in Section 6.

2. Configuration of AC Microgrid Testbed

The grid-tied AC-MG testbed used in this study consisted of a PV system, a battery storage, a diesel generator and two types of load (critical and non-critical) which is represented in Figure 1. The modelling of the MG was conducted in an RSCAD platform, using modules of different components available in the RSCAD library. In Appendix A Table A1, the specifications of all the components used in the MG are depicted, which were obtained from [38]. As shown in Figure 1, two VSIs are used to connect the PV and battery storage systems with the AC bus, and the AC-MG was integrated with the grid through a 3-ph transformer.
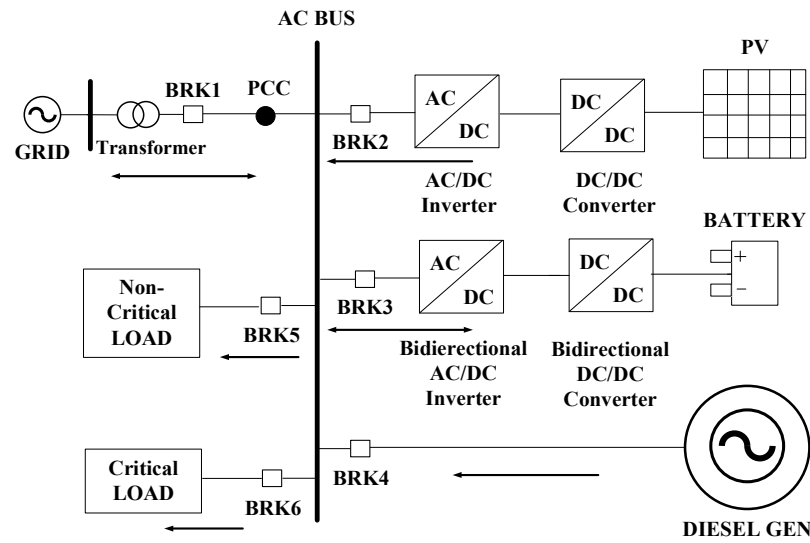
Figure 1. Schematic of Modelled Grid-tied AC Microgrid.

2.1. Photovoltaic (PV) System

The 0.1 MW-rated PV system used in this study, and the parameters of the system, are depicted in Table A1. To control the output of the PV-VSI, a PVMT-based FLDPC strategy was developed, which is described in Sections 3 and 4.

The relationship between the PV system's current and voltage can be represented as follows:

$$I_{PV} = I_{ph} - I_D - I_{sh} = I_{ph} - I_0[\exp\frac{q}{AKT(V_{PV} + I_{PV}R_s)} - 1] - \frac{V_{PV} + I_{PV}R_s}{R_{sh}} \tag{1}$$

where cell output voltage is V_{PV}, cell output current is I_{PV}, diode current is I_D, photocurrent is I_{ph}, reverse saturation current is I_0, electron charge is q, shunt resistance current is I_{sh}, temperature of cell is T, shunt resistance R_{sh}, series resistance R_s and quality factor is A.

A modified incremental conductance algorithm-based MPPT controller [39] is implemented to extract maximum power from the PV system. By using (2), the maximum power can be determined:

$$P_{pv}(t) = \eta_{pv}A_c I(t)(1 - 0.005(T_0(t) - 25)) \tag{2}$$

where cell array area is A_c, PV system efficiency is η_{pv}, solar irradiation is I and ambient temperature is T_0.

2.2. Battery Storage System (BSS)

In this study, the battery storage system (BSS) is comprised of strings of lithium-ion battery, a bidirectional DC-AC VSI, and a bidirectional DC-DC buck-boost converter. A control technique proposed in [5] was employed in this study to control the battery VSI. The size of the battery was chosen based on the critical load demand, so that in the case of any contingency the battery was able to provide back up. In charging mode, battery charged either by PV (power generation of PV is more than demand) or via the grid in grid-tied mode. In contrast, the battery operated in discharge mode when the MG was islanded, or the generation of PV was less than its capacity in grid-tied mode.

The crucial parameters of the battery are terminal voltage and SOC, which can be calculated based on (3) and (4) [40]:

$$V_{bat} = i_{bat}R_{bat} + V_{oc} + V_e e^{B\int i_{bat}dt} - k\frac{Ah}{Ah + \int i_{bat}dt} \tag{3}$$

$$SOC = \left(1 + \frac{\int i_{bat}dt}{Ah}\right) * 100 \tag{4}$$

where open circuit voltage is V_{oc}, terminal voltage of the battery is V_{bat}, battery internal resistance is R_{bat}, battery current is i_{bat}, exponential voltage is V_e, polarization voltage is k and B is the exponential capacity.

2.3. Diesel Generator

In this study, a diesel generator was used to provide backup supply to the MG when the grid fails. It comprised a diesel engine, a synchronous machine, and for regulating the machine's speed and frequency, an excitation system-driven speed governor. The modelling of the three different parts of the diesel generator was adopted from [41]. The dynamics of each diesel generator components can be given by (5) and (8).

The governor control system transfer function:

$$H_c = \frac{K_1(T_3 s + 1)}{(T_1 T_2 s^2 + T_1 s + 1)} \tag{5}$$

where, H_c is the transfer functions of governor control system, K_1 is the transfer function constants, and T_1 to T_3 are the time constants.

Actuator Transfer function:

$$H_a = \frac{(T_4 s + 1)}{s(T_5 s + 1)(T_6 s + 1)} \tag{6}$$

where H_a is the transfer functions actuator, and T_4 to T_6 are the time constants.

Diesel engine transfer function:

$$H_{eng} = e^{-T_D s} \tag{7}$$

where governor control system transfer functions is H_{eng} is and T_D is the time constant.

Excitation system transfer function:

$$H_e = \frac{1}{(T_e s + K_e)} \tag{8}$$

where transfer function constant is K_e, exciter transfer function is H_e and time constant is T_e.

2.4. Grid

By using (3), the power absorbed or supplied by the grid can be calculated [40]:

$$P_g(t) = P_l(t) + \sum (P_{pv}(t), P_b(t)) \tag{9}$$

where grid supplied/absorbed is P_g, load power is P_l, battery power is P_b, and PV power is P_{pv}.

2.5. Load

To verify the performance of the proposed PLL-less FLDPC method, two types of load were considered in this study, namely, critical and non-critical load. The load values were chosen based on the MG generation capacity, which changed with respect to time.

3. DPC and PVMT-Based PV-VSI Modelling

In this section, the mathematical modelling of PV-VSI based on DPC and PVMT is presented. L-filters were used at the output of PV-VSI to reduce the harmonics in current and voltage. In Figure 2a,b, the schematics of the dq CCS-based control method with PLL and the proposed PVMT-based FLDPC method without PLL are presented respectively.
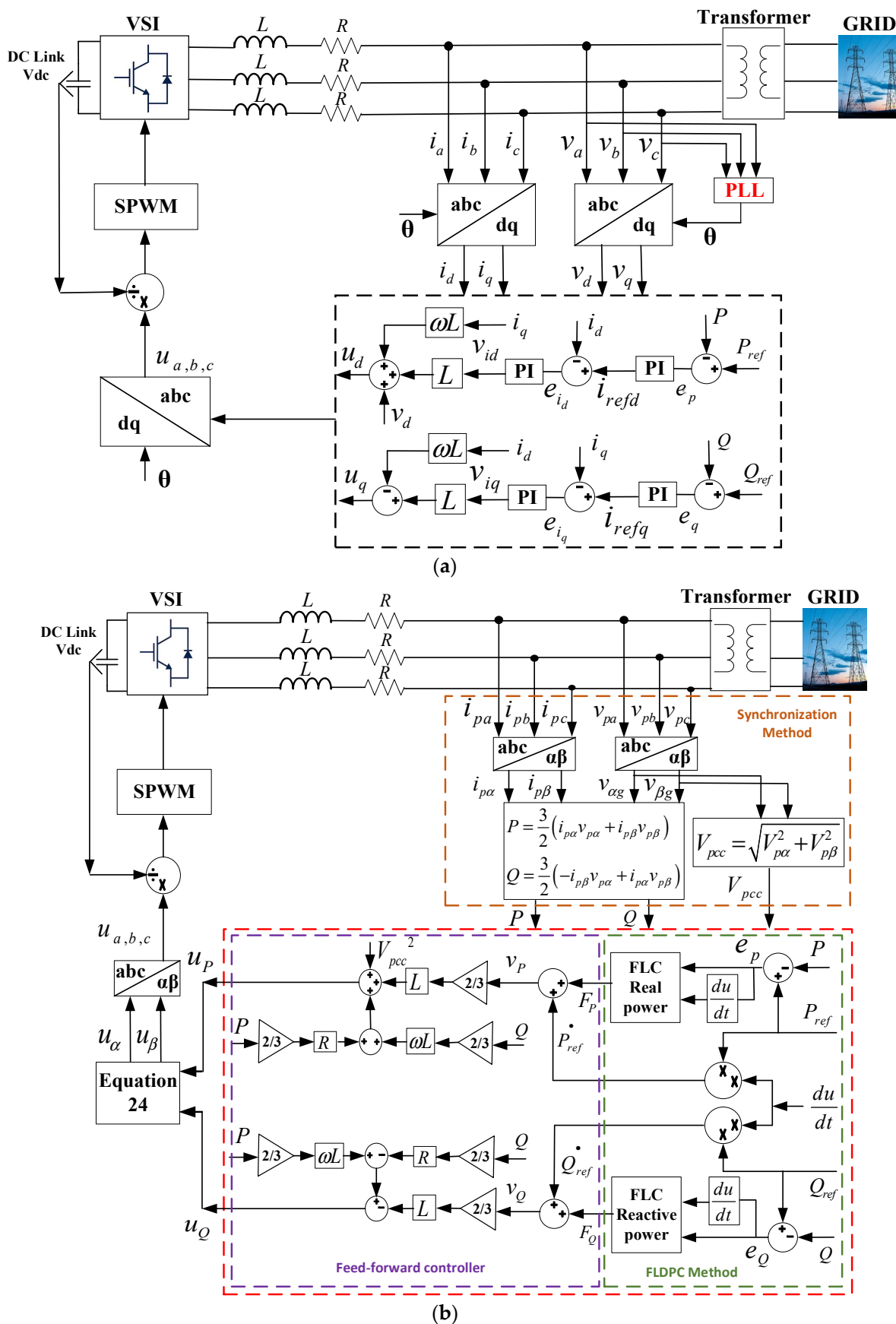
Figure 2. Power controllers for grid-tied AC-MG's PV-VSI, based on (**a**) PLL-PI-integrated dq CCS and (**b**) the proposed PVMT-based FLDPC.

The dynamic realtionships between VSI's output voltages, currents and PCC voltages can be represented using (10):

$$L\frac{di_{pa}}{dt} = -v_{pa} + u_a - Ri_{pa}$$
$$L\frac{di_{pb}}{dt} = -v_{bg} + u_b - Ri_{pb}$$
$$L\frac{di_{pc}}{dt} = -v_{cg} + u_c - Ri_{pc}$$

(10)

where, v_{pabc}, i_{pabc}, and u_{abc} are PCC voltages, VSI output currents and voltages, respectively. R and L are the resistance and inductance of filter, respectively.

The stationary reference frame of the equations presented in (10) can be transformed to (11) using Clarke's transformation:

$$L\frac{di_{p\alpha}}{dt} = u_\alpha - v_{p\alpha} - Ri_{p\alpha}$$
$$L\frac{di_{p\beta}}{dt} = u_\beta - v_{p\beta} - Ri_{p\beta}$$

(11)

where PCC voltages are $u_{\alpha\beta}$, and VSI currents and voltages are $i_{p\alpha\beta}$ and $v_{p\alpha\beta}$, respectively, in α–β frame.

The stationary reference frame representation of instant reactive and real power flow between the utility grid and VSI can be presented as (12):

$$P = \tfrac{3}{2}\left(i_{p\alpha}v_{p\alpha} + i_{p\beta}v_{p\beta}\right)$$
$$Q = \tfrac{3}{2}\left(-i_{p\beta}v_{p\alpha} + i_{p\alpha}v_{p\beta}\right)$$

(12)

where instant real and reactive powers supplied/injected by the grid are P and Q, respectively.

By differentiating (12), P and Q dynamic equations can be obtained as follows:

$$\frac{dP}{dt} = \tfrac{3}{2}\left(v_{p\alpha}\frac{di_\alpha}{dt} + i_{p\alpha}\frac{dv_{p\alpha}}{dt} + v_{p\beta}\frac{di_{p\beta}}{dt} + i_{p\beta}\frac{dv_{p\beta}}{dt}\right)$$
$$\frac{dQ}{dt} = \tfrac{3}{2}\left(-v_{p\alpha}\frac{di_{p\beta}}{dt} - i_{p\beta}\frac{dv_{p\alpha}}{dt} + v_{p\beta}\frac{di_{p\alpha}}{dt} + i_\alpha\frac{dv_{p\beta}}{dt}\right)$$

(13)

For simplifying the dynamics of P and Q in the balanced grid condition, the relationship of the PCC α–β voltage can be obtained as given in (14):

$$v_{p\alpha} = V_{pcc}\cos(\omega t)$$
$$v_{p\beta} = V_{pcc}\sin(\omega t)$$

(14)

where:

$$V_{pcc} = \sqrt{v_{p\alpha}{}^2 + v_{p\beta}{}^2}$$
$$\omega = 2\prod f$$

(15)

where *PCC* voltage amplitude is V_{pcc}, angular frequency is ω and grid voltage frequency is f.

The dynamic equations of *PCC* voltages are obtained as (16) by differentiating (14).

$$\frac{dv_{p\alpha}}{dt} = -\omega V_{pcc}\sin(\omega t) = -v_{p\beta}\omega$$
$$\frac{dv_{p\beta}}{dt} = \omega V_{pcc}\cos(\omega t) = v_{p\alpha}\omega$$

(16)

By substituting (10) and (16) in (13), the dynamic expression of real and reactive powers can be obtained as (17):

$$\frac{dp}{dt} = \frac{3}{2L}\left(-V_{pcc}{}^2 + u_\alpha v_{p\alpha} + u_\beta v_{p\beta}\right) - \omega q - p\frac{R}{L}$$

$$\frac{dq}{dt} = \frac{3}{2L}\left(-u_\beta v_{p\alpha} + u_\alpha v_{p\beta}\right) - \omega q - q\frac{R}{L} \tag{17}$$

where, dynamic real and reactive power control inputs and outputs are (p and q) and (u_α and u_β), respectively.

Since both the control inputs in (17) are coupled in P and Q states, by using voltage modulation theory [34], the dynamics of (17) can be simplified as (18) to define new voltage modulated control inputs:

$$u_P := u_\alpha v_{p\alpha} + u_\beta v_{p\beta}$$

$$u_Q := u_\beta v_{p\alpha} - u_\alpha v_{p\beta} \tag{18}$$

where the new control inputs are u_P and u_Q, and they are transformed into DC components as they satisfy (19):

$$\begin{bmatrix} u_P \\ u_Q \end{bmatrix} = V_{pcc} \begin{bmatrix} \cos(\omega t) & \sin(\omega t) \\ -\sin(\omega t) & \cos(\omega t) \end{bmatrix} \begin{bmatrix} u_\alpha \\ u_\beta \end{bmatrix} = V_{pcc} \begin{bmatrix} u_d \\ u_q \end{bmatrix} \tag{19}$$

where u_d and u_q are the *d-q* frame VSI voltages. Though the proposed method has no PLL system, the system is still presented in dq axis frame.

The dynamic expression of real and reactive powers presented in (17) can be expressed as (20), by substituting the control inputs of (17) with the new control inputs (u_P and u_Q).

$$\frac{dP}{dt} = \frac{3}{2L}\left(-V_{pcc}{}^2 + u_P\right) - \omega Q - P\frac{R}{L}$$

$$\frac{dQ}{dt} = \frac{3}{2L}u_Q - \omega Q - P\frac{R}{L} \tag{20}$$

4. Controller Design

4.1. FLC-based Direct Power Control

In this section, for the new PVMT and DPC-based VSI model presented in (20), a robust and simple controller consisting of feedforward and feedback control structure is designed. In Figure 2, the FLDPC method's schematic for the PV-VSI is depicted. In this control, the power (real and reactive) references are tracked by controlling their actual value using FLC.

The real and reactive power errors can be obtained using (21):

$$e_P := P_{ref} - P$$

$$e_Q := Q_{ref} - Q \tag{21}$$

where active and reactive power references are represented by P_{ref} and Q_{ref}, respectively, and real and reactive power errors are e_P and e_Q, respectively.

As shown in Figure 2, for obtaining zero steady state error, two error signals (e_P and e_Q) and their rate of change (*P-error_rate* and *Q-error_rate*) are given as inputs to two FLCs. The outputs of FLCs provided the control inputs F_P and F_Q for the feed-forward controllers. Due to non-availability of the FLC block in the RSCAD library, FLC is built in RSCAD software by writing codes using ANSI language in C-builder. Each FLC consisted of two inputs and one output, as depicted in Figure 2. The two inputs were the error and error-rates of power for each FLC. The membership functions of inputs and outputs were named identical for both real and reactive power. The variables representing error were NM (negative medium), ZV (zero value), and PM (positive medium). Similarly, error-rate variables were NM1 (negative medium 1), ZV1 (zero value 1), and PM1 (positive medium 1). The variables of output were BNE (big negative error), NME (negative medium error), ZE (zero error) and PME (positive medium error). In Figures 3 and 4, the real and reactive power FLCs' membership functions for error, error-rate and outputs are shown.

To ensure smooth control by FLC, triangular-based membership functions were considered in this study.
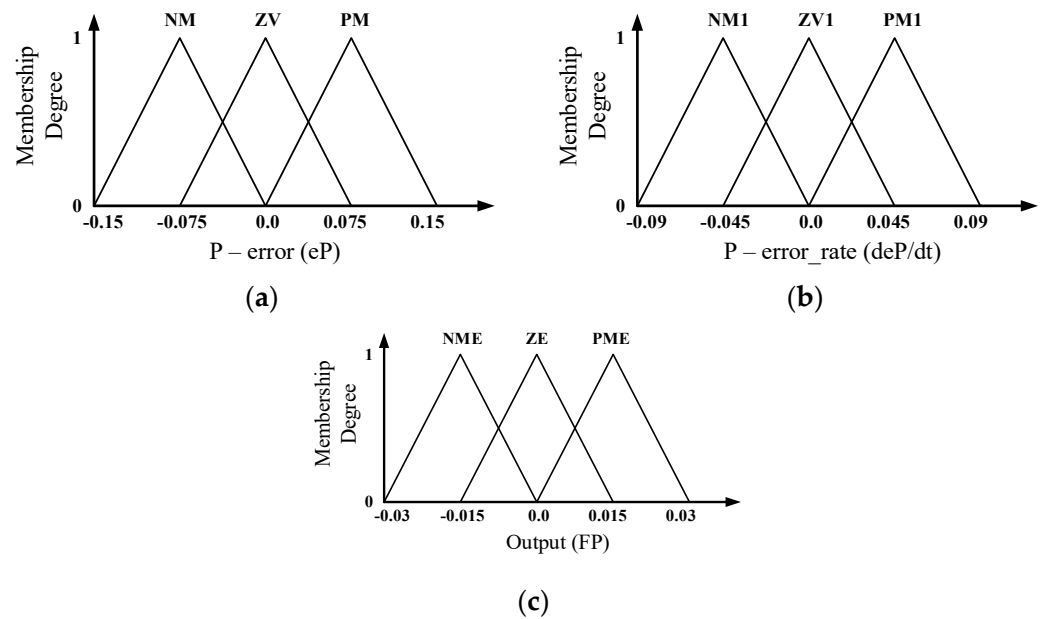

(a)

(b)

(c)

Figure 3. Membership functions of (**a**) P-error (e_P), (**b**) error_rate of P (de_P/dt) and (**c**) output of FLC (F_P).
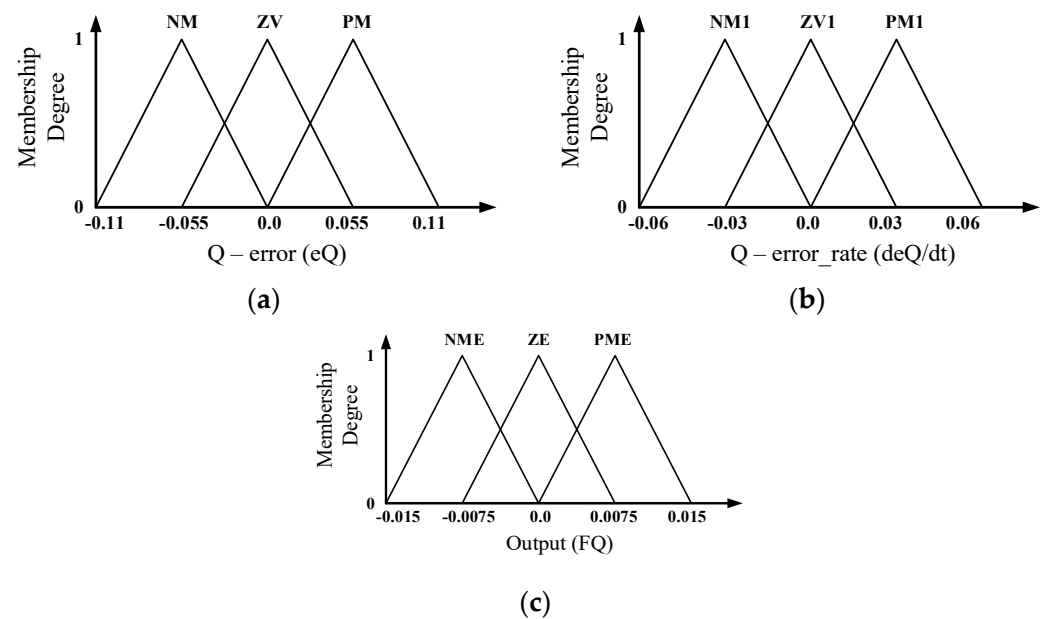

(a)

(b)

(c)

Figure 4. Membership functions of (**a**) Q-error (e_Q), (**b**) error_rate of Q (de_Q/dt) and (**c**) output of FLC (F_Q).

An important part in the design of FLC is choosing the scaling factors of input and output membership functions optimally. This can be obtained by implementing optimization techniques to minimize the deviation between inverter output powers and the reference powers. In this study, a black-box optimization technique known as the nonlinear Simplex method of Nelder and Mead is adopted for obtaining the optimal scaling factors of input and out membership functions [42]. The reason for choosing the black-box optimization technique is that it can be easily used in conjunction with time-domain or real-time simulation tools [24]. The process of black-box optimization entails the successive

evaluation of the objective function for the different sets of parameters for the membership functions. In this process, the real-time simulation program, i.e., RSCAD/RTDS, is used to evaluate the value of the objective function. First, an initial set of parameters was used to initialize the real-time simulation in RTDS, and the value of the objective function was numerically evaluated. Then, based on the optimization algorithm and the value of the objective function, a new set of parameters were obtained, and the process was repeated until an optimal set of parameters is determined.

To assign the input and output control, fuzzy rules were formed based on IF-THEN rules, which are summarized in Table 1. The rules were decided depending on the cooperation between the estimated error and complexity of FLC. In this paper, defuzzification was carried out by using the Sugeno-type weighted average method [43] to produce the real crisp output of F_P and F_Q.

Table 1. Rule table for FLCs of real and reactive power.

Membership Functions		ERROR RATE		
		NM1	ZV1	PM1
ERROR	NM	NME	NME	ZE
	ZV	NME	ZE	PME
	PM	ZE	PME	PME

4.2. Feed-Forward Controller

Due to the presence of coupling terms in the new MIMO system (20), and in this study, to eliminate the coupling terms, a feed-forward controller was designed, as expressed in (22):

$$u_P = \tfrac{2}{3}Lv_P + \tfrac{2}{3}L\omega Q + \tfrac{2}{3}RP + V_{pcc}{}^2$$
$$u_Q = -\tfrac{2}{3}Lv_Q - \tfrac{2}{3}RQ + \tfrac{2}{3}L\omega P \tag{22}$$

where feedback controller inputs are v_P and v_Q and can be calculated using (23):

$$v_P = F_P + \overset{\bullet}{P}_{ref}$$
$$v_Q = F_Q + \overset{\bullet}{Q}_{ref} \tag{23}$$

where F_p and F_Q are the de-fuzzified output of the real and reactive power FLCs.

Finally, the genuine control inputs u_α and u_β were obtained using (24).

$$u_\alpha = \frac{-u_Q v_{p\beta} + u_P v_{p\alpha}}{V_{pcc}{}^2}$$
$$u_\beta = \frac{u_P v_{p\beta} + u_Q v_{p\alpha}}{V_{pcc}{}^2} \tag{24}$$

These two control inputs using αβ-abc transformation were converted to 3-ph control signals, which were used to generate the control signals for the VSI switches using sinusoidal pulse width modulation (SPWM). SPWM was chosen in this study because the harmonics of lower and higher order can be reduced or eliminated easily using this technique.

4.3. Control of DC-Link Voltage

In Figure 5, the DC-link voltage controller is depicted, which aims to maintain a constant DC-link voltage during any disturbances or instabilities.
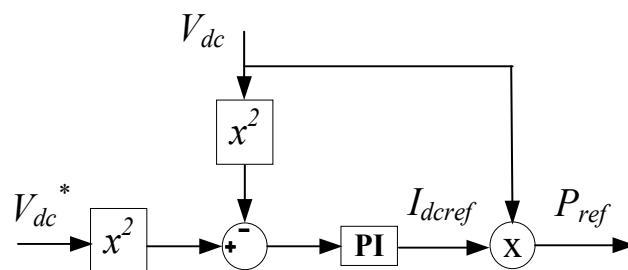
Figure 5. Schematic of controller of DC-link voltage.

The DC-link voltage error can be given by:

$$V_{dc\_error} = \left(V_{dc}{}^*\right)^2 - \left(V_{dc}\right)^2 \tag{25}$$

where, $V_{dc}{}^*$ is the reference of V_{dc}.

To generate the DC current reference I_{dcref}, this error signal was sent to the PI controller to the ensure DC bus voltage constant value. The DC current reference I_{dcref} is given by:

$$I_{dcref} = K_{p,dc}\left(\left(V_{dc}{}^*\right)^2 - \left(V_{dc}\right)^2\right) + K_{i,dc}\int_0^t \left(\left(V_{dc}{}^*\right)^2 - \left(V_{dc}\right)^2\right)dt \tag{26}$$

where, $K_{p,dc}$ and $K_{i,dc}$ are the PI controller gains. In Appendix A Table A2, the PI controller gain values for DC-link voltage controller are presented.

5. Results

The real-time simulation results obtained through the implementation of the proposed PLL-less PVMT-based FLDPC method for PV-VSI of grid-tied MG are presented in this section. The real-time simulations were carried out on RTDS, and the laboratory setup to validate the performance of the proposed power controller is shown in Figure 6.

Figure 6. Laboratory setup of the proposed controller in AC MG with RTDS.

Two case studies were conducted in this study to validate the performance of the proposed power controller. For the first case study, the steady-state and transient response of the proposed controller for PV-VSI was validated by changing both real and reactive power references, and by changing only real power references. The results were compared with those of the conventional PLL-PI-integrated dq CCS-based control method, proposed in [6]. For the second case study, load demand and solar irradiation were varied to test the proposed controller performance during MG's different operating modes. Finally, a comparative study was conducted to prove the preeminence of the proposed FLDPC method.

5.1. Case 1: Change of Both Real and Reactive Power References

This section presents the results related to the power tracking performance of the proposed FLDPC method, and subsequently compares its performance with the PLL-PI-integrated dq CCS-based control method for both real and reactive power reference change.

5.1.1. Tracking Performance Analysis of the Proposed Controller

The results obtained for both the controllers tracking performance analysis are depicted in Figures 7 and 8. To test the tracking performance of the controller's real power, references were varied between 0 MW and 0.1 MW (PV output is non-linear), whereas reactive power references were changed between 0 MVar and 0.02 MVar, respectively.
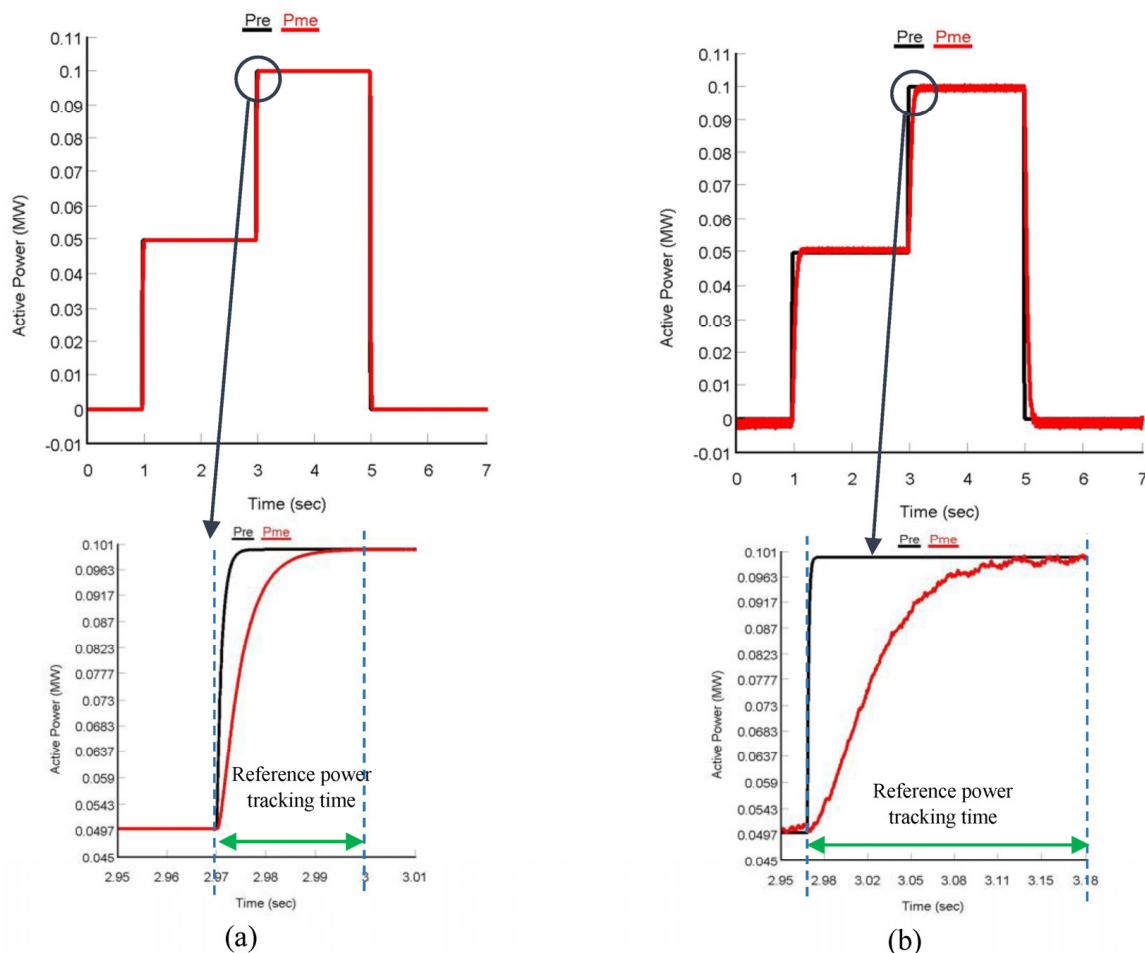
Figure 7. Real power tracking performance of (**a**) FLDPC method and (**b**) dq CCS-based power controller with PLL.

From Figure 7a, it is seen that, initially, real power reference was set to 0 MW, which was increased from 0 MW to 0.05 MW after 1 s. Then, it was set to 0.1 MW between 2.97 and 4.969 s, and the final reference was set to 0 MW again, between 4.97 and 7 s. For all the real power references, it was observed that the PV-VSI output real power, controlled by the proposed PVMT-based FLDPC, was tracking the real power references accurately. On the other hand, though from Figure 7b it seems that the conventional dq CCS-based power controller also tracked the reference powers, from the zoomed portion it is clear to see that the tracking speed of the proposed PLL-less PVMT-based FLDPC method is 0.03 s. This was 0.19 s faster than that of the conventional dq CCS-based power control method, whose real power reference tracking speed was 0.22 s. For reactive power, the reference power was kept to 0 MVar, initially, which increased to 0.01 MVar and 0.02 MVar at 1 s and 3 s, respectively. Finally, at 1 s reference reactive power decreased to 0 MVar. It can

be observed from Figure 8a that the VSI output reactive power controlled by the PVMT-based FLDPC method was following the reference reactive power accurately at different time intervals. In addition, the proposed PVMT-based FLDPC showed better tracking performance than that of CCS-based power controller, though the conventional CCS-based controller was able to track the reference reactive power, as shown in Figure 8b. According to the zoomed portion of Figure 8a,b, the time taken to reach a steady-state of reactive power by the proposed PVMT-based FLDPC was 0.03 s, where the conventional CCS-based power controller tracked it at 0.23 s. This was 0.20 s slower than the proposed controller.
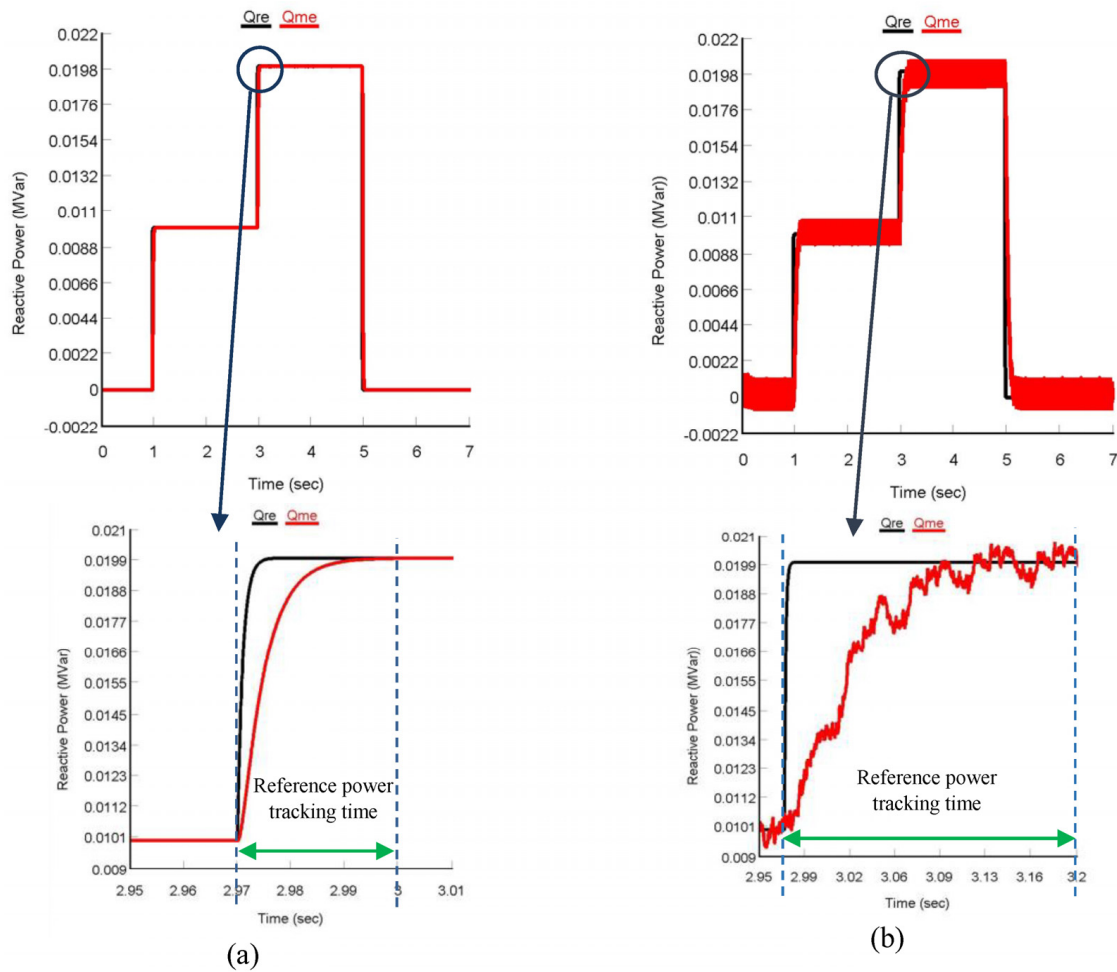
Figure 8. Reactive power tracking performance of (**a**) FLDPC method and (**b**) dq CCS based power controller with PLL.

5.1.2. Proposed Controller Steady-State Performance Analysis

In this section, the steady-state performance of the proposed PVMT-based FLDPC method is validated. From the results shown in Figures 9 and 10, it is clear that due to the use of the proposed PVMT-based FLDPC method, the ripples at VSI output power were significantly reduced. The time range considered for viewing the ripples in VSI output real and reactive power was 2.88–5 s. From Figure 9a, it can be observed that for the proposed PVMT-based FLDPC, very low ripple existed in the VSI real power output. However, a higher ripple was observed in the VSI real power output for the conventional PLL-based power controller, which ranged between 0.0984 and 0.1006 MW. Real power also did not follow the reference accurately, as seen from Figure 9b. For reactive power, it can be seen from Figure 10b that the ripple was very high for the conventional CCS-based power controller and it ranged from 0.019 to 0.0208 MVar. On the other hand, for the proposed PVMT-based FLDPC method, reactive power also had very low power ripple, as shown in Figure 10a.
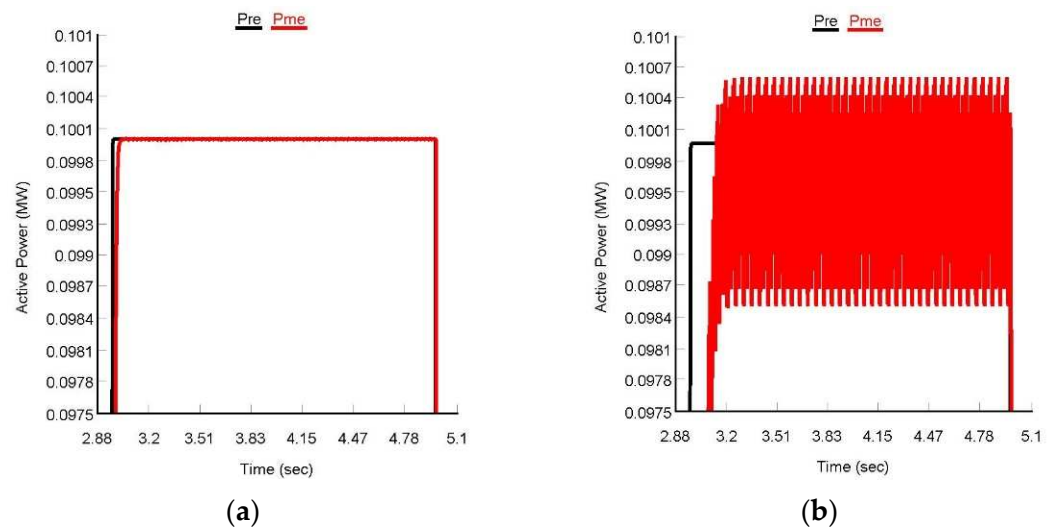
Figure 9. Real power steady-state performance of (**a**) FLDPC and (**b**) dq CCS-based power control method with PLL.
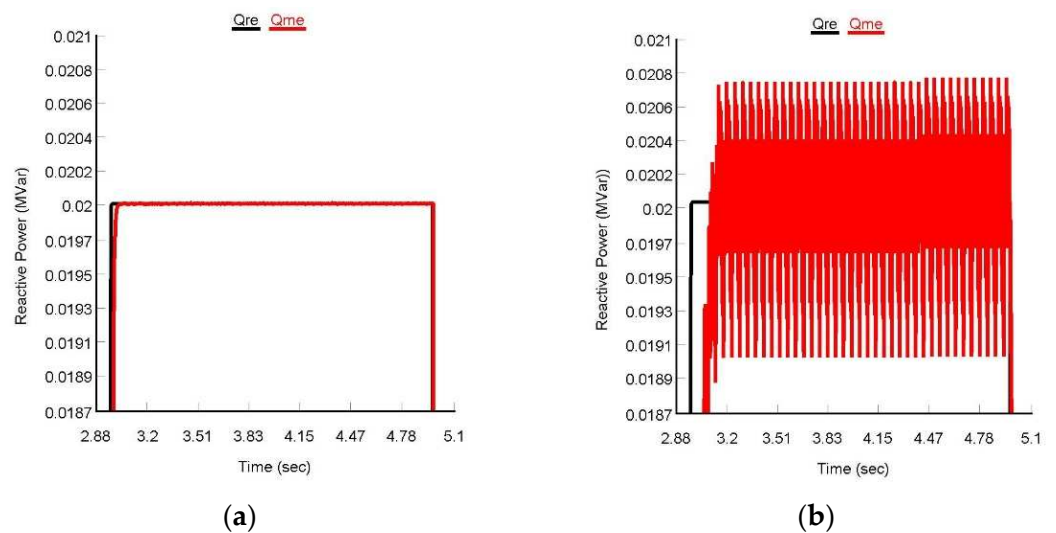

Figure 10. Reactive power steady-state performance of (**a**) FLDPC and (**b**) dq CCS-based power control method with PLL.

In Figures 11 and 12, the waveforms of the PV-VSI's output current and voltage are presented for both the controllers. From Figures 11a and 12a, it can be seen that for PLL-less PVMT-based FLDPC, the PV-VSI output voltage and current were sinusoidal in shape, and had negligible noises. In comparison, even though the PV-VSI output voltage and current for PLL-integrated CCS-based power controller were sinusoidal in shape, large distortion was observed, as shown in Figures 11b and 12b.

Further from Figure 13, it was observed that for both the controllers, the THD of the PV-VSI currents was less than 5%, which is in line with the IEC standard [44]; however, the current THD (4.967%) obtained by the PLL-CCS-based power control method was very high, compared with the PVMT-based FLDPC method's current THD (1.59%). As a result, oscillations in PV-VSI output power and current during steady-state were very low for PLL-less PVMT-based FLDPC, compared with the power control method based on PLL-integrated dq CCS.
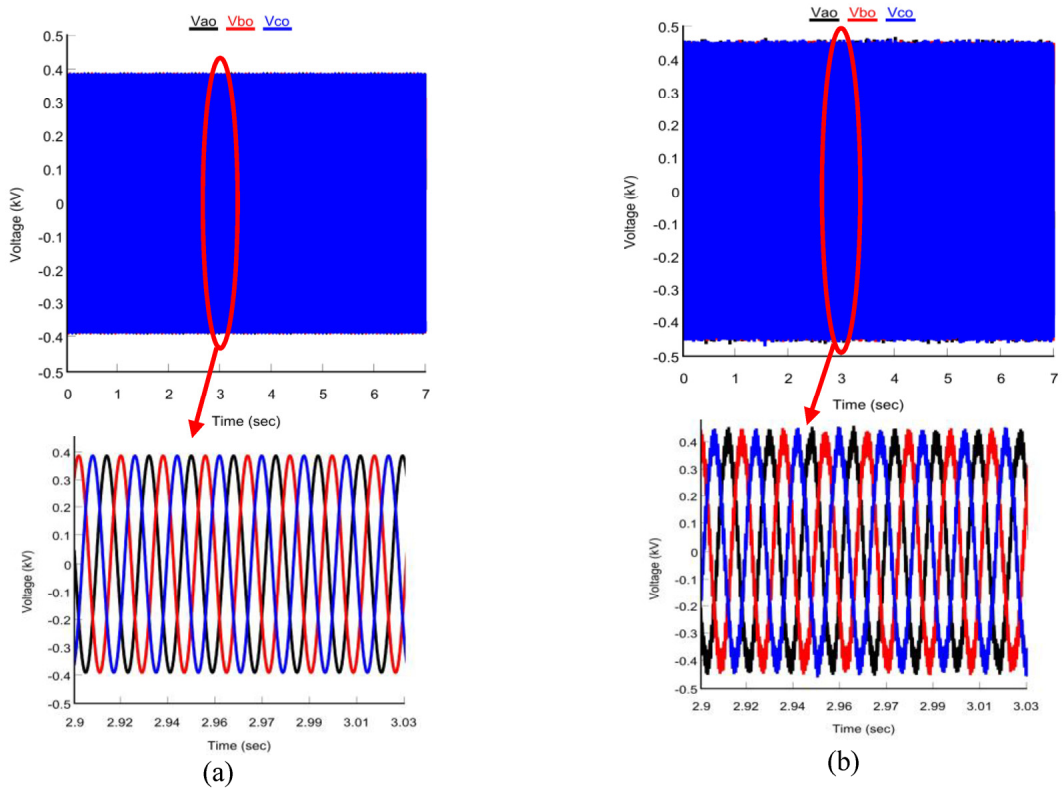
Figure 11. PV-VSI output voltage for (**a**) FLDPC method and (**b**) dq CCS-based power controller with PLL.
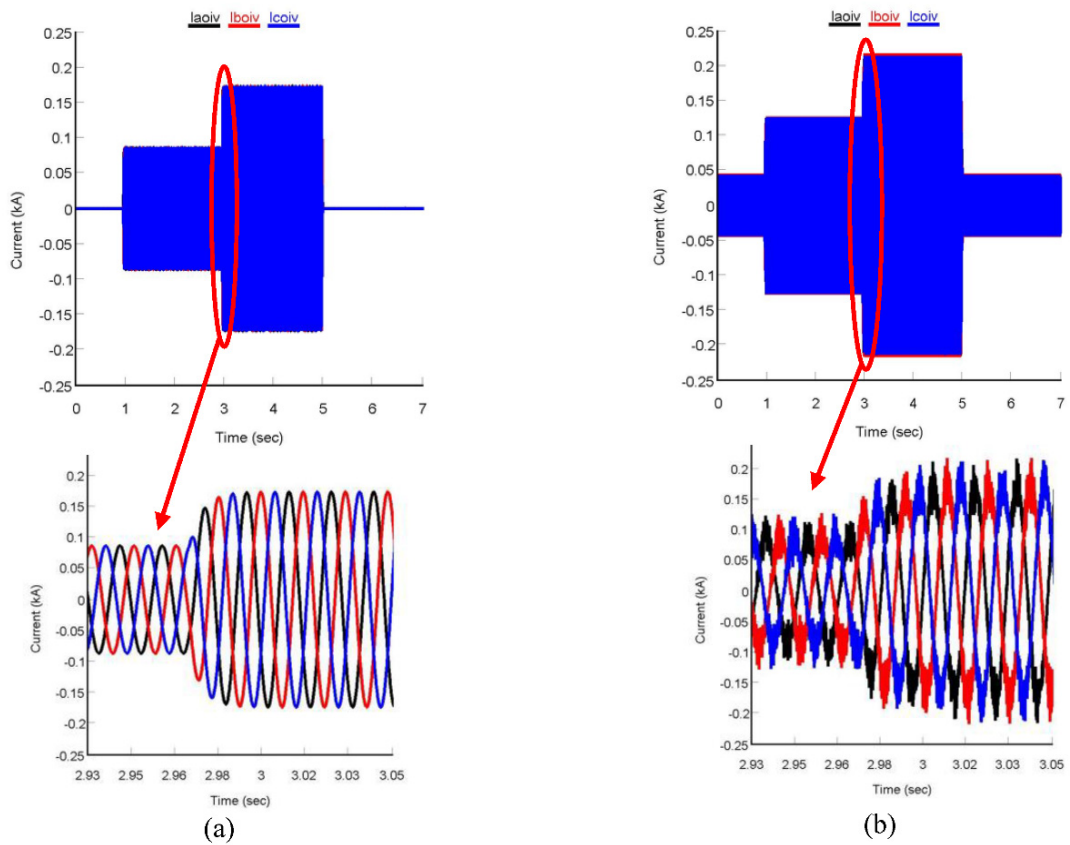

Figure 12. PV-VSI output current for (**a**) FLDPC method and (**b**) dq CCS-based power controller with PLL.
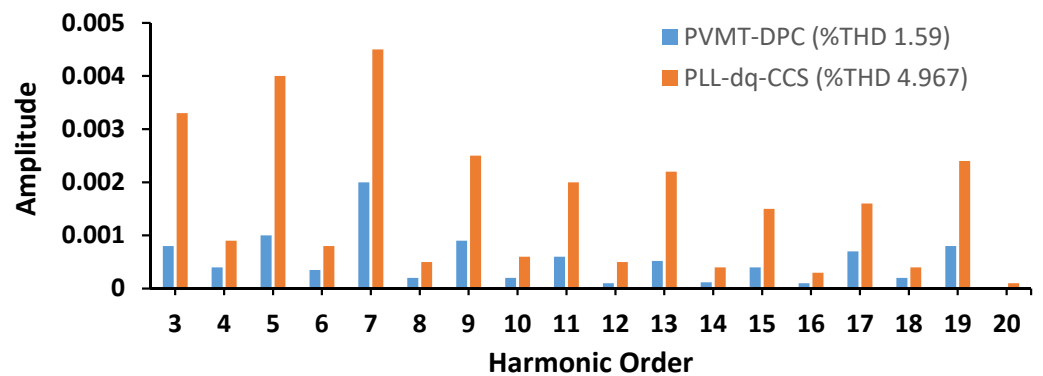
Figure 13. VSI output current THD for FLDPC and dq CCS-based power control method.

5.2. Case 2: Proposed Controllers Performance Analysis in Grid-Tied AC MG Application

It was essential to analyze the performance of the proposed PVMT-based FLDPC in grid-tied AC-MGs, to ensure that the controller was performing well in MG's different operating modes. In addition, the controller should be capable of operating in different real-world conditions such as varying load, and solar irradiation in MG. To verify these features in this section, the performance of the proposed PVMT-based FLDPC method was validated by varying both solar irradiation and load demand. Finally, a comparison is presented at the end of this section, to prove the superiority of the proposed FLDPC method over conventional MG power control methods for grid-tied VSIs. The results obtained after implementing the proposed controller for active power flow between different sources and loads are depicted in Figure 14 and Table 2. To regulate the power flow between different sources and load, a power management algorithm was adopted from [17].
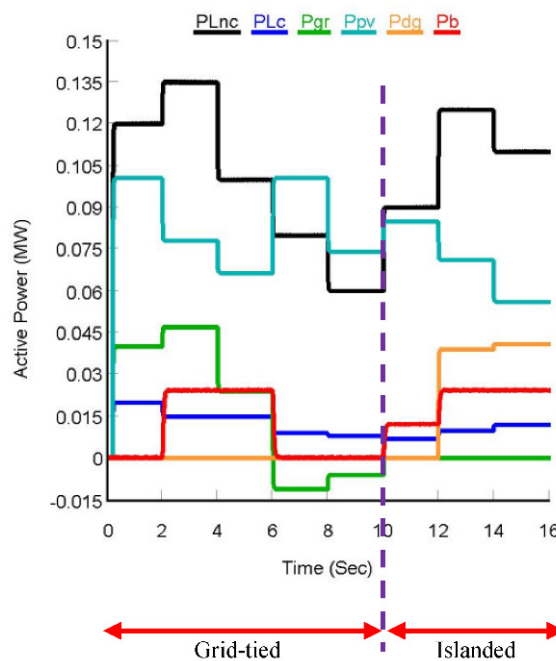

Figure 14. Active power flow from different power sources to loads.

The initial values of solar irradiation and varying load were set to 1000 W/m^2 and 0.14 MW (critical 0.02 MW + non-critical 0.12 MW, respectively). In between 0 and 2 s, PV was generating full power of 0.1 MW, which fulfilled 0.1 MW of the total load, and the remaining 0.04 MW demand was supplied by grid. At this period, the power from battery and diesel generator were nil. The solar irradiation was dropped to 850 W/m^2 between 2 and 4 s and, in contrast, load demand was increased to 0.15 MW. During this

period, PV provided a maximum of 0.078 MW power support to the load. Since PV power went down from the nominal value, the battery came into operation. In this case, the battery and grid supplied 0.025 MW and 0.047 MW power to fulfil the rest of the load demand. From 4 to 6 s, solar irradiation and load demand reduced to 700 W/m^2 and 0.115 MW, respectively. This situation compelled the grid to supply power of 0.024 MW to the load, since PV (0.066 MW) and battery (0.025 MW) together can support a maximum of 0.091 MW power. During 6–8 s, load demand decreased (0.089 MW) and solar irradiation increased (1000 W/m^2). Since the total load demand (0.089 MW) was less than the PV generation (0.1 MW), the remaining power (0.011 MW) from MG was delivered towards grid, and power from battery became zero. At 8 s, solar irradiation level reached 800 W/m^2 and the PV system generated a power of 0.074 MW. During 8–10 s, the load demand was 0.068 MW, which was supplied by the PV system fully, and remaining power (0.006 MW) of MG was supplied to the grid. For this period, power obtained from battery was nil and from 0 to 10 s, since MG was operating in grid-tied mode; therefore, the diesel generator did not provide any power support. The MG started operating in islanded mode at 10 s when the grid disconnected from the MG. During islanding, according to the power management algorithm, if PV and battery cannot fulfill the load demand, then the diesel generator will be activated. From 10 to 12 s, the generation of the PV system was 0.085 MW while the load demand was higher than the PV generation, i.e., 0.097 MW. As the battery had enough power (0.012 MW) to fulfil the remaining load demand, the diesel generator remained inactive during this duration. After 12 s, solar irradiation was reduced to 800 W/m^2 and load demand increased to 0.13 MW. During 12–14 s, the total generation (0.096 MW) from solar and battery (0.071 MW + 0.025 MW) was not sufficient to support the load demand. As a result, diesel generation turned on and supplied 0.034 MW power to fulfil the remaining load demand. Lastly, between 14 and 16 s, the PV generation further reduced to 0.056 MW. However, load demand did not reduce much (0.122 MW), which compelled the diesel generator to continue the power supply as PV, and the battery could not fulfill the total load demand.

Table 2. Summary of active power flow from different power sources to loads.

Duration (s)	Variables		Demand			Generation		
	Solar Irradiaion (W/m^2)	Total Load (MW)	Critical Load, P_{Lc} (MW)	Non-Critical Load, P_{Lnc} (MW)	Grid, P_{gr} (MW)	Solar, P_{pv} (MW)	Diesel Genrator, P_{dg} (MW)	Battery, P_b (MW)
0–2	1000	0.14	0.02	0.12	0.04	0.1	0	0
			Total = 0.14			Total = 0.14		
2–4	850	0.15	0.015	0.135	0.047	0.078	0	0.025
			Total = 0.15			Total = 0.15		
4–6	700	0.115	0.015	0.1	0.024	0.066	0	0.025
			Total = 0.115			Total = 0.115		
6–8	1000	0.089	0.009	0.08	−0.011	0.1	0	0
			Total = 0.089			Total = 0.089		
8–10	800	0.068	0.008	0.06	−0.006	0.074	0	0
			Total = 0.068			Total = 0.068		
10–12	900	0.097	0.007	0.09	0	0.085	0	0.012
			Total = 0.097			Total = 0.097		
12–14	750	0.13	0.01	0.12	0	0.071	0.034	0.025
			Total = 0.13			Total = 0.13		
14–16	600	0.122	0.012	0.11	0	0.056	0.041	0.025
			Total = 0.122			Total = 0.122		

In Figures 15 and 16, the output power, current and voltages of PV and battery VSIs are presented. Figure 15a shows that through the PV-VSI, the amount of delivered power was almost same as the power supplied by the PV with low ripple. In addition, the PV-VSI output current also had less distortion, as shown in Figure 15b, because the PVMT-based

FLDPC was implemented to control the PV-VSI. Similarly, from Figure 15c, it can be observed that the PV-VSI output voltage also had a pure sine wave shape, and negligible ripple. On the other hand, due to the use of PLL-integrated CCS-based controller battery VSI output power, current and voltage had high steady-state oscillations and distortions, which are presented in Figure 16a–c, respectively.
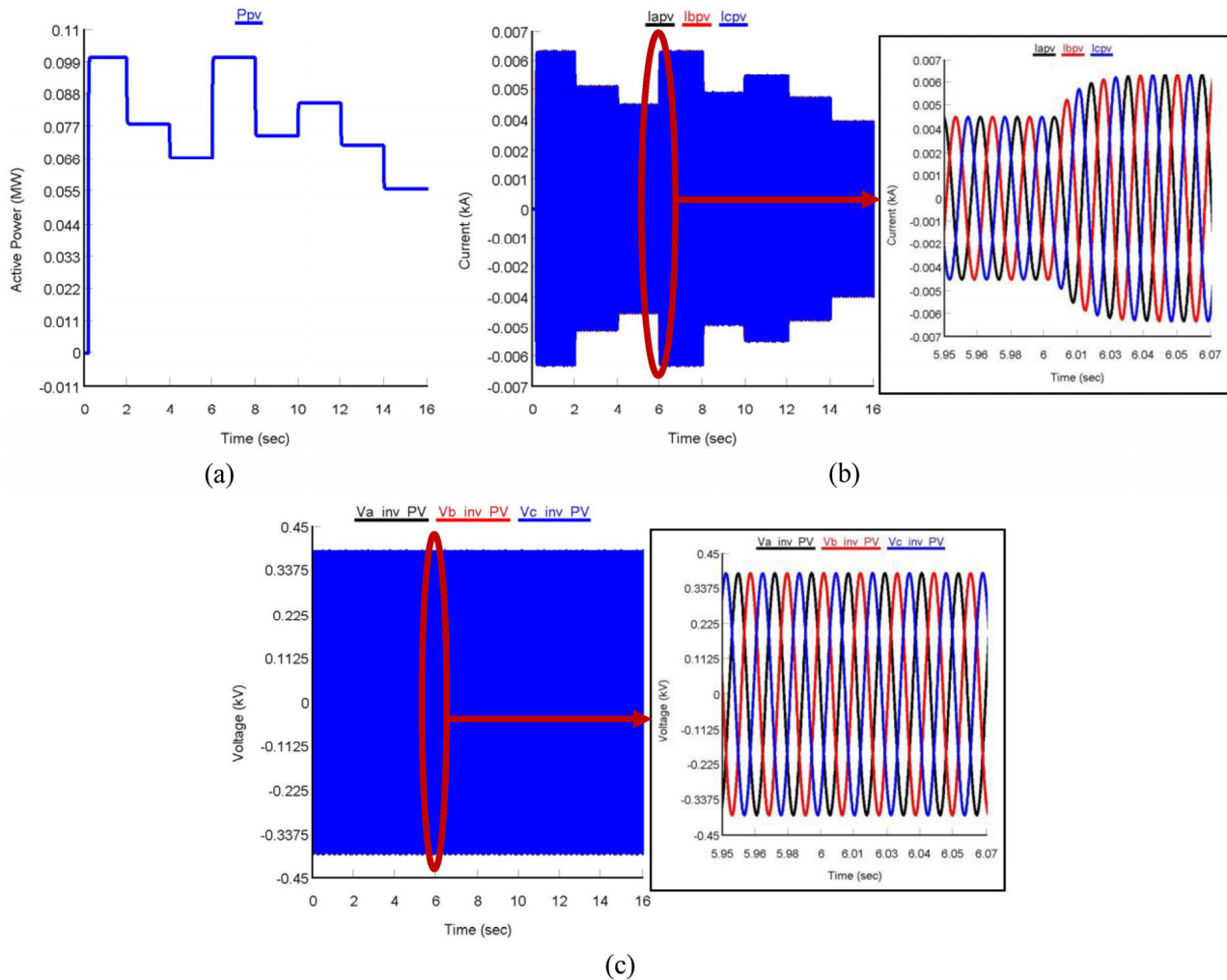

Figure 15. AC MG's PV-VSI output (**a**) power, (**b**) current and (**c**) voltage during solar irradiation and load changes.

The THD of PV and battery VSIs' output currents and voltages are depicted in Figure 17a–c, respectively. From the figures, it can be seen that the THD of PV-VSI output current was only 1.585%, whereas battery VSI output current THD was 4.718%, which was higher compared with PV-VSI current THD. In the case of voltages, battery VSI output voltage THD (2.592%) was higher than the PV-VSI output voltage THD (1.44%). The THDs were measured by considering three cycles (5.95–6 s) of current and voltage waveforms, as shown in the zoomed portion of Figure 15b,c and Figure 16b,c. Finally, in Figure 18a–c, grid power, current and voltage are presented, respectively. From the figures, it is clear that the power delivered or absorbed by the grid was according to the MG's requirement, and there were negligible ripples observed in the power. Furthermore, the shape of grid current and voltage were sinusoidal, which maintained 60 Hz frequency and had no distortions.
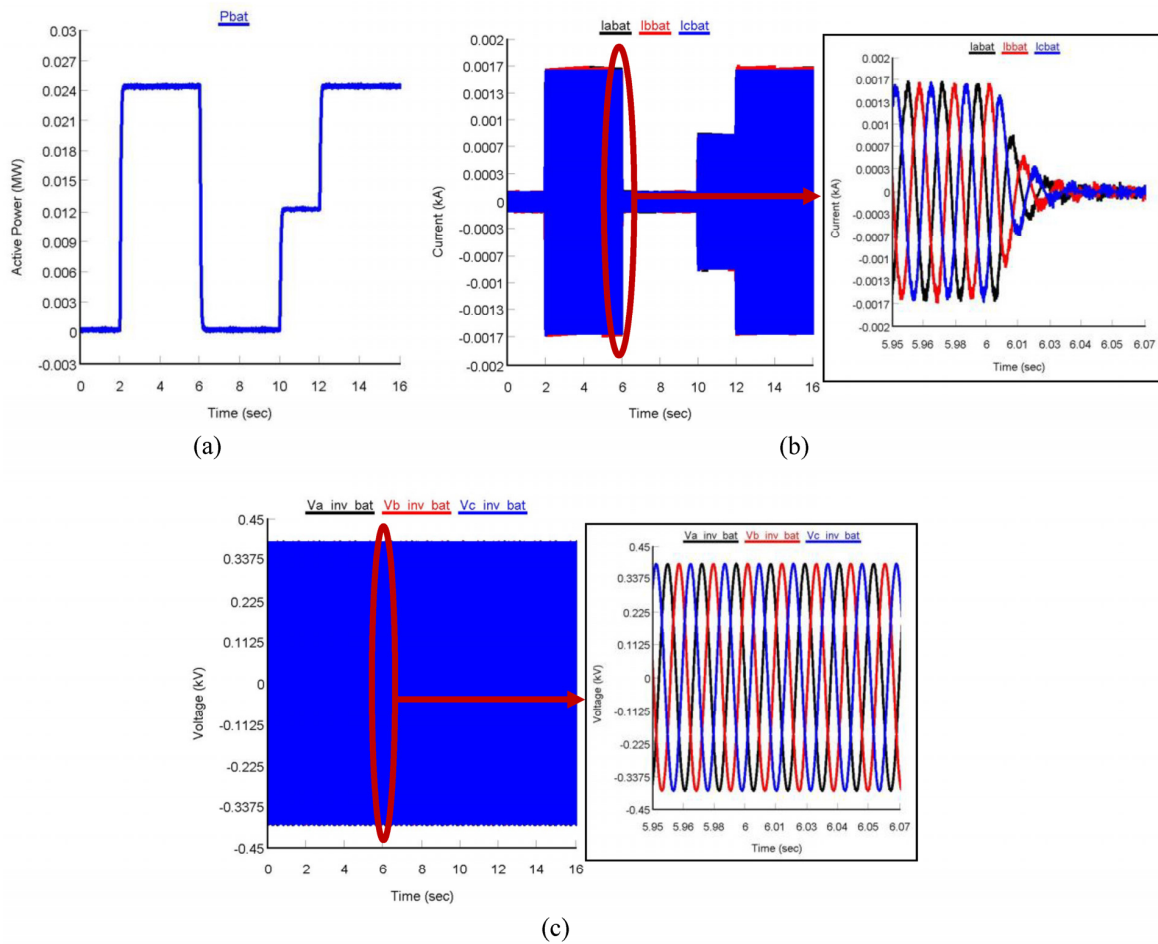
Figure 16. AC-MG's battery VSI output (**a**) power, (**b**) current and (**c**) voltage during solar irradiation and load changes.
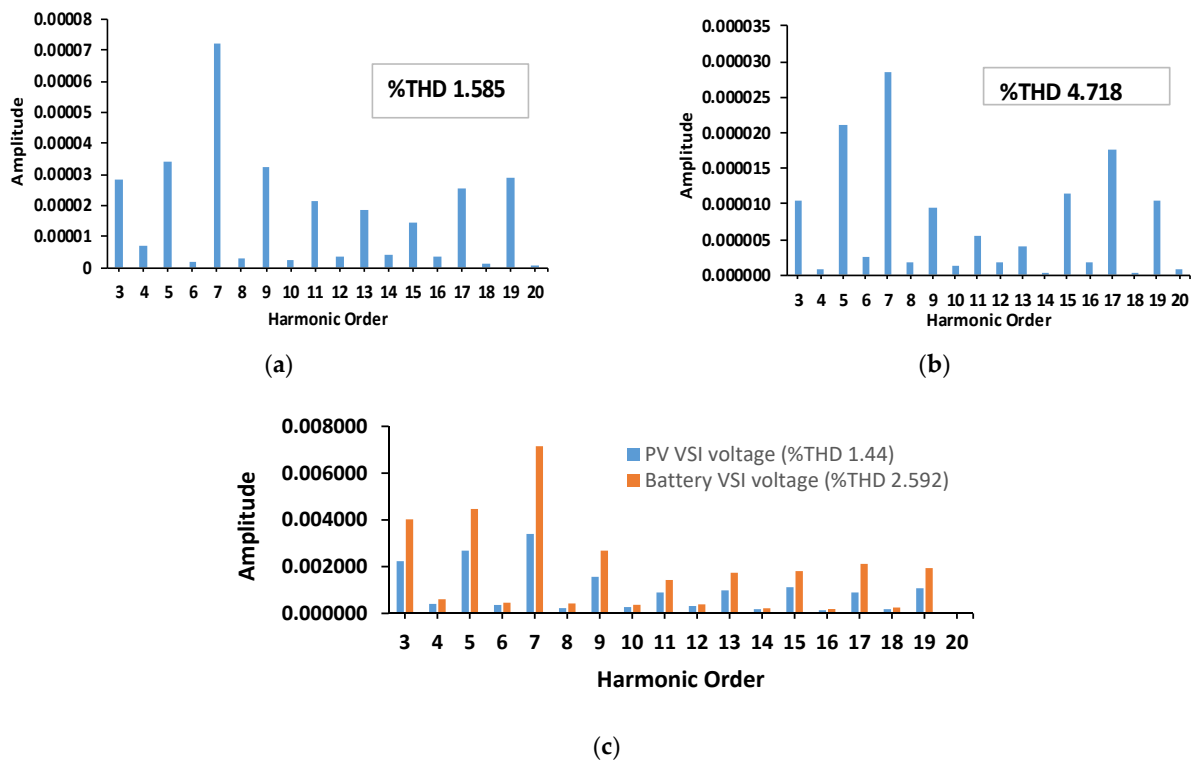

Figure 17. THD of (**a**) PV-VSI output current and (**b**) battery VSI output current and (**c**) PV and battery VSIs output voltage.
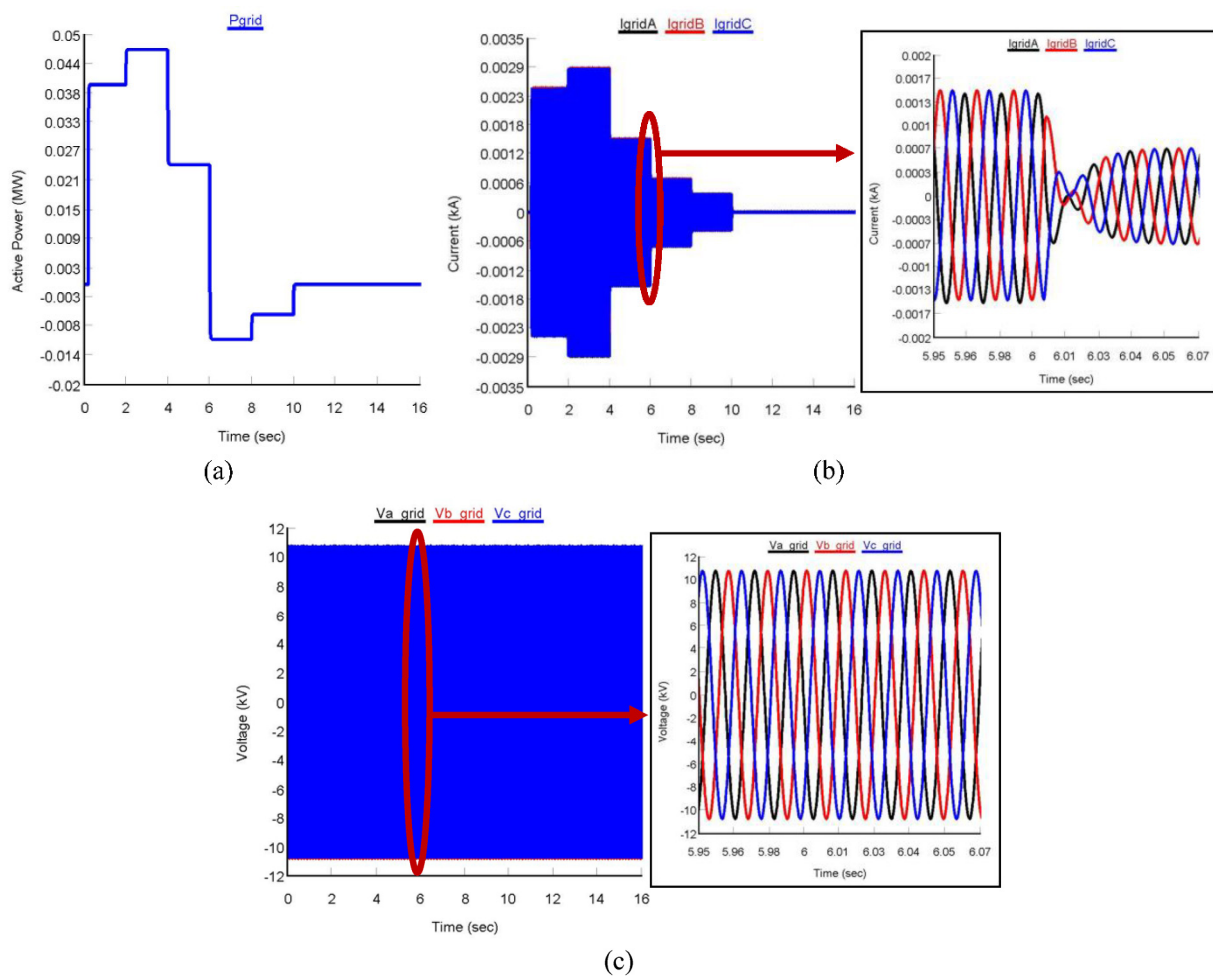
(a)

(b)

(c)

Figure 18. Grid (**a**) power, (**b**) current and (**c**) voltage during solar irradiation and load changes.

5.3. Comparison of the Proposed PVMT-Based FLDPC with Other MG Power Controllers

In this section, a comparative study is conducted between the proposed PLL-less PVMT-based FLDPC method and other grid-tied MG power control methods from [5–7,9,11]. The controllers were modelled in RSCAD, and their performances were tested by implementing them for controlling PV-VSI, as shown in Figure 1. The results were obtained by conducting real-time simulations in RTDS, and to make a fair comparison during simulations, all the parameters of MG were set similarly. The results of the comparative study are presented in Table 3 which shows that the proposed PVMT-based FLDPC method exhibited better performance than the other MG power control methods.

All the results are presented for the period of 1–2 s, when AC-MG was operating in grid-tied mode. For instance, the reference power tracking time of the proposed DPC controller was 0.20 s, 0.195 s, 0.185 s, 0.12 s, 0.14 s and 0.19 s faster than the controllers proposed in [5–7,9,11], respectively. Moreover, the PV-VSI output current THD was observed as 1.585%, approximately in the range of 2.264% to 3.289% lesser compared with the controllers in [5–7,9,11]. Furthermore, the power ripple in the output of PV-VSI controller by the proposed FLDPC was very low compared with the ripples that existed in the output power of PV-VSIs regulated by the controllers proposed in [5–7,9,11].

Table 3. Comparative analysis of the proposed PVMT-based FLDPC with other MG power controllers.

#	MG Power Controller	PLL System Presence	Active Power Ripples Range	Reference Power Tacking Time (s)	THD of VSI Output Voltage (%)	THD of VSI Output Current (%)
1	Proposed PVMT-based FLDPC	No	Very small (0.09999–0.10 MW)	0.03	1.44	1.585
2	Ref [5]	Yes	Large (0.0983–0.101 MW)	0.23	3.91	4.975
3	Ref [6]	Yes	Large (0.098–0.102 MW)	0.225	3.85	4.967
4	Ref [7]	Yes	Large (0.0985–0.1009 MW)	0.215	3.83	4.87
5	Ref [9]	Yes	Medium (0.0994–0.1003 MW)	0.15	2.59	3.95
6	Ref [11]	Yes	Large (0.0986–0.1009 MW)	0.22	3.80	4.76
7	Ref [27]	Yes	Medium (0.0993–0.1004 MW)	0.14	2.55	3.92

6. Discussion

From the real-time simulation results, it can be realized that the proposed PLL-less PVMT-based FLDPC method is capable of controlling the real and reactive power, irrespective of the load variability and solar irradiation variations. For different power references, it was observed that the PV-VSI output real power controlled by the proposed PVMT-based FLDPC was tracking the reference real and reactive powers accurately. On the other hand, though the conventional dq CCS-based power controller was also tracking the reference powers, the tracking speed of the proposed PLL-less PVMT-based FLDPC method was found to be faster than that of the conventional dq CCS-based power control method, because the proposed power control method PLL system and park transformation was omitted and the PCC voltage modulated the DPC method. Moreover, in the feedback controller, FLC was applied to minimize the errors between the reference powers and VSI output power, to ensure PV-VSI output powers were following the reference powers accurately.

Similar to the tracking performance the proposed PLL-less PVMT-based FLDPC method exhibited excellent performance during a steady-state. The proposed PVMT-based FLDPC overcame the steady-state oscillations issue, due to acquirement of an exponentially stable decoupled linear time invariant error dynamic by the proposed controller. It was observed that for the proposed PVMT-based FLDPC, there was very low ripple in the VSI real and reactive power output. However, there was higher ripple observed in the VSI power outputs for the conventional PLL-based power controller, and powers were also not following the reference accurately.

From the results presented in Table 2, it can be seen that the proposed controller also performed as outstanding while transferring power among different sources of MG, grid and load during MG's grid-tied, and islanding operating modes. From the real time simulation results, it was observed that during grid-tied mode the proposed PVMT-DPC method performed excellently by maintaining the required power flow between the MG and grid, as the PV system was capable of providing the power according to the solar irradiation changes. In addition, during the transition from grid-connected to islanded mode, the proposed PVMT-DPC method also showed a robust performance. Finally, from the comparison results presented in Table 3, it was observed that the proposed PLL-less PVMT-based FLDPC method integrated PV-VSI showed a better performance during both

the transient-state and the steady-state compared with the conventional power controller-integrated PV-VSIs connected to AC-MGs.

7. Conclusions

In this paper, a FLDPC scheme based on PVMT for a grid-tied MG's PV-VSI was introduced. The performance of the proposed power controller was validated by conducting real-time simulations using RTDS for two cases varying in both real and reactive power references, and in AC-MGs different operating modes. For case-1, the tracking and steady-state performance of the proposed FLDPC for a grid-tied PV-VSI was validated by changing real and reactive power references. On the other hand, for case-2 the performance of the proposed controller was validated for AC-MG's PV-VSI by varying the solar irradiation and load demand.

For case-1, real-time simulation results show that the proposed FLDPC method was able to track both real and reactive power to their reference powers accurately and quickly. The reference power tracking time required by the proposed FLDPC method for both real and reactive power was only 0.03 s, whereas the conventional PLL-integrated dq CCS-based power controller took 0.23 s, which was 0.20 s slower than the proposed controller. The proposed controller during steady-state also demonstrated outstanding performance as the ripples in the PV-VSI output power significantly reduced, and the THD of VSI output current achieved was 1.59%, which was well below the 5% set by the IEC standard. On the contrary, for a conventional PLL-integrated dq CCS-based power controller, the THD of VSI output current obtained was very high (4.975%) compared with the proposed FLDPC method.

Furthermore, for case-2, in MG application (grid-tied, and islanded operating modes), the proposed FLDPC method of PV-VSI showed an outstanding performance during the variation of solar irradiance and load. From the real-time simulation results, it was observed that during the grid-tied mode the proposed PVMT-based FLDPC method has performed excellently, by maintaining the required power flow between the MG and grid. Finally, a comparative study was conducted to prove the superiority of the proposed FLDPC method, with respect to other grid-tied MG power control methods. It was observed that the proposed FLDPC method outperformed all the other controllers, having a PI-based feedback controller and PLL-based synchronization methods, along with two control loops for parameters such as power ripples, THD and reference power tracking time.

In this work, the performance of the proposed FLDPC method was validated on AC-MG, which was connected to a healthy utility grid. In future, the performance of the FLDPC will also be validated for distorted grid conditions. Furthermore, for the grid re-synchronization process, the performance of the proposed FLDPC method was not validated. This will be conducted in the future.

Author Contributions: Conceptualization and methodology, S.A. (Shameem Ahmad) and M.K.; simulation and validation, S.A. (Shameem Ahmad), U.K.J., S.A. (Suhail Afzal) and A.P.; manuscript writing and editing, S.A. (Shameem Ahmad), S.M., H.M., M.K., S.A. (Suhail Afzal) and T.A.; supervision, S.M. and H.M. All authors have read and agreed to the published version of the manuscript.

Data Availability Statement: The data used in this research is enclosed within the manuscript. No external data sources are used in this research.

Conflicts of Interest: The authors declare no conflict of interest.

Nomenclature

VSI	Voltage source inverter
MG	Microgrid
PLL	Phase locked loop
DPC	Direct power control
FLC	Fuzzy logic controller
RTDS	Real time digital simulator
CCS	Current control scheme
PI	Proportional Integral
SOC	State of Charge
PVM	PCC voltage modulation
FLDPC	Fuzzy logic direct power control
PV	Photovoltaic
MPPT	Maximum power point tracker
BSS	Battery storage system
THD	Total harmonic distortion
SPWM	Sinusoidal pulse width modulation
MI	Modulation index
PCC	Point of common coupling
PVMT	PCC voltage modulation theory
ANN	Artificial neural network

Appendix A

Table A1. Parameters of AC MG components [38].

Parameters	Value
PV System (0.1 MW)	
PV modules connected in series	28
PV modules connected in parallel	68
Solar irradiation reference value	1000 W/m^2
Voltage at maximum power	17.3 V
Voltage at open circuit	21.5 V
Current at maximum power	3.05 A
PV module Temperature	25 °C
Current during short circuit (I_{sc})	3.33 A
Battery Storage (25 kWh)	
Nominal voltage per cell	3.6 V
Initial SOC of each cell	90%
Capacity of each cell	0.85 AH
State of charge (SOC) of battery	Greater than 60%
Cells connected in parallel	290
Cells connected in series	135
Diesel Generator (0.15 MVA)	
Machine power rating	0.15 MVA
Line to line voltage	0.48 kV

Table A1. *Cont.*

Parameters	Value
Grid	
Transformer primary/secondary voltage	0.48 kV/13.2 kV
Grid Voltage	13.2 kV
Frequency	60 Hz
Load	
Non-critical load	0.05–0.14 MW
Critical Load	0.005–0.015 MW
PV-VSI	
Voltage at DC link	975 V
PV-VSI switching frequency	2 kHz
DC-link capacitor	500 μF
$R_{a,b,c}$	0.1 Ω
$L_{a,b,c}$	5 mH
Battery VSI	
Voltage at DC link	975 V
PV-VSI switching frequency	2 kHz
DC-link capacitor	450 μF
$R_{a,b,c}$	0.01 Ω
$L_{a,b,c}$	5.5 mH
DC-DC Buck-Boost Converter (Battery Storage)	
Switching frequency	20 kHz
Capacitance	74 μF
Inductance	6 mH
DC-DC Boost Converter (PV System)	
Switching frequency	20 kHz
Capacitance	85 μF
Inductance	8 mH

Table A2. Values of PI controller coefficients for DC-link control.

Coefficients	Value
$K_{i,dc}$	0.015
$K_{p,dc}$	10

References

1. Bullich-Massagué, E.; Aragüés-Peñalba, M.; Prieto-Araujo, E.; Sumper, A.; Caire, R. Optimal feeder flow control for grid connected microgrids. *Int. J. Electr. Power Energy Syst.* **2019**, *112*, 144–155. [CrossRef]
2. Borhanazad, H.; Mekhilef, S.; Ganapathy, V.G.; Modiri-Delshad, M.; Mirtaheri, A. Optimization of micro-grid system using MOPSO. *Renew. Energy* **2014**, *71*, 295–306. [CrossRef]
3. Worku, M.Y.; Hassan, M.A.; Abido, M.A. Real time-based under frequency control and energy management of microgrids. *Electronics* **2020**, *9*, 1487. [CrossRef]
4. Hossain, M.A.; Pota, H.R.; Hossain, M.J.; Blaabjerg, F. Evolution of microgrids with converter-interfaced generations: Challenges and opportunities. *Int. J. Electr. Power Energy Syst.* **2019**, *109*, 160–186. [CrossRef]

5. Worku, M.Y.; Hassan, M.A.; Abido, M.A. Real time energy management and control of renewable energy based microgrid in grid connected and island modes. *Energies* **2019**, *12*, 276. [CrossRef]

6. Safa, A.; Berkouk, E.M.; Messlem, Y.; Gouichiche, A. A robust control algorithm for a multifunctional grid tied inverter to enhance the power quality of a microgrid under unbalanced conditions. *Int. J. Electr. Power Energy Syst.* **2018**, *100*, 253–264. [CrossRef]

7. Kaushal, J.; Basak, P. Power quality control based on voltage sag/swell, unbalancing, frequency, THD and power factor using artificial neural network in PV integrated AC microgrid. *Sustain. Energy Grids Netw.* **2020**, *23*, 100365. [CrossRef]

8. Smadi, I.A.; Albatran, S.; Alsyouf, M.A. Optimal control of a compact converter in an AC microgrid. *Electronics* **2018**, *7*, 102. [CrossRef]

9. Lou, G.; Gu, W.; Zhu, J.; Li, P.; Zhang, X. A novel control strategy for the seamless transfer of microgrids based on disturbance observer. *Int. J. Electr. Power Energy Syst.* **2020**, *118*, 105804. [CrossRef]

10. Abadlia, I.; Adjabi, M.; Bouzeria, H. Sliding mode based power control of grid-connected photovoltaic-hydrogen hybrid system. *Int. J. Hydrogen Energy* **2017**, *42*, 28171–28182. [CrossRef]

11. Feng, W.; Sun, K.; Guan, Y.; Guerrero, J.M.; Xiao, X. Active power quality improvement strategy for grid-connected microgrid based on hierarchical control. *IEEE Trans. Smart Grid* **2016**, *9*, 3486–3495. [CrossRef]

12. Adhikari, S.; Li, F. Coordinated Vf and PQ control of solar photovoltaic generators with MPPT and battery storage in microgrids. *IEEE Trans. Smart Grid* **2014**, *5*, 1270–1281. [CrossRef]

13. Mousavi, S.Y.M.; Jalilian, A.; Savaghebi, M.; Guerrero, J.M. Coordinated control of multifunctional inverters for voltage support and harmonic compensation in a grid-connected microgrid. *Electr. Power Syst. Res.* **2018**, *155*, 254–264. [CrossRef]

14. Go, S.-I.; Choi, J.-H. Design and dynamic modelling of pv-battery hybrid systems for custom electromagnetic transient simulation. *Electronics* **2020**, *9*, 1651. [CrossRef]

15. Sedaghati, R.; Shakarami, M.R. A novel control strategy and power management of hybrid PV/FC/SC/battery renewable power system-based grid-connected microgrid. *Sustain. Cities Soc.* **2019**, *44*, 830–843. [CrossRef]

16. Tang, X.; Zhang, D.; Xiao, D.; Li, M. Modeling and Stability Analysis of a Novel Voltage-Oriented Power Coordination Controlled Constant-Frequency AC Microgrid System. *Electronics* **2021**, *10*, 1935. [CrossRef]

17. Ahmad, S.; Mekhilef, S.; Mokhlis, H. DQ-axis Synchronous Reference Frame based PQ Control of Grid Connected AC Microgrid. In Proceedings of the 2020 IEEE International Conference on Computing, Power and Communication Technologies (GUCON), Greater Noida, India, 2–4 October 2020; pp. 842–847.

18. Lee, L.A.; Liu, C.C.; Xu, Y.; Schneider, K.P.; Tuffner, F.K.; Mo, K.; Ton, D.T. Dynamics and control of microgrids as a resiliency source. *Int. Trans. Electr. Energy Syst.* **2020**, *30*, e12610. [CrossRef]

19. Ali, Z.; Christofides, N.; Hadjidemetriou, L.; Kyriakides, E.; Yang, Y.; Blaabjerg, F. Three-phase phase-locked loop synchronization algorithms for grid-connected renewable energy systems: A review. *Renew. Sustain. Energy Rev.* **2018**, *90*, 434–452. [CrossRef]

20. Wang, X.; Harnefors, L.; Blaabjerg, F. Unified impedance model of grid-connected voltage-source converters. *IEEE Trans. Power Electron.* **2017**, *33*, 1775–1787. [CrossRef]

21. Wang, X.; Blaabjerg, F. Harmonic stability in power electronic-based power systems: Concept, modeling, and analysis. *IEEE Trans. Smart Grid* **2018**, *10*, 2858–2870. [CrossRef]

22. Harnefors, L.; Wang, X.; Yepes, A.G.; Blaabjerg, F. Passivity-based stability assessment of grid-connected VSCs—An overview. *IEEE J. Emerg. Sel. Top. Power Electron.* **2015**, *4*, 116–125. [CrossRef]

23. Gui, Y.; Kim, C.; Chung, C.C. Grid voltage modulated direct power control for grid connected voltage source inverters. In Proceedings of the 2017 American Control Conference (ACC), Seattle, WA, USA, 24–26 May 2017; pp. 2078–2084.

24. Hasanien, H.M.; Matar, M. A fuzzy logic controller for autonomous operation of a voltage source converter-based distributed generation system. *IEEE Trans. Smart Grid* **2014**, *6*, 158–165. [CrossRef]

25. Heydari, R.; Gheisarnejad, M.; Khooban, M.H.; Dragicevic, T.; Blaabjerg, F. Robust and fast voltage-source-converter (VSC) control for naval shipboard microgrids. *IEEE Trans. Power Electron.* **2019**, *34*, 8299–8303. [CrossRef]

26. Thao, N.G.M.; Uchida, K. Control the active and reactive powers of three-phase grid-connected photovoltaic inverters using feedback linearization and fuzzy logic. In Proceedings of the 2013 Australian Control Conference, Perth, Australia, 4–5 November 2013; pp. 133–140.

27. Omar, M.; El-Deib, A.; El Shafei, A.; Abdallah, M. Comparative study between PI and fuzzy-logic controllers for three-phase grid-connected photovoltaic systems. In Proceedings of the 2016 Eighteenth International Middle East Power Systems Conference (MEPCON), Cairo, Egypt, 27–29 December 2016; pp. 380–386.

28. Jamma, M.; Bennassar, A.; Barara, M.; Akherraz, M. Advanced direct power control for grid-connected distribution generation system based on fuzzy logic and artificial neural networks techniques. *Int. J. Power Electron. Drive Syst.* **2017**, *8*, 979. [CrossRef]

29. Islam, S.U.; Zeb, K.; Din, W.U.; Khan, I.; Ishfaq, M.; Hussain, A.; Busarello, T.D.C.; Kim, H.J. Design of robust fuzzy logic controller based on the levenberg marquardt algorithm and fault ride trough strategies for a grid-connected PV system. *Electronics* **2019**, *8*, 429. [CrossRef]

30. Shadoul, M.; Yousef, H.; Abri, R.A.; Al-Hinai, A. Adaptive Fuzzy Approximation Control of PV Grid-Connected Inverters. *Energies* **2021**, *14*, 942. [CrossRef]

31. Tahri, G.; Foitih, Z.A.; Tahri, A. Fuzzy logic control of active and reactive power for a grid-connected photovoltaic system using a three-level neutral-point-clamped inverter. *Int. J. Power Electron. Drive Syst.* **2021**, *12*, 453–462. [CrossRef]

32. Teekaraman, Y.; Kuppusamy, R.; Baghaee, H.R.; Vukobratović, M.; Balkić, Z.; Nikolovski, S. Current Compensation in Grid-Connected VSCs using Advanced Fuzzy Logic-based Fluffy-Built SVPWM Switching. *Energies* **2020**, *13*, 1259. [CrossRef]

33. Gui, Y.; Wang, X.; Blaabjerg, F. Vector current control derived from direct power control for grid-connected inverters. *IEEE Trans. Power Electron.* **2018**, *34*, 9224–9235. [CrossRef]

34. Gui, Y.; Kim, C.; Chung, C.C.; Guerrero, J.M.; Guan, Y.; Vasquez, J.C. Improved direct power control for grid-connected voltage source converters. *IEEE Trans. Ind. Electron.* **2018**, *65*, 8041–8051. [CrossRef]

35. Gui, Y.; Lee, G.H.; Kim, C.; Chung, C.C. Direct power control of grid connected voltage source inverters using port-controlled Hamiltonian system. *Int. J. Control Autom. Syst.* **2017**, *15*, 2053–2062. [CrossRef]

36. Choi, D.-K.; Lee, K.-B. Dynamic performance improvement of AC/DC converter using model predictive direct power control with finite control set. *IEEE Trans. Ind. Electron.* **2014**, *62*, 757–767. [CrossRef]

37. Gao, Y.; Ai, Q. Distributed cooperative optimal control architecture for AC microgrid with renewable generation and storage. *Int. J. Electr. Power Energy Syst.* **2018**, *96*, 324–334. [CrossRef]

38. Ahmad, S.; Mekhilef, S.; Mokhlis, H. An improved power control strategy for grid-connected hybrid microgrid without park transformation and phase-locked loop system. *Int. Trans. Electr. Energy Syst.* **2021**, *31*, e12922. [CrossRef]

39. Ahmad, S.; Rashid, M.T.; Ferdowsy, C.S.; Islam, S.; Mahmood, A.H. A technical comparison among different PV-MPPT algorithms to observe the effect of fast changing solar irradiation. In Proceedings of the 2015 IEEE International WIE Conference on Electrical and Computer Engineering (WIECON-ECE), Dhaka, Bangladesh, 19–20 December 2015; pp. 155–158.

40. Akram, U.; Khalid, M.; Shafiq, S. Optimal sizing of a wind/solar/battery hybrid grid-connected microgrid system. *IET Renew. Power Gener.* **2017**, *12*, 72–80. [CrossRef]

41. Sen, S.; Kumar, V. Microgrid modelling: A comprehensive survey. *Annu. Rev. Control* **2018**, *46*, 216–250. [CrossRef]

42. Filizadeh, S.; Gole, A.M.; Woodford, D.A.; Irwin, G.D. An optimization-enabled electromagnetic transient simulation-based methodology for HVDC controller design. *IEEE Trans. Power Deliv.* **2007**, *22*, 2559–2566. [CrossRef]

43. Ahmad, S.; Albatsh, F.M.; Mekhilef, S.; Mokhlis, H. Fuzzy based controller for dynamic Unified Power Flow Controller to enhance power transfer capability. *Energy Convers. Manag.* **2014**, *79*, 652–665. [CrossRef]

44. Photovoltaic, I. Systems. Characteristics of the Utility Interface. *IEC Std.* **2004**, *61*, 727.

Article

A Novel Three-Phase Harmonic Power Flow Algorithm for Unbalanced Radial Distribution Networks with the Presence of D-STATCOM Devices

Raavi Satish [1], Kanchapogu Vaisakh [2], Almoataz Y. Abdelaziz [3] and Adel El-Shahat [4,*]

[1]   Department of Electrical & Electronics Engineering, Anil Neerukonda Institute of Technology and Sciences (A), Visakhapatnam 531162, India; satish.eee@anits.edu

[2]   Department of Electrical Engineering, Andhra University, Visakhapatnam 530003, India; prof.kvaisakh@andhrauniversity.edu.in

[3]   Department of Electrical Power & Machines, Faculty of Engineering, Ain Shams University, Cairo 11517, Egypt; almoataz_abdelaziz@eng.asu.edu.eg

[4]   Energy Technology Program, School of Engineering Technology, Purdue University, West Lafayette, IN 47907, USA

*   Correspondence: asayedah@purdue.edu

Abstract: Due to the rapid advancement in power electronic devices in recent years, there is a fast growth of non-linear loads in distribution networks (DNs). These non-linear loads can cause harmonic pollution in the networks. The harmonic pollution is low, and the resonance problem is absent in distribution static synchronous compensators (D-STATCOM), which is the not case in traditional compensating devices such as capacitors. The power quality issue can be enhanced in DNs with the interfacing of D-STATCOM devices. A novel three-phase harmonic power flow algorithm (HPFA) for unbalanced radial distribution networks (URDN) with the existence of linear and non-linear loads and the integration of a D-STATCOM device is presented in this paper. The bus number matrix (BNM) and branch number matrix (BRNM) are developed in this paper by exploiting the radial topology in DNs. These matrices make the development of HPFA simple. Without D-STATCOM integration, the accuracy of the fundamental power flow solution and harmonic power flow solution are tested on IEEE−13 bus URDN, and the results are found to be precise with the existing work. Test studies are conducted on the IEEE−13 bus and the IEEE−34 bus URDN with interfacing D-STATCOM devices, and the results show that the fundamental r.m.s voltage profile is improved and the fundamental harmonic power loss and total harmonic distortion (THD) are reduced.

Keywords: unbalanced distribution networks; linear loads; non-linear loads; total harmonic distortion; harmonic power flow

1. Introduction

In terms of harmonics, the loads are classified into two types, linear loads and non-linear loads. A linear load [1] is one which, when supplied by an AC source at fundamental frequency, can produce only fundamental AC currents. Non-linear loads, however, generate harmonic currents. The use of non-linear loads can inject harmonic currents into URDN. These harmonic injections can cause overheating of the equipment, insulation stress on winding in electric machines, added power loss in the equipment, and interference with the communication. Therefore, HPFAs are essential for finding the harmonic distortion level on URDN. In [2], based on current injection, graph theory, and the sparse matrix technique, a three-phase HPFA is proposed. The authors of [3] utilized the decoupled harmonic power flow (DHPF) algorithm to present the results of harmonic power flow calculations. In [4,5], a forward/backward-based HPFA for DN is proposed that considered the special topology of radial distribution networks (RDN). The authors of [6] developed an iterative time-dependent, computer-aided HPFA by combining the time-dependent cross-coupled

harmonic model. To obtain this model, large data are received from the practical DNs. Tracing THD in secondary RDN with photovoltaic uncertainties by multiphase HPFA is discussed in [7]. The authors of [8] propose a new combined analytical technique (CAT) for HPFA in the presence of correlated input uncertainties from photovoltaic (PV) systems in RDN. In [9], static capacitors are allocated in shunt along RDN using a Cuckoo search optimization method. For allocating and sizing of capacitors optimally, a flower pollination algorithm is proposed in [10].In [11,12], a novel three-phase power flow algorithm for URDN with multiple integrations of distributed generations (DGs) and a D-STATCOM device is presented. In [13], an electrical energy management in unbalanced distribution networks using virtual power plant concept is presented. In [14], an efficient multi-objective optimization approach based on the supervised big bang–big crunch method for the optimal planning of a dispatchable distributed generator is presented. This approach aims to enhance the system performance indices by the optimal sizing and placement of distributed generators connected to balanced/unbalanced distribution networks. The optimal planning of distributed generators in unbalanced distribution networks using a modified firefly method is presented in [15].

The authors of [16] examine the utilization of D-STATCOM without a capacitor to compensate for power quality in DNs. The optimal D-STATCOM allocation in DNs is discussed in [17,18]. In [19], an optimal algorithm to control a three-phase D-STATCOM is proposed. This algorithm can give harmonic compensation as well as reactive power compensation in linear and non-linear loads, which are connected in three-phase. In [20], for minimizing the total real power loss in DNs with the interfacing of DGs, plug-in-hybrid electric vehicles (PHEVs), and D-STATCOM, a genetic algorithm is proposed. A control technique is developed in [21] for D-STATCOM for extracting the fundamental weight components from non-sinusoidal load currents to produce grid reference currents. For harmonics elimination, the injection of reactive power and balancing of load, this D-STATCOM is developed. The D-STATCOM's performance is examined in different working modes. The combination of two problems such as the reconfiguration and interfacing of D-STATCOM can be solved by using the grey wolf optimization (GWO) method proposed in [22].

The proposed power flow algorithm (PFA) can give both fundamental and harmonic solutions. The solution of the fundamental power flow algorithm (FPFA) discussed in this paper is used in modelling the linear and non-linear loads for HPFA. The BNM and BRNM developed in this paper make the implementation of the PFA simple. The bus numbers and branch numbers of newly created sections of RDN are stored in BNM and BRNM, respectively. This paper is arranged in the following order. The network components' modelling is addressed in Section 2. The algorithm to develop BNM and BRNM is discussed in Section 3. In Section 4, the three-phase HPFA with the integration of the D-STATCOM device is discussed. Section 5 presents the test studies and discussions on the IEEE−13 bus and IEEE−34 bus URDN. Section 6 discusses the concluding remarks.

2. Network Components and Their Modeling

The URDN includes the main components such as lines, three-phase transformers, three-phase capacitor banks, and loads. These components are briefly modeled in this section.

2.1. Overhead or Underground Distribution Lines

With the Carson's equations presented in [23], the primitive impedance matrices for three-phase overhead and underground lines can be formed. For a grounded neural system, these matrices are reduced to phase impedance matrices of 3×3 size using Kron reduction. Figure 1 shows the three-phase distribution line model, and its shunt admittance

is neglected due to its small effect. The phase impedance matrix for the line section 'jk' is given in Equation (1).

$$[Z_{abc}]_{jk} = \begin{bmatrix} Z_{aa} & Z_{ab} & Z_{ac} \\ Z_{ba} & Z_{bb} & Z_{bc} \\ Z_{ca} & Z_{cb} & Z_{cc} \end{bmatrix}_{jk} \tag{1}$$
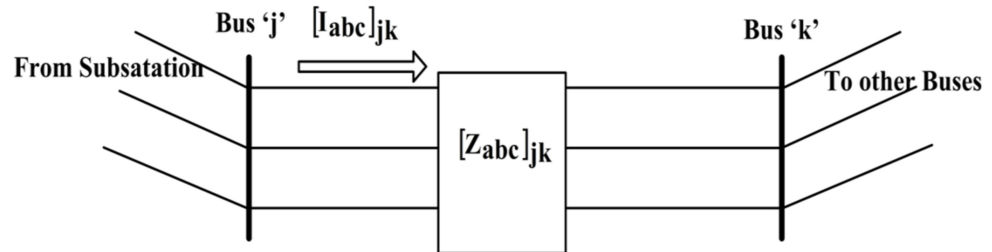

Figure 1. A sample three-phase distribution line.

From Figure 1, the relationship between the phase voltage matrices of bus-j and bus-k is given in Equation (2):

$$\begin{bmatrix} V_a \\ V_b \\ V_c \end{bmatrix}_k = \begin{bmatrix} V_a \\ V_b \\ V_c \end{bmatrix}_j - \begin{bmatrix} Z_{aa} & Z_{ab} & Z_{ac} \\ Z_{ba} & Z_{bb} & Z_{bc} \\ Z_{ca} & Z_{cb} & Z_{cc} \end{bmatrix}_{jk} \cdot \begin{bmatrix} I_a \\ I_b \\ I_c \end{bmatrix}_{jk} \tag{2}$$

The reactance of line is regarded as proportionate to the harmonic order for HPFA. For h-order harmonic frequency, the self-impedance of phase 'a' is given in Equation (3),

$$(Z_{aa})^h = R_{aa} + j \cdot h \cdot X_{aa} \tag{3}$$

2.2. Loads

The phase current matrix and line current matrix serving the different types of three-phase loads are outlined in Table 1. Detailed discussion on Table 1 is provided in [23].

2.2.1. Linear Loads

These loads produce only fundamental sinusoidal response upon supplied by sinusoidal source. The liner loads can be modelled in several ways [1]. Each model will show a different impact on harmonic analysis. The impedance modelling of these loads is taken as series combination of R and X.

2.2.2. Non-Linear Loads

With the harmonic spectrum of non-linear loads and their load current obtained from the fundamental power flow, these loads are modelled as constant current sources [24]. The magnitude of the current source is obtained with Equation (4), and its phase angle is obtained with Equation (5):

$$I_h = I_{rated} \frac{I_{h\_spectrum}}{I_{1\_spectrum}} \tag{4}$$

The phase angle of the current source is obtained as:

$$\theta_h = \theta_{h\_spectrum} + h\left(\theta_1 - \theta_{h\_spetrum}\right) \tag{5}$$

where:

θ_1 : Phase angle of the rated current at fundamental frequency;

$\theta_{h\_spectrum}$: Phase angle of the harmonic source current spectrum.

Table 1. Load modelling.

	Wye Connection	Delta Connection
Phase voltage matrix and specified load matrix at bus.	$\begin{bmatrix} \lvert V_{an} \rvert \angle \delta_a \\ \lvert V_{bn} \rvert \angle \delta_b \\ \lvert V_{cn} \rvert \angle \delta_c \end{bmatrix}, \begin{bmatrix} \lvert S_a \rvert \angle \theta_a \\ \lvert S_b \rvert \angle \theta_b \\ \lvert S_c \rvert \angle \theta_c \end{bmatrix}$	$\begin{bmatrix} \lvert V_{ab} \rvert \angle \delta_{ab} \\ \lvert V_{bc} \rvert \angle \delta_{bc} \\ \lvert V_{ca} \rvert \angle \delta_{ca} \end{bmatrix}, \begin{bmatrix} \lvert S_{ab} \rvert \angle \theta_{ab} \\ \lvert S_{bc} \rvert \angle \theta_{bc} \\ \lvert S_{ca} \rvert \angle \theta_{ca} \end{bmatrix}$
Phase current matrix serving constant power load	$\begin{bmatrix} IL_a \\ IL_b \\ IL_c \end{bmatrix} = \begin{bmatrix} \left(\frac{S_a}{V_{an}}\right)^* \\ \left(\frac{S_b}{V_{bn}}\right)^* \\ \left(\frac{S_c}{V_{cn}}\right)^* \end{bmatrix}$	$\begin{bmatrix} IL_{ab} \\ IL_{bc} \\ IL_{ca} \end{bmatrix} = \begin{bmatrix} \left(\frac{S_{ab}}{V_{ab}}\right)^* \\ \left(\frac{S_{bc}}{V_{bc}}\right)^* \\ \left(\frac{S_{ca}}{V_{ca}}\right)^* \end{bmatrix}$
Phase current matrix serving the constant impedance load	$\begin{bmatrix} ZL_a \\ ZL_b \\ ZL_c \end{bmatrix} = \begin{bmatrix} \frac{\lvert V_{an} \rvert^2}{S_a^*} \\ \frac{\lvert V_{bn} \rvert^2}{S_b^*} \\ \frac{\lvert V_{cn} \rvert^2}{S_c^*} \end{bmatrix}$ $\begin{bmatrix} IL_a \\ IL_b \\ IL_c \end{bmatrix} = \begin{bmatrix} \frac{V_{an}}{ZL_a} \\ \frac{V_{bn}}{ZL_b} \\ \frac{V_{cn}}{ZL_c} \end{bmatrix}$	$\begin{bmatrix} ZL_{ab} \\ ZL_{bc} \\ ZL_{ca} \end{bmatrix} = \begin{bmatrix} \frac{\lvert V_{ab} \rvert^2}{S_{ab}^*} \\ \frac{\lvert V_{bc} \rvert^2}{S_{bc}^*} \\ \frac{\lvert V_{ca} \rvert^2}{S_{ca}^*} \end{bmatrix}$ $\begin{bmatrix} IL_{ab} \\ IL_{bc} \\ IL_{ca} \end{bmatrix} = \begin{bmatrix} \frac{V_{ab}}{ZL_{ab}} \\ \frac{V_{bc}}{ZL_{bc}} \\ \frac{V_{ca}}{ZL_{ca}} \end{bmatrix}$
Phase current matrix serving the constant current load	$\begin{bmatrix} IL_a \\ IL_b \\ IL_c \end{bmatrix} = \begin{bmatrix} \lvert IL_a \rvert \angle (\delta_a - \theta_a) \\ \lvert IL_b \rvert \angle (\delta_b - \theta_b) \\ \lvert IL_c \rvert \angle (\delta_c - \theta_c) \end{bmatrix}$	$\begin{bmatrix} IL_{ab} \\ IL_{bc} \\ IL_{ca} \end{bmatrix} = \begin{bmatrix} \lvert IL_{ab} \rvert \angle (\delta_{ab} - \theta_{ab}) \\ \lvert IL_{bc} \rvert \angle (\delta_{bc} - \theta_{bc}) \\ \lvert IL_{ca} \rvert \angle (\delta_{ca} - \theta_{ca}) \end{bmatrix}$
Line current matrix entering the load	$\begin{bmatrix} IL_a \\ IL_b \\ IL_c \end{bmatrix}$	$\begin{bmatrix} IL_a \\ IL_b \\ IL_c \end{bmatrix} = \begin{bmatrix} 1 & 0 & -1 \\ -1 & 1 & 0 \\ 0 & -1 & 1 \end{bmatrix} \cdot \begin{bmatrix} IL_{ab} \\ IL_{bc} \\ IL_{ca} \end{bmatrix}$
Distributed Loads	Create a duplicate node at a distance of one-fourth the length from the sending end and connect a two-third of lode. At the receiving end one-third of load is connected.	

2.3. Capacitor Banks

Modelling of the capacitor banks is presented in Table 2.

Table 2. Capacitor banks modeling.

	Wye Connected	Delta Connected
Phase voltage matrix and specified reactive power matrix at bus.	$\begin{bmatrix} \lvert V_{an} \rvert \angle \theta_a \\ \lvert V_{bn} \rvert \angle \theta_b \\ \lvert V_{cn} \rvert \angle \theta_c \end{bmatrix} \begin{bmatrix} Q_a \\ Q_b \\ Q_c \end{bmatrix}$	$\begin{bmatrix} \lvert V_{ab} \rvert \angle \theta_{ab} \\ \lvert V_{bc} \rvert \angle \theta_{bc} \\ \lvert V_{ca} \rvert \angle \theta_{ca} \end{bmatrix} \begin{bmatrix} Q_{ab} \\ Q_{bc} \\ Q_{ca} \end{bmatrix}$
Phase current matrix serving the capacitor bank	$[B_{abc}] = \begin{bmatrix} \frac{Q_a}{\lvert V_a \rvert^2} \\ \frac{Q_b}{\lvert V_b \rvert^2} \\ \frac{Q_c}{\lvert V_c \rvert^2} \end{bmatrix}$ $\begin{bmatrix} IC_a \\ IC_b \\ IC_c \end{bmatrix} = \begin{bmatrix} j \cdot B_a \cdot V_{an} \\ j \cdot B_b \cdot V_{bn} \\ j \cdot B_c \cdot V_{cn} \end{bmatrix}$	$[B_{abc}] = \begin{bmatrix} \frac{Q_{ab}}{\lvert V_{ab} \rvert^2} \\ \frac{Q_{bc}}{\lvert V_{bc} \rvert^2} \\ \frac{Q_{ca}}{\lvert V_{ca} \rvert^2} \end{bmatrix}$ $\begin{bmatrix} IC_{ab} \\ IC_{bc} \\ IC_{ca} \end{bmatrix} = \begin{bmatrix} j \cdot B_{ab} \cdot V_{ab} \\ j \cdot B_{bc} \cdot V_{bc} \\ j \cdot B_{ca} \cdot V_{ca} \end{bmatrix}$
Line current matrix serving the capacitor bank	$\begin{bmatrix} IC_a \\ IC_b \\ IC_c \end{bmatrix}$	$\begin{bmatrix} IC_a \\ IC_b \\ IC_c \end{bmatrix} = \begin{bmatrix} 1 & 0 & -1 \\ -1 & 1 & 0 \\ 0 & -1 & 1 \end{bmatrix} \cdot \begin{bmatrix} IC_{ab} \\ IC_{bc} \\ IC_{ca} \end{bmatrix}$

For HPFA, the capacitive susceptance (B) is to be multiplied with 'h' for 'h' order frequency.

2.4. Tree-Phase Transformer

The fundamental voltage and current relationships between the primary and secondary sides for different transformer connections are presented in [25]. The modelling of the three-phase transformers for HPFA is given in [24,26].

2.5. D-STATCOM

The D-STATCOM is commonly regarded as a shunt compensator which supplies reactive power in PFAs. The voltage magnitude at the D-STATCOM bus can be controlled by adjusting the reactive power injection of D-STATCOM.

The interface of the D-STATCOM at i^{th} bus shown in Figure 2a, and its traditional modelling for PFAs is shown in Figure 2b. The specified reactive power of the load is combined with the reactive power output of D-STATCOM, so that reactive power varies as magnitude of V_i varies. This is absolutely a PV bus modelling with the real power output of the D-STATCOM set to zero [27,28]. The hypothesis in this model is that losses in the D-STATCOM and its connection are ignored. The D-STATCOMs have low harmonic content, so the harmonic current injected by the D-STATCOM is considered as zero for HPFA.
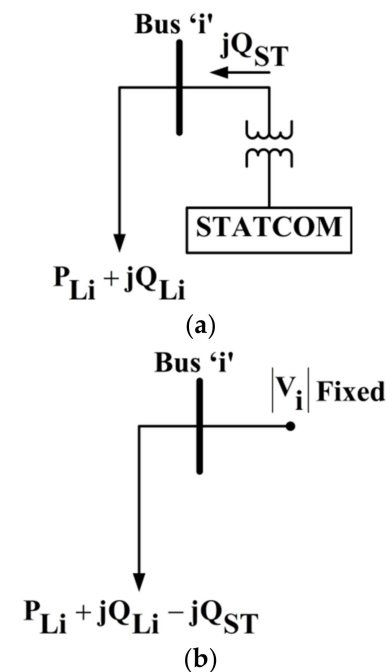
Figure 2. (**a**) D-STATCOM interface at i^{th} bus 2 (**b**) Traditional modelling of D-STATCOM as PV bus.

3. Algorithm for Developing BNM and BRNM

The performance of the HPFA of URDN is enhanced by the systematic numbering of buses and branches. From [29], the numbering scheme to buses and branches is taken. The following steps are to be followed to write a Software Code in order to split the URDN into different sections, as shown in Figure 3.
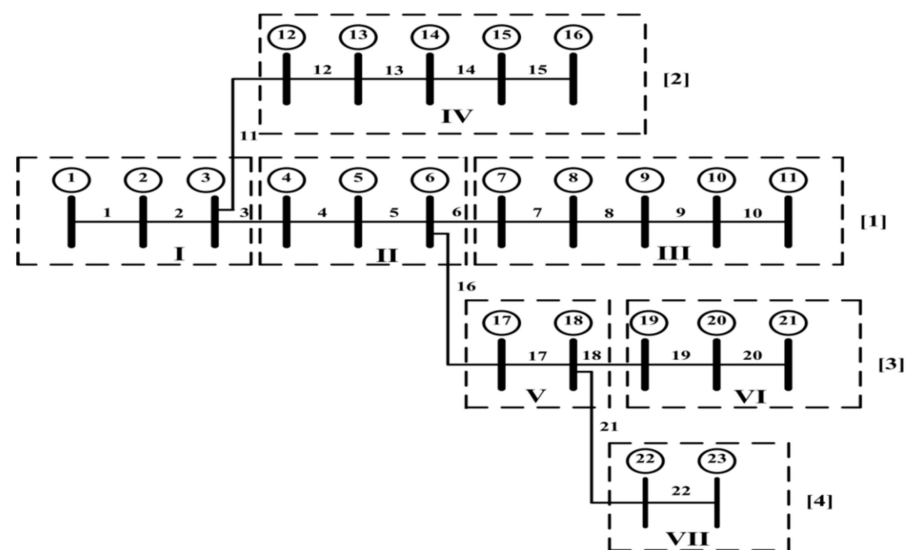
Figure 3. Divided sections for sample distribution network.

1. From the distribution network shown in Figure 3, form Table 3.

Table 3. Branch numbering of distribution network in Figure 2.

Branch Number(BN)	Sending Bus(SE)	Receiving Bus(RE)
1	1	2
2	2	3
3	3	4
4	4	5
5	5	6
6	6	7
7	7	8
8	8	9
9	9	10
10	10	11
11	3	12
12	12	13
13	13	14
14	14	15
15	15	16
16	6	17
17	17	18
18	18	19
19	19	20
20	20	21
21	18	22
22	22	23

2. Start with BN = 1.Read the RE of BN, i.e., 2. Then, check how many times this 2 appears in the SE row. Inthe above table, it appears one time. That means bus 2 is the sending end for only one branch. Fill these RE 2 and BN 1 in two different matrices (BNM and BRNM) as the first row and first column elements. Then, increase the column number by one.

3. Increase the BN (i.e., BN = 2), and read the RE of BN, i.e., 3. Then, as in step 1, check for the appearance of 3 in SE row. The bus 3 appears two times. That means that, from the bus 3, two branches are leaving. Then, fill these RE 3 and BN 2 into the same variables as the first row and present the column elements. Name this row elements as section-I. Now increase the row number by one and set the column number to one.

4. Similarly, increase the BN, and read the RE of BN. Then, check for the appearance of this RE in the SE row. If it appears one time, then fill these RE and BN values as the present row and present column elements of the variables BNM and BRNM. Then increase the column number by one and repeat step 4. If it does not appears or appears more than one time in the SE row, then fill the corresponding RE and BN values as present row and present column elements. Then identify this row as a section. Then increase the row number by one and set the column number to one and repeat the step 4.

The above steps are repeated until the BN value reaches the last branch number. At the end, the BNM and BRNM are obtained as follows:

$$
\mathbf{BNM} = \begin{bmatrix}
1 & 2 & 3 & 0 & 0 \\
4 & 5 & 6 & 0 & 0 \\
7 & 8 & 9 & 10 & 11 \\
12 & 13 & 14 & 15 & 16 \\
17 & 18 & 0 & 0 & 0 \\
19 & 20 & 21 & 0 & 0 \\
22 & 23 & 0 & 0 & 0
\end{bmatrix}
\begin{matrix}
\rightarrow \text{Section-I} \\
\rightarrow \text{Section-II} \\
\rightarrow \text{Section-III} \\
\rightarrow \text{Section-IV} \\
\rightarrow \text{Section-V} \\
\rightarrow \text{Section-VI} \\
\rightarrow \text{Section-VII}
\end{matrix}
\tag{6}
$$

$$
\mathbf{BRNM} = \begin{bmatrix}
1 & 2 & 0 & 0 & 0 \\
3 & 4 & 5 & 0 & 0 \\
6 & 7 & 8 & 9 & 10 \\
11 & 12 & 13 & 14 & 15 \\
16 & 17 & 0 & 0 & 0 \\
18 & 19 & 20 & 0 & 0 \\
21 & 22 & 0 & 0 & 0
\end{bmatrix}
\begin{matrix}
\rightarrow \text{Section-I} \\
\rightarrow \text{Section-II} \\
\rightarrow \text{Section-III} \\
\rightarrow \text{Section-IV} \\
\rightarrow \text{Section-V} \\
\rightarrow \text{Section-VI} \\
\rightarrow \text{Section-VII}
\end{matrix}
\tag{7}
$$

4. Three-Phase HPFA with Non-Linear Loads and D-STATCOM Devices

For modeling the linear and non-linear loads for HPFA, the fundamental power flow solution is required. Hence, the algorithm consists of two parts. PartA illustrates the iterative procedure for FPFA with the D-STATCOM device and PartB illustrates the iterative procedure for HPFA with linear loads, non-linear loads, and D-STATCOM devices.

After developing the BNM and BRNM for the URDN, the iterative procedure is explained with the following steps.

PartA: FPFA with D-STATCOM

1. The voltages at all busses are assigned as substation bus voltage.

$$
\begin{bmatrix}
V_a \\
V_b \\
V_c
\end{bmatrix} = \begin{bmatrix}
1\angle 0^o \\
1\angle -120^o \\
1\angle 120^o
\end{bmatrix}
\tag{8}
$$

2. Find the line current matrix serving the load at all buses.
3. Start with collecting line current matrix at bus-23 (the tail bus in section-VII in BNM), and thereby find the line current matrix for branch-22 (the tail branch in section-VII in BRNM). Then, continue to the bus-22 and branch-21 to find the line current matrix at the bus and line current matrix in branch, respectively. From Figure 4, the following equations are obtained by applying the KCL at every bus:

$$
[I_{abc}]_k = [IL_{abc}]_k + [Ish_{abc}]_k + [IC_{abc}]_k
\tag{9}
$$

$$[I_{abc}]_{jk} = [I_{abc}]_k \tag{10}$$

$$[I_{abc}]_j = [I_{abc}]_{jk} + [IL_{abc}]_j + [Ish_{abc}]_j + [IC_{abc}]_j \tag{11}$$

$$[I_{abc}]_{ij} = [I_{abc}]_j \tag{12}$$

$$[I_{abc}]_i = [I_{abc}]_{ij} \tag{13}$$

where:

$[I_{abc}]_k$: Line current matrix at bus-k;
$[IL_{abc}]_{jk}$: Line current in branch-jk;
$[IL_{abc}]_k$: Load current matrix at bus-k;
$[Ish_{abc}]_k$: Line current matrix drawn by shunt admittance at bus-k;
$[IC_{abc}]_k$: Line current matrix drawn by capacitor bank at bus-k, if any.

4. Now go to section-VI and repeat procedure as in step 5 to find the line current matrix at the head bus and line current matrix for head branch. Similarly, proceed up to section-I and find the line current matrix up to bus−1 and line current matrix up to branch−1.

5. Now start with head bus in section-I and continue to the tail bus in section-I by finding the phase voltage matrix at all buses with Equation (2). Then, go to the next section and repeat the same procedure.

6. Steps 4 to 6 are to be repeated until the convergence criterion as given in Equation (14) is satisfied:

$$\left| [V_{abc}]_i^r - [V_{abc}]_i^{r-1} \right| \le [\varepsilon_{abc}] \tag{14}$$

where 'r' is the iteration number.

7. D-STATCOM location is selected and model as PV bus for the outside γ^{th} iteration.

8. The mismatches in voltages at D-STATCOM buses are obtained with Equation (13):

$$\begin{bmatrix} \Delta V_a \\ \Delta V_b \\ \Delta V_c \end{bmatrix}^\gamma = \begin{vmatrix} V_a^{sp} \\ V_b^{sp} \\ V_c^{sp} \end{vmatrix} - \begin{vmatrix} V_a^{cal} \\ V_b^{cal} \\ V_c^{cal} \end{vmatrix}^\gamma \tag{15}$$

$$[\Delta V_{abc}]^\gamma \le [\varepsilon_{abc}] \tag{16}$$

where $[\Delta V]^\gamma$ is the mismatch matrix for the voltage and its size is $3 \cdot n \times 1$, and 'n' is the total number of PV buses.

9. If the Equation (16) is not satisfied, then the incremental current injection matrix at D-STATCOM bus is calculated with Equation (17) to maintain the specified voltages:

$$[\Delta I]^\gamma = [Z_{PV}]^{-1} \cdot [\Delta V]^\gamma \tag{17}$$

where $[Z_{PV}]$ is the sensitivity matrix for the PV bus with its size $3 \cdot n \times 3 \cdot n$. The formation of this matrix is presented in [30].

10. The incremental reactive current injection matrix at D-STATCOM bus is obtained with Equation (18):

$$\begin{bmatrix} \Delta I_{D,a} \\ \Delta I_{D,b} \\ \Delta I_{D,c} \end{bmatrix}_j^\gamma = \begin{bmatrix} |\Delta I_a| \cdot (\cos(90^0 + \delta_{v,a}) + j * \sin(90^0 + \delta_{v,a})) \\ |\Delta I_b| \cdot (\cos(90^0 + \delta_{v,b}) + j * \sin(90^0 + \delta_{v,b})) \\ |\Delta I_c| \cdot (\cos(90^0 + \delta_{v,c}) + j * \sin(90^0 + \delta_{v,c})) \end{bmatrix}_j^\gamma \tag{18}$$

11. In Figure 5, by applying the KCL at bus-j, the line current matrix in branch-ij is obtained as:

$$\begin{bmatrix} I_a \\ I_b \\ I_c \end{bmatrix}_{ij}^\gamma = \begin{bmatrix} IL_a \\ IL_b \\ IL_c \end{bmatrix}_j^\gamma - \begin{bmatrix} \Delta I_{D,a} \\ \Delta I_{D,b} \\ \Delta I_{D,c} \end{bmatrix}_j^\gamma \tag{19}$$

With $[V_{abc}]_j^\gamma$ and $[I_{abc}]_{ij}^\gamma$, the reactive power flow in the line $[Q_{abc}]_{ij}^\gamma$ is evaluated. Then, the incremental reactive current injection matrix is obtained with Equation (20):

$$
\begin{bmatrix} \Delta Q_{D,a} \\ \Delta Q_{D,b} \\ \Delta Q_{D,c} \end{bmatrix}_j^\gamma = \begin{bmatrix} QL_a \\ QL_b \\ QL_c \end{bmatrix}_j^\gamma - \begin{bmatrix} Q_a \\ Q_b \\ Q_c \end{bmatrix}_{ij}^\gamma
\tag{20}
$$

The reactive power generation matrix needed at D-STATCOM bus-j is obtained with Equation (21):

$$
\begin{bmatrix} Q_{D,a} \\ Q_{D,b} \\ Q_{D,c} \end{bmatrix}_j^\gamma = \begin{bmatrix} Q_{D,a} \\ Q_{D,b} \\ Q_{D,c} \end{bmatrix}_j^{\gamma-1} + \begin{bmatrix} \Delta Q_{D,a} \\ \Delta Q_{D,b} \\ \Delta Q_{D,c} \end{bmatrix}_j^\gamma
\tag{21}
$$

12. If the D-STATCOM device is able to generate limited reactive power, then find the total reactive power generation of D-STATCOM device with Equation (22). The total reactive power generation of D-STATCOM is now compared with the maximum and minimum limits of reactive power generation of D-STATCOM device limits. Equation (22) is calculated as follows:

$$
(Q_D)_j^\gamma = (Q_{D,a})_j^\gamma + (Q_{D,b})_j^\gamma + (Q_{D,c})_j^\gamma
\tag{22}
$$

If $Q_{j,min} \leq (Q_D)_j^\gamma \leq Q_{j,max}$
Then set complex power generation is as in Equation (21)
If $(Q_D)_j^\gamma \leq Q_{j,min}$
Then set $(Q_D)_j^\gamma = Q_{j,min}$ and $(Q_{D,a})_j^\gamma = (Q_{D,b})_j^\gamma = (Q_{D,c})_j^\gamma = Q_{j,min}/3$
If $(Q_D)_j^\gamma \geq Q_{j,max}$
Then set $(Q_D)_j^\gamma = Q_{j,max}$ and $(Q_{D,a})_j^\gamma = (Q_{D,b})_j^\gamma = (Q_{D,c})_j^\gamma = Q_{j,max}/3$

13. Now, find the complex power generation matrix at D-STATCM bus with Equation (23):

$$
\begin{bmatrix} S_{D,a} \\ S_{D,b} \\ S_{D,c} \end{bmatrix}_j^\gamma = \begin{bmatrix} P_{D,a} \\ P_{D,b} \\ P_{D,c} \end{bmatrix}_j + j \cdot \begin{bmatrix} Q_{D,a} \\ Q_{D,b} \\ Q_{D,c} \end{bmatrix}_j^\gamma
\tag{23}
$$

where $[P_{D,abc}]_j$ is the specified real power generation matrix of the D-STATCOM device and its value is set to zero.

14. The line current matrix injected by the D-STATCOM is obtained with the complex power generation matrix obtained in Equation (23) and bus voltage matrix as:

$$
[I_{D,abc}]_j^\gamma = \begin{bmatrix} (S_{D,a}/V_a)^* \\ (S_{D,b}/V_b)^* \\ (S_{D,c}/V_c)^* \end{bmatrix}_j^\gamma
\tag{24}
$$

15. Using the current injection matrix at the D-STATCOM buses, repeat from step 7 by setting $\gamma = \gamma+1$.
16. If Equation (16) is satisfied at all D-STATCOM buses, then stop the FPFA algorithm.
17. With the complex power loss in branch-ij in Equation (25), find the total power loss in the network by summing up the losses in all branches:

$$
\begin{bmatrix} SLoss_a \\ SLoss_b \\ SLoss_c \end{bmatrix}_{ij} = \begin{bmatrix} (V_a)_i \cdot (I_a)_{ij}^* \\ (V_b)_i \cdot (I_b)_{ij}^* \\ (V_c)_i \cdot (I_c)_{ij}^* \end{bmatrix} - \begin{bmatrix} (V_a)_j \cdot (I_a)_{ji}^* \\ (V_b)_j \cdot (I_b)_{ji}^* \\ (V_c)_j \cdot (I_c)_{ji}^* \end{bmatrix}
\tag{25}
$$

PartB: HPFA with non-linear loads and D-STATCOM device.

18. With the converged bus voltages and specified load, the impedances of the linear loads are calculated for the harmonic order-h of interest.
19. Find the harmonic current injection matrix for the non-linear loads for the selected h-order harmonic of interest. The harmonic current injection matrix of D-STATCOM is taken as zero.
20. The harmonic voltage at the substation bus is taken as zero since the supply voltage is assumed to bea pure sinusoidal voltage waveform.
21. The harmonic voltages at all other buses for the first iteration are assumed to be zeros as that of the substation bus:

$$
\begin{bmatrix} V_a \\ V_b \\ V_c \end{bmatrix}^h = \begin{bmatrix} 0 \\ 0 \\ 0 \end{bmatrix} \tag{26}
$$

22. Find the net harmonic current matrix at all the buses with the harmonic current matrix drawn by the linear loads and the harmonic current injection matrix of non-linear loads and the D-STATCOM device. The current matrix drawn by the linear loads at all the buses is zero for the first iteration as the harmonic voltage at all the buses is zero for the first iteration. This is illustrated with the sample section as shown in Figure 6. The net harmonic current matrix at bus-j is given by Equation (27), and the harmonic current matrix in branch-ij is given by Equation (28):

$$
[I_{abc}]_j^h = -[IS_{abc}]_j^h - [ID_{abc}]_j^h + [IL_{abc}]_j^h \tag{27}
$$

$$
[I_{abc}]_{ij}^h = [I_{abc}]_j^h \tag{28}
$$

where:

$[I_{abc}]_j^h$: Harmonic current matrix at bus-j for harmonic order-h;

$[I_{abc}]_{ij}^h$: Harmonic current matrix in branch-ij for harmonic order-h;

$[IL_{abc}]_j^h$: Harmonic current matrix drawn by linear load at bus-j for harmonic order-h;

$[IS_{abc}]_j^h$: Harmonic current injection matrix by non-linear load at bus-j for harmonic order-h;

$[ID_{abc}]_j^h$: Harmonic current injection matrix by D-STATCOM device at bus-j for harmonic order-h.

Likewise, the harmonic currents in all branches are to be obtained by moving up to the substation as explained in step 3 to step 4 in PartA for FPFA.

23. Then, start finding the harmonic voltages at all buses downstream from the substation bus with Equation (29) as explained in step 5 in PartA:

$$
\begin{bmatrix} V_a \\ V_b \\ V_c \end{bmatrix}_j^h = \begin{bmatrix} V_a \\ V_b \\ V_c \end{bmatrix}_i^h - \begin{bmatrix} Z_{aa} & Z_{ab} & Z_{ac} \\ Z_{ba} & Z_{bb} & Z_{bc} \\ Z_{ca} & Z_{cb} & Z_{cc} \end{bmatrix}_{ij}^h \cdot \begin{bmatrix} I_a \\ I_b \\ I_c \end{bmatrix}_{ij}^h \tag{29}
$$

24. Repeat the steps 22 to 23 until the magnitude mismatch of harmonic voltages of h-order at all the busses is within the tolerance limit.
25. Find the harmonic power loss in all branches using Equation (30). Then find the total harmonic power loss in the network for the selected harmonic order-h using Equation (31):

$$\begin{bmatrix} \text{SLoss}_a \\ \text{SLoss}_b \\ \text{SLoss}_c \end{bmatrix}_{ij}^h = \begin{bmatrix} (V_a)_i \cdot (I_a)_{ij}^* \\ (V_b)_i \cdot (I_b)_{ij}^* \\ (V_c)_i \cdot (I_c)_{ij}^* \end{bmatrix}^h - \begin{bmatrix} (V_a)_j \cdot (I_a)_{ji}^* \\ (V_b)_j \cdot (I_b)_{ji}^* \\ (V_c)_j \cdot (I_c)_{ji}^* \end{bmatrix}^h \tag{30}$$

$$[\text{TS\_loss}_{abc}]^h = \sum_{br=1}^{Nbr} \left[[\text{SLoss}_{abc}]_{br}^h \right] \tag{31}$$

26. Likewise, repeat the steps from 10 to 16 for all the harmonics of selected harmonic orders (h = 3, 5, 7, 9, 11, 13, and 15).
27. Find the total harmonic loss of the network using Equation (32):

$$[\text{Total\_loss}] = \sum_{h=h_o}^{h_m} \sum_{br=1}^{Nbr} \left[[\text{SLoss}_{abc}]_{br}^h \right] \tag{32}$$

28. The total r.m.s voltage at bus-i, say, phase '*a*', is calculated as:

$$(V_a)_i = \sqrt{ \left| (V_a)_i^1 \right|^2 + \sum_{h=h_o}^{h_m} \left| (V_a)_i^h \right|^2 } \tag{33}$$

29. The total harmonic distortion at every bus is calculated using Equation (34):

$$(\text{THD})_i^a = \frac{\sqrt{ \sum_{h=h_o}^{h_m} \left| (V_a)_i^h \right|^2 }}{\left| (V_a)_i^1 \right|} \tag{34}$$

where: h_o : Minimum harmonic order;
$\quad\quad\;\; h_m$: Maximum harmonic order;
$\quad\quad\;\;$ br : Branch number;
$\quad\quad\;\;$ Nbr : Total number of branches.
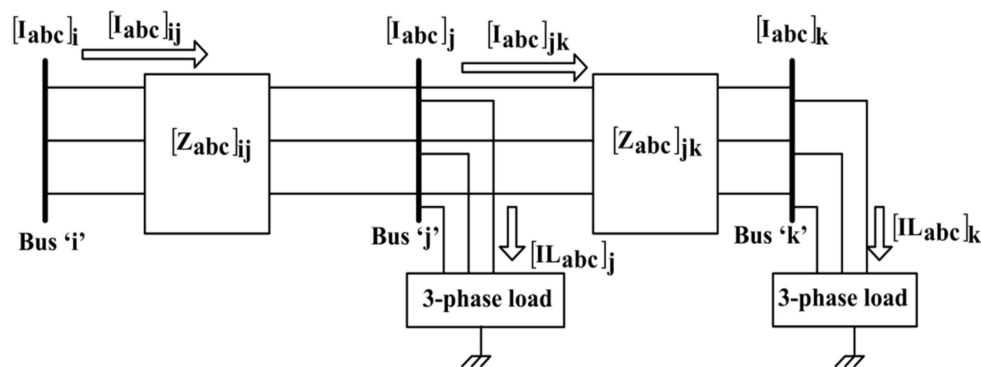
Figure 4. A simple URDN three busses.
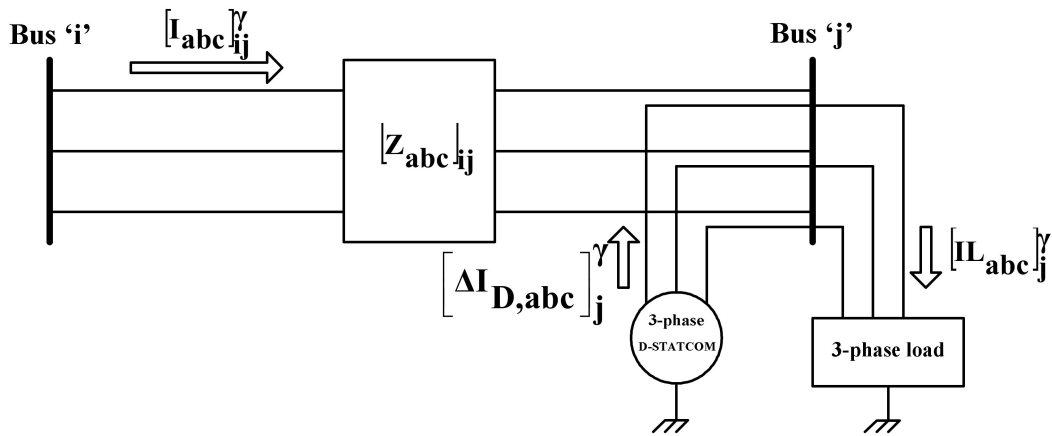
Figure 5. A simple URDN with two buses with D-STATCOM placed at bus-j.
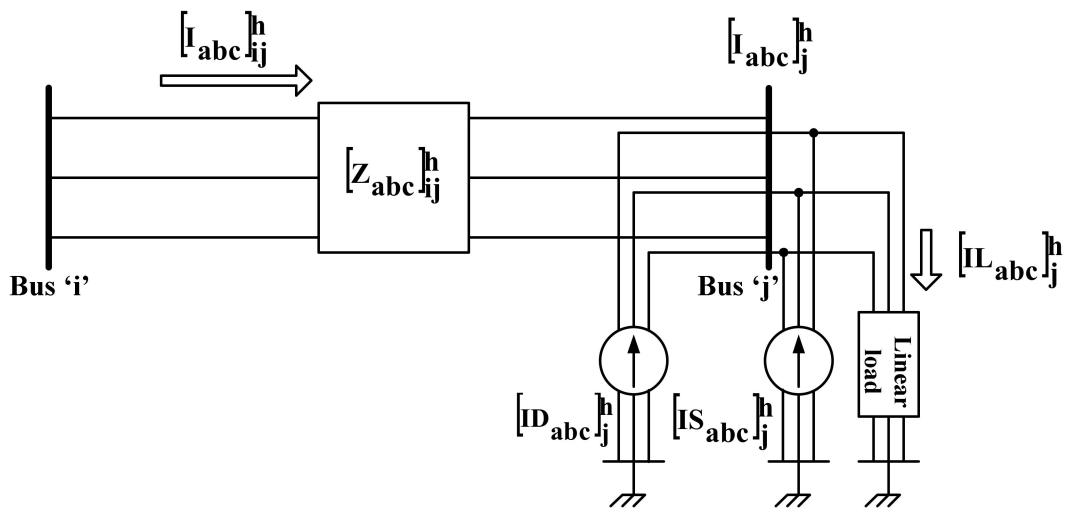
Figure 6. Sample section of two buses for HPFA.

5. Results and Discussions

5.1. IEEE−13 Bus URDN

5.1.1. Fundamental Power Flow Solution for Accuracy Test

The proposed three-phase FPFA is examined on IEEE−13 bus unbalanced test feeder without interfacing of D-STATCOM device. Figure 7 shows the IEEE−13 bus feeder and its data is collected from [31]. 5000 kVA and 4.16 kV are the chosen base values for this network. The FPFA is taken 5 iterations for its convergence with tolerance for convergence is 10^{-4}. The comparison of obtained power flow solution with IEEE solution and errors in voltage magnitudes and phase angles at every bus are presented in Table 4. Table 5 presents the comparison of obtained power loss with the IEEE losses. Insignificant values of maximum errors of 0.0005 p.u and 0.010º for voltage magnitudes and phase angles are observed in Table 6. So that, in terms of accuracy the test results are consistent with IEEE results.
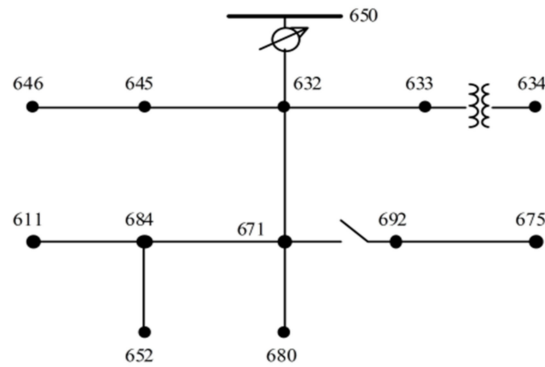
Figure 7. IEEE 13 Bus URDN.

Table 4. Fundamental voltage solution for IEEE−13 bus URDN.

Bus	Phase	Obtained Solution	IEEE Solution [31]	Error in Voltage Mag.	Error in Voltage Ang.
	a	$1 \angle 0^o$	$1 \angle 0^o$	0.0000	0.00
650	b	$1 \angle -120^o$	$1 \angle -120^o$	0.0000	0.00
	c	$1 \angle 120^o$	$1 \angle 120^o$	0.0000	0.00
	a	$1.0625 \angle 0^o$	$1.0625 \angle 0^o$	0.0000	0.00
RG	b	$1.0500 \angle -120^o$	$1.0500 \angle -120^o$	0.0000	0.00
	c	$1.0687 \angle 120^o$	$1.0687 \angle 120^o$	0.0000	0.00
	a	$1.0210 \angle -2.49^o$	$1.0210 \angle -2.49^o$	0.0000	0.00
632	b	$1.0420 \angle -121.72^o$	$1.0420 \angle -121.72^o$	0.0000	0.00
	c	$1.0175 \angle 117.83^o$	$1.0170 \angle 117.83^o$	−0.0005	0.00
	a	$0.9900 \angle -5.30^o$	$0.9900 \angle -5.30^o$	0.0000	0.00
671	b	$1.0529 \angle -122.34^o$	$1.0529 \angle -122.34^o$	0.0000	0.00
	c	$0.977 \angle 116.03^o$	$0.9778 \angle 116.02^o$	0.0001	−0.01
	a	$0.9900 \angle -5.30^o$	$0.9900 \angle -5.30^o$	0.0000	0.00
680	b	$1.0529 \angle -122.34^o$	$1.0529 \angle -122.34^o$	0.0000	0.00
	c	$0.9778 \angle 116.03^o$	$0.977 \angle 116.02^o$	0.0001	−0.01
	a	$1.0180 \angle -2.55^o$	$1.0180 \angle -2.56^o$	0.0000	0.01
633	b	$1.0401 \angle -121.77^o$	$1.0401 \angle -121.77^o$	0.0000	0.00
	c	$1.0148 \angle 117.82^o$	$1.0148 \angle 117.82^o$	0.0000	0.00
	a	$0.9940 \angle -3.23^o$	$0.9940 \angle -3.23^o$	0.0000	0.00
634	b	$1.0218 \angle -122.22^o$	$1.0218 \angle -122.22^o$	0.0000	0.00
	c	$0.9960 \angle 117.35^o$	$0.9960 \angle 117.34^o$	0.0000	−0.01
645	b	$1.0328 \angle -121.90^o$	$1.0329 \angle -121.90^o$	0.0001	0.00
	c	$1.0155 \angle 117.86^o$	$1.0155 \angle 117.86^o$	0.0001	0.00
646	b	$1.0311 \angle -121.98^o$	$1.0311 \angle -121.98^o$	0.0000	0.00
	c	$1.0134 \angle 117.90^o$	$1.0134 \angle 117.90^o$	0.0000	0.01
	a	$0.9900 \angle -5.30^o$	$0.9900 \angle -5.31^o$	0.0000	0.01
692	b	$1.0529 \angle -122.34^o$	$1.0529 \angle -122.34^o$	0.0000	0.00
	c	$0.9778 \angle 116.03^o$	$0.9777 \angle 116.02^o$	−0.0001	−0.01
	a	$0.9835 \angle -5.55^o$	$0.9835 \angle -5.56^o$	0.0000	0.01
675	b	$1.0553 \angle -122.52^o$	$1.0553 \angle -122.52^o$	0.0000	0.00
	c	$0.9759 \angle 116.04^o$	$0.9758 \angle 116.03^o$	−0.0001	−0.01
684	a	$0.9881 \angle -5.32^o$	$0.9881 \angle -5.32^o$	0.0000	0.00
	c	$0.9758 \angle 115.92^o$	$0.9758 \angle 115.92^o$	0.0000	0.00
611	c	$0.9738 \angle 115.78^o$	$0.9738 \angle 115.78^o$	0.0000	0.00
652	a	$0.9825 \angle -5.24^o$	$0.9825 \angle -5.25^o$	0.0000	0.01

Table 5. Power loss in IEEE−13 bus URDN.

Phase	Obtained Power Loss		IEEE Loss [31]	
	Active (kW)	Reactive (kVAR)	Active (kW)	Reactive (kVAR)
a	39.13	152.62	39.11	152.59
b	−4.74	42.27	−4.70	42.22
c	76.59	129.69	76.65	129.85
Total	110.98	324.57	111.13	324.66

Table 6. Power loss in IEEE−13 bus URDN.

Harmonic Order	Harmonic Power Loss	
	APL (kW)	RPL (kVAR)
3	0.7958	6.5165
5	0.0856	1.1483
7	0.0072	0.1183
9	0.0043	0.0902
11	0.0008	0.0164
13	0.0008	0.0226
15	0.0010	0.0340
Total harmonic loss	0.8983	7.9464
Fundamental loss	147.33	433.54
Total power loss	148.23	441.49

5.1.2. Fundamental and Harmonic Power Flow Solutions without D-STATCOM

The regulator between buses 650 and 632 is removed and the capacitor banks at bus 675 and 611 are removed from the network. The data for the harmonic load composition and current spectra of harmonic loads aretaken from [32]. The convergence tolerance is taken as 10^{-4}. Table 6 presents the harmonic power losses and total power loss of the network including fundamental and harmonic loss. The harmonic voltage solutions for the selected range of harmonics of order 3, 5, 7, 9, 11, 13, and 15 are presented in Table 7. Table 8 presents the fundamental r.m.s profile, the total harmonic voltage profile, and the THD %. It is observed from Table 8 that the maximum THD % on the network is 5.2263 at bus−611 for c-phase, and in [2], it was reported that the maximum THD % at bus−611 is 5.23. Therefore, the results of the proposed HPFA are almost matches the literature in terms of accuracy. To see the impact of the D-STATCOM on the fundamental r.m.s voltage profile, the total r.m.s voltage profile, the fundamental and harmonic power loss, and the THD %, the results of this case study are taken as benchmarks.

5.1.3. IEEE−13 Bus URDN with D-STATCOM

In this case, a three-phase D-STATCOM is integrated at bus 680. The D-STATCOM is modelled as a PV model with its real power generation set to zero and the lower limit and upper limit for the three-phase reactive power generation are 100 kVAR and 1000 kVAR, respectively. The phase voltages specified at this bus are 1 p.u. Table 8 presents the harmonic power loss and total power loss (including fundamental and harmonic power loss). In comparison with Table 6, it is observed that the integration of the D-STATCOM into the network reduces both the fundamental and harmonic power losses, thereby the total power loss in the network is also reduced. Table 9 presents the fundamental r.m.s voltage profile, the total r.m.s voltage profile, and the THD %.In comparison with Table 7, it is observed that there is an improvement in fundamental r.m.s voltage profile. The minimum fundamental r.m.s voltage in the network without D-STATCOM is 0.8651 p.uat bus−611 for c-phase, whereas its value is 0.8763 p.u at bus−611 for c-phase with integration of D-STATCOM. The maximum THD % in the network is reduced from 5.2263 to 5.1133 with integration of D-STATCOM. Figure 8 shows the comparison of THD % with and

without integration of D-STATCOM. Figure 9 presents the comparison of fundamental r.m.s voltages on the network for the two case studies.

Table 7. Fundamental r.m.s voltage, total r.m.s voltages, and THD % in IEEE−13 bus URDN.

Bus	Phase	S. No	Fundamental r.m.s Voltage	Total r.m.s Voltage	THD %
650	a	1	$1 \angle 0^o$	1	0
	b	2	$1 \angle -120^o$	1	0
	c	3	$1 \angle 120^o$	1	0
632	a	4	$0.9498 \angle -2.7462^o$	0.9500	1.9173
	b	5	$0.9839 \angle -121.6817^o$	0.9839	0.4974
	c	6	$0.9300 \angle 117.8000^o$	0.9302	2.2737
671	a	7	$0.9109 \angle -5.8987^o$	0.9117	4.0623
	b	8	$0.9875 \angle -122.2091^o$	0.9875	1.0363
	c	9	$0.8717 \angle 115.9500^o$	0.8728	4.9409
680	a	10	$0.9109 \angle -5.8987^o$	0.9117	4.0623
	b	11	$0.9875 \angle -122.2091^o$	0.9875	1.0363
	c	12	$0.8717 \angle 115.9500^o$	0.8728	4.9409
633	a	13	$0.9466 \angle -2.8223^o$	0.9468	1.9098
	b	14	$0.9819 \angle -121.7315^o$	0.9819	0.4919
	c	15	$0.9271 \angle 117.7946^o$	0.9273	2.2648
634	a	16	$0.9207 \angle -3.6073^o$	0.9209	1.8801
	b	17	$0.9624 \angle -122.2445^o$	0.9624	0.4873
	c	18	$0.9064 \angle 117.2178^o$	0.9066	2.2406
645	b	19	$0.9745 \angle -121.8646^o$	0.9745	0.4991
	c	20	$0.9283 \angle 117.8225^o$	0.9286	2.2769
646	b	21	$0.9729 \angle -121.9382^o$	0.9729	0.5000
	c	22	$0.9264 \angle 117.8696^o$	0.9267	2.2815
692	a	23	$0.9109 \angle -5.8987^o$	0.9117	4.0623
	b	24	$0.9875 \angle -122.2091^o$	0.9875	1.0363
	c	25	$0.8717 \angle 115.9500^o$	0.8728	4.9409
675	a	26	$0.9025 \angle -6.0795^o$	0.9034	4.3128
	b	27	$0.9887 \angle -122.3037^o$	0.9887	1.0491
	c	28	$0.8678 \angle 116.0660^o$	0.8689	5.0687
684	a	29	$0.9093 \angle -5.9502^o$	0.9100	4.0765
	c	30	$0.8684 \angle 115.9163^o$	0.8695	5.0741
611	c	31	$0.8651 \angle 115.8365^o$	0.8663	5.2263
652	a	32	$0.9041 \angle -5.8755^o$	0.9049	4.0900

Table 8. Fundamental and Harmonic power loss for IEEE−13 URDN with D-STATCOM.

Harmonic Order	Harmonic Power Loss	
	Active (kW)	Reactive (kVAR)
3	0.7836	6.3935
5	0.0841	1.1282
7	0.0071	0.1168
9	0.0043	0.0886
11	0.0008	0.0160
13	0.0008	0.0223
15	0.0009	0.0336
Total harmonic loss	0.8816	7.7991
Fundamental Loss	135.34	396.63
Total power loss	136.22	404.43

Table 9. Fundamental r.m.s voltages, total r.m.s voltages, and THD % in IEEE−13 bus URDN with D-STATCOM.

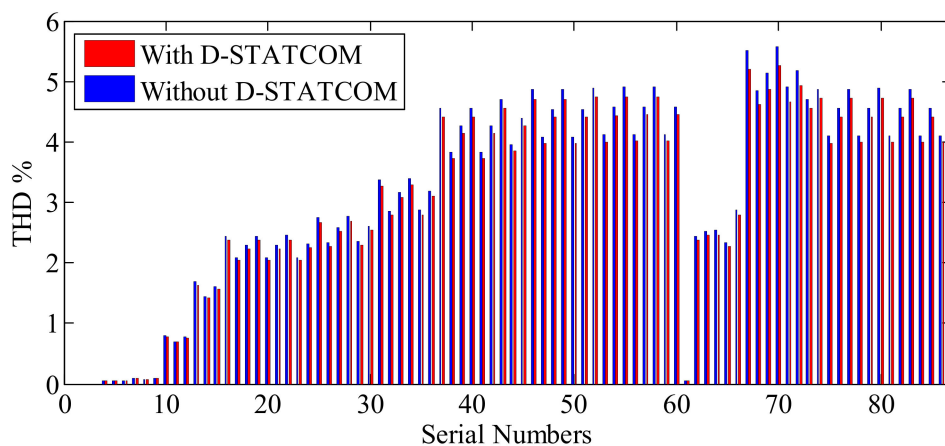| Bus	Phase	Fundamental r.m.s Voltage	Total r.m.s Voltage in p.u	THD %
650	a	$1.0000\angle 0°$	1	0
	b	$1.0000\angle -120°$	1	0
	c	$1.0000\angle 120°$	1	0
632	a	$0.9545\angle -2.8433°$	0.9547	1.8920
	b	$0.9883\angle -121.7039°$	0.9883	0.4923
	c	$0.9355\angle 117.6975°$	0.9357	2.2404
671	a	$0.9204\angle -6.0689°$	0.9211	3.9865
	b	$0.9961\angle -122.2496°$	0.9962	1.0211
	c	$0.8829\angle 115.7512°$	0.8839	4.8346
680	a	$0.9227\angle -6.1274°$	0.9234	3.9764
	b	$0.9983\angle -122.2605°$	0.9983	1.0189
	c	$0.8855\angle 115.6856°$	0.8865	4.8205
633	a	$0.9512\angle -2.9186°$	0.9514	1.8846
	b	$0.9863\angle -121.7535°$	0.9863	0.4869
	c	$0.9326\angle 117.6923°$	0.9329	2.2317
634	a	$0.9255\angle -3.6957°$	0.9256	1.8556
	b	$0.9669\angle -122.2618°$	0.9669	0.4823
	c	$0.9121\angle 117.1225°$	0.9123	2.2082
645	b	$0.9789\angle -121.8864°$	0.9789	0.4940
	c	$0.9338\angle 117.7205°$	0.9341	2.2436
646	b	$0.9773\angle -121.9600°$	0.9773	0.4948
	c	$0.9319\angle 117.7674°$	0.9322	2.2482
692	a	$0.9204\angle -6.0689°$	0.9211	3.9865
	b	$0.9961\angle -122.2496°$	0.9962	1.0211
	c	$0.8829\angle 115.7512°$	0.8839	4.8346
675	a	$0.9121\angle -6.2456°$	0.9129	4.2312
	b	$0.9973\angle -122.3429°$	0.9973	1.0335
	c	$0.8790\angle 115.8645°$	0.8801	4.9586
684	a	$0.9187\angle -6.1203°$	0.9194	4.0007
	c	$0.8796\angle 115.7184°$	0.8807	4.9647
611	c	$0.8763\angle 115.6396°$	0.8775	5.1133
652	a	$0.9135\angle -6.0456°$	0.9142	4.0140
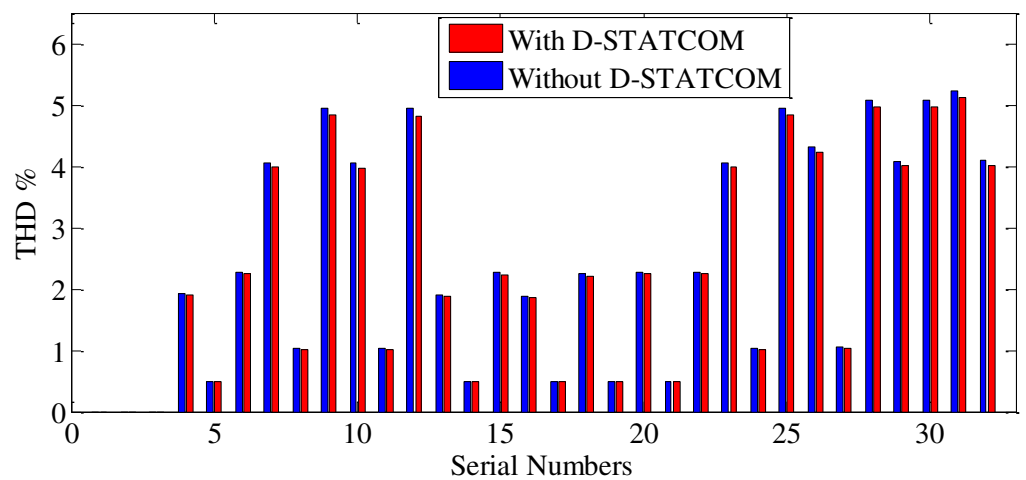
Figure 8. Comparison of THD % for case studies on IEEE−13 URDN.
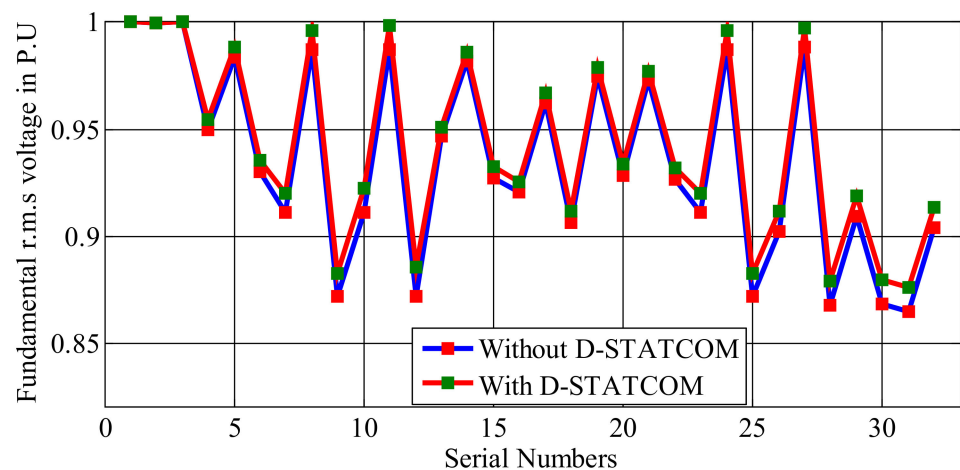
Figure 9. Comparison of fundamental r.m.svoltages for case studies on IEEE−13 URDN.

5.2. IEEE−34 Bus URDN

The date for the IEEE−34 bus URDN is taken from [31]. The base values selected for the system are 2500 kVA and 24.9 kV. The load composition at spot loads for harmonic analysis is presented in Table 10. The data for the current spectra of harmonic loads aretaken from [32]. The convergence tolerance for both fundamental and harmonic power flows is 10^{-4}. The case studies on the network are presented in Table 11. The rating and location of the D-STATCOM device for Case2 is presented in Table 11. Table 12 presents the fundamental r.m.s voltage profile, the total r.m.s voltage profile, and the THD % for Case1. The test results of Case1 are used as a benchmark to see the fundamental and harmonic impacts of D-STATCOM on the network. The summary of results for the case studies is presented in Table 13. In Case2, which has integrations of two D-STATCOM devices, the maximum THD% is observed to be 5.2567 which is less than in Case 1. The number of phases effected with a THD% more than fiveis reduced from fourto twofrom Case 1 to Case 2. From Case 1 to Case 2, it is found that the minimum fundamental voltage on the network is improved from 0.7641 p.u to 0.8137 p.u at bus 890 for the a-phase.The fundamental power loss and the total power loss including harmonic loss of the network reduced in Case 2 in comparison with Case 1. Figure 10 shows the comparison of THD % with and without the integration of the D-STATCOM. Figure 11 shows the comparison of the fundamental r.m.s voltages on the network for the two case studies.

Table 10. Load composition of spot loads in IEEE−34 bus URDN.

| | Load Composition | | | |
| | Non-Linear Loads | | | Linear Loads |
Bus No.	Fluorescent Light Banks	Adjustable Speed Drives	Composite Residential Loads	
830	None	None	80%	20%
844	30%	30%	30%	10%
848	30%	30%	30%	10%
890	30%	None	60%	10%
860	30%	30%	30%	10%
840	30%	30%	30%	10%

Table 11. Case studies on IEEE−34 bus URDN.

Case Study	Description
Case 1 (Without D-STATCOM)	• Voltage regulator is taken off between bus−614 and bus−650 and bus−852 and bus−832. • Capacitor banks are taken off at bus−844 and bus−848. • Load composition of spot loads as in Table 9
Case 2 (With D-STATCOM)	• Three-phase D-STATCOM placed at bus 890 is modeled as PV bus with P = 0 and three-phase reactive power limits: $100 \leq Q \leq 500$ kVAR. • Three-phase D-STATCOM placed at bus 650 is modeled as PV bus with P = 0 and three-phase reactive power limits: $100 \leq Q \leq 500$ kVAR.

Table 12. Fundamental r.m.s voltages, total r.m.s voltages, and THD % in the IEEE−34 bus URDN for Case 1.

Bus No.	S. No.	Ph.	Total r.m.s Voltages in p.u	THD %	Bus No	S. No.	Ph.	Total r.m.s Voltages in p.u	THD %
800	1	a	1	0	834	46	a	0.8169	4.8628
	2	b	1	0		47	b	0.8531	4.0835
	3	c	1	0		48	c	0.8570	4.5399
802	4	a	0.9972	0.0541	842	49	a	0.8168	4.8691
	5	b	0.9980	0.0481		50	b	0.8530	4.0888
	6	c	0.9981	0.0531		51	c	0.8569	4.5458
806	7	a	0.9953	0.0908	844	52	a	0.8164	4.8990
	8	b	0.9967	0.0808		53	b	0.8524	4.1147
	9	c	0.9969	0.0891		54	c	0.8565	4.5742
808	10	a	0.9605	0.7955	846	55	a	0.8162	4.9094
	11	b	0.9745	0.6983		56	b	0.8519	4.1261
	12	c	0.9742	0.7706		57	c	0.8562	4.5841
812	13	a	0.9200	1.6825	848	58	a	0.8162	4.9109
	14	b	0.9488	1.4531		59	b	0.8518	4.1276
	15	c	0.9479	1.6045		60	c	0.8562	4.5855
814	16	a	0.8880	2.4435	810	61	b	0.9975	0.0562
	17	b	0.9284	2.0813	818	62	a	0.8869	2.4466
	18	c	0.9271	2.2994	820	63	a	0.8599	2.5235
850	19	a	0.8880	2.4438	822	64	a	0.8564	2.5339
	20	b	0.9284	2.0815	826	65	b	0.9169	2.3333
	21	c	0.9271	2.2997	856	66	b	0.8954	2.8693
816	22	a	0.8877	2.4526	888	67	a	0.7875	5.5150
	23	b	0.9281	2.0888		68	b	0.8248	4.8565
	24	c	0.9268	2.3079		69	c	0.8275	5.1312
824	25	a	0.8778	2.7468	890	70	a	0.7853	5.5791
	26	b	0.9171	2.3328		71	b	0.8228	4.9085
	27	c	0.9173	2.5798		72	c	0.8252	5.1873
828	28	a	0.8769	2.7713	864	73	a	0.8203	4.7018
	29	b	0.9162	2.3529		74	a	0.8164	4.8734
	30	c	0.9165	2.6025	860	75	b	0.8526	4.0921
830	31	a	0.8574	3.3823		76	c	0.8566	4.5493
	32	b	0.8961	2.8557	836	77	a	0.8162	4.8779
	33	c	0.8974	3.1673		78	b	0.8522	4.0967
854	34	a	0.8569	3.3981		79	c	0.8565	4.5531
	35	b	0.8956	2.8688	840	80	a	0.8162	4.8790
	36	c	0.8969	3.1820		81	b	0.8522	4.0976
852	37	a	0.8233	4.5667		82	c	0.8564	4.5542
	38	b	0.8603	3.8340	862	83	a	0.8162	4.8779
	39	c	0.8634	4.2626		84	b	0.8522	4.0968
832	40	a	0.8233	4.5671		85	c	0.8565	4.5530
	41	b	0.8603	3.8342	838	86	b	0.8520	4.0977
	42	c	0.8634	4.2629					
858	43	a	0.8203	4.7018				—	
	44	b	0.8570	3.9475					
	45	c	0.8604	4.3890					

Table 13. Summary of results for the case studies on IEEE−34 bus URDN.

Case Study	Min. Fundamental Voltage, p.u	Min. Total r.m.sVoltage, p.u	Max. THD%	No. of Phases of Buses (THD > 5%)
Case 1	0.7841 at bus−890, a-phase	0.7853 at bus−890, a-phase	5.5791 at bus−890, a-phase	4
Case 2	0.8137 at bus−890, a-phase	0.8148 at bus−890, a-phase	5.2567 at bus−890, a-phase	2
Case study	Total fundamental power loss		Total power loss including total harmonic loss	
	Active (kW)	Reactive (kVAR)	Active (kW)	Reactive (kVAR)
Case 1	260.89	180.49	264.56	188.15
Case 2	227.69	155.82	231.23	163.21

Figure 10. Comparison of THD% for case studies on IEEE−34 URDN.
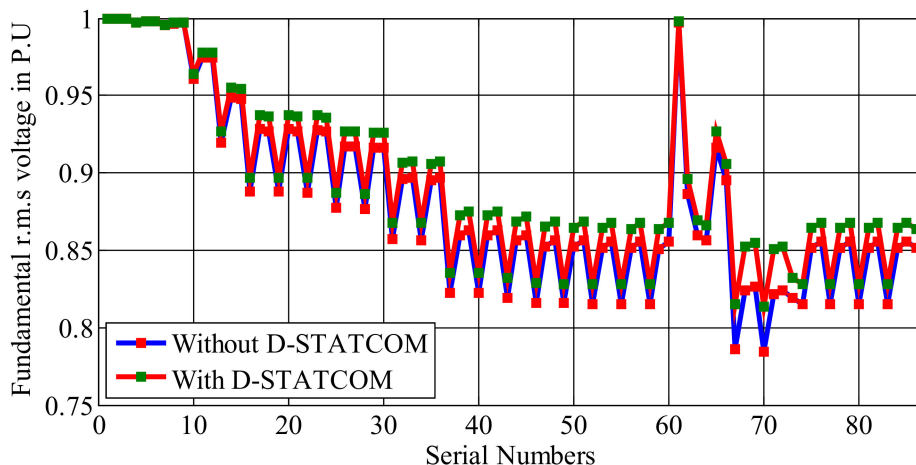
Figure 11. Comparison of fundamental r.m.svoltages for case studies on IEEE−34 URDN.

6. Conclusions

This paper proposes new three-phase PFAs for URDN with the presence of linear and non-linear loads and D-STATCOM devices. These PFAs can give both fundamental and harmonic power flow solutions with/without the presence of D-STATCOM devices. The developed BNM and BRNM make both the FPFA and HPFA simple. These matrices are developed by exploiting the radial topology in distribution networks. This method uses the

basic concepts of circuit theory, and they can be easily understood. In this paper, the linear loads are modeled as a series combination of resistance and reactance, and non-linear loads are modeled as constant current sources with its magnitude and angle obtained from the current spectra. The harmonic current injections from the D-STATCOM are assumed as zero. The proposed FPFA and HPFA are tested on the IEEE−13 bus URDN, and the results are found to be accurate with the literature. The test studies are carried on the IEEE−13 bus and IEEE−34 bus URDN, and the results of the case studies show thatthere is an improvement in the fundamental voltage profile, a reduction in the fundamental and harmonic power loss, and a reduction in THD% with the integration of D-STATCOM devices.

References

1. Burch, R.; Chang, G.K.; Grady, M.; Hatziadoniu, C.; Liu, Y.; Marz, M.; Ortmeyer, T.; Xu, W.; Ranade, S.; Ribeiro, P. Impact of aggregate linear load modeling on harmonic analysis: A comparison of common practice and analytical models. *IEEETrans. Power Deliv.* **2003**, *18*, 625–630. [CrossRef]
2. Yang, N.-C.; Le, M.-D. Three-phase harmonic power flow by direct ZBUS method for unbalanced radial distribution systems with passive power filters. *IET Gener. Transm. Distrib.* **2016**, *10*, 3211–3219. [CrossRef]
3. Milovanović, M.; Radosavljević, J.; Perović, B.; Dragičević, M. Power flow in radial distribution systems in the presence of harmonics. *Int. J. Electr. Eng. Comput.* **2018**, *2*, 11–19. [CrossRef]
4. Amini, M.A.; Jalilian, A.; Behbahani, M.R.P. Fast network reconfiguration in harmonic polluted distribution network based on developed backward/forward sweep harmonic load flow. *Electr. Power Syst. Res.* **2019**, *168*, 295–304. [CrossRef]
5. Milovanović, M.; Radosavljević, J.; Perović, B. A backward/forward sweep power flow method for harmonic polluted radial distribution systems with distributed generation units. *Int. Trans. Electr. Energy Syst.* **2019**, *30*, e12310. [CrossRef]
6. Nduka, O.S.; Ahmadi, A.R. Data-driven robust extended computer-aided harmonic power flow analysis. *IET Gener. Transm. Distrib.* **2020**, *14*, 4398–4409. [CrossRef]
7. Hernandez, J.C.; Ruiz-Rodriguez, F.J.; Jurado, F.; Sanchez-Sutil, F. Tracing harmonic distribution and voltage unbalance in secondary radial distribution networks with photovoltaic uncertainties by a multiphase harmonic load flow. *Electr. Power Syst. Res.* **2020**, *185*, 1–18. [CrossRef]
8. Ruiz-Rodriguez, F.J.; Hernandez, J.C.; Jurado, F. Iterative harmonic load flow by using the point-estimate method and complex affine arithmetic for radial distribution systems with photovoltaic uncertainties. *Electr. Power Energy Syst.* **2020**, *118*, 1–16. [CrossRef]
9. El-Fergany, A.; Abdelaziz, A.Y. Cuckoo Search-based Algorithm for Optimal Shunt Capacitors Allocations in Distribution Networks. *Electr. Power Compon. Syst.* **2013**, *41*, 1567–1581. [CrossRef]
10. Abdelaziz, A.Y.; Ali, E.S.; Abd Elazim, S.M. Flower Pollination Algorithm for Optimal Capacitor Placement and Sizing in Distribution Systems. *Electr. Power Compon. Syst. J.* **2016**, *44*, 544–555. [CrossRef]
11. Satish, R.; Kantarao, P.; Vaisakh, K. A new algorithm for impacts of multiple DGs and D-STATCOM in unbalanced radial distribution networks. *Int. J. Renew. Energy Technol.* **2021**, *12*, 221–242. [CrossRef]
12. Satish, R.; Vaisakh, K.; Abdelaziz, A.Y.; El-Shahat, A. A Novel Three-phase Power Flow Algorithm for Evaluation of Impact of Renewable Energy Sources and D-STATCOM Device in Unbalanced Radial Distribution Networks. *Energies* **2021**, *14*, 6152. [CrossRef]
13. Othman, M.M.; Hegazy, Y.G.; Abdelaziz, A.Y. Electrical Energy Management in Unbalanced Distribution Networks using Virtual Power Plant Concept. *Electr. Power Syst. Res.* **2017**, *145*, 157–165. [CrossRef]
14. Abdelaziz, A.Y.; Hegazy, Y.G.; El-Khattam, W.; Othman, M.M. A Multi objective Optimization for Sizing and Placement of Voltage Controlled Distributed Generation Using Supervised Big Bang Big Crunch Method. *Electr. Power Compon. Syst.* **2015**, *43*, 105–117. [CrossRef]
15. Abdelaziz, A.Y.; Hegazy, Y.G.; El-Khattam, W.; Othman, M.M. Optimal Planning of Distributed Generators in Distribution Networks Using Modified Firefly Method. *Electr. Power Compon. Syst.* **2015**, *43*, 320–333. [CrossRef]
16. Rohouma, W.; Balog, R.S.; Peerzada, A.A.; Begovic, M.M. D-STATCOM for harmonic mitigation in low voltage distribution network with high penetration of nonlinear loads. *Renew. Energy* **2020**, *145*, 1449–1464. [CrossRef]
17. Sirjani, R.; Jordehi, A.R. Optimal placement and sizing of distribution static compensator (D-STATCOM) in electric distribution networks: A review. *Renew. Sustain. Energy Rev.* **2017**, *77*, 688–694. [CrossRef]

18. Rezaeian-Marjani, S.; Galvani, S.; Talavat, V.; Farhadi-Kangarlu, M. Optimal allocation of D-STATCOM in distribution networks including correlated renewable energy sources. *Electr. Power Energy Syst.* **2020**, *122*, 1–14. [CrossRef]

19. Patel, S.K.; Arya, S.R.; Maurya, R. Optimal Step LMS-Based Control Algorithm for DSTATCOM in Distribution System. *Electr. Power Compon. Syst.* **2019**, *47*, 675–691. [CrossRef]

20. Singh, B.; Singh, S. GA-based optimization for integration of DGs, STATCOM and PHEVs in distribution systems. *Energy Rep.* **2019**, *5*, 84–103. [CrossRef]

21. Badoni, M.; Singh, A.; Singh, B.; Saxena, H. Real-time implementation of active shunt compensator with adaptive SRLMMN control technique for power quality improvement in the distribution system. *Int. Trans. Electr. Energy Syst.* **2020**, *14*, 1598–1606. [CrossRef]

22. Selvaraj, G.; Rajangam, K. Multi-objective grey wolf optimizer algorithm for combination of network reconfiguration and D-STATCOM allocation in distribution system. *Int. Trans. Electr. Energy Syst.* **2019**, *29*, e12100. [CrossRef]

23. Kersting, W.H. *Distribution System Modeling and Analysis*, 4th ed.; CRC Press: Boca Raton, FL, USA, 2017.

24. Task Force on Harmonics Modeling and Simulation. Modeling and simulation of the propagation of harmonics in electric power networks I. Concepts, models, and simulation techniques. *IEEE Trans. Power Deliv.* **1996**, *11*, 452–465. [CrossRef]

25. Chen, T.H.; Chang, J.D.; Chang, Y.L. Models of grounded mid-tap open-wye and open-delta connected transformers for rigorous analysis of a distribution system. *IEEE Proc. Gener. Transm. Distrib.* **1996**, *143*, 82–88. [CrossRef]

26. Arrillaga, J.; Bradley, D.A.; Bodger, P.S. *Power System Harmonics*, 1st ed.; Wiley: Hoboken, NJ, USA, 1985.

27. Yang, Z.; Shen, C.; Crow, M.L.; Zhang, L. An improved STATCOM model for power flow analysis. In Proceedings of the 2000 Power Engineering Society Summer Meeting, Seattle, WA, USA, 16–20 July 2000; pp. 1121–1126.

28. Jazebi, S.; Hosseinian, S.H.; Vahidi, B. DSTATCOM allocation in distribution networks considering reconfiguration using differential evolution algorithm. *Energy Convers. Manag.* **2011**, *52*, 2777–2783. [CrossRef]

29. Das, D.; Nagi, H.S.; Kothari, D.P. Novel method for solving radial distribution networks. *IEEE Proc. Gener. Transm. Distrib.* **1994**, *141*, 291–298. [CrossRef]

30. Shirmohammadi, D.; Carol, S.; Cheng, A. A Three phase power flow method for real time distribution system analysis. *IEEE Trans. Power Syst.* **1995**, *10*, 671–679.

31. Radial Distribution Test Feeders. Available online: http://sites.ieee.org/pes-testfeeders/resources (accessed on 28 September 2021).

32. Abu-Hashim, R.; Burch, R.; Chang, G.; Grady, M.; Gunther, E.; Halpin, M.; Xu, W.; Marz, M.; Sim, T.; Liu, Y.; et al. Test systems for harmonic modeling and simulation. *IEEE Trans. Power Deliv.* **1999**, *14*, 579–587. [CrossRef]

A Novel Opposition-Based Arithmetic Optimization Algorithm for Parameter Extraction of PEM Fuel Cell

Abhishek Sharma [1,2], **Rizwan Ahamad Khan** [3], **Abhinav Sharma** [4,*], **Diwakar Kashyap** [5,*] and **Shailendra Rajput** [1,*] ![ORCID]

[1] Department of Electrical and Electronic Engineering, Ariel University, Ariel 40700, Israel; abhishek15491@gmail.com

[2] Department of Research & Development, University of Petroleum and Energy Studies, Dehradun 248007, India

[3] Department of Mathematics, Shri Krishna University, Chhatarpur 471001, India; rizwankhanchp@gmail.com

[4] Department of Electrical and Electronics Engineering, University of Petroleum and Energy Studies, Dehradun 248007, India

[5] Institut National de la Recherche Scientifique—Énergie, Matériaux et Télécommunications, Montréal, QC J3X 1S2, Canada

[*] Correspondence: abhinav.sharma@ddn.upes.ac.in (A.S.); diwakar.cct@gmail.com (D.K.); shailendrara@ariel.ac.il (S.R.)

Abstract: The model-identification and parameter extraction are a well-defined method for modeling and development purposes of a proton exchange membrane fuel cell (PEMFC) to improve the performance. This paper introduces a novel opposition-based arithmetic optimization algorithm (OBAOA) for identifying the unspecified parameters of PEMFCs. The cost function is defined as the sum of the square deviations between the experimentally measured values and the optimal achieved values from the algorithm. Ballard Mark V PEM fuel cell is employed and analyzed to demonstrate the capability of the proposed algorithm. To demonstrate system efficiency, simulation results are compared to those of other optimizers under the same conditions. Furthermore, the proposed algorithm is validated through benchmark functions. The final results revealed that the proposed opposition-based arithmetic optimization algorithm can accurately retrieve the parameters of a PEMFC model.

Keywords: proton exchange membrane fuel cell; parameter identification; optimization; energy storage; arithmetic optimization

1. Introduction

The demand for clean energy has kept increasing in recent years due to global warming and depleting oil reserves [1,2]. Fuel cells have drawn significant attention in recent years due to high efficiency and no emission of greenhouse gases. In recent years, fuel cell research has grown significantly due to possible applications such as stationary power generation and automotive applications [3]. PEMFCs have particularly drawn attention for transport applications. It has many advantages such as low operating temperature, short start-up and shut-down time, high efficiency, no waste is generated as the by-product is water [4,5]. Due to compact size, low operating temperature, and quick start-up time makes PEMFCs a reliable candidate for medium power applications like smart grid, micro gird, and power electronic devices [6]. The fuel cell has three main components: anode, cathode, and electrolyte. Both anode and cathode contain a layer of catalyst, which is separated by an electrolyte membrane to perform the redox reaction. However, the voltage (1.0 V) and current density (500–1000 mA/cm^2) delivered by a single cell is too low for any practical application, so a number of stacks are connected in series to deliver sufficient power for practical application. The performance of a fuel cell depends on multiple parameters such as operating temperature, inlet pressure of fuel and reactant, and conductivity of the membrane. In order to utilize fuel cell for wide range of application evaluation of

performance under various operating conditions is necessary. Moreover, development of a mathematical model to simulate the dynamic variation in operating conditions and fuel cell performance is necessary for its integration in smart grid/microgrid [7].

Both theoretical and experimental studies have been performed to optimize the factors affecting performance such as pressure, temperature, flow rate of fuel and oxidant, reaction kinetics, and membrane thickness to get the maximum power density from fuel cell [8]. As the fuel cell performance depends on multiple interdependent factors, which makes it really difficult to develop a mathematical model to evaluate the multivariable, complex, and interrelated parameters affecting the fuel cell performance [9]. In recent years, remarkable research and development has been performed to get a better understanding of the function of PEMFC characteristics via mathematical modeling. The modeling achieves great significance in the outlook of simulation, design, exploration, and progress of high-efficiency fuel cell systems [10–12]. A reliable model facilitates monitoring of fuel cell behavior for process monitoring and designing a suitable power conditioning unit for various power applications. The development of a precise parameter estimation method using the experimental data is a pre-requisite to develop a mathematical model of fuel cell and design an appropriate power control algorithm [13]. Two different approaches have been utilized to develop a mathematical model of the fuel cell systems. In the first approach, a mechanistic model is built to simulate the heat, mass transfer, reaction kinetics, membrane conductivity, and crossover of reactants through the electrolyte membrane encountered in fuel cells [14,15]. In this approach, a three-dimensional multiphase model of fuel cell system is developed, in which the gas and liquid two-phase flow in channel and porous electrodes are investigated in detail. This approach of precise estimation of model parameters is hindered by the nonlinear and complex relations of the electrochemical equations. In the second approach, a mathematical model is developed on the basis of empirical or semi-empirical equations, which are utilized to predict the effect of different input parameters on the voltage–current characteristics of the fuel cell, without examining the physical and electrochemical phenomena taking place in fuel cell system [16]. The electrical equivalent models of fuel cell are mainly divided into static and dynamic models. The static models depends on steady-state operation of fuel cell based on polarization curve [17,18] and the dynamic models rely on characteristics of electrical terminal represented by a set of passive elements [19,20]. Although mechanistic models have been developed to evaluate the optimum parameters to get the maximum output from the fuel cell system, the actual performance of fuel cell observed in experimental studies is not precisely the same as observed in theoretical studies, irrespective of models, because of assumptions and approximations are made in modelling [21]. In order to develop the precision of the models and make it reflect the actual fuel-cell performance, it is essential to improve the parameters of the models. However, a little effort has been put forward in the area of parameters optimization.

Generally, the statistics contained in any PEMFC datasheet are insufficient to determine the effective set of parameters. However, if the precise parameters are not specified, there are significant variations between the data obtained from the model and that listed in the manufacturer's datasheet. PEMFC parameter identification can be approached as an optimization challenge, and a variety of meta-heuristic techniques can be implemented to find the best solution. Over the last ten years, various meta-heuristic optimization techniques have been applied to address the issue of PEMFC parameter estimation, which utilizes two important search strategies: (a) exploration/diversification and (b) exploitation/intensification [22,23]. The first method explores the search space globally, which avoids local optima and resolving local optima entrapment, whereas the second method explores the nearby promising solutions to improve their quality locally [24]. A proper balance between these two strategies is required to get the optimum performance. The classification of meta-heuristics method is based in the evolutionary algorithms, swarm intelligence algorithms, physics-based methods, and human-based methods. However, there is no single optimized algorithm, which can solve all optimization problems. Most

of the researchers either modify an existing algorithm or propose a new algorithm to get better result [25]. Different meta-heuristic algorithms have been utilized for parameter optimization of PEMFCs such as particle swarm optimization (PSO) [26], genetic algorithm (GA) [27], artificial neural network (ANN) [28], differential evolution (DE) [29], artificial immune system (AIS) [30], artificial bee colony (ABC) [31], bird mating optimization (BMO) [32], biography-based optimization (BMO) [33], seeker optimization algorithm (SOA) [34], backtracking search algorithm (BSA) [35], improved teaching learning-based optimization (ITLBO) [36]. Slime mold algorithm (SMA) [37], moth-flame optimization (MFO) [38], Archimedes optimization algorithm [39], Jellyfish search algorithm (JSA) [40], bonobo optimizer [41], and hybrid GWO algorithm [42] have been implemented to identify the unknown parameters of PEMFC. In this article, the authors have proposed an improved opposition-based arithmetic optimization algorithm for parameter extraction of PEMFC. To the best of the authors' knowledge, arithmetic optimization algorithm (AOA) has not been explored in this field, therefore, in this article authors have examined the performance of improved AOA for parameter extraction of fuel cells.

The main contribution of this research paper is as follows:

- An improved arithmetic optimization algorithm (AOA) algorithm is formulated that employs the opposition-based learning method for population initialization, preventing the accumulation of too many solutions in one location and resulting in a more efficient global search.
- The performance of the proposed algorithm is evaluated on ten benchmark functions and experimental results clearly depicts that the OBAOA is very efficient and accurate.
- The performance of proposed OBAOA algorithm is further accessed for parameter extraction of Ballard Mark V PEFMC.

The manuscript is organized as follows: Section 2 describes the theoretical and mathematical model of the PEMFC, Section 3 includes the formulation of OAOA technique. Section 4 discusses the results and findings. Finally, Section 5 provides the overall conclusive remarks of the proposed study.

2. Theory and Modeling of Proton Exchange Membrane Fuel Cell

There are three main components of a fuel cell: anode, cathode, and electrolyte. The fuel oxidation and oxygen reduction take place at anode and cathode, respectively. An electrolyte membrane separates the anode and cathode and allows conduction of protons to complete the electric circuit. The oxidation and reduction reaction are shown by Equations (1) and (2), respectively. The overall reaction is represented by Equation (3) [43,44].

$$\text{Oxidation: } 2H_2 \rightarrow 4H^+ + 4e^- \tag{1}$$

$$\text{Reduction: } O_2 + 4H^+ + 4e^- \rightarrow 2H_2O \tag{2}$$

$$\text{Complete reaction: } 2H_2 + O_2 \rightarrow 2H_2O \tag{3}$$
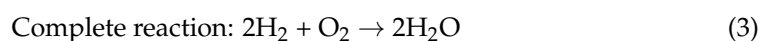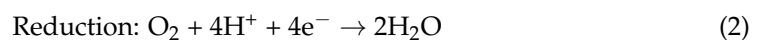
At open circuit potential the cell voltage can be expressed by Equation (4):

$$V_{\text{Cell}}^{\text{OCV}} = E_{O_2/H_2O}^r - E_{H_2/H^+}^r \tag{4}$$

At standard conditions (1.0 atm pressure and 25 °C), the fuel cell open circuit voltage (OCV) should be 1.229 V. However, the measured OCV at room temperature is around 1.0 V, due to the losses associated with the fuel cell. The cell voltage (V_{cell}) is expressed by Equation (5) when the current (I_{cell}) is drawn from the cell.

$$V_{\text{cell}} = E_{\text{Nernst}} - V_{\text{activation}} - V_{\text{concentration}} - V_{\text{ohmic}} \tag{5}$$

$$E_{\text{Nernst}} = 1.229 - 0.85 \times 10^{-4}(T - 298.15) + 4.3085 \times 10^{-5}T\left[ln\left(P_{H_2}\right) + 0.5\,ln\left(P_{O_2}\right)\right] \tag{6}$$

The activation overpotential of anode and cathode can be expressed as:

$$V_{\text{activation}} = -\left[\xi_1 + \xi_2 + \xi_3 \times T \times ln\left(C_{O_2}\right) + \xi_4\, ln(i)\right] \tag{7}$$

where $V_{\text{activation}}$ is the voltage drop due to the activation of redox processing the anode and cathode. The ξ_n represents the parametric coefficients for each cell model, whose values are defined based on theoretical equations with kinetic, thermodynamic, and electrochemical foundations (Mann et al., 2000). The oxygen concentration at the catalyst layer of the cathode (C_{O_2}, mol/cm^3) is given by:

$$C_{O_2} = \frac{P_{O_2}}{5.08 \times 10^6 \times e^{\frac{498}{T}}} \tag{8}$$

The mass transport affects the concentrations of hydrogen and oxygen at the anode and cathode, which affects the partial pressures of gases. The change in partial pressure of fuel and reductant rely on the electrical current and on the physical features of the system. The voltage drop due to concentration polarization is represented as:

$$V_{\text{concentration}} = -b\, ln\left(1 - \frac{i}{i_{max}}\right) \tag{9}$$

where b is a parametric coefficient (V) that depends on the cell and its operation state, and i represents the actual current density of the cell (A/cm^2).

The ohmic drop (V_{Ohmic}) in Equation (5) is represented as:

$$V_{\text{Ohmic}} = i\,(R_M + R_c) \tag{10}$$

$$R_M = \rho_M \frac{l}{A} \tag{11}$$

where R_M is the resistance to the transfer of protons through the membrane (Ω), R_c is the charge transfer resistance, ρ_M is the specific resistivity of the membrane for the electron flow (Ω-m), A is the active area of the cell (cm^2) and l is the thickness of the membrane, which separate electrodes. The following numerical expression for the resistivity of the Nafion membrane is used:

$$\rho_M = \frac{181.6 \times \left[1 + 0.03\left(\frac{i_{FC}}{A}\right) + 0.062\left(\frac{T}{303}\right)^2 \left(\frac{i_{FC}}{A}\right)^{2.5}\right]}{\left[\lambda - 0.634 - 3\left(\frac{i_{FA}}{A}\right) exp\left(4.18\left(\frac{T-303}{T}\right)\right)\right]} \tag{12}$$

where $181.6/(\lambda - 0.634)$ is the specific resistivity (Ω-cm) at OCV at 30 °C, the exponential term in the denominator is the temperature factor correction if the cell is operating at different temperature. The parameter λ is an adjustable parameter with a maximum value of 24. This parameter is influenced by the preparation procedure of the membrane and is a function of relative humidity and stoichiometry relation of the anode gas.

If 'n' number of stacks are combined then the cell voltage is defined as:

$$V_{\text{cell}} = n \times (E_{\text{Nernst}} - V_{\text{activation}} - V_{\text{concentration}} - V_{\text{ohmic}}) \tag{13}$$

At a given temperature (T), the partial pressure of fuel (P_{H_2}) and oxidant (P_{O_2}) is given by following equations:

$$P_{H_2} = \frac{0.79}{0.21} P_{O_2} \tag{14}$$

$$P_{O_2} = P_c - RH_c P^*_{H_2O} - P_{N_2} \exp\left(\frac{0.291 \frac{i}{A}}{T^{0.832}}\right) \tag{15}$$

If H_2 and O_2 are used as reactant then the partial pressure of oxygen and hydrogen is given as:

$$P_{O_2} = RH_c P_{H_2O}^* \left[\left(\frac{\exp\left(\frac{4.192\left(\frac{i}{A}\right)}{T^{1.334}} \right) \left(RH_c P_{H_2O}^* \right)}{P_c} \right)^{-1} - 1 \right] \tag{16}$$

$$P_{H_2} = RH_a P_{H_2O}^* \left[\left(\frac{\exp\left(\frac{1.635\left(\frac{i}{A}\right)}{T^{1.334}} \right) \left(RH_a P_{H_2O}^* \right)}{P_a} \right)^{-1} - 1 \right] \tag{17}$$

where RH_c and RH_a are relative humidity at the cathode and anode, respectively. P_c and P_a are the inlet pressure at cathode and anode, respectively. The P_{N_2} is partial pressure of nitrogen at the cathode. The $P_{H_2O}^*$ is saturated vapor pressure (atm), which is calculated as:

$$log_{10}\left(P_{H_2O}^* \right) = 2.95 \times 10^{-2}(T - 273.15) - 9.18 \times 10^{-5}(T - 273.15)^2 + 1.44 \times 10^{-7}(T - 273.15)^3 - 2.18 \tag{18}$$

Formulation of Objective Function

In this research work, sum of squared error (SSE) is adopted as an optimization function (OF) for the identification of unknown parameters (ζ_1, ζ_2, ζ_3, ζ_4, λ, R_c, and b) of PEMFC, which is generally used by the authors in the existing literature [45–47]. The objective function is defined as follows:

$$OF = \text{Minimize}(SSE) = \text{Minimize}\left(\sum_{i=1}^{N} [V_{\text{measured}}(i) - V_{\text{estimated}}(i)]^2 \right) \tag{19}$$

where N represents the number of measured values, i denotes the number of iterations, V_{measured} denotes the measured voltage while $V_{\text{estimated}}$ denotes the estimated value of voltage for PEMFC.

3. Optimization Method

3.1. Conventional Arithmetic Optimization Algorithm

Arithmetic optimization algorithm (AOA) is a stochastic population-based metaheuristic optimization algorithm proposed by Abualigah et al. [48] in the year 2021. The algorithm is motivated by the distribution behavior of four key arithmetic operators in the field of mathematics, which includes addition, subtraction, multiplication, and division. In the area of science and engineering, there are complex, non-convex, and high dimension problems, which are difficult to solve using conventional gradient-based optimization algorithms. Metaheuristic is a high-level search algorithm that easily finds the optimal solution for diverse problems without getting stuck in local optimal solution. These algorithms first create a random solution in the search space and iteratively discovers the solution through different search strategies. The phenomenon of how these algorithms update its solution is defined by mathematical behavior of algorithms. Based on these mathematical-concepts, these algorithms are classified as evolutionary, swarm, physics-based, and human-based algorithms. Genetic algorithm (GA), particle swarm optimization (PSO), gravitational search algorithm (GSA), whale optimization algorithm (WOA), and grey wolf optimization (GWO) are some of the metaheuristic algorithms that have efficiently solved non-linear and high-computational engineering design problems. Exploration and exploitation are other unique characteristics that define the functionality of these algorithms. Exploration is defined as the global search capability of the algorithm, while exploitation is defined as the capability of algorithm to explore the nearby promising regions. The efficiency of a metaheuristic algorithm depends on how efficiently the algorithm maintains the balance between exploration and exploitation. AOA uses high and low dispersion nature of arithmetic operators to creates this balance. Multiplication and division operators have high

distributed values, therefore these operators are used in the exploration phase to discover the optimal solution in a diverse region of search space with the following equations:

$$x_{i,j}(C_{\text{Iter}} + 1) = \begin{cases} best(x_j) \div (MOP + \epsilon) \times ((UB_j - LB_j) \times \mu + LB_j), & r_2 < 0.5 \\ best(x_j) \times MOP \times ((UB_j - LB_j) \times \mu + LB_j), & \text{otherwise} \end{cases} \quad (20)$$

where $x_{i,j}$ represents the jth position of the ith solution, $best(x_j)$ is the jth position of the best obtained solution, UB_j and LB_j are the upper and the lower bound of the jth position, ϵ is a constant parameter, μ is the control parameter that regulates the search process, and r_2 is the random number in the range [0, 1]. The MOP is math optimizer probability and defined as:

$$MOP(C_{\text{Iter}}) = 1 - \frac{(C_{\text{Iter}})^{1/\alpha}}{(M_{\text{Iter}})^{1/\alpha}} \quad (21)$$

where C_{Iter} represents the current iteration, M_{Iter} represents the maximum number of iterations, and α is the constant parameter.

Subtraction and multiplication operators have low distributed values, therefore, these operators easily find the optimal solution in the areas that were discovered in the exploration phase. These exploitation operators iteratively reach the solution with the following equations :

$$x_{i,j}(C_{\text{Iter}} + 1) = \begin{cases} best(x_j) - (MOP + \epsilon) \times ((UB_j - LB_j) \times \mu + LB_j), & r_3 < 0.5 \\ best(x_j) + MOP \times ((UB_j - LB_j) \times \mu + LB_j), & \text{otherwise} \end{cases} \quad (22)$$

where r_3 is the random number defined in range [0, 1].

The exploration and exploitation phases are balanced by Math Optimizer accelerated (*MOA*) function, which is defined as:

$$MOA(C_{\text{Iter}}) = Min + C_{\text{Iter}} \times \left(\frac{Max - Min}{M_{\text{Iter}}} \right) \quad (23)$$

where *min* and *max* represent the minimum and the maximum value of the accelerated function. Exploration phase is executed when the value of r_1, which is a random number in range [0, 1] is greater than MOA, otherwise the exploitation phase is executed.

3.2. Opposition-Based Learning

In 2005, Tizhoosh et al. introduced the phenomenon of opposition-based learning (OBL) [49]. The basic principle of OBL is that it imitates the opposite relationship among agents. Over the last few years, artificial intelligence field has experienced tremendous growth and researchers are exploring and building innovative algorithms so as to enhance the performance of existing algorithms. OBL is one of the novel concepts that finds application in metaheuristic [50] and other artificial intelligence algorithms. OBL considers agents and their opposite counterpart in order to better explore the search space and find global optimal solution. Figure 1 shows the mechanism of OBL. The fundamental concept of OBL is outlined as follows:

Let N be a real number in the search space $[k_L, k_U]$, then its opposite counterpart is defined as follows:

$$\vec{N} = k_L + k_U - N \quad (24)$$

In the higher dimensional space, the N is expressed as:
$N_k = [N_{k_1}, N_{k_2}, \ldots, N_{k_t}]$ and defined in the search space $[k_{Lt}, k_{Ut}]$, where $t = 1, 2, 3, \ldots, n$. Then, the opposite points are defined as:

$$\vec{N}_k = k_{Lt} + k_{Ut} - \left[\vec{N}_{k1}, \vec{N}_{k2}, \ldots\ldots\ldots\ldots\ldots \vec{N}_{kt} \right] \quad (25)$$
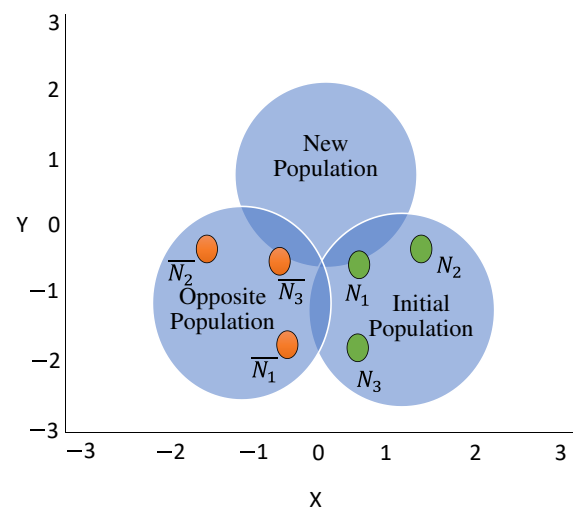
Figure 1. Illustration of opposition-based learning mechanism [2].

3.3. Proposed Algorithm

This section outlines the proposed opposition-based arithmetic optimization algorithm (OBAOA). In the field of optimization, local optima avoidance capability and convergence rate are two critical parameters, which define the performance of the algorithm. Most of the metaheuristic algorithms quickly converges and avoids local optimal solution. However, some algorithms fail to explore entire search space and get trapped in local optimal solution. In this area, researchers are exploring new ways such as modification of existing algorithm, hybridization of two or more algorithms to overcome these limitations.

AOA also has poor exploration capability and did not discover a global optimal solution and have slow rate of convergence. Thus, in this article, authors have enhanced the performance of AOA by incorporating the opposition mechanism and have proposed opposition OBAOA. OBL mechanism allows the algorithm to discover global optimal solution and improve convergence rate and thereby boost exploration capability of the algorithm. In OBAOA, the opposition-based principle is first incorporated in the initialization phase and later in the operational phase. The flow chart of OBAOA is shown in Figure 2 and the mathematical model is outlined as follows:

Step 1 Initialization: Generate the random candidate solution in the defined space as:

$$X = \begin{bmatrix} p_{1,1} & p_{1,2} & \cdots & \cdots & p_{1,d} \\ p_{2,1} & p_{2,2} & \cdots & \cdots & p_{2,d} \\ p_{n,1} & p_{n,2} & \cdots & \cdots & p_{n,d} \end{bmatrix} \tag{26}$$

where n is the number of solution and d is the dimension.

Step 2 Opposition Based Learning: Generate the opposite solution in the search space using Equation (25);

Step 3 (Initialize the constant parameters): Initialize the parameters α, μ and ϵ;

Step 4 (Fitness evaluation): Evaluate the fitness of opposite candidate solution;

Step 5 (Ranking): Sort the fitness and determine the best solution;

Step 6 (Evaluate constant and time varying parameters): Use Equations (21) and (23) to estimate the MOA function and MOP and generate random numbers r_1, r_2, r_3 in the range [0, 1];

Step 7 (AOA candidate solution position updating mechanism):
if $r_1 >$ MOA;
update position of each candidate solution using the following mechanism.

Implement exploration phase:

if $r_1 > 0.5$;

update the position using multiplication model of Equation (20).
Else;
update the position using division model of Equation (20).
Else;

Implement exploitation phase:

if $r_3 > 0.5$;
update the position using addition model of Equation (22).
Else;
update the position using subtraction model of Equation (22).

Step 8 (Monitor the positions of each candidate solution): Determine the opposite candidate solution that moves beyond the search space and reinitialize their position within the boundaries;

Step 9 (Termination criteria): If minimum error or maximum number of iterations is accomplished the algorithm ends. Otherwise repeat Steps (5) to (8);

Step 10 (Final result): The position of best candidate solution represents the global optimal solution.
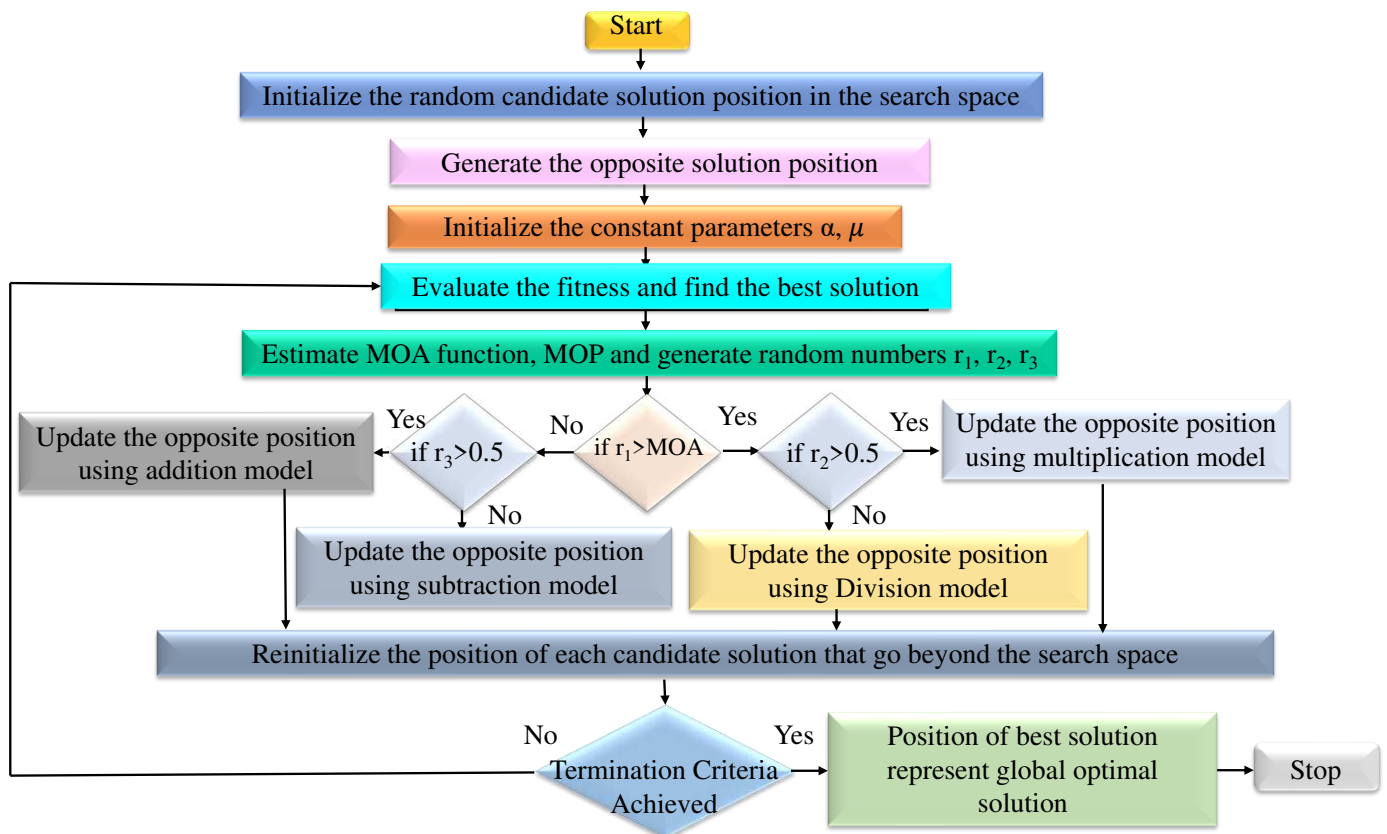
Figure 2. Flow chart of opposition-based arithmetic optimization algorithm.

4. Results and Discussion

In this section, a benchmark test research approach was used to evaluate the proposed algorithm in the case of parameter identification for PEMFC. Table 1 displays the ten benchmark test functions, one to seven of which are unimodal and the remaining functions are multimodal. Some well-known meta-heuristic algorithms, such as ant lion optimizer (ALO) [51], dragonfly algorithm (DA) [52], grasshopper optimization algorithm (GOA) [53], and multiverse optimization (MVO) [54] are especially compared to assess the precision and efficiency of the suggested algorithm. The statistical outcomes of benchmark test functions are shown in Table 2. In this research paper, the benchmark functions are denoted by the letter "F" accompanied by a number (e.g., F1).

According to Table 2, the proposed algorithm has the least mean and standard deviation (SD) values except for the F6. In the case of F6, ALO generates the best optimized value. Based on the benchmark test function, it is asserted that the proposed algorithm outperforms and outperforms the other compared algorithms in terms of effectiveness and precision.

Table 1. Benchmark functions.

ID	Mathematical Expression	Dim	Lower	Upper	Type
F1	$f_1(x) = \sum_{i=1}^{n} x^2$	30	-100	100	Unimodal
F2	$f_2(x) = \sum_{i=1}^{n} |x_i| + \prod_{i=1}^{n} |x|$	30	-10	10	Unimodal
F3	$f_3(x) = \sum_{i=1}^{n} \left(\sum_{j-1}^{i} x_j \right)$	30	-100	100	Unimodal
F4	$f_4(x) = max_i[|x|, 1 \leq i \leq n]$	30	-100	100	Unimodal
F5	$\sum_{i=1}^{n-1} \left[100(x_{i+1} - x_i^2)^2 + (x_i - 1)^2 \right]$	30	-30	30	Unimodal
F6	$\sum_{i=1}^{n} (|x_i + 0.5|)^2$	30	-100	100	Unimodal
F7	$\sum_{i=1}^{n} i x_i^4 + random[0, 1]$	30	-1.28	1.28	Unimodal
F8	$\sum_{i=1}^{n} -x_i \sin\left(\sqrt{|x_i|}\right)$	30	-500	500	Multimodal
F9	$\sum_{i=1}^{n} \left[x_i^2 - 10\cos(2\pi x_i) + 10 \right] . n$	30	-5.12	5.12	Multimodal
F10	$-20\exp\left(-0.2\sqrt{\frac{1}{n}\sum_{i=1}^{n} x_i^2}\right) - \exp\left(\frac{1}{n}\sum_{i=1}^{n}\cos(2\pi x_i)\right) + 20 + e$	30	-32	32	Multimodal

Table 2. Statistical results of benchmark test functions.

Algorithms		F1	F2	F3	F4	F5	F6	F7	F8	F9	F10
OBAOA	MEAN	1.54×10^{-122}	0	4.05×10^{-112}	3.81×10^{-125}	2.88×10^{-17}	6.8817×10^{-2}	7.17×10^{-16}	-1.4632×10^4	6×10^{-51}	5.33×10^{-43}
	SD	3.0876×10^{-32}	0	1.099×10^{-18}	0	2.71×10^{-3}	5.4317×10^{-3}	1.15×10^{-4}	3.0044×10^{-2}	1.63×10^{-4}	1.82×10^{-11}
ALO	MEAN	9.06×10^{-10}	1.56×10^{-5}	8.02×10^{-5}	3.36×10^{-5}	5.8065×10^{-3}	4.3×10^{-9}	4.7488×10^{-2}	-2.1542×10^2	1.9899×10^{-3}	1.63×10^{-5}
	SD	7.9531×10^{-5}	2.33×10^{-2}	4.4256×10^{-4}	2.647×10^{-3}	4.1108×10^{-2}	2.0335×10^{-3}	7.6×10^{-1}	2.1278×10^3	2.5977×10^{-1}	2.001×10^{-2}
DA	MEAN	1.2477×10^{-2}	5.789×10^{-1}	5.137×10^{-2}	2.6485×10^{-3}	1.5026×10^{-3}	1.115×10^{-2}	8.381×10^{-3}	-2.3522×10^3	1.8527×10^{-1}	2.0353×10^{-3}
	SD	1.485×10^{-1}	4.5855×10^{-2}	3.1780×10^{-1}	9.9573×10^{-2}	2.2829×10^{-2}	8.8613×10^{-1}	2.6488×10^{-1}	2.211×10^1	4.2195×10^{-2}	6.7603×10^{-2}
GOA	MEAN	7.64×10^{-1}	2.2149×10^{-2}	3.71×10^{-8}	1.38×10^{-5}	4.5656×10^{-3}	1.43×10^{-9}	8.905×10^{-3}	-3.0710×10^4	3.7095×10^{-3}	1.6462×10^{-2}
	SD	5.2897×10^{-6}	2.8652×10^{-1}	4.5226×10^{-3}	3.6148×10^{-3}	4.132×10^{-2}	3.9632×10^{-1}	1.12×10^{-2}	1.3627×10^2	5.2491×10^{-2}	2.0027×10^{-1}
MVO	MEAN	4.279×10^{-3}	1.1512×10^{-2}	1.7761×10^{-2}	2.7901×10^{-2}	2.8803×10^{-3}	9.359×10^{-3}	1.664×10^{-3}	-3.0448×10^1	6.9657×10^{-2}	2.245×10^{-2}
	SD	9.591×10^{-2}	3.173×10^{-1}	1.622×10^{-1}	6.75×10^{-1}	4.325×10^{-1}	9.839×10^1	2.0981×10^{-1}	2.301×10^1	1.0753×10^1	2.62×10^0

To further validate the effectiveness of the proposed OBAOA algorithm, the practical case of Ballard Mark V PEMFC is considered. The experimental values of voltage and current are taken from [55,56]. The operating condition and technical specification of Ballard Mark V PEMFC is illustrated in Table 3. Table 4 depicts the lower and upper search bounds for the parameters similar to the other authors [57,58]. The simulation results are compared with the other optimization methods existing in the literature review. Moreover, to show the competence of OBAOA algorithm, four pre-existing algorithms: AOA [48], PSO [59], gravitational search algorithm (GSA) [60], and acquilla optimizer (AO) [61] are employed. For a reasonable comparative evaluation, the number of population and iterations are set at 30 and 1000, respectively. All simulations were run on a PC with an Intel (R) Core i5- CPU M370@2.4 GHz 8 GB and the MATLAB R2018b software.

Table 3. Technical specification and operating condition of PEMFC.

Parameters	Ballard Mark V
Number of cells	35
A [cm^2]	50.6
l [μm]	178
J_{max} [A/cm^2]	1.5
P_{H2} [bar]	1
Po_2 [bar]	1
Power [W]	1000
T [K]	343.15

Table 4. Lower and upper bounds of parameters for PEMFC.

Parameters	Upper Bound	Lower Bound
ζ_1	−0.08532	−1.1997
$\zeta_2 \times 10^{-3}$	6.00	0.8
$\zeta_3 \times 10^{-5}$	9.80	3.60
$\zeta_4 \times 10^{-4}$	−0.954	−2.60
λ	24.00	10.00
$R_C \times 10^{-4}$	8.00	1
b	0.5	0.0136

4.1. Parameter Optimization of BALLARD MARK V PEMFC

Table 5 demonstrates the optimized value of all parameters by implementing the OBAOA algorithm. The number of cells connected in series in the Ballard Mark V model is 35, and the membrane thickness is 178 μm. It is clearly depicted in Table 3 that the proposed OBAOA method is able to produce the least SSE of 9.03×10^{-4} in comparison to other optimization methods. Here, SSE is taken for performance evaluation, which is same as considered by the other authors [58,62].

Table 5. Optimized value of parameters for Ballard Mark V PEM fuel cell.

Parameter/ Algorithm	ζ_1	ζ_2	ζ_3	ζ_4	λ	R_C	b	SSE	Time (s)
OBAOA	−1.245	1.539×10^{-3}	9.45×10^{-5}	-1.84×10^{-4}	11.315	6.03×10^{-4}	0.0490	9.03×10^{-4}	3.20
AOA	−1.784	3.415×10^{-3}	5.13×10^{-5}	-1.058×10^{-5}	14.711	6.316×10^{-4}	0.0856	2.16×10^{-3}	11.40
PSO	−1.917	4.338×10^{-3}	7.19×10^{-5}	-1.602×10^{-5}	16.285	2.285×10^{-4}	0.4635	1.489×10^{-3}	15.70
GSA	−1.044	8.545×10^{-3}	3.60×10^{-5}	-9.54×10^{-5}	18.345	1×10^{-4}	0.0136	1.665×10^{2}	12.34
AO	−1.419	2.116×10^{-3}	3.62×10^{-5}	-2.391×10^{-5}	22.558	7.793×10^{-4}	0.4301	1.985×10^{2}	14.67
IFSO [63]	−1.120	3.57×10^{-3}	8.01×10^{-5}	-15.94×10^{-5}	22	1×10^{-4}	0.015	0.784	3.80
CGOA [64]	−2.120	3.8×10^{-3}	7.19×10^{-5}	-17.03×10^{-5}	23	1×10^{-4}	0.042	2.613	5.61
MRFO [65]	−1.090	3.82×10^{-3}	7.73×10^{-5}	-16.28×10^{-5}	23	1×10^{-4}	1.36	0.85	6.19
FSO [66]	−0.950	3.36×10^{-3}	7.42×10^{-5}	-15.83×10^{-5}	22	1×10^{-4}	0.029	0.952	6.13
HGWO [57]	−0.974	3.451×10^{-3}	8.38×10^{-5}	-1.129×10^{-4}	21.70	8×10^{-4}	0.0136	2.369×10^{-3}	-

Furthermore, as depicted in Table 6, the minimum and maximum value of internal absolute error (IAE) between experimental and simulated values is 0.0003 and 0.0139, respectively. The characteristics curve of current-voltage and power-voltage for Ballard Mark V PEMFC is redrawn and presented in Figure 3, based on best-optimized parameters obtained by executing the OBAOA algorithm. This implies that the presented OBAOA technique outperforms other methods.

4.2. Convergence Analysis

Figure 4 describes the convergence curve for the Ballard Mark V PEMFC to evaluate the computational capability of the OBAOA technique. Figure 4 shows that the developed OBAOA algorithm significantly outperformed the AOA, PSO, GSA, and AO algorithms in terms of convergence speed and produces a realistic solution for the same number of function evaluations (i.e., 1000).

Table 6. Estimated values of voltage and power for Ballard Mark V PEMFC.

$I_{measured}$ (A)	$V_{measured}$ (V)	$V_{estimated}$ (V)	Absolute Error	$P_{measured}$ (W)	$P_{estimated}$ (W)	Absolute Error
5.4	0.92	0.9067	0.0132	4.968	4.8965	0.0714
10.8	0.88	0.8782	0.0017	9.504	9.4846	0.0193
16.2	0.85	0.8496	0.0003	13.77	13.7641	0.0058
21.6	0.82	0.8210	0.0010	17.712	17.7352	0.0232
27	0.79	0.7925	0.0025	21.33	21.3977	0.0677
32.4	0.77	0.7639	0.0060	24.948	24.7517	0.1962
37.8	0.74	0.7353	0.0046	27.972	27.7973	0.1746
43.2	0.72	0.7068	0.0131	31.104	30.5343	0.5696
48.6	0.69	0.6782	0.0117	33.534	32.9628	0.5711
54	0.66	0.6496	0.0103	35.64	35.0829	0.5570
59.4	0.62	0.6211	0.0011	36.828	36.8944	0.0664
64.8	0.6	0.5925	0.0074	38.88	38.3974	0.4825
70.2	0.55	0.5639	0.0139	38.61	39.5919	0.9819
Sum of AE			8.68×10^{-2}			
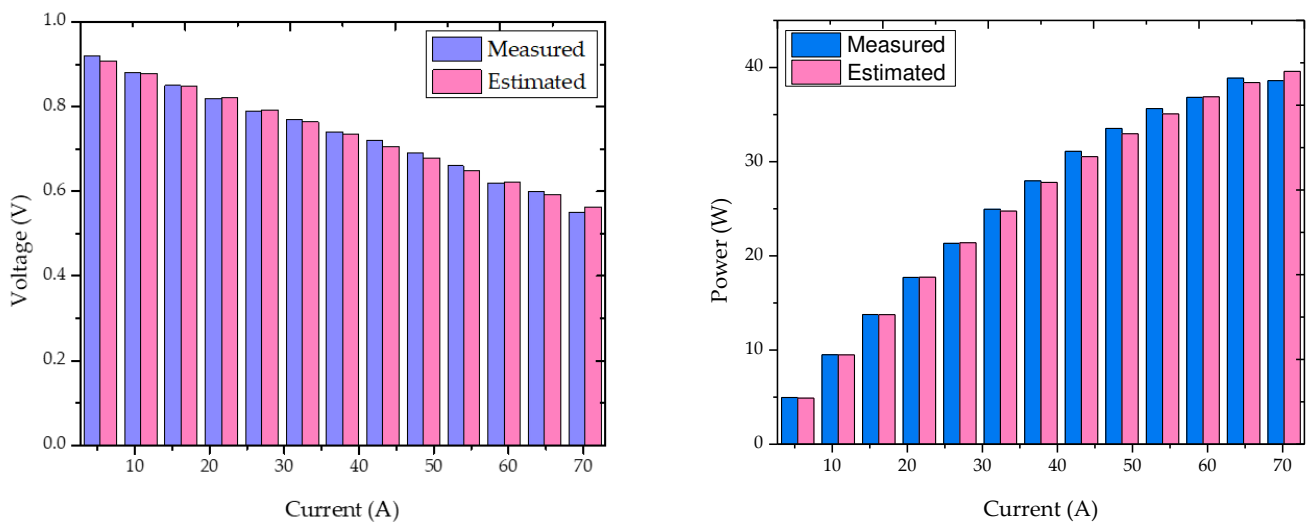
Figure 3. Evaluation between the experimental and the simulated data produced by OBAOA technique for Ballard Mark V PEMFC.
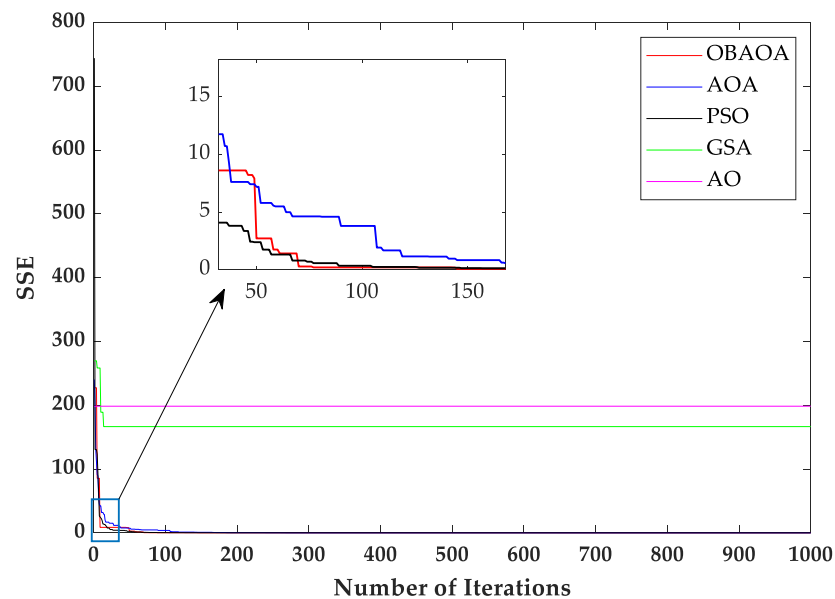
Figure 4. Convergence graph of different algorithms for Ballard Mark V fuel cell.

The minimum value of SSE is produced by OBAOA. The values of SSE are 9.03×10^{-4}, 2.16×10^{-3}, 1.489×10^{-3}, 1.665×10^{2}, and 1.985×10^{2}, respectively for OBAOA, AOA, PSO, GSA, and AO.

4.3. Statistical and Robustness Analysis

This section provides the statistical evaluations based on mean, minimum, maximum, and standard deviation in terms of SSE for all earlier suggested methodologies, as well as a comparison with the accuracy and robustness of the various algorithms in a total of thirty runs, as shown in Table 7. The mean of the SSE is calculated to evaluate the algorithms' accuracy, and the standard deviation is calculated to evaluate the dependability of the implemented parameter estimation technique.

Table 7. Statistical results of Ballard Mark V Fuel cell.

Algorithms	Minimum	Maximum	Average	SD
OBAOA	9.030×10^{-4}	2.274×10^{2}	1.694×10^{-3}	2.054×10^{-5}
AOA	2.166×10^{-3}	2.403×10^{2}	1.957×10^{-2}	3.185×10^{-3}
PSO	1.489×10^{-3}	3.357×10^{1}	1.818×10^{-2}	1.101×10^{-3}
GSA	1.665×10^{2}	5.767×10^{2}	1.675×10^{-1}	1.506×10^{-2}
AO	1.985×10^{2}	1.985×10^{1}	1.983×10^{-2}	2.116×10^{-3}

The statistical analysis outcomes reveal that the developed OBAOA is the most accurate and efficient technique for parameter estimation because it has a very low standard deviation.

The Friedman rank test [67] is applied to determine the relevance of the data in addition to the conventional statistical analysis, i.e., best, mean, worst, and standard deviation. Furthermore, for each analyzed PV module, this non-parametric test is used to rank the algorithms. The null hypothesis H_0 (*p*-value > 5%) in the Friedman test suggests no notable change between the compared algorithms. The opposite hypothesis H_1 signifies a notable difference between the compared algorithms for all 30 runs. In this test, each algorithm is given a rank based on its performance. Small ranks determine the best algorithms. Table 8 displays the Friedman rank test results at a 95% confidence level. According to Table 8, the OBAOA has the first rank based on the Friedman ranking test results, followed by PSO, AOA, GSA, and AO.

Table 8. Friedman ranking test for Ballard Mark V PEMFC.

Algorithms	Friedman Ranking
OBAOA	1
AOA	3
PSOF	2
GSA	4
AO	5

5. Conclusions

The OBAOA algorithm is proposed in this paper to recognize the complicated parameters of the PEMFC model. In the present work, the practical reading of Ballard Mark V PEMFC is considered for the identification of seven unknown parameters (ζ_1, ζ_2, ζ_3, ζ_4, λ, R_c, and b). Based on the results obtained, the findings are as follows.

- An enhanced version of OBAOA is introduced by incorporating the opposition-based learning mechanism.
- SSE is taken as an objective function for the optimization of parameters.
- The proposed algorithm is tested using ten benchmark test functions (seven unimodal and three multimodal). Furthermore, the convergence graph as well as the I-V and P-V characteristics curves support the precision of the anticipated algorithm.

- The proposed OBAOA technique is easy to implement with low computational complexity.
- The SSE value is minimum (9.03×10^{-4}) compared to standard AOA and other predefined algorithms with least computational time i.e., 3.20 s.
- Friedman ranking test is carried out, which clearly depicts that the OBAOA algorithm outperforms the other compared algorithms.

It is also worth noting that the proposed formulation will pique the attention of the fuel cell community, both researchers and practitioners, due to its capacity to solve problems effectively.

References

1. Goldemberg, J. The promise of clean energy. *Energy Policy* **2006**, *34*, 2185–2190. [CrossRef]
2. Sharma, A.; Sharma, A.; Dasgotra, A.; Jately, V.; Ram, M.; Rajput, S.; Averbukh, M.; Azzopardi, B. Opposition-Based Tunicate Swarm Algorithm for Parameter Optimization of Solar Cells. *IEEE Access* **2021**, *9*, 125590–125602. [CrossRef]
3. Rajashekara, K. Hybrid fuel-cell strategies for clean power generation. *IEEE Trans. Ind. Appl.* **2005**, *41*, 682–689. [CrossRef]
4. Mekhilef, S.; Saidur, R.; Safari, A. Comparative study of different fuel cell technologies. *Renew. Sustain. Energy Rev.* **2012**, *16*, 981–989. [CrossRef]
5. Sharaf, O.Z.; Orhan, M.F. An overview of fuel cell technology: Fundamentals and applications. *Renew. Sustain. Energy Rev.* **2014**, *32*, 810–853. [CrossRef]
6. Bankupalli, P.T.; Ghosh, S.; Kumar, L.; Samanta, S. A noniterative approach for maximum power extraction from PEM fuel cellusing resistance estimation. *Energy Convers. Manag.* **2019**, *187*, 567–577. [CrossRef]
7. Priya, K.; Satishkumar, K.; Rajasekhar, N. A comprehensive review on parame-ter estimation techniques for Proton Exchange Membrane fuel cell modelling. *Renew. Sustain. Energy Rev.* **2018**, *93*, 121–144. [CrossRef]
8. Seo, M.H.; Choi, S.M.; Lim, E.J.; Kwon, I.H.; Seo, J.K.; Noh, S.H.; Kim, W.B.; Han, B. Toward New Fuel Cell Support Materials: A Theoretical and Experimental Study of Nitrogen-Doped Graphene. *ChemSusChem* **2014**, *7*, 2609–2620. [CrossRef]
9. Friede, W.; Raël, S.; Davat, B. Mathematical model and characterization of the transient behavior of a PEM fuel cell. *IEEE Trans. Power Electron.* **2004**, *19*, 1234–1241. [CrossRef]
10. Tremblay, O.; Dessaint, L.-A. A generic fuel cell model for the simulation of fuel cell vehicles. In Proceedings of the 2009 IEEE Vehicle Power and Propulsion Conference, Dearborn, MI, USA, 7–10 September 2009.
11. Ahmadi, P.; Kjeang, E. Realistic simulation of fuel economy and life cycle metrics for hydrogen fuel cell vehicles. *Int. J. Energy Res.* **2017**, *41*, 714–727. [CrossRef]
12. Spiegel, C. *PEM Fuel Cell Modeling and Simulation Using MATLAB*; Elsevier: Amsterdam, The Netherlands, 2011.
13. Bankupalli, P.T.; Ghosh, S.; Sahu, L.K.; Dwivedi, A.K. Parameter estimation of PEM fuel cell electrical equivalent model using hybrid optimization. In Proceedings of the 8th International Conference on Power Systems (ICPS), Jaipur, India, 20–22 December 2019; pp. 1–6.
14. Amphlett, J.C.; Baumert, R.M.; Mann, R.F.; Peppley, B.A.; Roberge, P.R.; Harris, T.J. Performance modeling of the Ballard Mark IV solid polymer electrolyte fuel cell: I. Mechanistic model development. *J. Electrochem. Soc.* **1995**, *142*, 1. [CrossRef]
15. Ariza, H.E.; Correcher, A.; Sánchez, C.; Pérez-Navarro, Á.; García, E. Thermal and Electrical Parameter Identification of a Proton Exchange Membrane Fuel Cell Using Genetic Algorithm. *Energies* **2018**, *11*, 2099. [CrossRef]
16. Hu, M.; Gu, A.; Wang, M.; Zhu, X.; Yu, L. Three dimensional, two phase flow mathematical model for PEM fuel cell: Part I. Model development. *Energy Convers. Manag.* **2004**, *45*, 1861–1882. [CrossRef]
17. Mzoughi, D.; Allagui, H.; Bouaicha, A.; Mami, A. Modeling and testing of a 1.2-kW Nexa fuel cell using bond graph methodology. *IEEJ Trans. Electr. Electron. Eng.* **2015**, *10*, 527–538. [CrossRef]

18. Haji, S. Analytical modeling of PEM fuel cell i–V curve. *Renew. Energy* **2011**, *36*, 451–458. [CrossRef]

19. Wang, C.; Nehrir, M.; Shaw, S.R. Dynamic Models and Model Validation for PEM Fuel Cells Using Electrical Circuits. *IEEE Trans. Energy Convers.* **2005**, *20*, 442–451. [CrossRef]

20. Sharma, A.; Sharma, A.; Averbukh, M.; Jately, V.; Azzopardi, B. An Effective Method for Parameter Estimation of a Solar Cell. *Electronics* **2021**, *10*, 312. [CrossRef]

21. Abdin, Z.; Webb, C.; Gray, E. PEM fuel cell model and simulation in Matlab–Simulink based on physical parameters. *Energy* **2016**, *116*, 1131–1144. [CrossRef]

22. Abualigah, L.; Diabat, A. A comprehensive survey of the Grasshopper optimization algorithm: Results, variants, and applications. *Neural Comput. Appl.* **2020**, *32*, 15533–15556. [CrossRef]

23. Abualigah, L.; Diabat, A.; Geem, Z.W. A Comprehensive Survey of the Harmony Search Algorithm in Clustering Applications. *Appl. Sci.* **2020**, *10*, 3827. [CrossRef]

24. Abualigah, L. Group search optimizer: A nature-inspired meta-heuristic optimization algorithm with its results, variants, and applications. *Neural Comput. Appl.* **2021**, *33*, 2949–2972. [CrossRef]

25. Abualigah, L.; Diabat, A.; Mirjalili, S.; Abd Elaziz, M.; Gandomi, A.H. The arithmetic optimization algorithm. *Comput. Methods Appl. Mech. Eng.* **2021**, *376*, 113609. [CrossRef]

26. Ye, M.; Wang, X.; Xu, Y. Parameter identification for proton exchange membrane fuel cell model using particle swarm optimization. *Int. J. Hydrog. Energy* **2009**, *34*, 981–989. [CrossRef]

27. Priya, K.; Babu, T.S.; Balasubramanian, K.; Kumar, K.S.; Rajasekar, N. A novel approach for fuel cell parameter estimation using simple Genetic Algorithm. *Sustain. Energy Technol. Assess.* **2015**, *12*, 46–52. [CrossRef]

28. Razbani, O.; Assadi, M. Artificial neural network model of a short stack solid oxide fuel cell based on experimental data. *J. Power Sources* **2014**, *246*, 581–586. [CrossRef]

29. Gong, W.; Cai, Z. Parameter optimization of PEMFC model with improved multi-strategy adaptive differential evolution. *Eng. Appl. Artif. Intell.* **2014**, *27*, 28–40. [CrossRef]

30. Askarzadeh, A.; Rezazadeh, A. Artificial immune system-based parameter extraction of proton exchange membrane fuel cell. *Int. J. Electr. Power Energy Syst.* **2011**, *33*, 933–938. [CrossRef]

31. Zhang, W.; Wang, N.; Yang, S. Hybrid artificial bee colony algorithm for parameter estimation of proton exchange membrane fuel cell. *Int. J. Hydrog. Energy* **2013**, *38*, 5796–5806. [CrossRef]

32. Askarzadeh, A. Parameter estimation of fuel cell polarization curve using BMO algorithm. *Int. J. Hydrog. Energy* **2013**, *38*, 15405–15413. [CrossRef]

33. Niu, Q.; Zhang, L.; Li, K. A biogeography-based optimization algorithm with mutation strategies for model parameter estimation of solar and fuel cells. *Energy Convers. Manag.* **2014**, *86*, 1173–1185. [CrossRef]

34. Dai, C.; Chen, W.; Song, Y.; Zhu, Y. Seeker optimization algorithm: A novel stochastic search algorithm for global numerical optimization. *J. Syst. Eng. Electron.* **2010**, *21*, 300–311. [CrossRef]

35. Askarzadeh, A.; dos Santos Coelho, L. A backtracking search algorithm combined with Burger's chaotic map for parameter estimation of PEMFC electrochemical model. *Int. J. Hydrog. Energy* **2014**, *39*, 11165–11174. [CrossRef]

36. Niu, Q.; Zhang, H.; Li, K. An improved TLBO with elite strategy for parameters identification of PEM fuel cell and solar cell models. *Int. J. Hydrog. Energy* **2014**, *39*, 3837–3854. [CrossRef]

37. Gupta, J.; Nijhawan, P.; Ganguli, S. Optimal parameter estimation of PEM fuel cell using slime mould algorithm. *Int. J. Energy Res.* **2021**, *45*, 14732–14744. [CrossRef]

38. Messaoud, R.B.; Midouni, A.; Hajji, S. PEM fuel cell model parameters extraction based on moth-flame optimization. *Chem. Eng. Sci.* **2021**, *229*, 116100. [CrossRef]

39. Houssein, E.H.; Helmy, B.E.; Rezk, H.; Nassef, A.M. An enhanced Archimedes optimization algorithm based on Local escaping operator and Orthogonal learning for PEM fuel cell parameter identification. *Eng. Appl. Artif. Intell.* **2021**, *103*, 104309. [CrossRef]

40. Gouda, E.A.; Kotb, M.F.; El-Fergany, A.A. Jellyfish search algorithm for extracting unknown parameters of PEM fuel cell models: Steady-state performance and analysis. *Energy* **2021**, *221*, 119836. [CrossRef]

41. Sultan, H.M.; Menesy, A.S.; Kamel, S.; Tostado-Véliz, M.; Jurado, F. Parameter identification of proton exchange membrane fuel cell stacks using bonobo optimizer. In Proceedings of the 2020 IEEE International Conference on Environment and Electrical Engineering and 2020 IEEE Industrial and Commercial Power Systems Europe (EEEIC/I&CPS Europe), Madrid, Spain, 9–12 June 2020; pp. 1–7.

42. Miao, D.; Chen, W.; Zhao, W.; Demsas, T. Parameter estimation of PEM fuel cells employing the hybrid grey wolf optimization method. *Energy* **2020**, *193*, 116616. [CrossRef]

43. O'Hayre, R.; Cha, S.-W.; Colella, W.; Prinz, F.B. *Fuel Cell Fundamentals*; John Wiley & Sons: Hoboken, NJ, USA, 2016.

44. Steele, B.C.; Heinzel, A. Materials for fuel-cell technologies. In *Materials for Sustainable Energy: A Collection of Peer-Reviewed Research and Review Articles from Nature Publishing Group*; World Scientific: Singapore, 2011; pp. 224–231.

45. Rajasekar, N.; Jacob, B.; Balasubramanian, K.; Priya, K.; Sangeetha, K.; Babu, T.S. Comparative study of PEM fuel cell parameter extraction using Genetic Algorithm. *Ain Shams Eng. J.* **2015**, *6*, 1187–1194. [CrossRef]

46. Ali, M.; El-Hameed, M.; Farahat, M. Effective parameters' identification for polymer electrolyte membrane fuel cell models using grey wolf optimizer. *Renew. Energy* **2017**, *111*, 455–462. [CrossRef]

47. El-Fergany, A.A. Electrical characterisation of proton exchange membrane fuel cells stack using grasshopper optimiser. *IET Renew. Power Gener.* **2018**, *12*, 9–17. [CrossRef]

48. David, R.C.; Precup, R.E.; Petriu, E.M.; Rădac, M.B.; Preitl, S. Gravitational search algorithm-based design of fuzzy control systems with a reduced parametric sensitivity. *Inf. Sci.* **2013**, *247*, 154–173. [CrossRef]

49. Tizhoosh, H.R. Opposition-based learning: A new scheme for machine intelligence. In Proceedings of the International Conference on Computational Intelligence for Modelling, Control and Automation and International Conference on Intelligent Agents, Web Technologies and Internet Commerce (CIMCA-IAWTIC'06), Vienna, Austria, 28–30 November 2005.

50. Mahdavi, S.; Rahnamayan, S.; Deb, K. Opposition based learning: A literature review. *Swarm Evol. Comput.* **2018**, *39*, 1–23. [CrossRef]

51. Mirjalili, S. The ant lion optimizer. *Adv. Eng. Softw.* **2015**, *83*, 80–98. [CrossRef]

52. Meraihi, Y.; Ramdane-Cherif, A.; Acheli, D.; Mahseur, M. Dragonfly algorithm: A comprehensive review and applications. *Neural Comput. Appl.* **2020**, *32*, 16625–16646. [CrossRef]

53. Mirjalili, S.Z.; Mirjalili, S.; Saremi, S.; Faris, H.; Aljarah, I. Grasshopper optimization algorithm for multi-objective optimization problems. *Appl. Intell.* **2018**, *48*, 805–820. [CrossRef]

54. Mirjalili, S.; Mirjalili, S.M.; Hatamlou, A. Multi-verse optimizer: A nature-inspired algorithm for global optimization. *Neural Comput. Appl.* **2016**, *27*, 495–513. [CrossRef]

55. Correa, J.; Farret, F.A.; Canha, L.; Simoes, M. An Electrochemical-Based Fuel-Cell Model Suitable for Electrical Engineering Automation Approach. *IEEE Trans. Ind. Electron.* **2004**, *51*, 1103–1112. [CrossRef]

56. Amphlett, J.; Baumert, R.; Mann, R.; Peppley, B.; Roberge, P.; Rodrigues, A. Parametric modelling of the performance of a 5-kW proton-exchange membrane fuel cell stack. *J. Power Sources* **1994**, *49*, 349–356. [CrossRef]

57. Nelwamondo, F.V.; Golding, D.; Marwala, T. A dynamic programming approach to missing data estimation using neural networks. *Inf. Sci.* **2013**, *237*, 49–58. [CrossRef]

58. Balasubramanian, K.; Jacob, B.; Priya, K.; Sangeetha, K.; Rajasekar, N.; Babu, T.S. Critical evaluation of genetic algorithm-based fuel cell parameter extraction. *Energy Procedia* **2015**, *75*, 1975–1982. [CrossRef]

59. Kennedy, J.; Eberhart, R. Particle swarm optimization. In Proceedings of the Proceedings of ICNN'95-International Conference on Neural Networks, Perth, WA, Australia, 27 November–1 December 1995.

60. Rashedi, E.; Nezamabadi-Pour, H.; Saryazdi, S. GSA: A gravitational search algorithm. *Inf. Sci.* **2009**, *179*, 2232–2248. [CrossRef]

61. Abualigah, L.; Yousri, D.; Elaziz, M.A.; Ewees, A.A.; Al-Qaness, M.A.; Gandomi, A.H. Aquila Optimizer: A novel meta-heuristic optimization algorithm. *Comput. Ind. Eng.* **2021**, *157*, 107250. [CrossRef]

62. Rezk, H.; Ferahtia, S.; Djerioui, A.; Chouder, A.; Houari, A.; Machmoum, M.; Abdelkareem, M.A. Optimal parameter estimation strategy of PEM fuel cell using gradient-based optimizer. *Energy* **2022**, *239*, 122096. [CrossRef]

63. Qin, F.; Liu, P.; Niu, H.; Song, H.; Yousefi, N. Parameter estimation of PEMFC based on Improved Fluid Search Optimization Algorithm. *Energy Rep.* **2020**, *6*, 1224–1232. [CrossRef]

64. Arora, S.; Anand, P. Chaotic grasshopper optimization algorithm for global optimization. *Neural Comput. Appl.* **2019**, *31*, 4385–4405. [CrossRef]

65. Selem, S.I.; Hasanien, H.M.; El-Fergany, A.A. Parameters extraction of PEMFC's model using manta rays foraging optimizer. *Int. J. Energy Res.* **2020**, *44*, 4629–4640. [CrossRef]

66. Leng, H.; Li, X.; Zhu, J.; Tang, H.; Zhang, Z.; Ghadimi, N. A new wind power prediction method based on ridgelet transforms, hybrid feature selection and closed-loop forecasting. *Adv. Eng. Inform.* **2018**, *36*, 20–30. [CrossRef]

67. Digalakis, J.G.; Margaritis, K.G. An Experimental Study of Benchmarking Functions for Genetic Algorithms. *Int. J. Comput. Math.* **2002**, *79*, 403–416. [CrossRef]

Design of a Charge Pump Circuit and System with Input Impedance Modulation for a Flexible-Type Thermoelectric Generator with High-Output Impedance

Kazuma Koketsu and Toru Tanzawa *

Graduate School of Integrated Science and Technology, Shizuoka University, Hamamatsu 432-8561, Japan; kohketsu.kazuma.15@shizuoka.ac.jp

* Correspondence: toru.tanzawa@shizuoka.ac.jp

Abstract: This paper describes a charge pump system for a flexible thermoelectric generator (TEG). Even though the TEG has high-output impedance, the system controls the input voltage to keep it higher than the minimum operating voltage by modulating the input impedance of the charge pump using two-phase operation with low- and high-input impedance modes. The average input impedance can be matched with the output impedance of the TEG. How the system can be designed is also described in detail. A design demonstration was performed for the TEG with 400 Ω. The fabricated system was also measured with a flexible-type TEG based on carbon nanotubes. Even with an output impedance of 1.4 kΩ, the system converted thermal energy into electric power of 30 μW at 2.5 V to the following sensor ICs.

Keywords: charge pump; energy harvesting; thermoelectric; IoT

1. Introduction

The Internet of Things (IoT) currently is attracting researchers' attention, which is a system for the interaction of information from things such as sensing edge devices to the cloud and servers via the Internet and vice versa [1]. The maintenance costs to replace batteries can be a large portion of the costs of edge devices. Therefore, it is expected that sensing devices should be battery free based on the energy transducer generating electric power from environmental energy such as sunlight and vibration kinetic energy. A thermoelectric generator (TEG) extracts power from a temperature gradient. The open-circuit voltage V_{OC} of the TEG increases in proportion to the temperature difference between hot and cold heat sources [2]. Bulk-type TEGs [3] have a low output impedance (R_{TEG}) of the order of Ω and are in production together with boost converters. Flexible-type thin film TEGs [4] are expected to have various applications because they can be placed on curved surfaces. A drawback of the flexible-type TEG is the high-output impedance of the order of 10–100 Ω, especially in the case of a small form-factor. Even worse, a low-cost small form-factor TEG generates V_{OC} as low as a few hundred mV. To operate sensor ICs, boost converters are required [5–7]. In this research, the design of boost charge pump circuits (CPs) is proposed for a flexible-type TEG with high-output impedance, as illustrated in Figure 1. Such a system is used for heat pipes [8] and wrist watches [9].

To design systems with TEGs and integrated CPs, the circuit area and power conversion efficiency (PCE) are key figures of merit. Table 1 summarizes the key features of existing designs and this work. In [10], the design of low-voltage CPs was developed to strike a balance between the circuit area and power efficiency under the conditions of a given output voltage and current. In this design, CPs are driven by voltage sources with zero impedance, while TEGs have a finite output impedance. In [11], both TEGs and CPs were optimally designed to minimize their areas when CPs were driven by TEGs. However, design constraints such as temperature differences and the number of TEG units connected

in parallel and in series were not taken into consideration. A design methodology was proposed when V_{OC} and R_{TEG} were given in [12,13]. In [12], an optimum design was provided to determine the dimensions of switching devices and the clock frequency to maximize the output power of the CP when the number of stages N and stage capacitors C of the CP and the V_{OC} and R_{TEG} of TEG were given. However, the output voltage of the CP was not given, whereas the input voltage of the load circuit must be controlled with a specific voltage. In [13], how the input voltage of the CP or the output voltage of the TEG is determined theoretically was discussed when the circuit area of the CP was minimized or, in other words, when the output power of the CP was maximized with a given CP circuit area to generate a target output current at a specific output voltage, as shown in Figure 2a, which is the same target design of this work. However, the minimum operation voltage of circuits was not considered in [13], but it was assumed that the input voltage of the CP can be set at any voltage. Furthermore, no control circuit was disclosed to control the input voltage of the CP in [13]. In this work, the minimum operating voltage of the circuits was taken into consideration in the design, as shown in Figure 2b. This can be a key design point especially for TEGs with a high-output impedance, which have a potentially large IR drop at V_{DD}.
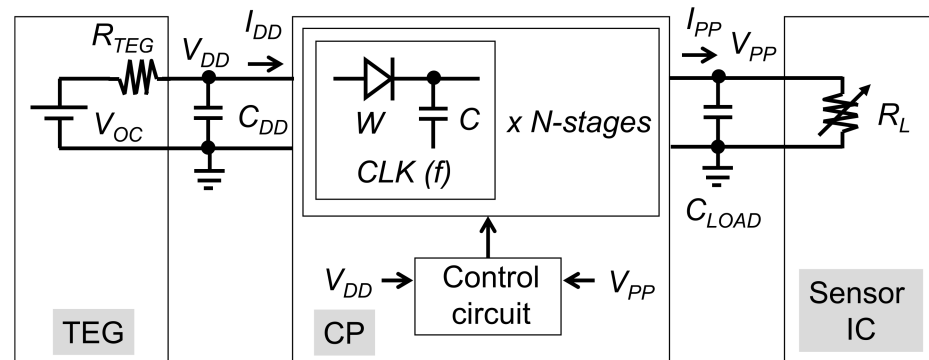
Figure 1. Block diagram of the energy harvesting system based on the TEG and CP.

Table 1. Comparison of the key features of this work with existing designs.

	Optimum Design Target	Given Design Parameters	Parameter to Be Optimized	Parameters to Be Determined
Tokuda [10]	CP	$V_{PP}, I_{PP}, V_{DD}, f$	Area of the CP to be minimized and the PCE to be maximized	N, C
Koketsu [11]		V_{PP}, I_{PP}, f	Area of the TEG and CP to be minimized	V_{OC}, R_{TEG}, N, C
Lu [12]	TEG + CP	V_{OC}, R_{TEG}, N, C	P_{PP} to be maximized	W, f
Tanzawa [13]		$V_{OC}, R_{TEG}, V_{PP}, f$	$I_{PP} @ V_{PP}$ to be maximized	N, C
This work		$V_{OC}, R_{TEG}, V_{PP}, f, V_{DD}{}^{MIN}$		

This paper is an extended version of a conference paper [14] to describe its details. A control circuit to operate the CP was proposed to meet the demand that the output current be generated as high as the target current at a specific voltage while the input voltage of the CP is controlled at a voltage higher than the minimum operating voltage. The designs of the CP system and building blocks are presented in Sections 2.1 and 2.2, respectively, to discuss how the circuits can be optimally designed. The entire system was fabricated in 65 nm CMOS. Experimental results are shown in Section 2.3, and Section 3 gives a summary of this work.
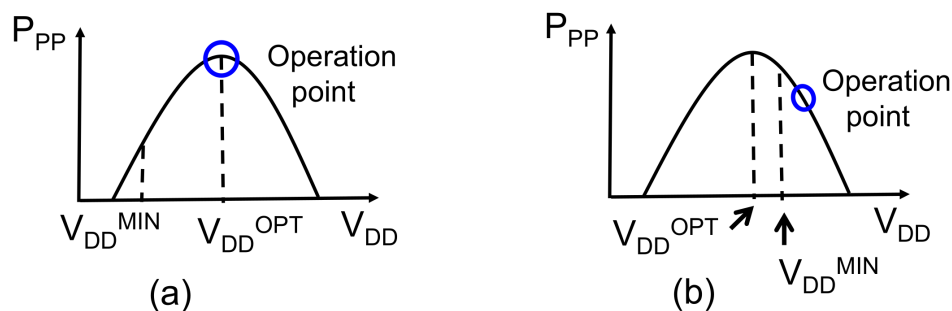
Figure 2. Operating points of [8] (**a**) and of this work (**b**).

2. Circuit Design

2.1. System Design

Figure 3 illustrates the proposed CP system to extract power from the TEG with high-output impedance and to drive the following sensor ICs. Table 2 shows the condition to resume or suspend CP operation. A detector DETi monitors V_{DD} and outputs ENi. A detector DETo monitors V_{PP} and outputs ENo. Only when both signals become high, an oscillator OSC outputs a clock to drive the CP. Otherwise, the OSC stops working to not drive the CP. The third detector DETpp generates a signal VPP_OK to let the sensor ICs know the supply voltage is sufficiently high to work.
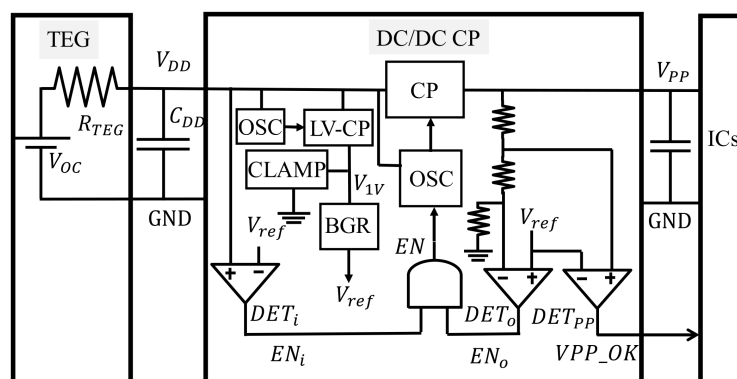
Figure 3. Building blocks of the proposed CP circuit system.

Table 2. Operation condition of the main CP against V_{DD} and V_{PP}.

	$V_{PP} < V_{PPT}$	$V_{PP} > V_{PPT}$
$V_{DD} > V_{DDT}$	Resume	Suspend
$V_{DD} < V_{DDT}$	Suspend	Suspend

Figure 4 shows two operation phases in steady state. In Phase (a), the CP inputs the current mainly from C_{DD}. Even though R_{TEG} is much larger than the input impedance of CP, V_{DD} can be controlled to be higher than V_{DD_MIN}. Phase (a) starts with EN high when V_{PP} hits $V_{PPM} = V_{PPT}$, where V_{PPM} and V_{PPT} are the minimum voltage of V_{PP} and the target voltage of V_{PP}, respectively. V_{PP} increases while V_{DD} decreases due to CP operation. EN goes low when (1) ENo goes low or (2) ENi goes low. In the case of (1), the ripple $\triangle V_{PP}$ is determined by the loop response from the output node of the CP to EN. V_{DDM} must be higher than V_{DDT}. In the case of (2), V_{DDM} is equal to V_{DDT}. In Phase (b), V_{DD} increases with the charging current from the TEG, while V_{PP} decreases with the discharging load current. The input impedance of the CP becomes very large because the main charge pump CP is suspended with EN low, even though a small amount of current flows into small building blocks such as LV-CP. Thus, even though the TEG has high-output impedance, the system controls the input voltage to keep it higher than the minimum operating voltage by

modulating the input impedance of the charge pump using two-phase operation with low- and high-input impedance modes. The average input impedance can be matched with the output impedance of the TEG. On the other hand, such an operation is not required when the output impedance of TEGs such as the bulk-type is much lower than the input impedance of the CP in operation. The operating point approaches V_{OC}, but the system can work as long as V_{OC} is higher than the minimum operating voltage.
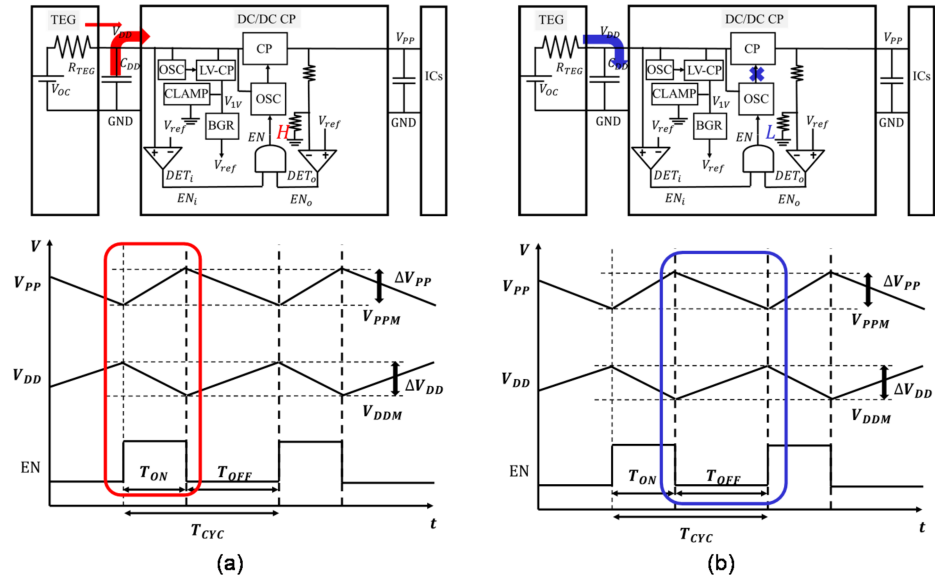
Figure 4. Two phases of the circuit operation. (**a**) Low and (**b**) high input impedance modes

The following equations hold among T_{ON}, T_{OFF}, ΔV_{PP} and ΔV_{DD}, where it is assumed that I_{PP} and I_{DD} are the steady-state currents and can be treated as constant when $\Delta V_{PP} \ll V_{PP}$, $\Delta V_{DD} \ll V_{DD}$, and $I_{TEG} \ll I_{DD}$.

$$T_{ON} = \frac{C_{DD}\,\Delta V_{DD}}{I_{DD}} = \frac{C_{PP}\,\Delta V_{PP}}{I_{PP} - I_{LOAD}} \tag{1}$$

$$T_{OFF} = R_{TEG}C_{DD}\ln\frac{V_{OC} - V_{DDM}}{V_{OC} - V_{DDM} - \Delta V_{DD}} = \frac{C_{PP}\,\Delta V_{PP}}{I_{LOAD}} \tag{2}$$

I_{PP} and I_{LOAD} are related as Equation (3).

$$I_{LOAD} = \frac{T_{ON}}{T}I_{PP} \tag{3}$$

When one can regard I_{TEG} as constant in the case of $\Delta V_{DD} \ll V_{DD}$, I_{DD} and I_{TEG} are related as Equation (4).

$$I_{TEG} = \frac{T_{ON}}{T}I_{DD} \tag{4}$$

2.2. Building Blocks' Design

B1: Main charge pump

The given design parameters are the minimum open-circuit voltage of the TEG (V_{OCMIN}), R_{TEG}, V_{PPT}. The number of stages N was designed to maximize I_{PP} at V_{PPT} when the circuit area is given. Based on [15], N is given by Equation (5).

$$N = [1.7 \times N_{MIN}] = \left\lceil 1.7 \times \frac{V_{PP} - V_{DD} + V_{TH}^{EFF}}{V_{DD}/(1 + \alpha_T) - V_{TH}^{EFF}} \right\rceil, \tag{5}$$

where $[x]$ indicates the floor function of x, N_{MIN} is the minimum number of stages to barely generate V_{PP}, and V_{TH}^{EFF} is an effective threshold voltage of switching transistors, which were called ultra-low power diodes in [16]. The capacitance of each stage capacitor C is related with I_{PP} and I_{DD} as Equations (6) and (7), where the clock frequency f is determined to maximize I_{PP}.

$$I_{PP} = \frac{fC(1+\alpha_T)}{N}\left[\left(\frac{N}{1+\alpha_T}+1\right)V_{DD} - (N+1)V_{TH}^{EFF} - V_{PP}\right], \tag{6}$$

$$I_{DD} = \left(\frac{N}{1+\alpha_T}+1\right)I_{PP} + \left(\frac{\alpha_T}{1+\alpha_T}+\alpha_B\right)fNCV_{DD} + I_{CTRL}, \tag{7}$$

where α_T and α_B are the ratios of the top (C_{TOP}) and bottom plate parasitic capacitance (C_{BTM}) to C, C_{TOP}/C and C_{BTM}/C, respectively. Note that C_{BTM} includes the parasitic capacitance of an oscillator to drive the main CP. I_{CTRL} is the input current for the control circuits, which was assumed to be βI_{DD} using the design parameter β (<1) in this paper because the auxiliary circuits assumed in this paper as shown later steadily ran regardless of T_{ON}. I_{DD} is also given by Equation (8) at the extreme case of $T_{ON} = T$ and $T_{OFF} = 0$.

$$I_{DD} = \frac{V_{OC} - V_{DD}}{R_{TEG}} \tag{8}$$

From Equations (6)–(8), the minimum C needs to meet Equation (9).

$$C = \frac{(1-\beta)N(V_{OC}-V_{DD})}{fR_{TEG}\left[(N+1+\alpha_T)\left\{\left(\frac{N}{1+\alpha_T}+1\right)V_{DD} - (N+1)V_{TH}^{EFF} - V_{PP}\right\} + \left(\frac{\alpha_T}{1+\alpha_T}+\alpha_B\right)N^2V_{DD}\right]} \tag{9}$$

To have a duty ratio of T_{ON}/T smaller than a factor of γ, the C to be designed must be increased by a factor of $1/\gamma$.

The parameters shown in Table 3 were used for design demonstration. V_{DDMIN} was mainly determined by the technology used to design, e.g., the availability of low-Vt CMOS and circuits used in the system. As will be shown later, it was limited by an oscillator to generate a clock with 10 MHz. Such a moderate frequency was required to have a sufficiently small circuit system built in the same sensor ICs. From Equations (5) and (9), N and C were calculated to be 19 and 4.8 pF at $V_{DDT} = 0.5$ V, respectively. Figure 5 shows P_{PP} and CP area NC/γ as a function of V_{DD}.

Table 3. Design parameters used in this work.

V_{DDMIN}	V_{DDT}	V_{TH}^{EFF}	V_{PPT}	R_{TEG}	V_{OCMIN}	f	α_T	α_B	β	γ
0.45 V	0.5 V	0.25 V	2.5 V	400 Ω	0.6 V	10 MHz	0.1	0.2	0.2	0.33
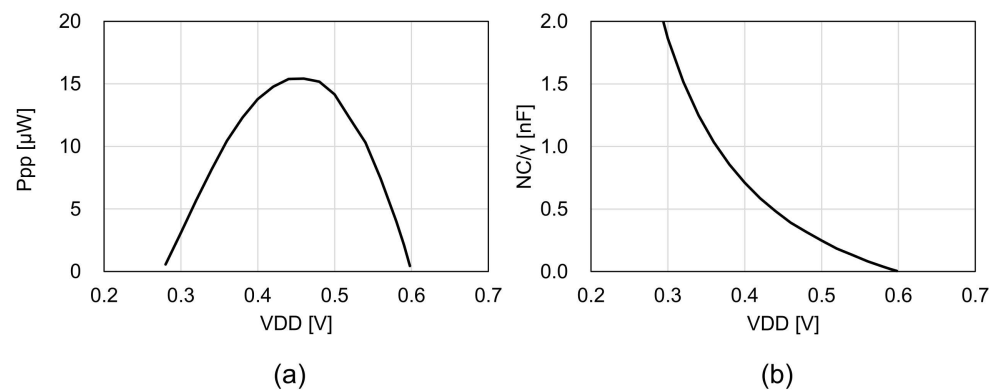
Figure 5. (**a**) P_{PP} vs. V_{DD}; (**b**) CP area NC/γ vs. V_{DD}.

B2: Auxiliary circuits

As illustrated in Figure 3, the detectors compare V_{DD} and V_{PP} with a reference voltage V_{REF} generated by bandgap reference BGR [17]. To provide a supply voltage $V_{1V} \sim 1$ V to the BGR, another small CP (LV-CP) was implemented. The LV-CP is operated in open loop not to affect the V_{DDMIN} of the system. A dedicated oscillator starts running without any input signal other than V_{DD}. When LV-CP converts power to the output terminal and V_{1V} reaches about 1 V, a clamping circuit CLAMP with NMOSFETs connected in series with the output terminal clamps the output voltage. V_{1V} is also used as the supply voltage of all the logic gates and the detectors. Figure 6 shows a simulated result of the BGR. V_{REF} is saturated when $V_{1V} > 0.8$ V.
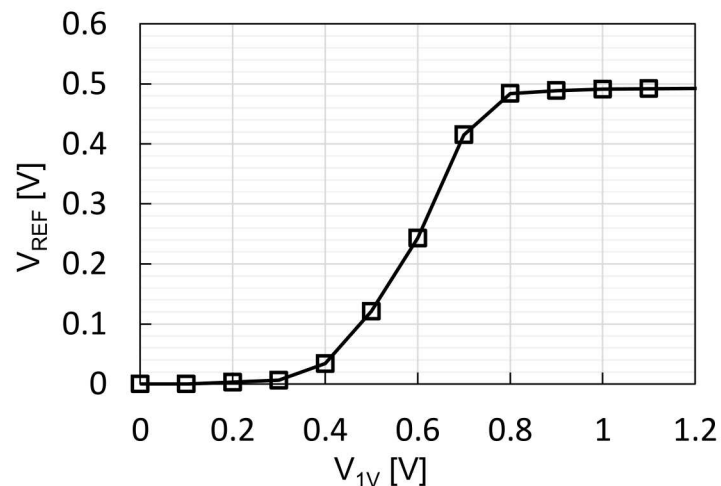
Figure 6. V_{REF} vs. V_{DD}.

2.3. Experimental Results

The system was designed in 65 nm low-Vt CMOS technology, as shown in Figure 7. The entire area was 0.28 μm^2. The CPs had an N of 20 and a C of 15 pF. The LV-CP had an N of six and a C of 3 pF to generate the supply current of 10 μA at 1 V, which was sufficiently high for the following circuits while keeping $\gamma < 0.2$.
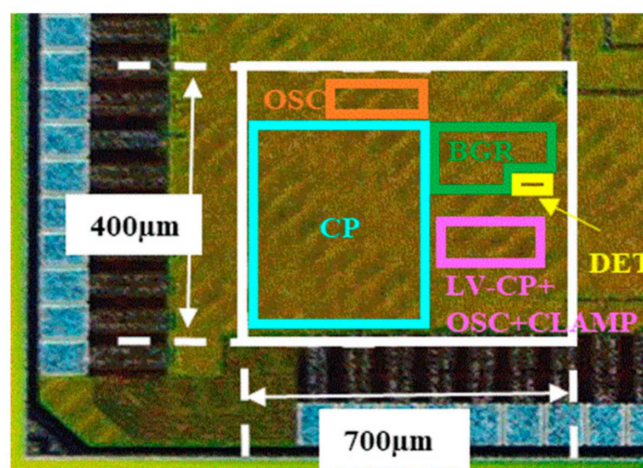
Figure 7. Die photo.

The input terminal was connected to an equivalent circuit of the TEG with V_{OC} and R_{TEG}. A C_{DD} of 300 nF and a C_{PP} of 1 nF were connected to the input and output terminals of the CP system, respectively. Since the system did not work at a V_{OC} of 0.6 V probably because the V_{TH} of MOSFETs was close to the slow corner while the simulation was performed at the typical corner, the experiments were performed at V_{OC} of 0.8 V. Figure 8

shows I_{PP}, I_{DD}, V_{DD}, and P_{PP} as a function of V_{PP} where V_{PP} was varied by varying the load resistance. All the simulations were performed with the slow-corner model. The measured results were matched with the simulated ones with an error of about 10%. V_{PP} was regulated at 2.5 V when I_{PP} was 25 μA or lower. The average V_{DD} was 0.6 V or higher when V_{PP} was regulated.
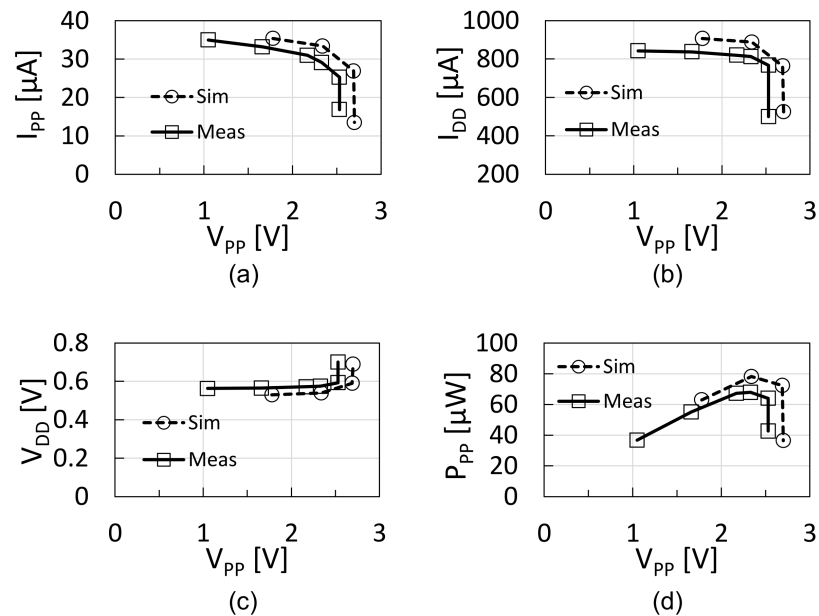
Figure 8. (**a**) I_{PP}, (**b**) I_{DD}, (**c**) V_{DD}, and (**d**) P_{PP} as a function of V_{PP}.

To see the dynamic response of V_{PP} and V_{DD} against V_{OC}, V_{OC} was made to go up and down between 0.5 V and 1 V in 200 μs, as shown in Figure 9. A signal EN was also monitored using a buffer whose supply voltage was V_{1V}. In the period T_1, because V_{DD} was lower than V_{DDT}, EN stayed low. In the period T_2, because V_{DD} was higher than V_{DDT}, but V_{PP} was lower than V_{PPT}, EN stayed high. Once V_{PP} reached V_{PPT}, in the period T_3, the system stayed in the steady state where the T_{ON}/T_{OFF} operation was repeated to keep V_{PP} and V_{DD} at V_{PPT} and V_{DDT}, respectively.
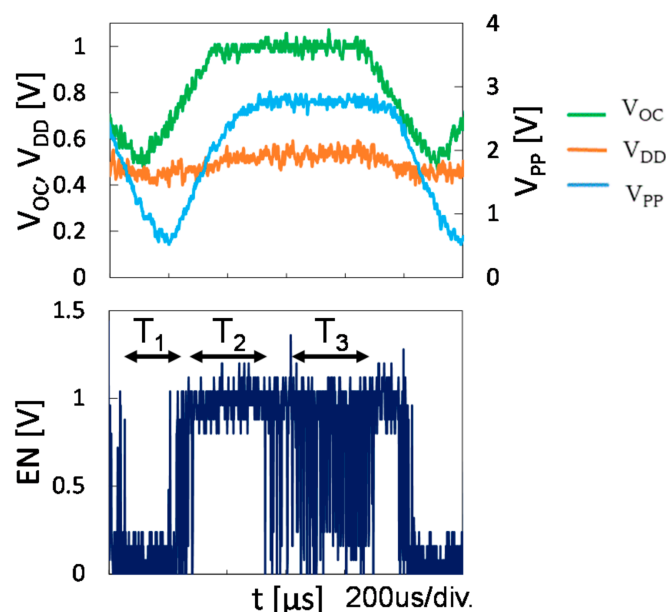
Figure 9. Dynamic behavior of V_{PP} and V_{DD} against V_{OC}.

The system was also tested with the TEG using a thermal source, as shown in Figure 10. The TEG was based on carbon nanotubes [18]. The TEG module was built to fit with a pipe, which flowed hot liquid or gas. Because the TEG module had an R_{TEG} of 1.4 kΩ, V_{OC} needed to be set at a higher voltage of 1.1 V with a temperature difference of 66 K to enable the fabricated converter system to be functional, as shown in Figure 11.

(a)   (b)
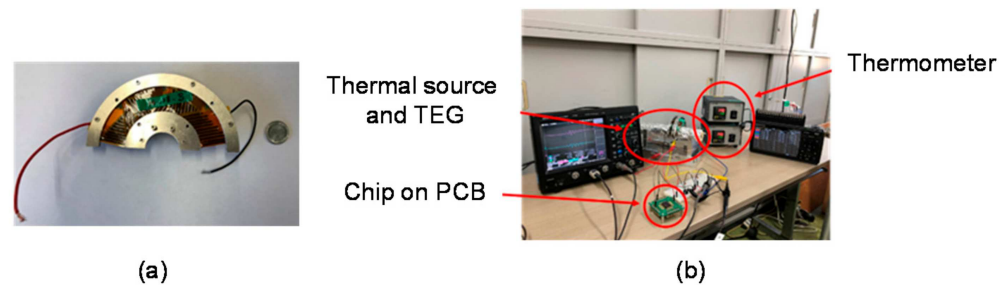
Figure 10. The TEG module (**a**) and experimental setup with the TEG (**b**).

(a)   (b)
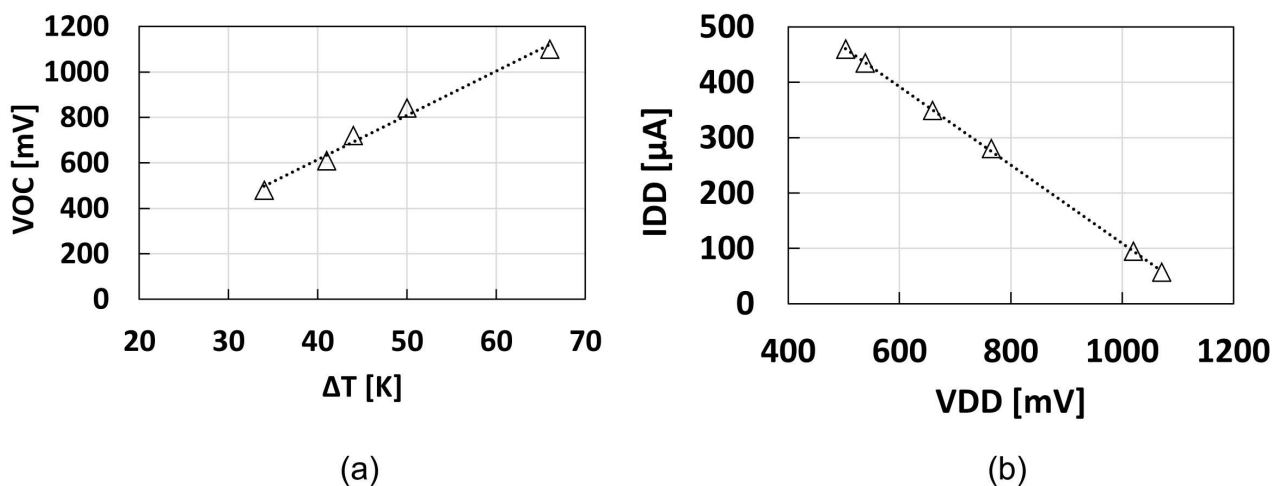
Figure 11. V_{OC} vs. ΔT (**a**) and I_{DD} vs. V_{DD} at ΔT of 66 K (**b**).

Figure 12 shows I_{PP}, I_{DD}, V_{DD}, P_{PP}, η_{SYS}, and η_{CP} as a function of V_{PP}. η_{SYS} and η_{CP} are defined by $(V_{PP} \times I_{PP})/(V_{OC} \times I_{DD})$ and $(V_{PP} \times I_{PP})/(V_{DD} \times I_{DD})$, respectively. The V_{PP} regulation point was different by 0.3 V between measured and simulated, but the electric values except for it were in good agreement. It was confirmed that the converter system with the TEG module under the experimental condition could supply power of 30 μW at 2.5 V to the following sensor ICs. The overall power conversion efficiency η_{SYS} was hit at about 7% against a theoretical limit with no loss of 50%. The power conversion efficiency of the converter system η_{CP} was 15% when V_{DD} was 0.55 V at V_{PP} of 2.5 V, i.e., a voltage ratio (V_{PP}/V_{DD}) of 4.5. For comparison, η_{CP} of 20%, 32%, and 45% was realized with a V_{DD} of 0.1 V, 0.2 V, and 0.3 V at a V_{PP} of 0.5 V, respectively, in [10]. Thus, the η_{CP} of the proposed converter system was a little lower than that of [10] at the voltage ratio of 4.5. The design optimization may need to be improved to increase power conversion efficiency by including the TEG electrical parameters in the design parameters.
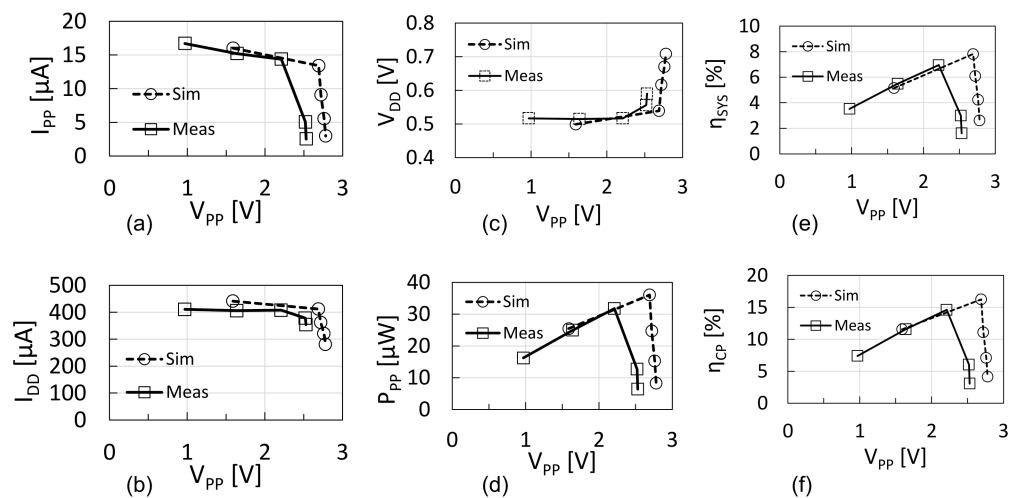
Figure 12. (**a**) I_{PP}, (**b**) I_{DD}, (**c**) V_{DD}, (**d**) P_{PP}, (**e**) η_{SYS}, and (**f**) η_{CP} as a function of V_{PP}.

3. Conclusions

A charge pump circuit system was presented for energy harvesting based on a flexible-type thermoelectric generator with high-output impedance. Even though the charge pump was operated with a highly resistive TEG, the input voltage could be controlled at a voltage higher than V_{DDMIN} by modulating the input impedance of the CP using two-phase operation with low- and high-input impedance modes. The average input impedance could be matched with the output impedance of TEG. The design methodology was proposed to determine the N and C of the main charge pump when V_{OC}, R_{TEG}, V_{PP}, f, and V_{DD}^{MIN} were given. The system was fabricated in 65 nm CMOS to demonstrate the functionality of the system with the TEG. Using an equivalent circuit for the TEG, the system was validated with a V_{OC} of 0.8 V and an R_{TEG} of 400 Ω. V_{PP} regulation was successfully observed. The circuit system was also measured with a flexible-type TEG and a thermal source. The system converted thermal energy into power to 30 µW at 2.5 V. By adding a full-bridge rectifier between the energy transducer and the proposed converter, the control circuit would be able to work even with other energy transducers such as piezoelectric or electrostatic vibration energy transducers with an AC equivalent voltage source and high-output impedance.

Author Contributions: Conceptualization, T.T.; methodology, K.K. and T.T.; software, K.K.; validation, K.K. and T.T.; formal analysis, K.K. and T.T.; investigation, K.K. and T.T.; writing—original draft preparation, K.K.; writing—review and editing, T.T.; funding acquisition, T.T. All authors have read and agreed to the published version of the manuscript.

Nomenclature

C	Capacitance per stage
C_{DD}	Capacitor connected to V_{DD}
C_{PP}	Capacitor connected to V_{PP}
f	Clock frequency
I_{CP}	Input current of CP
I_{CTRL}	Input current of control circuits

I_{DD}	Operating current of the TEG and CP
I_{LOAD}	Load current of the CP
I_{TEG}	Output current of the TEG
N	Stage number of the CP
P_{DD}	Input power of the CP
P_{PP}	Output power of the CP
P_{TEG}	Generated power of the TEG
α_T	Ratio of top plate capacitance to C
α_B	Ratio of bottom plate capacitance to C
R_{TEG}	Output impedance of the TEG
T	Operation period, $T_{ON} + T_{OFF}$
T_{OFF}	Suspended period
T_{ON}	Resumed period
V_{DD}	Input voltage of the CP
V_{DDT}	Target input voltage of the CP to be controlled
V_{DDM}	Minimum V_{DD} in operation
ΔV_{DD}	Ripple in V_{DD}
V_{PP}	Output voltage of the CP
V_{PPT}	Target output voltage of the CP to be controlled
V_{PPM}	Minimum V_{PP} in operation
ΔV_{PP}	Ripple in V_{PP}
β	Ratio of I_{CTRL} to I_{DD}
γ	Operation duty; T_{ON}/T

References

1. Lu, C.; Raghunathan, V.; Roy, K. Efficient Design of Micro-Scale Energy Harvesting Systems. *IEEE J. Emerg. Sel. Top. Circuits Syst.* **2011**, *1*, 254–266. [CrossRef]
2. Huesgen, T.; Woias, P.; Kockmann, N. Design and fabrication of MEMS thermoelectric generators with high temperature efficiency. *Sens. Actuators A Phys.* **2008**, *145*, 423–429. [CrossRef]
3. Date Sheet of TGP-651, Micropelt. Available online: http://www.micropelt.com/ (accessed on 2 April 2021).
4. Du, Y.; Xu, J.; Paul, B.; Eklund, P. Flexible thermoelectric materials and devices. *Appl. Mater. Today* **2018**, *12*, 366–388. [CrossRef]
5. Priya, S.; Inman, D.J. Chapter 18: Energy Harvesting for Active RF Sensors and ID Tags. In *Energy Harvesting Technologies*; Springer: New York, NY, USA, 2009.
6. Li, Y.; Buddharaju, K.; Singh, N.; Lo, G.Q.; Lee, S.J. Chip-Level Thermoelectric Power Generators Based on High-Density Silicon Nanowire Array Prepared with Top-Down CMOS Technology. *IEEE Electron Device Lett.* **2011**, *32*, 674–676. [CrossRef]
7. Shrivastava, A.; Wentzloff, D.; Calhoun, B.H. A 10mV-input boost converter with inductor peak current control and zero detection for thermoelectric energy harvesting. In Proceedings of the IEEE 2014 Custom Integrated Circuits Conference, San Jose, CA, USA, 15–17 September 2014. [CrossRef]
8. Remeli, M.F.; Kiatbodin, L.; Singh, B.; Verojporn, K.; Date, A.; Akbarzadeh, A. Power Generation from Waste Heat Using Heat Pipe and Thermoelectric Generator. *Energy Procedia* **2015**, *75*, 645–650. [CrossRef]
9. Priya, S.; Inman, D.J. Chapter 11: Thermoelectric Energy Harvesting. In *Energy Harvesting Technologies*; Springer: New York, NY, USA, 2009.
10. Tokuda, S.; Tanzawa, T. Toward a Minimum-Operating-Voltage Design of DC-DC Charge Pump Circuits for Energy Harvesting. In Proceedings of the 2019 IEEE International Symposium on Circuits and Systems (ISCAS), Sapporo, Japan, 26–29 May 2019; pp. 1–4. [CrossRef]
11. Koketsu, K.; Tanzawa, T. An Optimum Design of Thermal Energy Transducers and Power Converters for Small Form-Factor Thermoelectric Energy Harvester. In Proceedings of the IEICE General Conference, Tokyo, Japan, 19–22 March 2019. Available online: http://hdl.handle.net/10297/00026345 (accessed on 27 March 2019).
12. Lu, C.; Park, S.P.; Raghunathan, V.; Roy, K. Analysis and Design of Ultra Low Power Thermoelectric Energy Harvesting Systems. In Proceedings of the 16th ACM/IEEE International Symposium on Low-Power Electronics and Design, Austin, TX, USA, 11 October 2010; pp. 183–188. [CrossRef]
13. Tanzawa, T. Design of DC-DC Switched-Capacitor Voltage Multiplier driven by DC Energy Transducer. In Proceedings of the 2014 21st IEEE International Conference on Electronics Circuits and Systems, Marseille, France, 7–10 December 2014; pp. 327–330. [CrossRef]
14. Koketsu, K.; Tanzawa, T. A Design of Cold Start Charge Pump for Flexible Thermoelectric Generator with High Output Impedance. In Proceedings of the 2020 27th IEEE International Conference on Electronics, Circuits and Systems, Glasgow, UK, 23–25 November 2020. [CrossRef]
15. Tanzawa, T. An Optimum Design for Integrated Switched-Capacitor Dickson Charge Pump Multipliers with Area Power Balance. *IEEE Trans. Power Electron.* **2014**, *29*, 534–538. [CrossRef]

16. Haddad, P.-A.; Gosset, G.; Raskin, J.-P.; Flandre, D. Automated Design of a 13.56 MHz 19 μW Passive Rectifier With 72% Efficiency Under 10 μA load. *IEEE J. Solid-State Circuits* **2016**, *51*, 1290–1301. [CrossRef]
17. Banba, H.; Shiga, H.; Umezawa, A.; Miyaba, T.; Tanzawa, T.; Atsumi, S.; Sakui, K. A CMOS bandgap reference circuit with sub-1-V operation. *IEEE J. Solid-State Circuits* **1999**, *34*, 670–674. [CrossRef]
18. Suemori, K.; Hoshino, S.; Kamata, T. Flexible and lightweight thermoelectric generators composed of carbon nanotube— Polystyrene composites printed on film substrate. *Appl. Phys. Lett.* **2013**, *103*, 153902. [CrossRef]

A Fully Integrated AC-DC Converter in 1 V CMOS for Electrostatic Vibration Energy Transducer with an Open Circuit Voltage of 10 V

Yosuke Ishida [†] and Toru Tanzawa *

Graduate School of Integrated Science and Technology, Shizuoka University, Hamamatsu 432-8561, Japan; ishida.yohsuke.15@shizuoka.ac.jp
*   Correspondence: toru.tanzawa@shizuoka.ac.jp
†   Current address: Anritsu Corp., Atsugi 243-8555, Japan.

Abstract: This paper proposes an AC-DC converter for electrostatic vibration energy harvesting. The converter is composed of a CMOS full bridge rectifier and a CMOS shunt regulator. Even with 1 V CMOS, the open circuit voltage of the energy transducer can be as high as 10 V and beyond. Bandgap reference (BGR) inputs a regulated voltage, which is controlled by the output voltage of the BGR. Built-in power-on reset is introduced, which can minimize the silicon area and power to function normally found upon start-up. The AC-DC converter was fabricated with a 65 nm low-Vt 1 V CMOS with 0.081 mm^2. 1 V regulation was measured successfully at 20–70 °C with a power conversion efficiency of 43%.

1. Introduction

Energy harvesting (EH) is technology for harvesting power for IoT edge devices from environmental energy using energy transducers [1]. Eliminating the replacement of batteries based on EH can reduce the total cost of IoT devices. Electrostatic energy transducers (ES-ETs) can convert vibration energy into electronic power [2,3]. Due to the high output impedance of 1 MΩ or larger, open circuit voltages have to go beyond 10 V to generate power of 10 μW or larger. In [4], a battery charger is proposed using two variable capacitors based on ES-ETs. Capacitance varies with vibration, resulting in variable voltage at the capacitor node. Two capacitors vary out of phase. Thus, the diode connected with those two capacitors flows current from one to the other. The latter capacitor is connected to the battery via another diode. As a result, with sufficient amplitude in the voltage at the capacitor node, the battery can be charged with vibration energy. Another power converter is proposed in [5,6] based on a full bridge rectifier (FBR) followed by a DC-DC buck converter, as shown in Figure 1a. An HV rectifier is composed of four diodes for converting the AC power of ES-ETs into DC power to the converter. As the DC voltage is much higher than the maximum voltage acceptable to sensor CMOS ICs, power management circuits (PMC) in DC/DC converters need to be fabricated using a BCD process, which provides an HV CMOS operating even at high voltages of 10 V or higher. Buck converters require external components such as inductors, capacitors, and resistor (LCRs) to convert the DC input voltage of an order of 10 V into an output voltage of an order of 1 V. The priority in design was power conversion efficiency at a power of 1 mW rather than the cost and form factor. What if the priority should be the cost and form factor? In this work, we focus on the full integration of a converter into the same chip for a sensor/RF, as shown in Figure 1b. Section 2 discusses key design features. Power-on-reset (POR) is a critical block to starting up the operation. A built-in POR with no additional power is proposed. The circuit was

fabricated in 65 nm low-Vt CMOS. Experimental results are shown in Section 3. Section 4 compares the circuit features of the proposed circuit with previously reported converters.
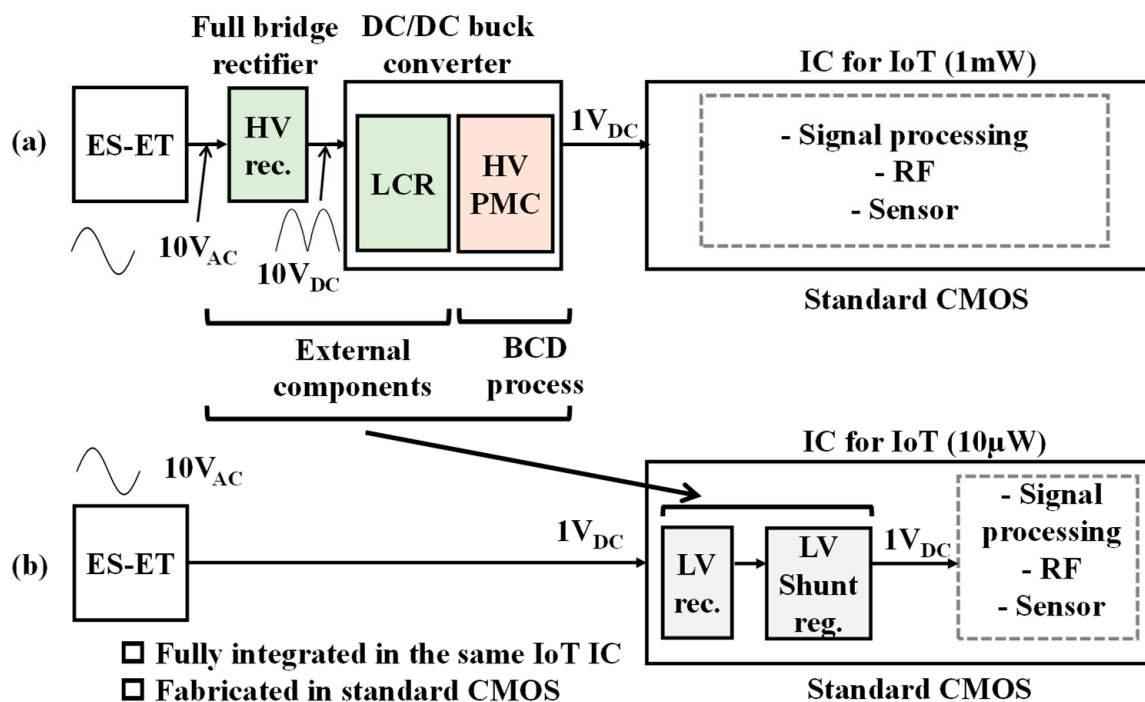
Figure 1. IoT edge device with an ES-ET and (**a**) a buck converter with FBR and PMC in a BCD process [6] or (**b**) a proposed shunt regulator integrated into an IoT chip.

2. Circuit Design

2.1. System Design

Figure 2 illustrates a proposed fully integrated AC-DC converter. A cross-coupled CMOS bridge circuit [7] is used in a full bridge rectifier (FBR). An additional diode-connected NMOS (N_D) is needed in order to not flow reverse current when the voltages at IN1 and IN2 become lower than the regulated output voltage V_{DD}. An active diode [8] can be placed in parallel with N_D to reduce the voltage drop. In this design, low power is prioritized. An active diode requires an opamp, which consumes power. Bandgap reference (BGR) operates with V_{DD}, which is controlled by the output voltage V_{REF}.
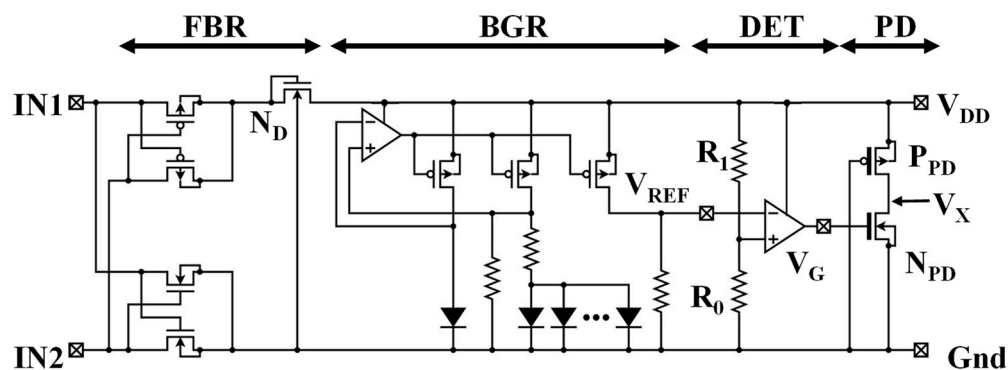
Figure 2. AC-DC converter for an ES-EH proposed in this work.

2.2. Power Conversion Efficiency

Figure 3 is used to estimate the power conversion efficiency (PCE). When the voltage drop at a rectifier is sufficiently low in comparison with the amplitude of the voltage source (V_A) and the DC output (V_{DD}), an average output power can be estimated by (1) in a steady state. The maximum available power P_{AV}, which is defined by the output power when the load resistance is as large as the output impedance of the transducer $|Z_S|$, is given by (2). Then, PCE is calculated by (3). Figure 4 shows η vs. V_{DD} at V_A = 10 V, 30 V, 60 V, and 100 V. When V_{DD} is controlled to be 1 V, η decreases as V_A (>10 V) increases, which is the weakest point for the proposed circuit. Lower V_A, or, in other words, lower output impedance, is preferred for an electrostatic energy transducer.

$$\overline{P_{OUT}} = \frac{2V_{OUT}^2}{\pi|Z_S|}\left\{\sqrt{\left(\frac{V_m}{V_{OUT}}\right)^2 - 1} - \cos^{-1}\left(\frac{V_{OUT}}{V_m}\right)\right\} \tag{1}$$

$$\overline{P_{AV}} = \frac{V_m^2}{8|Z_S|} \tag{2}$$

$$\eta = \frac{\overline{P_{OUT}}}{\overline{P_{AV}}} \tag{3}$$
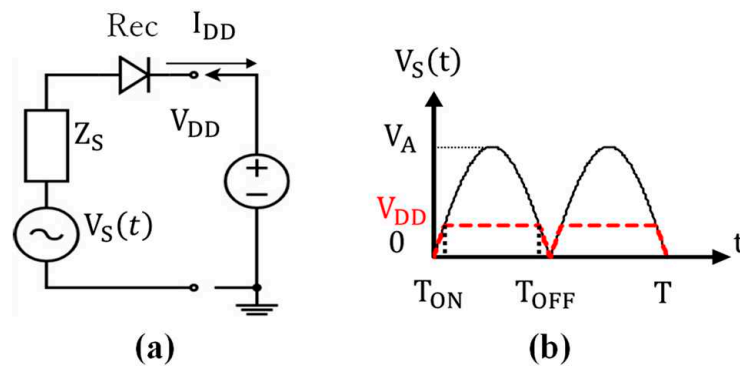
Figure 3. Circuit model for estimating the power conversion efficiency. (**a**) Circuit model; (**b**) voltage waveform.
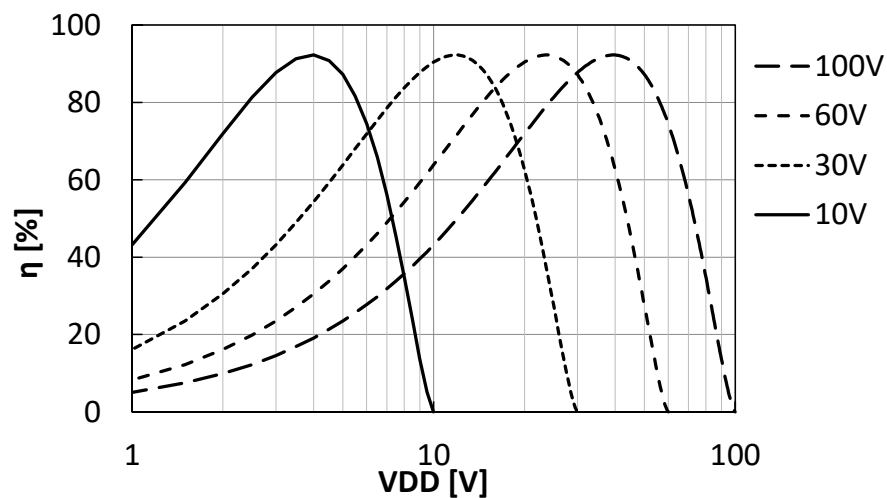
Figure 4. PCE η vs. V_{DD} at V_A = 10 V, 30 V, 60 V, and 100 V.

2.3. Bandgap Reference (BGR)

As the target V_{DD} is 1 V, a current-mode bandgap reference (BGR) [9] was selected in this work. Using low-Vt CMOS, the reference voltage V_{REF} is stable at 0.8 V and higher, as shown in Figure 5a. Operation current I_{DD}, including a current generator, is about 200 nA at V_{DD} = 1 V, as shown in Figure 5b. The detector (DET) controls V_{DD} to be 2X V_{REF} with $R_0 = R_1$ (see Figure 2). Table 1 summarizes the simulated results of the AC-DC converter at corner conditions.
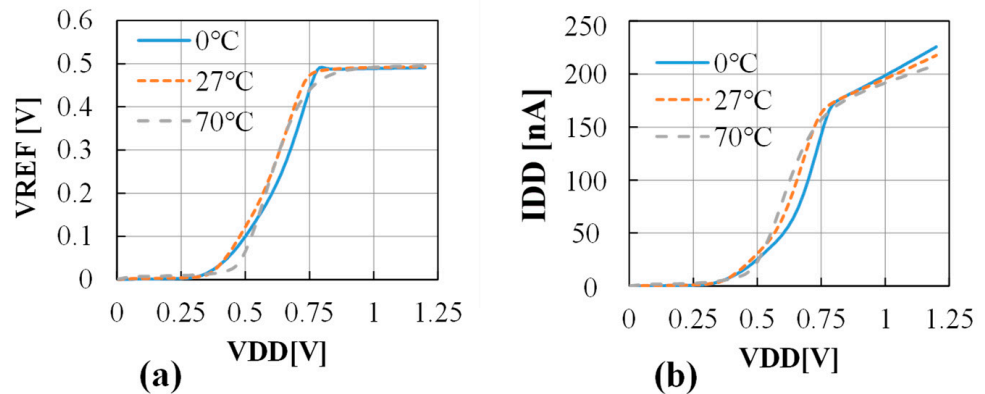
Figure 5. (**a**) Simulated V_{REF} vs. V_{DD} and (**b**) I_{DD} vs. V_{DD}.

Table 1. Simulation result of V_{DD} at corner conditions.

VDD[V]	FF	TT	SS
0 °C	1.0	1.0	1.0
27 °C	1.0	1.0	1.0
70 °C	0.90	1.0	1.0

2.4. Built-In Power-On Reset (POR)

After the transducer starts generating power, V_{DD} is gradually increased from 0 V. Every building block has its own minimum operating V_{DD}. If pull-down (PD) is enabled below the minimum V_{DD}, the system is latched in that state and therefore V_{DD} should no longer be increased. Power-on reset (POR) aims to remove such misbehavior. Additional low-power POR requires more silicon area and more power. As a result, we simply added a blocking PMOS (P_{PD}), which has a standard threshold voltage in the pull-down path, as shown in Figure 2. As shown in Figure 6a, while V_{DD} is low, V_{REF} can be also lower than $V_{DD}/2$ because of the misbehavior of the OPAMPs. In that case, the gate voltage V_G of the pull-down NMOS (N_{PD}) stays high. Even in such a case, P_{PD} disconnects the path from V_{DD} to ground. The necessary condition for normal operation is that P_{PD} starts conducting after $V_{REF} > V_{DD}/2$. Figure 6b shows the simulated waveform of the entire system to verify the normal operation during power-up.

2.5. Decoupling Capacitor

To stabilize V_{DD} even with AC input, a decoupling capacitor C_{VDD} needs to be placed. When a maximum output current of 10 μA at AC power frequency of 100 Hz is needed, the capacitance of C_{VDD} is required to be 10 μA X 5 ms/10 mV~5 μF for a ripple in V_{DD} of 10 mV. The entire AC-DC converter is simulated in AC mode, as well as with different capacitance values of C_{VDD}, as shown in Figure 7. The system can be stable with C_{VDD} of 20 nF or larger.
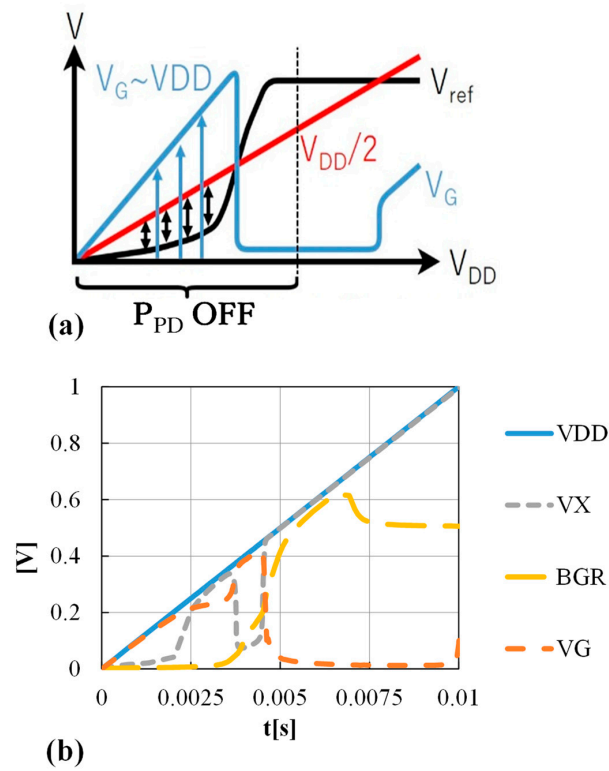
Figure 6. (**a**) Idea of a built-in POR and (**b**) the simulated waveform.
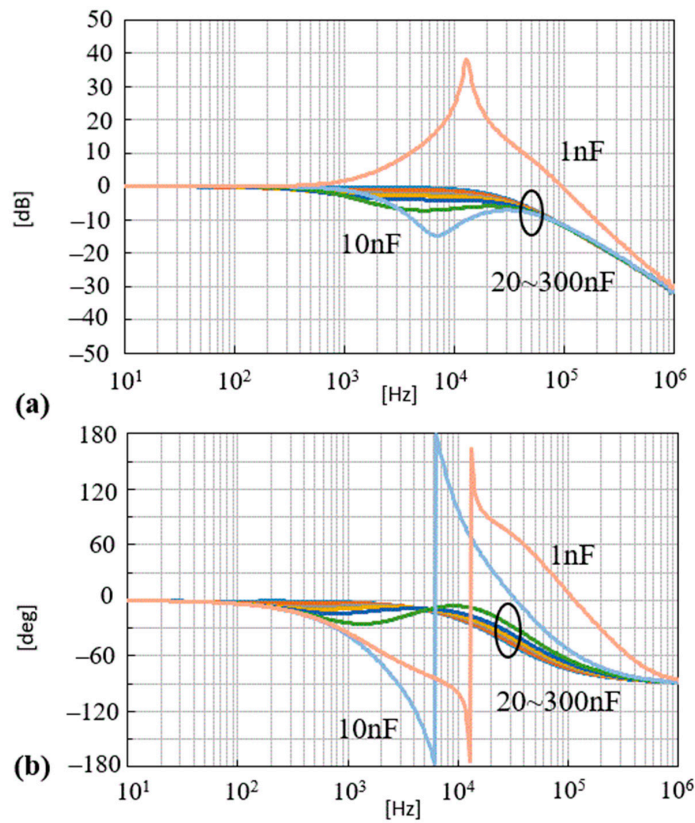
Figure 7. Bode plots with C_{VDD} varied. (**a**) Gain vs. freq.; (**b**) Phase vs. freq.

3. Experiments

The proposed AC-DC converter was designed and fabricated in 65 nm low-Vt CMOS, as shown in Figure 8. The majority block was BGR in terms of area. The entire area was 0.081 mm^2, which is so small that it can be integrated into the same IoT IC chip. The pulse generator available at the lab only generated an AC peak of 10 V. As a result, the AC-DC converter was measured with a 100 kΩ resistor connected with the AC voltage source to an input power larger than 10 μW. A 6 μF capacitor was connected with V_{DD}.
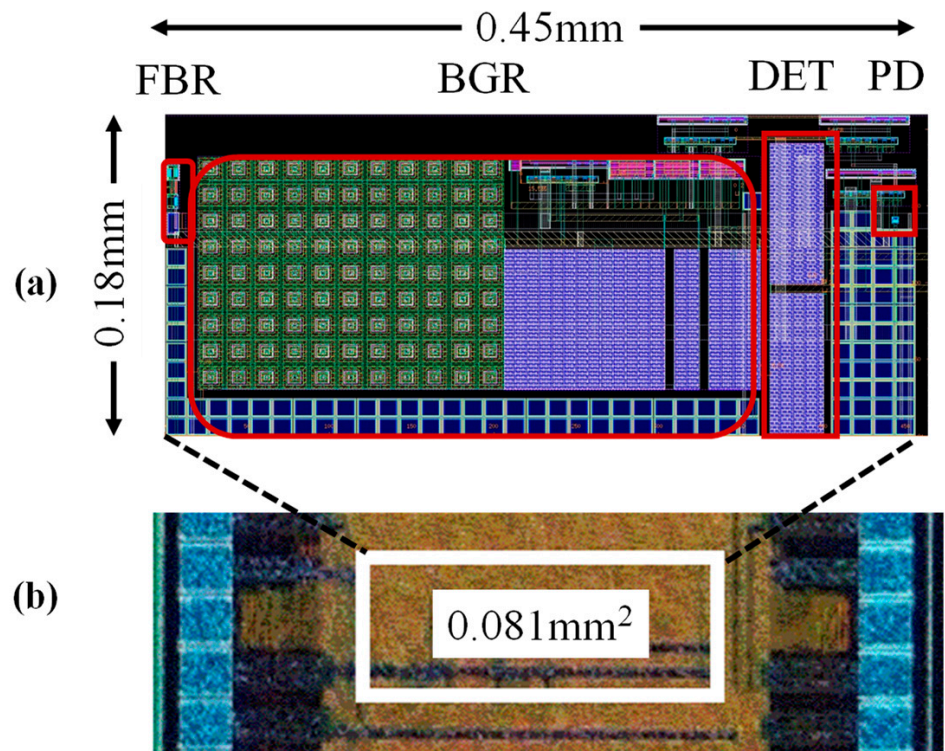
Figure 8. (**a**) Layout of the AC-DC converter and (**b**) a die photo.

Figure 9a shows I_{DD} vs. V_{DD} by varying the load resistance R_L. The AC-DC converter regulates V_{DD} at 1 V with 10 μA or below. Figure 9b shows the measured waveform at different temperatures. The voltage source starts at 0.1 s with an amplitude of 10 V at 100 Hz. The converter charges up the load capacitance C_{VDD} for 0.25 s until V_{DD} reaches about 1 V. The measured average and ripple of V_{DD} are summarized in Table 2.
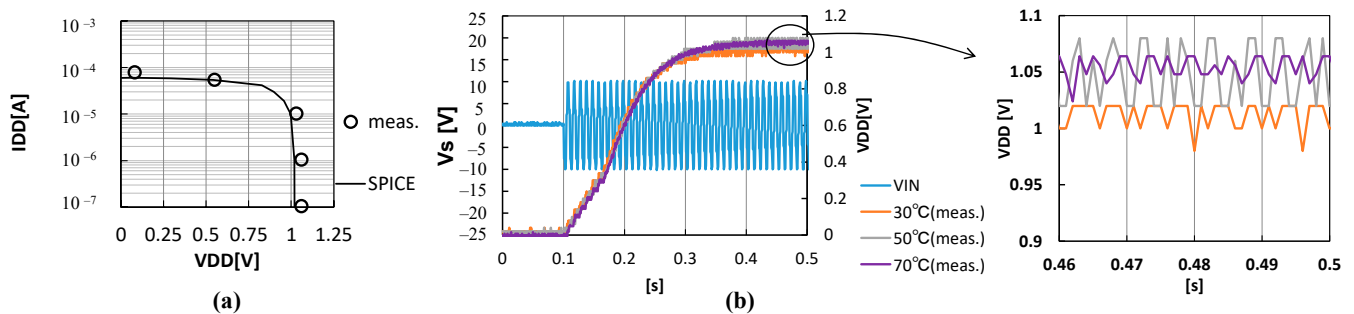
Figure 9. Measured I_{DD} vs. V_{DD} (**a**) and waveform (**b**).

Table 2. Measured V$_{DD}$ vs. temperature.

Temp.	VDD
0 °C	1.00 V $\pm$ 20 mV
27 °C	1.05 V $\pm$ 30 mV
70 °C	1.05 V $\pm$ 22 mV

To verify the effect of the built-in POR, measurements were also performed by connecting the source and drain of P$_{PD}$. As shown by "V$_{DD}$ without PMOS" in Figure 10, V$_{DD}$ was stuck at the ground level.
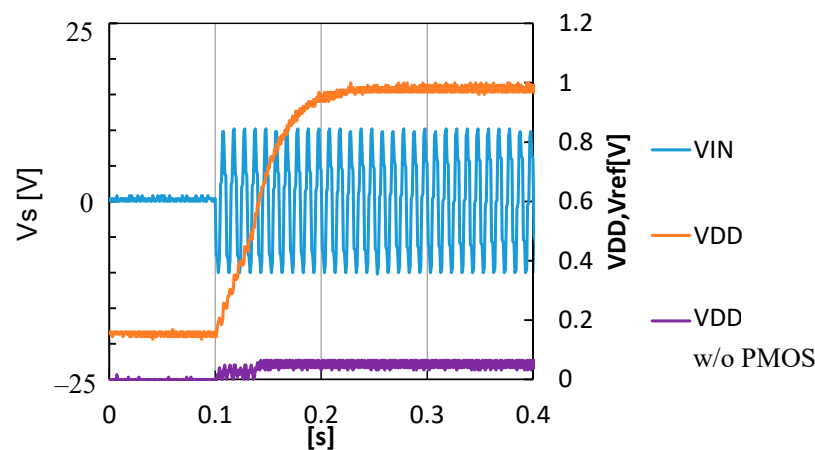
Figure 10. Measured waveform with and without P$_{PD}$.

4. Discussions

4.1. Comparison with Previously Reported Converters

Circuit features are compared in Table 3. In [6], the AC-DC converter was composed of FBR and a buck DC-DC converter. To allow for a high voltage input of 60 V at the peak, a BCD process was used, which provided 60 V transistors. Discrete diodes for FBR were required in addition to a converter chip. A high power efficiency of 85% was realized by the buck converter. In [10], another AC-DC converter was presented, which was composed of capacitor divider, switched capacitor converter, and FBR to convert power from 120 V mains. Wiring capacitors were used to manage a high voltage of 168 V without adding extra process steps or devices. As capacitance density was quite low, the converter size needed to be as large as 9.8 mm^2. In [11], another AC-DC converter was proposed to generate a standard CMOS-compatible voltage of 2 V from the magnetostrictive energy harvester (MS-EH) with a peak open circuit voltage of 0.5 V. Due to the on-chip oscillator running at 5 MHz to drive a charge pump circuit (CP), the control circuit consumed power of 18 μW. In [12], a DC-DC charge pump was developed for piezo-electric energy harvesting. The voltage conversion ratio was varied for energy efficient power conversion according to V$_A$. Area per maximum output power was realized with 3.1 [mm^2/mW]. On the other hand, a shunt regulator was used instead of the buck converter in this work at the cost of a reduction in PCE. However, when the transducer can generate sufficient power for the IoT chip even with the AC-DC converter with 43% PCE, it can be integrated into the same IoT chip without additional discrete components and the buck converter chip. Area per maximum output power was realized with 8.1 [mm^2/mW] in measurement and 0.81 [mm^2/mW] in simulation under the conditions of R$_S$ = 100 kΩ, R$_L$ = 10 kΩ, and V$_A$ = 30 V.

Table 3. Comparison table with previously reported converters.

	Stanzione [6]	De Pelecijn [10]	Kawauchi [11]	Chen [12]	This Work
Energy source	ES-EH	AC mains	MR-EH	PZ-EH	ES-EH
Voltage conversion: Up or Down?	Down	Down	Up	Up/Down	Down
Architecture	FBR and Buck	Cap-div, SC, and FBR	FBR and AC-DC CP	FBR and DC-DC CP	FBR and Shunt
External components	FBR (4 diodes)/LCR (1L,1C,2R)	None (except for C_{VDD})			
CMOS	0.25 μm 60 V BCD and 3 V CMOS	0.35 μm 12 V HV-CMOS	65 nm 1 V low-Vt CMOS	0.18 μm CMOS	65 nm 1 V low-Vt CMOS
VDD regulation	N. A.	N. A.	No regulation	N. A.	±5%
Control power	500 nW	50 nW	18 μW	4 μW (*1)	700 nW
Maximum input peak voltage	60 V	168 V	1 V	N. A.	10 V (measured), 100 V (potentially)
Input power	1 μW–1 mW	20 μW	22 μW	N.A.	1 μW–100 μW
Output power	1 μW–1 mW	20 μW	4 μW	0.5–64 μW	1 μW–100 μW
Power conversion efficiency	85%	81%	23%	72% (*1)	43%
Die/circuit area	BCD (3 mm^2) and CMOS (N.A.)	9.8 mm^2	0.11 mm^2	0.2 mm^2	0.081 mm^2
Area [mm^2]/Max. output power [mW]	4.6	612.5	27.5	3.1	8.1 (meas.), 0.81 (sim.) (*2)

(*1) The data were taken from the condition of V_{OUT} = 2 V and V_A = 3 V. (*2) The data were simulated under the conditions of R_S = 100 kΩ, R_L = 10 kΩ, and V_A = 30 V.

4.2. Limination of the Proposed Converter on V_A and R_S of ES-EH

To see which electrical parameters of ES-EH allowed the converter to output a regulated voltage of 1 V, SPICE simulation was performed with various amplitude voltages V_A and output resistances R_S of ES-EH under the condition of a load resistance of 1 MΩ, as shown in Figure 11. The middle area in blue shows that V_{DD} is regulated between 0.95 V and 1.0 V. ES-EH with too high Rs inputs insufficient power into the regulator against the output power, whereas ES-EH with too low Rs injects too much power so that the PD path cannot pull down to the target regulation point. The lower bound on Rs can be reduced with a larger PD size.
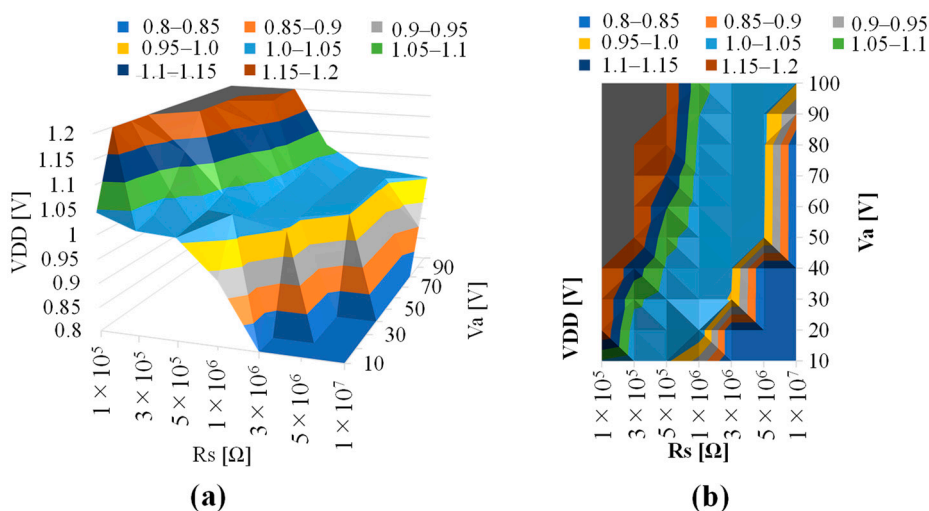
Figure 11. Simulated VDD with different V_A and R_S under a load resistance of 1 MΩ in (**a**) 3D and (**b**) top view plots.

5. Conclusions

This paper proposed an AC-DC converter which does not require external components for rectification and power conversion. It can be integrated in the same IoT chip with a small overhead area of 0.1 mm^2. This converter can provide a better option for electrostatic energy harvesting where the cost is the highest priority.

Author Contributions: Conceptualization, T.T.; methodology, Y.I. and T.T.; software, Y.I.; validation, Y.I. and T.T.; formal analysis, Y.I. and T.T.; investigation, Y.I. and T.T.; writing—original draft preparation, Y.I.; writing—review and editing, T.T.; funding acquisition, T.T. Both authors have read and agreed to the published version of the manuscript.

References

1. Kazmiersuki, T.; Beedy, S. *Energy Harvesting Systems: Principles, Modeling and Applications*; Springer: Berlin/Heidelberg, Germany, 2010; pp. 1–78.
2. Fu, Q.; Suzuki, Y.; Suzuki, Y. MEMS vibration electret energy harvester with combined electrodes. In Proceedings of the 2014 IEEE 27th International Conference on Micro Electro Mechanical Systems (MEMS), San Francisco, CA, USA, 26–30 January 2014; pp. 409–412. [CrossRef]
3. Hashiguchi, G. Electromechanical theory of microelectromechanical devices. *IEICE Electron. Express* **2014**, *11*, 20142007. [CrossRef]
4. De Queiroz, A.C.M.; Domingues, M. The Doubler of Electricity Used as Battery Charger. *IEEE Trans. Circuits Syst. II Express Briefs* **2011**, *58*, 797–801. [CrossRef]
5. Stanzione, S.; Van Liempd, C.; Van Schaijk, R.; Naito, Y.; Yazicioglu, R.F.; Van Hoof, C. A self-biased 5-to-60 V input voltage and 25-to-1600 μW integrated DC-DC buck converter with fully analog MPPT algorithm reaching up to 88% end-to-end efficiency. In Proceedings of the 2013 IEEE International Solid-State Circuits Conference Digest of Technical Papers, San Francisco, CA, USA, 17–21 February 2013; IEEE: Piscataway, NJ, USA, 2013; pp. 74–75.
6. Stanzione, S.; Van Liempd, C.; Nabeto, M.; Yazicioglu, F.R.; Van Hoof, C. 20.8 A 500 nW batteryless integrated electrostatic energy harvester interface based on a DC-DC converter with 60 V maximum input voltage and operating from 1 μW available power, including MPPT and cold start. In Proceedings of the 2015 IEEE International Solid-State Circuits Conference—(ISSCC) Digest of Technical Papers, San Francisco, CA, USA, 22–26 February 2015; IEEE: Piscataway, NJ, USA, 2015; pp. 1–3.
7. Peters, C.; Kessling, O.; Henrici, F.; Ortmanns, M.; Manoli, Y. CMOS Integrated Highly Efficient Full Wave Rectifier. In Proceedings of the 2007 IEEE International Symposium on Circuits and Systems, Los Alamitos, CA, USA, 27–30 May 2007; IEEE: Piscataway, NJ, USA, 2007; pp. 2415–2418.
8. Ulusan, H.; Gharehbaghi, K.; Zorlu, O.; Muhtaroglu, A.; Kulah, H. A Fully Integrated and Battery-Free Interface for Low-Voltage Electromagnetic Energy Harvesters. *IEEE Trans. Power Electron.* **2014**, *30*, 3712–3719. [CrossRef]
9. Banba, H.; Shiga, H.; Umezawa, A.; Miyaba, T.; Tanzawa, T.; Atsumi, S.; Sakui, K. A CMOS bandgap reference circuit with sub-1-V operation. *IEEE J. Solid-State Circuits* **1999**, *34*, 670–674. [CrossRef]
10. De Pelecijn, E.; Steyaert, M.S.J. A Fully Integrated Switched-Capacitor-Based AC–DC Converter for a 120 VRMS Mains Interface. *IEEE J. Solid-State Circuits* **2019**, *54*, 2009–2018. [CrossRef]
11. Kawauchi, H.; Tanzawa, T. A Fully Integrated Clocked AC-DC Charge Pump for Mignetostrictive Vibration Energy Harvesting. *Electronics* **2020**, *9*, 2194. [CrossRef]
12. Chen, Z.; Law, M.-K.; Mak, P.-I.; Zeng, X.; Martins, R.P. Piezoelectric Energy-Harvesting Interface Using Split-Phase Flipping-Capacitor Rectifier with Capacitor Reuse for Input Power Adaptation. *IEEE J. Solid-State Circuits* **2020**, *55*, 2106–2117. [CrossRef]

Battery Management System Algorithm for Energy Storage Systems Considering Battery Efficiency

Jeong Lee [1], Jun-Mo Kim [2] [ID], Junsin Yi [1] and Chung-Yuen Won [1],*

1   Department of Electrical and Computer Engineering, Sungkyunkwan University, Suwon 16419, Korea; leejeong1@skku.edu (J.L.); junsin@skku.edu (J.Y.)
2   Interdisciplinary Program in Photovoltaic System Engineering, Sungkyunkwan University, Suwon 16419, Korea; ksho4807@skku.edu
*   Correspondence: woncy@skku.edu; Tel.: +82-031-290-7164

Abstract: Aging increases the internal resistance of a battery and reduces its capacity; therefore, energy storage systems (ESSs) require a battery management system (BMS) algorithm that can manage the state of the battery. This paper proposes a battery efficiency calculation formula to manage the battery state. The proposed battery efficiency calculation formula uses the charging time, charging current, and battery capacity. An algorithm that can accurately determine the battery state is proposed by applying the proposed state of charge (SoC) and state of health (SoH) calculations. To reduce the initial error of the Coulomb counting method (CCM), the SoC can be calculated accurately by applying the battery efficiency to the open circuit voltage (OCV). During the charging and discharging process, the internal resistance of a battery increase and the constant current (CC) charging time decrease. The SoH can be predicted from the CC charging time of the battery and the battery efficiency, as proposed in this paper. Furthermore, a safe system is implemented during charging and discharging by applying a fault diagnosis algorithm to reduce the battery efficiency. The validity of the proposed BMS algorithm is demonstrated by applying it in a 3-kW ESS.

Keywords: energy storage system (ESS); battery management system (BMS); battery efficiency; state of charge (SoC); state of health (SoH)

1. Introduction

Energy storage systems (ESSs) store electricity when surplus electricity is generated or electricity rates are low and supply the stored electricity to the unit when electricity is in high demand or prices are high; therefore, for the efficient operation of power facilities, the development of an energy management system (EMS) algorithm is imperative.

Battery characteristics [1–3] and the sizing of ESSs have been extensively investigated [4–6] because the battery accounts for most of the budget when designing ESSs; therefore, battery selection and management are important, as the aging problems caused by inappropriate battery management costs account for a large part of the replacement budget.

Many ESSs use lithium-ion batteries, since they offer a high energy density and high efficiency [7,8]; however, it is crucial to identify the charging state of batteries because there is a risk of fire during charge-discharge cycles and because there is a need to predict the state of health (SoH) and state of charge (SoC) for battery state management [9]. The ESS consists of cells in series-parallel [10,11] with a large capacity. To solve the safety problems related to fires and explosions [12], a system that manages the battery status is required [13].

The purpose of a battery management system (BMS) is to manage the battery [14,15]. To improve the reliability and safety of the battery [16,17], many BMS functions are being developed [18]. The functions of BMS can be classified as real-time monitoring, calculation and prediction, protection, and optimization. The battery voltage, current, temperature, SoC,

SoH, and other factors can be confirmed via monitoring [19–21]. In addition, the SoC, SoH, and internal impedance can be calculated and predicted [19,22–25]. The protection process limits overcurrent, overvoltage, and overheating and performs fault diagnosis [26–29]. The optimization process maintains the optimal state of charge of a battery by considering the amount of charge between cells [30–32]. As the cycle of a battery increases, the battery ages and its state changes [33]; therefore, to manage a battery, it is necessary to improve the performance of BMSs. The performance of a BMS varies according to the estimation accuracy of the SoC and SoH, indicators of the battery state [10,34,35].

Charge-discharge cycles, temperature, overcharge and overdischarge, and increased internal resistance cause batteries to age, which reduces their capacity. The calculation of battery efficiency can be performed based on the current and SoC [36], via aging analysis based on charge-discharge capacities [37], or via charging-discharging power differences [38,39]; however, it is difficult to accurately estimate the battery state using this approach, as it does not consider the internal resistance changes arising from the aging phenomenon.

Since the internal resistance increases along with the aging phenomenon of the battery, it should be estimated during the operation, therefore, a battery efficiency estimation method is proposed in this paper. The efficiency of the battery is obtained based on the charging and discharging power losses. Since the internal resistance varies according to the battery efficiency, the battery states can be identified using this variation of internal resistance.

A battery efficiency calculation formula is used to predict the SoC and SoH of the battery. The conventional methods used for estimating battery SoC for BMS performance improvements include deep neural network-based methods for error rating reduction [40], extended Kalman filter (EKF)-based methods with the Thevenin model [41], particle swarm optimization (PSO) [42], and hysteresis voltage of the open circuit voltage (OCV) [43]. Additionally, SoC and internal resistance estimation methods based on an unscented Kalman filter (UKF) with analysis of model parameters [44] and estimation based on the adaptive cubature Kalman filter (ACKF) with neural networks are proposed in [45]. In addition, there are other related studies on SoC estimation, such as equivalent circuit model (ECM)-based estimation with noise compensation [46], OCV error compensation based on DNN [47], the open circuit voltage–charge amount (OCV-Q) curve fitting method using a convolutional neural network (CNN) [48], the event-driven Coulomb counting method (CCM) algorithm for unbalanced SoCs [49], and CCM based on modified parameters [50]; however, DNN- and KF-based methods require high computational power and an additional learning process. The OCV and CCM are primarily used to indicate the charging state of a battery [51,52]; however, because OCV is used when the internal battery state is stabilized, it is not sufficiently stable for a nonlinear battery [9]. Furthermore, because another CCM calculates the SoC by accumulating the charge current, the CCM has the disadvantage of increasing the SoC if an error occurs in the initial current measurement value [53].

In this paper, an SoC estimation method combining OCV with CCM is proposed to improve upon the drawbacks of both OCV and CCM. This estimation algorithm does not require excessive computational power and can improve the estimation accuracy. The proposed algorithm uses the OCV equation with the internal resistance and efficiency of the battery. Additionally, the equation can calculate the charge-discharge of the battery by accurately considering the initial value of the CCM by applying OCV while considering the state of the battery.

Based on the battery efficiency formula, a formula that predicts the SoH of a battery based on the charging time required to safely operate the battery is also applied to the BMS algorithm to improve the reliability.

Research related to SoH estimation to improve BMS performance includes the multi-layer perceptron (MLP)-based method [54], the self-adaptive weight particle swarm optimization (SWPSO)-based estimation method using a dynamic recurrent neural network

(DRNN) with the ability to conduct dynamic mapping [55], and the XGBoost-based estimation method [56]. Additionally, a state estimation method combining the battery model with a data-based method [57] and a voltage–power-curve-based estimation method [58] has been researched. In [59], a more accurate SoH estimation method was proposed by considering the charging time of the battery, although it did not consider the internal resistance variation and showed estimation error; however, as the SoH estimated without considering the internal resistance is incorrect, some researchers have considered it a constant value [60,61]. Although the SoH is also predicted based on its constant current (CC) charging time [62–64], the internal resistance and temperature [65] of a battery are considered when a system is operated for a long time, while the accurate characteristics of a battery cannot be numerically represented; however, this research used the battery efficiency equation, allowing for a more accurate estimation of the battery state by numerically defining the capacity reduction and the internal resistance of a battery.

The BMS measures the battery's initial SoH and stores the value. The BMS stores the current SoH by comparing the current values with the initial SoH based on the changing values as the battery is used. According to the battery status, the temperature of the battery arises and internal resistance increases along with it. Because of the increase in the internal resistance, the SoH of a battery decreases and it takes less time to charge-discharge the battery; therefore, the CC time period decreases. Based on this time period difference among the charge-discharge cycles, the SoH estimation method is proposed in this paper. The proposed SoH estimation method uses the integral value of the CC time period difference among the charge-discharge cycles for more accurate SoH estimation. In this paper, the battery efficiency equation is used to predict the SoH of a battery considering the decrease in the CC charging time of the SoH due to the increase in the internal resistance of the battery and the fact that the capacity of a battery decreases when it heats up.

An algorithm for predicting battery-related system safety and accurate SoC and SoH by determining a battery fault using the battery efficiency equation is proposed.

The literature on the fault diagnosis of batteries shows that the estimated SoH method is typically used. Many studies on battery fault diagnosis have focused on SoH estimation, since it is a major part of fault diagnosis. For example, in [66], the fault diagnosis method is based on the estimated SoH using the surface temperature of the battery, while fault detection is performed using the SoH estimated based on a multilayer neural network (MNN) in [67].

In this paper, a novel fault diagnosis algorithm that detects the fault state based on the SoH and the efficiency of the battery is proposed for more accurate fault detection. With the proposed method, the battery can be managed more safely because battery faults can be detected beforehand, since the battery efficiency plummets in the fault state before the SoH reaches its fault range.

In this study, we implement the SoC calculation combined with the OCV and CCM, SoH based on the charging time, as well as a fault diagnosis algorithm in a 3 kW ESS. Furthermore, the validity of the proposed BMS algorithm is investigated.

2. Battery Efficiency for Predicting Battery State

Figure 1 illustrates the factors affecting the performance of a battery.

As the number of charge-discharge cycles increases, a chemical reaction occurs in the battery, causing aging, which reduces the SoH of the battery. Aging increases the internal resistance of a battery and decreases its charge-discharge capacity. As the capacity of a battery decreases, its charge voltage reaches the maximum value.

Identifying the occurrence of aging during the charge-discharge operation of a battery requires determination of the magnitude by which its capacity decreases by calculating its internal resistance or efficiency.

Although accurate modeling of a battery is required to understand its state, it is difficult to perform accurate modeling because of the nonlinear characteristics. Furthermore, given the various factors for batteries, the system costs increase because the roles of the

BMS managing the battery vary and the number of computations increases. This paper proposes a battery efficiency calculation formula that considers the internal resistance, which significantly affects the performance of a battery, as well as a system that considers the nonlinear characteristics.
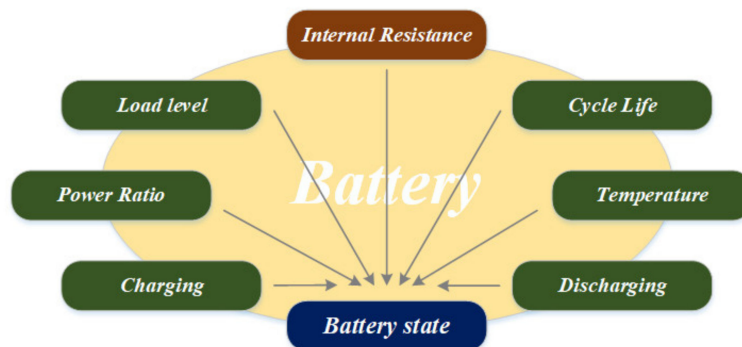

Figure 1. Factors affecting the state of a battery.

Figure 2 shows an ESS system, in which the proposed algorithm was implemented. The ESS consisted of a battery system and a power conversion system (PCS). The battery system consisted of a battery and a BMS. The ac-dc of the PCS comprised a two-level converter that was easy to control with high efficiency, while the dc-dc comprised a full-bridge converter [68].
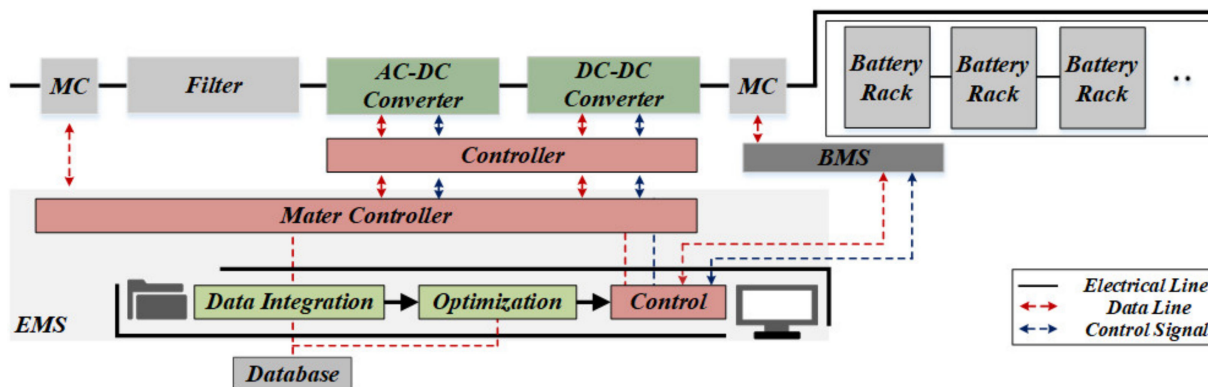
Figure 2. Proposed ESS configuration diagram.

Figure 3 illustrates the BMS configuration of the battery system. The BMS received data regarding the battery voltage, current, and temperature and predicted the SoC and SoH. Furthermore, the data were transmitted using controller area network (CAN) communication. When any abnormalities occurred in the battery voltage, current, or state, the charge-discharge state of the battery was cut off to protect it. Furthermore, the BMS provided a protection function to secure the battery safety when an abnormality in the battery temperature occurred [69]. By applying the proposed algorithm, the BMS sensed the battery voltage, current, and temperature; accumulated data; calculated the battery efficiency; and predicted the SoC and SoH. In addition, battery's efficiency protected it in from faults.
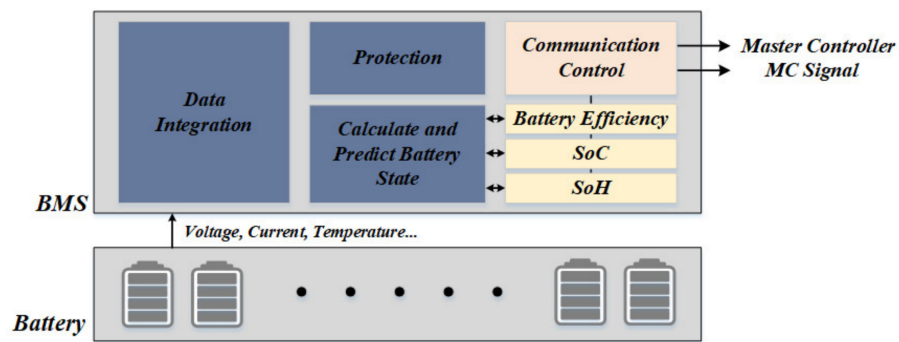
Figure 3. Proposed BMS configuration diagram.

3. ESS Considering Battery Efficiency

Figure 4 illustrates the proposed EMS algorithm and shows a day-ahead EMS algorithm based on the proposed battery management algorithm.
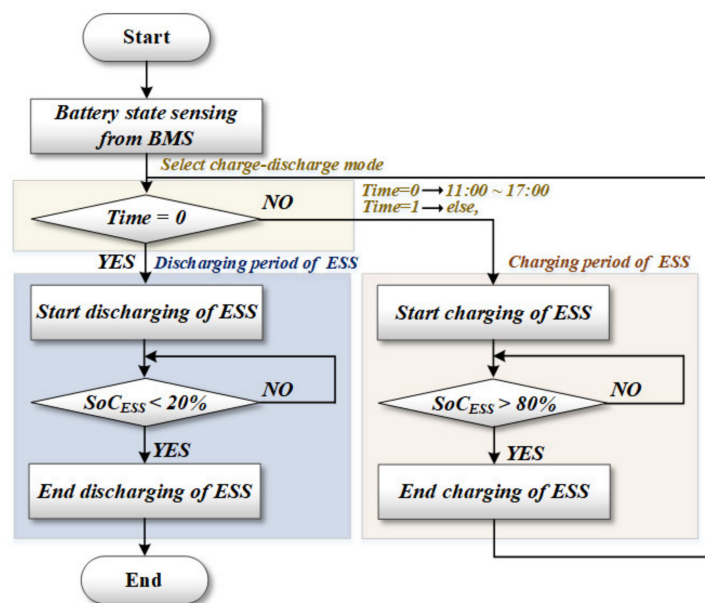
Figure 4. EMS charge-discharge algorithm according to time.

The ESS supported the grid by discharging during the daytime (when there are many power users) and charging at night. During the charge-discharge process, the proposed algorithm could sense the battery state through CAN communication using the BMS algorithm and proceeded with charging. If the SoC of the ESS battery was below 80%, the battery was charged, while if it was above 80%, charging was terminated. The minimum and maximum values of the battery SoC could be redefined by the user, and this paper defines the operational SoC as that defined between 20% and 80%. After charging, if the power required by the grid increased, the ESS proceeded with discharging. Furthermore, the ESS used an algorithm that terminated the discharging of the battery when the SoC dropped below 20%.

The EMS algorithm is an algorithm for the charge-discharge process of a battery, which ensures high safety when connected with the BMS. The paper did not separately consider the system fault diagnosis performed by the EMS because the EMS algorithm was proposed considering the battery state; however, further studies are necessary to investigate the fault diagnosis and response in EMS, which are critical factors affecting the charge-discharge process required for the grid.

3.1. Proposed BMS Algorithm

The ESS, which charges and discharges energy from a battery, is directly affected by battery performance; thus, a BMS that manages and protects the battery and communicates with the outside is critical.

One of the problems in nonlinear batteries is that their internal characteristics change based on the number of charge-discharge cycles; thus, the primary goal of a BMS is to accurately follow these changes.

This paper proposes a method to improve battery safety and performance based on the reduction in its efficiency (which occurs during battery use), derive a battery efficiency equation, and apply it to calculate and predict the SoC and SoH of the battery. Furthermore, based on the battery efficiency calculation, this paper proposes an algorithm for terminating the use of the battery and diagnosing faults.

Figure 5 illustrates the proposed BMS algorithm. The proposed BMS algorithm can sense the battery voltage, current, and temperature and calculate its efficiency. When the efficiency of a battery is calculated, its charge-discharge current is measured to determine whether the ESS is in the charge-discharge state. When the ESS is charged or discharged, the SoC is calculated using the combination of the OCV and CCM.
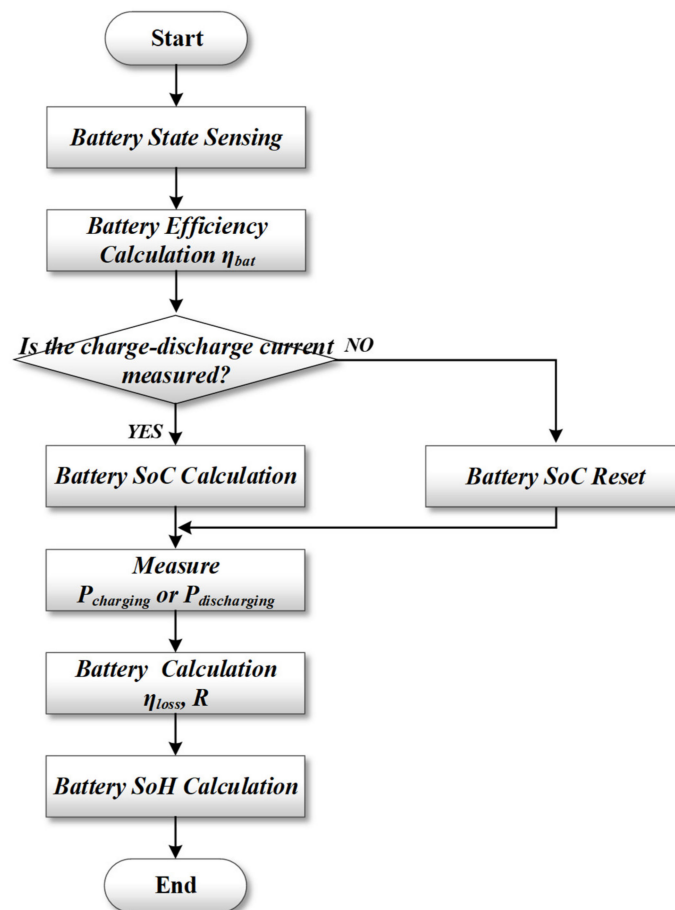
Figure 5. BMS algorithm that considers the battery efficiency.

When the ESS is not in the charge-discharge state, the SoC of the battery is reset to increase the accuracy of the initial value of the SoC.

At the end of the charging and discharging operation of the battery, the charging power $P_{charging}$ or discharging power $P_{discharging}$ is measured to estimate battery loss and internal resistance for the next cycle. As a day-ahead EMS was used in this paper, one cycle represents a day of operation; therefore, the internal resistance of the battery was estimated based on the difference between the charging and discharging energies for a day.

After the charge-discharge process, the SoH, to which the battery efficiency was applied, was calculated and predicted to improve the battery safety and performance.

Battery Efficiency

Battery efficiency can be used as an indicator of the current usage time compared to the initial time. A battery efficiency equation was proposed to express the relationship between the capacity and voltage of the battery model. Because the internal resistance of a battery affects the battery output, the battery's internal resistance must be accurately calculated.

The internal resistance of a battery is the key indicator of its state. The internal resistance of a battery increases with an increase in the heat generated during the charge-discharge of the battery.

Figure 6 illustrates the current capacity of the ESS with aging.
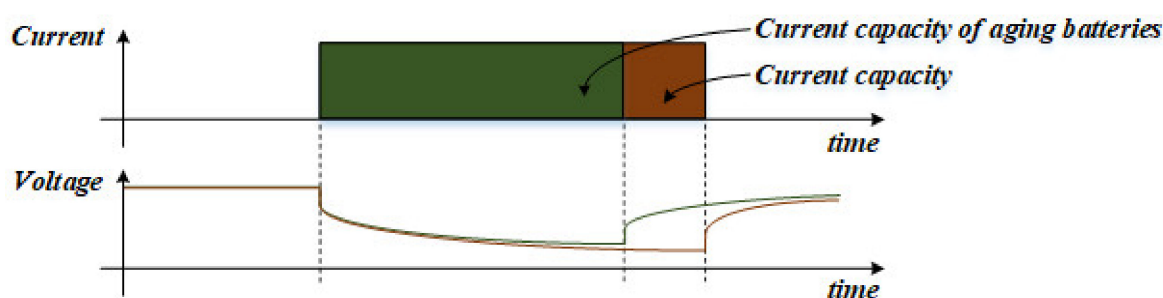
Figure 6. The current capacity of a battery during aging.

As the battery aged, its internal resistance increased and the current capacity decreased, which significantly affected the performance of the ESS when the capacity was large. Furthermore, the use of a battery with reduced performance causes overcharging and overdischarging, which limits battery safety.

The current battery capacity is the amount of current that a fully charged battery can discharge for one hour. Compared to a battery in the birth of life (BOL) state, an aging battery, upon discharge, reaches the terminal voltage limit faster because of its reduced current capacity.

The efficiency of a battery decreases when it is used. As a battery shows the maximum efficiency at the initial state, its efficiency can only decrease when it is in operation.

Equation (1) defines the efficiency of a battery. The efficiency of a battery η_{bat} can be expressed by subtracting the battery loss η_{loss} from the initial battery efficiency, 100%.

As the decrease in the efficiency can be expressed as the increase in the internal resistance, η_{loss} can be calculated based on the charging and discharging powers, as shown in Equation (2).

I_{bat} is the charge-discharge current, R is the battery's internal resistance, and V_{bat} is the battery voltage.

$$\eta_{bat} = 100 - \eta_{loss} \tag{1}$$

$$\eta_{loss} = \frac{I_{bat}^2 \times R}{V_{bat} \times I_{bat}} \tag{2}$$

In this case, the charge-discharge current of the battery can be represented by Equation (3).

During the charge-discharge of a battery, the current can be calculated as the amount of charge (battery capacity) and the C-rates at which the battery has been charged or discharged over time. Q_{bat} is the battery capacity, while t is the charge-discharge time of the battery. Equation (3) uses the electric charge equation.

Equations (2) and (3) give the total loss in battery efficiency, as represented in Equation (4). Using Equation (4), the battery loss equation, as well as Equation (1), the battery

efficiency can be calculated. Equation (4) can be used to determine the internal resistance of a battery. Equation (5) gives the internal resistance of the battery. In this paper, as the charge-discharge process progressed, the battery efficiency decreased.

$$I_{bat} = \frac{Q_{bat}}{t} \tag{3}$$

$$\eta_{loss} = \frac{\left(\frac{Q_{bat}}{t}\right) \times R}{V_{bat}} \tag{4}$$

$$R = \frac{\eta_{loss} \times V_{bat} \times t}{Q_{bat}} \tag{5}$$

3.2. Improved SoC and SoH Prediction Method

A battery protection system monitors the battery state and prevents it from overcharging and overdischarging, improving its safety and performance. The performance of a BMS is evaluated based on how accurately it predicts the SoC and SoH of the battery [34].

CCM is used to track the SoC with the value calculated by integrating the current during the charge-discharge of the battery to the initial value of the SoC; however, because the current is accumulated to the initial value of the CCM, errors are accumulated if the precise initial value is unknown [70,71]. Because errors gradually increase, the paper propose following the SoC with an improved method combining the OCV and CCM to improve the initial value.

Equation (6) expresses the voltage calculated using the open circuit voltage formula of the battery through Equation (5). The battery state can be more accurately predicted using the internal resistance obtained through Equation (5) and the OCV of the battery.

The final CCM is depicted in Equation (7). The accuracy of the prediction of the battery state can be improved by applying the internal resistance value derived from the battery efficiency equation to the conventional CCM. $SoC(t)$ is the SoC at time t, $SoC(t-1)$ is the initial SoC, C_n is the battery capacity, and V_{ocv} is the battery voltage in the open state [72,73].

$$SoC(t-1) = V_{ocv} + \left(I_{bat} \times \frac{\eta_{loss} \times V_{bat} \times t}{Q_{bat}} \right) \tag{6}$$

$$SoC(t) = SoC(t-1) + \int_0^t \frac{I(t)}{C_n} dt \tag{7}$$

SoH, which is an indicator of the battery life time, is essential for managing the battery charge-discharge process. Various models for predicting SoH have been proposed to improve the battery safety and performance. The standard method predicts the life time of a battery by analyzing it according to the chemical principle of the battery and through mathematical or physical modeling [74–76]; however, these methods do not consider the internal resistance of a battery, which significantly affects its life time.

Figure 7 illustrates the constant current–constant voltage (CC–CV) charging curve of a battery.
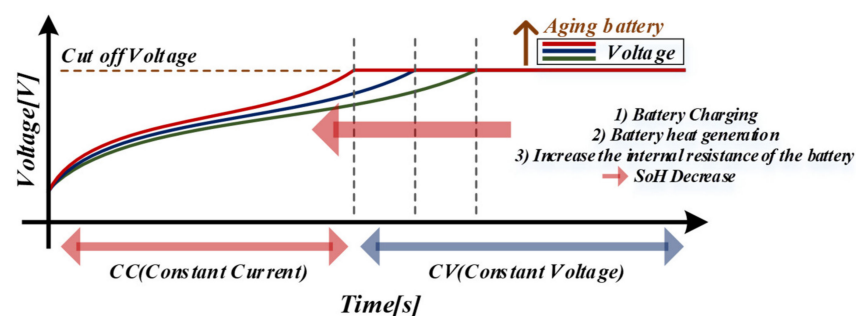
Figure 7. Voltage and SoH of a battery during charging.

A battery is typically charged through the CC–CV [77]. Whenever the battery is charged, its CC charging time decreases, while the CV charging time increases. As the battery charging proceeds, the battery temperature increases and internal resistance increases, resulting in a decrease in its SoH.

Figure 8 shows the discharge characteristics of a battery.
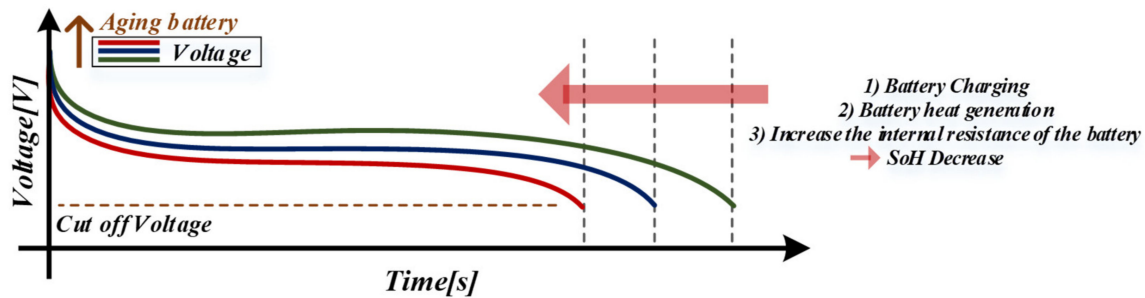
Figure 8. Voltage and SoH of a battery during discharging.

As in the charging cycle, the time to reach the cut-off voltage is also reduced during charging because the SoH decreases as the temperature and internal resistance of the battery increase, as shown in the charging curve.

This paper considered the internal resistance of a battery, which significantly affects the SoH, to propose a method for predicting the battery SoH based on the charging time after the charge-discharge process. Although previous studies [62,64] did not accurately predict the internal resistance value, they numerically derived and applied the internal resistance value based on the battery efficiency.

To calculate a battery's SoH, the equation should be rearranged by *t* using the SoC derived from Equations (6) and (7) after the SoC charge-discharge process, resulting in Equation (8). By applying the internal resistance equation derived from the battery efficiency equation, the charge-discharge time is compared based on the charge-discharge cycle of the battery. Here, t_{after} is the time after the charge-discharge process, which can be used to predict the battery SoH using the battery characteristics by comparing the values after the charge-discharge process (Equations (8) and (9)). SoH_{after} is the SoH of the battery compared to the time after charging and discharging. The SoH of the battery can be predicted using the charge-discharge time of the battery. Here, t_{before} is the battery charge-discharge time before t_{after}.

$$t_{after} = \frac{C_n \times (SoC(t) - V_{ocv} - \eta_{loss} \times V_{bat})}{I_{bat}} \tag{8}$$

$$SoH_{after} = \frac{t_{after}}{t_{before}} \times 100\% \tag{9}$$

3.3. Method Used to Diagnose Battery Fault

Figure 9 illustrates the proposed battery fault diagnosis algorithm.

The fault diagnosis algorithm considers two situations. After the battery information is sensed through the BMS and the battery efficiency is evaluated regarding whether the value corresponds to the over range, charging proceeds. If the battery efficiency is not higher than the over range, the charge-discharge process is performed; however, if the battery efficiency is higher than the over range and the battery SoH is 40% or less, the charge-discharge process is terminated.

This over range value changes depending on the battery state, battery type, and other factors, and this value should be set before the operation. In this paper, the fault state was set when the efficiency was below 80% and the SoH was below 40%.

Although the battery's charge-discharge SoC is used correctly at 0–100% for the ESS, in this paper, the SoC was charged at 20–80%, the optimal operation region for lithium-ion batteries from a safety viewpoint. Furthermore, the SoH was subjected to charge-discharge cycles up to the maximum region of the battery. Charging was terminated based on the experimental requirements and safety considerations—when the SoH reached 40% or less—to confirm the disposal of the battery through a signal.
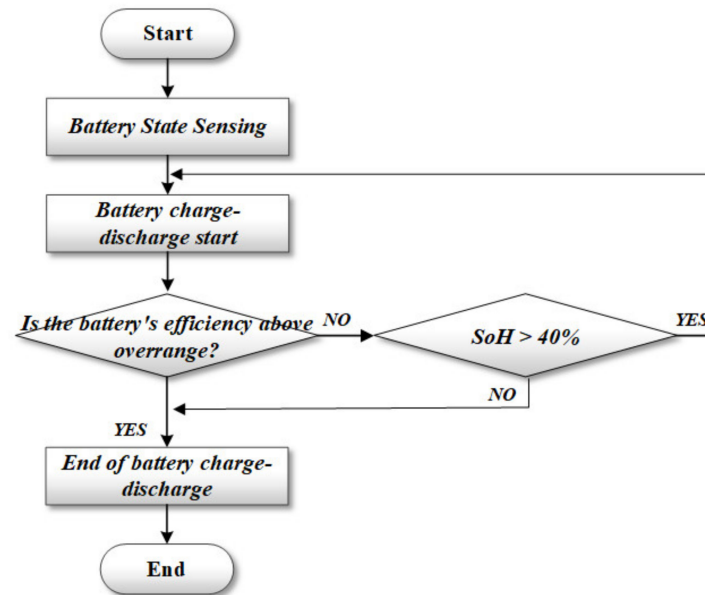
Figure 9. Proposed fault diagnosis algorithm.

The BMS senses the final output values of Equations (1) and (9), then a charge-discharge termination signal is transmitted through CAN communication if the value is within the over range. The paper predicted the correct battery state through BMS and diagnosed the fault using the proposed method during the charge-discharge process to propose a BMS algorithm for an ESS that uses a large battery capacity.

4. Experiments to Verify the Proposed Algorithm

A 3-kW ESS was implemented to verify the BMS algorithm of the ESS considering the battery efficiency.

The BMS algorithm proposed in this paper was applied to the ESS and the battery efficiency was tested during the charge-discharge process by charging several battery modules.

The internal resistance calculated from the battery efficiency was applied to the SoC. Then, the OCV, CCM, and proposed algorithm were compared and the SoC was confirmed in the case of a battery fault. The charge-discharge cycle was performed by converting the SoC calculated from the internal resistance of the battery into the charging-discharging time. Furthermore, the termination of the charge-discharge cycle was confirmed through the connection between the ESS and BMS in the case of a fault. In the additional part of the algorithm, the total efficiency of the ESS was further confirmed to verify its validity.

Figure 10 illustrates the ESS experiment hardware used in this paper, while Table 1 lists the experiment parameters. The PCS of the ESS consists of a two-level inverter, a full bridge converter, and a master controller. The output side comprised three lithium-ion battery modules (1 module: 24 cells × 4.2 V) and a BMS. The experiment was conducted using an oscilloscope and a laptop computer to confirm the operation.
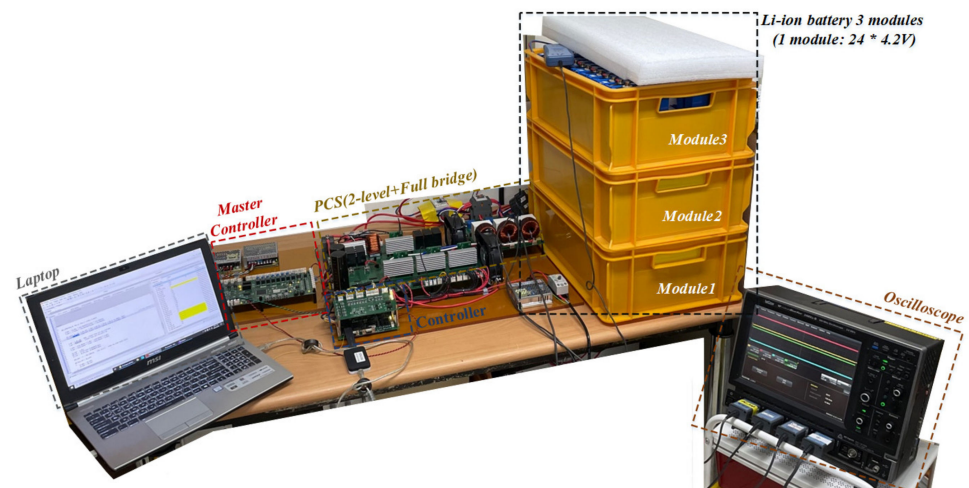
Figure 10. ESS hardware configuration for the application of the proposed algorithm.

Table 1. ESS experimental parameters for the application of the proposed algorithm.

Parameter	Symbols	Values	Units
Rated power	P_{ESS}	3	kW
Input voltage	V_{ac_in}	220	V_{ac}
DC link voltage	V_{dc_link}	400	V
Output voltage	V_{dc_out}	96	V
Output Current	I_{dc_out}	30	A
Switching frequency	f_{acdc}	40	kHz
Switching frequency	f_{dcdc}	100	kHz

For the battery efficiency experiment, battery efficiency was confirmed by the charge-discharge of a faulty battery module and a normal battery module.

The profiling of the battery was carried out in four steps. The data were confirmed in the order of (1) securing the charge-discharge data, (2) deriving an equation through curve fitting, (3) performing the charge-discharge cycle, and (4) extracting the target data from the implemented correlation equation.

An experiment battery was proposed to verify the battery efficiency by configuring the battery with three modules and assigning modules 1 and 2 as the normal batteries and module 3 as the battery subjected to repeated charge-discharge cycles.

Figure 11 illustrates efficiency graph of the battery module.

During battery charging, the difference in the final internal resistance values of the battery was confirmed, as depicted in Figure 11. If a specific range was set during the charge-discharge cycle for testing, the change in the state of the battery caused by aging was detected.

The battery efficiency test revealed a significant change in the efficiency of the battery after investigating the changes in the efficiency of the faulty or abnormal batteries that occurred during the charge-discharge cycle of the ESS and those of the normal battery. The difference between the efficiencies of the faulty (aged) and normal batteries was 38.4%. The results suggest that the battery efficiency of the proposed algorithm could be applied for predicting the SoC and SoH, which requires improved accuracy, while the change in the internal resistance (which has the greatest impact on the battery state) could also be applied to increase the accuracy of the battery state prediction.
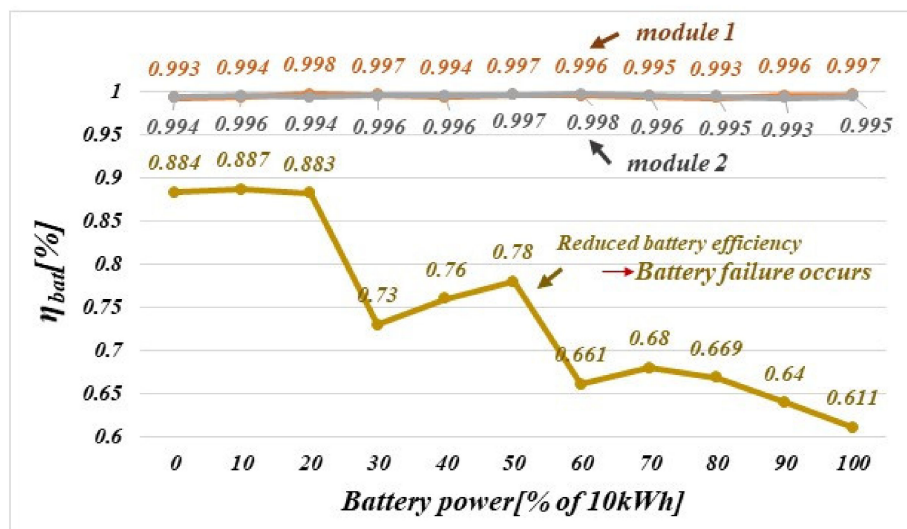
Figure 11. Battery efficiency difference profile graph according to battery power.

Figure 12 and Table 2 illustrate the SoC profile of the battery to which the proposed battery efficiency equation was applied.
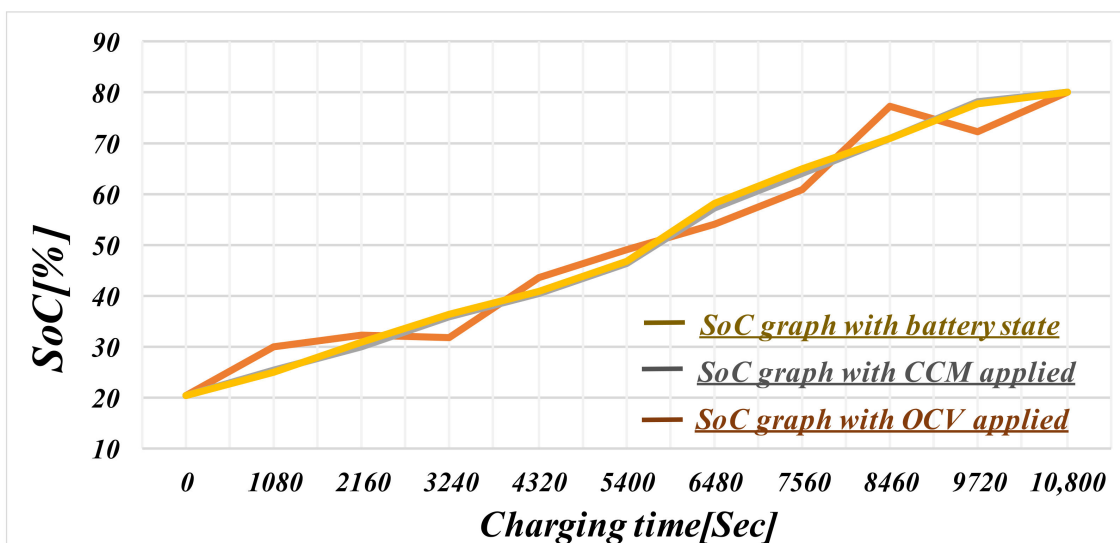
Figure 12. SoC comparison profile graph.

Table 2. SoC profile of the batteries according to the algorithm.

Algorithm	0 s	1080 s	2160 s	3240 s	4320 s	5400 s	6480 s	7560 s	8460 s	9720 s	10,800 s
OCV	20.3%	30.1%	32.1%	31.5%	43.5%	49.1%	54.1%	60.8%	77.3%	72.1%	80%
CCM	20.3%	25.3%	30.1%	35.8%	40.3%	46.3%	57.2%	64.2%	70.8%	78.2%	80%
Proposed	20.2%	25.1%	30.6%	36.1%	40.7%	46.8%	58.2%	65.1%	70.9%	80.3%	80%

All three normal battery modules were discharged up to 20% and charged up to 80% of the maximum SoC.

By applying the battery efficiency, the OCV, CCM, and proposed SoC algorithm could be compared.

The SoC profile was confirmed using the proposed algorithm.

To confirm the SoC calculation, the OCV and CCM were compared with the proposed SoC calculation algorithm. The CCM was charged after accurately determining the initial

value. The OCV could not accurately determine the SoC during charging. The CCM and proposed SoC operation seemed to accurately calculate the SoC; however, when using the actual CCM, the user could not directly and accurately set the initial value. As such, using the algorithm proposed in this paper, the SoC can be determined more accurately.

Figure 13 illustrates the SoH profile to which the proposed algorithm was applied, while Table 3 presents the CC termination time based on the battery state.
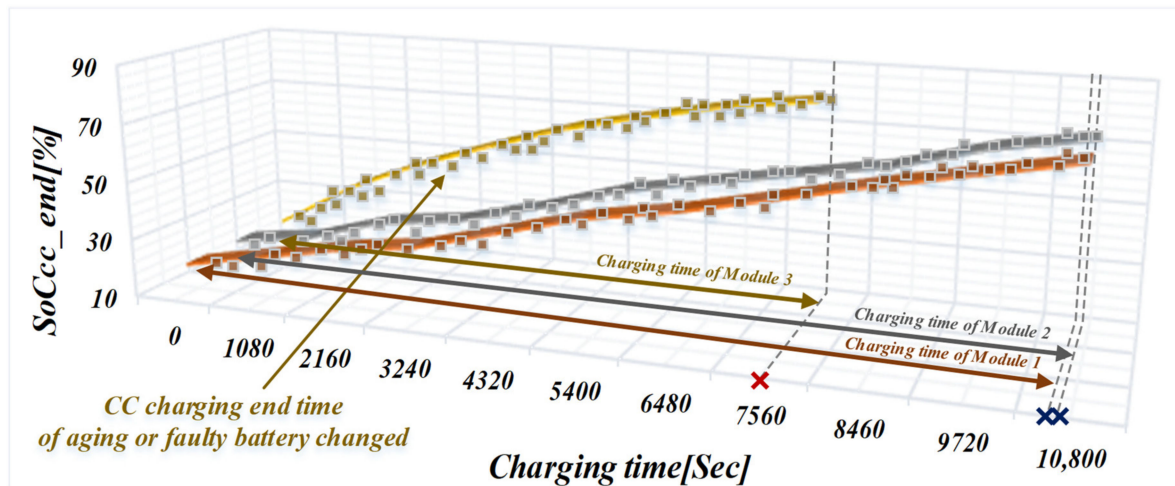
Figure 13. SoH profile with CC charging time, to which the battery efficiency was applied.

Table 3. SoH table for three battery modules to which the battery efficiency was applied.

Parameter	Charging Time (Before)	Charging Time (After)	ΔSoC
Module 1	10,740 s	10,610 s	0.02%
Module 2	10,760 s	10,700 s	0.01%
Module 3	10,740 s	7430 s	31%

50 cycles were charged and discharged at 0.3 C-rate, and CC charging time was compared in the 51st cycle.

The battery was charged by applying the internal resistance to which the battery efficiency was applied. The results demonstrated that the CC charging time of the module decreased when the battery failed or had other problems.

Equation (10), which compared the *SoH* profiles obtained using the three methods investigated, confirmed that the *SoH* prediction was possible based on the CC termination time of the battery. The Δ*SoH* is the amount of change between SoH_{before} and SoH_{after}, while SoH_{before} is the *SOH* before SoH_{after}.

$$\Delta SoH = \left(1 - \frac{SoH_{after}}{SoH_{before}} \right) \times 100 \tag{10}$$

It is difficult to accurately diagnose faulty batteries based on environmental changes, such as battery aging. Because the characteristics of the battery vary when a cell comprises modules, the internal resistance and capacity deviation occurs, causing overdischarge; thus, because the safety and energy efficiency of the battery system is significantly reduced, in this paper we diagnosed the battery state using two methods, whereby faulty batteries were diagnosed based on when the (1) battery efficiency and (2) SoH battery efficiency were reached.

Figure 14a shows the charging voltage and current waveform at the time of a fault signal, while Figure 14b is the discharge voltage and current waveform at the time of a

fault signal. Figure 14 illustrates the fault signals when the battery efficiency is reduced and the SoH is 40% or less. If a fault is detected, the charge–discharge cycle of the battery is terminated with the general purpose input output (GPIO) signal, which cuts off the battery MC through the BMS. The main controller then terminates the pulse width modulation signal, causing the ESS to enter into a stop state.
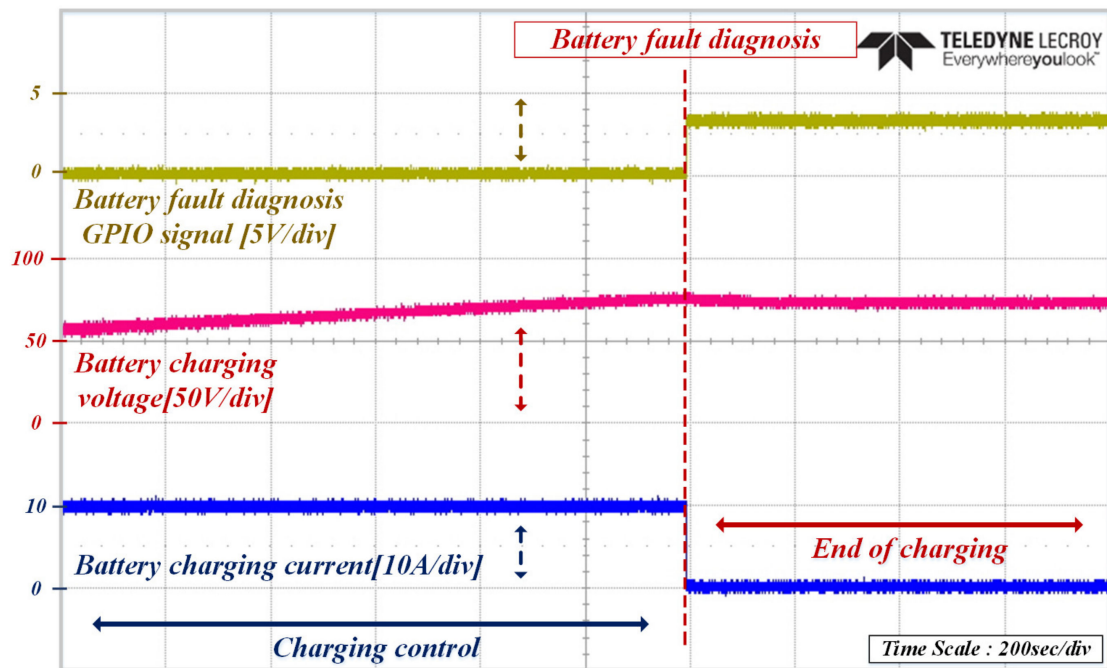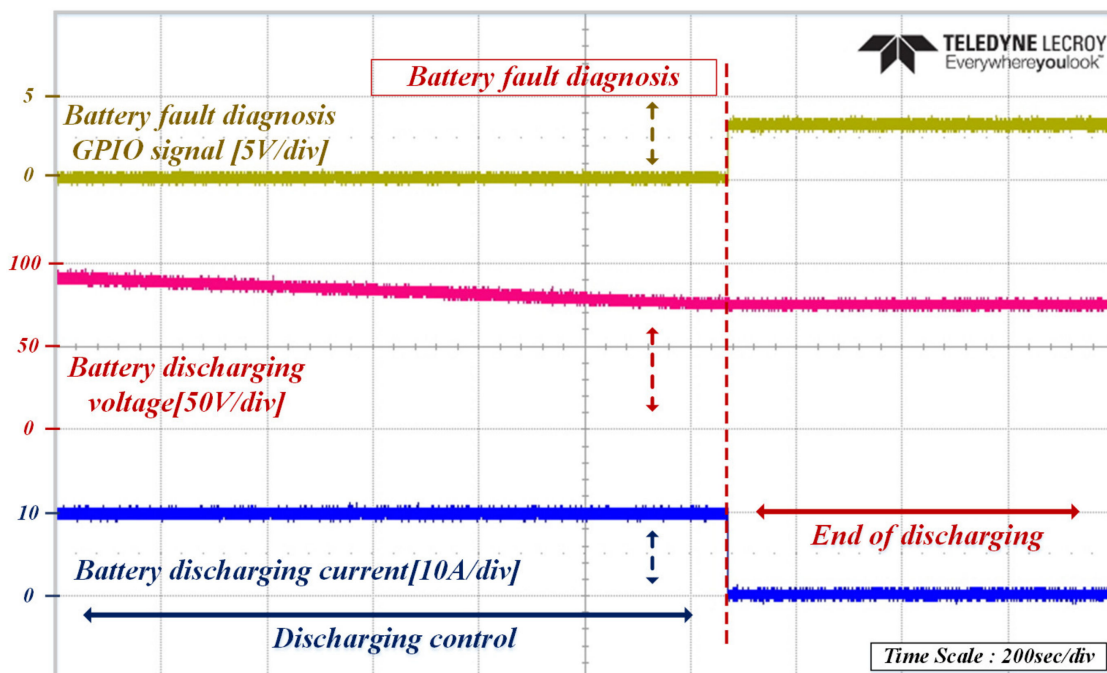
Figure 14. Waveforms for battery fault diagnosis: (**a**) charging voltage and charging current waveform; (**b**) discharging voltage and discharging current waveform.

Figure 15 illustrates the efficiency waveform of the ESS when the system was implemented by applying the proposed algorithms.
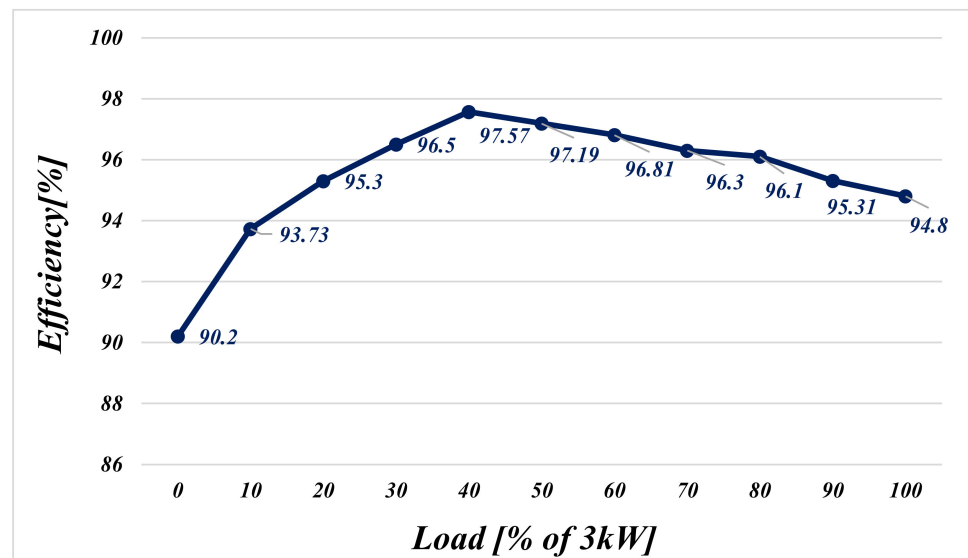
Figure 15. ESS efficiency waveform when the proposed algorithm was implemented.

The efficiency of ESS is caused by the decrease in the difference between the power consumed by charging and the power generated by discharging; therefore, the operating cost for using the battery increases. Efficiency was measured when applying the proposed EMS and BMS algorithms. When the algorithm proposed in this paper was applied, the maximum efficiency was 97.57%.

This paper proposes a BMS algorithm for an ESS. To apply the BMS algorithm to the ESS, the experiment was conducted by deriving the internal resistance of the battery from its efficiency. Moreover, the increase in battery state accuracy was verified through experiments by applying the battery efficiency to the SoC with the OCV and CCM and the SoH considering the charging time. Furthermore, increased safety through the diagnosis of faulty batteries was verified through experiments.

5. Conclusions

In this paper we proposed a BMS algorithm that considers battery efficiency. The algorithm was applied to an ESS to improve the battery safety and performance. The algorithm proposed in this paper was divided into three parts.

First, the efficiency of the battery was used to estimate the state of the battery. The internal resistance of the battery was estimated based on the difference between the charging and discharging power to obtain the value of the variable internal resistance. The variation in the internal resistance was confirmed by the experimental results, which showed the increase in the charging-discharging power difference during the battery's operation.

Second, the SoC and SoH estimation methods were proposed. For SoC estimation, the method of combining OCV and CCM with the estimated battery states was proposed to compensate for both low initial estimation accuracies of CCM and incorrect estimation of OCV. An SoH estimation algorithm based on the charging time was also proposed. This proposal was based on the fact that an increase in the temperature of a battery results in an increase in its internal resistance and a decrease in the CC charging time. This charging time decrement according to the internal resistance variation was confirmed in the experiment. Based on the estimated SoH, the battery lifespan estimation method, which observes the charging-discharging SoH difference for a long period of time, was proposed. Additionally, the proposed method is more flexible than conventional methods, since it does not require any additional analysis of different kinds of battery cells for SoH estimation.

Third, this paper proposed a battery fault diagnosis algorithm that aims to improve battery safety. Using this method, faults are diagnosed through efficiency and SoH, and this fault diagnosis algorithm was validated through experiments.

In conclusion, accurate SoC and SoH estimations were proposed by applying battery efficiency to the estimation process. The estimated SoC and SoH were used to improve not only the performance of BMS but also the battery safety via a fault diagnosis algorithm with accurate SoH estimation.

References

1. Diouf, B.; Pode, R. Potential of lithium-ion batteries in renewable energy. *Renew. Energy* **2015**, *76*, 375–380. [CrossRef]
2. Zubi, G.; Dufo-López, R.; Carvalho, M.; Pasaoglu, G. The lithium-ion battery: State of the art and future perspectives. *Renew. Sustain. Energy Rev.* **2018**, *89*, 292–308. [CrossRef]
3. Raijmakers, L.; Danilov, D.; Eichel, A.; Notten, P. A review on various temperature-indication methods for Li-ion batteries. *Appl. Energy* **2019**, *240*, 918–945. [CrossRef]
4. Fossati, J.P.; Galarza, A.; Martín-Villate, A.; Fontan, L. A method for optimal sizing energy storage systems for microgrids. *Renew. Energy* **2015**, *77*, 539–549. [CrossRef]
5. Xia, S.; Chan, K.W.; Luo, X.; Bu, S.; Ding, Z.; Zhou, B. Optimal sizing of energy storage system and its cost-benefit analysis for power grid planning with intermittent wind generation. *Renew. Energy* **2018**, *122*, 472–486. [CrossRef]
6. Yang, Y.; Bremner, S.; Menictas, C.; Kay, M. Battery Energy Storage System Size Determination in Renewable Energy Systems: A review. *Renew. Sustain. Energy Rev.* **2018**, *91*, 109–125. [CrossRef]
7. Nadeem, F.; Hussain, S.M.S.; Tiwari, P.K.; Goswami, A.K.; Ustun, T.S. Comparative Review of Energy Storage Systems, Their Roles, and Impacts on Future Power Systems. *IEEE Access* **2019**, *7*, 4555–4585. [CrossRef]
8. Santos-Pereira, K.; Pereira, J.D.; Veras, L.S.; Cosme, D.L.; Oliveira, D.Q.; Saavedra, O.R. The requirements and constraints of storage technology in isolated microgrids: A comparative analysis of lithium-ion vs. lead-acid batteries. *Energy Syst.* **2021**, 1–24. [CrossRef]
9. Shahriari, M.; Farrokhi, M. On-line state of health estimation of VRLA batteries using state of charge. *IEEE Trans. Ind. Electron.* **2013**, *1*, 191–202. [CrossRef]
10. Lim, N.G.; Kim, J.Y.; Lee, S. Estimation of the Hot Swap Circulation Current of a Multiple Parallel Lithium Battery System with an Artificial Neural Network Model. *Electronics* **2021**, *10*, 1448. [CrossRef]
11. Lee, H.; Park, J.; Kim, J. Incremental Capacity Curve Peak Points—Based Regression Analysis for the State-of-Health Prediction of a Retired LiNiCoAlO2 Series/Parallel Configured Battery Pack. *Electronics* **2019**, *8*, 1118. [CrossRef]
12. Wang, Q.; Mao, B.; Stoliarov, S.I.; Sun, J. A review of lithium ion battery failure mechanisms and fire prevention strategies. *Prog. Energy Combust. Sci.* **2019**, *73*, 95–131. [CrossRef]
13. Gabar, H.A.; Othman, A.M.; Abdussami, M.R. Review of Battery Management Systems(BMS) Development and Industrial Standards. *Technologies* **2021**, *9*, 28. [CrossRef]
14. Wei, Z.; Zhao, J.; He, H.; Ding, G.; Cui, H.; Liu, L. Future smart battery and management: Advanced sensing from external to embedded multi-dimensional measurement. *J. Power Sources* **2021**, *489*, 229462. [CrossRef]
15. Xiong, R.; Ma, S.; Li, H.; Sun, F.; Li, J. Toward a safer battery management system: A critical review on diagnosis and prognosis of battery short circuit. *Iscience* **2020**, *23*, 101010. [CrossRef] [PubMed]
16. Hemavathi, S. Li-ion Battery Health Estimation Based on Battery Internal Impedance Measurement. In *Innovations in Sustainable Energy and Technology*; Springer: Singapore, 2021; pp. 183–193.
17. Aiello, O. Electromagnetic Susceptibility of Battery Management Systems' ICs for Electric Vehicles: Experimental Study. *Electronics* **2020**, *9*, 510. [CrossRef]
18. Nordmann, H.; Frisch, M.; Sauer, D.U. Thermal Fault-Detection Method and Analysis of Peripheral Systems for Large Battery Packs. *EES J. Meas.* **2017**, *114*, 484–491. [CrossRef]
19. Lee, C.-J.; Kim, B.-K.; Kwon, M.-K.; Nam, K.; Kang, S.-W. Real-Time Prediction of Capacity Fade and Remaining Useful Life of Lithium-Ion Batteries Based on Charge/Discharge Characteristics. *Electronics* **2021**, *10*, 846. [CrossRef]

20. Samanta, A.; Chowdhuri, S.; Williamson, S.S. Machine Learning-Based Data-Driven Fault Detection/Diagnosis of Lithium-Ion Battery: A Critical Review. *Electronics* **2021**, *10*, 1309. [CrossRef]

21. Lelie, M.; Braun, T.; Knips, M.; Nordmann, H.; Ringbeck, F.; Zappen, H.; Sauer, D.U. Battery management system hardware concepts: An overview. *Appl. Sci.* **2018**, *8*, 534. [CrossRef]

22. Kurzweil, P.; Scheuerpflug, W. State-of-charge monitoring and battery diagnosis of NiCd cells using impedance spectroscopy. *Batteries* **2020**, *6*, 4. [CrossRef]

23. Ko, Y.; Choi, W. A New SOC Estimation for LFP Batteries: Application in a 10 Ah Cell (HW 38120 L/S) as a Hysteresis Case Study. *Electronics* **2021**, *10*, 705. [CrossRef]

24. Meddings, N. Application of electrochemical impedance spectroscopy to commercial Li ion cells: A review. *J. Power Sources* **2020**, *480*, 228742. [CrossRef]

25. Laadjal, K.; Cardoso, A.J.M. Estimation of Lithium-Ion Batteries State-Condition in Electric Vehicle Applications: Issues and State of the Art. *Electronics* **2021**, *10*, 1588. [CrossRef]

26. Raj, A.; Rodrigues, M.T.F.; Abraham, D.P. Rate-dependent aging resulting from fast charging of Li-ion cells. *J. Electrochem. Soc.* **2020**, *167*, 120517. [CrossRef]

27. Juarez-Robles, D.; Vyas, A.A.; Fear, C.; Jeevarajan, J.A.; Mukherjee, P.P. Overcharge and Aging Analytics of Li-Ion Cells. *J. Electrochem. Soc.* **2020**, *167*, 090547. [CrossRef]

28. Bhattacharjee, A.; Mohanty, R.K.; Ghosh, A. Design of an Optimized Thermal Management System for Li-Ion Batteries under Different Discharging Conditions. *Energies* **2020**, *13*, 5695. [CrossRef]

29. Werner, D.; Paarmann, S.; Wiebelt, A.; Wetzel, T. Inhomogeneous temperature distribution affecting cyclic aging of Li-ion cells. Part ii: Analysis and correlation. *Batteries* **2020**, *6*, 12. [CrossRef]

30. Luo, X.; Kang, L.; Lu, C.; Linghu, J.; Lin, H.; Hu, B. An Enhanced Multicell-to-Multicell Battery Equalizer Based on Bipolar-Resonant LC Converter. *Electronics* **2021**, *10*, 293. [CrossRef]

31. Pham, V.L.; Duong, V.T.; Choi, W.J. A Low Cost and Fast Cell-to-Cell Balancing Circuit for Lithium-Ion Battery Strings. *Electronics* **2020**, *9*, 248. [CrossRef]

32. Van, C.N.; Vinh, T.N.; Ngo, M.D.; Ahn, S.J. Optimal SoC Balancing Control for Lithium-Ion Battery Cells Connected in Series. *Energies* **2021**, *14*, 2875. [CrossRef]

33. Venet, P.; Redondo-Iglesias, E. Batteries and Supercapacitors Aging. *Batteries* **2020**, *6*, 18. [CrossRef]

34. Xiong, R.; Li, L.; Tian, J. Towards a smarter battery management system: A critical review on battery state of health monitoring methods. *J. Power Sour.* **2018**, *405*, 18–29. [CrossRef]

35. Wei, Z.; Zhao, D.; He, H.; Cao, W.; Dong, G. A noise-tolerant model parameterization method for lithium-ion battery management system. *Appl. Energy* **2020**, *268*, 114932. [CrossRef]

36. Kang, J.; Yan, F.; Zhang, P.; Du, C. Comparison of comprehensive properties of Ni-MH (nickel-metal hydride) and Li-ion(lithium-ion) batteries in terms of energy efficiency. *Energy* **2014**, *70*, 618–625. [CrossRef]

37. Eddahech, A.; Briat, O.; Vinassa, J.M. Performance comparison of four lithium-ion battery technologies under calendar aging. *Energy* **2015**, *84*, 542–550. [CrossRef]

38. Ahmadi, L.; Fowler, M.; Young, S.; Fraser, R.; Gaffney, B.; Walker, S. Energy efficiency of Li-ion battery packs re-used in stationary power applications. *Sustain. Energy Technol. Assess.* **2014**, *8*, 9–17. [CrossRef]

39. Meister, P.; Jia, H.; Li, J.; Kloepsch, R.; Winter, M.; Placke, T. Best Practice: Performance and Cost Evaluation of Lithium Ion Battery Active Materials with Special Emphasis on Energy Efficiency. *Chem. Mater.* **2016**, *28*, 7203–7217. [CrossRef]

40. How, D.N.; Hannan, M.A.; Lipu, M.S.H.; Sahari, K.S.; Ker, P.J.; Muttaqi, K.M. State-of-Charge Estimation of Li-Ion Battery in Electric Vehicles: A Deep Neural Network Approach. *IEEE Trans. Ind. Appl.* **2020**, *56*, 5565–5574. [CrossRef]

41. Zhi, L.; Peng, Z.; Zhifu, W.; Qiang, S.; Yinan, R. State of Charge Estimation for Li-ion Battery Based on Extended Kalman Filter. *Energy Procedia* **2017**, *105*, 3515–3520. [CrossRef]

42. Bian, X.; Wei, Z.; He, J.; Yan, F.; Liu, L. A two-step parameter optimization method for low-order model-based state of charge estimation. *IEEE Trans. Transp. Electrif.* **2020**, *7*, 399–409. [CrossRef]

43. Baccouche, I.; Jemmali, S.; Manai, B.; Omar, N.; Essoukri Ben Amara, N. Improved OCV model of a Li-ion NMC battery for online SOC estimation using the extended Kalman filter. *Energies* **2017**, *10*, 764. [CrossRef]

44. Chen, Z.; Yang, L.; Zhao, X.; Wang, Y.; He, Z. Online state of charge estimation of Li-ion battery based on an improved unscented Kalman filter approach. *Appl. Math. Modell.* **2019**, *70*, 532–544. [CrossRef]

45. Tian, Y.; Lai, R.; Li, X.; Xiang, L.; Tian, J. A combined method for state-of-charge estimation for lithium-ion batteries using a long short-term memory network and an adaptive cubature Kalman filter. *Appl. Energy* **2020**, 337–339. [CrossRef]

46. Wei, Z.; He, H.; Pou, J.; Tsui, K.L.; Quan, Z.; Li, Y. Signal-Disturbance Interfacing Elimination for Unbiased Model Parameter Identification of Lithium-Ion Battery. *IEEE Trans. Ind. Inform.* **2020**, *17*, 5887–5897. [CrossRef]

47. Kamrueng, C.; Kittiratsatcha, S.; Polmai, S. Fast Approach of Open Circuit Voltage Estimation for Li-ion Battery Based on OCV Error Compensation. In Proceedings of the 2020 23rd International Conference on Electrical Machines and Systems (ICEMS), IEEE, Hamamatsu, Japan, 24–27 November 2020; pp. 1583–1586.

48. Tian, J.; Xiong, R.; Shen, W.; Sun, F. Electrode ageing estimation and open circuit voltage reconstruction for lithium ion batteries. *Energy Storage Mater.* **2021**, *37*, 283–295. [CrossRef]

49. Qaisar, S.M. Event-Driven Approach for an Efficient Coulomb Counting Based Li-Ion Battery State of Charge Estimation. *Procedia Comput. Sci.* **2020**, *168*, 202–209. [CrossRef]

50. Zhang, S.; Guo, X.; Dou, X.; Zhang, X. A data-driven coulomb counting method for state of charge calibration and estimation of lithium-ion battery. *Sustain. Energy Technol. Assess.* **2020**, *40*, 100752.

51. Ouyang, T.; Xu, P.; Lu, J.; Hu, X.; Liu, B.; Chen, N. Co-estimation of state-of-charge and state-of-health for power batteries based on multi-thread dynamic optimization method. *IEEE Trans. Ind. Electron.* **2021**. [CrossRef]

52. Swarup, S.; Tan, S.X.D.; Liu, Z.; Wang, H.; Hao, Z.; Shi, G. Battery state of charge estimation using adaptive subspace identification method. In Proceedings of the 2011 9th IEEE International Conference on ASIC, IEEE, Xiamen, China, 25–28 October 2011; pp. 91–94.

53. Yang, K.; Tang, Y.; Zhang, Z. Parameter Identification and State-of-Charge Estimation for Lithium-Ion Batteries Using Separated Time Scales and Extended Kalman Filter. *Energies* **2021**, *14*, 1054. [CrossRef]

54. Jungsoo, K.; Jungwook, Y. Estimation of Li-ion Battery State of Health based on Multilayer Perceptron: As an EV Application. *IFAC-Pap. Line* **2018**, *51*, 392–397.

55. Che, Y.; Liu, Y.; Cheng, Z.; Zhang, J. SOC and SOH Identification Method of Li-ion Battery Based on SWPSO-DRNN. *IEEE Journal of Emerging and Selected Topics in Power Electronics* **2020**, *9*, 4050–4061. [CrossRef]

56. Shuxiang, S.; Chen, F.; Haiying, X. Lithium-Ion Battery SOH Estimation Based on XG Boost Algorithm with Accuracy Correction. *Energies* **2020**, *13*, 812.

57. Bian, X.; Wei, Z.; He, J.; Yan, F.; Liu, L. A Novel Model-based Voltage Construction Method for Robust State-of-health Estimation of Lithium-ion Batteries. *IEEE Trans. Ind. Electron.* **2020**, *1*. [CrossRef]

58. He, J.; Wei, Z.; Bian, X.; Yan, F. State-of-Health Estimation of Lithium-Ion Batteries Using Incremental Capacity Analysis Based on Voltage–Capacity Model. *IEEE Trans. Transp. Electrif.* **2020**, *6*, 417–426. [CrossRef]

59. Zhang, S.; Guo, X.; Dou, X.; Zhang, X. A Rapid Online Calculation Method for State of Health of Lithium-Ion Battery based on Coulomb Counting Method and Differential Voltage Analysis. *J. Power Sources* **2020**, *479*, 228740. [CrossRef]

60. Li, N.; Gao, F.; Hao, T.; Ma, Z.; Zhang, C. SOH Balancing Control Method for the MMC Battery Energy Storage System. *IEEE Trans. Ind. Electron.* **2018**, *65*, 6581–6591. [CrossRef]

61. Yang, Y.; Wen, J.; Shi, Y.; Zeng, J. State of Health Prediction of Lithium-Ion Batteries Based on the Discharge Voltage and Temperature. *Electronics* **2020**, *10*, 1497. [CrossRef]

62. Lee, J.; Kim, J.; Ryu, K.; Won, C. An Energy Storage System's Operational Management and Control Method Considering a Battery System. *Electronics* **2020**, *9*, 356. [CrossRef]

63. Huang, W.X.; Abu Qahouq, J.A. An Online Battery Impedance Measurement Method Using DC-DC Power Converter Control. *IEEE Trans. Ind. Electron.* **2014**, *61*, 5987–5995. [CrossRef]

64. Kim, J. A Study on SOH Estimation Method for Lithium Ion Battery Using Charging Time. Master's Thesis, Korea University, Seoul, Korea, 2015; pp. 1–94.

65. Yang, R.; Xiong, R.; Shen, W.; Lin, X. Extreme Learning Machine Based Thermal Model for Lithium-ion Batteries of Electric Vehicles under External Short Circuit. *Engineering* **2020**, *7*, 395–405. [CrossRef]

66. Tian, J.; Xiong, R.; Shen, W. State-of-Health estimation based on differential temperature for lithium ion batteries. *IEEE Trans. Power Electron.* **2020**, *35*, 10363–10373. [CrossRef]

67. Lee, J.H.; Kim, H.S.; Lee, I.S. Multilayer Neural Network-Based Battery Module SOH Diagnosis. *Int. J. Eng. Res. Technol.* **2020**, *13*, 316–319. [CrossRef]

68. Copper Development Association. *Market Evaluation for Energy Storage in the United States*; KEMA, Inc.: Burlington, MA, USA, 2012.

69. Andrea, D. *Battery Management Systems for Large Lithium-Ion Battery Packs*; Artech House: Norwood, MA, USA, 2010.

70. Shin, D.; Yoon, B.; Yoo, S. Compensation Method for Estimating the State of Charge of Li-Polymer Batteries Using Multiple Long Short-Term Memory Networks Based on the Extended Kalman Filter. *Energies* **2020**, *14*, 349. [CrossRef]

71. Meng, J.; Ricco, M.; Luo, G.; Swierczynski, M.; Stroe, D.I.; Stroe, A.I.; Teodorescu, R. An overview and comparison of online implementable soc estimation methods for lithium-ion battery. *IEEE Trans. Ind. Appl.* **2018**, *54*, 1583–1591. [CrossRef]

72. Movassagh, K.; Raihan, A.; Balasingam, B.; Pattipati, K. A Critical Look at Coulomb Counting Approach for State of Charge Estimation in Batteries. *Energies* **2021**, *14*, 4074. [CrossRef]

73. Lu, L.; Han, X.; Li, J.; Hua, J.; Ouyang, M. A review on the key issues for lithium-ion battery management in electric vehicles. *J. Power Sources* **2013**, *226*, 272–288. [CrossRef]

74. Topan, P.A.; Ramadan, M.N.; Fathoni, G.; Cahyadi, A.I.; Wahyunggoro, O. State of charge (SOC) and state of health (SOH) estimation on lithium polymer battery via Kalman filter. In Proceedings of the 2nd International Conference on Science and Technology-Computer (ICST), Yogyakarta, Indonesia, 27–28 October 2016; pp. 93–96.

75. Mo, B.; Yu, J.; Tang, D.; Liu, H. A remaining useful life prediction approach for lithium-ion batteries using Kalman filter and an improved particle filter. In Proceedings of the 2016 IEEE International Conference on Prognostics and Health Management (ICPHM), Ottawa, ON, Canada, 20–22 June 2016; pp. 1–5.

76. Pola, D.; Navarrete, H.F.; Orchard, M.E.; Rabie, R.S.; Cerda, M.A.; Olivares, B.E.; Silva, J.F.; Espinoza, P.A.; Perez, A. Particle-Filtering-Based Discharge Time Prognosis for Lithium-Ion Batteries With a Statistical Characterization of Use Profiles. *IEEE Trans. Reliab.* **2015**, *64*, 1–11. [CrossRef]
77. Zun, C.Y.; Park, S.U.; Mok, H.S. New Cell Balancing Charging System Research for Lithium-ion Batteries. *Energies* **2020**, *13*, 1393. [CrossRef]

Article

An Ultra-Low-Power CMOS Supercapacitor Storage Unit for Energy Harvesting Applications

Vasiliki Gogolou [1] [iD], **Konstantinos Kozalakis** [1] [iD], **Eftichios Koutroulis** [2] [iD], **Gregory Doumenis** [3] and **Stylianos Siskos** [1,*]

1 Electronics Lab, Department of Physics, Aristotle University of Thessaloniki, 54124 Thessaloniki, Greece; vgogolou@physics.auth.gr (V.G.); kkozalak@physics.auth.gr (K.K.)
2 School of Electrical & Computer Engineering, Technical University of Crete, 73100 Chania, Greece; efkout@electronics.tuc.gr
3 Department of Informatics and Telecommunications, University of Ioannina, 47150 Arta, Greece; greg@uoi.gr
* Correspondence: siskos@physics.auth.gr

Abstract: This work presents an ultra-low-power CMOS supercapacitor storage unit suitable for a plethora of low-power autonomous applications. The proposed unit exploits the unregulated voltage output of harvesting circuits (i.e., DC-DC converters) and redirects the power to the storage elements and the working loads. Being able to adapt to the input energy conditions and the connected loads' supply demands offers extended survival to the system with the self-startup operation and voltage regulation. A low-complexity control unit is implemented which is composed of power switches, comparators and logic gates and is able to supervise two supercapacitors, a small and a larger one, as well as a backup battery. Two separate power outputs are offered for external load connection which can be controlled by a separate unit (e.g., microcontroller). Furthermore, user-controlled parameters such as charging and discharging supercapacitor voltage thresholds, provide increased versatility to the system. The storage unit was designed and fabricated in a 0.18 um standard CMOS process and operates with ultra-low current consumption of 432 nA at 2.3 V. The experimental results validate the proper operation of the overall structure.

Keywords: energy harvesting; on-chip integration; power management; supercapacitor; storage unit

1. Introduction

With the emergence of the Internet of Things (IoT) concept, the number of interconnected devices is rapidly growing. An issue that arises is the power autonomy of the nodes. Often, the energy harvesting concept is adopted [1]. The main idea is that ambient energy is harnessed and converted to electrical energy in order to power up the connected electrical loads. The most used environmental sources are light, heat, RF energy and mechanical stresses, exploited by piezoelectric or triboelectric devices [2–7]. Considering that an autonomous system should be functional, even in periods of input energy absence, the integration of an energy storage unit is crucial.

The type of the comprised storage medium should be carefully considered. Batteries offer very high storage capacitance (high energy density) but low power density, elevated cost and limited charge/discharge cycles. On the other hand, supercapacitors have numerous benefits, such as high-power density and long lifetime, with low degradation between charging cycles, however, they present lower storage capacitance [8]. Hybrid energy storage solutions, which exploit the benefits of both types of storage devices, have been proposed [9]. The most common approach relies on a battery for long-term energy storage, combined with a supercapacitor element, connected to the power output. This way a storage scheme is created, which presents all the advantages of the battery and also high-power density for short periods of time. Such circuits find use in multiple applications, such as healthcare assistive tools [10], DC microgrids deployment [11] and electric

vehicles [12]. A similar approach employs a battery at the power output and makes use of a bidirectional voltage converter and a supercapacitor to increase the power density of the energy storage unit. This concept is often adopted in energy harvesting applications for autonomous nodes [13–15]. However, the above works are discrete and bulky solutions. Since today's world demands miniature implementations for portable devices, on-chip integration becomes imperative.

Based on the energy availability conditions (continuous or interrupted) the integration of a battery can be omitted. In the case of continuous energy flow, a battery-less scheme can be used. A relative work is a four-supercapacitor CMOS storage bank, which offers high energy utilization [16]. In case of interrupted energy flow, the supercapacitors are not able to provide long-term storage, and a battery should be used. However, the simultaneous integration of a supercapacitor, along with the necessary control circuit, besides increasing the output power density, can also significantly extend the life expectancy of the battery, minimizing its charge/discharge cycles. Such an approach is presented in [17] where the proposed unit utilizes additional switching voltage conversion circuits (i.e., charge pumps) for the battery charging and discharging operations, which offer high power conversion efficiency but present limited working power range and increase the volume of the system.

In this work, a novel ultra-low-power integrated storage unit is proposed, suitable for a plethora of energy harvesting autonomous applications (Figure 1). This design is an improved and more versatile version of previous work [18] and presents experimental results. It can be connected to the output of various energy harvesting circuit types (DC-DC converters, charge pumps, etc.) and transfer the harvested energy to the storage media, providing regulated voltage supply to the internal control units of the harvesting circuit and the output loads (e.g., low-power sensors).
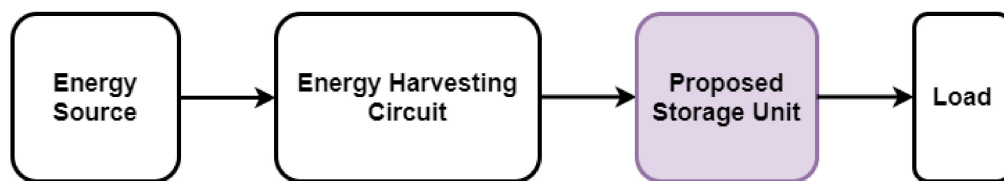
Figure 1. Block diagram of an energy harvesting system.

The proposed unit achieves minimization of the internal power consumption, deployment area and design complexity. The main storage element is a supercapacitor of small value, while a second larger supercapacitor can be used to provide energy to high-power modules. Depending on the energy availability conditions (continuous or interrupted), a backup battery can be used to avoid the energy starvation of the system during time periods of low input energy. Any type of battery can be used, depending on the use case application. Due to technology restrictions of the proposed unit, its maximum voltage must not exceed 3.6 V. For example, in Section 5.1, two 1.2 V Ni-MH AAA batteries are used to validate the unit's operation.

The proposed unit provides self-startup operation and sub-μW consumption, highly desired properties that contribute to high energy utilization and power autonomy of the applied harvesting system. Furthermore, it presents enhanced adaptability since it can be integrated into a wide range of energy harvesting systems, considering that the control parameters (supercapacitor thresholds, produced supply voltage) can be modified by the user. Moreover, significant versatility is offered, since external control, e.g., a microcontroller unit, can be added to the topology.

This paper is organized as follows. Section 2 presents the proposed supercapacitor storage unit and its operational principle. Section 3 describes the control logic of the unit. Sections 4 and 5 show the simulated and experimental results, respectively. Section 6 discusses the utilization of the storage unit in wireless sensor nodes (WSN) applications. Finally, Section 7 concludes this paper.

2. Proposed Topology and Operational Principle

The proposed storage unit is comprised of two supercapacitors, a small (SCsmall), a larger one (SCbig) and a backup battery (Figure 2). The small supercapacitor is mandatory since it is the main storage element that provides power to the control unit. The large supercapacitor and the battery elements are considered optional and their integration on the unit depends on the needs of each specific application.
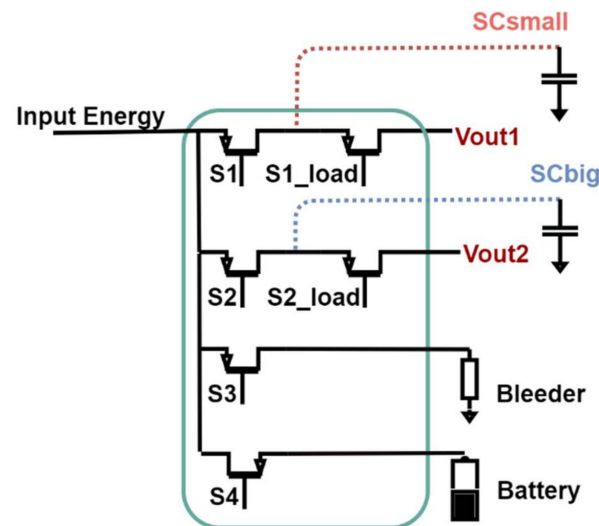

Figure 2. The topology of the proposed energy storage unit.

Specifically, SCsmall provides a regulated supply voltage with a 50 mV voltage ripple for the internal control circuits of the energy harvesting system and power output for connection of external loads (e.g., sensors, processing units, low-range RF modules). The 50 mV voltage ripple is selected to minimize the switching frequency — hence the power consumption — and at the same time, it is considered safe for most load types. SCbig offers an extra unregulated output to the system, for more power demanding loads (e.g., wide-range RF modules, GSM modules), since many off-the-shelf components operate in a wide supply voltage range. The voltage window of this output can be adjusted by the user regarding the specifications of the connected module, with a minimum window of 200 mV. To ensure the extended survival of systems that their continuous operation is critical a backup battery can be connected to the unit. Finally, a bleeder resistor is used to protect the system from excess input energy, which is activated whenever the supercapacitor(s) are fully charged.

The flowchart depicted in Figure 3 summarizes the operational principle of the unit which is described as follows:

Self-Startup: PMOS switches are used to control the charging of the supercapacitors (i.e., switches S1, S2 in Figure 2). Initially, all control signals are at zero potential since the control unit is inactive. Thus, the PMOS switches are ON, and energy is provided to both supercapacitors. As soon as the small supercapacitor voltage (VSCsmall) reaches a sufficient level, the control unit is activated, monitoring the charging of the supercapacitors.

Charging: Initially, the SCsmall supercapacitor starts to charge through switch S1. Meanwhile, SCbig remains disconnected as the main objective is the power-up of the system. The charging process continues until VSCsmall reaches a maximum threshold (Vmax1). At this state, SCbig begins to charge. The charging of SCbig continues until its voltage level reaches a high threshold value (Vmax2), but only if VSCsmall remains within a small voltage window (i.e., $\Delta V_1 = Vmax1 - Vmin1 = 50$ mV). This way, SCsmall has always charging priority and supply voltage regulation is achieved for the system internal control unit.

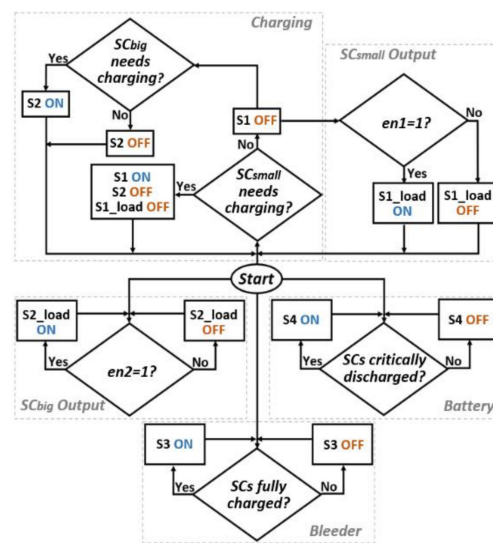**Figure 3.** A flowchart of the proposed system operational logic.

Loads Connection: Two power outputs are available for load connection. A light load can be connected to SCsmall through the switch S1_load. Granted that VSCsmall is above Vmin1, the load supply can be enabled. Power demanding modules can be connected to SCbig. If VSCbig is higher than a lower threshold (Vmin2), the load can be supplied through switch S2_load.

Preservation: In the worst-case scenario, where input energy is not available, a backup battery can provide energy to SCsmall in order to sustain the operation of the system. If needed, the unit can be configured to provide energy to SCbig as well. The battery support is triggered if the supercapacitor's voltage level drops below the predefined thresholds, Vlow1 and Vlow2, respectively. These thresholds are set lower than Vmin1 and Vmin2, to avoid unnecessary battery activation and the external loads enabling during energy starvation periods. The charging priority feature is also applied here.

Protection: When the supercapacitors are fully charged, a bleeder resistor is connected to the input in order to dump any excess input energy and protect the system from overvoltage stresses.

External control: The charging and discharging thresholds for the supercapacitors are externally selected using resistor dividers. Large value resistor networks should be utilized, for ultra-low power consumption. Alternatively, digital-to-analog converters can be used along with a microcontroller unit (MCU), to dynamically change the thresholds, or even deactivate unnecessary modes by monitoring the available energy and voltage level at the input. Finally, the load outputs can be enabled or disabled by the MCU, through the en1 and en2 pins.

The selection of the supercapacitors values should be based on the needs of each specific application and be decided according to the available input energy and the load's demands. For instance, if long starvation periods are expected, large supercapacitors should be used, which may increase the required start-up time but will secure the extended survival of the system. Generally, demanding loads that can draw large instant currents during activation (e.g., wide-range RF transmitters) should be connected to SCbig. For SCsmall, a relatively low capacitance is recommended, as it provides fast startup to the system. Finally, for ultra-low-power systems the leakage current of the selected supercapacitors should be considered.

In the proposed design the maximum input current is set to 500 mA and the maximum output current is set to 100 mA. The working voltage thresholds of both supercapacitors can be set anywhere between 1.2 V and 3.6 V.

3. Implementation of the Control Unit

The control circuit of the proposed storage unit, composed of comparators, logic gates and power switches, is depicted in Figure 4. The power switches are implemented with 10,000 um/0.30 um 3.3 V PMOS transistors, which present low on-resistance and sufficient response time. The power switch's length is set to a minimum in order to present a small layout area. A bulk regulation circuit is added on S1 and S2 switches to prevent supercapacitors from discharging towards the input. To supervise the voltage levels of the storage media, low-power comparators are designed, utilizing resistive MOSFETs and nA bias current (Figure 4). The topology of the used comparator [19] creates a hysteresis window (ΔV) which can be implemented by adjusting the cross-coupled (M5, M6) and diode-connected (M3, M4) transistors aspect ratio as follows:

$$\Delta V = \pm \frac{1 - \sqrt{(W/L)_{5,6}/(W/L)_{3,4}}}{\sqrt{1 + (W/L)_{5,6}/(W/L)_{3,4}}} V_{ov_{diffpair}} \tag{1}$$

where W is the width of each transistor, L is the length of each transistor and $V_{ovdiffpair}$ is the overdrive voltage of the differential pair of the comparator. Thus, by properly selecting the values of the transistors' widths, the desired hysteresis window can be achieved. Specifically:
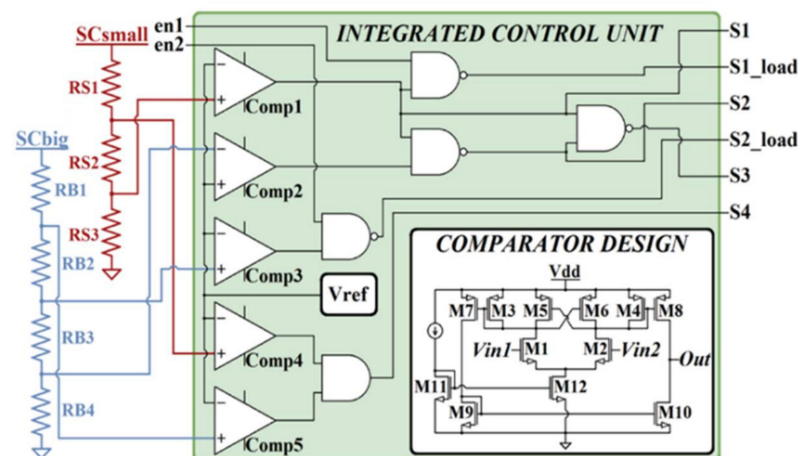
Figure 4. Control logic and comparator design.

For SCsmall, a comparator with a 50 mV hysteresis window (comp1) is designed. It controls the charging and discharging mode of the supercapacitor through switches S1 and S1_load respectively. This small hysteresis window provides regulated supply voltage for the internal circuits of the harvesting system, with low voltage ripple as well as protection from excessive switching. Additionally, pin en1 is available for external control of the load connection via the S1_load switch (Vout1).

The SCbig charging mode is also supervised by a 50 mV hysteresis window comparator (comp2). Additionally, a 200 mV hysteresis window comparator (comp3) controls the SCbig discharging, via the output switch, S2_load. Since two different comparators are used for the charging and discharging mode of SCbig, the output voltage window (Vout2) can be adjusted to the load needs, with a minimum ΔV_2 of 200 mV. For a 5 F capacitor and 100 mA load current the frequency of the voltage ripple is extremely low (<1 mHz). This supply voltage ripple is acceptable for many off-the-shelf components (e.g., MSP430i204x MCU, etc.). As external control is offered (pins en1 and en2), the supply of the loads can be enabled or disabled as needed. Otherwise, the enable pins can be tied to low (inactive) or high (active) potential.

Two additional comparators (comp4 and comp5), monitor VSCsmall and VSCbig voltage levels and activate the battery support if one or both supercapacitors are critically

discharged. The S4 switch closes, and the battery provides energy to the supercapacitor in need. The bleeder mode (switch S3) is triggered only in case that both supercapacitors are fully charged.

The combination of the comparators signals along with the external enable signals, is implemented with digital logic circuits (NAND, AND, NOT gates) which are also custom-designed with resistive transistors, to further decrease the power consumption of the control unit.

The voltage thresholds are determined by external voltage divider networks (Figure 4), with multiple voltage tapping points. A fraction of VSCsmall or VSCbig is compared with a stable voltage reference. Since bandgap voltage references are too power-demanding for low-power applications, a 1.08 V voltage reference circuit was implemented, which is based on the circuit presented in [20], with pW power consumption.

4. Simulation Results

In order to verify the operation of the proposed storage unit, simulations were carried out via the Cadence Virtuoso suite. The input voltage of the storage unit was set to 2.4 V, emulating the output voltage of a harvesting circuit, i.e., a step-up DC-DC converter. The charging and discharging voltage thresholds of the supercapacitors were set as follows:

$$
\begin{array}{lll}
V_{max1} = 2.3 \text{ V} & V_{min1} = 2.25 \text{ V} & V_{low1} = 2.15 \text{ V} \\
V_{max2} = 2.3 \text{ V} & V_{min2} = 1.8 \text{ V} & V_{low2} = 1.6 \text{ V}
\end{array}
\tag{2}
$$

The voltage levels in (2) were implemented with voltage dividers, each with a total resistance of 82 MΩ. An AVX BZ015A104Z_B Bestcap supercapacitor of 100 mF was selected as SCsmall and an SCMT22C505PRBA0 supercapacitor of 5 F as SCbig. To extract realistic results, ESR and leakage resistors were added to the schematic models, according to the supercapacitors datasheets. Figure 5 shows the charging mode when both supercapacitors are fully empty. At startup, a 350 mV early-state charging phase is observed for SCbig, due to the insufficient power supply of the control unit. The duration of this phenomenon depends on the available input power as well as the selected supercapacitors values and their leakage current. For the components under consideration, the charging of SCbig stops after approximately 100 ms.
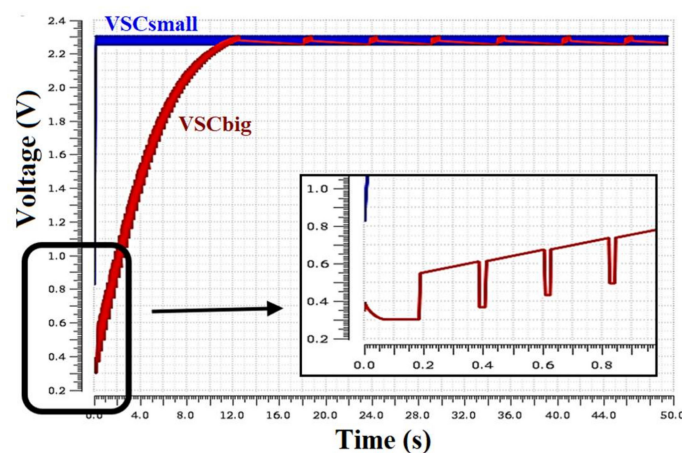

Figure 5. Supercapacitors charging mode and startup (inset).

The supply of the output loads is depicted in Figure 6a,b. A 100 Ω resistor is connected to Vout1 and a 22 Ω resistor to Vout2, drawing approximately 20 mA and 100 mA, respectively. As shown, the loads are connected when the voltage levels of the supercapacitors exceed the minimum thresholds. Figure 7a presents the activation of the bleeder resistor. Figure 7b shows the battery support mode. The battery input voltage is set to 2.5 V, providing energy to the critically discharged supercapacitors, with the defined charging

priority. The SCsmall is recharged to the higher desired voltage (i.e., 2.3 V) to provide proper operation to the internal control circuits, while SCbig voltage is maintained to the minimum threshold (i.e., 1.6 V) to avoid unnecessary usage of the backup battery.
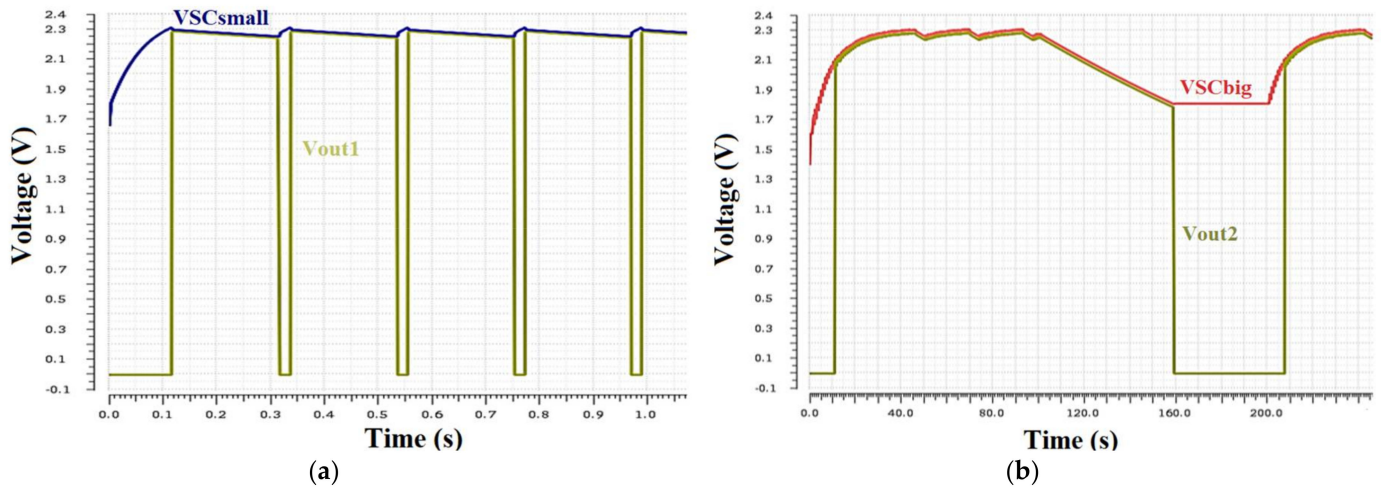

Figure 6. Connection of the external loads according to the predefined voltage thresholds of the supercapacitors. The output loads are disconnected in low-input energy conditions to preserve the operation of the system. (**a**) SCsmall voltage level and Vout1 load output. (**b**) SCbig voltage and Vout2 load output.
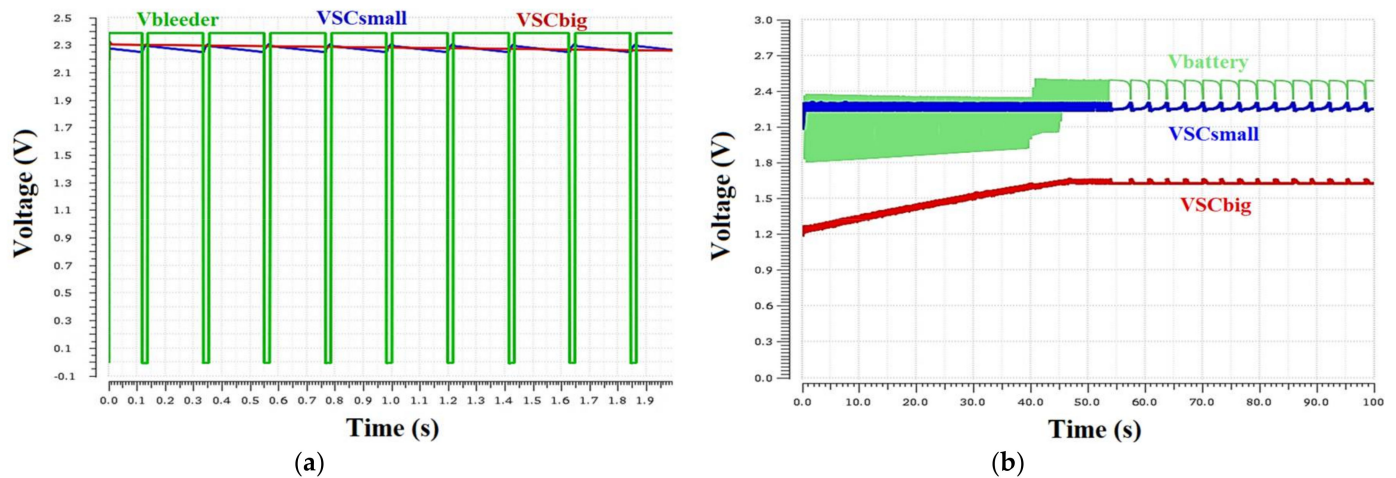
Figure 7. (**a**) Bleeder mode activation. The bleeder mode is activated only when both supercapacitors are fully charged. (**b**) Battery energy support. Initially, the battery charges both supercapacitors. SCbig charging stops when its voltage reaches the lower voltage threshold (1.6 V). SCsmall is charged to its high threshold (2.3 V).

The simulated total current consumption of the storage unit is 374 nA at 2.3 V. The voltage dividers of the comparators consume 56 nA (28 nA each) and the integrated control circuit draws 318 nA.

5. Experimental Results

The proposed self-adaptive storage scheme was implemented in a 0.18 um standard CMOS process. The physical design and the chip die are shown in Figure 8. The control unit layout occupies a low die area of 125 um × 50 um.
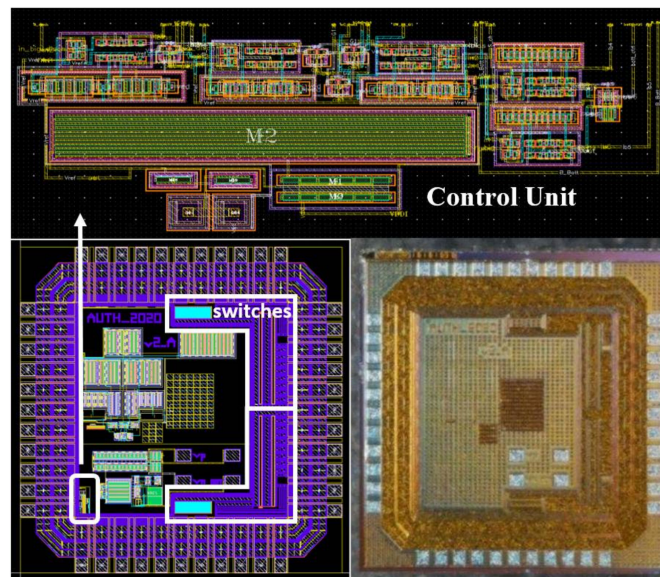
Figure 8. Physical design of the unit and the fabricated die.

5.1. Laboratory Measurements

To test the fabricated design, laboratory measurements were carried out using a digital oscilloscope (RIGOL DS1052E), as depicted in Figures 9–11. Voltage dividers with a total resistance of 82 MΩ were utilized for the thresholds of the comparators, according to Equation (2). Additionally, the AVX supercapacitors mentioned in Section 4 were used. A voltage source unit provides 2.4 V to the storage scheme input.

Figure 9 demonstrates the supercapacitors charging mode. Initially, SCsmall begins to charge and only when it is fully charged at the voltage of 2.3 V determined from the thresholds of the comparators, SCbig is connected at the input. As shown, the early-state charging of SCbig stops at about 50 mV, lower than the simulation result, and the overall charging duration is longer. These phenomena are due to the charging path resistance (i.e., chip pins and breadboard PCB resistance), which reduces the charging current. The peak current drawn is 2.1 A in the simulation, while its experimentally measured value is 0.45 A.
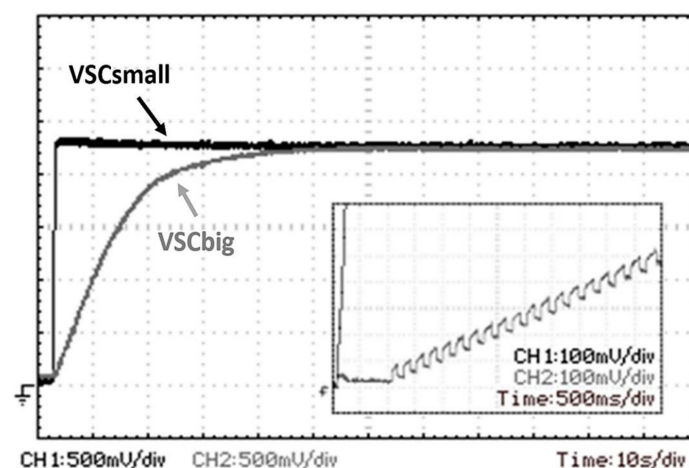
Figure 9. Oscilloscope view of SCsmall (CH1) and SCbig (CH2) voltage signals during charging and startup (inset), following the predefined charging priority feature. The SCbig supercapacitor is connected to the input only when SCsmall is fully charged at 2.3 V.
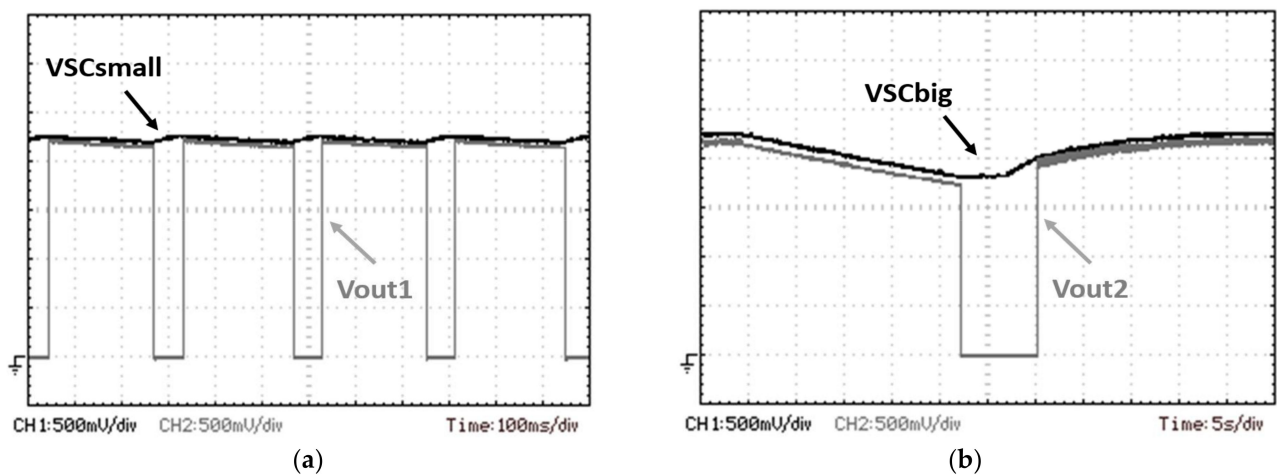
Figure 10. Oscilloscope view of (**a**) SCsmall voltage (CH1) and Vout1 (CH2) load output. (**b**) SCbig voltage (CH1) and Vout2 (CH2) load output. The output loads are disconnected in low-input energy conditions to preserve the operation of the system.
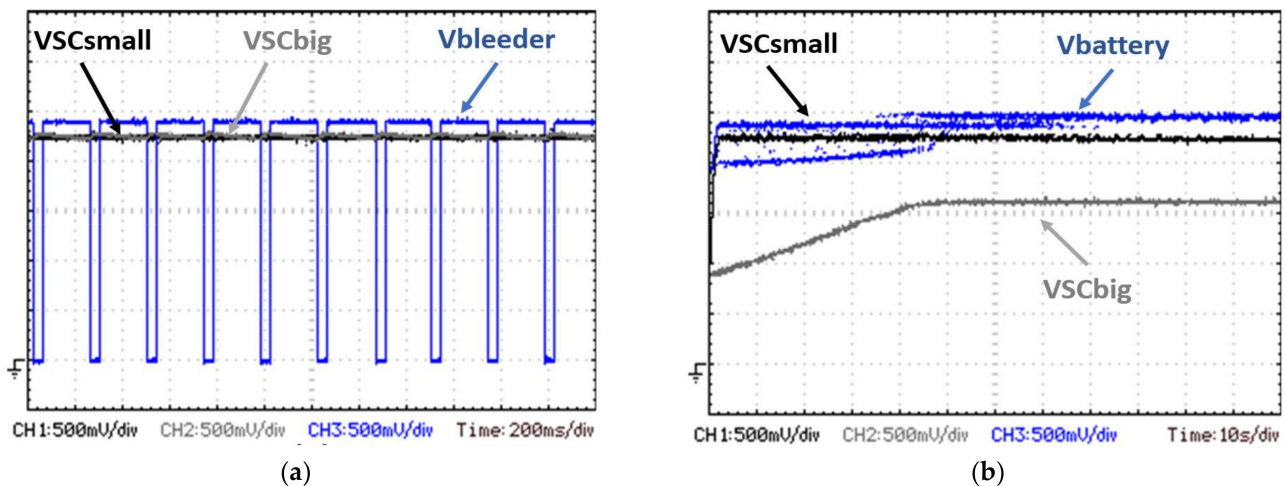

Figure 11. (**a**) SCsmall voltage (CH1), SCbig voltage (CH2) and bleeder output (CH3) during bleeder mode activation. (**b**) SCsmall voltage (CH1), SCbig voltage (CH2) and battery input (CH3) during battery energy support.

The load's connection modes are depicted in Figure 10a,b. A 100 Ω resistor is connected to Vout1 and a 22 Ω resistor to Vout2, similarly to the simulation setup. The loads draw energy from the supercapacitors, as long as the voltage levels do not fall below the predetermined minimum thresholds. Figure 11a presents the bleeder activation, drawing the excess energy. Figure 11b curves are obtained without input power supply. The supercapacitors are discharged, and two 1.2 V Ni-MH AAA batteries, connected in series (measured at 2.5 V), provide power to the system.

The measured current consumption of the integrated control unit is 376 nA at 2.3 V. Combined with the two 82 MΩ voltage dividers consumption, the total current consumption of the proposed unit is 432 nA at 2.3 V.

In Table 1, this work is compared with other state-of-the-art implementations. As shown, the proposed design offers many advantages such as low-complexity, small size integrated solution, ultra-low-power consumption and wide voltage and current range. Thus, this design is suitable for a wide variety of autonomous energy harvesting applications.

Table 1. State-of-the-art storage units implementations.

Ref No.	Target Application	Topology	Technology/Area	Voltage Converters/Inductors/Super capacitors/Battery	Voltage Range/Maximum Current	Power Consumption
[10]	Electric powered wheelchair	Battery, voltage converter, supercapacitor	Discrete	2/3/Array/Yes	60 V/100 A	mW [1]
[11]	DC Microgrid	Battery, voltage converter, supercapacitor	Discrete	1/2/Array/Yes	50 V/3 A	n/a
[13]	Energy harvesting, wireless sensor node	Supercapacitor, bidirectional converter, battery	Discrete	1/1/1/Yes	7–12 V/1.25 A	mW [1]
[14]	Energy harvesting, wireless sensor node	Supercapacitor, bidirectional converter, battery	Discrete	1/1/1/Yes	3.3 V/1.51 A	mW [1]
[15]	Energy harvesting, wireless sensor node	Battery, voltage converter, supercapacitor	Discrete	1/2/1/Yes	3.3 V/151 mA	uW [1]
[16]	Energy harvesting, wireless sensor node	Four supercapacitor reconfigurable power bank	0.35 um/n/a	0/0/4/No	2.6–5.5 V/50 mA	185 uW
[17]	Energy harvesting, wireless sensor node	Supercapacitor (main), battery and converter (secondary)	65 nm/ 0.48 mm^2	2/0/1/Yes	0.45 V/300 mA	uW [1]
This work	Energy harvesting, wireless sensor node	Up to two supercapacitors, optional battery	0.18 um/ 0.19 mm^2	0/0/2/Optional	1.2V–3.6 V/100 mA	0.99 uW

[1] Actual value not available.

5.2. Energy Harvesting

The storage unit was also tested during the energy harvesting operation. A BQ25504 energy harvesting IC combined with an 80 mm × 72 mm PV cell were utilized, harnessing energy at office lighting conditions (approximately 600 Lux of light intensity). The measurement setup is depicted in Figure 12. As this is a low power demanding use case scenario, the values of SCsmall and SCbig were set at 1 mF and 4.4 mF (two 2.2 mF capacitors connected in parallel) respectively.

Figure 13 presents the charging phase of the storage unit, with zero initial stored energy in the two supercapacitors. Since the available current is about 100 uA, the charging of the small supercapacitor requires about 30 s.

As stated, the supercapacitor's values should be properly selected, according to the power supply requirements of the target system. For this test case, smaller capacitors can reduce the charging time duration, at the expense of extended energy autonomy or connection of demanding external loads.
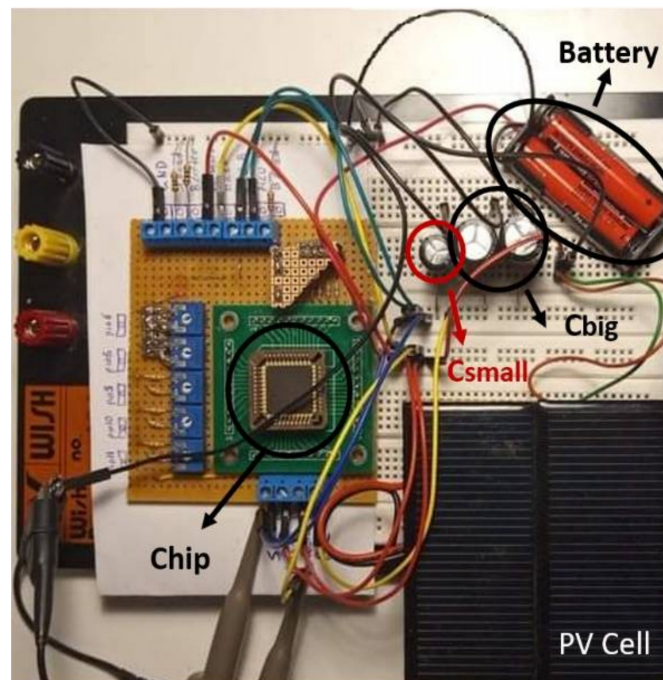
Figure 12. Experimental setup for testing the storage unit in indoor light energy harvesting conditions.
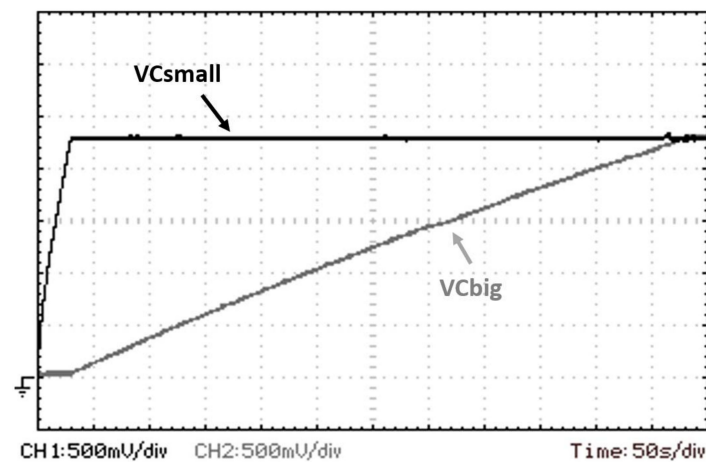

Figure 13. SCsmall (CH1) and SCbig (CH2) charging via BQ25504.

The proposed unit was also tested with a piezoelectric transducer providing power at the input. Figure 14 depicts the measurement setup. A V25W PZT transducer from MIDE is used to convert the vibrations to electrical energy and a vibrating speaker is used to trigger the piezoelectric transducer. A mass of 1.9 g. is fixed on the tip of the transducer, to further increase the power offered to the storage unit. A rectifier comprised of four Schottky diodes is connected between the output of the PZT element and the proposed storage unit. The vibrations frequency is set at 25 Hz and the open circuit peak-to-peak voltage is measured at 20 V. The observed mechanical displacement of the tip of the transducer was observed at 1 cm peak-to-peak. The values of SCsmall and SCbig were set at 1 mF and 4.4 mF respectively, and also, loads of 100 Ω are connected at the supercapacitors outputs. Finally, Figure 15 presents the charging phase of the two supercapacitors.
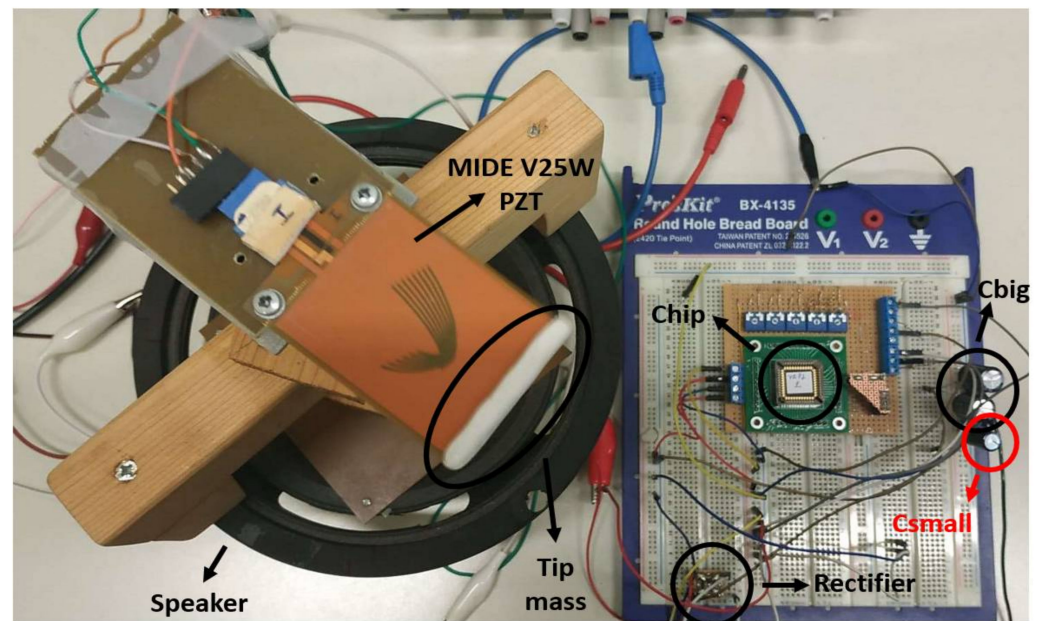
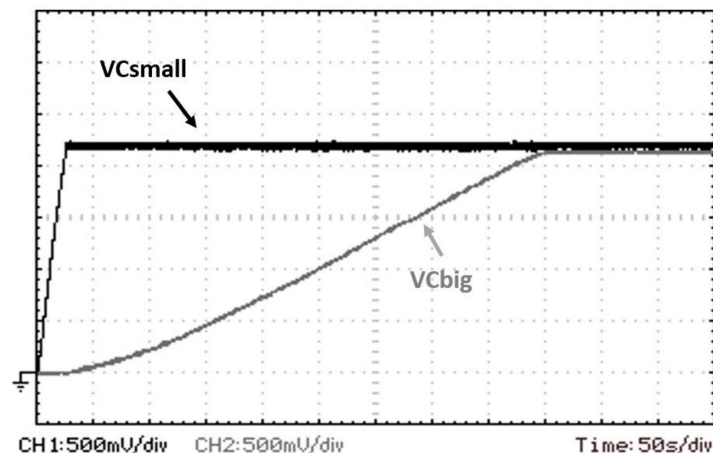**Figure 14.** Experimental setup for testing the storage unit with mechanical vibrations harvesting.

Figure 15. SCsmall (CH1) and SCbig (CH2) charging phase from the piezoelectric transducer.

6. Future Work and Discussion

The proposed storage unit is suitable for energy-harvesting-based, wireless sensor node (WSN) applications. The unit can autonomously supervise the charging and discharging of two supercapacitors (SCsmall, SCbig) and a backup battery, exploiting the energy provided by a harvester module. It can be combined with any type of energy harvesting module, such as photovoltaic, triboelectric, piezoelectric, or thermoelectric micro/nano-generators. Depending on the used harvester, a step-up/down converter and/or an AC-DC rectifier might be required (e.g., BQ25504 in case of the small photovoltaic panel or thermoelectric harvester). The proposed storage unit provides two separate power outputs. The SCsmall output, which provides a regulated output voltage (50 mV ripple) has the highest charging priority. Thus, it is considered as the main power output of the unit and should be used for the primary system circuits. Additionally, the SCbig output, provides an unregulated output voltage, however within an adjustable voltage window, with a minimum ΔV of 200 mV. This output has low charging priority and should be used for the secondary circuits of the system. This way extended operation is achieved for the primary system circuits, and additionally, the idle consumption of the secondary ones is eliminated. For embedding an RF transceiver module, an MCU, as well as the required sensors, and in case that real-time acquiring of the sensor data is not mandatory,

the SCsmall output can be used for the MCU supply and the sensors supply (for local data logging) and the SCbig output can be used for the power demanding RF transceiver module (so the transmission of the data will take place during energy-rich periods of time).

In the case of continuous energy availability (e.g., continuous vibrations), a battery is not required and can be omitted. However, to ensure undisrupted operation a backup non-rechargeable battery can be added. For ultra-low-power WSN systems and sparse energy starvation periods, a multiyear duration is expected from a coin-size battery cell (e.g., cr2032 3V 230 mah). In case of discontinuous energy availability conditions and for a scenario that the undisrupted operation of the supported system is crucial, the use of a battery is mandatory. Depending on the use-case application and the power requirements, the use of a separate external battery charger module should also be considered. Finally, in systems embedding an MCU, the direct power supply of the MCU from the SCsmall is possible. This way the MCU supply has the highest priority and the longest possible power autonomy. A future work WSN approach is shown in Figure 16.
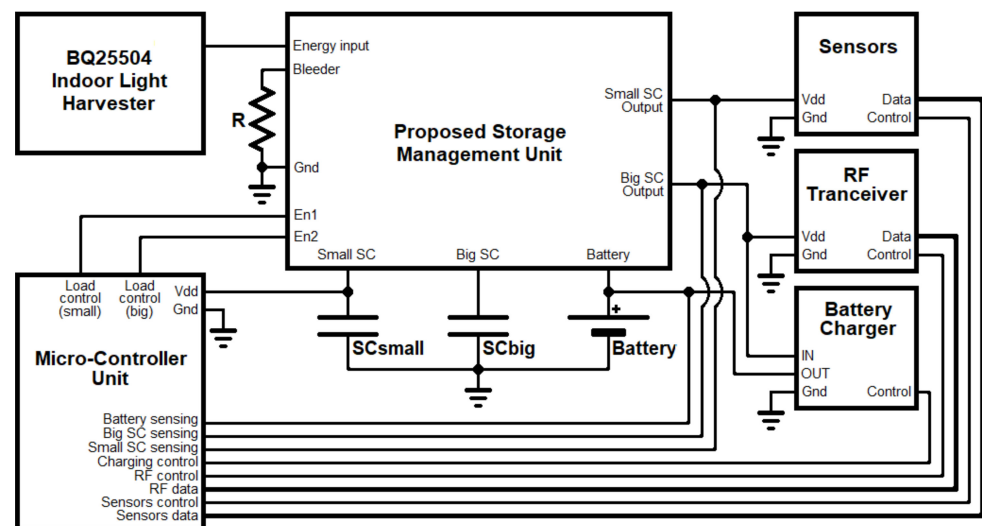

Figure 16. Future work WSN topology.

In the WSN shown in Figure 16, an indoor light harvester based on the BQ25504 IC was used. Additionally, an ultra-low-power MCU (e.g., MSP430FR5969 consuming 20 nA in deep sleep mode and 250 nA with calendar and timekeeping ON) is directly supplied by the small supercapacitor. Since continuous energy availability is not expected and an MCU is used, a rechargeable battery and a battery charger are added to the topology. The MCU is measuring the voltage levels of the two supercapacitors and the battery, in order to select a preferable power plan that matches the available energy. For example, only calendar and timekeeping during very-low energy levels, sensor reading during low energy levels, data transmission during high energy levels and battery charging during very-high-energy levels. The MCU is also controlling all the peripheral modules (sensors, RF transceiver and battery charger), as well as the load control signals (en1, en2) of the proposed storage unit.

7. Conclusions

In this work, an ultra-low-power supercapacitor-based storage unit with an integrated control scheme was presented, offering flexibility to the applied energy harvesting system. The ultra-low current consumption of only 432 nA at 2.3 V proves the proposed storage unit ideal for energy harvesting systems, even for cases of a few μW input power range. Furthermore, extra modes can be added to the topology with the usage of external control (e.g., an MCU), expanding the operational capabilities of the proposed unit. For instance, the control of an additional charging unit for the backup battery is a highly beneficial mode that will be added in future work.

References

1. Elahi, H.; Munir, K.; Eugeni, M.; Atek, S.; Gaudenzi, P. Energy Harvesting towards Self-Powered IoT Devices. *Energies* **2020**, *13*, 5528. [CrossRef]
2. Chen, I.-C.; Liang, C.-W.; Tsai, T.-H. A single-inductor dual-input dual-output DC–DC converter for photovoltaic and piezoelectric energy harvesting systems. *IEEE Trans. Circuits Syst. II Express Briefs* **2019**, *66*, 1763–1767. [CrossRef]
3. Charris, D.; Gomez, D.; Ortega, A.R.; Carmona, M.; Pardo, M. A Thermoelectric Energy Harvesting Scheme with Passive Cooling for Outdoor IoT Sensors. *Energies* **2020**, *13*, 2782. [CrossRef]
4. Sanislav, T.; Mois, G.D.; Zeadally, S.; Folea, S.C. Energy Harvesting Techniques for Internet of Things (IoT). *IEEE Access* **2021**, *9*, 39530–39549. [CrossRef]
5. Salauddin, M.; Halim, M.A.; Park, J.Y. A magnetic-spring-based, low-frequency vibration energy harvester comprising a dual halbach array. *Smart Mater. Struct.* **2016**, *25*, 095017. [CrossRef]
6. Toyabur, R.M.; Salauddin, M.; Park, J.Y. Design and experiment of piezoelectric multimodal energy harvester for low frequency vibration. *Ceram. Int.* **2017**, *43*, 675–681. [CrossRef]
7. Salauddin, M.; Toyabur, R.M.; Maharjan, P.; Rasel, M.S.; Cho, H.; Park, J.Y. Design and experimental analysis of a low-frequency resonant hybridized nanogenerator with a wide bandwidth and high output power density. *Nano Energy* **2019**, *66*, 104122. [CrossRef]
8. Prauzek, M.; Konecny, J.; Borova, M.; Janosova, K.; Hlavica, J.; Musilek, P. Energy harvesting sources storage devices and system topologies for environmental wireless sensor networks: A review. *Sensors* **2018**, *18*, 2446. [CrossRef] [PubMed]
9. Babu, T.S.; Vasudevan, K.R.; Ramachandaramurthy, V.K.; Sani, S.B.; Chemud, S.; Lajim, R.M. A comprehensive review of hybrid energy storage systems: Converter topologies control strategies and future prospects. *IEEE Access* **2020**, *8*, 148702–148721. [CrossRef]
10. Khan, M.A.; Zeb, K.; Sathishkumar, P.; Ali, M.U.; Uddin, W.; Hussain, S.; Ishfaq, M.; Khan, I.; Cho, H.-G.; Kim, H.-J. A Novel Supercapacitor/Lithium-Ion Hybrid Energy System with a Fuzzy Logic-Controlled Fast Charging and Intelligent Energy Management System. *Electronics* **2018**, *7*, 63. [CrossRef]
11. Ravada, B.R.; Tummuru, N.R.; Ande, B.N.L. Photovoltaic-Wind and Hybrid Energy Storage Integrated Multi-Source Converter Configuration for DC Microgrid Applications. *IEEE Trans. Sustain. Energy* **2021**, *12*, 83–91. [CrossRef]
12. Hussain, S.; Ali, M.U.; Park, G.-S.; Nengroo, S.H.; Khan, M.A.; Kim, H.-J. A Real-Time Bi-Adaptive Controller-Based Energy Management System for Battery–Supercapacitor Hybrid Electric Vehicles. *Energies* **2019**, *12*, 4662. [CrossRef]
13. Pellitteri, F.; Livreri, P.; Schirone, L.; Miceli, R. A hybrid storage system for wireless sensor nodes powered with energy harvesting. In Proceedings of the 2019 International Conference on Clean Electrical Power (ICCEP), Otronto, Italy, 2–4 July 2019; pp. 221–226.
14. Saggini, S.; Ongaro, F.; Galperti, G.; Mattavelli, P. Supercapacitor-based hybrid storage systems for energy harvesting in wireless sensor networks. In Proceedings of the 2010 Twenty-Fifth Annual IEEE Applied Power Electronics Conference and Exposition (APEC), Palm Springs, CA, USA, 21–25 February 2010; pp. 2281–2287.
15. Qi, N.; Yin, Y. Comprehensive optimized hybrid energy storage system for long-life solar-powered wireless sensor network nodes. *Appl. Energy* **2021**, *290*, 116780. [CrossRef]
16. Siskos, A.; Mahboubi, F.E.; Boitier, V.; Laopoulos, T.; Bafleur, M. A power management system using reconfigurable storage scheme for batteryless wireless sensor nodes. In Proceedings of the 2018 7th International Conference on Modern Circuits and Systems Technologies (MOCAST), Thessaloniki, Greece, 7–9 May 2018; pp. 1–4.
17. Li, J.; Seo, J.-S.; Kymissis, I.; Seok, M. Triple-mode hybrid-storage energy harvesting power management unit: Achieving high efficiency against harvesting and load power variabilities. *IEEE J. Solid-State Circuits* **2017**, *52*, 2550–2562. [CrossRef]
18. Gogolou, V.; Siskos, S.; Laopoulos, T. A reconfigurable storage unit for autonomously powered IoT nodes. In Proceedings of the 2019 Panhellenic Conference on Electronics & Telecommunications (PACET), Volos, Greece, 8–9 November 2019; pp. 1–4.
19. Amin, S.S.; Mercier, P.P. MISIMO: A multi-input single-inductor multi-output energy harvesting platform in 28-nm FDSOI for powering net-zero-energy systems. *IEEE J. Solid-State Circuits* **2018**, *53*, 3407–3419. [CrossRef]
20. Ji, Y.; Lee, J.; Kim, B.; Park, H.-J.; Sim, J.-Y. A 192-pW voltage reference generating bandgap–Vth with process and temperature dependence compensation. *IEEE J. Solid-State Circuits* **2019**, *54*, 3281–3291. [CrossRef]

MDPI